PhD Thesis

Backanalysis Methodology Based on Multiple Optimization Techniques for Geotechnical Problems

Author
Cristian de Santos

Advisors
Prof. Alberto Ledesma
Prof. Antonio Gens

Thesis Committee
Prof. Eduardo Alonso (Universitat Politècnica de Catalunya)
Prof. César Sagaseta Millán (Universidad de Cantabria)
Prof. Cristina Jommi (Delft University of Technology)

External Reviewers
Prof. Kenichi Soga (University of Cambridge)
Prof. Cristina Jommi (Delft University of Technology)

Universitat Politècnica de Catalunya - BarcelonaTECH
Department of Geotechnical Engineering and Geo-Sciences
Barcelona, 2015

Abstract

Nowadays, thanks to the increase of computers capability to solve huge and complex problems, and also thanks to the endless effort of the geotechnical community to define better and more sophisticated constitutive models, the challenge to predict and simulate soil behavior has been eased. However, due to the increase in that sophistication, the number of parameters that define the problem has also increased. Moreover, frequently, some of those parameters do not have a real geotechnical meaning as they just come from mathematical expressions, which makes them difficult to identify. As a consequence, more effort has to be placed on parameters identification in order to fully define the problem.

This thesis aims to provide a methodology to facilitate the identification of parameters of soil constitutive models by backanalysis. The best parameters are defined as those that minimize an objective function based on the differences between measurements and computed values. Different optimization techniques have been used in this study, from the most traditional ones, such as the gradient based methods, to the newest ones, such as adaptive genetic algorithms and hybrid methods. From this study, several recommendations have been put forward in order to take the most advantage of each type of optimization technique. Along with that, an extensive analysis has been carried out to determine the influence on soil parameters identification of what to measure, where to measure and when to measure in the context of tunneling. The Finite Element code Plaxis has been used as a tool for the direct analysis. A FORTRAN code has been developed to automate the entire backanalysis procedure. The Hardening Soil Model (HSM) has been adopted to simulate the soil behavior. Several soil parameters of the HSM implemented in Plaxis, such as E_{50}^{ref}, E_{ur}^{ref}, c and φ, have been identified for different geotechnical scenarios. First, a synthetic tunnel case study has been used to analyze all the different approaches that have been proposed in this thesis. Then, two complex real cases of a tunnel construction (Barcelona Metro Line 9) and a large excavation (Girona High-Speed Railway Station) have been presented to illustrate the potential of the methodology. Special focus on the influence of construction procedures and instruments error structure has been placed for the tunnel backanalysis, whereas in the station backanalysis, more effort has been devoted to the potential of the concept of adaptive design by backanalysis. Moreover, another real case, involving a less conventional geotechnical problem, such as Mars surface exploratory rovers, has been also presented to test the backanalysis methodology and the reliability of the Wong & Reece wheel-terrain model; widely adopted by the terramechanics community, but nonetheless, still not fully accepted when analyzing lightweight rovers as the ones that have been used in recent Mars exploratory missions.

Key words: Backanalysis, Parameters Identification, Gradient Based Methods, Adaptive Genetic Algorithms, Hybrid Methods, Plaxis, Tunnels, Excavations and Mars Surface Exploratory Rovers.

Resumen

Actualmente, gracias al aumento de la capacidad de los ordenadores para resolver problemas grandes y complejos, y gracias también al gran esfuerzo de la comunidad geotécnica de definir mejores y más sofisticados modelos constitutivos, se ha abordado el reto de predecir y simular el comportamiento del terreno. Sin embargo, debido al aumento de esa sofisticación, también ha aumentado el número de parámetros que definen el problema. Además, frecuentemente, muchos de esos parámetros no tienen un sentido geotécnico real dado que vienen directamente de expresiones puramente matemáticas, lo cual dificulta su identificación. Como consecuencia, es necesario un mayor esfuerzo en la identificación de los parámetros para poder definir apropiadamente el problema.

Esta tesis pretende proporcionar una metodología que facilite la identificación mediante el análisis inverso de los parámetros de modelos constitutivos del terreno. Los mejores parámetros se definen como aquellos que minimizan una función objetivo basada en la diferencia entre medidas y valores calculados. Diferentes técnicas de optimización han sido utilizadas en este estudio, desde las más tradicionales, como los métodos basados en el gradiente, hasta las más modernas, como los algoritmos genéticos adaptativos y los métodos híbridos. De este estudio, se han extraído varias recomendaciones para sacar el mayor provecho de cada una de las técnicas de optimización. Además, se ha llevado a cabo un análisis extensivo para determinar la influencia sobre qué medir, dónde medir y cuándo medir en el contexto de la excavación de un túnel. El código de Elementos Finitos Plaxis ha sido utilizado como herramienta de cálculo del problema directo. El desarrollo de un código FORTRAN ha sido necesario para automatizar todo el procedimiento de Análisis Inverso. El modelo constitutivo de *Hardening Soil* ha sido adoptado para simular el comportamiento del terreno. Varios parámetros del modelo constitutivo de *Hardening* implementado en Plaxis, como E_{50}^{ref}, E_{ur}^{ref}, c y φ, han sido identificados para diferentes escenarios geotécnicos. Primero, se ha utilizado un caso sintético de un túnel donde se han analizado todas las distintas técnicas que han sido propuestas en esta tesis. Después, dos casos reales complejos de una construcción de un túnel (Línea 9 del Metro de Barcelona) y una gran excavación (Estación de Girona del Tren de Alta Velocidad) se han presentado para ilustrar el potencial de la metodología. Un enfoque especial en la influencia del procedimiento constructivo y la estructura del error de las medidas se le ha dado al análisis inverso del túnel, mientras que en el análisis inverso de la estación el esfuerzo se ha centrado más en el concepto del diseño adaptativo mediante el análisis inverso. Además, otro caso real, algo menos convencional en términos geotécnicos, como es la exploración de la superficie de Marte mediante robots, ha sido presentado para examinar la metodología y la fiabilidad del modelo de interacción suelo-rueda de Wong y Reece; extensamente adoptado por la comunidad que trabajo en Terramecánica, pero aún no totalmente aceptada para robots ligeros como los que se han utilizado recientemente en las misiones de exploración de Marte.

Palabras clave: Análisis Inverso, Identificación de Parámetros, Métodos basados en el Gradiente, Algoritmos Genéticos Adaptativos, Métodos Híbridos, Plaxis, Túneles, Excavaciones y Robots de Exploración de la Superficie de Marte.

Acknowledgments

First and foremost, I would like to thank Professor Alberto Ledesma, one of my advisors, firstly, for encouraging me to take the passionate path of a PhD, and secondly and more important, for his guidance and endless support throughout this adventure that have made of geotechnics my passion. I also want to acknowledge Professor Antonio Gens, my other advisor, for his tireless commitment to my work.

A special note of appreciation to my family whose unconditional support and patience have provided me with a constant source of encouragement. I cannot remember how many times I told them that I was close to finish my thesis, but that day never seemed to arrive, until now. So, many thanks for everything, and I sincerely hope that you feel this thesis as yours, because without you this wouldn't have been possible.

Also a special appreciation to Dr Paul Bonnier, Plaxis Scientific Researcher, who did not hesitate to share or answer any question related to the internal functioning of the geotechnical software Plaxis. Thanks to Daniel Garolera for helping me to overcome any problem related to FORTRAN. Thanks to Maria Teresa Yubero and Infraestructures de la Generalitat de Catalunya S.A.U (Infraestructures.cat) for sharing with me the instruments data of the construction of the new Barcelona metro line 9. Thanks to everyone of the "Girona Station Team" who let me put my feet on the ground and see at firsthand how a real project is ultimately built. Thanks to Professor Jose Andrade (Caltech) for making me feel as part of the Caltech family during my stay there, and also thanks to you for giving me the opportunity to participate in the task of trying to define a potential methodology to identify the Mars surface soil parameters, which has expanded my geotechnical knowledge *to infinity and beyond*. Subsequently, I must extend my gratitude to Professor Karl Iagnemma and Dr Carmine Senatore from the Robotic Mobility Group at MIT, who introduced me into the field of terramechanics and provided me with the experimental data.

I also want to thank my friend and colleague Ignasi Aliguer who has been sharing with me office and knowledge throughout these years, and who, without doubt, has also become an expert on backanalysis by listening to me talking and talking, day after day, about my research and how interesting I thought it was.

Furthermore, I would like to show my deepest gratitude to everybody that have been around me during these years, whether I was discussing my work with you or not, you helped me to achieve, in one way or another, my goal to become a doctor. For all of that: many thanks to all of you; especially to my UPC colleagues (PhD students, Administrative Staff and Professors).

Last but not least, I would like to express my gratitude to the institutions and companies that have been financially supporting my research: Spanish Ministry of Education and Science (Project: BIA 2006-27031-E), European Science Foundation (Eurocores S3T Program: Micro-Measurement and Monitoring Systems for Ageing Underground Infrastructures - Underground M^3. Project led by Professor Kenichi Soga from University of Cambridge), UTE AVE GIRONA (FCC, Dragados, Tecsa and Copisa), and Adif (Spanish Railway Infrastructures Administrator).

Table of Contents

List of Abbreviations and Notations

ABBREVIATIONS

AGA ..... Adaptive Genetic Algorithm
EPB ..... Earth Pressure Balanced
FEM ..... Finite Element Method
GA ..... Genetic Algorithm
HPD ..... Healthy Population Diversity
HSM ..... Hardening Soil Model
PCA ..... Principal Component Analysis
Q-Q ..... Quantile-Quantile
SGA ..... Simple Genetic Algorithm
SPD ..... Standard Population Diversity
TBM ..... Tunnel Boring Machine

NOTATIONS

$\boldsymbol{A}$ ..... Measurements Sensitivity Matrix
AF ..... Amplifier Factor of the Standard Deviation
a^x ..... Relative Difference Between Measurement and Calculation
b ..... Wheel Width
$\boldsymbol{C}_p$ ..... Parameters Covariance Matrix
$\boldsymbol{C}_p^0$ ..... *Priori* Parameters Covariance Matrix
$\boldsymbol{C}_x$ ..... Measurements Covariance Matrix
$\boldsymbol{C}_{x\_cv2}$ ..... Matrix of the Square Coefficient of Variation of the Measurements
c ..... Effective Cohesion
$c_{increment}$ ..... Increase of Cohesion per Unit of Depth
c_1 ..... Empirical Parameter to Locate the Maximum Stress
c_2 ..... Empirical Parameter to Locate the Maximum Stress
d_{eq} ..... Equivalent Thickness
DP ..... Drawbar Pull
E ..... Young's Modulus
EA ..... Axial Stiffness
EI ..... Flexural Rigidity
E_i^{inter} ..... Auxiliary Internal Parameter Defining the Initial Stiffness
E_{oed}^{ref} ..... Tangent Stiffness for Primary Oedometer Loading
E_{ur}^{ref} ..... Unloading/Reloading Stiffness
$\boldsymbol{E}_x$ ..... Instruments Error Structure Matrix (Absolute Error)
$\boldsymbol{E}_{x\_cv2}$ ..... Instruments Error Structure Matrix (Relative Error)
E_{50}^{ref} ..... Secant Stiffness in Standard Drained Triaxial Test
f ..... Individual Fitness
f_{max} ..... Highest Fitness of the Population
f_{min} ..... Lowest Fitness of the Population
f_{parent_i} ..... Parents Fitness of Individual i
f^c ..... Hardening Compression Yield Surface
f^s ..... Hardening Shear Yield Surface
f^* ..... Modified Individual Fitness Value

$\bar{f}$ ..... Average Fitness of the Population
$\overline{f^*}$ ..... Modified Average Fitness of the Population
GAP ..... Reproduction gap
g^c ..... Plastic Potential
G_{i,j,k_j} ..... Value of the Bit k_j of Parameter j and Individual i
G_{j,k_j}^{ave} ..... Average Value of G_{i,j,k_j}
$G_i^{ref\_inter}$ ..... Internal Reference Initial Shear Modulus
HPD_j ..... Weighted Average of the Euclidian Distance between G_{i,j,k_j} and $G_{i,j,k_j}^{w_{ave}}$
$HPD_{i,j}$ ..... HPD Individual i Contribution to HPD_j
HPD_{max} ..... Maximum Value of HPD
$\boldsymbol{I}$ ..... Identity Matrix
i ..... Slip Ratio
J ..... Objective Function
J_{axis_i} ..... Objective Function Value at the End of the Principal Axis i
$J_{frontier}$ ..... Objective Function Frontier Value
j ..... Shear Displacement
K_s ..... Elastic Swelling Modulus
K_s/K_c ..... Swelling-Compression Ratio
K_x ..... Shear Modulus in Direction x
K_0 ..... Coefficient of Lateral Earth Pressure
K_0^{NC} Coefficient of Lateral Earth Pressure Associated with Normally Consolidated States of Stress
k_c ..... Pressure-Sinkage Parameter
k_x ..... Horizontal Permeability
k_y ..... Vertical Permeability
k_φ ..... Pressure-Sinkage Parameter
L ..... Maximum Likelihood Function
$\boldsymbol{M}$ ..... Independent Instruments Error Structure Matrix (Relative Error)
m ..... Power for Stress-Level Dependency of Stiffness
n ..... Pressure-Sinkage Exponent
OCR ..... Over-Consolidated Ratio
P_c ..... Crossover Probability
$P_{c\_adaptive_j}$ ..... Adaptive Crossover Probability of Parameter j
P_{c_max} ..... Maximum Crossover Probability
P_{c_min} ..... Minimum Crossover Probability
P_m ..... Mutation Probability
P_{m_max} ..... Maximum Mutation Probability
$P_{m\_adaptive_j}^{Diversity}$ ..... Diverse Adaptive Mutation Probability of Parameter j
$P_{m\_adaptive_i}^{Fitness}$ ..... Fitness Adaptive Mutation Probability of individual i
$P_{m\_adaptive_{i,j}}$ ..... Adaptive Mutation Probability of Individual i and Parameter j
$P_{roulette}$ ..... Roulette Wheel Selection Probability
$P_{roulette_{limited}}$ ..... Modified Roulette Wheel Selection Probability
$\boldsymbol{p}$ ..... Set of Parameters
p^{ref} ..... Stiffness Reference Pressure
p' ..... Effective Mean Stress
p'_p ..... Effective Pre-Consolidation Stress
$\boldsymbol{p}^0$ ..... *Priori* Set of Parameters
q ..... Deviatoric Stress for Triaxial Loading
q_a ..... Asymptotic Deviatoric Stress
q_f ..... Ultimate Deviatoric Stress

$\tilde{q}$ ..... Special Deviatoric Stress Measurement (Plaxis)
r ..... Wheel Radius
R_f ..... Failure Ratio
S ..... Supporting Likelihood Function
SPD_j ..... Average of the Euclidian Distance between G_{i,j,k_j} and G_{i,j,k_j}^{ave}
$SPD_{i,j}$ ..... SPD Individual i Contribution to SPD_j
SPD_{max} ..... Maximum Value of SPD
T ..... Torque
$T_{size\_adaptive}$ ..... Adaptive Tournament Size
T_{size_max} ..... Maximum Tournament Size
u_x ..... Horizontal Displacements
u_y ..... Vertical Displacements
v ..... Velocity
W ..... Vertical Load
$\boldsymbol{W}$ ..... Markov Matrix
w ..... Weight
w_i ..... HPD Weighted Factor
x^{cal} ..... Computed Variable
x^{me} ..... Measured Variable
z ..... Sinkage
z_f ..... Front Sinkage
z_r ..... Rear Sinkage
α ..... Steepness of the Hardening Compression Yield Surface
ε_i^e ..... Elastic Strains in Direction i
ε_i^p ..... Plastic Strains in Direction i
$\varepsilon_i^{p\_c}$ ..... Plastic Compression Strains in Direction i
$\varepsilon_i^{p\_s}$ ..... Plastic Shear Strains in Direction i
ε_v^p ..... Plastic Volumetric Strains
μ ..... Marquardt Iterative Parameter
μ_0 ..... Initial Marquardt Iterative Parameter
φ ..... Effective Angle of Internal Friction
γ_{sat} ..... Saturated Specific Weight
γ_{unsat} ..... Unsaturated Specific Weight
γ^p ..... Internal Material Variable for the Accumulated Plastic Deviatoric Strain
ν ..... Poisson's Ratio
ν_{ur} ..... Poisson's Ratio for Unloading-Reloading
ω ..... Angular Velocity
ψ ..... Angle of Dilatancy
ρ ..... Marquardt Iterative Parameter
σ ..... Normal Stress
σ ..... Standard Deviation
σ_{DP} ..... Drawbar Pull Standard Deviation
σ_f ..... Front Stress
σ_m ..... Maximum Stress
σ_p ..... Pre-Consolidation Stress
σ_T ..... Torque Standard Deviation
σ_r ..... Rear Stress
$\sigma_{tension}$ ..... Tensile Strength
σ_z ..... Sinkage Standard Deviation
σ^2 ..... Variance
σ_i' ..... Effective Confining Stress in Direction i

τ ..... Shear Stress
τ_f ..... Front Shear Stress
τ_r ..... Rear Shear Stress
θ_f ..... Front Angle
θ_m ..... Angle of Maximum Stress
θ_r ..... Rear Angle

List of Figures

List of Tables

Chapter 1

Introduction

As a consequence of the new challenges that engineers are currently facing, more sophisticated techniques and powerful tools are required to tackle and solve the problems associated with those challenges. The widely used geotechnical Finite Element Method (FEM) is one of the best examples of those sophisticated techniques and powerful tools that have been used over the past decades to meet those challenges. On the one hand, FEM allows defining numerical models that closely fit the physical system; complex geometry can be introduced, sophisticated constitutive models can be used, different stages and processes can be defined. On the other hand, the more complex the numerical models are, the more information needs to be introduced, and often that information, such as the parameters that define the constitutive models, is extremely difficult to obtain.

Simplifying the scenario, where the geometry of the system is supposed to be known and where the constitutive model that captures better the soil behavior is also known and fixed, soil parameters remain as the only unknown variable of the problem before being capable of predicting the soil behavior. Therefore, that is part of the reason why estimating the parameters properly is crucially important.

Traditionally, soil parameters have been estimated from laboratory testing and in situ tests. However, in the majority of the cases, sample extraction from the soil environment causes, to some degree, disturbances on them, and consequently on the parameters too. Moreover, even though supposing that the sample is not affected by any type of disturbance derived from

the extraction, the relatively small size of the sample often makes difficult to consider the sample representative of a geotechnical soil layer, and consequently, its parameters neither. Those drawbacks are slightly attenuated when performing in situ tests due to: 1) No samples are extracted from the soil, and 2) The soil volume involved in "in situ" tests is usually bigger than the standard laboratory test samples, which makes in situ tests more likely to be representative of a geotechnical soil layer. Nevertheless, the boundary conditions for in situ tests are highly uncertain while in laboratory tests they are strictly defined and known.

Taking a step forward along the path of parameters estimation, there is a methodology, called backanalysis (also known as inverse analysis), with a strong potential to identify soil parameters based on the interaction of a conceptual model and the physical system. The conceptual model (i.e. numerical model) is evaluated and compared with the physical system while changing the model's input parameters (soil parameters) until the model matches the physical system. Usually, the model represents the real problem globally, while the physical system is represented by a set of measurements, usually extracted from in situ instrumentation, such as inclinometers, sliding micrometers and piezometers. That makes of backanalysis a technique capable of addressing the problem of parameters identification globally. However, if laboratory tests are only used to apply the backanalysis procedure, it has to be taken into account the loss of global representation derived from the reduction of soil domain involved in the analysis.

As a result, the current thesis aims to define a methodology to estimate soil parameters from numerical applications, as well as answering, if possible, some traditional questions related to backanalysis such as what, where and when to measure in order to estimate reliable soil parameters.

In order to achieve that, it was necessary to develop a software program (HBCode) capable of managing and linking all different parts involved in a full backanalysis procedure in an automatic manner. A novel optimization algorithm (hybrid method) and some improvements on existing algorithms (adaptive genetic algorithms) have also been defined with that purpose.

Chapter 2 presents the backanalysis framework, where different objective functions, along with the instrumentation error structure, the optimal layout of measuring points and the constitutive model, used to simulate the soil behavior, are fully described.

In Chapter 3, the different optimization algorithms used in this thesis are presented in detail, from local search methods, such as the Gauss-Newton method and the Marquardt method, to global search techniques such as genetic algorithms, as well as a hybrid method that attempts to optimize the two different types of techniques (local and global).

The main aspects of the HBCode are described in Chapter 4, where especial attention has been paid to the management and manipulation of the numerical model files (Plaxis 2D - Version 9).

In Chapter 5, an extensive analysis of the methodology, applied to a synthetic case representing a shallow tunnel, has been conducted in order to verify the applicability of the backanalysis methodology presented in this thesis. First, a two parameter identification case (E_{50}^{ref} and c) has been studied to evaluate the strengths and weaknesses of all optimization

algorithms presented in the thesis. Subsequently, an analysis of the in situ instrumentation layout was also conducted, using two different tunnel scenarios (far from collapse and close to collapse). Finally, a four parameters identification problem (E_{50}^{ref}, E_{ur}^{ref}, φ and c) has been carried out.

The first real case study is presented in Chapter 6, involving the construction of the new Barcelona Metro Line 9. Obviously, the ultimate goal of a geotechnical backanalysis is to identify the soil parameters. However, in Chapter 6, the influence of the tunnel construction procedure, the type of measurements involved in the analysis, and the use or not use of the instruments error structure have been additionally studied.

In Chapter 7, the large excavation of the Girona High-Speed Railway Station has been chosen as the second real case study. Apart from identifying the soil parameters and verifying whether or not the hypotheses used in design were valid, the concept of adaptive design by backanalysis has been introduced to optimize, if possible, the construction in real time. Adaptive design by backanalysis refers to the evolution of the design caused by the update of soil parameters values as construction progresses.

To confirm the applicability and robustness of the backanalysis methodology presented in this thesis, in Chapter 8, it has been applied to a less conventional geotechnical scenario: Mars surface exploratory rovers. The backanalysis performed has brought into question the reliability of the Wong and Reece wheel-terrain model, widely accepted and used by the terramechanics community.

Finally, in Chapter 9, the conclusions and future research are presented.

Chapter 2

Backanalysis

2.1 Introduction

The use of commercial software based on the Finite Element Method (FEM) has become very popular in geotechnical engineering. Moreover, those programs continuously incorporate more sophisticated constitutive models to simulate soil behavior, and consequently, more parameters are required to define them. Frequently, some parameters, especially in sophisticated constitutive models, do not have a real geotechnical meaning as they just come from a mathematical expression, which makes them difficult to identify.

Traditionally, soil parameters have been obtained from laboratory tests. However, in many cases samples used in laboratory tests do not represent the whole soil profile. In addition to that, sample extraction itself causes some disturbance and changes of the soil properties that are difficult to quantify.

As a consequence of that, the use of backanalysis to identify soil parameters has received significant attention from the geotechnical community. The basis of backanalysis consists in comparing a set of measurements, extracted from the physical system, with a conceptual model (i.e. a finite element model). The parameters that best represent the physical system are those that minimize the difference between measurements and calculations expresses as an objective function. Usually, the model represents the real problem globally, while the physical system is represented by a set of measurements, generally extracted from in situ

instrumentation, such as inclinometers, sliding micrometers and piezometers. That makes backanalysis a global technique. However, as previously mentioned, if only laboratory tests are used in the backanalysis procedure, it is necessary to take into account the loss of global representation due to the reduction of soil domain.

The adoption of backanalysis by the geotechnical community began in the early 80s. Gioda (1980) and Gioda & Maier (1980) presented one of the first geotechnical backanalysis, where the identification of rock mass parameters during a tunnel excavation was carried out. The least squares criterion was used to define the objective function, while a direct method was applied to minimize it.

In Cividini et al. (1981, 1983) and Cancelli & Cividini (1984), backanalysis applied to earth dam problems were studied. Subsequently, Gioda (1985) presented some remarks on backanalysis and characterization problems in geomechanics.

Simultaneously to the trend initiated by Gioda, the known as the Japanese group (formed by the universities of Kobe, Kyoto and Tokyo) was strongly working on the field of backanalysis applied to geotechnics. Several backanalyses for tunnel excavations were conducted by Sakurai (1983), Sakurai & Takeuchi (1983) and Hisatake & Ito (1985), as well as for consolidation in Arai et al. (1984) and test embankments on soft clay deposits in Arai et al. (1986).

Later, Ledesma (1987) introduced a full definition of the backanalysis problem based on the concept of maximum likelihood in order to generalize the objective function and formally define it from a statistical point of view. Moreover, he defined the structure of the error for several well-known in situ instruments such as inclinometers and sliding micrometers.

Using the methodology presented in Ledesma (1987), several real cases for tunnels and excavation were carried out in Gens et al. (1988), Ledesma et al. (1996), Gens et al. (1996) and Ledesma & Romero (1997).

Calvello (2002) employed the results of conventional drained and undrained triaxial compression tests performed on clay specimens in order to identify several soil parameters of four different constitutive models: the Duncan-Chang model, the Modified Cam-clay model, the Anisotropic Modified Cam-clay model and the Hardening Soil model.

Malécot et al. (2004) applied the backanalysis procedure to identify parameters of the Mohr-Coulomb constitutive model from the horizontal displacements of a synthetic sheet pile wall. Two different optimization algorithms were used and subsequently compared; one based on a gradient method and the other on genetic algorithms. Later, in Levasseur (2007), Levasseur et al. (2007) and Rechea et al. (2007), a full backanalysis definition using genetic algorithms was presented. Several cases were studied; from pressuremeter tests to real excavations. Moreover, in Levasseur (2007) and Levasseur et al. (2009 and 2010) the concept of using a principal component analysis, as a genetic algorithm post-process, was introduced to better deal with the non-uniqueness of the problem; a feature strongly associated with the nature of geomechanics.

In Finno & Calvello (2005), an inverse analysis of a real supported excavation performed in five stages was presented. The field observations were obtained from inclinometer data and the Hardening Soil model was used as the constitutive model to reproduce the soil behavior. The results indicated that a recalibration of the model at an early construction stage may affect the predictions throughout construction.

Hashash et al. (2010) discussed the advantages and disadvantages of using genetic algorithms and self-learning simulations for inverse analysis in a deep urban excavation. The authors concluded with the general idea that self-learning simulations allows to discover new soil behavior while genetic algorithms assist engineers to better select the parameters of existing soil constitutive models.

Finally, in de Santos et al. (2014), a simple synthetic tunnel excavation was used to illustrate the potential of the hybrid methodology presented in this thesis. For that particular case, a simple genetic algorithm and the Gauss-Newton method were combined to define the hybrid method.

From what has been presented above, it can be noted that in the last decade the majority of the backanalysis effort has been focused on optimization algorithms and their application to challenging real problems. Indeed, the effort to create more robust and computational efficient backanalysis procedures is still strongly pursued.

2.2 Performance of the Parameter Identification Process

Like all inverse problems, parameter identification problems are usually ill-posed, which means that at least one of the following properties given by Jacques Hadamard (Engl et al., 1996) is violated.

- For all admissible data, a solution exists.

- For all admissible data, the solution is unique.

- The solution depends continuously on the data.

In the following subparts of section 2.2, the properties mentioned above are briefly discussed. In Xiang et al. (2003), the full discussion is presented in detail.

2.2.1 Existence

The violation of the first property happens when the numerical model fails to describe the mechanism of the physical problem or the measurements contain very poor data. If a proper numerical model cannot be found to describe a physical problem, it means the direct problem has not been solved satisfactory, so the problem of parameter identification is beyond discussion.

2.2.2 Uniqueness

Physically, satisfying the second property requires that the measurements contain enough information to determine a unique solution. Mathematically, according to the contraction

mapping theorem and some hypotheses (Chicone, 1999), the uniqueness of the problem can be guaranteed. This is a sufficient condition, not a necessary one.

2.2.3 Stability

The discussion of the last property is directly related to the continuity of the objective function. This is probably the main reason why parameter identification problems are often unstable. Usually, as pointed out in Engl et al (1996), some kind of regularization will be used to compensate the loss of continuity.

2.3 Objective Function

Using a model that relates parameters to measurable variables ($x^{cal} = M(p)$), and having m measurements of these variables x_1^{me}, x_2^{me}, x_3^{me}, … x_m^{me}; the parameters of the model, p_1, p_2, p_3, … p_n, that better adjust the measurements are the solution of the problem. Therefore, the objective function can be defined as the function that quantifies the degree of adjustment between the model and the measurements. There are several ways to define the objective function. The most extended methods are presented in Eykhoff (1974). In the current document, only the least-squares method, the Markov or generalized least-squares method, the maximum likelihood method and the maximum likelihood method with prior information are presented.

2.3.1 The Least-Squares Method

Even though the least-squares method is one of the simplest objective function types, it is one of the most extended methods to define the objective function.

The best parameters are those that minimize a function that depends on the square difference between measured and computed variables.

$$J = \sum_{i=1}^{m} \left(x_i^{me} - x_i^{cal}\right)^2 \tag{2.1}$$

where m is the number of measurements.

Equation (2.1) can be represented in matrix notation as equation (2.2) shows.

$$J = [\boldsymbol{x}^{me} - \boldsymbol{x}^{cal}]^T [\boldsymbol{x}^{me} - \boldsymbol{x}^{cal}] \tag{2.2}$$

2.3.2 The Markov Method (or the Generalized Least-Squares Method)

The Markov method is a generalization of the least-squares method; where a "weighted" diagonal matrix ($\boldsymbol{W}$) is introduced in order to reflect the quality of the measurements.

$$J = [\boldsymbol{x}^{me} - \boldsymbol{x}^{cal}]^T \boldsymbol{W} [\boldsymbol{x}^{me} - \boldsymbol{x}^{cal}] \tag{2.3}$$

The error associated with the measuring process is reflected in $\boldsymbol{W}$, where higher weights are assigned to more reliable measurements. Usually, the definition of $\boldsymbol{W}$ is directly related to the standard deviation of the apparatus that has been used to extract the measurements. However, $\boldsymbol{W}$ can be defined as desired in order to take into account more aspects related to

the process of extracting the measurements, such as the skills of the technician or any other specific condition that can alter the reliability of the measure.

2.3.3 The Maximum Likelihood Method

Using the maximum likelihood method, the difference between the measurements and the model is attributed to the observational procedure (measurements). That discrepancy is considered as a random variable, and its probability density function must be known. Thanks to the statistical point of view of the method, the objective function defined by the maximum likelihood method can be considered as a more general criterion than the ones based on the least-squares and Markov methods. However, more knowledge of the problem is required to properly define it.

The solution of the problem is the one that maximized the probability to obtain the field measurements actually observed, in other words, the best parameters estimation is found by maximizing the likelihood (L) of an hypothesis ($\boldsymbol{p}$) given a set of error measurements ($\boldsymbol{x}^{me} - \boldsymbol{x}^{cal}$). As shown in Edwards (1972) and Tarantola (1987), the likelihood of a hypothesis is proportional to the conditional probability of $\boldsymbol{x}^{me}$ given a set of parameters $\boldsymbol{p}$. Therefore, the criterion can be expressed as:

$$L = kP(\boldsymbol{x}^{me}/\boldsymbol{p}) \tag{2.4}$$

where k is a proportionally constant.

Carrera (1988) demonstrated that this formulation has theoretical and conceptual advantages:

- There is no need to define the probability of a hypothesis, which has become a controversial concept in probability theory.

- The model is not required to reproduce the true system exactly (Baram & Sandell, 1978).

- Prior parameters information can be systematically introduced to the parameter identification procedure (see section 2.2.4).

Assuming that the error of the measurements follows a normal distribution (Gaussian distribution), the likelihood can be rewritten as:

$$P(\boldsymbol{x}^{me}/\boldsymbol{p}) = \frac{1}{\sqrt{(2\pi)^m |\boldsymbol{C}_x|}} \exp\left[-\frac{1}{2}\left(\boldsymbol{x}^{me} - \boldsymbol{x}^{cal}\right)^T (\boldsymbol{C}_x)^{-1}\left(\boldsymbol{x}^{me} - \boldsymbol{x}^{cal}\right)\right] \tag{2.5}$$

where m is the number of measurements, and $\boldsymbol{C}_x$ the measurements covariance matrix, which represents the structure of the error associated with the measurements.

Maximizing (2.5) is equivalent to minimize the supporting function (2.6):

$$S = -2\ln L \tag{2.6}$$

Thanks to the monotonous growth of the logarithm function, the use of the function S appeared to be more appropriate, especially while working with normal distributed functions. The full expression of equation (2.6) is shown as follows:

$$S = \left(\boldsymbol{x}^{me} - \boldsymbol{x}^{cal}\right)^T (\boldsymbol{C}_x)^{-1}\left(\boldsymbol{x}^{me} - \boldsymbol{x}^{cal}\right) + \ln|\boldsymbol{C}_x| + m\ln(2\pi) - 2\ln k \tag{2.7}$$

On the assumption that the covariance matrix $\boldsymbol{C}_x$ is fixed and the last three terms of equation (2.7) are constant, the objective function using the maximum likelihood method can be finally defined as:

$$J = [\boldsymbol{x}^{me} - \boldsymbol{x}^{cal}]^T \boldsymbol{C}_x^{-1} [\boldsymbol{x}^{me} - \boldsymbol{x}^{cal}] \tag{2.8}$$

In equation (2.8) the "weighted" matrix has a clear statistical meaning represented by the inverted measurements covariance matrix. In the case, where measurements are independent among them, $\boldsymbol{C}_x^{-1}$ is a diagonal matrix, and the objective function obtained by the maximum likelihood method (eq. 2.8) is equivalent to the one obtained by the Markov method (eq. 2.3). Moreover, if the elements of the diagonal of $\boldsymbol{C}_x^{-1}$ are also identical, the objective function obtained by the maximum likelihood method (eq. 2.8) is equivalent to the one obtained by the least-squares method (eq. 2.2).

2.3.4 The Maximum Likelihood Method with Prior Information

In order to make the objective function more general, prior information (in this case the *a priori* parameter values, $\boldsymbol{p}^0$) can be introduced into the problem. Following a statistical representation of the problem, as shown in the previous section 2.2.3, the new objective function must incorporate a term representing the error of the prior parameters estimation. Therefore, equation (2.4) can be rewritten as equation (2.9), where the likelihood is defined as proportional to the joint probability of the measurements and the prior parameter values.

$$L = kP(\boldsymbol{x}^{me}/\boldsymbol{p}, \boldsymbol{p}^0) = kP(\boldsymbol{x}^{me}/\boldsymbol{p})P(\boldsymbol{p}^0) \tag{2.9}$$

Both probability functions, $P(\boldsymbol{x}^{me}/\boldsymbol{p})$ and $P(\boldsymbol{p}^0)$ are considered normal or Gaussians.

Therefore:

$$P(\boldsymbol{x}^{me}/\boldsymbol{p}) = \frac{1}{\sqrt{(2\pi)^m |\boldsymbol{C}_x|}} \exp\left[-\frac{1}{2}\left(\boldsymbol{x}^{me} - \boldsymbol{x}^{cal}\right)^T (\boldsymbol{C}_x)^{-1}\left(\boldsymbol{x}^{me} - \boldsymbol{x}^{cal}\right)\right] \tag{2.10}$$

and

$$P(\boldsymbol{p}^0) = \frac{1}{\sqrt{(2\pi)^n \left|\boldsymbol{C}_{p^0}\right|}} \exp\left[-\frac{1}{2}(\boldsymbol{p}^0 - \boldsymbol{p})^T \left(\boldsymbol{C}_p^0\right)^{-1} (\boldsymbol{p}^0 - \boldsymbol{p})\right] \tag{2.11}$$

where m is the number of measurements, n the number of parameters, $\boldsymbol{C}_p^0$ the *a priori* parameters covariance matrix, and $(\boldsymbol{p}^0 - \boldsymbol{p})$ the vector of differences between prior information and parameters being estimated.

As presented in section 2.2.3, it is more useful to work with a supporting function S (eq. 2.6), rather than working with function L (eq. 2.9). Then, using equations (2.10) and (2.11) the new supporting function is defined as follows:

$$S = \left(\boldsymbol{x}^{me} - \boldsymbol{x}^{cal}\right)^T (\boldsymbol{C}_x)^{-1}\left(\boldsymbol{x}^{me} - \boldsymbol{x}^{cal}\right) + (\boldsymbol{p}^0 - \boldsymbol{p})^T \left(\boldsymbol{C}_p^0\right)^{-1} (\boldsymbol{p}^0 - \boldsymbol{p}) + \ln|\boldsymbol{C}_x| + \ln\left|\boldsymbol{C}_p^0\right| + \\ + m\ln(2\pi) + n\ln(2\pi) - 2\ln k \tag{2.12}$$

On the assumption that the covariance matrices $\boldsymbol{C}_x$ and $\boldsymbol{C}_p^0$ are fixed and the last three terms of equation (2.12) are constants, the objective function using the maximum likelihood method with prior information can be finally defined as:

$$J = [\boldsymbol{x}^{me} - \boldsymbol{x}^{cal}]^T \boldsymbol{C}_x^{-1} [\boldsymbol{x}^{me} - \boldsymbol{x}^{cal}] + [\boldsymbol{p}^0 - \boldsymbol{p}]^T \boldsymbol{C}_p^{0^{-1}} [\boldsymbol{p}^0 - \boldsymbol{p}] + \ln|\boldsymbol{C}_x| + \ln\left|\boldsymbol{C}_p^0\right| \quad (2.13)$$

2.3.5 Objective Function using a Relative Error

The objective functions shown in the previous sections (2.2.1, 2.2.2, 2.2.3 and 2.2.4) are usually applied to cases where the same kind of measurements are used (i.e. displacements). However, in cases where different kinds of measurements or large differences among the magnitude of the measurements are involved, an objective function defined by the concept of relative error is considered appropriate.

Using the structure of the maximum likelihood method (eq. 2.8), and defining the components of $\boldsymbol{a}^x$ as in equation 2.14, an objective function (eq. 2.15) is properly defined for cases where different kinds of measurements or large differences among the magnitude of the measurements are involved.

$$a_i^x = \left(\frac{x_i^{me} - x_i^{cal}}{x_i^{me}}\right) \quad (2.14)$$

$$J = [\boldsymbol{a}^x]^T \boldsymbol{C}_{x\_cv2}^{-1} [\boldsymbol{a}^x] \quad (2.15)$$

where $\boldsymbol{C}_{x\_cv2}^{-1}$ is the inverse matrix of the square coefficient of variation of the measurements, which represents the structure of the error associated with the measurements.

2.4 Instrumentation Error Structure

As presented before, $\boldsymbol{C}_x$ and $\boldsymbol{C}_{x\_cv2}$ represent in some way the structure of the error associated with the measurements. If an instrument performs independent measurements and its errors have a Gaussian distribution of probability with the same variance (σ^2), then $\boldsymbol{C}_x$ and $\boldsymbol{C}_{x\_cv2}$ are diagonal, and they can be represented as in equations (2.16) and (2.17).

$$\boldsymbol{C}_x = \sigma^2 \boldsymbol{I} \quad (2.16)$$

$$\boldsymbol{C}_{x\_cv2} = \sigma^2 \boldsymbol{M} \quad (2.17)$$

where $\boldsymbol{I}$ is the identity matrix and $\boldsymbol{M}$ a diagonal matrix (see equation 2.18).

$$\boldsymbol{M} = \begin{bmatrix} \frac{1}{x_1^{me^2}} & \cdots & 0 \\ \vdots & \ddots & \vdots \\ 0 & \cdots & \frac{1}{x_m^{me^2}} \end{bmatrix} \quad (2.18)$$

However, in some instruments, especially those designed for linewise observations (Kovari & Amstad, 1983), the errors of the measurements are not independent. For instance, if an

inclinometer device is used to measure horizontal displacements along a borehole, the value of the displacement i is based on all the previously measured displacements.

In this section, the covariance matrix ($\boldsymbol{C}_x$) and the square coefficient variation matrix ($\boldsymbol{C}_{x\_cv2}$) for two instruments performing linewise observations (sliding micrometer and inclinometer) are presented. In order to do that, it was considered useful to express the covariance matrix and the square coefficient variation matrix for each type of instrument as:

$$(\boldsymbol{C}_x)_k = \sigma_k^2 (\boldsymbol{E}_x)_k \tag{2.19}$$

$$\left(\boldsymbol{C}_{x\_cv2}\right)_k = \sigma_k^2 \left(\boldsymbol{E}_{x\_cv2}\right)_k \tag{2.20}$$

where σ_k^2 is a scale factor which represents the global variance of the measurements made using the instrument k, and $(\boldsymbol{E}_x)_k$ and $\left(\boldsymbol{E}_{x\_cv2}\right)_k$ contains the error structure of the instrument. Obviously, if the measurements are independent and have the same variance, $(\boldsymbol{E}_x)_k$ is the identity matrix, while $\left(\boldsymbol{E}_{x\_cv2}\right)_k$ is $\boldsymbol{M}$ (see equations (2.16) and (2.17)).

$(\boldsymbol{E}_x)_k$ has been obtained from Ledesma (1987) and Ledesma et al (1996) and subsequently adapted to define $\left(\boldsymbol{E}_{x\_cv2}\right)_k$ for use in the objective function based on the relative error.

2.4.1 Sliding Micrometer

A sliding micrometer consists in a probe that is introduced into a borehole where a tube with measuring marks is previously installed. The probe measures with high accuracy (Δz= ±0.002mm/m) the distance between adjacent measuring marks, before, during and after the ground experiences deformation.

It is assumed that the line, over the measurements are taken, is divided in p sections of length l_i, and that the sliding micrometer measures the change of length (δ_{y_i}) between adjacent measuring marks. Then, the longitudinal displacement of the measuring mark n is:

$$u_{y_n} = \sum_{i=1}^{n} \delta_{y_i} + A \tag{2.21}$$

where A is an integration constant that allows to transform the measurements from relative measurements to absolute measurements. Typically, the movement of one of the extremes of the line of measurement is used to define A.

In order to determine $(\boldsymbol{E}_x)_k$ and $\left(\boldsymbol{E}_{x\_cv2}\right)_k$, the measurements ($\delta_{y_i}$) are assumed to be independent with variance σ^2 and A being exactly known. The procedure to obtain the error structure of a sliding micrometer is fully described in Ledesma (1987) and Ledesma et al. (1996); herein, $(\boldsymbol{E}_x)_k$ and $\left(\boldsymbol{E}_{x\_cv2}\right)_k$ are directly presented.

$$(\boldsymbol{E}_x)_{i,j} = \begin{cases} i & if\ i \le j \\ j & if\ j < i \end{cases} \tag{2.22}$$

$$\left(\boldsymbol{E}_{x\_cv2}\right)_{i,j} = \begin{cases} \frac{i}{x_i^{me2}} & if\ i \le j \\ \frac{j}{x_j^{me2}} & if\ j < i \end{cases} \tag{2.23}$$

where:

$$i = 1, \dots, n$$

$$j = 1, \dots, n$$

In equations (2.24) and (2.25) the matrices of the error structure of the measurements, obtained using a sliding micrometer, are shown.

$$(\boldsymbol{E}_x)_{sliding\ micrometer} = \begin{bmatrix} 1 & 1 & 1 & \cdots & 1 \\ 1 & 2 & 2 & \cdots & 2 \\ 1 & 2 & 3 & \cdots & 3 \\ \vdots & \vdots & \vdots & \ddots & \vdots \\ 1 & 2 & 3 & \cdots & n \end{bmatrix} \tag{2.24}$$

$$\left(\boldsymbol{E}_{x\_cv2}\right)_{sliding\ micrometer} = \begin{bmatrix} \frac{1}{x_1^{me^2}} & \frac{1}{x_1^{me^2}} & \frac{1}{x_1^{me^2}} & \cdots & \frac{1}{x_1^{me^2}} \\ \frac{1}{x_1^{me^2}} & \frac{2}{x_2^{me^2}} & \frac{2}{x_2^{me^2}} & \cdots & \frac{2}{x_2^{me^2}} \\ \frac{1}{x_1^{me^2}} & \frac{2}{x_2^{me^2}} & \frac{3}{x_3^{me^2}} & \cdots & \frac{3}{x_3^{me^2}} \\ \vdots & \vdots & \vdots & \ddots & \vdots \\ \frac{1}{x_1^{me^2}} & \frac{2}{x_2^{me^2}} & \frac{3}{x_3^{me^2}} & \cdots & \frac{n}{x_n^{me^2}} \end{bmatrix} \tag{2.25}$$

If the variance of the integration constant A is taken into account, then equations (2.22) and (2.23) are rewritten as:

$$(\boldsymbol{E}_x)_{i,j} = \begin{cases} i + \left(\frac{varA}{\sigma^2}\right) & i\ if\ i \le j \\ j + \left(\frac{varA}{\sigma^2}\right) & j\ if\ j < j \end{cases} \tag{2.26}$$

$$\left(\boldsymbol{E}_{x\_cv2}\right)_{i,j} = \begin{cases} \frac{i}{x_i^{me^2}} + \left(\frac{varA}{\sigma^2}\right) & if\ i \le j \\ \frac{j}{x_j^{me^2}} + \left(\frac{varA}{\sigma^2}\right) & if\ j < i \end{cases} \tag{2.27}$$

2.4.2 Inclinometer

The inclinometer is used to obtain the horizontal displacements in the ground. It also consists on a probe that is introduced into a borehole where a tube is previously installed. The probe measures with high precision the angle with respect to the vertical. The integration of these angles provides the horizontal displacement. Therefore, the horizontal displacement in point n, assuming that the line over the measurements are taken is divided in p sections of length l_i, is:

$$u_{x_n} = \sum_{i=1}^{n} \tan \alpha_i \cdot l_i + B \tag{2.28}$$

where B is an integration constant that expresses the horizontal displacement of the initial point of measurement.

Since α usually takes small values ($\tan \alpha \approx \alpha$), equation (2.28) can be rewritten as:

$$u_{x_n} = \sum_{i=1}^{n} \alpha_i \cdot l_i + B \tag{2.29}$$

In order to determine $(\boldsymbol{E}_x)_k$ and $\left(\boldsymbol{E}_{x\_cv2}\right)_k$, the measurements ($\alpha_i$) are assumed to be independent with variance σ^2 and B being exactly known. The procedure to obtain the error structure of an inclinometer is fully described in Ledesma (1987) and Ledesma et al. (1996); herein, $(\boldsymbol{E}_x)_k$ and $\left(\boldsymbol{E}_{x\_cv2}\right)_k$ are directly presented.

$$(\boldsymbol{E}_x)_{i,j} = \begin{cases} \sum_{n=1}^{i} l_k^2 & if\ i \le j \\ \sum_{n=1}^{j} l_k^2 & if\ j < i \end{cases} \tag{2.30}$$

$$\left(\boldsymbol{E}_{x\_cv2}\right)_{i,j} = \begin{cases} \sum_{n=1}^{i} \frac{l_k^2}{x_k^{me^2}} & if\ i \le j \\ \sum_{n=1}^{j} \frac{l_k^2}{x_k^{me^2}} & if\ j < i \end{cases} \tag{2.31}$$

In equations (2.32) and (2.33) the matrices of the error structure of the measurements, obtained using an inclinometer, are shown.

$$(\boldsymbol{E}_x)_{inclinometer} = \begin{bmatrix} l_1^2 & l_1^2 & \cdots & l_1^2 \\ l_1^2 & l_1^2 + l_2^2 & \cdots & l_1^2 + l_2^2 \\ \vdots & \vdots & \ddots & \vdots \\ l_1^2 & l_1^2 + l_2^2 & \cdots & l_1^2 + l_2^2 + \cdots + l_n^2 \end{bmatrix} \tag{2.32}$$

$$\left(\boldsymbol{E}_{x\_cv2}\right)_{inclinometer} = \begin{bmatrix} \frac{l_1^2}{x_1^{me^2}} & \frac{l_1^2}{x_1^{me^2}} & \cdots & \frac{l_1^2}{x_1^{me^2}} \\ \frac{l_1^2}{x_1^{me^2}} & \frac{l_1^2}{x_1^{me^2}} + \frac{l_2^2}{x_2^{me^2}} & \cdots & \frac{l_1^2}{x_1^{me^2}} + \frac{l_2^2}{x_2^{me^2}} \\ \vdots & \vdots & \ddots & \vdots \\ \frac{l_1^2}{x_1^{me^2}} & \frac{l_1^2}{x_1^{me^2}} + \frac{l_2^2}{x_2^{me^2}} & \cdots & \frac{l_1^2}{x_1^{me^2}} + \frac{l_2^2}{x_2^{me^2}} + \cdots + \frac{l_n^2}{x_n^{me^2}} \end{bmatrix} \tag{2.33}$$

If the variance of the integration constant B is taken into account, then equations (2.30) and (2.31) are rewritten as:

$$(\boldsymbol{E}_x)_{i,j} = \begin{cases} \sum_{n=1}^{i} l_k^2 + \left(\frac{varB}{\sigma^2}\right) & if\ i \le j \\ \sum_{n=1}^{j} l_k^2 + \left(\frac{varB}{\sigma^2}\right) & if\ j < i \end{cases} \tag{2.34}$$

$$\left(\boldsymbol{E}_{x\_cv2}\right)_{i,j} = \begin{cases} \sum_{n=1}^{i} \frac{l_k^2}{x_k^{me^2}} + \left(\frac{varB}{\sigma^2}\right) & if\ i \le j \\ \sum_{n=1}^{j} \frac{l_k^2}{x_k^{me^2}} + \left(\frac{varB}{\sigma^2}\right) & if\ j < i \end{cases} \tag{2.35}$$

2.5 Optimal Layout of Measuring Points

A very interesting and important aspect is defining what to measure, where to measure, when to measure and how many measurements are needed in order to solve the parameters

identification problem. In fact, the quality and the quantity of measurements exert a major influence on the accuracy of the identified parameters.

The answer to *what to measure* would be measuring the variables (type of measurement), on which the system parameters have an obvious impact. Sensitivity analyses are usually carried out for this purpose (Beck & Woodbury 1998).

In order to answer *where to measure*, the concept of sensitivity matrix, being defined as the matrix of the partial derivative of measurements with respect to the unknown parameters, has been used to locate the best measurement points. The general idea is focused on determine the most sensitive points of the system (high quality measurements), and used them to extract the measurements to subsequently use them as inputs to better solve the objective function. Murakami & Hasegawa (1988) and Shoji et al. (1990) implemented that idea for cases where just one parameter was intended to be identified. However, this method is difficult to apply when there is more than one parameter. Haftka et al. (1998) proposed the concept of maximizing all the sensitivities by finding a single compromise measure, when identifying more than one parameter. Supposing that all measurements are independent and have the same associated error defined by σ^2, the resultant objective function is defined by the least-squares method. As a consequence, the parameters covariance matrix (Bury, 1975) can be defined as:

$$\boldsymbol{C}_p = \sigma^2(\boldsymbol{A}^T\boldsymbol{A})^{-1} \tag{2.36}$$

where σ^2 is the variance of the measurements, and $\boldsymbol{A}$ the matrix containing the derivatives of the computed variables with respect to the parameters, commonly referred as the sensitivity matrix.

From equation (2.36) it can be realized that highly sensitive measurements (high coefficient values in $\boldsymbol{A}$) cause low coefficient values in $\boldsymbol{C}_p$. Low coefficient values in $\boldsymbol{C}_p$ indicate high accuracy in the parameters identified. Using that idea, Haftka et al (1998) defined the single compromise measure based on the maximization of the determinant of the matrix $\boldsymbol{A}^T\boldsymbol{A}$.

The same approach, as the one already presented to answer the question *where to measure*, can be adopted to answer the question *when to measure*. However, while trying to determine when to measure or when it is more appropriate to measure, the results of the sensitivities have to be analyzed in temporal terms rather than in spatial terms. Basically, the idea is to study the evolution of the sensitivity of the different measurement points over time.

Referring to the quantity, *how many measurements are needed*, the well-known principle is that the number of measurements should be at least the same as the number of the parameters (Cividini et al. 1981; Gioda & Sakurai 1987; Venclik 1994). Otherwise, the identification process will fail, due to the lack of input information. However, the view of "more measurements are better" was not confirmed by Cividini et al. (1981) and Venclik (1994). Nevertheless, Ledesma et al. (1996) found some differences in the reliability of the solution for a fixed measurement error, represented by the parameters covariance matrix. As expected, the variance of the parameters identified, were smaller when using a higher number of measurements.

2.6 Constitutive Model

The equations that are intended to reproduce the soil behavior are what are known as constitutive models. Many different constitutive models have been defined to reproduce the many different types of soils, from the simplest one, using a linear stress-strain relationship, to the very sophisticated ones, as the Hardening Soil Model (HSM) described in the following section.

Therefore, because of the complexity in terms of strains and stresses associated with tunnels and excavations, the sophisticated HSM was considered the most appropriate constitutive model to tackle them. The well-known and widely used geotechnical commercial software Plaxis, which among its different constitutive models the HSM is available, was used to simulate the different geotechnical scenarios studied in this thesis.

2.6.1 The Hardening Soil Model (HSM)

The original HSM was developed by Schanz (1998) and Schanz et al. (1999) on the basis of the Double Hardening model by Vermeer (1978). The HSM also incorporates ideas by Kondner & Zelasko (1963), Duncan & Chang (1970), Ohde (1951) or Janbu (1963), and Rowe (1962).

The HSM is an elastoplastic double-yield surface model that uses the Mohr-Coulomb failure criteria and takes into account the soil dilatancy effect. By using a double-yield surface, distinction is made between two main types of hardenings, shear hardening and compression hardening. The shear hardening is mainly used to model irreversible strains due to primary deviatoric loading, while the compression hardening is mainly used to model irreversible plastic strains due to compression in oedometer loading and isotropic loading.

Extending the hypoelastic Duncan-Chang model (Duncan & Chang, 1970) to an elastoplastic formulation, Schanz (1998) proposed a shear hardening yield surface as shown in equation (2.37).

$$f^s = \frac{2}{E_i^{inter}} \frac{q}{1-{}^{q}/_{q_a}} - \frac{2q}{E_{ur}} - \gamma^p \tag{2.37}$$

where $q = \sigma_1 - \sigma_3$ is defined for triaxial loading, q_a is the asymptotic deviatoric stress as defined in the original Duncan-Chang model (Duncan & Chang, 1970), E_{ur} is the Young's modulus for unloading and reloading, and E_i^{inter} is an auxiliary internal parameter defining the initial stiffness and γ^p is an internal material variable for the accumulated plastic deviatoric strain (eq. 2.38).

$$\gamma^p = \varepsilon_1^p - \varepsilon_2^p - \varepsilon_3^p = 2\varepsilon_1^p - \varepsilon_v^p \approx 2\varepsilon_1^p \tag{2.38}$$

where ε_1^p, ε_2^p, ε_3^p are the plastic principal strains, and ε_v^p the plastic volumetric strains due to primary deviatoric loading.

The meaning of E_i^{inter} in the full HSM implemented in Plaxis is not as closely related to the hyperbolic model defined by Kondner & Zelasko (1963), where E_{50}, the stiffness modulus

when mobilizing 50% of the maximum shear strength, can be explicitly related to E_i. The transition from E_{50}, as used in Kondner & Zelasko (1963), to E_i^{inter}, as used in Plaxis (Brinkgreve & Broere, 2008), is made because of the existence of a second yield surface. The interaction between E_i^{inter} and E_{50} is fully described in section 2.6.1.2.

In reality, plastic volumetric strains are never precisely equal to zero, but for hard soils plastic volume changes tend to be small when compared with the axial strain ε_1^p. However, by introducing the soil dilatancy, a non-insignificant plastic volumetric strain is taken into account. The plastic volumetric strain due to the soil dilatancy follows from the theory described in Rowe (1962), and it was fully adapted to the HSM by Schanz & Vermeer (1998). The introduction of the soil dilatancy makes the plastic strains on the shear hardening yield surface non-associated.

The second yield surface, known as compression hardening yield surface or also namely yield cap, is basically introduced in order to fully delimit the elastic region. The compression hardening yield surface mainly accounts for plastic volumetric strains due to compression in oedometer loading and isotropic loading. However, part of the plastic shear strains of the model are also contributed by the yield cap. The hardening compression yield surface is defined as:

$$f^c = \frac{\tilde{q}^2}{\alpha^2} - p'^2 - p_p'^2 \tag{2.39}$$

where p_p' is an internal material variable for effective pre-consolidation stress, p' is the effective mean stress, α is the steepness of the yield surface, and $\tilde{q}$ is a special stress measure.

$$\tilde{q} = \sigma_1' + \left(\frac{3+\sin\varphi}{3-\sin\varphi} - 1\right)\sigma_2' - \left(\frac{3+\sin\varphi}{3-\sin\varphi}\right)\sigma_3' \tag{2.40}$$

All the details of both yield surfaces, as well as the entire HSM, can be seen in Schanz (1998), Schanz et al. (1999), Benz (2007) and Brinkgreve & Broere (2008).

Figure 2.1 illustrates the hardening yield surfaces in $p' - \tilde{q}$ space for triaxial compression conditions.

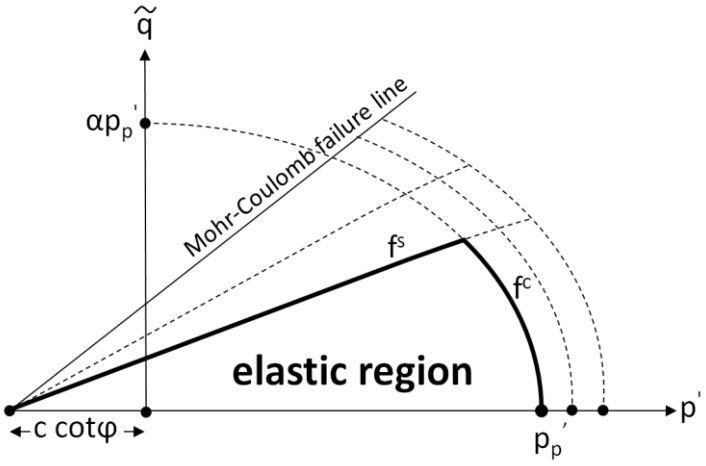

Figure 2.1. Hardening yield surfaces. Shear Hardening yield surface (f^s), Compression Hardening yield surface (f^c) and Mohr-Coulomb failure line represented in $p' - \tilde{q}$ space for compression triaxial conditions.

2.6.1.1 Input Parameters of the HSM implemented in Plaxis

One of the advantages of using the HSM over more simple models is not only the hyperbolic stress-strain relationship, but also the control of stress level dependency. The effect of that stress dependency is basically represented by the different stiffness moduli.

The reference moduli (E_{50}^{ref}, E_{oed}^{ref} and E_{ur}^{ref}), to the reference pressure (p^{ref}), and the stress-level dependency parameter (m) are the main parameters in charge of defining the stiffness.

- E_{50}^{ref}: Reference secant stiffness in standard drained triaxial test.

- E_{oed}^{ref}: Reference tangent stiffness for primary oedometer loading.

- E_{ur}^{ref}: Reference unloading / reloading stiffness.

In the following equations (2.41, 2.42 and 2.43), the relationships between the reference values and the actual values of each stiffness moduli are shown.

$$E_{50} = E_{50}^{ref} \left(\frac{\sigma_3' \sin\varphi + c\cos\varphi}{p^{ref} \sin\varphi + c\cos\varphi} \right)^m \tag{2.41}$$

$$E_{oed} = E_{oed}^{ref} \left(\frac{\frac{\sigma_3'}{K_0^{NC}} \sin\varphi + c\cos\varphi}{p^{ref} \sin\varphi + c\cos\varphi} \right)^m \tag{2.42}$$

$$E_{ur} = E_{ur}^{ref} \left(\frac{\sigma_3' \sin\varphi + c\cos\varphi}{p^{ref} \sin\varphi + c\cos\varphi} \right)^m \tag{2.43}$$

where c is the effective cohesion, φ the effective angle of internal friction, K_0^{NC} the coefficient of lateral earth pressure associated with normally consolidated states of stress.

Figure 2.2 illustrates a standard drained triaxial test, where the physical meaning of E_{50} and E_{ur} can be visualized, as well as E_i.

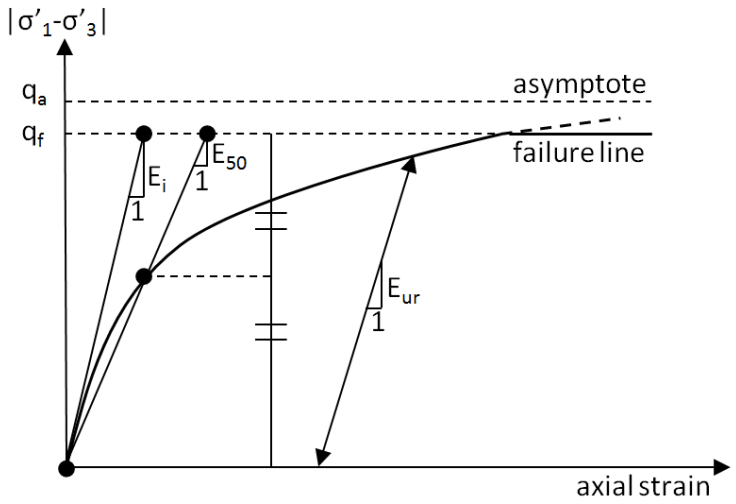

Figure 2.2. Hyperbolic stress-strain relation in primary loading for standard drained triaxial test.

Figure 2.3 illustrates an oedometer test where the definition of E_{oed}^{ref} can be observed.

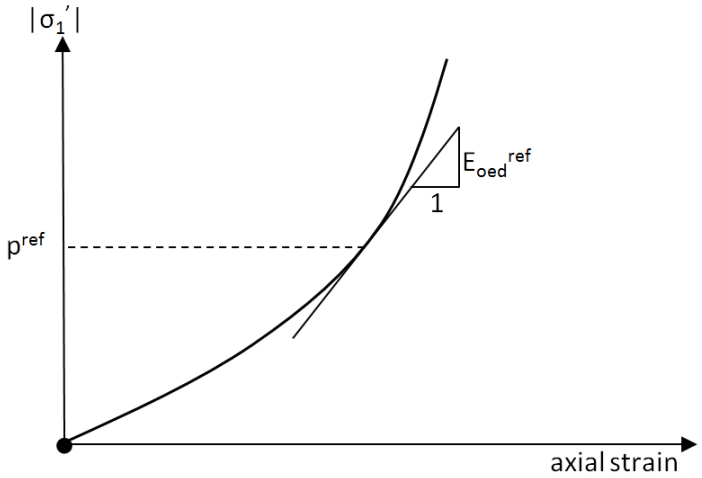

Figure 2.3. Definition of E_{oed}^{ref} in oedometer test results.

Apart from the basic parameters for soil stiffness, already presented, additional parameters have to be introduced to fully define the HSM. In table 2.1, all the input HSM parameters are presented.

Parameter	Description	Units
	Basic parameters for soil stiffness	
E_{50}^{ref}	Secant stiffness in standard drained triaxial test	[kN/m^2]
E_{oed}^{ref}	Tangent stiffness for primary oedometer loading	[kN/m^2]
E_{ur}^{ref}	Unloading / Reloading stiffness (by default $E_{ur}^{ref} = 3E_{50}^{ref}$)	[kN/m^2]
m	Power for stress-level dependency of stiffness	[-]
	Failure parameters	
c	Effective cohesion	[kN/m^2]
φ	Effective angle of internal friction	[deg]
ψ	Angle of dilatancy	[deg]
	Advanced parameters	
ν_{ur}	Poisson's ratio for unloading-reloading (by default $\nu_{ur} = 0.2$)	[-]
p^{ref}	Reference stress for stifnesses (by default $p^{ref} = 100kN/m^2$)	[kN/m^2]
K_0^{NC}	Coefficient of lateral earth pressure associated with normally consolidated states of stress (by default $K_0^{NC} = 1 - \sin\varphi$)	[-]
R_f	Failure ratio q_f/q_a (by default $R_f = 0.9$)	[-]
$\sigma_{tension}$	Tensile strength (by default $\sigma_{tension} = 0kN/m^2$)	[kN/m^2]
$c_{increment}$	Increase of cohesion per unit of depth (by default $c_{increment} = 0kN/m^3$)	[kN/m^3]

Table 2.1. Input parameters of the Hardening Soil Model implemented in Plaxis.

2.6.1.2 Internal Parameters of the HSM implemented in Plaxis

Once the input parameters are defined, the internal parameters (α, K_s/K_c and $G_i^{ref\_inter}$) are determined by an internal iterative procedure carried out by the program Plaxis itself.

On the one hand, α and K_s/K_c are the internal parameters controlling the compression hardening yield surface definition, namely cap parameters. On the other hand, $G_i^{ref\_inter}$ is related to the shear hardening yield surface.

α is the steepness of the cap, and K_s/K_c is the ratio between the elastic swelling modulus and the elastoplastic compression modulus for isotropic compression. K_s/K_c relates the plastic volumetric strain rate ($\dot{\varepsilon}_v^{p\_c}$) to the evolution of the isotropic pre-consolidation stress ($\dot{p}_p'$) by equation (2.44).

$$\dot{\varepsilon}_v^{p\_c} = \frac{\dot{p}_p'}{H} \tag{2.44}$$

H is defined as:

$$H = \frac{1}{(K_s/K_c)-1} K_s \tag{2.45}$$

and K_s as:

$$K_s = \frac{E_{ur}}{3(1-2\nu_{ur})} \tag{2.46}$$

$G_i^{ref\_inter}$ is the internal reference initial shear modulus used to obtained the auxiliary internal parameter E_i^{inter} that is needed to define the shear hardening yield surface. $G_i^{ref\_inter}$ is firstly converted to $E_i^{ref\_inter}$ by using Hooke's law of isotropic elasticity represented by equation (2.47) and then transformed from its reference form to its global expression by equation (2.48).

$$E_i^{ref\_inter} = 2(1+\nu_{ur}) G_i^{ref\_inter} \tag{2.47}$$

$$E_i^{inter} = E_i^{ref\_inter} \left(\frac{\sigma_3' \sin\varphi + c\cos\varphi}{p^{ref} \sin\varphi + c\cos\varphi} \right)^m \tag{2.48}$$

The internal iterative procedure that Plaxis carries out in order to define and validate the internal parameters, with respect the input parameters, is based on performing a triaxial and an oedometer test. Below, this internal iterative procedure is schematically described.

- Initial Guess

The iterative procedure starts with an initial guess of the internal parameters values (α, K_s/K_c and G_i^{inter}).

- Triaxial Test Simulation

A simulation of a standard drained triaxial test at $\sigma_3 = p^{ref}$ is carried out, where G_i^{inter} is modified until E_{50}^{ref} is reproduced. As the stress path of the simulation is known, the problem can be defined incrementally, and consequently, the total vertical strains can be calculated.

$$\varepsilon_{1_{n+1}} = \varepsilon_{1_{n+1}}^{e} + \varepsilon_{1_{n+1}}^{p\_s} + \varepsilon_{1_{n+1}}^{p\_c} \tag{2.49}$$

where $\varepsilon^{e}_{1_{n+1}}$ is the elastic vertical strain at stress step $n+1$, $\varepsilon^{p\_s}_{1_{n+1}}$ is the plastic vertical strain from the shear hardening yield surface at stress step $n+1$, and $\varepsilon^{p\_c}_{1_{n+1}}$ is the plastic vertical strain from the compression hardening yield surface at stress step $n+1$.

$$\varepsilon^{e}_{1_{n+1}} = \frac{q_{n+1}}{E^{ref}_{ur}} \tag{2.50}$$

$$\varepsilon^{p\_s}_{1_{n+1}} = \frac{1}{E^{ref\_inter}_{i}} \frac{q_{n+1}}{1-{q_{n+1}}/{q_a}} - \frac{q_{n+1}}{E^{ref}_{ur}} \tag{2.51}$$

$$\varepsilon^{p\_c}_{1_{n+1}} = \varepsilon^{p\_c}_{v_{n+1}} \tan^{-1}\theta_{n+1} \tag{2.52}$$

where θ_{n+1} is the parameter that relates $\varepsilon^{p\_c}_{v_{n+1}}$ to $\varepsilon^{p\_c}_{1_{n+1}}$. In contrast to the shear hardening yield surface (f^2), the compression hardening yield surface (f^c) uses an associated flow rule for the definition of the plastic potential (g^c), as $g^c = f^c$.

$$\varepsilon^{p\_c}_{v_{n+1}} = \frac{\Delta p_p|^{n+1}_{n}}{H} + \varepsilon^{p\_c}_{v_n} \tag{2.53}$$

$$\theta_{n+1} = \tan^{-1}\left(\frac{{\partial f^c}/{\partial q_{n+1}}}{{\partial f^c}/{\partial p_{n+1}}}\right) = \tan^{-1}\left(\frac{\left({2q_{n+1}}/{\alpha^2}\right)}{2p_{n+1}}\right) \tag{2.54}$$

Figure 2.4 illustrates the procedure where G^{inter}_{i} is modified until E^{ref}_{50} is reproduced taking into account the vertical strains from the elastic region, the shear hardening yield surface and the compression hardening yield surface.

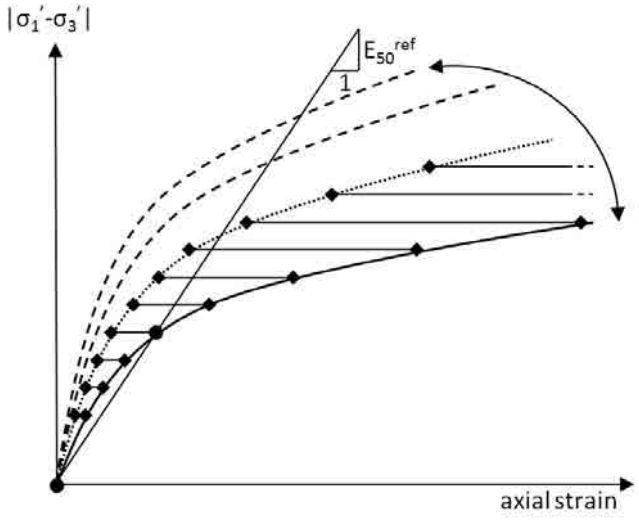

Figure 2.4. Simulation of a standard drained triaxial test at $\sigma_3 = p^{ref}$, where $G^{ref\_inter}_{i}$ is modified until E^{ref}_{50} is obtained. The dashed lines represent the curves $q-\varepsilon_1$, without taking into account $\varepsilon^{p\_c}_{1}$, while using the not proper guessed values of G^{inter}_{i}; the dotted line represents the curve $q-\varepsilon_1$, without taking into account $\varepsilon^{p\_c}_{1}$, while using the proper guessed value of G^{inter}_{i}. The horizontal lines with diamonds at the ends represent $\varepsilon^{p\_c}_{1}$, and its combination with the curve $q-\varepsilon_1$ (for the proper value of G^{inter}_{i}) matches the actual curve $q-\varepsilon_1$ (solid line) defined by E^{ref}_{50} .

- Oedometer Test Simulation

A simulation of an oedometer test is then performed. The initial stress conditions are defined as: $\sigma_1' = p^{ref}$ and $\sigma_3' = K_0^{NC} p^{ref}$. Then, several small vertical stress increments are applied, while checking the vertical and horizontal strains. If the horizontal strain is not zero, the value of K_0^{NC} is changed until the horizontal strain is zero ($K_0^{NC\_inter}$). After that, the oedometer modulus from the simulated test can be identified ($E_{oed}^{ref\_inter}$). Figure 2.5 illustrates the simulated oedometer.

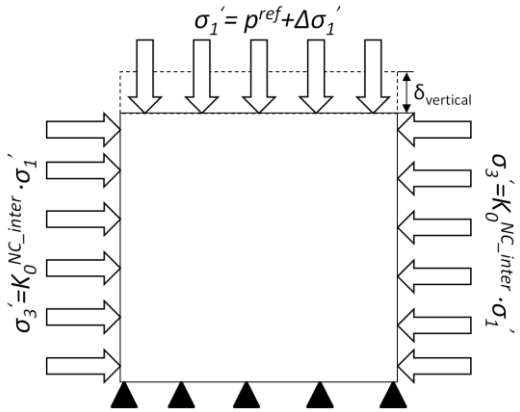

Figure 2.5. Simulation of the oedometer carried out during the internal iterative process.

If the values of $K_0^{NC\_inter}$ and $E_{oed}^{ref\_inter}$ are not close enough to the input values of K_0^{NC} and E_{oed}^{ref}, the entire internal iterative procedure is started again by defining a new guessed values of α, K_s/K_c and $G_i^{ref\_inter}$. However, if the values are close enough, a Newton iteration process is carried out in order to finally get a full match between $K_0^{NC\_inter}$ and K_0^{NC}, and $E_{oed}^{ref\_inter}$ and E_{oed}^{ref}. Then, the internal iterative procedure is considered completed.

- Limitations

In some cases, it is not possible to match all the input parameters and the final values of α, K_s/K_c and $G_i^{ref\_inter}$. In those cases, Plaxis suggests to the user the values of $K_0^{NC\_inter}$ and $E_{oed}^{ref\_inter}$ as input parameters for K_0^{NC} and E_{oed}^{ref}. In general, the reason of the failure is associated with values of α smaller than the horizontal ($\alpha \to 0$), values of α higher than the vertical ($\alpha \to \infty$), or values of $K_s/K_c < 1$, which completely deactivate the compression hardening yield surface.

Chapter 3

Optimization Algorithms

3.1 Introduction

As indicated in Chapter 2, the backanalysis problem can be reduced to minimize or maximize a function that compares measurements with calculations. Many optimization methods have been defined and adapted to specific functions; and thereby the classification of the different types of methods. In this thesis, three main categories of methods have been used:

1) Gradient Based Methods

2) Direct Methods

3) Hybrid Methods

The gradient based methods are those methods that require the evaluation of the gradient of the objective function, while the direct methods are those ones that evaluate directly the objective function without the need of using the gradient of the function. However, the majority of the direct methods use some sort of criteria to properly and efficiently drive the optimization procedure. The hybrid methods represent the category of those methods that combine more than one method. Here, only a limited number of methods representing the three different categories are presented. The gradient based methods are represented by the Gauss-Newton method and the Marquardt method; the direct methods are represented by genetic algorithms (quite often genetic algorithms are included in some subcategories like the

stochastic or evolutionary ones) and, finally, the hybrid methods are represented by a method based on the combination of a gradient based method and genetic algorithms.

More comprehensive classifications can be consulted in Eykhoff (1974), Fletcher (1981), Scales (1986) and Goldberg (1989a).

3.2 Gradient Based Methods

3.2.1 Introduction

As its name points out, the gradient based methods are based on evaluating the gradient of the objective function. As a consequence, the objective function has to be continuous in the whole domain.

Traditionally, the gradient based methods have been widely used, especially for smooth functions with few local minima, and usually with few parameters to be identified. For cases like non-smooth functions or too many parameters, the gradient based methods can become quite unstable and their efficiency may rapidly decrease. Moreover, a initial guess of the parameters ($\boldsymbol{p}_t$, for $t = 0$) is needed to define a starting point, which in many cases is not straightforward and, unfortunately, it has an strong impact on the performance of the optimization process and on the final result.

In general, the gradient based methods can be described as an iterative procedure driven by a scheme such as:

$$\boldsymbol{p}_{t+1} = \boldsymbol{p}_t + \Delta\boldsymbol{p} \tag{3.1}$$

and

$$J_{t+1} < J_t \tag{3.2}$$

where J is the value of the objective function, $\boldsymbol{p}_{t+1}$ is the new guess of the parameters, and $\Delta\boldsymbol{p}$ is the increment of parameters from the previous guess.

Figure 3.1 illustrates the scheme followed by the gradient based methods, for a case where two parameter are identified (p_1 and p_2).

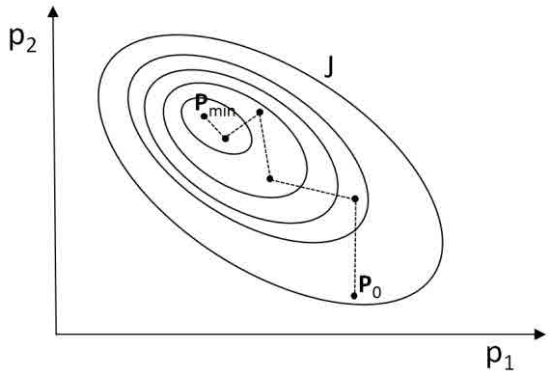

Figure 3.1. Gradient based methods scheme. P_0 is the starting point and P_{min} the value of p_1 and p_2 in the minimum.

Many different gradient based methods have been defined depending on the procedure applied to define $\Delta \boldsymbol{p}$. In the following two sections (3.2.2 and 3.2.3), the Gauss-Newton method and the Marquardt method are presented.

3.2.2 Gauss-Newton Method

While using an objective function defined by the maximum likelihood method, the advancing parameter vector ($\Delta \boldsymbol{p}$), using the Gauss-Newton method, is as shown in equation (3.3).

$$\Delta \boldsymbol{p} = (\boldsymbol{A}^T \boldsymbol{C}_x^{-1} \boldsymbol{A})^{-1} \boldsymbol{A}^T \boldsymbol{C}_x^{-1} \left(\boldsymbol{x}^{me} - \boldsymbol{x}^{cal} \right) \tag{3.3}$$

where $\boldsymbol{A}$ is the matrix that contains the derivatives of the computed variables with respect to the parameters, commonly referred as the sensitivity matrix, $\boldsymbol{C}_x$ is the measurements covariance matrix (see section 2.4), $\boldsymbol{x}^{me}$ are the measured variables, and $\boldsymbol{x}^{cal}$ are the computed variables.

In equation (3.3), the importance of $\boldsymbol{A}$ is evident. However, getting $\boldsymbol{A}$ is not usually easy. Here, the forward finite difference scheme has been used to define $\boldsymbol{A}$.

$$(\boldsymbol{A})_{i,j} = \frac{\partial x_i^{cal}}{\partial p_j} \approx \frac{x_i^{cal}\left(p_j + \Delta p_{FFD_j}\right) - x_i^{cal}(p_j)}{\Delta p_{FFD_j}} \tag{3.4}$$

$$i = 1, \dots, number\ of\ measurements$$

$$j = 1, \dots, number\ of\ parameters$$

where Δp_{FFD_j} is a very small increment of the parameter j.

When using an objective function based on the maximum likelihood method using a relative error (section 2.3.5), $\Delta \boldsymbol{p}$ is defined as shown in equation (3.5).

$$\Delta \boldsymbol{p} = \left(\boldsymbol{A}^T \boldsymbol{B}^T \boldsymbol{C}_{x\_cv2}^{-1} \boldsymbol{B} \boldsymbol{A} \right)^{-1} \boldsymbol{A}^T \boldsymbol{B}^T \boldsymbol{C}_{x\_cv2}^{-1} \boldsymbol{a}^x \tag{3.5}$$

where $\boldsymbol{C}_{x\_cv2}$ is the matrix of the square coefficient of variation of the measurements (see section 2.4), $\boldsymbol{B}$ is an auxiliary diagonal matrix defined in equation (3.6), and $\boldsymbol{a}^x$ is the vector of the relative difference between $\boldsymbol{x}^{me}$ and $\boldsymbol{x}^{cal}$ (eq. 2.14). The sensitivity matrix ($\boldsymbol{A}$) used in equation (3.5) is exactly equal to the one that appears in equation (3.3).

$$(\boldsymbol{B})_{i,j} = \begin{cases} i = j \rightarrow \frac{1}{x_i^{me}} \\ i \neq j \rightarrow 0 \end{cases} \tag{3.6}$$

$$i = 1, \dots, number\ of\ measurements$$

$$j = 1, \dots, number\ of\ measurements$$

If $\boldsymbol{C}_x$ and $\boldsymbol{C}_{x\_cv2}$ are changed to a "weighted" diagonal matrix, equations (3.3) and (3.5) are adapted in the case where the objective function is based on the Markov method. Subsequently, if this "weighted" diagonal matrix is represented by the identity matrix, (3.3) and (3.5) correspond to the case where the objective function is based on the Least-Squares method.

3.2.3 Marquardt Method

In order to improve the convergence properties of the Gauss-Newton method, especially while having ill conditioned matrices, Levenberg (1944) and subsequently Marquardt (1963) introduced some modifications. Those modifications to the Gauss-Newton method are known as the Marquardt method.

The expression for the advancing vector ($\Delta\boldsymbol{p}$) when using an objective function based on the maximum likelihood method is as follows:

$$\Delta\boldsymbol{p} = (\boldsymbol{A}^T\boldsymbol{C}_x^{-1}\boldsymbol{A} + \mu\boldsymbol{I})^{-1}\boldsymbol{A}^T\boldsymbol{C}_x^{-1}\left(\boldsymbol{x}^{me} - \boldsymbol{x}^{cal}\right) \tag{3.7}$$

while for the case where using an objective function based on the maximum likelihood method using a relative error, $\Delta\boldsymbol{p}$ is obtained from:

$$\Delta\boldsymbol{p} = \left(\boldsymbol{A}^T\boldsymbol{B}^T\boldsymbol{C}_{x\_cv2}^{-1}\boldsymbol{B}\boldsymbol{A} + \mu\boldsymbol{I}\right)^{-1}\boldsymbol{A}^T\boldsymbol{B}^T\boldsymbol{C}_{x\_cv2}^{-1}\boldsymbol{a}^x \tag{3.8}$$

where μ is the Marquardt parameter ($\mu \in [0, \infty)$), and $\boldsymbol{I}$ is the identity matrix.

Obviously, the Gauss-Newton method is a particular case of the Marquardt method when $\mu = 0$.

From an efficiency point of view, the Gauss-Newton method has a lower computational cost than the Marquardt method. However, for cases where $\boldsymbol{C}_x$ and $\boldsymbol{C}_{x\_cv2}$ are ill conditioned, the use of the Marquardt method is more appropriate.

The Marquardt method can be geometrically interpreted as figure 3.2 illustrates. If $\mu = 0$, the method goes towards the minimum of a tangent paraboloid of the objective function; while, if $\mu \to \infty$, the method follows the local gradient direction.

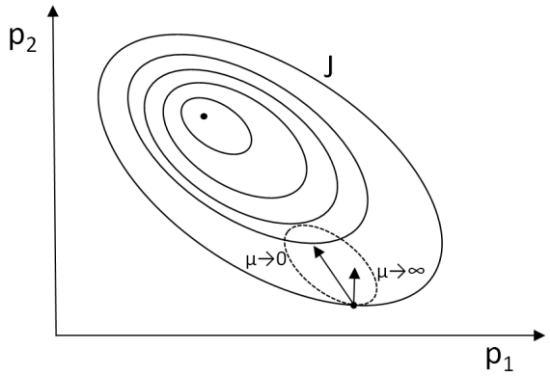

Figure 3.2. Marquardt direction scheme. For $\mu = 0$ the method goes towards the minimum of a tangent paraboloid of the objective function (J), while if $\mu \to \infty$ the method follows the gradient direction.

Marquardt (1963) proposed a scheme to modify μ along the iterative process in order to optimize the number of iterations (see figure 3.3). First, μ is set to an initial value ($\mu = \mu_{k=1}$). Then, Δp_k is computed according to equation (3.7) or (3.8) and the value of the objective function (J_k) is compared with the value of the objective function (J_{k+1}) from the possible next iteration $k + 1$. The definition of the possible next iteration is mainly controlled by the value of μ_k. On the one hand, if $J_{k+1} \leq J_k$, it means that the iterative process is working properly, the

value of μ_{k+1} is defined as $\mu_{k+1} = \mu_k/\rho$, and the iterative process keeps running forward. ρ is a Marquardt parameter modifying μ. As a consequence, the closer to the minimum is, the closer the value of μ_{k+1} is to 0 ($\rho > 1$). On the other hand, if $J_{k+1} > J_k$, it means that the iterative process is not working properly, a new value of μ_k has to be defined as $\mu_k^* = \mu_k\rho$. Then, the new value of the objective function (J_{k+1}^*) from the new possible next iteration $k+1$ is evaluated. This last step is repeated as many times as needed to get $J_{k+1}^* < J_k$.

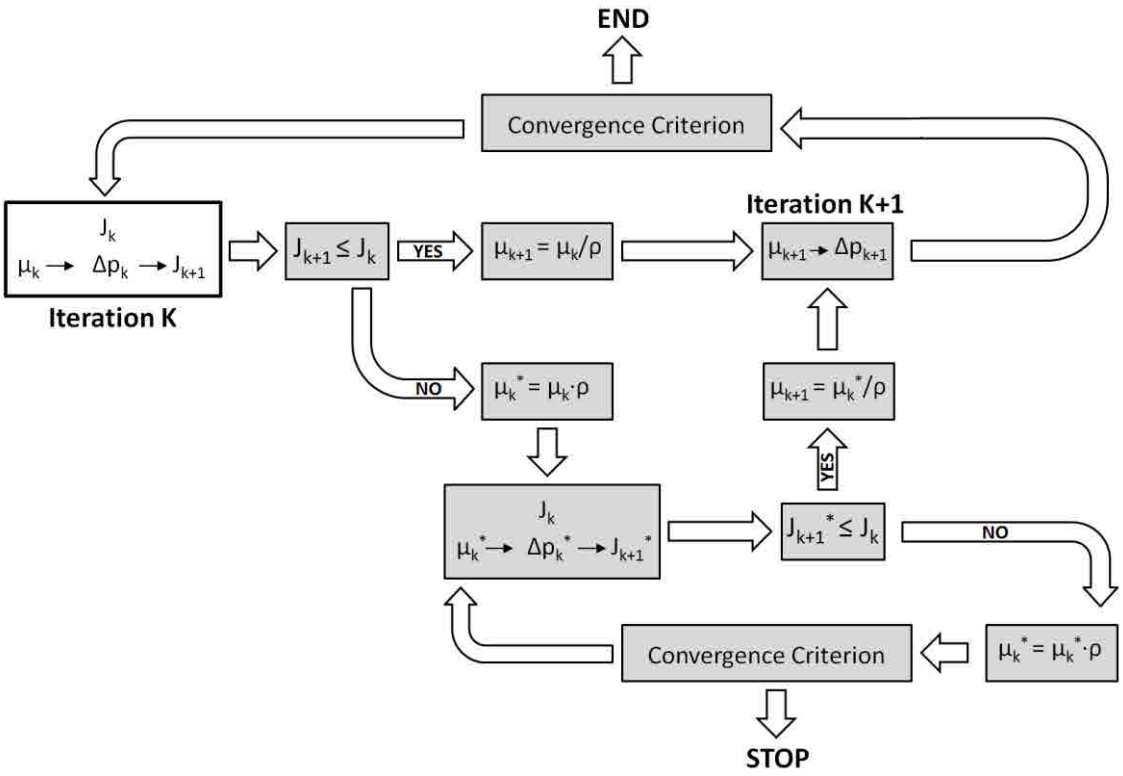

Figure 3.3. Marquardt iterative scheme.

3.3. Genetic Algorithms

3.3.1. Introduction

Genetic algorithms (GAs) are defined as a search procedure based on the mechanism of natural evolution where selection and genetics are involved. Any mention of evolution is strongly linked to Charles Darwin (1859). He introduced the idea of natural selection as the mechanism whereby small heritable variations in individuals can induce an increase in fitness (a measure of the adaptation degree of an organism to the environment). What might cause such variations was something that Darwin could only speculate on, and not until Gregor Mendel (1865) discovered the basis of genetic inheritance that Darwin's ideas were formally defined.

The vision of defining an artificial algorithm capable of mimicking the evolutionary process of nature was initially developed by Holland (1975) and subsequently fully defined by Goldberg (1989a), one of Holland's pupils at the University of Michigan. From those studies the following features were identified:

- Evolution occurs on chromosome level.

- Reproduction is the exact moment when evolution takes place.

- Selection is the process where individuals are chosen for reproduction.

- Good individuals (high fitness) are more likely to be involved in the reproductive process.

- Crossover produces new individuals (offspring) from combining the chromosomes of the parents (selected individuals).

- Mutation introduces new genetic material into the population.

- All the knowledge needed for producing good individuals is enclosed in the genes of the chromosomes.

Robustness is the main reason of using genetic algorithm. However, that robustness is often associated with high computational cost compared to more conventional optimization procedures. The most distinctive features of genetic algorithms are:

- GAs work with a coding of the parameter set, not the parameters themselves.

- GAs search from a population of points, not from a single point.

- GAs use objective function information, instead of derivatives or other auxiliary knowledge.

- GAs use probabilistic transition rules, instead of deterministic ones.

3.3.2. Basic Genetic Algorithm Foundations

Schematically the structure of a genetic algorithm can be described as shown in figure 3.4; where: First, an initial population of possible solutions (individuals) is created. Then, the goodness of the individuals is evaluated (fitness). Subsequently, the operators involved in the evolutionary process are applied (selection, crossover and mutation). After that, the new population is created. This sequence is looped until the convergence criterion is reached.

Concepts as initial population, fitness, selection, crossover and mutation are fully defined in following sections.

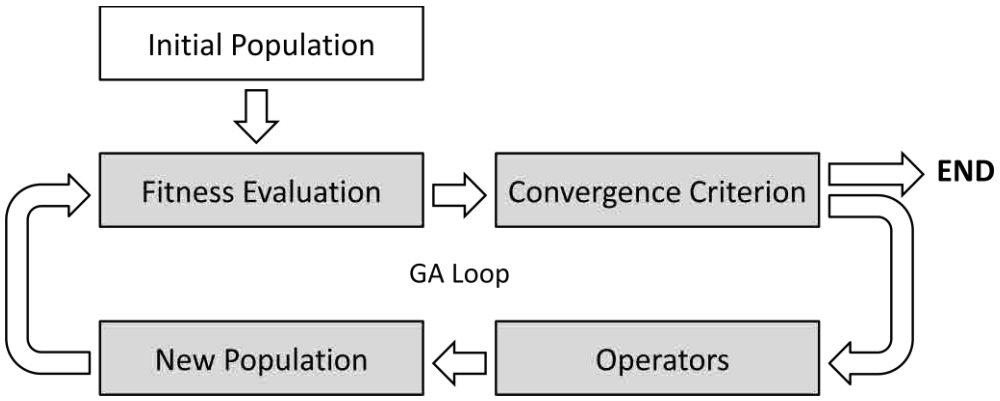

Figure 3.4. Schematic genetic algorithms structure.

The mathematical foundations of genetic algorithms laid on the Schema Theorem, also known as the Fundamental Theorem of Genetic Algorithms, defined by Goldberg (1989a).

Prior to presenting the Theorem it is required to introduce the concept of schema and the notion of length and order of a schema.

A schema is a subset of the space A^l (search space of l-*dimensions*) in which all chromosomes share a particular set of defined values.

This can be represented by using the alphabet AU*, where the * symbol is a free bit. In the binary case (1**1), for example, represents the subset of the 4-dimensional hypercube {0, 1}^{4} in which both, the first and the last bit takes the value 1. All individuals sharing the schema (1**1) are represented by the chromosomes {(1001), (1011), (1101), (1111)}.

Schema can thus be thought of in set-theoretic terms, as defining subsets of similar chromosomes, or geometrically, as defining hyperplanes in l-dimension space.

It is clear that any specified chromosome is an instance of many schemata. In general, if the string has length l, each chromosome is an instance of $|A|^l$ distinct schemata, since at each bit it can take either a * or its actual value (it's assumed that the full chromosome itself and the all * string are also schemata). As a consequence, each time the fitness of a given chromosome is evaluated, Information about the average fitness of each schema of the given chromosome is being gathered. Using binary alphabet, a population of *N* individuals could contain $N \cdot 2^l$ schemata. However, in practice there will be considerable overlapping between strings and not all schemata will be equally represented. In fact, what it is wanted is an unequal representation where the genetic algorithm focuses its attention on those that are fitter.

The distance between the first and the last defined position on the schema is the length of the schema ($\delta(schema)$). And the number of defined positions is the order of the schema ($o(schema)$). Hence the schema (1**1) has length 3 and order 2.

3.3.2.1. Fundamental Theorem of Genetic Algorithms

Supposing that at a given time step *t* (generation) there are *m* individuals of a particular schema *H* contained within the population *A(t)*; the expected number of individuals of a particular schema *H* contained within the population *A(t+1)* at time step *t+1* is:

$$m(H, t+1) = m(H, t) \cdot \frac{f(H)}{\bar{f}} \tag{3.9}$$

where $f(H)$ is the average fitness of the individuals representing schema *H* at time *t* and $\bar{f}$ the average fitness of the entire population.

Then, it can be inferred that a particular schema grows as the ratio of the average fitness of the schema to the average fitness of the population. In other words, schemata with fitness values above the population average will receive higher number of samples in the next generation, while schemata with fitness value below the population average will receive a lower number of samples. It is interesting to observe that this expected behavior is carried out with every schema *H* contained in a particular population *A* in parallel.

If it's assumed that a particular schema *H* remains above average an amount $c\bar{f}$ with c a constant, equation (3.9) can be rewritten as follows:

$$m(H,t+1) = m(H,t) \cdot \frac{(\bar{f}+c\bar{f})}{\bar{f}} = (1+c) \cdot m(H,t) \tag{3.10}$$

Starting at t=0 and assuming a stationary value of c, the previous equation (3.10) can be rewritten as:

$$m(H,t) = m(H,0) \cdot (1+c)^t \tag{3.11}$$

Equation (3.11) can be recognized as a geometric progression or the discrete analog of an exponential form. To some extent it can be stated that the number of good individuals (individuals with fitness above the average) of a particular schema *H* increases exponentially in future generations.

In order to fully define the mechanism of genetic algorithms, it is needed to introduce the effect of crossover and mutation in equation (3.11), which represents the effect of reproduction.

If crossover is itself performed by random choice with probability P_c at a particular mating, the survival probability against crossover may be given by the expression (3.12).

$$P_{cs} \geq 1 - P_c \cdot \frac{\delta(H)}{l-1} \tag{3.12}$$

Defining mutation as the random alteration of a single position with probability P_m, and since a single bit survives with probability (1 - P_m), and since each mutation is statistically independent, a particular schema survives against mutation when each of the *o(H)* positions within the schema survives. The expression of mutation survival probability is as followed:

$$P_{ms} \geq (1 - P_m)^{o(H)} \tag{3.13}$$

For small values of P_m ($P_m << 1$), expression (3.13) may be approximated by expression (3.14):

$$P_{ms} \geq 1 - o(H) \cdot P_m \tag{3.14}$$

Therefore, if equations (3.9), (3.12) and (3.14) are finally combined, the mechanism of genetic algorithms are fully defined by equation (3.15), known as the Schema Theorem or the Fundamental Theorem of Genetic Algorithms.

$$m(H,t+1) \geq m(H,t) \cdot \frac{f(H)}{\bar{f}} \left[1 - P_c \cdot \frac{\delta(H)}{l-1} - o(H) \cdot P_m\right] \tag{3.15}$$

In conclusion, it can be stated that: high-performance, short-defining-length and low-order schemata receive at least exponentially increasing number of trials in successive generations.

3.3.3. Simple Genetic Algorithm (SGA)

The structure of a simple genetic algorithm is shown in figure 3.5. All the different elements involved in a SGA are fully described in the following sections.

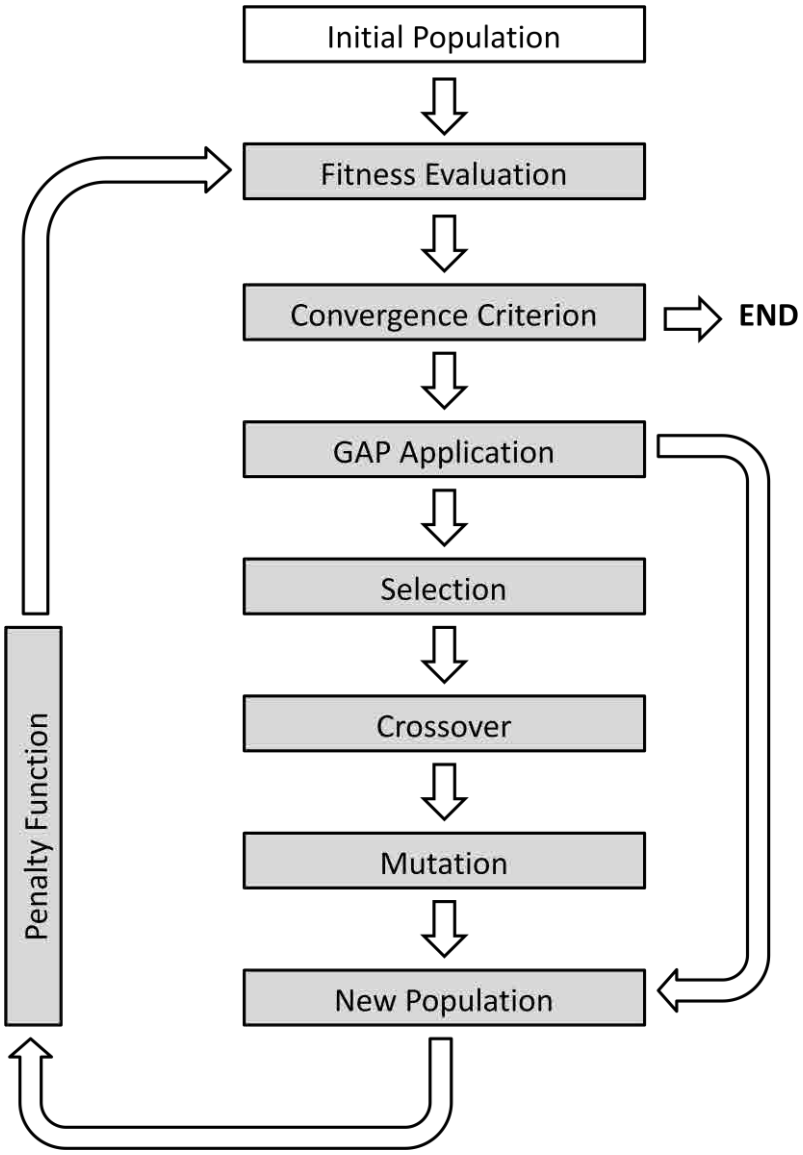

Figure 3.5. Simple Genetic Algorithm structure.

3.3.3.1 Initial Population

The major questions to consider are firstly the size of the population, and secondly the method by which the individuals are chosen. The choice of the population size has been approached from several theoretical points of view, although the underlying idea is always of a trade-off between efficiency and effectiveness. Intuitively, it would seem that there should be some "optimal" value for a given string length on the grounds that too small populations would not allow sufficient room for exploring the search effectively, while too large populations would penalize the efficiency of the method such as no solution could be expected in a reasonable computational cost.

Many empirical studies were carried out during the 70's and 80's. The most representative ones were done by De Jong (1975), Brindle (1981), Grefenstette (1986) and Schaffer et al. (1989), where a population size between 20 and 100 individuals was found optimal; for the problems studied in those cases.

Goldberg (1985) attempted to solve the population size issue by using the idea of schemata. Unfortunately, from this point of view, it appeared that the population size should increase as an exponential function of the string length. Some refinements of this work were reported by Goldberg (1989b), but they do not change the overall conclusions significantly.

A later analysis from a different perspective was done by Goldberg et al. (1992), where it was found that a linear dependence of population size on string length was adequate. The population should grow with string length. However, even a linear growth rate would lead to quite large population in some cases.

Referring to how the initial population has to be chosen, it is nearly always assumed that initialization should be random. However, individuals chosen in this way do not necessary cover the search space uniformly, and there may be advantages in terms of covering if more sophisticated statistical method is used, especially for more complex alphabets than the binary alphabet. Recent studies have been done for binary alphabet where the concept of diversity was used to quantify the "quality" of an initial population. In Diaz-Gomez & Hougen (2007a) a metric approach to measure diversity at a population level was introduced. Some empirical results of the relationship between initial diversity and GA's performance were presented in Diaz-Gomez & Hougen (2007b). However, Diaz-Gomez & Hougen (2009) pointed out that there was not such strong correlation between initial diversity and GA performance, at least for the standard range of diversity often encountered in binary random initial populations.

3.3.3.2. Fitness Evaluation

The fitness evaluation is the genetic algorithm stage where the goodness of the individuals, with respect to the environment, is evaluated. The objective function is the function in charge of defining the fitness of all individuals.

$$f = \frac{1}{J} \tag{3.16}$$

where f is the fitness of an individual and J is the value of the objective function associated to the individual.

As shown in section 2.3 (Objective Function), different objective functions can be used to evaluate the goodness of the individuals.

3.3.3.3. Convergence Criterion

The method to terminate the GA procedure is by applying a convergence criterion. Because of its multi-point evaluation nature (population rather than points), usually, several tolerance parameters are simultaneously used. The most frequently used tolerance parameters for genetic algorithms are:

- The maximum number of generations.

- The fitness of the best individual.

- The average fitness of the population.

- The diversity of the population.

- The number of new individuals for generation.

3.3.3.4. GAP Application

The GAP application controls the fraction of new individuals *A(t+1)* generated by the reproductive process (selection + crossover + mutation). The fraction of individuals that skip the reproductive process are randomly chosen. The main goal of applying a generation GAP is to avoid premature convergence. An extensive analysis on GAP application and its implications was done by De Jong (1975), where high values of generation GAP (between 0.8 and 1) were found suitable ($0 \leq GAP \leq 1$, if GAP = 0 => no new individual is generated by reproduction, while if GAP = 1 => all new individuals are generated by reproduction) .

3.3.3.5. Selection

Selection is the process of choosing individuals for birth according to their fitness. Many methods have been studied, especially by Goldberg & Deb (1991), of how to carry out this selection. The most used selection methods are: the roulette wheel selection (De Jong, 1975) and the tournament selection (attributed to an unpublished work of Wetzel and subsequently studied in Brindle, 1981).

The probability of selecting a specific individual at the step time t (generation t) by the roulette wheel is as follows:

$$P_{roulette}(t) = \frac{f}{N \cdot \bar{f}} \tag{3.17}$$

where f is the fitness of the specific individual, $\bar{f}$ the average fitness of the entire population at the step time t and *N* is the population size.

Figure 3.6 illustrates equation (3.17).

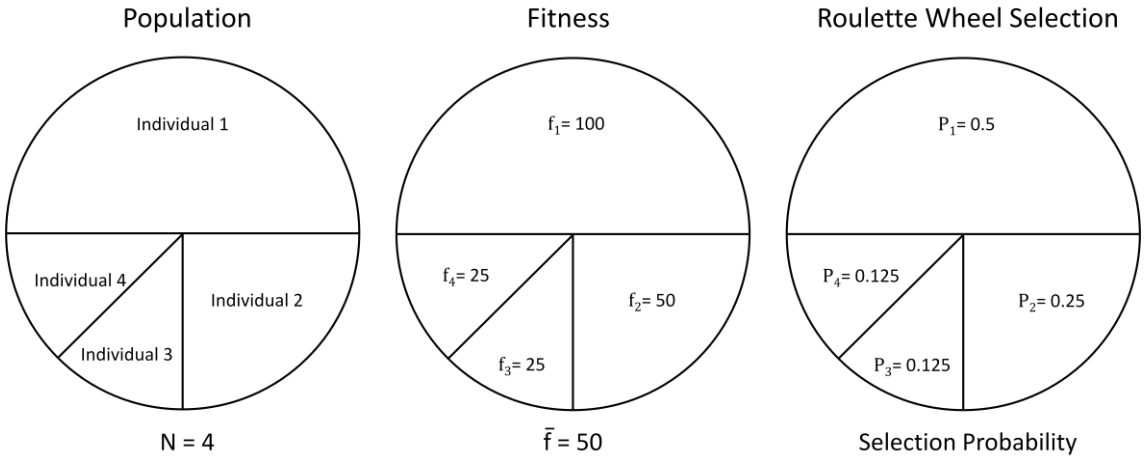

Figure 3.6. Roulette Wheel Selection.

The concept of tournament selection is based on selecting the best individual from a randomly selected group of individuals (see figure 3.7). The size of this group is known as tournament

size. The bigger the tournament size is, the higher the selection pressure is. And, the lower the tournament size is, the lower the selection pressure is. Selection pressure quantifies the weight given to the fitness during the selection process.

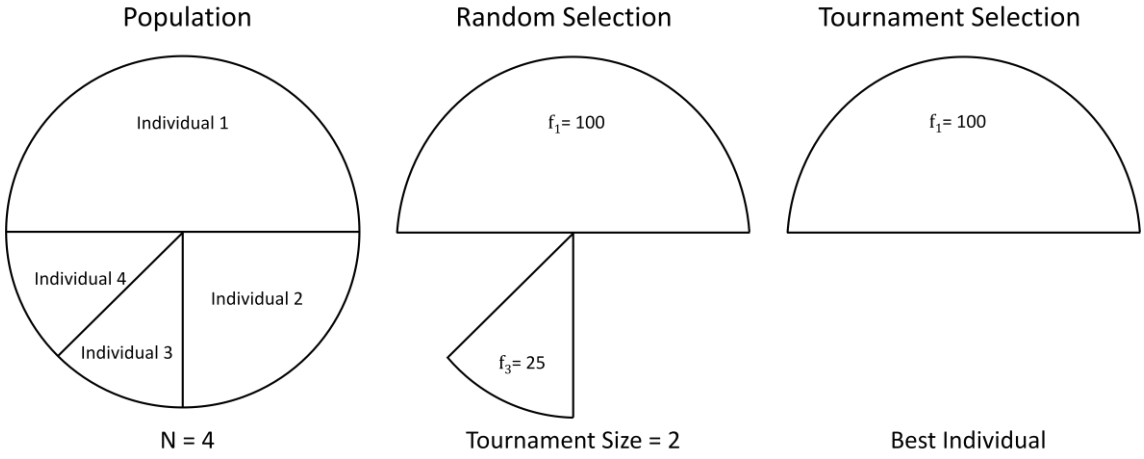

Figure 3.7. Tournament Selection.

3.3.3.6. Crossover

The crossover stage is where the chromosomes of the parents are combined to create their offspring. The combination of the parents "DNA" is done by concatenating part of the father chromosome with part of the mother chromosome. The chromosome portions from each other are defined by the crossover point. Usually, the crossover point is a random single point, which specifies the point where the chromosome is going to be cut and subsequently concatenated. In De Jong & Spears (1992), an exhaustive analysis was carried out in order to study the effect of applying multi-point crossover. However, it was concluded that single point crossover was the most suitable manner to cut the parents chromosomes for recombination.

The application of the crossover operator is controlled by the crossover probability P_c. Several empirical studies have been done in order to set a suitable value of P_c. However, significant discrepancies were obtained due to the high problem dependency. De Jong (1975) concluded that 0.6 was the most suitable value of P_c, Grefenstette (1986) P_c=0.95 and Schaffer et al (1989) P_c=0.75-0.95.

The crossover procedure is illustrated in figure 3.8.

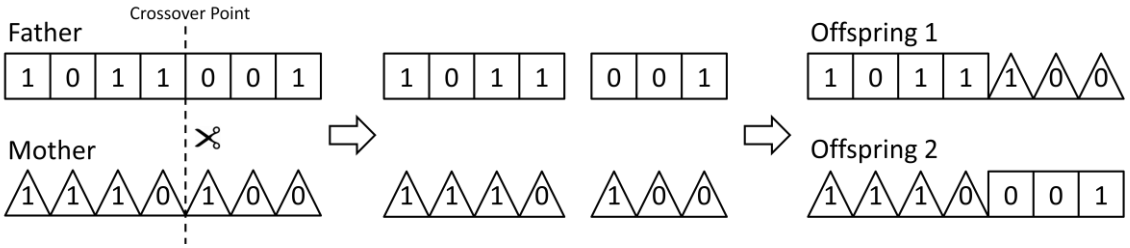

Figure 3.8. Crossover Procedure.

The main role of crossover is searching around good individuals in order to promote potential high fitness domains (see figure 3.9). This process is known as EXPLOITATION.

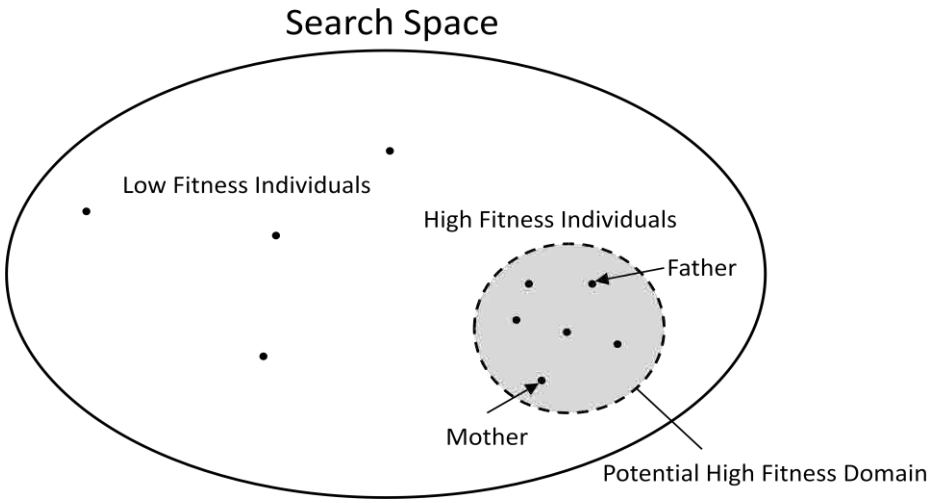

Figure 3.9. Exploitation of Potential High Fitness Domains by Crossover Operator.

3.3.3.7. Mutation

Mutation is the process where bits of a chromosome are randomly replaced by another to yield a new structure.

The application of mutation is commanded by the mutation probability P_m. Several empirical studies have been done in order to set a suitable value of P_m. However, similarly to crossover, significant discrepancies were obtained due to the high problem dependency. De Jong (1975) concluded that 0.001 was the most suitable value of P_m, Grefenstette (1986) P_m=0.01 and Schaffer et al. (1989) P_m=0.005-0.01.

The mutation process is illustrated in figure 3.10.

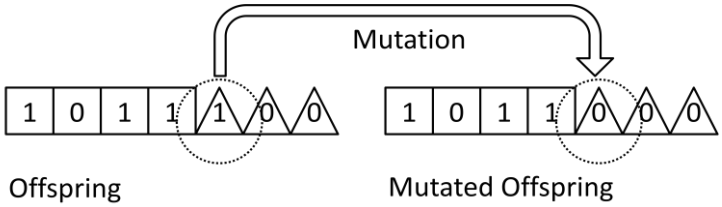

Figure 3.10. Mutation Procedure.

The main role of mutation is searching for new potential high fitness domains. This process is known as EXPLORATION.

3.3.3.8. New Population

The new population is constituted by the offspring (from the reproductive process) and the fraction of individuals not involved in the reproductive process (GAP application). It is assumed that generation after generation the individuals forming the more evolved populations will have higher fitness, or at least some of them.

Frequently, in order to avoid the loss of the best individual, the survival of the best individual is ensured by preserving it and replacing only the remaining (*N* - 1) members of the new population. This is what De Jong (1975) defined as *Elitism*.

3.3.3.9 Penalty Function

Commonly, there is no guarantee that two feasible parents will provide feasible offspring. The most obvious solution to the problem of constraints is simply to ignore them (if an infeasible solution is encountered, it is not allowed to enter the next population). However, this fails to recognize that the degree of infeasibility does supply some information too. It is common to find the global minimum on or near a constraint boundary, so that solutions that are slightly unfeasible my actually help to drive the search procedure to the optimum. This is reflected in Golver & Laguna (1993).

A frequent way of dealing with candidate solutions that violate the constraints is to generate potential solutions without considering the constraints and then penalizing them by decreasing the value of their fitness. In other words, a constrained problem is transformed to an unconstrained problem by combining a penalty function with the objective function. However, though the objective function is usually well defined, there is no accepted methodology for combining it with the penalty function. Davis (1987) studied the advantages and disadvantages of using high, moderate, or light penalties, and concluded that:

If one incorporates a high penalty into the evolution routine and the domain is one in which production of an individual violating the constraint is likely, one runs the risk of creating a genetic algorithm that spends most of its time evaluating illegal individuals. Further, it can happen that when a legal individual is found, it drives the others out and the population converges on it without finding better individuals, since the likely paths to other legal individuals require the production of illegal individuals as intermediate structures, and the penalties for violating the constraint make it unlikely that such intermediate structure will reproduce. If one imposes moderate penalties, the system may evolve individuals that violate the constraint but are rated better than those that do not because of the objective function can be satisfied better by accepting the moderate constraint penalty than by avoiding it.

Some approaches for using penalty functions in genetic algorithms can be found in Siedlecki & Skanska (1989), and Richardson et al. (1989).

3.3.3.10 SGA Limitation

After defining in detail the different steps of a simple genetic algorithm and the operators involved in it, the basic performance of a genetic algorithm can be understood as a process focused on finding high fitness individuals in high fitness domains (EXPLOITATION) and trying to find new high fitness individuals in order to define new potential high fitness domains (EXPLORATION). Therefore, the proper performance of a genetic algorithm is based on the balance between EXPLOITATION and EXPLORATION. All parameters involved in the algorithm (population size, selection type, P_c, P_m, etc) affect that balance in some way; the main factors are the probability of crossover (P_c) to promote EXPLOITATION and the probability of mutation (P_m) to promote EXPLORATION. High values of P_c encourage EXPLOITATION, while high values

of P_m encourage EXPLORATION. Depending on the state of the evolution (generation, diversity of the population, etc) strong EXPLOITATION may drive the algorithm to a premature convergence, while if too much effort is focused on EXPLORATION, the computational cost may become unacceptable to make the algorithm competitive.

Figure 3.11 illustrates the balance between EXPLOITATION and EXPLORATION, as well as its implications for performance.

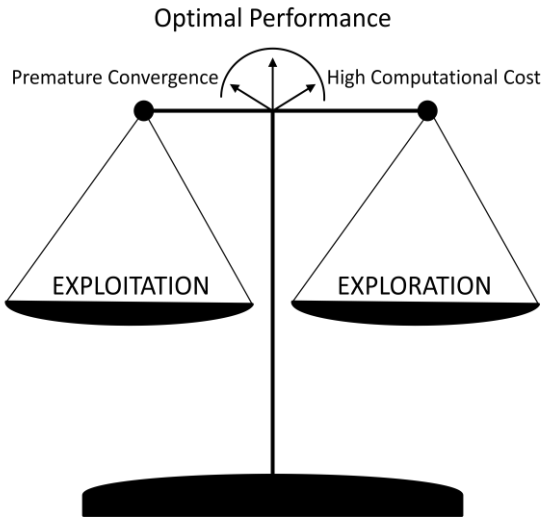

Figure 3.11. Balance between EXPOITATION and EXPLORATION.

Unfortunately, the evolutionary nature of genetic algorithms makes it impossible to define a suitable fixed proportion of EXPLOITATION and EXPLORATION. In addition, there is the limitation on parameter changes while using Simple Genetic Algorithm. That makes SGAs less reliable for complex problems.

3.3.4 Adaptive Genetic Algorithm (AGA)

3.3.4.1 Introduction

As mentioned in the previous section, the proper performance of a genetic algorithm is based on the balance between EXPLOITATION and EXPLORATION. The fact that no parameter changes occur suggests a modification of the Simple Genetic Algorithms (fixed parameters) to some kind of genetic algorithm capable to adapt its parameters while running. In general, the new genetic algorithm is known as Adaptive Genetic Algorithm. However, many authors often change slightly the name of the algorithm based on the method of varying the parameters and the parameters themselves.

Fogarty (1989) experimentally defined a dynamical mutation probability that decreases exponentially over the number of generations. Even though, the results showed an increase of performance, the experimental setup was rather specific. Hesser & Männer (1991, 1992) defined a more general expression for decreasing the mutation probability.

Schaffer & Morishma (1987) studied a crossover mechanism wherein the distribution of crossover points is adapted based on the parent fitness. In Thierens (2002) and Liu & Feng (2004) the same approach (based on fitness) was used to adapt the value of the mutation rate.

The concept of combining the parent fitness with the population diversity to adapt the crossover and the mutation rate was first introduced in Srinivas & Patnaik (1994). More recently, many researchers have used the work by Srinivas & Patnaik (1994) and adapted it for their problems. Zhu (2003) and Hagras et al. (2004) took the concept of diversity to adapt the crossover and mutation rate to their particular problems. A drawback of the Srinivas and Patnaik's method is that the population convergence is detected according to a fitness-based measure. The degree of diversity loss is calculated as $f_{max} - f_{ave}$, where f_{max} is the maximum fitness value in the population, and f_{ave} is the average population fitness. Srinivas and Patnaik hypothesize that the closer f_{ave} is to f_{max} the more converged the population is. In multimodal fitness landscapes, however, many different chromosomes can share the same fitness score, so although an average fitness value may be identical to the best fitness value, the population may be widely scattered. Mc Ginley et al. (2011) defined a new methodology based on diversity measures calculated from the genetic diversity rather than the fitness diversity within a population.

Affenzeller & Wagner (2005) presented an adaptive selection mechanism, where selection pressure is varied by adjusting the proportion of individuals involved in the reproductive procedure. In Eiben et al. (2006a, 2006b) and Mc Ginley (2011) the selection pressure is adapted by changing the tournament size (only applicable when using the tournament selection method).

3.3.4.2 Adaptive Genetic Algorithm Definition

Based on the ideas shown in Mc Ginley et al. (2011), where crossover, mutation and selection pressure is adapted, a new Adaptive Genetic Algorithm is presented. The objective of the new AGA is to create and maintain a diverse population of good individuals capable of adapting to difficult fitness landscapes.

Two measures of population diversity are employed to make the algorithm adaptable. The first measure is named Standard Population Diversity (SPD) and it describes a population's solution space diversity with no regard to the fitness of the individuals. SPD is similar to other diversity measures described in the literature, like the one described in Zhu (2003). The second measure is named Healthy Population Diversity (HPD) and it was firstly defined in Mc Ginley et al. (2011). HPD describes a population's solution space diversity from a fitness perspective.

SPD controls the crossover and mutation rates, while HPD is used to regulate selection pressure. Crossover employs SPD to divide the population into an EXPLOITATION section and an EXPLORATION section (see figure 3.11). The relative size of each section is controlled by SPD. Mutation is applied adaptively with higher probability in the EXPLORATION section to explore potentially unvisited domains, while low probability is employed in the EXPLOITATION section of the population.

Selection pressure (tournament size) is adapted according to the value of HPD. Tournament size is reduced when HPD is low (converged population) permitting lower-fitness outliers to reproduce and, by that means, protecting innovation. When HPD is high, tournament size is increased to promote "survival of the fittest".

3.3.4.2.1 Calculating SPD (SPD_j)

Because of the fact that chromosomes may represent more than one parameter, the same number of SPDs (SPD_j) as parameters represented in the chromosome have to be calculated.

If the population consists of *N* individuals, where their chromosomes are formed by concatenating strings of bits representing different parameters (see figure 3.12), SPD_j can be defined as follows:

$$SPD_j = \frac{1}{N}\sum_{i=1}^{N} SPD_{i,j} \tag{3.18}$$

where $SPD_{i,j}$ is contribution of the individual i to SPD_j. $SPD_{i,j}$ represents the average of the Euclidean distance between G_{i,j,k_j} and G_{j,k_j}^{ave}. G_{i,j,k_j} is the value of the bit k_j (parameter j and individual i) and G_{j,k_j}^{ave} is the average of G_{i,j,k_j}. Because of using binary alphabet the only possible values of G_{i,j,k_j} are 0 or 1, while the value of G_{j,k_j}^{ave} must be a value between 0 and 1. *N* represents the number of individuals in the population.

$$SPD_{i,j} = \frac{1}{l_j}\sum_{k_j=1}^{l_j} \left\| G_{i,j,k_j} - G_{j,k_j}^{ave} \right\| \tag{3.19}$$

l_j is the number of bits used to represent parameter j.

$$G_{j,k_j}^{ave} = \frac{1}{N}\sum_{i=1}^{n} G_{i,j,k_j} \tag{3.20}$$

where:

$$i = 1, \dots, N$$

$$j = 1, \dots, p$$

$$k_j = 1, \dots, l_j \begin{cases} j = 1 \rightarrow k_1 = 1, \dots, l_1 \\ j = 2 \rightarrow k_2 = 1, \dots, l_2 \\ \vdots \\ \vdots \\ j = p \rightarrow k_p = 1, \dots, l_p \end{cases}$$

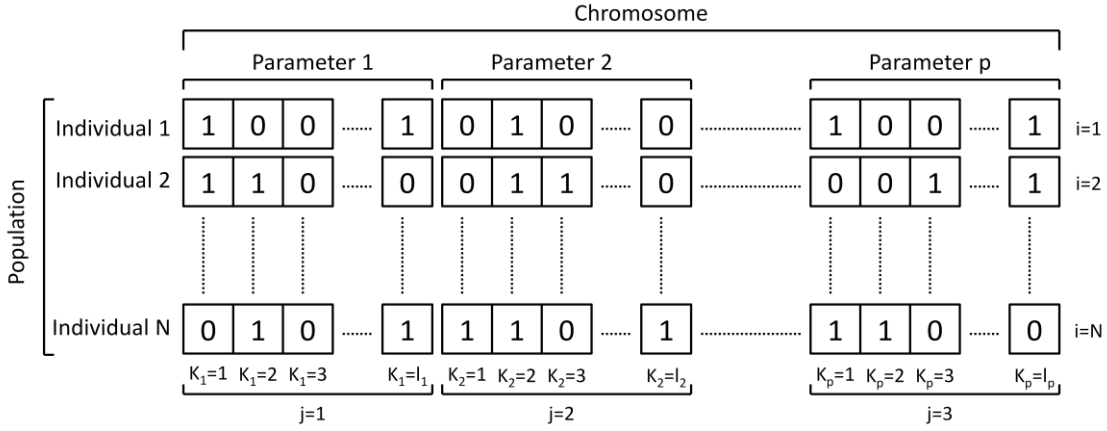

Figure 3.12. Population and individual structure.

3.3.4.2.2 Calculating HPD (HPD_j)

In contrast to SPD, HPD merges both fitness and solution spaces weighting each individual distance contribution in the solution space according to its score in the fitness space. Therefore, HPD_j can be defined as follows:

$$HPD_j = \frac{1}{N}\sum_{i=1}^{N} HPD_{i,j} \tag{3.21}$$

where $HPD_{i,j}$ is the contribution of the individual i to HPD_j. $HPD_{i,j}$ represents the average of the "weighted" Euclidean distance between G_{i,j,k_j} and $G_{j,k_j}^{w_{ave}}$. G_{i,j,k_j} is the value of the bit k_j (parameter j and individual i) and $G_{j,k_j}^{w_{ave}}$ is a "weighted" average of G_{i,j,k_j} .Because of using binary alphabet the only possible values of G_{i,j,k_j} are 0 or 1, while the value of $G_{j,k_j}^{w_{ave}}$ must be a value between 0 and 1. *N* represents the number of individuals in the population.

$$HPD_{i,j} = w_i \cdot \frac{1}{l_j}\sum_{k_j=1}^{l_j} \left\| G_{i,j,k_j} - G_{j,k_j}^{w_{ave}} \right\| \tag{3.22}$$

w_i represents the weighted factor.

$$w_i = \frac{log(f_i)}{log\ (f_{max})} \tag{3.23}$$

f_i is the fitness of the individual i and f_{max} is the maximum fitness of the population.

$$G_{j,k_j}^{w_{ave}} = \frac{1}{N}\sum_{i=1}^{n} \Phi\left(G_{i,j,k_j}, w_i\right) \tag{3.24}$$

If $G_{i,j,k_j} = 0$ then: $\Phi\left(G_{i,j,k_j}, w_i\right) = w_i$

Else if $G_{i,j,k_j} = 1$ then: $\Phi\left(G_{i,j,k_j}, w_i\right) = 1 - w_i$

3.3.4.2.3 Adaptive Crossover ($P_{c\_adaptive}$)

The mechanism to make adaptable the crossover procedure is controlled by an adaptive crossover probability ($P_{c\_adaptive}$). It should be noticed that there are as many values of $P_{c\_adaptive}$ as parameters. The value of $P_{c\_adaptive}$ is obtained by the equation (3.25) proposed by Mc Ginley et al. (2011).

$$P_{c\_adaptive_j} = \left(\frac{SPD_j}{SPD_{max}} \cdot \left(P_{c\_max} - P_{c\_min}\right)\right) + P_{c\_min} \tag{3.25}$$

where SPD_{max} = 0.5 for binary alphabet and represents the maximum value of diversity. Using binary alphabet that means that there is the same number of 0's as 1's represented in the chromosomes. P_{c_max} is the maximum crossover probability and P_{c_min} the minimum (values defined by the user).

If $SPD_j \rightarrow 0.5 \Rightarrow P_{c\_adaptive_j} \rightarrow P_{c\_max}$

Else if $SPD_j \rightarrow 0 \Rightarrow P_{c\_adaptive_j} \rightarrow P_{c\_min}$

Increasing the value of $P_{c\_adaptive}$ promotes the EXPOITATION section, while decreasing the value of $P_{c\_adaptive}$ promotes the EXPLORATION section.

3.3.4.2.4 Adaptive Mutation ($P_{m\_adaptive}$)

The adaptive mutation probability ($P_{m\_adaptive}$) is defined by combining two mechanisms. One of them is controlled by SPD (diversity) and the other one by the fitness of the parents.

Equation (3.26), also proposed by Mc Ginley et al. (2011), defines the mutation probability determined from population diversity (SPD).

$$P_{m\_adaptive_j}^{Diversity} = \left(\frac{SPD_{max} - SPD_j}{SPD_{max}}\right) \cdot P_{m\_max} \tag{3.26}$$

where P_{m_max} is the maximum applicable mutation probability.

If $SPD_j \rightarrow 0.5 \Rightarrow P_{m\_adaptive_j}^{Diversity} \rightarrow 0$

Else if $SPD_j \rightarrow 0 \Rightarrow P_{m\_adaptive_j}^{Diversity} \rightarrow P_{m\_max}$

Low diverse populations are forced to explore in order to introduce diversity.

Equation (3.27) defines the mutation probability determined from parent's fitness.

$$P_{m\_adaptive_i}^{Fitness} = P_{m\_max} \cdot \left(\frac{f_{max} - f_{parent_i}}{f_{max} - f_{min}}\right) \tag{3.27}$$

where f_{max} is the highest fitness of the population, f_{min} is the lowest fitness of the population and f_{parent_i} is the fitness of the parent of the offspring i. It should be noticed that there are as many values of $P_{m\_adaptive_i}^{Fitness}$ as individuals involved in the reproductive process.

Finally, the expression that controls the adaptive mutation procedure is shown in equation (3.28).

$$P_{m\_adaptive_{i,j}} = \frac{P_{m\_adaptive_j}^{Diversity} + P_{m\_adaptive_i}^{Fitness}}{2} \tag{3.28}$$

3.3.4.2.5 Adaptive Selection ($T_{size\_adaptive}$)

The mechanism to adapt the selection pressure is defined by the adaptable tournament size ($T_{size\_adaptive}$). Tournament selection involves selecting a number (T_{size}) of individuals randomly from the population, with the best individual from this group being selected as a parent (see section 3.3.3.5). It should be noted that the adaptive selection procedure (in this work) is only applied when using the tournament selection method. When using the roulette wheel method of selection, there is no application of any kind of adaptive selection procedure.

Equation (3.29) defines the adaptable tournament size (Mc Ginley et al. 2011).

$$T_{size\_adaptive} = \frac{\frac{1}{p}\sum_{j=1}^{p} HPD_j}{HPD_{max}} \cdot T_{size\_max} \quad (3.29)$$

where p is the number of parameters, HPD_{max} is set to 0.5 and represents the maximum diversity of population health. T_{size_max} is the maximum admissible tournament size.

The higher the tournament size is, the lower selection pressure is, while the smaller the tournament size is, the higher the selection pressure is.

If $T_{size\_adaptive} \rightarrow Population\ Size \Rightarrow Selection \rightarrow Random\ Selection$

Else if $T_{size\_adaptive} \rightarrow 1 \Rightarrow Selection \rightarrow Elitism\ Selection$

3.3.4.2.6 Adaptive Genetic Algorithm Structure

The structure of an adaptive genetic algorithm (from the GAP application stage to the new population stage) is:

1) Application of the adaptive selection operator (adaptive tournament selection). If the tournament selection method is not chosen as selection method, the selection process will not be adaptable. Nonetheless, the algorithm can still be adaptive, if in the following stages (crossover and mutation) the adaptive forms ($P_{c\_adaptive}$ and $P_{m\_adaptive}$) are used.

2) EXPLOITATION vs. EXPLORATION. Crossover defines whether EXPLOITATION or EXPLORATION is going to be applied.

On the one hand, if finally the crossover operator is applied to the chromosome, a low mutation rate is also applied. This procedure is known as EXPLOITATION section and is when the search is focused on domains represented by good individuals. On the other hand, if the crossover operator is not applied, the adaptive mutation rate is applied.

3) Construction of the new population by combining the offspring from both sections (EXPLOITATION and EXPLORATION).

It should be noticed that the processes of crossover and mutation are applied for each string of bits representing the different parameters codified in the chromosome.

Figure 3.13 illustrates the structure of an adaptive genetic algorithm.

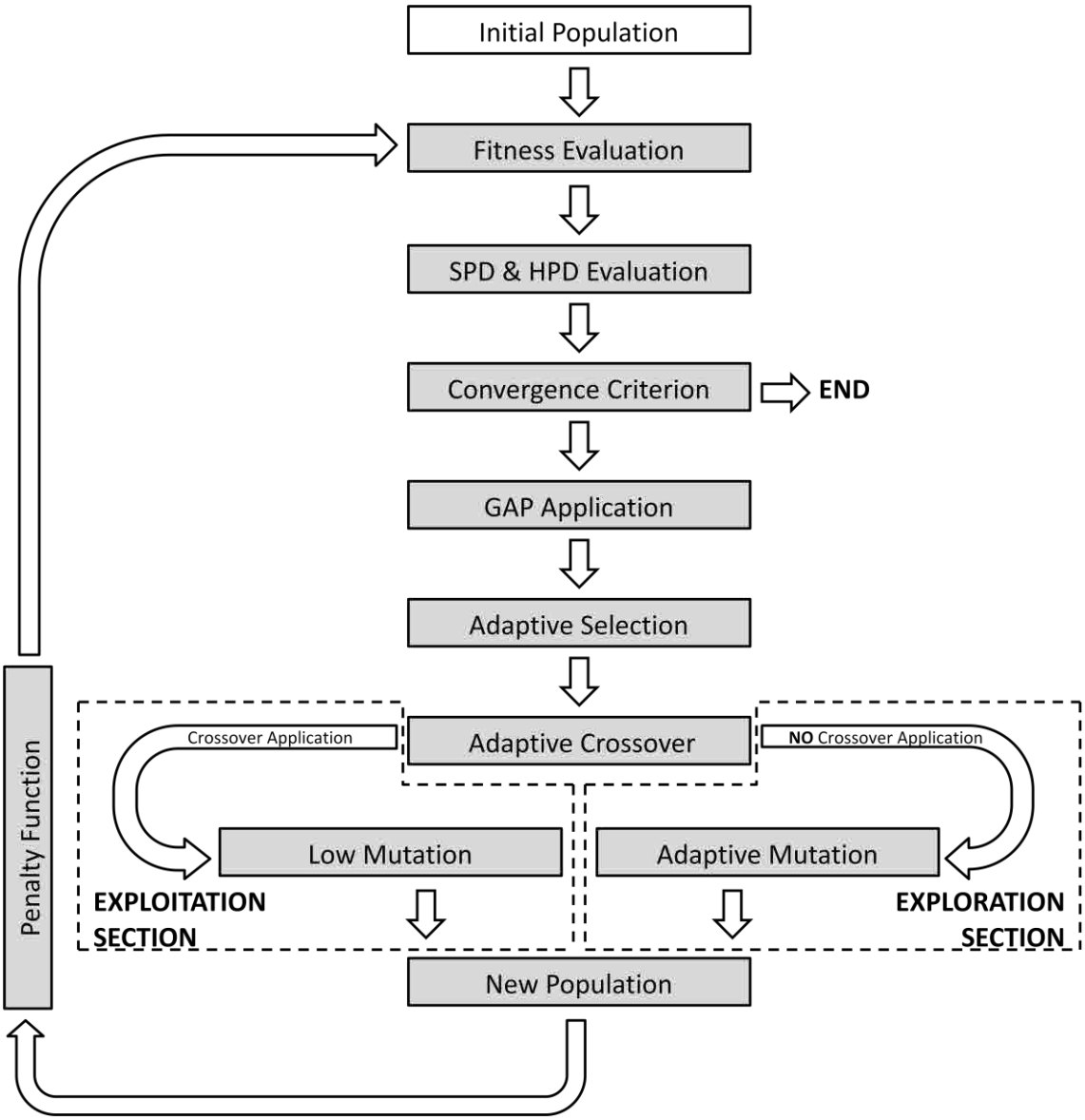

Figure 3.13. AGA structure.

3.3.5 Genetic Algorithm Post-Process

As it has been mentioned before, mathematically, according to the contraction mapping theorem and some hypothesis (Chicone, 1999), the uniqueness of the problem can be guaranteed (this is a sufficient condition, but not a necessary one). However, due to the nature of geotechnical problems, the guarantee of having uniqueness is rather difficult or even not possible. The inherent heterogeneity and complexity of the soil behavior lead to a model of geotechnical structures that is inevitably both uncertain and simplified; along with the intrinsic error associated with the different methods of measurements. As a consequence, rather than having one exact unique solution or focusing on getting the best possible solution (the best individual), a set of approximated solutions can be identified as the final solution of the parameter identification problem. A statistical method based on a principal component analysis (PCA) has been considered as genetic algorithm post-process to evaluate the representativeness of this set of approximated solutions (Levasseur, 2007; Levasseur et al., 2009 and 2010).

3.3.5.1 Principal Component Analysis (PCA)

The PCA is a statistical procedure that uses an orthogonal transformation to convert a set of solutions (points) of possibly correlated variables into a set of points of linearly uncorrelated variables called principal components (also known as principal axes). The number of principal components is less than or equal to the number of original variables. The property of maximum variation is represented by the first principal component. The successive principal components are determined with the property that they are orthogonal to the previous principal component and that they maximize the variance of the points projected onto them. The representation of principal components in the search space permits to visualize the first-order orientation of the points and its spread.

Practically, the method is based on calculating the correlation matrix and then obtaining its eigenvalues and eigenvectors to represent de distribution and correlation of the different variables (parameters). The correlation matrix is defined by the Pearson product-moment correlation coefficients, commonly called simply "the correlation coefficients" (eq. 3.30), which are obtained by dividing the covariance of two variables ($p_i,\ p_j$) by the product of their standard deviation (Pearson, 1895).

$$corr(p_i, p_j) = \frac{cov(p_i,p_j)}{\sigma_{p_i}\sigma_{p_j}} = \frac{E\left[\left(p_i-\mu_{p_i}\right)\left(p_j-\mu_{p_j}\right)\right]}{\sigma_{p_i}\sigma_{p_j}} \tag{3.30}$$

$$i = 1, \dots, number\ of\ parameters$$

$$j = 1, \dots, number\ of\ parameters$$

where σ_{p_i} and σ_{p_j} are the standard deviations, μ_{p_i} and $\mu_{p_j}$are the expected value of p_i and p_j, and E is the expected value operator.

Figure 3.14 illustrates the scheme of a PCA for a case of two variables (parameters).

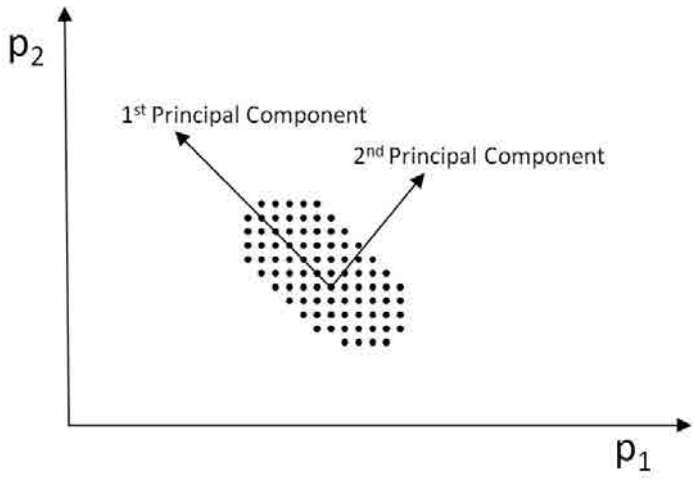

Figure 3.14. Scheme of a Principal Component Analysis (PCA).

3.3.5.2 Post-Process Definition

Frontier Definition

Previous to starting the PCA, the set of points involved in the analysis have to be selected. The method used to define the frontier between the points accepted for the PCA and the ones that are not, is based on the expression proposed by Wiggins (1972).

$$\sigma = \sqrt{\frac{J}{m-n}} \tag{3.31}$$

where σ represents an average value of the standard deviation of the measurements, J is the value of the objective function, and m and n are the number of measurements and the number of parameters respectively.

Then, once σ is fully defined, based on the type of instruments used to carry out the measurements and the global reliability of the measurements, the frontier value ($J_{frontier}$) can be directly obtained by:

$$J_{frontier} = (m-n) \cdot \sigma^2 \tag{3.32}$$

The points susceptible to be analyzed for the PCA can be restricted just to the ones represented in the last generation or they can be expanded to all the individuals involved in the different generations (from the initial generation to the last generation). The implications of using more or less individuals from different generations are discussed in Chapter 5.

Principal Component Analysis Application

Once the set of points used for carrying out the PCA is defined, the PCA is performed and then the eigenvectors and eigenvalues of the correlation matrix are obtained.

Definition of the Solution of the Parameter Identification Problem

After obtaining the eigenvectors and eigenvalues of the correlation matrix, an ellipsoid is defined in order to create an envelope curve of the solution set. The axes directions of the ellipsoid correspond to the eigenvectors orientation, whereas the axes sizes are equal to twice the variance of the associated component.

Thanks to this method; from a discrete set of solutions (points or individuals) identified by genetic algorithms, a continuous space of solutions is estimated. The space included in the ellipsoid is a first-order approximation of the set of solutions of the parameter identification problem.

Figure 3.15 illustrates the different steps presented above.

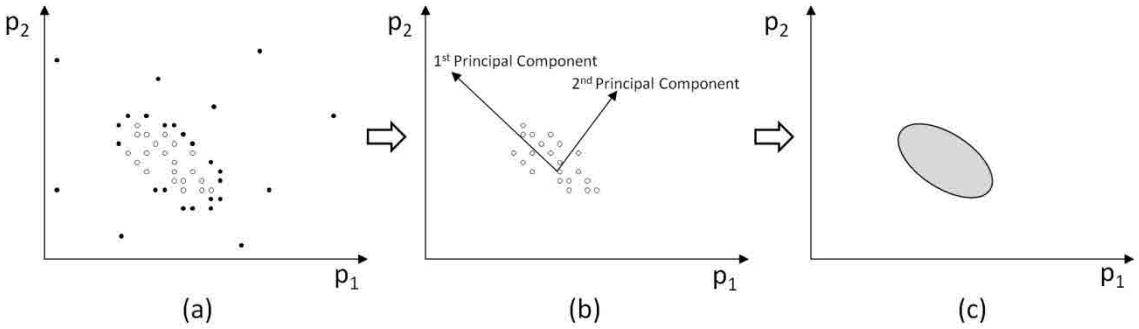

Figure 3.15. Genetic Algorithm Post-Process Scheme. Figure (a) represents the last genetic algorithm generation, where the black points are the individuals not selected for the PCA and the empty ones are the individuals selected for the PCA. Figure (b) shows the resultant principal components from the PCA, and finally, figure (c) illustrates the ellipsoid that defines the continuous space of the parameter identification solution.

Verification

Sometimes the ellipsoid does not represent properly the shape of the objective function, meaning that many solutions enclosed inside the ellipsoid are not satisfying the condition of having a value of the objective function lower than the frontier value. In those cases, the solutions represented by this method of post-process cannot be considered satisfactory.

When three or fewer parameters are being identified, the verification of this method is relatively easy; it just requires to check graphically whether or not the layout of the solutions are well represented by the ellipsoid (see figure 3.16).

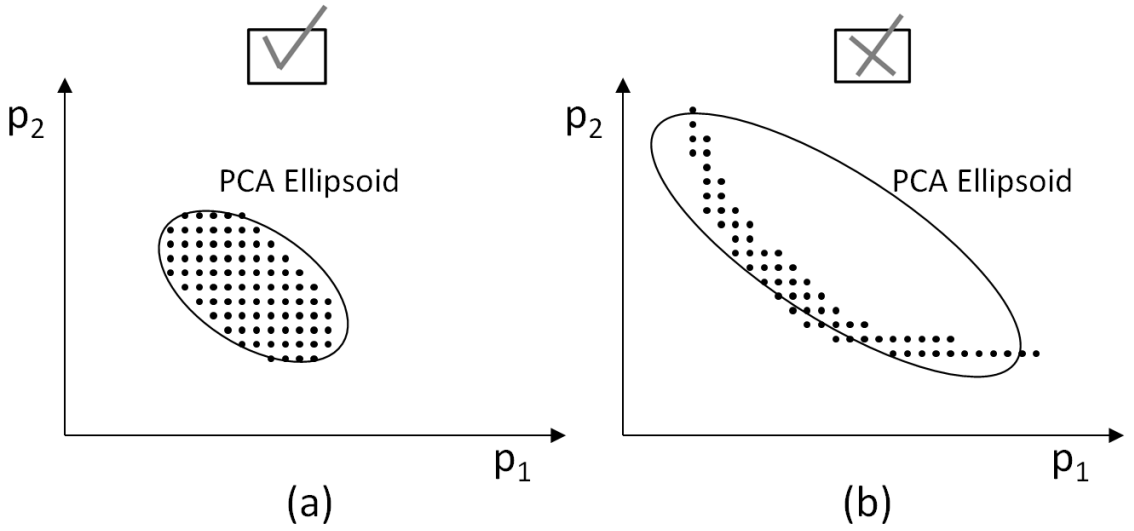

Figure 3.16. Graphical verification of the PCA ellipsoid. Figure (a) illustrates a satisfactory representation of the solution, while figure (b) illustrates a non-satisfactory case.

However, for cases where more than 3 parameters are involved, the graphical strategy is not possible. Then, in order to generalize a criterion to verify the representativeness of the ellipsoid, a novel verification criterion has been defined.

The verification criterion consists in evaluating the objective function at the end of the principal axes that defined the ellipsoid, and then, compare (eq. 3.33) those values with the value defined as frontier in the PCA.

$$Ver_i = \left(\frac{J_{frontier} - J_{axis_i}}{J_{frontier}}\right)^2 \tag{3.33}$$

$$i = 1, \dots, ellipsoid\ dimension\ (number\ of\ principal\ components) \times 2$$

where $J_{frontier}$ is the objective function value defined as frontier, and J_{axis_i} is the objective function evaluated at the end of the principal axis i.

Then, the ellipsoid can be considered representative (satisfactory) if and only if all values of Ver_i are lower than a tolerance. The definition of that tolerance will depend on each problem, so, it must be defined specifically for each case, as for the frontier value.

In the case of obtaining a non-representative ellipsoid, the transformation of some original variables can turn out in a representative ellipsoid, as shown in Levasseur (2007) and Levasseur et al. (2010). Defining a stricter frontier can also help to define a representative ellipsoid for the solution. However, if none of that works, the final solution will be only represented by the best individual of the population.

3.4 Hybrid Method

3.4.1. Introduction

As mentioned before, there are, on the one hand, gradient based methods that can be seen as efficient methods, when they have the proper conditions to work well, and, on the other hand there are the genetic algorithms that present a high robustness, but also a high computational cost. Then, in order to keep the characteristic robustness of genetic algorithms and the efficiency of the gradient based methods, a hybrid method that makes the most of both has been defined.

Yang et al. (1997) introduce this concept of combining genetic algorithms with a local search method, a linear recursive least-squares, into an on-line identification of continuous time-delay systems from sampled input-output data. The presence of the unknown time delay greatly complicates the parameter identification problem, essentially because the parameters of the model are not linear with respect to the time delay. However, once the time delay is determined, the model becomes linear for the other parameters. Motivated by this fact, Yang et al. (1997) proposed a novel hybrid approach where the time delay is firstly determined by the genetic algorithm, whereas the system parameters are subsequently estimated by the local search method.

Using the opposite scheme, first local search and then genetic algorithm, Lee & Lee (2002) and Chen et al. (2002) defined a method based on generating the initial population of genetic algorithm by applying previously the local search technique, and then reduce the search space and consequently improving the efficiency of the optimization. Such approach was well suited for some specific problems, but not for its general application.

Tsai (2002) and Tsai et al. (2003a and 2003b) developed a methodology for parameter structure identification in groundwater modeling, where a genetic algorithm is allied with a grid search method and a quasi-Newton algorithm to solve the inverse problem. The genetic algorithm is first used to search for the near-optimal parameter pattern and values. Next, a

grid search method and a quasi-Newton algorithm iteratively improve the genetic algorithm estimation. A similar work was presented by Kasprzyk & Jaskula (2004). In this case the genetic algorithm was combined with the simplex downhill minimization method in order to identify six parameters of the model describing overlapping semidefferential voltammetric curves.

Misevicius (2004) developed a type of hybrid method for solving quadratic assignment problems, where the local search technique is used as one of the operators of the genetic algorithm for improving each member of the population in each generation, which was found to give a better performance as far as efficiency is concerned. Related to the work of Misevicius (2004), Wang & Wu (2004) and Kim et al. (2004) showed that this type of hybrid algorithm affects the control of the genetic algorithm parameters more than the genetic algorithm itself. Consequently, finding the global optimum is not assured as usually happens when using genetic algorithms only.

In this thesis, the method briefly presented in de Santos et al (2014), where a hybrid method for backanalysis was applied for the first time in the field of geotechnics, has been used and is described here. The method is based on combining in serial form genetic algorithms with gradient based methods. The genetic algorithm is used as a first stage to define a smaller search space, located near the minimum, and the gradient method is used as a second stage to finally find the minimum in an efficient manner (see figure 3.17). Once the genetic algorithm analysis is finished, a principal component analysis is carried out in order to obtain an ellipsoid, which is going to define the new search space used by the gradient method.

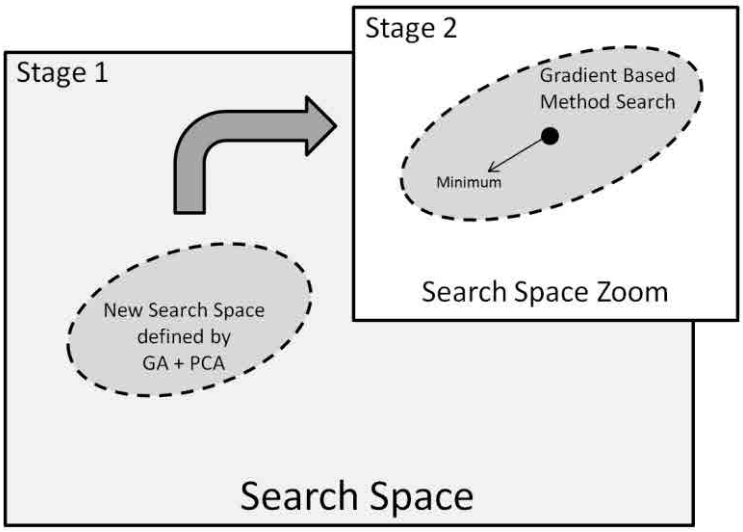

Figure 3.17. Hybrid Method Scheme.

3.4.2 Hybrid Method Definition

3.4.2.1 Stage 1: Global Search

Genetic Algorithm Analysis

As mentioned before, the first stage is where the genetic algorithm is carried out in order to reduce the search space. Reducing the search space is expected to help the gradient based method with not getting stuck in local minima. Usually, when using genetic algorithms as a

part of a hybrid method, the maximum number of generations is reduced with respect to cases where genetic algorithms work alone. In Chapter 5, it has been noticed that after few generations, the representativeness of the set of solutions does not increase significantly to justify the increase on computational cost of generating new generations.

Principal Component Analysis

Once the genetic algorithm is finished the PCA is carried out in order to define the new search space. The mechanism used in this step is as defined in the previous section (3.3.5). The new search space is supposed to be close enough to the global minimum and representative enough to keep local minima out of the new domain. Apart from defining the new search space, the PCA is used to define the starting point for the gradient based method. The center of the ellipsoid defined by the PCA is used as the starting point.

3.4.2.2 Stage 2: Local Search

Starting from the center of the ellipsoid, a gradient based method is used with the objective of improving the genetic algorithm solution. The aim of that combination is achieving a good solution with a reasonable computational cost.

Chapter 4

Backanalysis Dedicated Code: HBCode

4.1 Introduction

The methodology and the results presented in this thesis have been possible thanks to the use of a backanalysis code that has automated all the different steps involved in a problem of parameters identification. The Backanalysis code, named HBCode, which stands for Hybrid Backanalysis Code, was written in FORTRAN 90 by the author of the thesis and its development was focused on solving backanalysis problems using the commercial geotechnical software Plaxis 2D v9.

The wide application of Plaxis by the geotechnical community, and its large number of features to define and reproduce complex problems, has made Plaxis a powerful tool to solve direct problems. Consequently, it was considered appropriate to face the complexity of backanalysis by using Plaxis to define and calculate the numerical models. Because of the use of Plaxis, HBCode is currently capable to identify any parameter that defines the Hardening Soil model implemented in Plaxis.

Moreover, most of the objective functions presented in Chapter 2, and all the optimization algorithms presented in Chapter 3, are implemented in HBCode, as well as the principal component analysis that is used when applying the hybrid algorithm.

In table 4.1, the main characteristics of HBCode are shown.

HBCode by C. de Santos	
Language Code	FORTRAN 90
Numerical Models	Plaxis v9
Objective Functions	Least-Squares Markov Maximum Likelihood
Type of measurements	Vertical Displacements Horizontal Displacements Water Pressure
Instrumentation error structures	Sliding Micrometer Inclinometer Extensometer Surface Vertical Displacement Point Piezometer
Optimization Algorithms	Gradient Based Methods: Gauss-Newton Marquardt Genetic Algorithms: Simple Genetic Algorithm (SGA) Adaptive Genetic Algorithm (AGA) Hybrid Algorithms (+ Principal Component Analysis): SGA + Gauss-Newton SGA + Marquardt AGA + Gauss-Newton AGA + Marquardt

Table 4.1. HBCode main characteristics.

4.2 HBCode-Plaxis Interaction

In addition to the optimization algorithms and the essential operations needed for a backanalysis that have been implemented and extensively presented in chapter 2 and chapter 3, only the manner of how the Plaxis files have been manipulated to define, evaluate and extract the possible new solutions is presented here.

The most representative Plaxis files that have been used to carry out the backanalysis are schematically presented in figure 4.1.

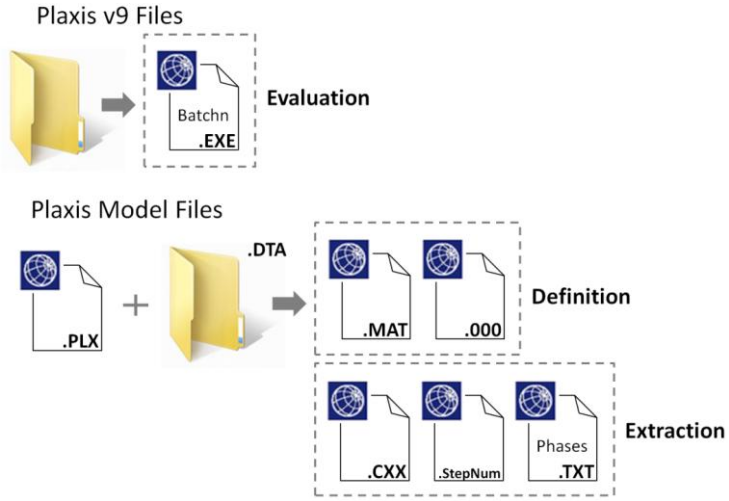

Figure 4.1. The main Plaxis files manipulated by HBCode.

Definition

Before evaluating any combination of parameters, it is needed to redefine the Plaxis MatFile (.MAT), which contains all the information related to the soil parameter values, and the Initial Stress State File (.000), which contains all the information related to the initial stress state, the Shear Hardening yield surface and the Compression Hardening yield surface.

The scheme followed by the HBCode to redefine the MatFile and the Initial Stress State file is presented in detail in the following sections (4.2.1 and 4.2.2).

Evaluation

Once the MatFile and the Initial Stress State file are redefined, it is necessary to recalculate the numerical model. The method used by HBCode to calculate the Plaxis models is based on the application of a batch file, containing the address of the Plaxis Calculus Module (batchn.exe), the Plaxis PLX file (.PLX) of the model that has to be calculated, and the sentence *calculate (/C)*.

An example would be as follows:

*C:\Program Files (x86)\Plaxis v9**batchn.EXE** "Plaxis_Model**.PLX**" **/C***

Extraction

Finally, when the model with the new parameter values is calculated, the results are extracted and the objective function evaluated. Two different strategies have been defined in HBCode to extract the results depending on the number of measurements used in the analysis in order to try to optimize the time and the computational cost of the extraction. The fastest way to extract the results is using the CXX file (.CXX), which contains the results from pre-selected displacements and stress points. Unfortunately, Plaxis only permits the pre-selection of a maximum of ten displacement points and ten stress points, which in terms of backanalysis can represent a too small number of points. The other way to extract the results, which has no limitation on the number of displacements and stress points is using the general results file, where the results of all displacements and stress points are stored. Plaxis generates one general results file for each calculation step; using the number of the calculation step as a file extension (.StepNum). So, before opening the file the step number of the last step associated with the Plaxis phase that is going to be compared with the measurements has to be determined; to do that it has to be read the Phases.txt, which contains the information related to the number of steps involved in calculating each Plaxis phase. Once the step number is identified, the general file can be selected and subsequently manipulated. As mentioned before, the general file contains information of all displacements and stress points, and that makes the process of extraction extremely time consuming comparing to the other method (.CXX). Nonetheless, the use of the general file has been considered more useful than the use of the CXX file, especially when working on complicated problems where having more measurements makes the difference between solving or not solving the backanalysis problem.

4.2.1 MatFile Definition (.MAT)

Prior to start introducing the new soil parameter values into the MatFile, it has to be transformed from binary alphabet to "human" text file (ASCII). The transformation is conducted by an executable file (cbin.exe) provided from *Plaxis bv*. The executable file is capable to perform the transformation in the two directions: from binary to "human", and from "human" to binary. Then, after transforming the MatFile into text file, the new soil parameter values can replace the old values. Then, the MatFile is again transformed to binary form to finally redefine the internal Hardening Soil Model (HSM) parameters (α, K_s/K_c and $G_i^{ref\_inter}$) that control the coupling of the Shear Hardening yield surface with the Compression Hardening yield surface (see section 2.6.1.2). The evaluation of the new internal HSM parameters has been conducted by an executable file provided from *Plaxis bv* (HsCapItr.exe).

4.2.2 Initial Stress State Definition (.000)

Depending on whether K_0 is one of the parameters to be identified or not, the values of effective horizontal stresses (σ_x'), stored in the initial stress state file (.000), will be recalculated or not. In the case of identifying K_0, σ_x' has to be recalculated and stored in the initial stress state file. The new value of σ_x' is directly obtained by $\sigma_y' \cdot K_0$.

Independently of whether K_0 is involved in the analysis or not, in the majority of cases where parameters such as E_{50}^{ref}, E_{oed}^{ref}, E_{ur}^{ref}, c and φ are varied, two parameters associated with the hardening yield surfaces, as the isotropic pre-consolidation stress (p_p') and the accumulated plastic deviatoric strain (γ^p), must be recalculated to properly define the yield surfaces. The scheme used to calculate p_p' and γ^p that has been implemented in HBCode is the same one implemented in Plaxis (Brinkgreve & Broere, 2008). The values of p_p' and γ^p stored in the initial stress state file are the highest values obtained from two different scenarios, assuming pre-consolidation stress and unloading stress.

Stress state from pre-consolidation and unloading stress

1) Pre-consolidation stress

$$\sigma_y' = \sigma_p = \sigma_y'^0 \cdot OCR \tag{4.1}$$

$$\sigma_x' = K_0^{NC} \cdot \sigma_y' \tag{4.2}$$

where σ_y' is the effective vertical stress, σ_p is the vertical pre-consolidation stress, $\sigma_y'^0$ is the in situ effective vertical stress, OCR is Over-Consolidated Ratio, σ_x' is the effective horizontal stress, and K_0^{NC} is the coefficient of lateral earth pressure associated with normally consolidated state stress.

2) Unloading stress

$$\sigma_y' = \sigma_y'^0 \tag{4.3}$$

$$\sigma_x' = \sigma_y' \cdot K_0^{NC} \cdot \frac{K_0 - \left(\nu_{ur}/_{1-\nu_{ur}}\right)}{K_0^{NC} - \left(\nu_{ur}/_{1-\nu_{ur}}\right)} - \frac{\nu_{ur}}{1-\nu_{ur}} \cdot (OCR - 1) \tag{4.4}$$

where K_0 is the current coefficient of lateral earth pressure, and ν_{ur} is the Poisson's ratio for unloading-reloading.

Calculating p_p'

The value of p_p' can be obtained by imposing in equation 2.39 $f^c = 0$. Then:

$$p_p' = \left[\left(\frac{\sigma_1' + \left(\frac{3+\sin\varphi}{3-\sin\varphi} - 1\right) \cdot \sigma_2' - \left(\frac{3+\sin\varphi}{3-\sin\varphi}\right) \cdot \sigma_3'}{\alpha} \right)^2 + \left(\frac{\sigma_1' + \sigma_2' + \sigma_3'}{3} \right)^2 \right]^{0.5} \tag{4.5}$$

where α is the steepness of the compression hardening yield surface obtained from the MatFile after executing HsCapItr.exe.

Calculating γ^p

The value of γ^p can be obtained by prescribing $f^s = 0$ in equation 2.37. Then:

$$\gamma^p = \frac{1}{E_i^{inter}} \cdot \frac{\sigma_1' - \sigma_3'}{1 - \frac{\sigma_1' - \sigma_3'}{q_a}} - \frac{2 \cdot (\sigma_1' - \sigma_3')}{E_{ur}} \tag{4.6}$$

where E_i^{inter} is an auxiliary internal parameter defining the initial stiffness that is obtained from the MatFile after executing HsCapItr.exe , E_{ur} is the unloading-reloading stiffness, and q_a is the asymptotic deviatoric strain originally defined by Duncan & Chang (1970) as:

$$q_a = \frac{q_f}{R_f} = \left((c \cdot \cot\varphi - \sigma_3') \cdot \frac{2 \cdot \sin\varphi}{1 - \sin\varphi} \right) / R_f \tag{4.7}$$

where q_f is the ultimate deviatoric stress, and R_f is the ratio between q_a and q_f, which should be less than 1.

Once the new values of p_p' and γ^p are stored in the initial stress state file (.000), the numerical model is ready to be calculated again.

Chapter 5

Application and Validation of the Methodology (Synthetic Case)

5.1 Introduction

In this chapter the backanalysis methodology has been applied and validated for a synthetic case represented by a tunnel excavation. All the different optimization methods described in chapter 3 have been used in order to study the strengths and weaknesses of each method. The aim of using a synthetic case is because its simplicity helps to focus the study on the understanding of the behavior of the backanalysis technique rather than on the final parameter values.

5.2 Synthetic Case

5.2.1 Description

The case study is a symmetric circular tunnel 10 m deep and 10 m in diameter (see figure 5.1). The model, defined in Plaxis 2D (Version 9), is 80 meters wide and 40 meter high. The hypothesis of plane strain was adopted. 1476 15-node triangle elements were used to discretize the geometry of the problem, and consequently 12142 nodes and 17712 stress points were created (see figure 5.2). The hardening soil model was used as constitutive model. Only one material was considered to define the stratigraphy of the model. The soil parameters of the model are shown in table 5.1. In order to simulate the soil-structure interaction, an interface was defined adjacent to the outer side of the tunnel lining. The tunnel was considered impervious and water flow through the lining was not allowed.

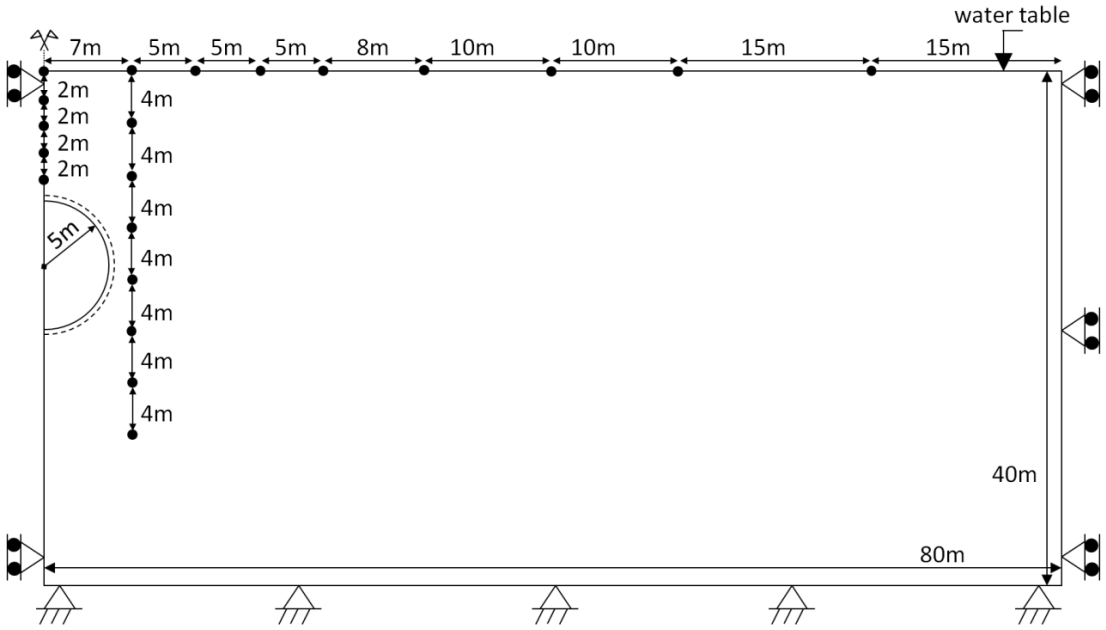

Figure 5.1. Geometric scheme of the model. (•) measurement points.

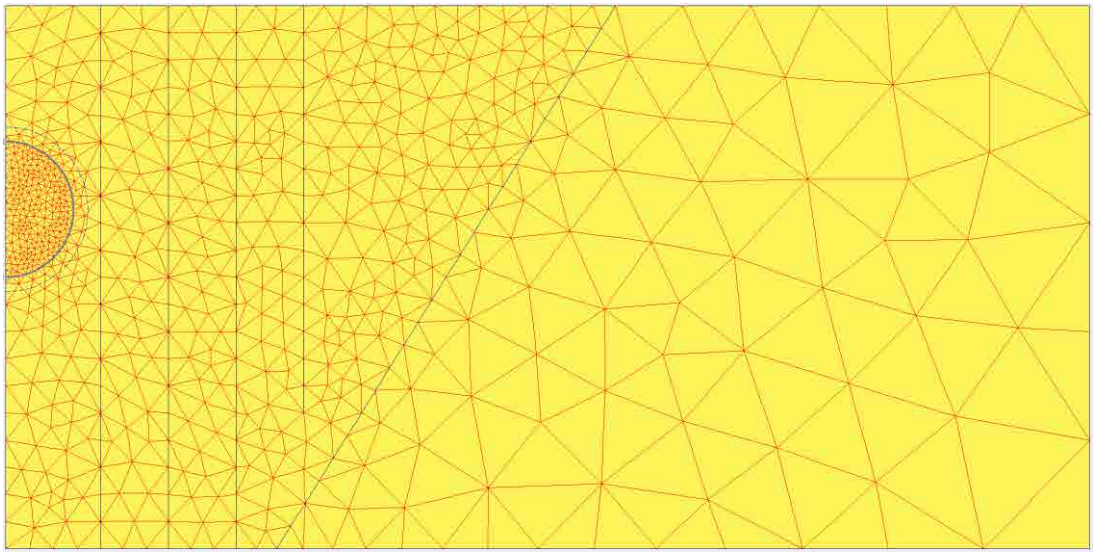

Figure 5.2. Plaxis geometric model.

Parameter	Description	Value
γ_{unsat}	Unsaturated specific weight	19 [kN/m^2]
γ_{sat}	Saturated specific weight	21 [kN/m^2]
$k_x = k_y$	Horizontal and vertical permeability	8.64·10^{-4} [m/day]
E_{50}^{ref}	Secant stiffness in standard drained triaxial test	5000 - 37500 [kN/m^2]
E_{oed}^{ref}	Tangent stiffness for primary oedometer loading	0.8·E_{50}^{ref} [kN/m^2]
E_{ur}^{ref}	Unloading / Reloading stiffness ($20E_{50}^{ref} \geq E_{ur}^{ref} \geq 3E_{50}^{ref}$)	10000 - 200000 [kN/m^2]
m	Power for stress-level dependency of stiffness	1 [-]
c	Effective cohesion	0 - 50 [kN/m^2]
φ	Effective angle of internal friction	25 - 35 [deg]
ψ	Angle of dilatancy	0 [deg]
ν_{ur}	Poisson's ratio for unloading-reloading (by default $\nu_{ur} = 0.2$)	0.2 [-]
p^{ref}	Reference stress for stifnesses	100 [kN/m^2]
K_0^{NC}	Coefficient of lateral earth pressure associated with normally consolidated states of stress (by default $K_0^{NC} = 1 - \sin\varphi$)	0.531 [-]
R_f	Failure ratio q_f/q_a	0.9 [-]

$\sigma_{tension}$	Tensile strength	0 [kN/m^2]
$c_{increment}$	Increase of cohesion per unit of depth	0 [kN/m^3]
R_{inter}	Interface strength factor	0.64 [-]

Table 5.1. Soil parameters.

The parameters of the lining are shown in table 5.2

Parameter	Description	Value
Material type	Constitutive model	elastic
EA	Axial stiffness	1.25·10^7 [kN/m]
EI	Flexural rigidity	2.6042·10^5 [kNm^2/m]
d_{eq}	Equivalent thickness	0.50 [m]
w	Weight	12.5 [kN/m/m]
ν	Poisson's ratio	0.2 [-]

Table 5.2. Parameters of the tunnel lining.

Three different stage constructions, plus the initial stress generation, were defined to simulate the tunnel construction.

- *Phase 0:* Definition of the initial stresses by the Plaxis K_0 procedure. The material was initially considered normally consolidated (OCR=1) and the value of K_0 was defined by the equation of Jaky (1948).

$$K_0 = 1 - \sin\varphi \tag{5.1}$$

- *Phase 1:* Tunnel excavation using the Plaxis method ΣMStage to simulate a volume loss close to 0.8% (ΣMStage=0.2).

- *Phase 2:* Tunnel construction activating the lining.

- *Phase 3:* Dissipation of all the excess of water pressure caused by the tunnel construction process (consolidation).

5.2.2 Measurements

Twenty points with information on vertical displacements were chosen as in situ instrumentation data. The locations of these points try to simulate an extensometer, located along the vertical tunnel axis, an extensometer, 2 meters away from the tunnel side, and various surface points. Figure 5.1 shows the location of those 20 points used as in situ instrumentation data.

The measurements used in this study were directly extracted from the last calculation phase (phase 3) after evaluating the Plaxis model with:

E_{50}^{ref}=25000 kN/m^2

$E_{oed}^{ref} = 0.8E_{5o}^{ref}$

E_{ur}^{ref}=75000 kN/m^2

c=10 kN/m^2

φ=28^o

Two different set of data were created by defining two levels of data noise. The noise was randomly created following a normal distribution defined by the mean (μ) and the standard deviation (σ). One set of data, named exact data, was defined by μ=0 m and σ=0 m. The other set of data, named noisy data, was defined by μ=0 m and σ=0.5·10^{-3} m. Table 5.3 contains the values of the vertical displacements used as measurement points.

Point	Exact Data / μ=0 m and σ=0 m	Noisy Data / μ=0 m and σ=0.5·10^{-3} m
1	-0.020792 m	-0.020524 m
2	-0.021996 m	-0.021079 m
3	-0.022404 m	-0.023533 m
4	-0.022707 m	-0.022276 m
5	-0.023304 m	-0.023144 m
6	-0.017748 m	-0.018401 m
7	-0.018290 m	-0.018507 m
8	-0.017949 m	-0.017778 m
9	-0.014081 m	-0.012292 m
10	0.0000129 m	0.0013976 m
11	0.0053286 m	0.0046537 m
12	0.0047475 m	0.0062650 m
13	0.0033345 m	0.0036972 m
14	-0.012231 m	-0.012262 m
15	-0.006986 m	-0.006629 m
16	-0.003269 m	-0.003372 m
17	-0.001233 m	-0.001295 m
18	-0.00628 m	0.0001168 m
19	-0.000344 m	0.0003608 m
20	-0.000112 m	0.0005969 m

Table 5.3. In situ measurement data from a direct calculation using Plaxis. The points represent the measurement points in the model, from top to bottom and from left to right (see figure 5.1).

Figure 5.3 illustrates the values of the vertical displacements shown in table 5.3.

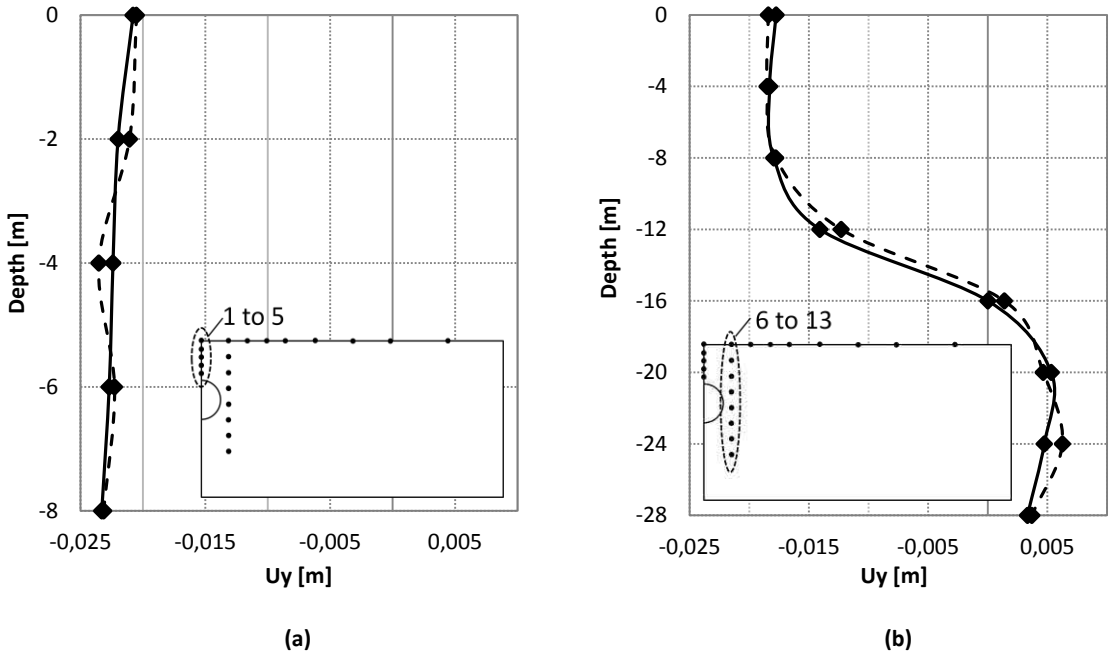

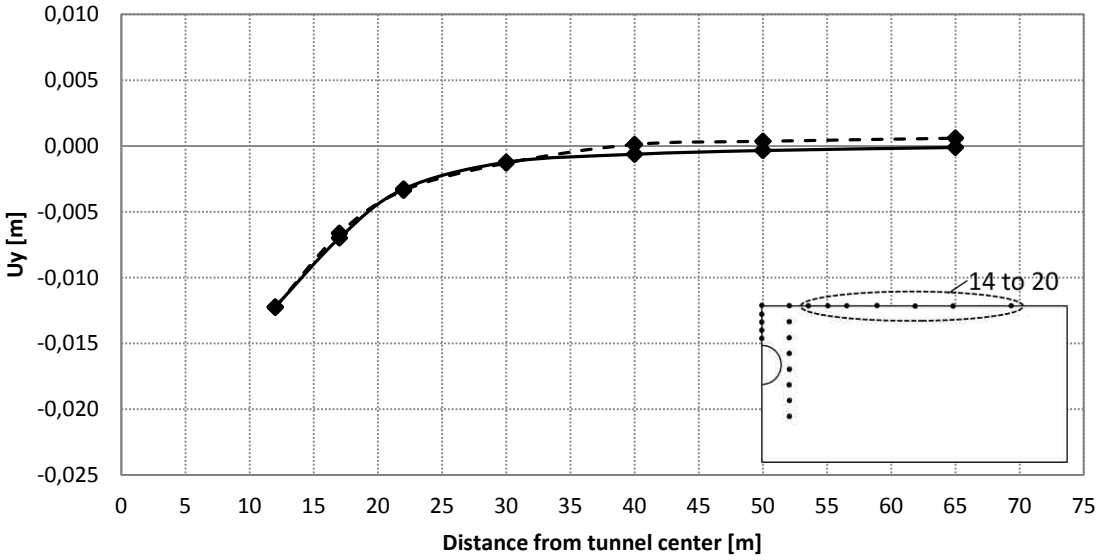

(c)

Figure 5.3. Vertical displacements used as measurements. (a) measurements from point 1 to point 5 (from top to bottom). (b) measurements from point 6 to point 13 (from top to bottom). (c) measurements from point 14 to point 20 (from left to right). The solid line represents the exact data and the dashed line represents the noisy data.

5.2.3 Stress and Strain Overview of the Model

In this section some outputs of the numerical model are presented in order to better understand the behavior of the particular case study of a shallow tunnel construction. Due to the fact that a tunnel construction is a combined system where loading and unloading states occur simultaneously, knowing the stresses with respect to the yield surfaces and the strains can be very useful in terms of parameter identification.

From figure 5.4 the regime of the stress points can be extracted, and subsequently the relevance associated to the different stiffness moduli can also be derived. Using the hardening soil model, six different regimes are possible: Elastic regime, Mohr-Coulomb regime, Tension cut-off regime, Hardening regime, Cap regime and Cap & Hardening regime. All different regimes are fully described in the manual of Plaxis (Brinkgreve & Broere, 2008). Simplifying, it can be pointed out that:

- The elastic behavior is mainly controlled by the unloading-reloading modulus (E_{ur}^{ref}).

- The stress state at failure, described by the Mohr-Coulomb failure criterion, is defined by the effective strength parameters φ and c.

- The tension cut-off is totally controlled by the tensile strength ($\sigma_{tension}$).

- The hardening regime, which affects all the stress points located in the shear hardening yield surface, is mainly controlled by the stiffness parameter E_{50}^{ref}.

- The stress points located in the compression hardening yield surface (cap regime) are mainly controlled by the stiffness parameter E_{oed}^{ref}.

- The regime defined by the intersection of the both hardening yield surfaces is mainly controlled by E_{50}^{ref} and E_{oed}^{ref}.

In order to better follow the evolution of the system under a tunnel construction, five stress points were selected to study their behavior in depth. Figure 5.5 shows the location of those selected points.

As it was expected (see figure 5.6), due to the unloading phenomenon of a tunnel construction, the stresses at the point closer to the bottom of the tunnel (point E) have varied the most with respect to the other points. However, even considering a tunnel construction as an unloading system, not all points can be considered under unloading conditions. This phenomenon has some implications with respect to where to measure in terms of what parameter is wanted to be identified, especially when using the hardening soil model that uses three different stiffness moduli with dependence to the stress state. Therefore, it must be taken into account that in sophisticated constitutive models, such as the hardening model that has many interactions among parameters, it cannot be easy or even possible to fully distinguish when and how each parameter is affecting the behavior of the model. Consequently, in order to better define where to measure (the optimal layout of measuring points), it is highly recommended to proceed with a sensitivity analysis as presented in section 2.5.

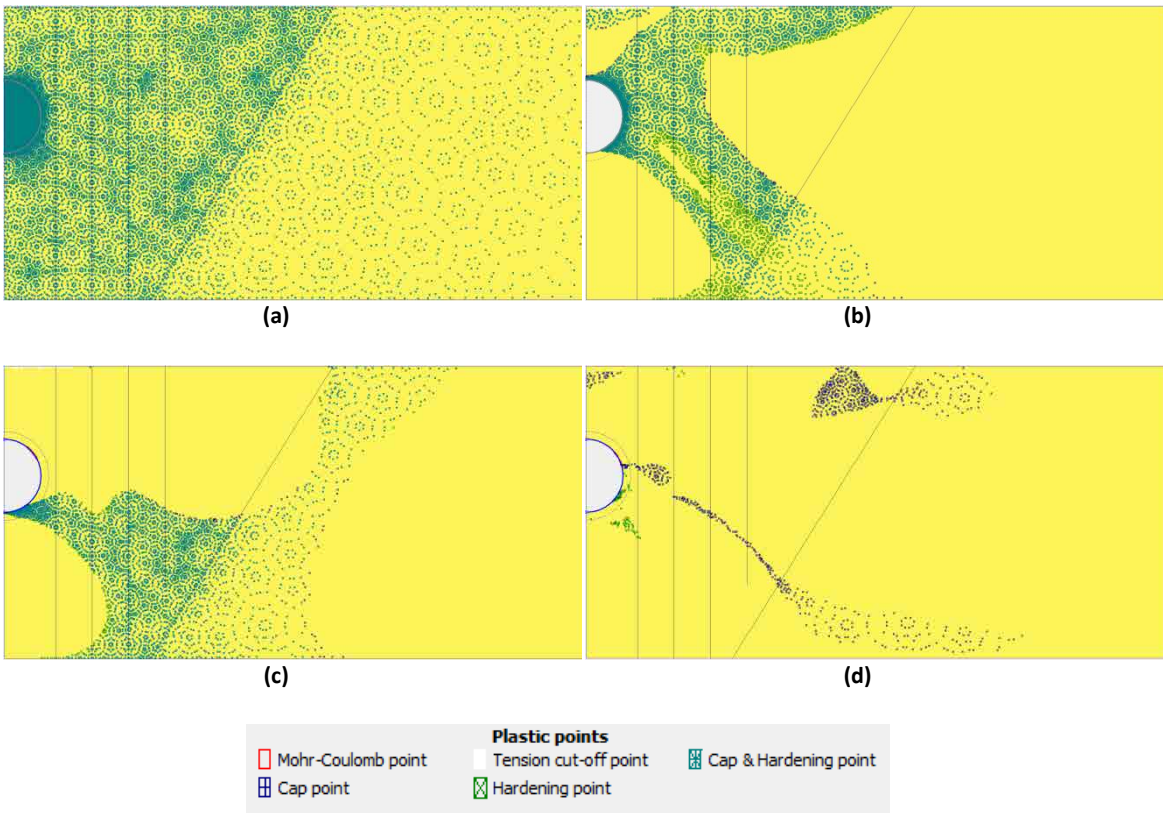

Figure 5.4. Plastic points of the model used to generate the measurements. (a) shows the plastic points from the calculation phase 0, (b) shows the plastic points from the calculation phase 1, (c) shows the plastic points from the calculation phase 2 and (d) shows the plastic points from the calculation phase 3.

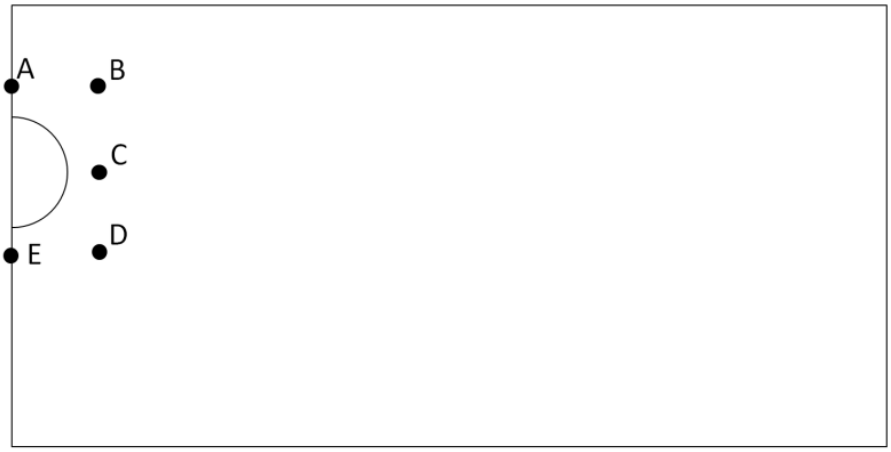

Figure 5.5. Location of the selected points.

Observing figures 5.7 and 5.8, it can be noticed that the majority of the strains are shear strains due to the soil relaxation previous to the installation of the lining. And as expected for an undrained situation, no volumetric strains occurred until the consolidation phase (phase 3).

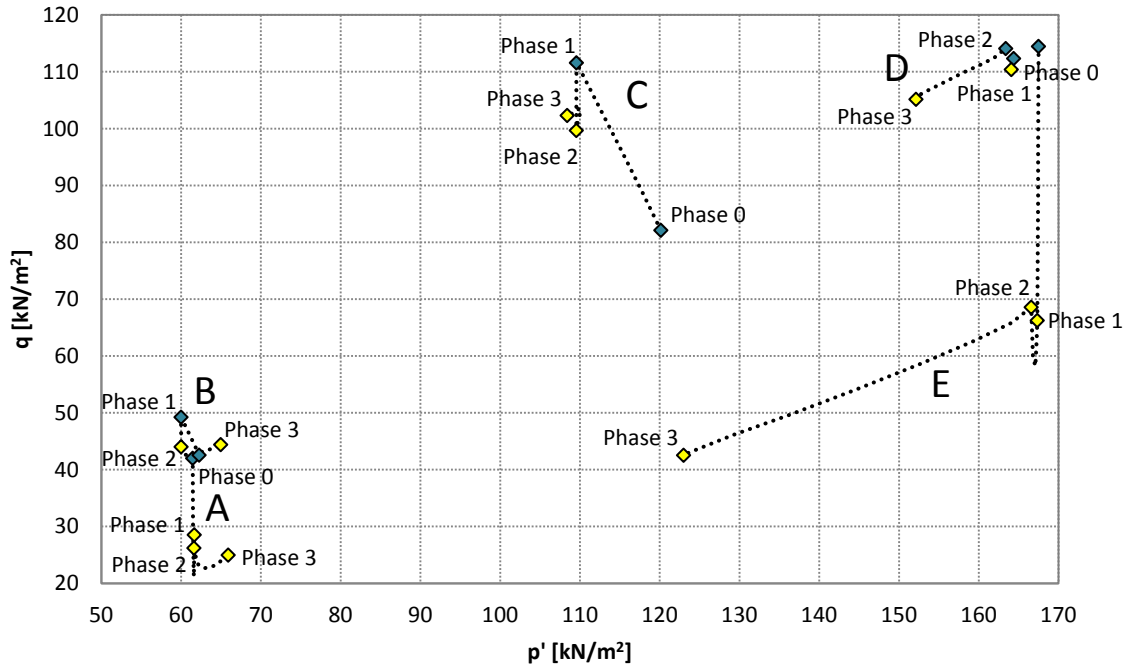

Figure 5.6. Stress paths of the points A, B, C, D and E. The blue-green diamonds represent the Cap & Hardening regime and the yellow diamonds represent the Elastic regime.

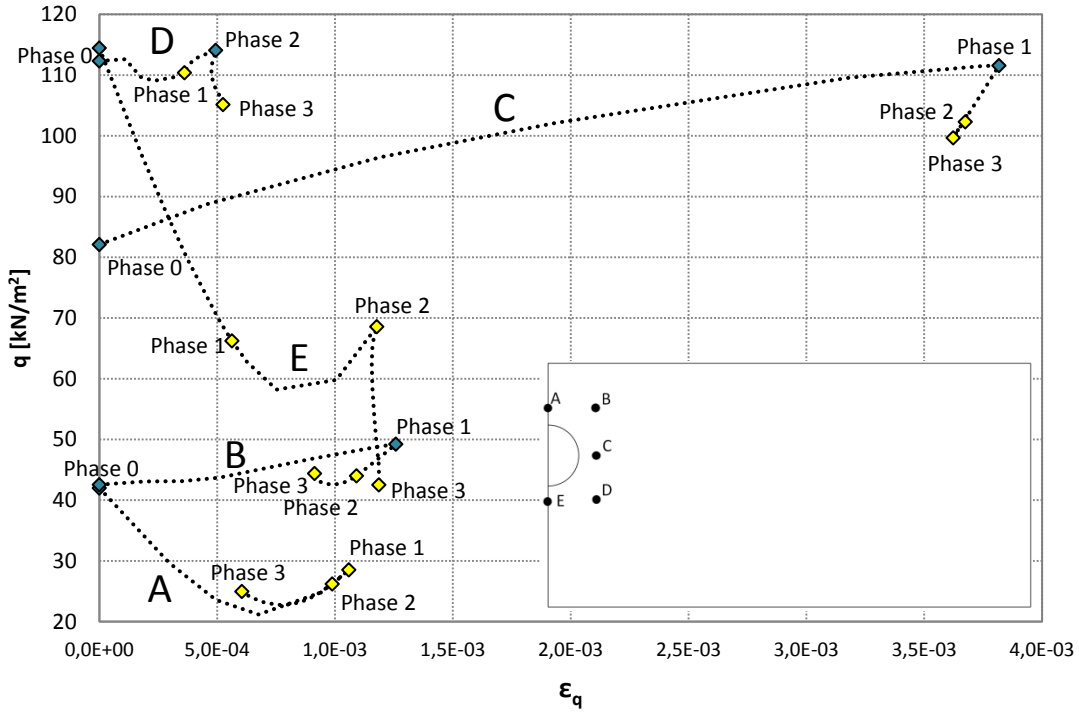

Figure 5.7. Shear strain paths of the points A, B, C, D and E. The blue-green diamonds represent the Cap & Hardening regime and the yellow diamonds represents the Elastic regime.

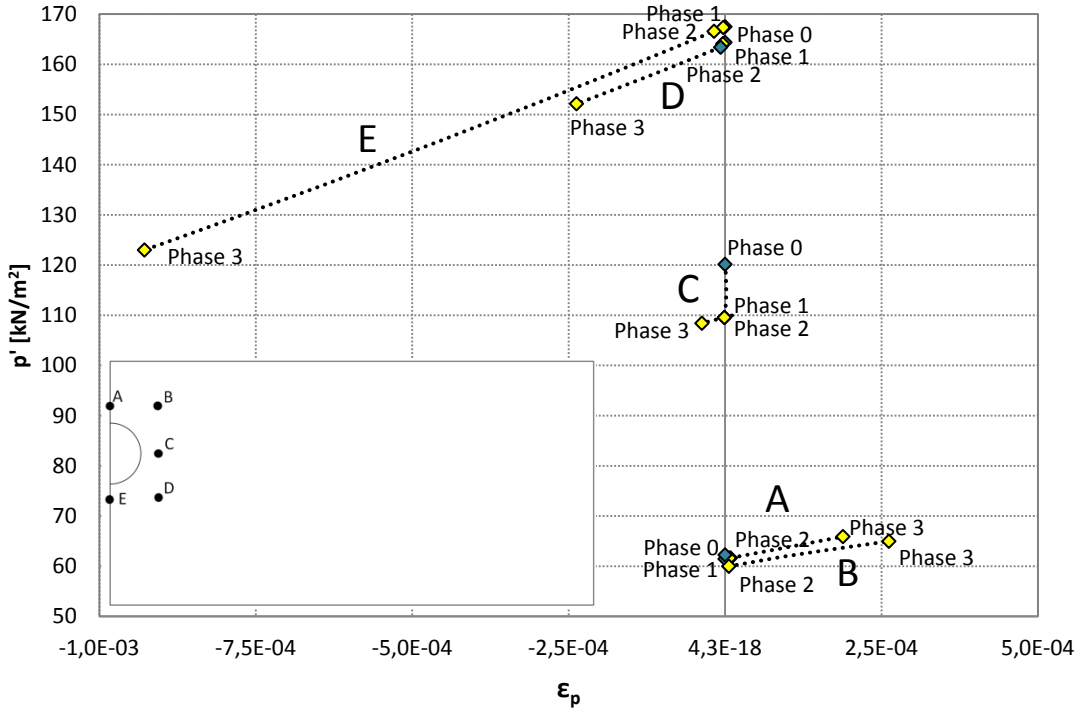

Figure 5.8. Volumetric strain paths of the points A, B, C, D and E. The blue-green diamonds represent the Cap & Hardening regime and the yellow diamonds represent the Elastic regime. (-) for compression and (+) for swelling behavior.

5.3 Two Parameters Identification Case (E_{50}^{ref} and c)

5.3.1 Introduction

In this section, the identification of the secant stiffness in standard drained triaxial test (E_{50}^{ref}) and the cohesion (c), for two different measurements scenarios (exact data and noisy data), is presented. The selection of these two parameters is based on a sensitivity analysis where E_{50}^{ref} and c were determined as the parameters more relevant with respect to vertical displacements. As it is shown in table 5.1, the tangent stiffness for primary oedometer loading (E_{oed}^{ref}) has been directly correlated with E_{50}^{ref}. The reason for forcing this relationship between E_{50}^{ref} and E_{oed}^{ref} is just to avoid problems derived from the computation of the internal parameters of the Hardening Soil Model that try to fit simultaneously both yield surfaces (see section 2.6).

The fact of identifying two parameters has permitted to visualize the actual shape of the objective function in the search space. 3366 direct problems were solved in order to properly represent the shape of the objective function. The search space was defined by:

- Minimum value of E_{50}^{ref} = 5000 kN/m^2

- Maximum value of E_{50}^{ref} = 37500 kN/m^2

- Step size value of E_{50}^{ref} = 500 kN/m^2

- Minimum value of c = 0 kN/m^2

- Maximum value of c = 50 kN/m^2

- Step size value of c = 1 kN/m^2

The global minimum is of course located in E_{50}^{ref} = 25000 kN/m^2 and c = 10 kN/m^2.

Usually, in real cases or cases where the computational cost is so high, this kind of exhaustive previous analysis or pre-visualizations of the objective function are not possible or worth it. However, due to the objective of showing the methodology presented in this thesis, the visualization of the objective function was considered useful.

The least-squares method (see section 2.3.1) was used to define the objective function applied in this synthetic case study.

Figure 5.9 shows the shape of the objective function for the case of exact data.

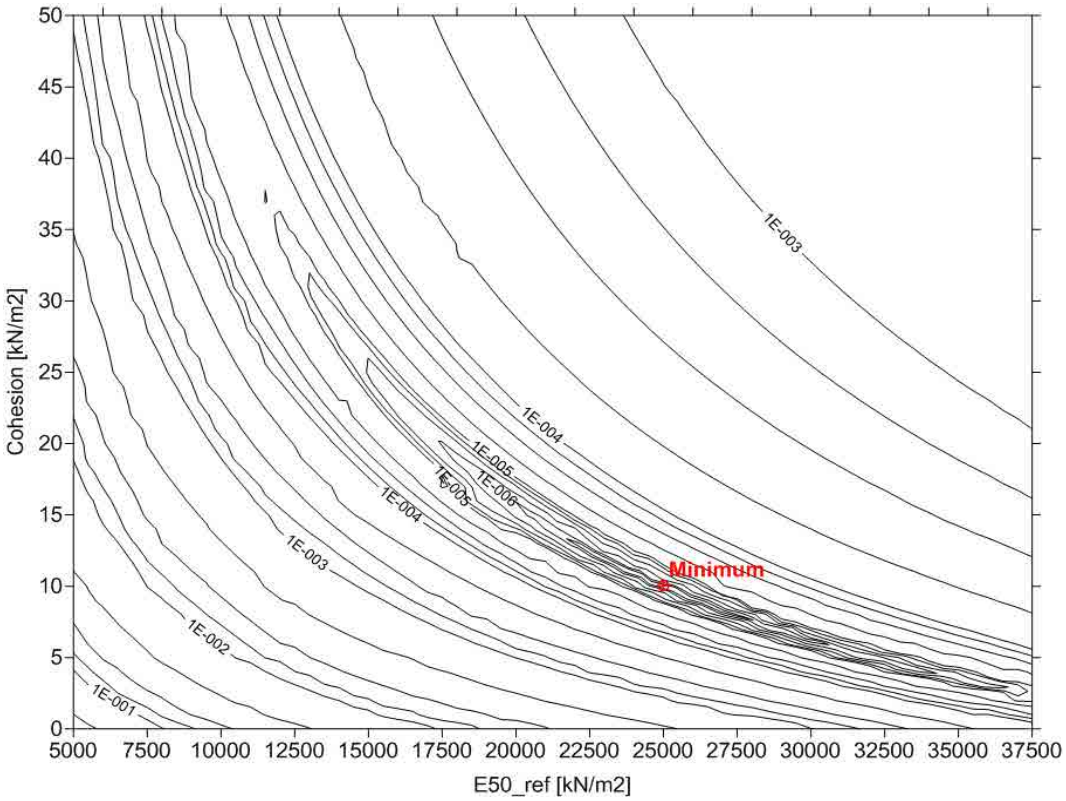

Figure 5.9. Mapping of the objective function [m^2] for the case of exact data.

Thanks to figure 5.9, the relationship between E_{50}^{ref} and c can be appreciated, where very different combinations of E_{50}^{ref} and c have low values of error, as well as the sensitivity of the objective function with respect to E_{50}^{ref} and c, which is represented by the distance between the isolines. Graphically, an extensive narrow valley encloses the surroundings of the global minimum, which often increases the difficulty of the parameter identification. In theory, the easiest problem (for two parameters) would be defined by an objective function represented by perfect concentric circles, where both parameters would be equally sensitive. Unfortunately, this scenario rarely occurs.

Figure 5.10 illustrates the effect of adding a certain amount of noise into de measurements (noisy data case), where the narrow valley shown in figure 5.9 has flattened. That makes the parameters identification even more difficult, and unfortunately, this situation occurs quite often in geotechnical problems.

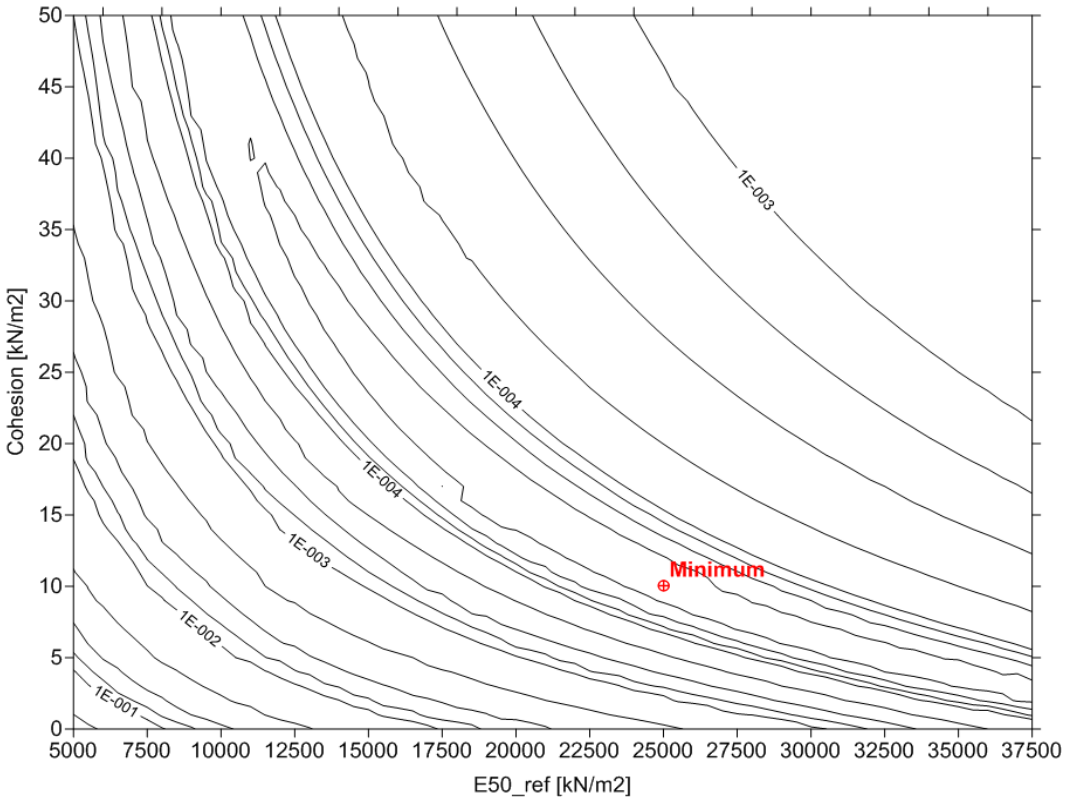

Figure 5.10. Mapping of the objective function [m^2] for the case of noisy data.

5.3.2 Using the Gauss-Newton Method

The Gauss-Newton method, presented in section 3.2.2, was used to find the parameter values that best represented the measurements. Because of the high dependency of the solution with respect to the starting point, while using gradient based methods, three different starting points were selected.

- Starting Point 1: E_{50}^{ref} = 17500 kN/m^2 and c = 30 kN/m^2

- Starting Point 2: E_{50}^{ref} = 30000 kN/m^2 and c = 40 kN/m^2

- Starting Point 3: E_{50}^{ref} = 7500 kN/m^2 and c = 5 kN/m^2

5.3.2.1 Exact Data Case Results

The following three figures (5.11, 5.12 and 5.13) illustrate the path followed by the iterative procedure throughout the objective function surface for the case of exact data. For a better understanding of the optimization method behavior and its stability, the method was permitted to run freely until reaching a maximum number of iterations (no error tolerance was imposed). A maximum of ten iterations were considered appropriate to reach the global optimum from all starting points.

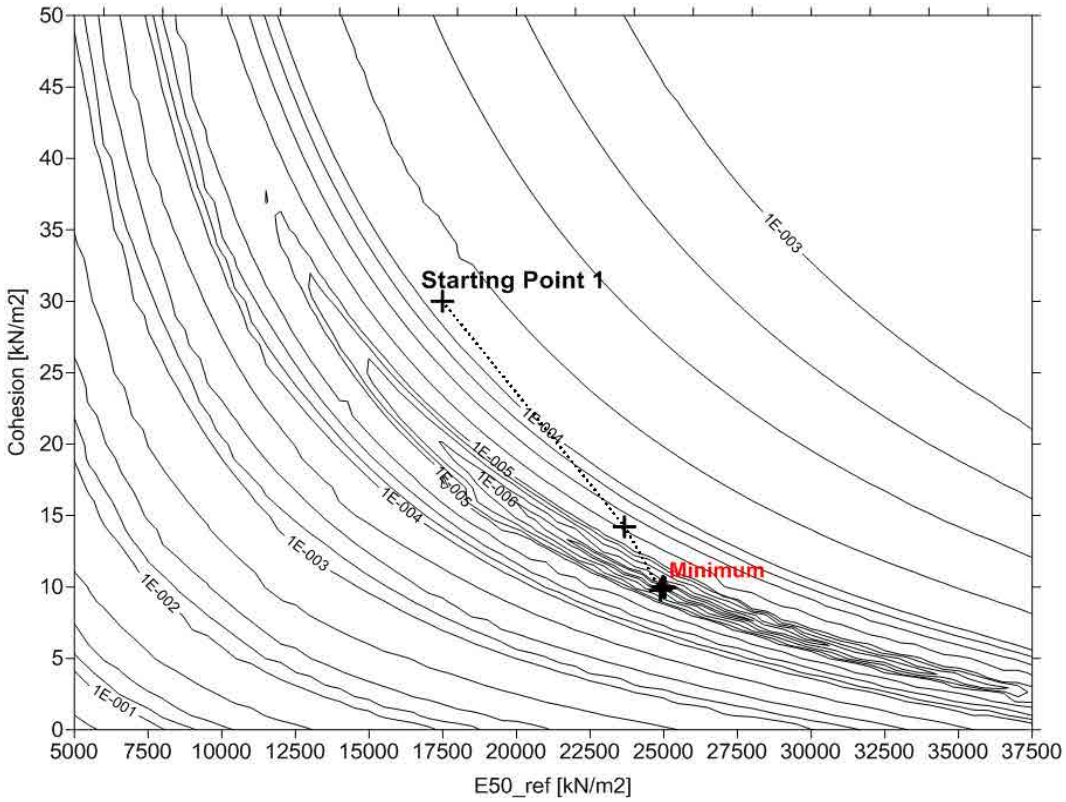

Figure 5.11. Gauss-Newton path from the starting point 1 - Objective function [m^2] (exact data).

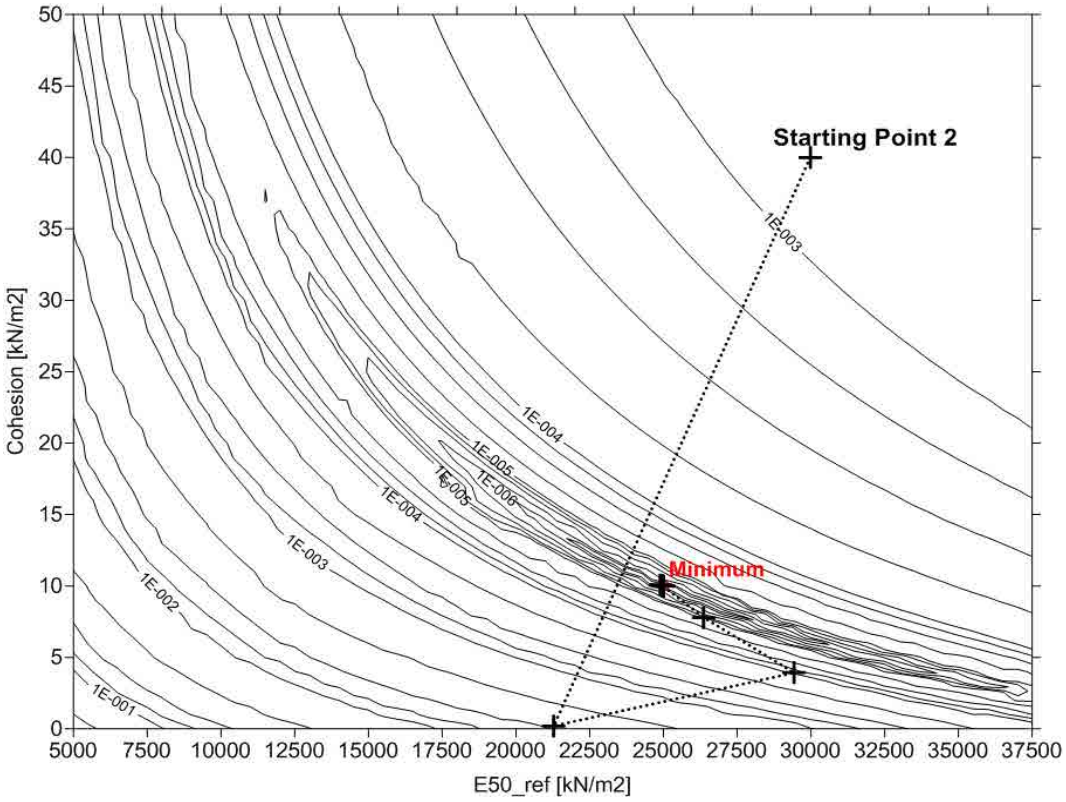

Figure 5.12. Gauss-Newton path from the starting point 2 - Objective function [m^2] (exact data).

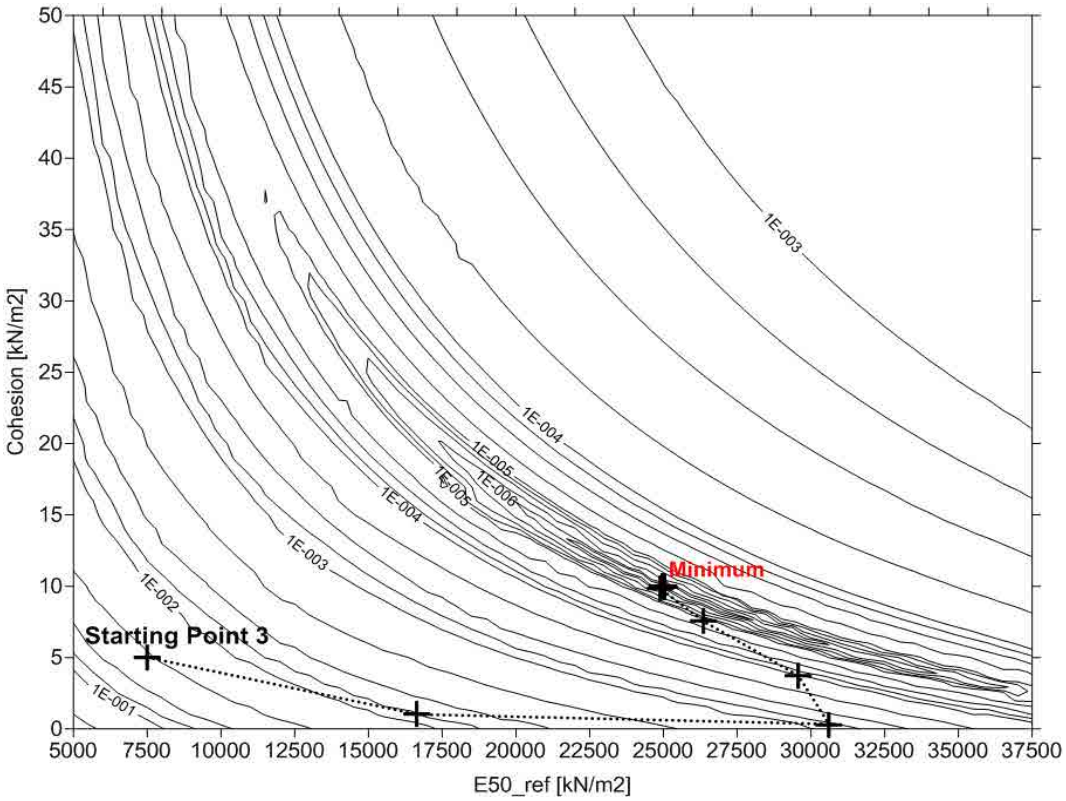

Figure 5.13. Gauss-Newton path from the starting point 3 - Objective function [m^2] (exact data).

From figure 5.11, 5.12 and 5.13 it can also be observed, especially for the first iterations where the step size is large, how the method drives the search towards the minimum of the tangent paraboloid to the objective function.

In figure 5.14, 5.15 and 5.16, the evolution of the algorithm, in terms of objective function and parameters values, is illustrated.

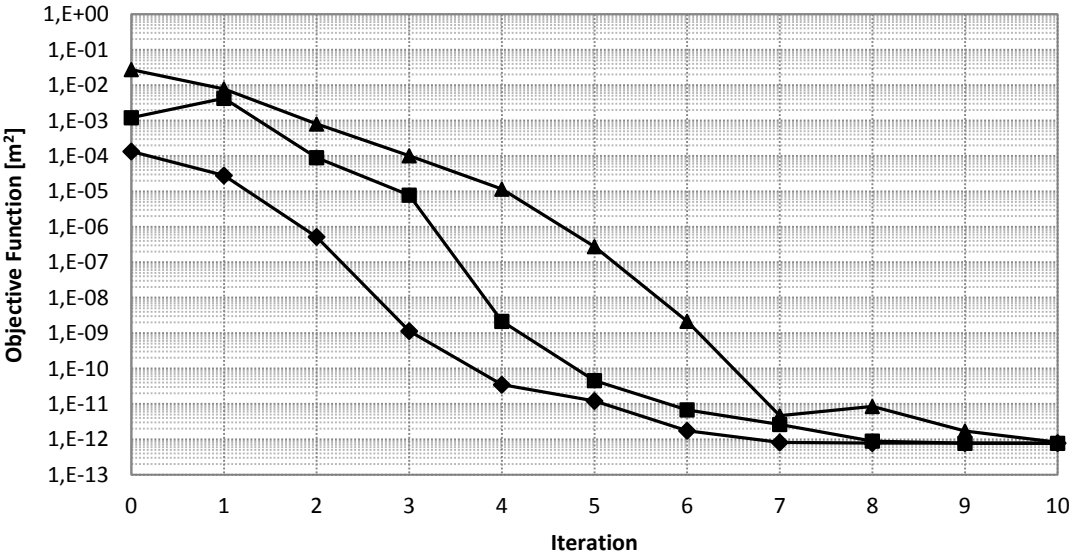

Figure 5.14. Evolution of the objective function using the Gauss-Newton method with exact data. The diamonds represent the starting point 1 case, the squares represent the starting point 2 case and the triangles represent the starting point 3 case.

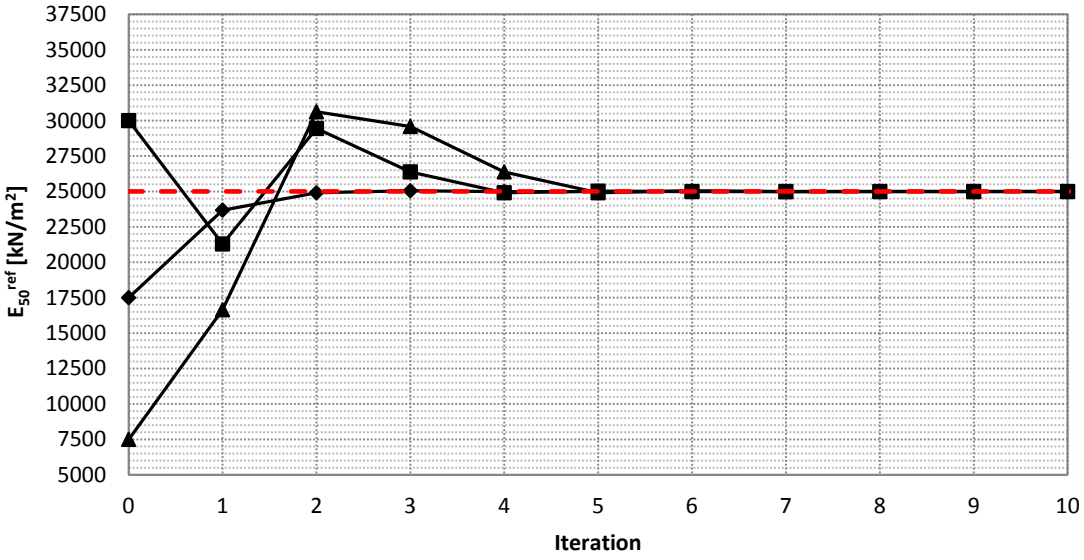

Figure 5.15. Evolution of the E_{50}^{ref} value using the Gauss-Newton method with exact data. The diamonds represent the starting point 1 case, the squares represent the starting point 2 case, the triangles represent the starting point 3 case and the red dashed line represents the actual parameter value.

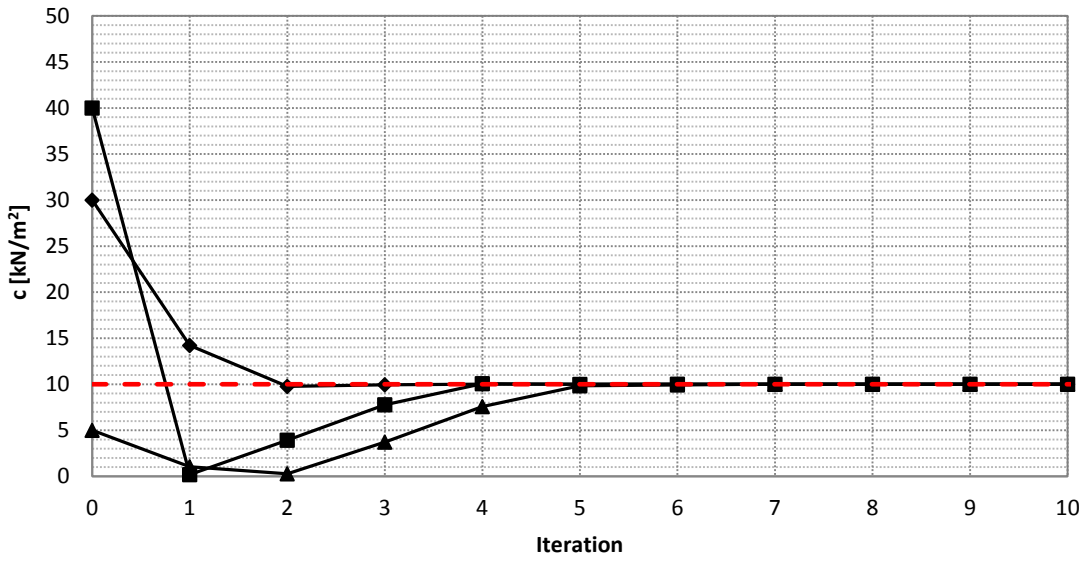

Figure 5.16. Evolution of the cohesion value using the Gauss-Newton method with exact data. The diamonds represent the starting point 1 case, the squares represent the starting point 2 case, the triangles represent the starting point 3 case and the red dashed line represents the actual parameter value.

For the case study of a shallow tunnel relatively far from collapse, it is pointed out that the Gauss-Newton method works properly on identifying the secant stiffness in standard drained triaxial test (E_{50}^{ref}) and the cohesion (c) when using exact data from vertical displacement measurements. Moreover, even having a narrow banana shape valley surrounding the global minimum, the optimization algorithm shows itself as a highly stable iterative procedure. This is reflected in figure 5.14, where in almost each new iteration the value of the objective function diminishes along the process.

A summary of the results is shown in table 5.4 where the computational cost is also presented.

Case	Initial Values		Final Values		Computational Cost
	E_{50}^{ref} [kN/m^2]	c [kN/m^2]	E_{50}^{ref} [kN/m^2]	c [kN/m^2]	[Plaxis evaluations]
Starting Point 1	17500	30	24995.99	10.00	30
Starting Point 2	30000	40	24996.00	10.00	30
Starting Point 3	7500	5	24996.00	10.00	30

Table 5.4. Results summary using the Gauss-Newton method with exact data. Plaxis evaluations is referred to the number of direct problems solved by the geotechnical program Plaxis.

The difference between the final values of E_{50}^{ref} and its actual value (25000 kN/m^2) is associated to a numerical error derived from the computer precision and the HBCode itself.

5.3.2.2 Noisy Data Case Results

In this section the measurements used in the analysis were altered by introducing noise. As indicated above, the noise was randomly created following a normal distribution defined by the mean μ=0 and the standard deviation σ=0.5·10^{-3} m.

The following three figures (5.17, 5.18 and 5.19) illustrate the path followed by the iterative procedure throughout the objective function surface for the case of noisy data. Due to the fact that it was expected a more unstable scenario due to the introduction of noise, the maximum number of iteration was raised from 10 to 15.

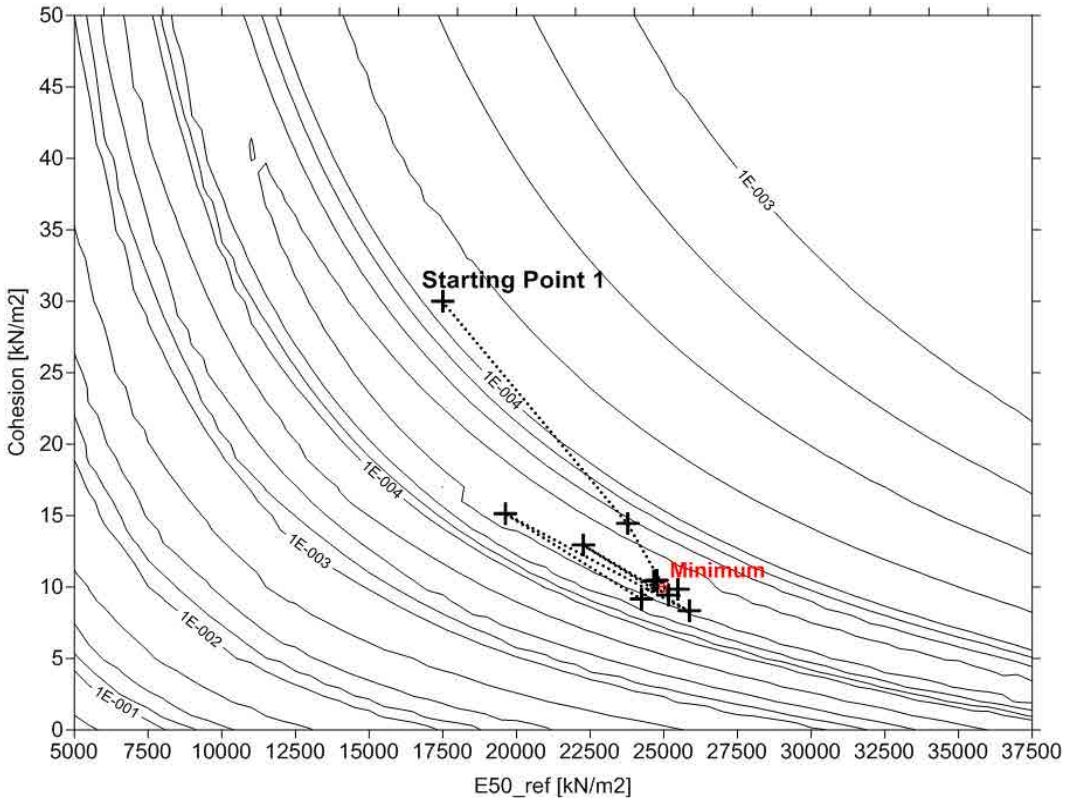

Figure 5.17. Gauss-Newton path from the starting point 1 - Objective function [m^2] (noisy data).

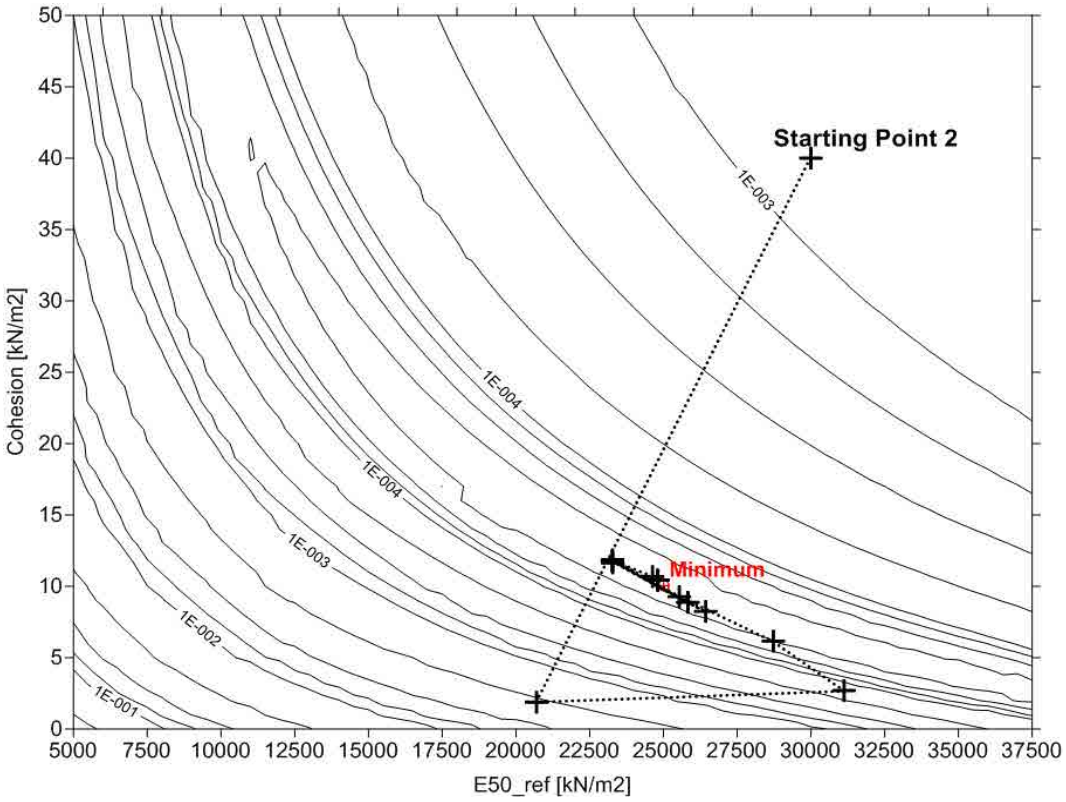

Figure 5.18. Gauss-Newton path from the starting point 2 - Objective function [m^2] (noisy data).

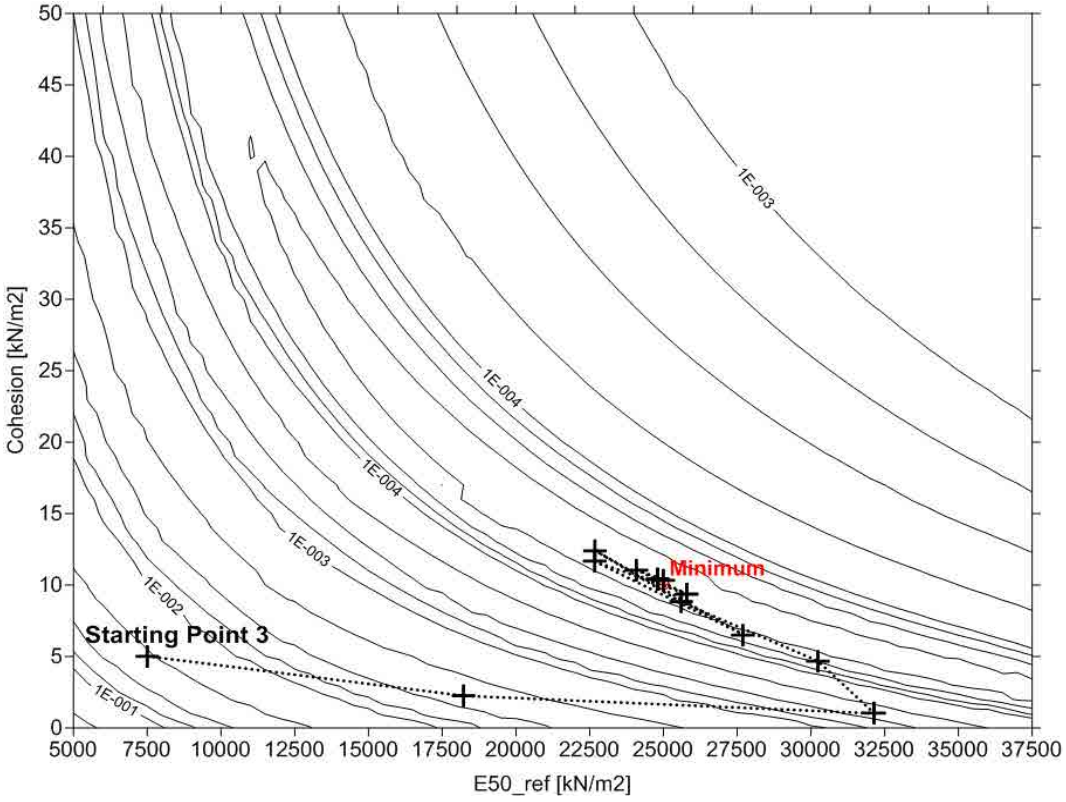

Figure 5.19. Gauss-Newton path from the starting point 3 - Objective function [m^2] (noisy data).

As expected, close to the minimum the procedure has jumped around it. This behavior is derived from the difficulties that a gradient based method has to move around relatively flat

and noisy domains. However, in terms of soil parameter values, the results obtained from the Gauss-Newton method are still good enough to be considered satisfactory (see figures 5.20 and 5.21).

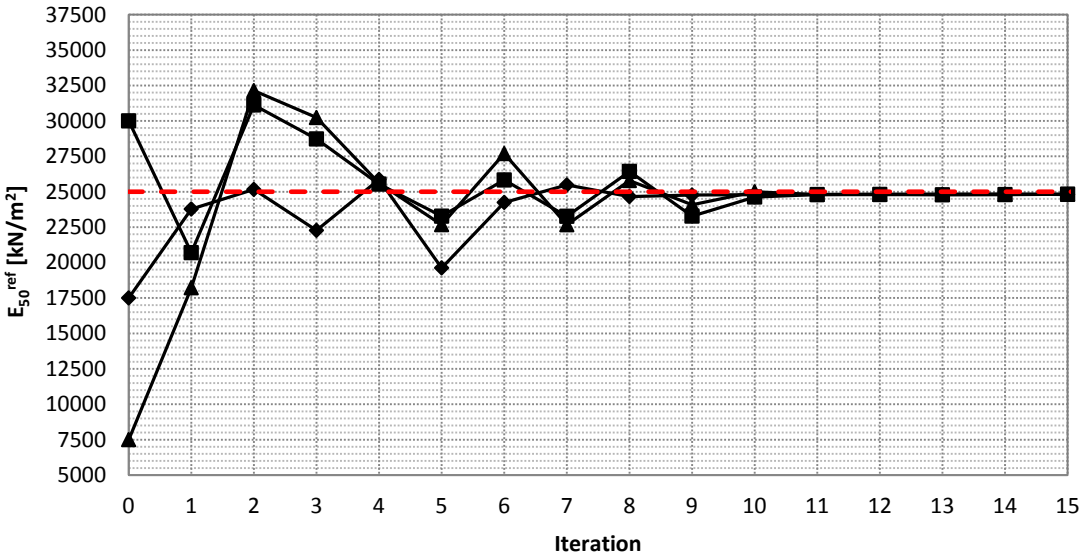

Figure 5.20. Evolution of the E_{50}^{ref} value using the Gauss-Newton method with noisy data. The diamonds represent the starting point 1 case, the squares represent the starting point 2 case, the triangles represent the starting point 3 case and the red dashed line represents the actual parameter value.

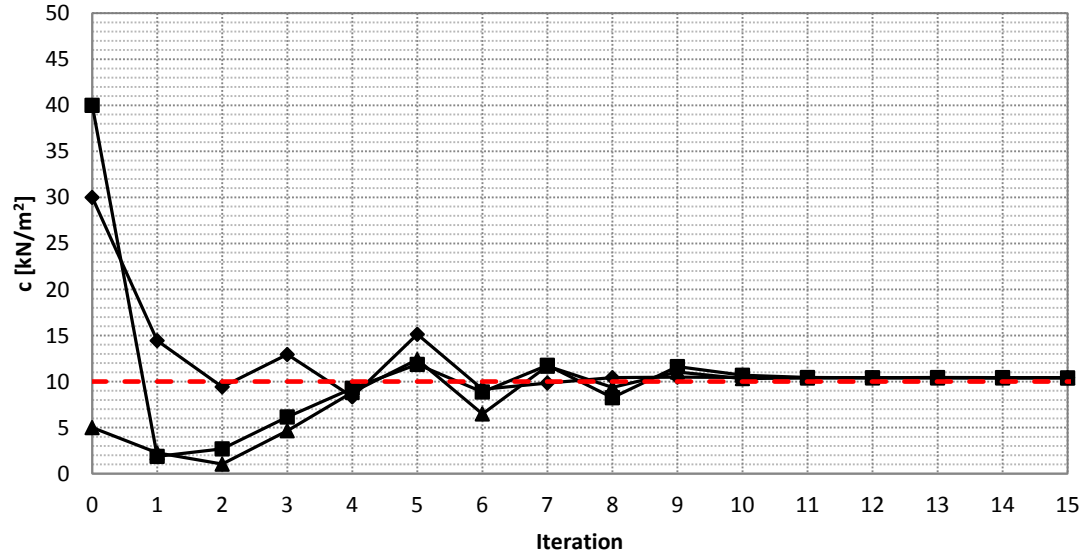

Figure 5.21. Evolution of the cohesion value using the Gauss-Newton method with noisy data. The diamonds represent the starting point 1 case, the squares represent the starting point 2 case, the triangles represent the starting point 3 case and the red dashed line represents the actual parameter value.

In terms of objective function (see figure 5.22), the significant increase in the objective function value, especially close to the minimum, is a direct consequence of the noise that has flattened the surroundings of the minimum and has caused that different parameters combinations have similar values of objective function. This phenomenon, typical in geotechnical problems, is reflected in the oscillatory behavior of the parameter values

throughout the iterative procedure (see figures 5.20 and 5.21), while the objective function value remains constant (see figure 5.22). In these cases, depending on the value of the objective function defined as solution of the parameter identification problem (objective function tolerance), taking into account that the accuracy of the measurements and the nature of the geotechnical problem have to be reflected in some way in the objective function tolerance, a domain of different possible solutions would be determined as solution of the problem instead of having a one unique solution.

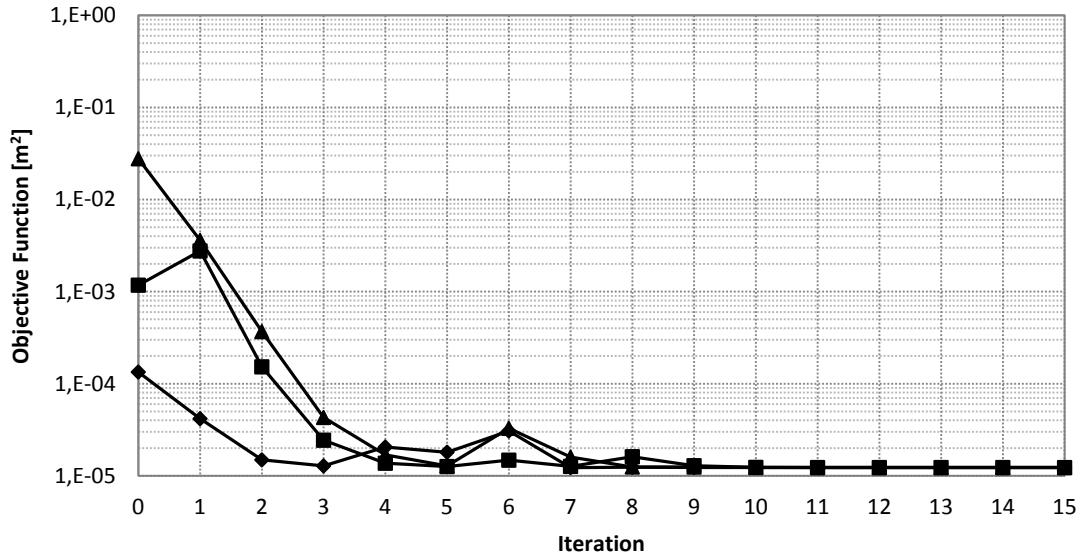

Figure 5.22. Evolution of the objective function using the Gauss-Newton method with noisy data. The diamonds represent the starting point 1 case, the squares represent the starting point 2 case and the triangles represent the starting point 3 case.

Because of the presence of noise in the measurements, a deviation is associated with the parameters values obtained from the analysis.

From the diagonal elements of the parameter covariance matrix ($\boldsymbol{C}_p$), the variance of each parameter can be extracted, and subsequently its standard deviation (Bury, 1975).

The parameter covariance matrix is defined as:

$$\boldsymbol{C}_p = (\boldsymbol{A}^T \boldsymbol{C}_x^{-1} \boldsymbol{A})^{-1} \tag{5.2}$$

where $\boldsymbol{A}$ is the sensitivity matrix and $\boldsymbol{C}_x$ is the measurement covariance matrix (see chapter 2). Assuming the measurements independent, and knowing the standard deviation of each measurement, the measurement covariance matrix is defined as:

$$\boldsymbol{C}_x = \begin{bmatrix} \sigma_1^2 & \cdots & 0 \\ \vdots & \ddots & \vdots \\ 0 & \cdots & \sigma_n^2 \end{bmatrix} \tag{5.3}$$

where σ is the standard deviation of each measurement and n is the number of measurements.

A summary of the results is shown in table 5.5 including the standard deviation of the parameters identified and the computational cost.

Case	Initial Values		Final Values		Computational Cost
	E_{50}^{ref} [kN/m^2]	c [kN/m^2]	E_{50}^{ref} [kN/m^2]	c [kN/m^2]	[Plaxis evaluations]
Starting Point 1	17500	30	24803.57 ± 1805.4	10.42 ± 1.47	44
Starting Point 2	30000	40	24830.13 ± 1817.0	10.41 ± 1.47	44
Starting Point 3	7500	5	24813.70 ± 1820.3	10.41 ± 1.47	44

Table 5.5. Results summary using the Gauss-Newton method with noisy data. Plaxis evaluations is referred to the number of direct problems solved by the geotechnical program Plaxis.

Finally, it can be pointed out that, even with the presence of noise, the Gauss-Newton method works satisfactory on identifying the secant stiffness in standard drained triaxial test (E_{50}^{ref}) and the cohesion (c) for a case study of a shallow tunnel relatively far from collapse. The real values are within the interval of confidence.

5.3.3 Using the Marquardt Method

Due to the fact that the Marquardt method is also a gradient based method, the same three starting points that were presented in the previous section were used.

- Starting Point 1: E_{50}^{ref} = 17500 kN/m^2 and c = 30 kN/m^2

- Starting Point 2: E_{50}^{ref} = 30000 kN/m^2 and c = 40 kN/m^2

- Starting Point 3: E_{50}^{ref} = 7500 kN/m^2 and c = 5 kN/m^2

When using the Marquardt method, two parameters related to the optimization method must be initially defined in order to fully define the iterative procedure. Those two parameters are: the initial value of μ (μ_0), which is in charge of driving the search, and ρ, which controls the value of μ along the iterative procedure. The full description of the method was presented in section 3.2.3, as well as the implications caused by different values of μ_0 and ρ.

Due to the fact that the Marquardt method tends to iterate by smaller steps than the Gauss-Newton method, the maximum value of iterations was set to 45.

5.3.3.1 Exact Data Case Results

Initially, the values of μ_0 and ρ were set to μ_0=1·10^{-2} and ρ=10, as adopted in Ledesma (1987). However, as explained later, the right values of μ_0 and ρ are strongly problem dependent, and usually, several trials are required in order to find them. A general guideline to find those suitable values between the extreme cases of μ=0 and μ=∞, is to set values with respect to the size of the result of the multiplication of $\boldsymbol{A}^T\boldsymbol{C}_x^{-1}\boldsymbol{A}$. Nonetheless, the task of finding the right values of μ_0 and ρ is still difficult, and many times that penalize the use of the Marquardt method.

In the following three figures (5.23, 5.24 and 5.25), the path followed by the algorithm, for the case of exact data with μ_0=1·10^{-2} and ρ=10, is shown.

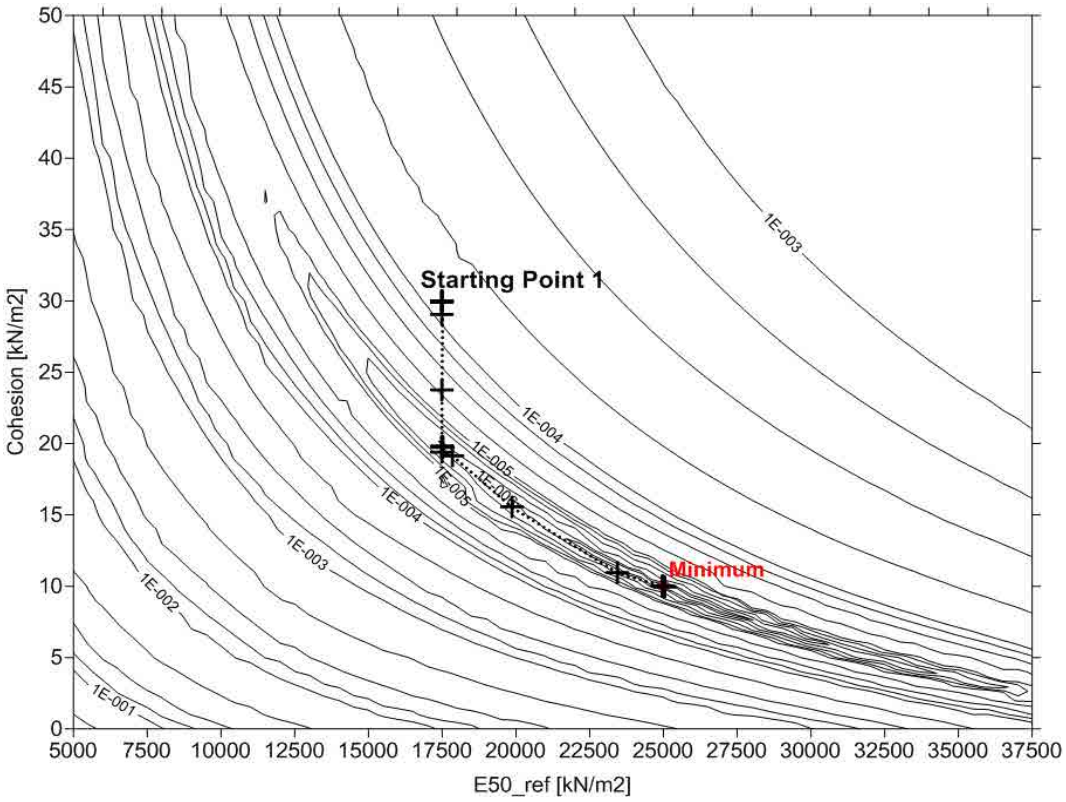

Figure 5.23. Marquardt path from the starting point 1 - Objective function [m^2] (exact data with μ_0=1·10^{-2} and ρ=10).

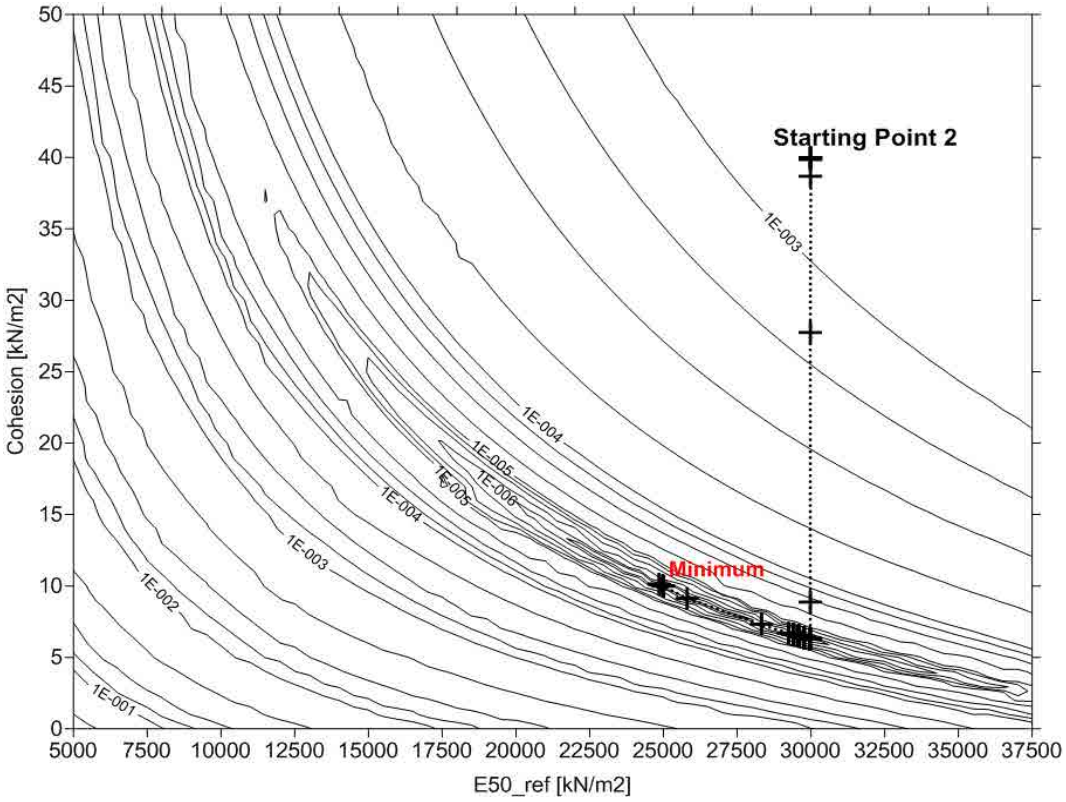

Figure 5.24. Marquardt path from the starting point 2 - Objective function [m^2] (exact data with μ_0=1·10^{-2} and ρ=10).

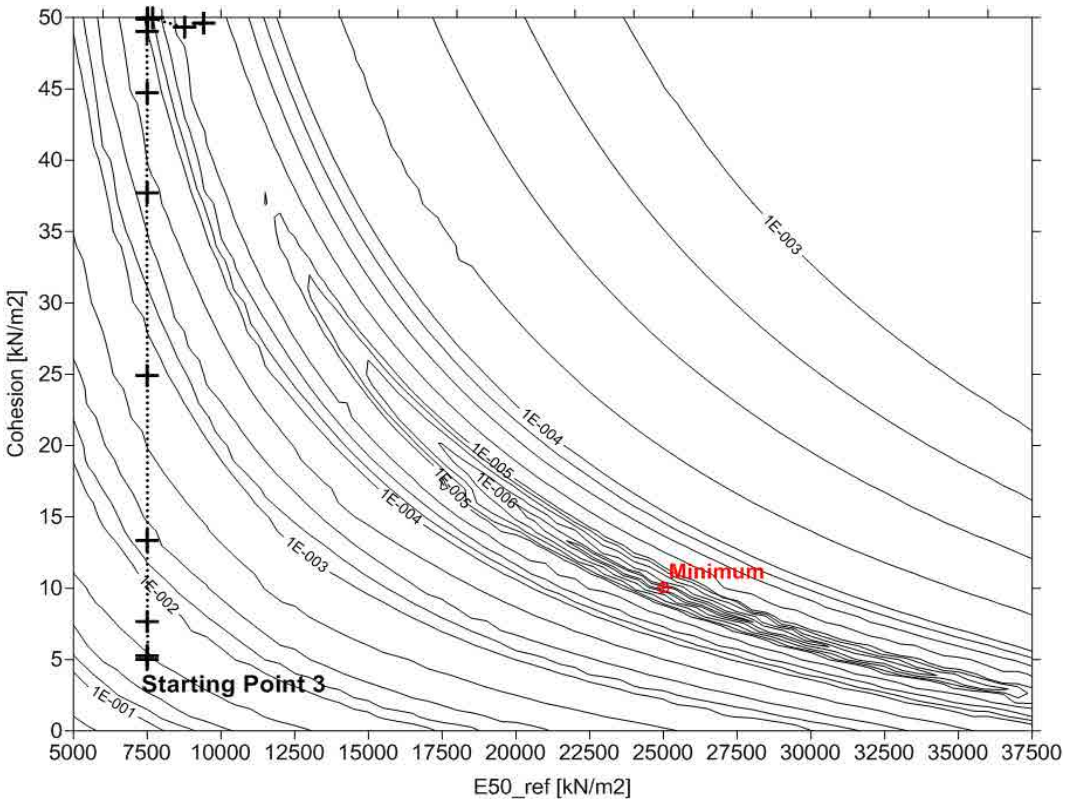

Figure 5.25. Marquardt path from the starting point 3 - Objective function [m^2] (exact data with μ_0=1·10^{-2} and ρ=10).

Except for the starting point 3, which got stuck in a corner of the narrow valley, with no further improvement occurring; the Marquardt method has reached the global optimum by following a path similar to the gradient of the objective function.

In order to reach the global optimum from all starting points and also trying to decrease the number of iterations, a new value of μ_0 was set to μ_0=1·10^{-12}, keeping in line with the size of $\boldsymbol{A}^T\boldsymbol{C}_x^{-1}\boldsymbol{A}$.

With the new value of μ_0 it was possible to reach the minimum for all starting points and the number of iterations was substantially reduced to 10.

As expected, decreasing the value of μ_0 has made the algorithm to advance with longer steps, as well as driving the search closer to the direction defined by the minimum of the tangent paraboloid of the objective function.

The following three figures (5.26, 5.27 and 5.28) illustrate the path followed by the iterative procedure throughout the surface of objective function, for the case of exact data with μ_0=1·10^{-12} and ρ=10, while figures 5.29, 5.30 and 5.31 show in detail the evolution of the search in terms of the objective function and the parameters values.

From the results presented in this section, it can be pointed out that good results can be obtained from applying the Marquardt method (for exact data). However, in order to obtain those good results, a not insignificant effort must be placed into the definition of μ_0, and depending on the complexity of the problem, this task can be difficult and time consuming.

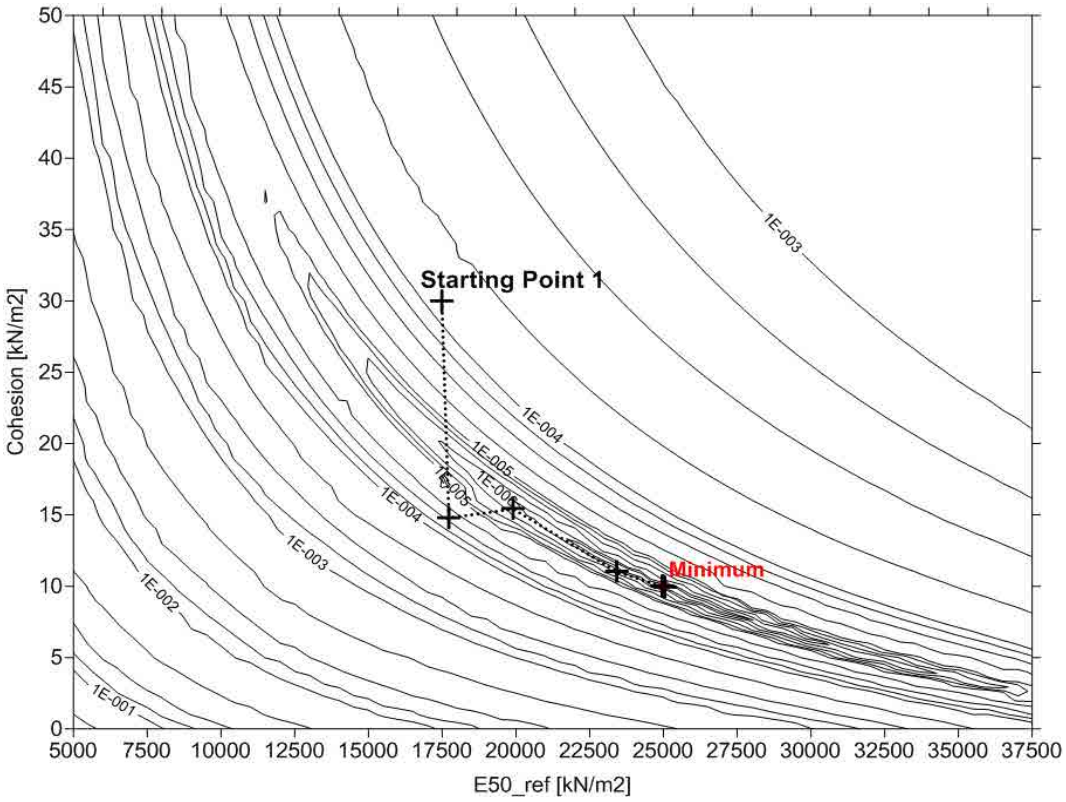

Figure 5.26. Marquardt path from the starting point 1 - Objective function [m^2] (exact data with μ_0=1·10^{-12} and ρ=10).

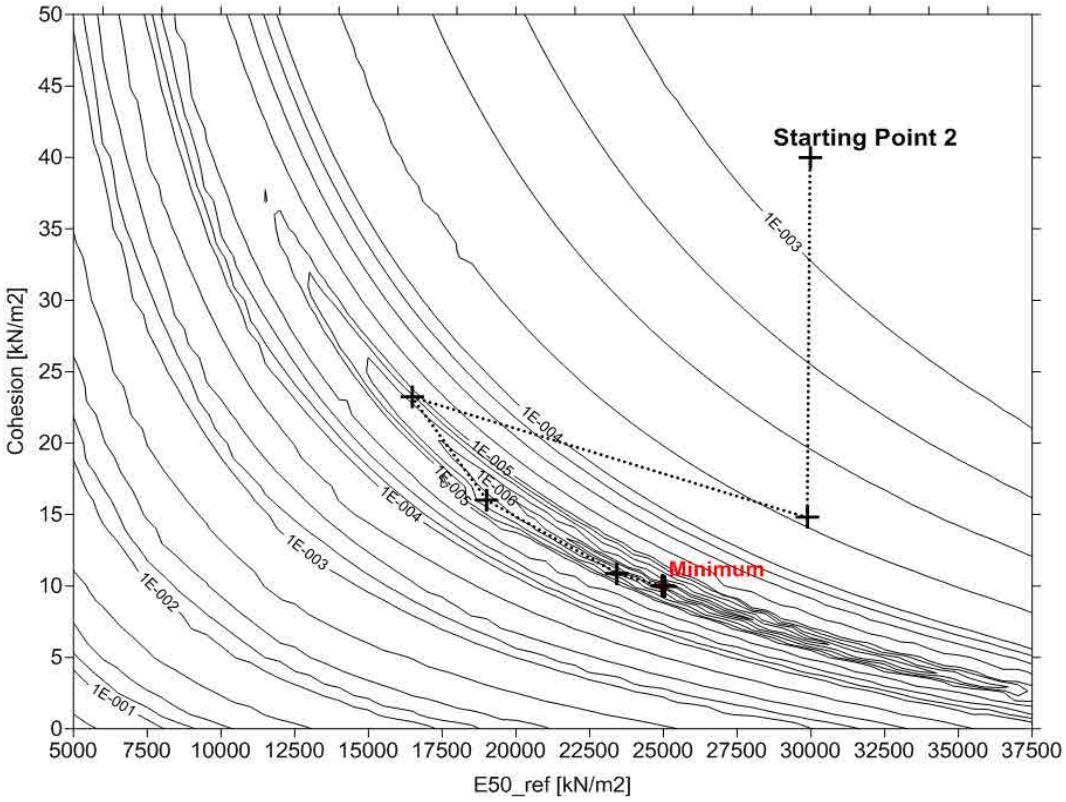

Figure 5.27. Marquardt path from the starting point 2 - Objective function [m^2] (exact data with μ_0=1·10^{-12} and ρ=10).

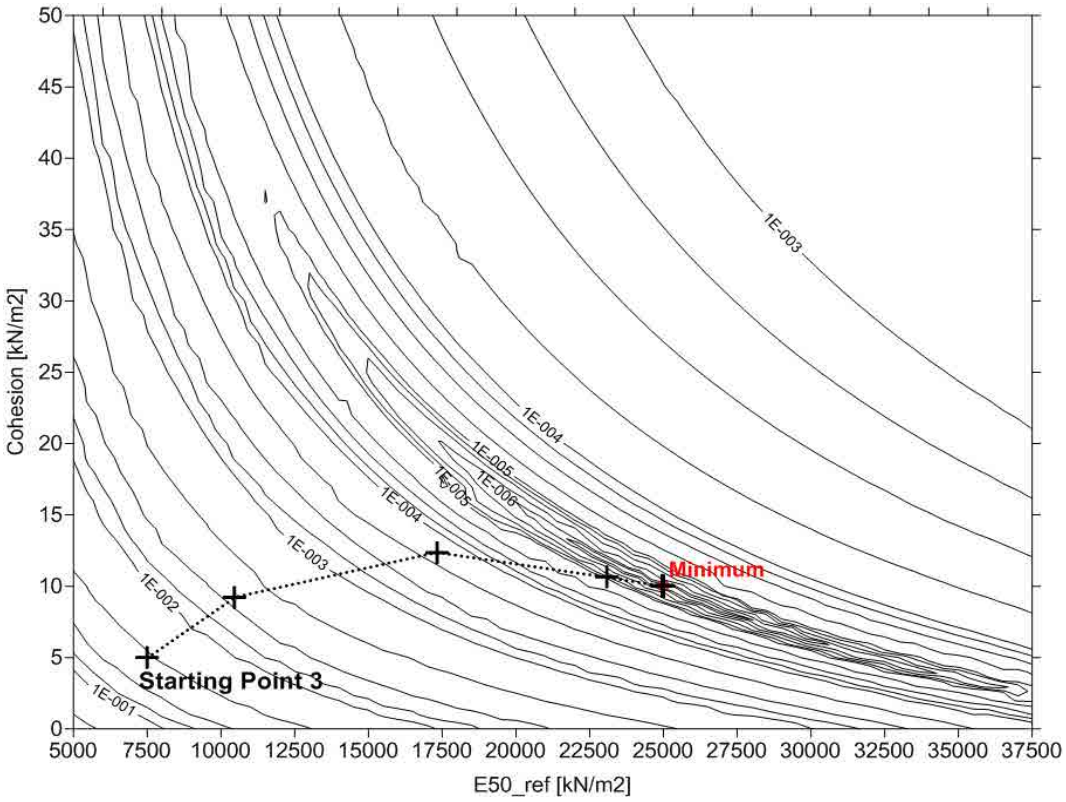

Figure 5.28. Marquardt path from the starting point 3 - Objective function [m^2] (exact data with μ_0=1·10^{-12} and ρ=10).

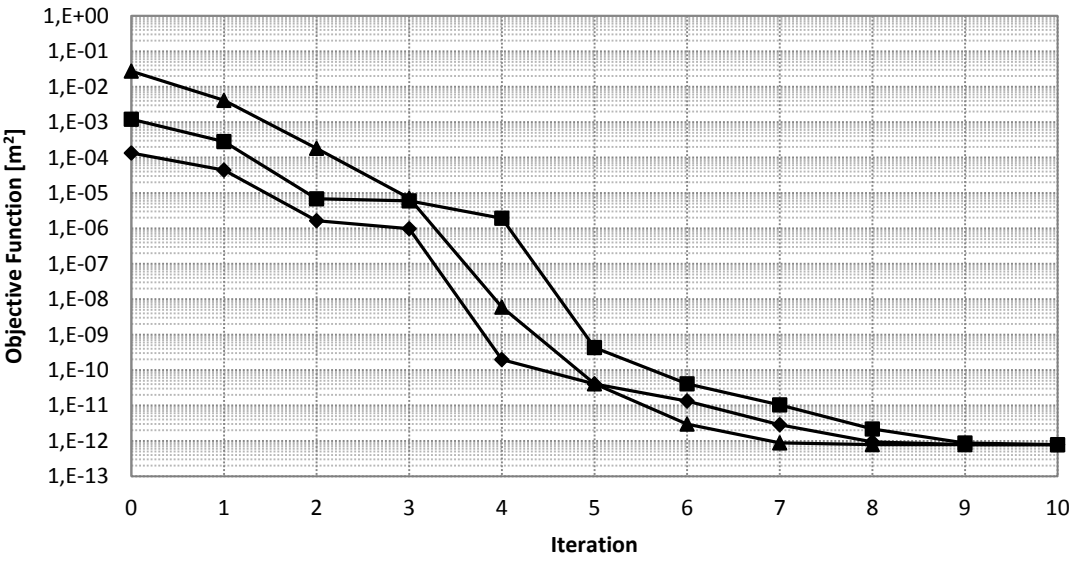

Figure 5.29. Evolution of the objective function using the Marquardt method with exact data and μ_0=1·10^{-12} and ρ=10. The diamonds represent the starting point 1 case, the squares represent the starting point 2 case and the triangles represent the starting point 3 case.

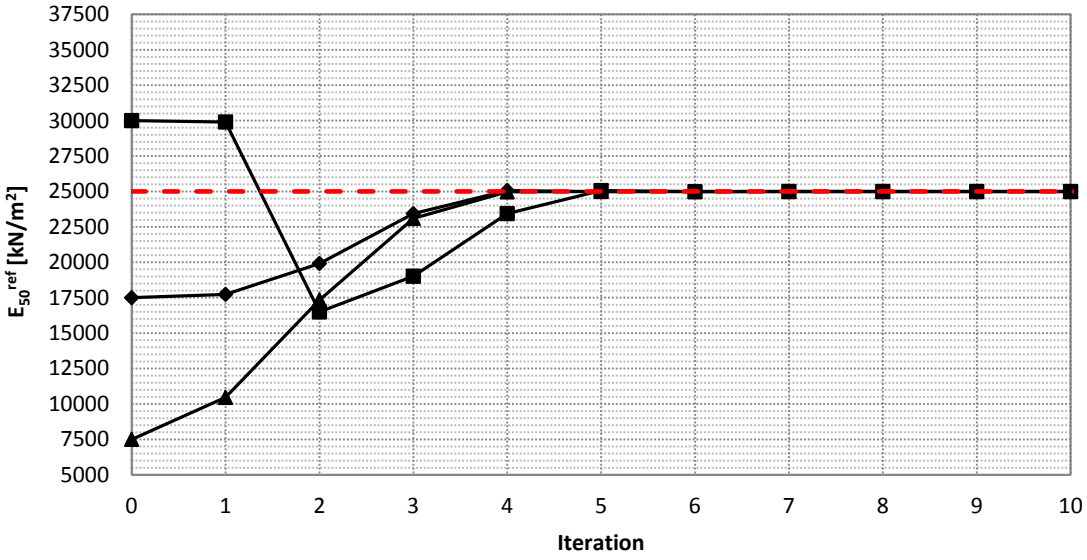

Figure 5.30. Evolution of the E_{50}^{ref} value using the Marquardt method with exact data and μ_0=1·10^{-12} and ρ=10. The diamonds represent the starting point 1 case, the squares represent the starting point 2 case, the triangles represent the starting point 3 case and the red dashed line represents the actual parameter value.

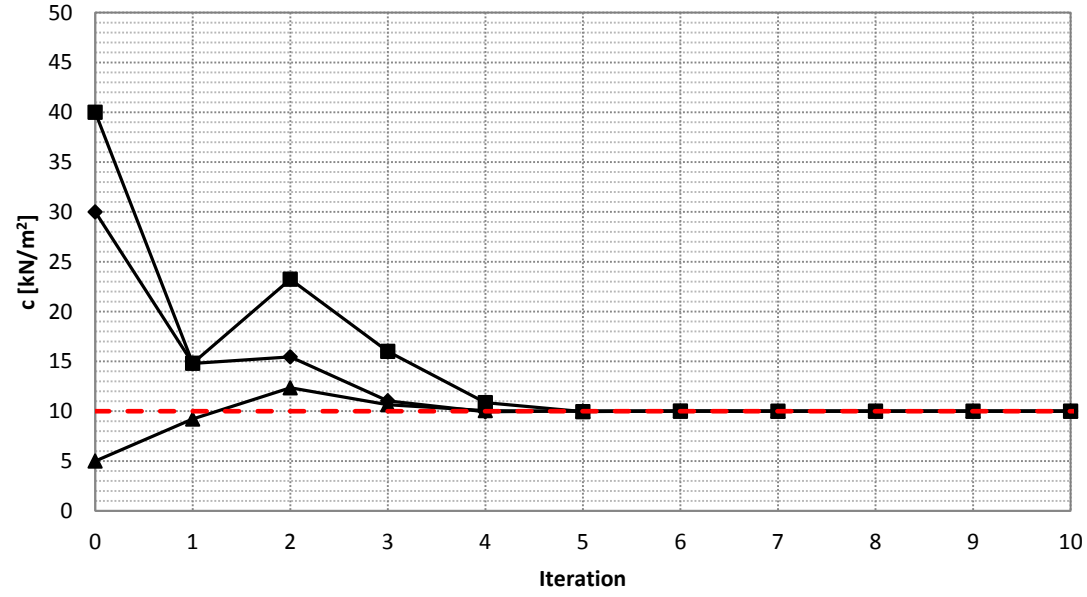

Figure 5.31. Evolution of the cohesion value using the Marquardt method with exact data and μ_0=1·10^{-12} and ρ=10. The diamonds represent the starting point 1 case, the squares represent the starting point 2 case, the triangles represent the starting point 3 case and the red dashed line represents the actual parameter value.

A summary of the results is shown in table 5.6 where the computational cost is also presented.

Case	Initial Values		Final Values		Computational Cost
	E_{50}^{ref} [kN/m^2]	c [kN/m^2]	E_{50}^{ref} [kN/m^2]	c [kN/m^2]	[Plaxis evaluations]
Starting Point 1	17500	30	24995.99	10.00	30
Starting Point 2	30000	40	24995.98	10.00	33
Starting Point 3	7500	5	24995.99	10.00	78

Table 5.6. Results summary using the Marquardt method with exact data and μ_0=1·10^{-12} and ρ=10. Plaxis evaluations is referred to the number of direct problems solved by the geotechnical program Plaxis.

5.3.3.2 Noisy Data Case Results

As it was appreciated from the previous section, the performance of the Marquardt method is strongly problem dependent, and the selection of the values of μ_0 and ρ has a high influence on the final results. As a consequence, and expecting a more difficult resolution of the problem, due to the introduction of noise, several values of μ_0 and ρ were used to try to solve the problem. However, here, only the results obtained from the case of $\mu_0=1\cdot10^{-15}$ and $\rho=10$ (the better case) are presented.

Unfortunately, even though all of them were capable to reach the narrow valley surrounding the minimum, none of them was capable of finally arriving at the global minimum. In fact, for the starting point 1 and 3, the algorithm passed close to the minimum but was not capable to reach it.

Figures 5.32, 5.33 and 5.34 show the path followed by the algorithm throughout the surface of objective function for the case of noisy data with $\mu_0=1\cdot10^{-15}$ and $\rho=10$, and illustrate what has been already mentioned.

To see in more detail the evolution of the algorithm, in terms of objective function and parameters values, figures 5.35, 5.36 and 5.37 are presented.

It has to be mentioned that if the results are strictly evaluated in terms of geotechnical representation, as parameters of a soil material, the results are not as bad as they are if they are evaluated in mathematical terms. It has to be noticed that in reality there is a high variability on the parameters values to characterize a soil stratum.

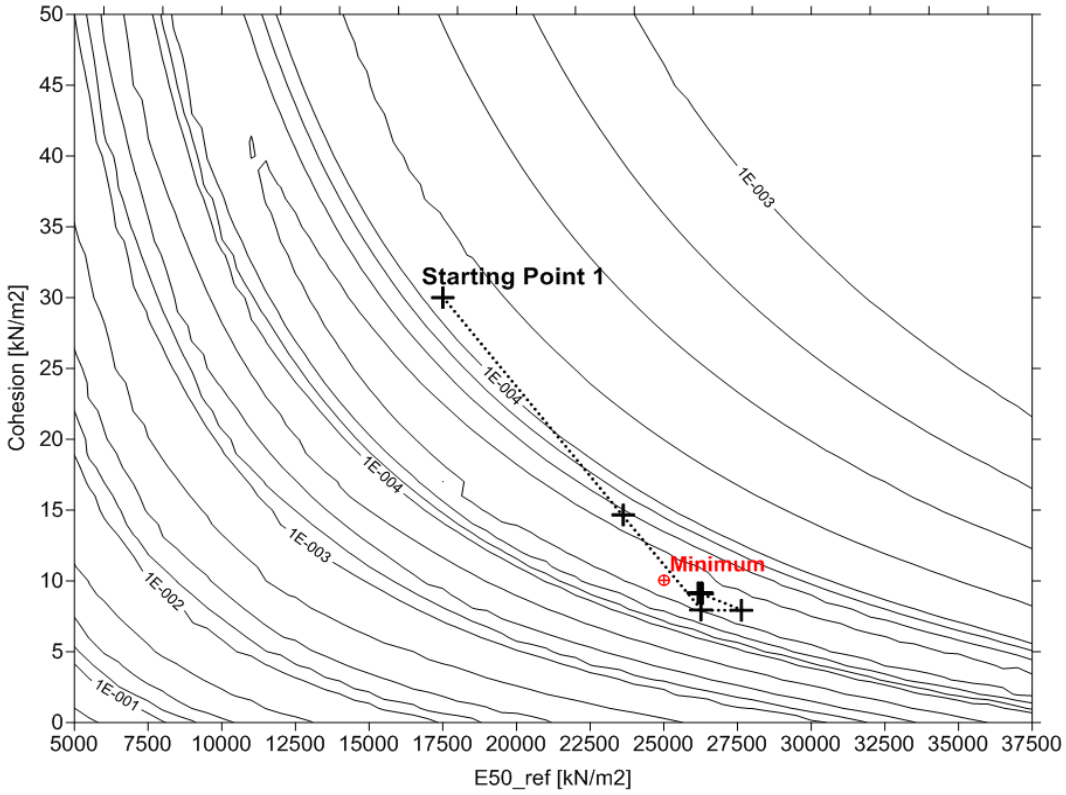

Figure 5.32. Marquardt path from the starting point 1 - Objective function [m^2] (noisy data with $\mu_0=1\cdot10^{-15}$ and $\rho=10$).

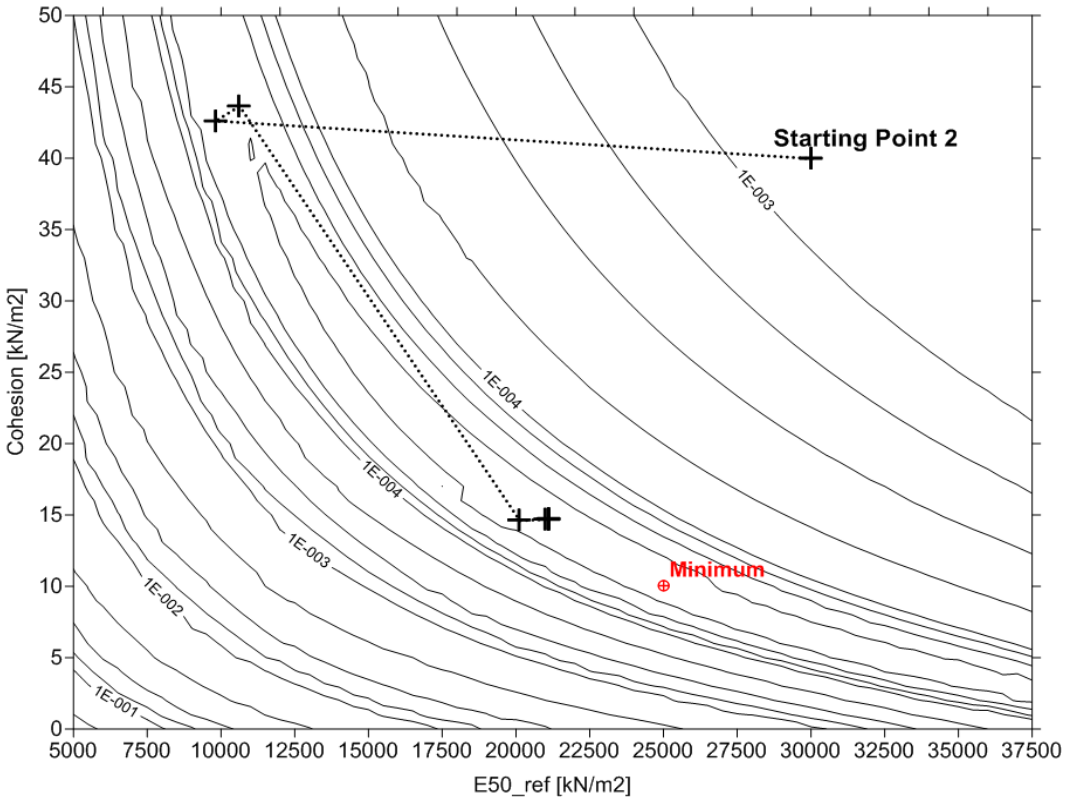

Figure 5.33. Marquardt path from the starting point 2 - Objective function [m^2] (noisy data with μ_0=1·10^{-15} and ρ=10).

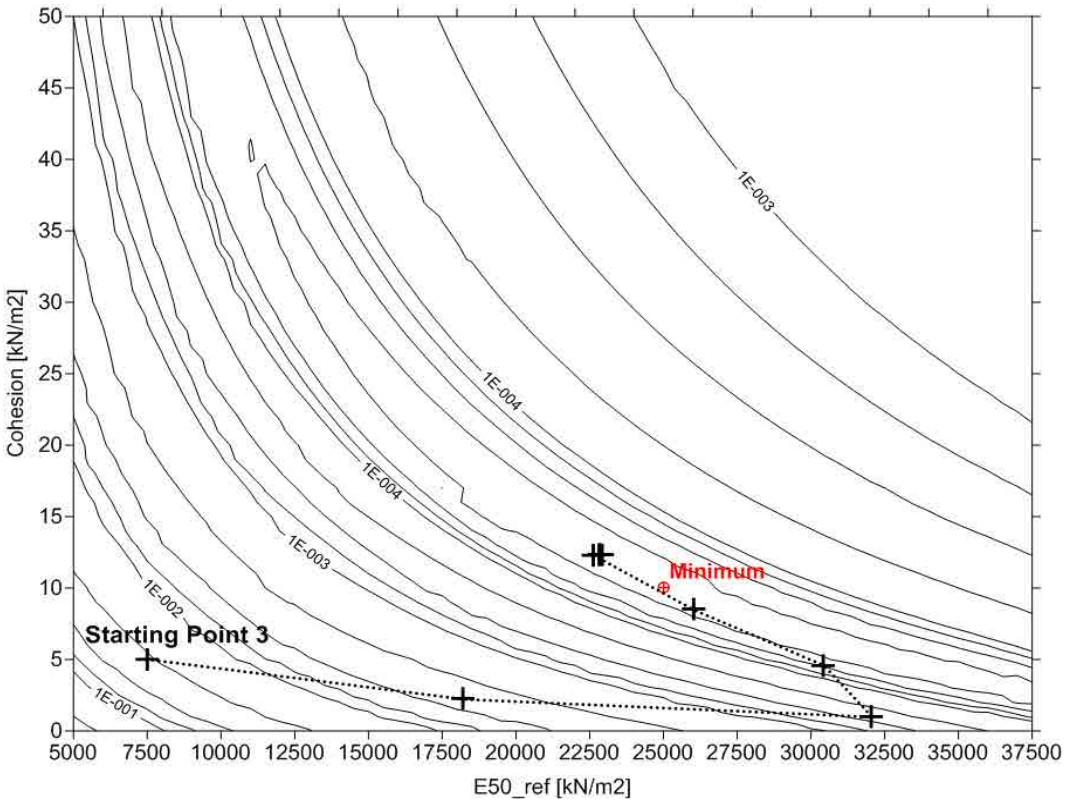

Figure 5.34. Marquardt path from the starting point 3 - Objective function [m^2] (noisy data with μ_0=1·10^{-15} and ρ=10).

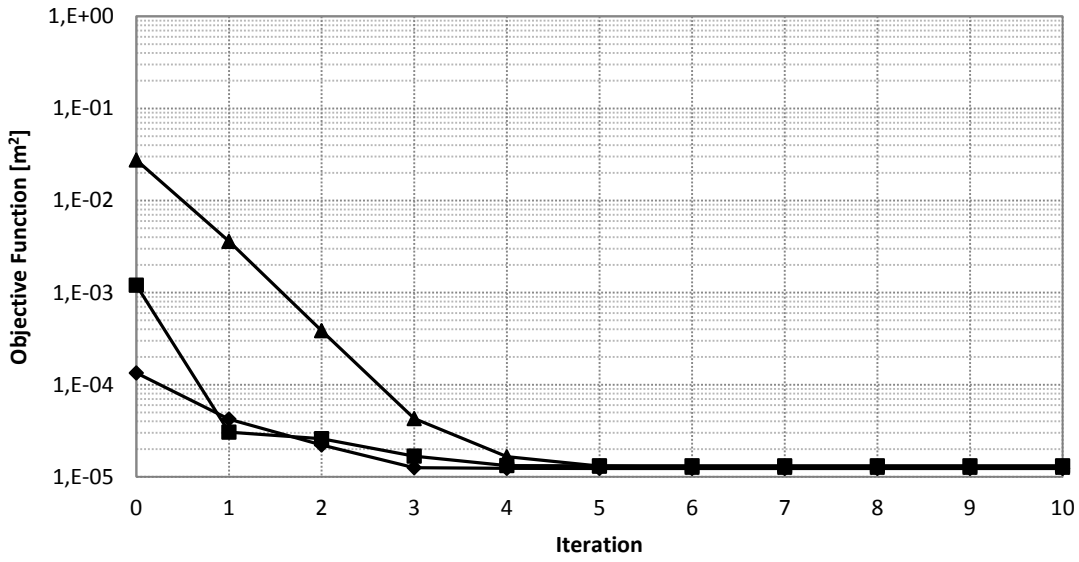

Figure 5.35. Evolution of the objective function using the Marquardt method with noisy data and μ_0=1·10^{-15} and ρ=10. The diamonds represent the starting point 1 case, the squares represent the starting point 2 case and the triangles represent the starting point 3 case.

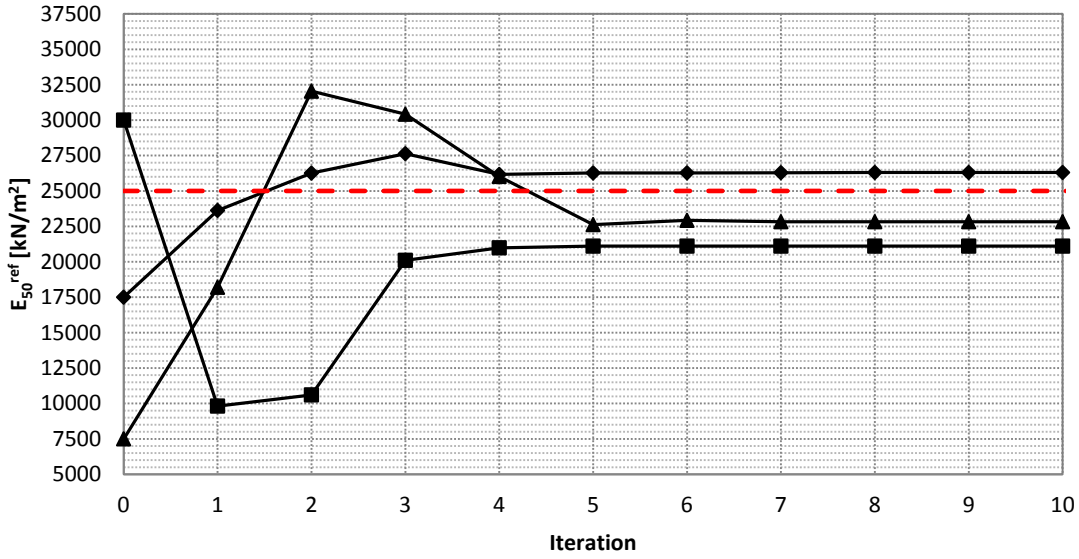

Figure 5.36. Evolution of the E_{50}^{ref} value using the Marquardt method with noisy data and μ_0=1·10^{-15} and ρ=10. The rhombuses represent the starting point 1 case, the squares represent the starting point 2 case, the triangles represent the starting point 3 case and the red dashed line represents the actual parameter value.

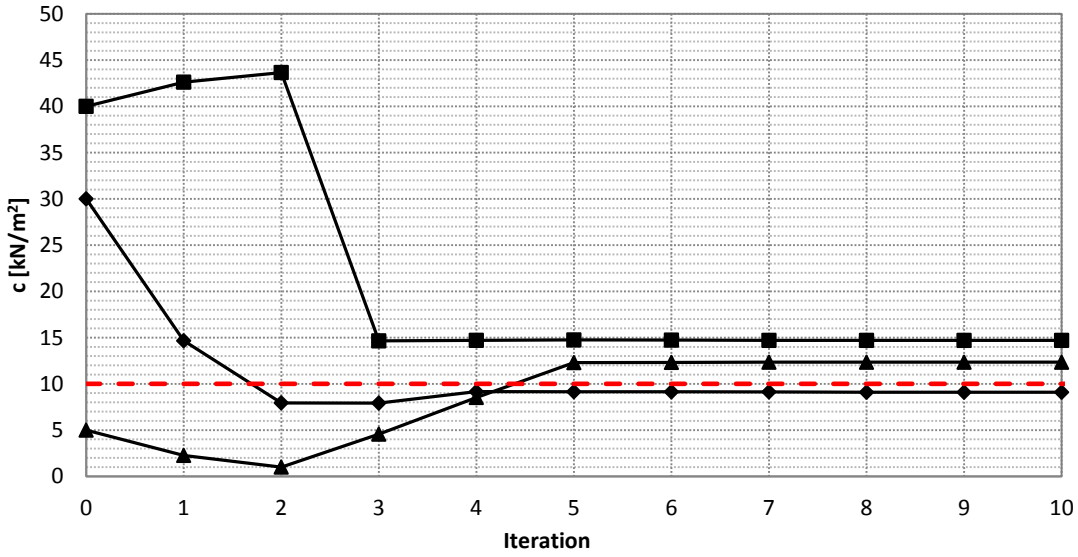

Figure 5.37. Evolution of the cohesion value using the Marquardt method with noisy data and μ_0=1·10^{-15} and ρ=10. The diamonds represent the starting point 1 case, the squares represent the starting point 2 case, the triangles represent the starting point 3 case and the red dashed line represents the actual parameter value.

A summary of the results is shown in table 5.7 where the computational cost is also presented after ten iterations. Actually, more than ten iterations were forced, but no improvement was obtained. As a consequence, it was decided to define the results just using the first ten iterations. However, when using the Marquardt method, it has to be taken into account that for each actual iteration, many internal iterations may be required depending on the evolution of the error (see section 3.2.3). Therefore, as shown in table 5.7, even defining the same number of iterations, different computational costs are obtained.

Case	Initial Values		Final Values		Computational Cost
	E_{50}^{ref} [kN/m^2]	c [kN/m^2]	E_{50}^{ref} [kN/m^2]	c [kN/m^2]	[Plaxis evaluations]
Starting Point 1	17500	30	26301.64 ± 2089.6	9.09 ± 1.82	93
Starting Point 2	30000	40	21104.67 ± 1978.6	14.69 ± 2.66	120
Starting Point 3	7500	5	22827.13 ± 1133.8	12.34 ± 1.50	87

Table 5.7. Results summary using the Marquardt method with nosy data and μ_0=1·10^{-15} and ρ=10. Plaxis evaluations is referred to the number of direct problem solved by the geotechnical program Plaxis.

5.3.4 Using a Simple Genetic Algorithm (SGA)

5.3.4.1 Previous Sensitivity Analysis (Population Size and Selection Pressure)

As mentioned in section 3.3, the key factor of the good performance of genetic algorithms is based on the balance between exploitation and exploration. Many parameters of the algorithm can be tuned up in order to reach the desirable balance between exploitation and exploration. The population size and the selection pressure are some of the parameters that have a major role on that balance.

Increasing the size of the population has a direct impact on the capability of the algorithm to keep a high level of individuals' diversity. The importance of having a diverse population is based on the fact that diverse populations keep the algorithm out of premature convergence, where the algorithm is incapable of generating enough new individuals to keep evolving the population until a satisfactory individual is found.

Another way to keep individuals' diversity is lowering the selection pressure. Lowering the selection pressure increases the chance of the less fitted individuals to be selected. The involvement of less fitted individuals on the reproduction spreads the individuals of the next generation, and subsequently increases the population diversity.

The more common way to increase or decrease the selection pressure is changing the value of the tournament size when using the tournament selection method (see section 3.3.3.5). However, for this particular case study, better results were obtained when using the roulette wheel selection method (see section 3.3.3.5). Therefore, due to the fact that the roulette wheel method has not an explicit way to modify its selection pressure, because the method is exclusively based on the fitness of the individuals, a fitness limit was introduce to lower the selection pressure. The idea is to associate, for those individuals that have the fitness higher than the fitness limit, a probability of selection equivalent to the fitness limit. As a consequence, the probability of selecting a specific individual at the step time t (generation t) by the roulette wheel (eq. 3.17) has been modified to:

$$P_{roulette_{limited}}(t) = \frac{f^*}{N \cdot \overline{f^*}} \tag{5.4}$$

where f^* is the fitness of the specific individual, if the individual fitness is lower than the fitness limit; or the limit fitness, if the individual fitness is higher than the fitness limit. $\overline{f^*}$ is the average fitness of the population, using the fitness limit for the individuals with higher fitness than the limit, and N is the size of the population.

Regardless the importance of keeping a high diverse population, oversized populations and low selection pressure, on the other hand, can make the computational cost too high. For this reason, different population sizes and the application of a fitness limit was studied in terms of diversity and computational cost before trying to solve the actual problem.

The fitness limit was defined by extracting the value of the objective function (eq. 3.31) associated with measurements with approximately one millimeter of standard deviation, which was considered acceptable, and then applying equation 3.16 to finally define the fitness limit. The numerical value of the fitness limit is 40000 m^{-2}, which comes from an objective function value of $2.5 \cdot 10^{-5}$ m^2.

The results of the sensitivity analysis presented in this section were only carried out by the case of noisy data, where three different population sizes (51, 101 and 201) were used in combination with the application and non-application of the fitness limit. The search space discretization was defined as it is shown in table 5.8.

Parameter	Minimum Value	Maximum Value	Step Size Value	Total number of individuals in the search space
E_{50}^{ref} [kN/m^2]	5000	37500	500	3366
c [kN/m^2]	0	50	1	

Table 5.8. Genetic algorithm search space discretization.

Figure 5.38 shows the evolution of the standard population diversity (SPD) for all combinations of population size and application and non-application of the fitness limit.

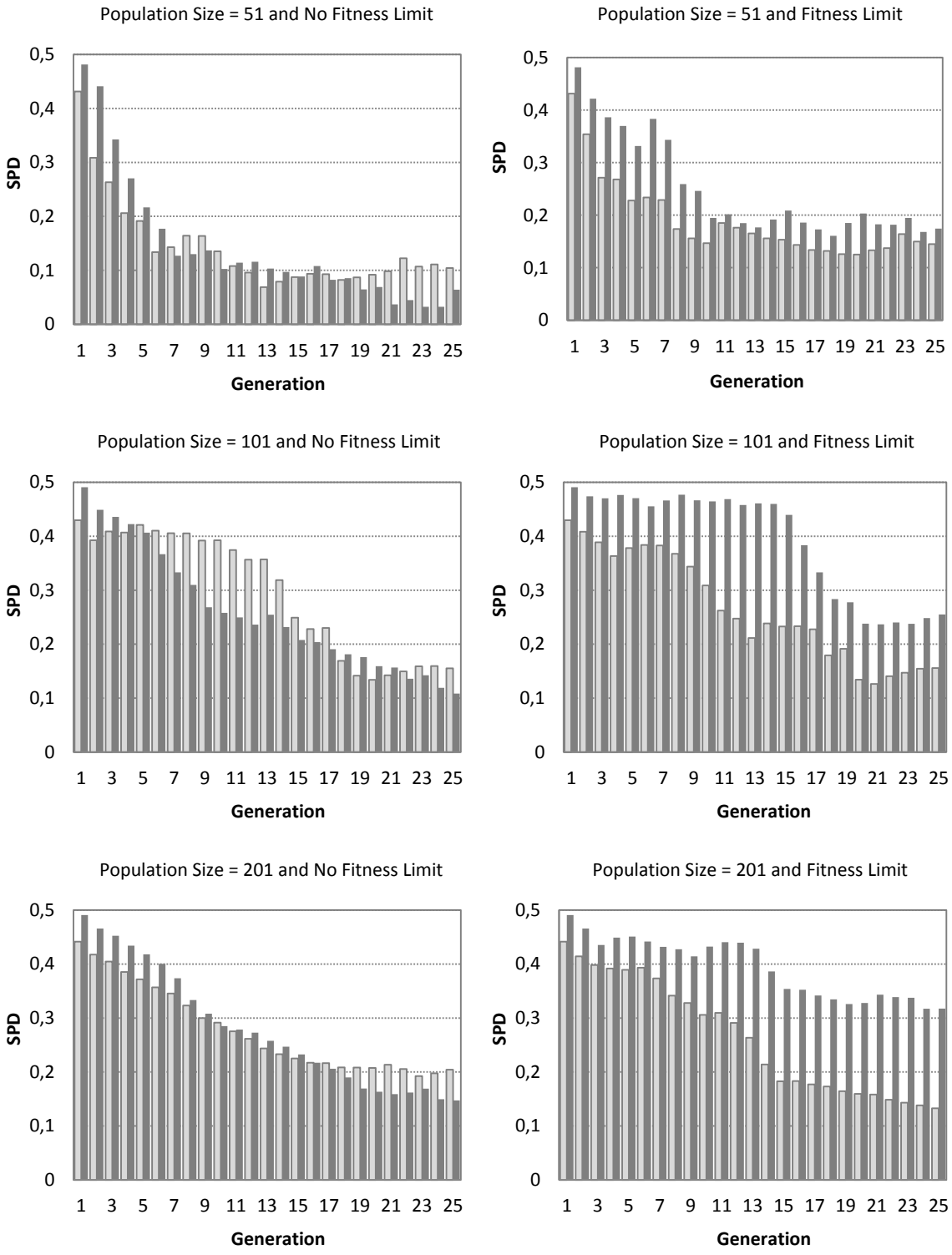

Figure 5.38. Evolution of the standard population diversity (SPD) using a SGA with noisy data. The light grey bars represent the SPD of the E_{50}^{ref} while the dark grey bars represent the SPD of the cohesion.

From the different scenarios (population size and fitness limit) presented in figure 5.38, two main conclusions can be drawn:

1) The application of a fitness limit helps to maintain population's diversity for more generations.

2) For this case study, populations bigger than 101 individuals don't cause any significant increase on terms of population's diversity, independently of the application or not application of a fitness limit.

In order to study directly the capability of the algorithm to generation new individuals in each new generation, the evolution of the percentage of new individuals in each generation is presented in figure 5.39.

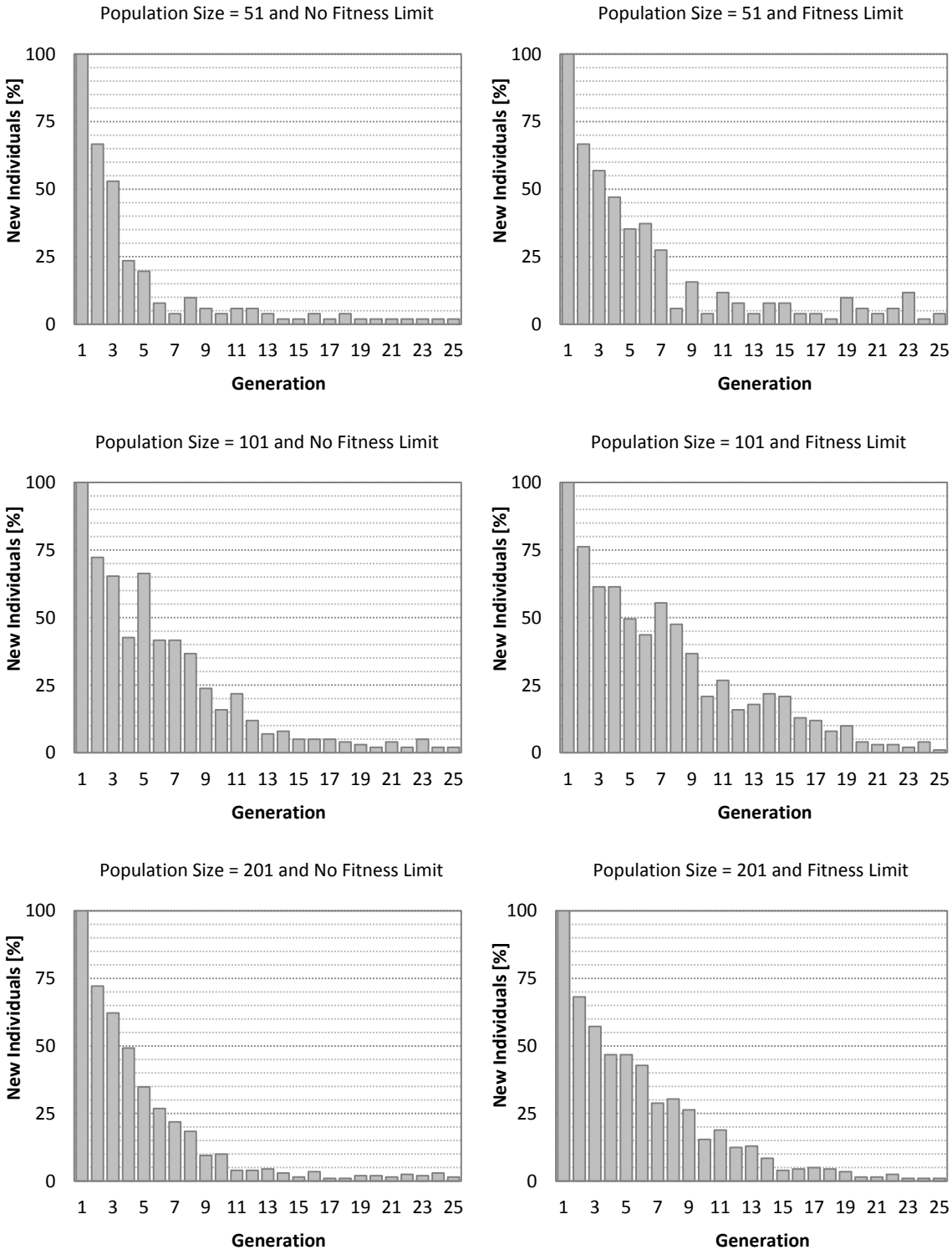

Figure 5.39. Evolution of the percentage of new individuals per generation using a SGA with noisy data.

Clearly, and especially for the smallest population size (51 individuals), the use of a fitness limit makes the algorithm more capable of generating new individuals. However, as a consequence, the computational cost increases. As an example, for the case of 51 individuals, the computational cost goes from 172 direct evaluations, while using no fitness limit, to 249 direct evaluations, when using a fitness limit.

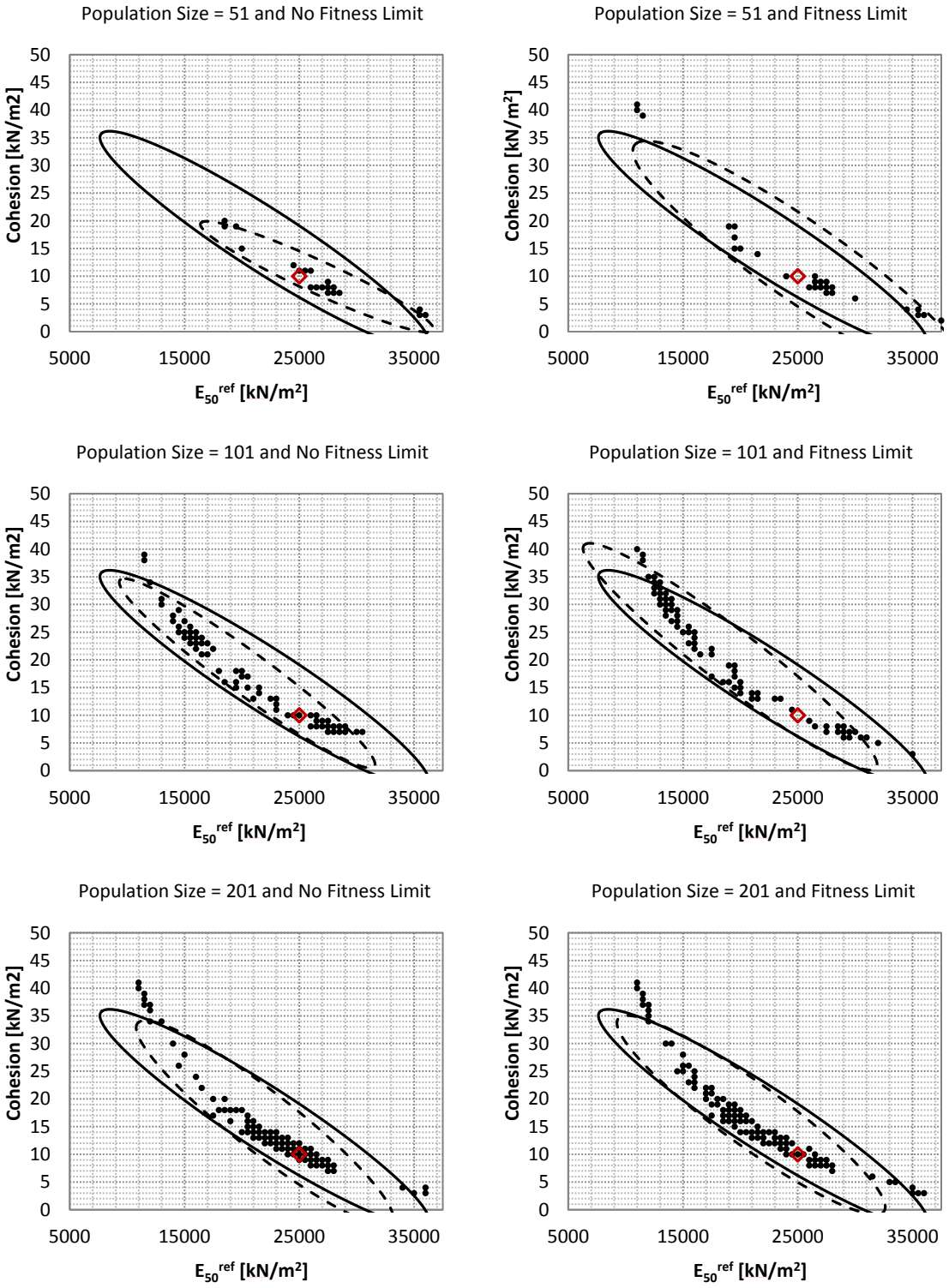

Figure 5.40. Representativeness of the individuals involved in the PCA using a SGA with noisy data (theoretical PCA ellipse versus calculated PCA ellipse). The solid line represents the theoretical PCA ellipse, the dashed line represents the calculated PCA ellipse, the black points are the individuals involved in the PCA and the red rhombus is the individual that represents the solution of the problem.

Another main aspect related to population size and selection pressure, it is its implication on the representativeness of the individuals considered satisfactory for the later principal component analysis (PCA). In figure 5.40, the theoretical PCA ellipse, which is the PCA ellipse defined by all good individuals represented in the entire space search, is compared with the PCA ellipses obtained from the genetic algorithm procedures (calculated PCA ellipse).

The use of a fitness limit makes the problem of representativeness from the population size more independent. All calculated PCA ellipses almost match the theoretical PCA ellipse. Whereas, for the case where a fitness limit is not used, the problem of representativeness remains and it is dependent on the population size. This effect is clearly reflected in figure 5.40a where the calculated PCA ellipse does not match the theoretical PCA ellipse.

To illustrate the phenomenon of promoting exploitation or exploration, the two extreme cases of maximum exploitation and maximum exploration are presented.

The next two figures (5.41 and 5.42) illustrate the case where exploitation was highly promoted; from an initial population of 51 individuals to 172 evaluated individuals after 25 generations applying a simple genetic algorithm without fitness limit.

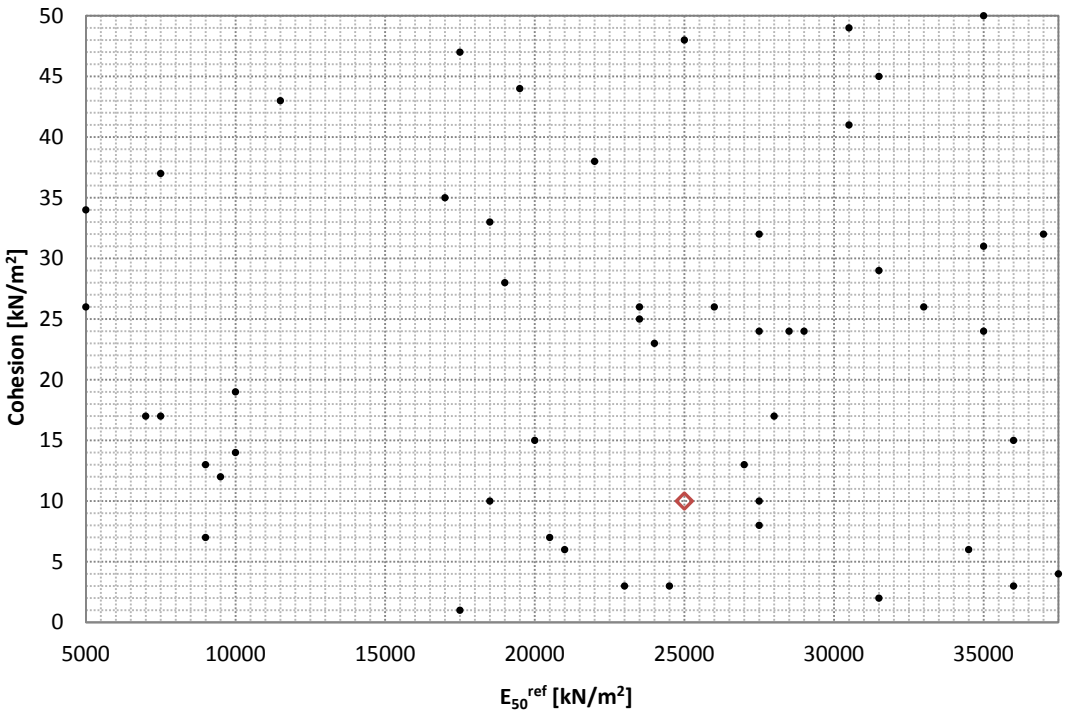

Figure 5.41. Initial population of 51 individuals randomly generated (promoting exploitation).

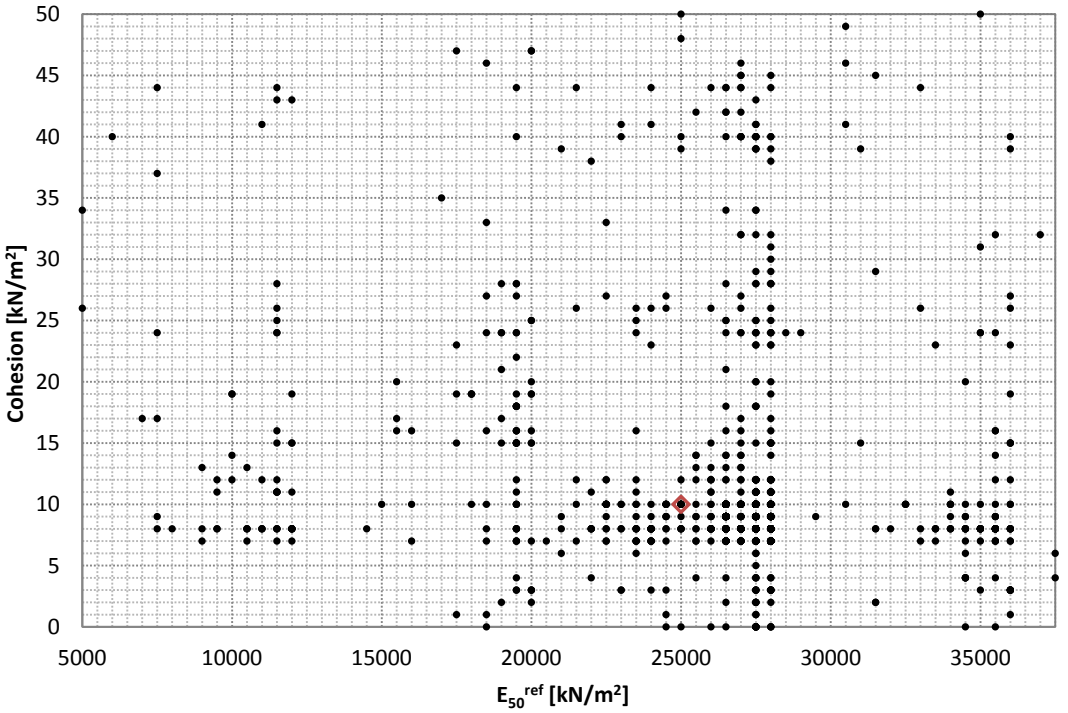

Figure 5.42. Total evaluated individuals (172 individuals) after 25 generations applying a simple genetic algorithm without fitness limit and a population of 51 individuals (promoting exploitation).

On the other hand, in the next two figures (5.43 and 5.44) the promotion of exploration is illustrated. The highly promoted exploration case is represented by a simple genetic algorithm with fitness limit and a population size of 201 individuals.

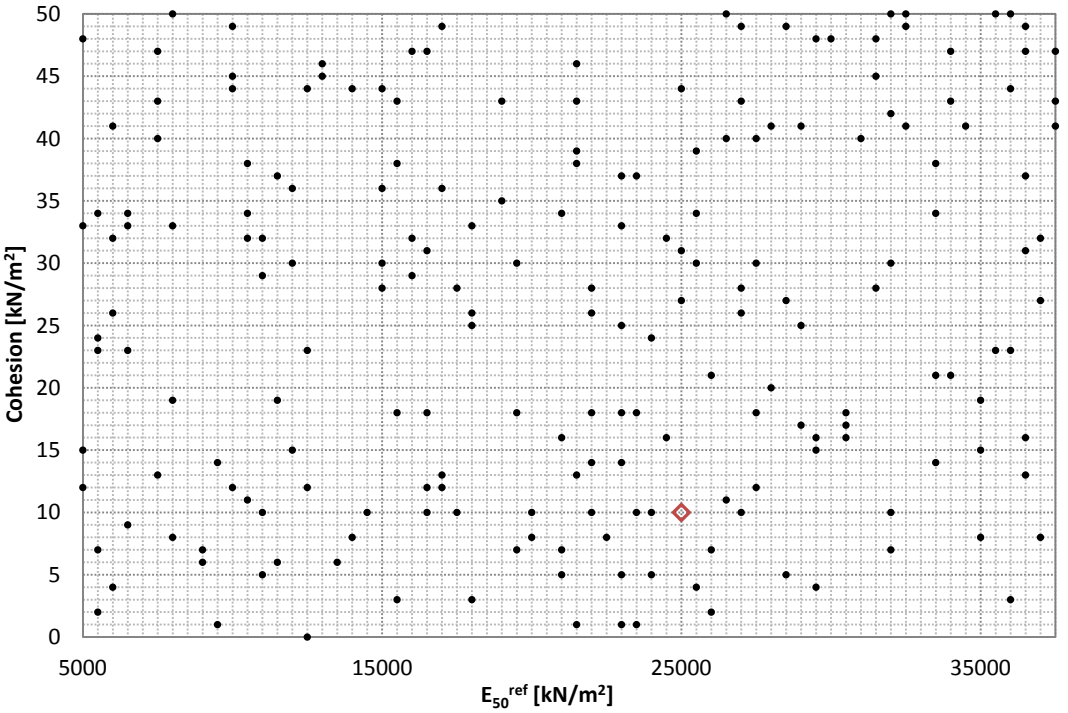

Figure 5.43. Initial population of 201 individuals randomly generated (promoting exploration).

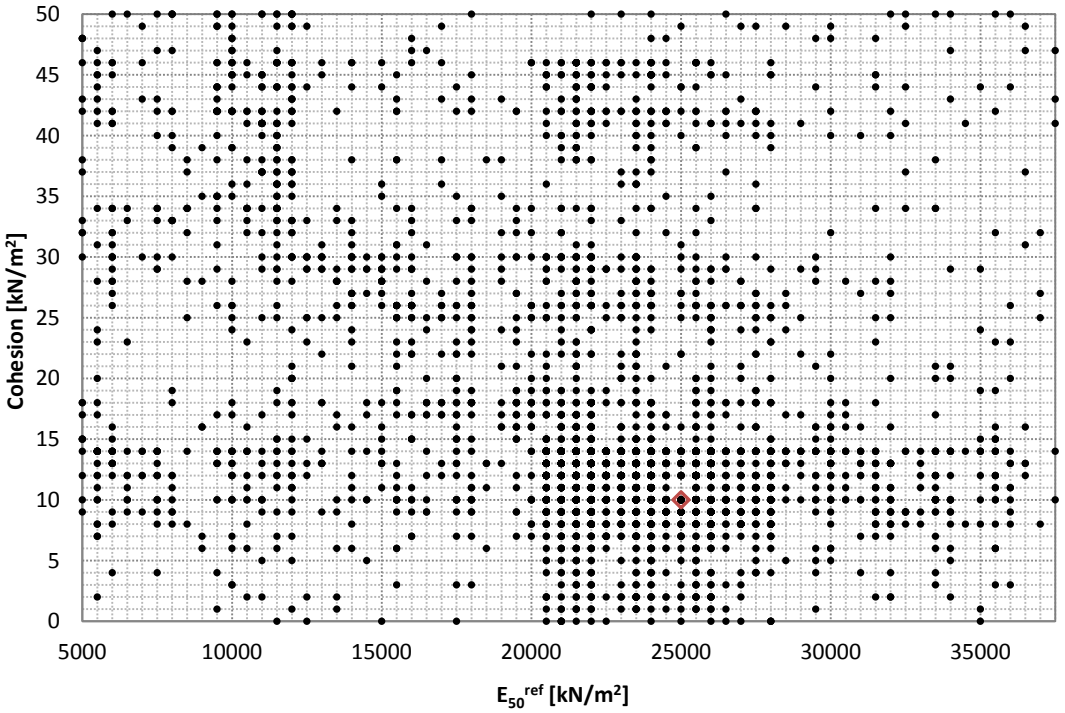

Figure 5.44. Total evaluated individuals (1096 individuals) after 25 generations applying a simple genetic algorithm with fitness limit and a population of 201 individuals (promoting exploration).

Based on the results presented in this section, the population size and the application or non-application of the fitness limit have been defined.

On the one hand, when looking for the best individual, rather than the best set of individuals, a simple genetic algorithm without a fitness limit and a population size of 101 individuals, was considered appropriate for trying to find the best individual, keeping a sufficient population's diversity with a reasonable computational cost. On the other hand, when looking for the best set of individuals, rather than one unique best individual, a simple genetic algorithm with a fitness limit and a population of 101 individuals was considered appropriate.

It is really important to mention that these recommendations are only valid for the case study presented here. Therefore, a new sensitivity analysis would be required for a new problem. However, in the absence of any sensitivity analysis, it is recommended to use a fitness limit (low selection pressure) and the biggest possible population, taking into account the computational cost of the problem.

5.3.4.2 Looking for the best individual

As mentioned before, genetic algorithm can be focused on just finding a good solution, represented by the best individual of all generations, or defining a solution domain represented by individuals considered good enough to represent the solution.

In this section, the problem is focused on trying to find the best individual represented in the search space.

The main characteristics and parameters needed to fully define the problem of parameters estimation, presented in this section, are shown in table 5.9.

Optimization Algorithm	
Type of algorithm	SGA + Elitism
Selection type	Roulette Wheel (without fitness limit)
GAP	1
Probability of applying crossover (P_c)	0.95
Probability of applying mutation (P_m)	0.01
Population size	101
Search Space Discretization	
$E_{50\ min}^{ref}$ [kN/m^2]	5000
$E_{50\ max}^{ref}$ [kN/m^2]	37500
$E_{50\ step\ size}^{ref}$ [kN/m^2]	500
c_{min} [kN/m^2]	0
c_{max} [kN/m^2]	50
$c_{step\ size}$ [kN/m^2]	1
Objective Function	
Type of objective function	Least-Squares Method
Measurements	
Type of measurement	Vertical Displacements (20 measurement points)

Table 5.9. Main characteristics and parameters of the problem of parameters estimation (SGA / Looking for the best individual).

5.3.4.2.1 Exact Data Case Results

The results of the soil parameters identification using a simple genetic algorithm, with exact data, and looking for the best individual, are presented in this section.

In figure 5.45 the initial population, represented altogether with the surface of the objective function, is shown, whereas in figure 5.46 it is shown the population after 25 generations.

As observed in figure 5.46, after 25 generations the best individual of the population does not coincide with the actual value of the minimum. The best individual found by the algorithm is represented by E_{50}^{ref} = 29000 kN/m^2 and c = 7 kN/m^2, while the value of the minimum is E_{50}^{ref} = 25000 kN/m^2 and c = 10 kN/m^2.

Part of the reason of not finding the real best individual is due to the quick loss of individuals' diversity that has made the algorithm incapable to explore new potential domains. Moreover, even though a sensitivity analysis was carried out to better define the genetic algorithm parameters, such as the population size and the selection pressure, the fact of using exact data, instead of noisy data as it was used in the sensitivity analysis, has pointed out how different the results can be, just by slightly varying the shape of the objective function (exact data versus noisy data).

The loss of individuals' diversity is illustrated in figure 5.47 where the evolution of the SPD and the percentage of new individuals are shown.

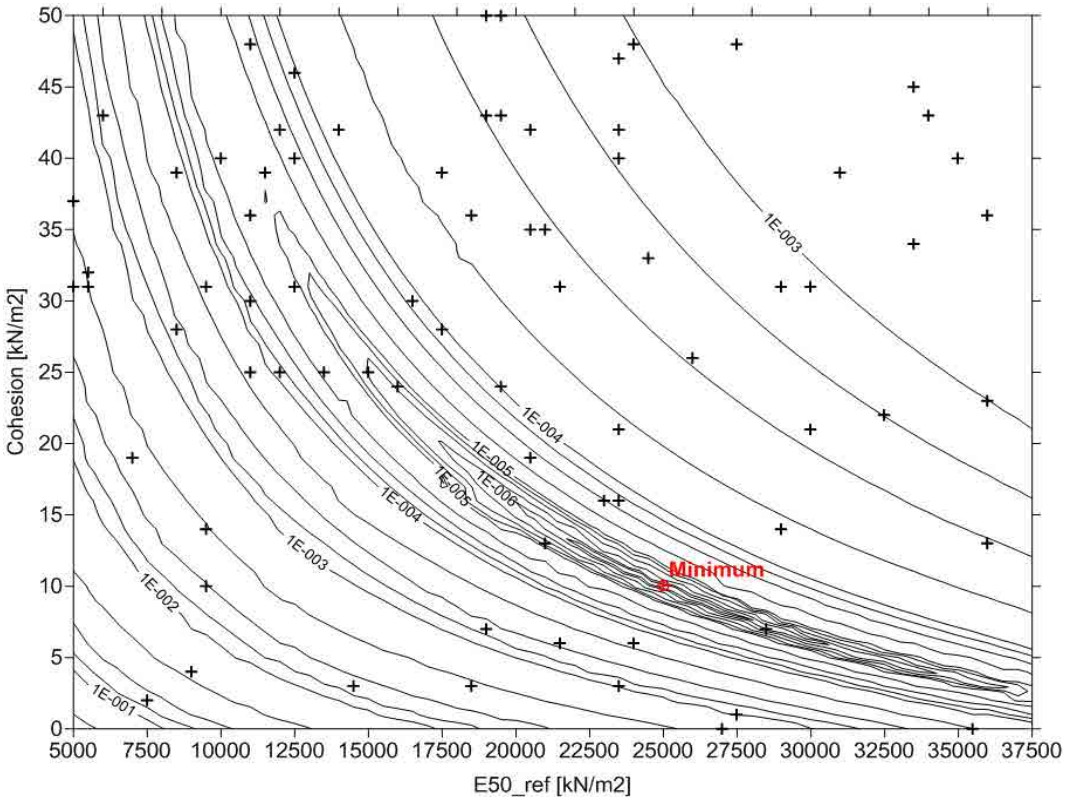

Figure 5.45. Initial population of 101 individuals randomly generated - Objective function [m^2]. The black crosses represent the individuals (SGA / looking for the best individual / exact data case).

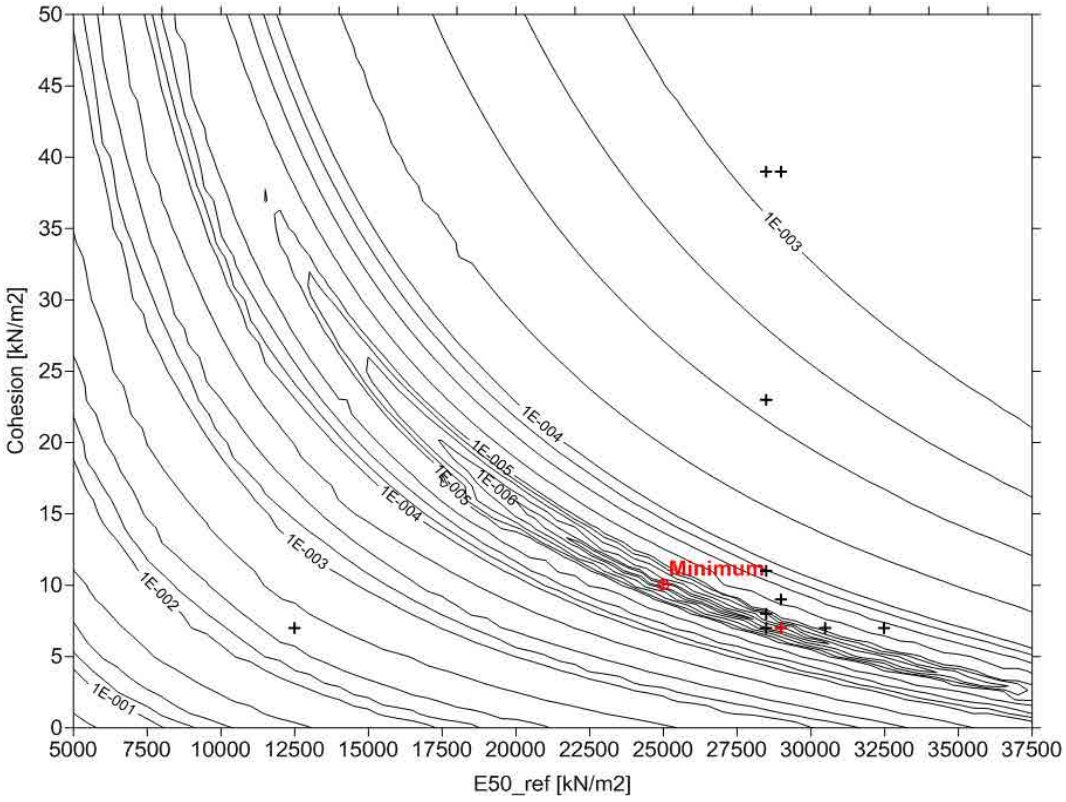

Figure 5.46. Population after 25 generations (last generation) - Objective function [m^2]. The black crosses represent the individuals of the last generation and the red cross represents the best individual of the generation (SGA / looking for the best individual / exact data case).

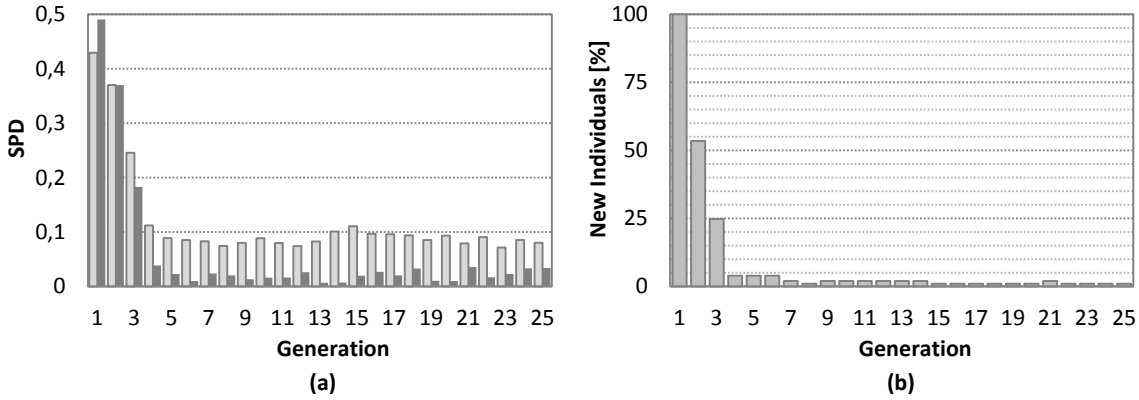

Figure 5.47. (a) evolution of the Standard Population Diversity (SPD), and (b) evolution of the percentage of new individuals in the population (SGA / looking for the best individual / exact data).

The evolution, in terms of objective function value is shown in figure 5.48, where there is a large difference between the best individual and the average value of the general population.

This non-insignificant difference has very likely caused the genetic algorithm to work with a high selection pressure due to high selection probability associated to the best individual with respect to the average of the population, and consequently this has also contributed to miss the actual minimum of the search space.

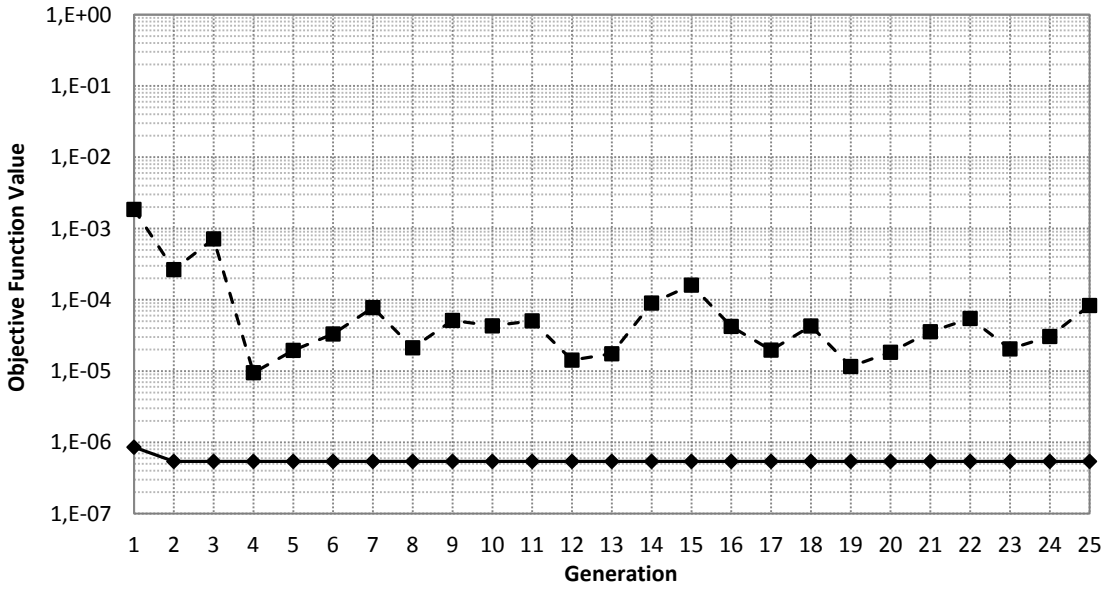

Figure 5.48. Evolution of the objective function. The solid line with diamonds represents the value of the best individual and the dashed line with squares represents the average value of the population (SGA / looking for the best individual / exact data).

Similarly, figure 5.49 and figure 5.50 illustrate the poor evolution of the best individual, where in fact, there was only one evolution of the best individual after 25 generations.

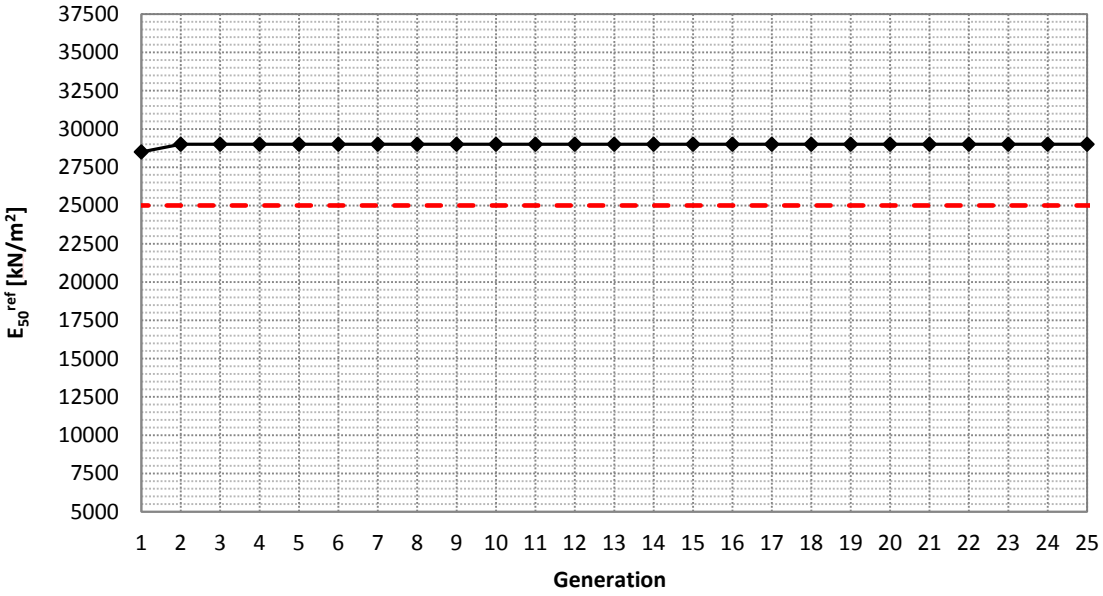

Figure 5.49. Evolution of the E_{50}^{ref} value (SGA / looking for the best individual / exact data).

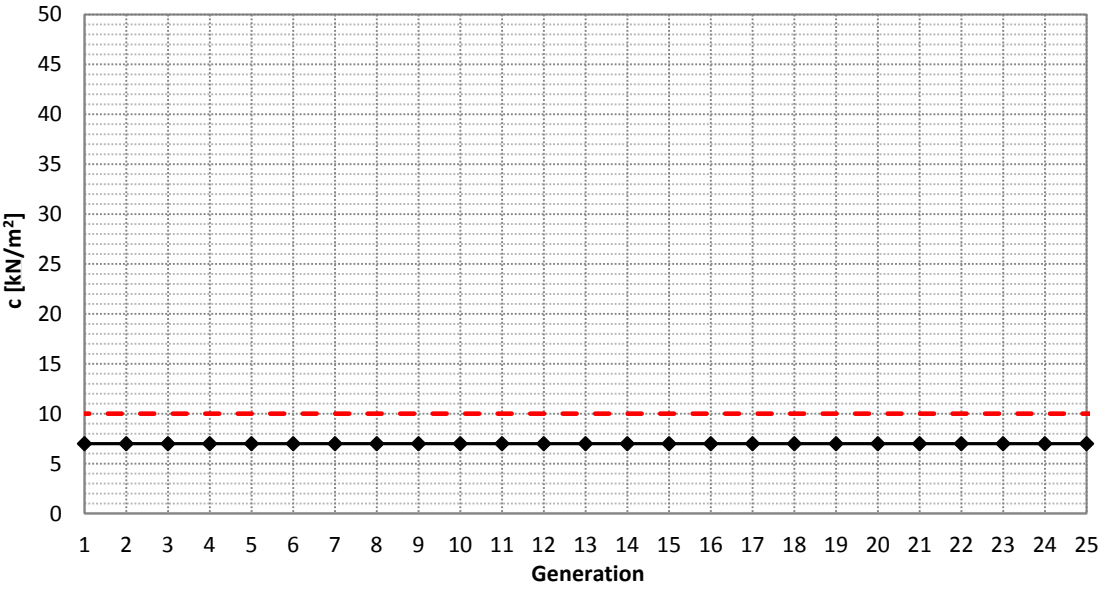

Figure 5.50. Evolution of the cohesion value (SGA / looking for the best individual / exact data).

In order to illustrate in more detail what has been already explained, the full evolution of the population is shown in figure 5.51.

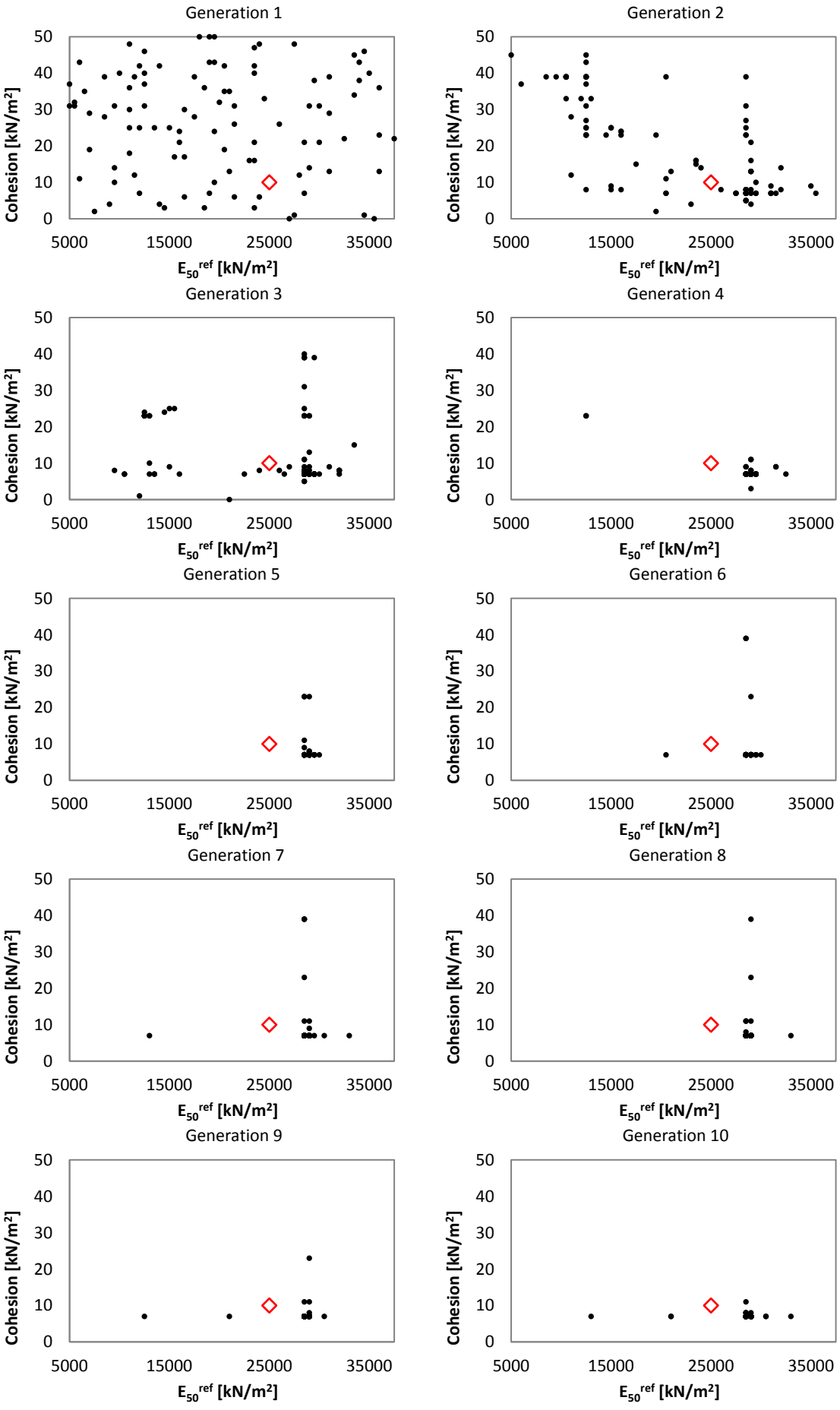
Generation 1
Generation 2
Generation 3
Generation 4
Generation 5
Generation 6
Generation 7
Generation 8
Generation 9
Generation 10
Cohesion [kN/m²]
E50ref [kN/m²]
0
10
20
30
40
50
5000
15000
25000
35000

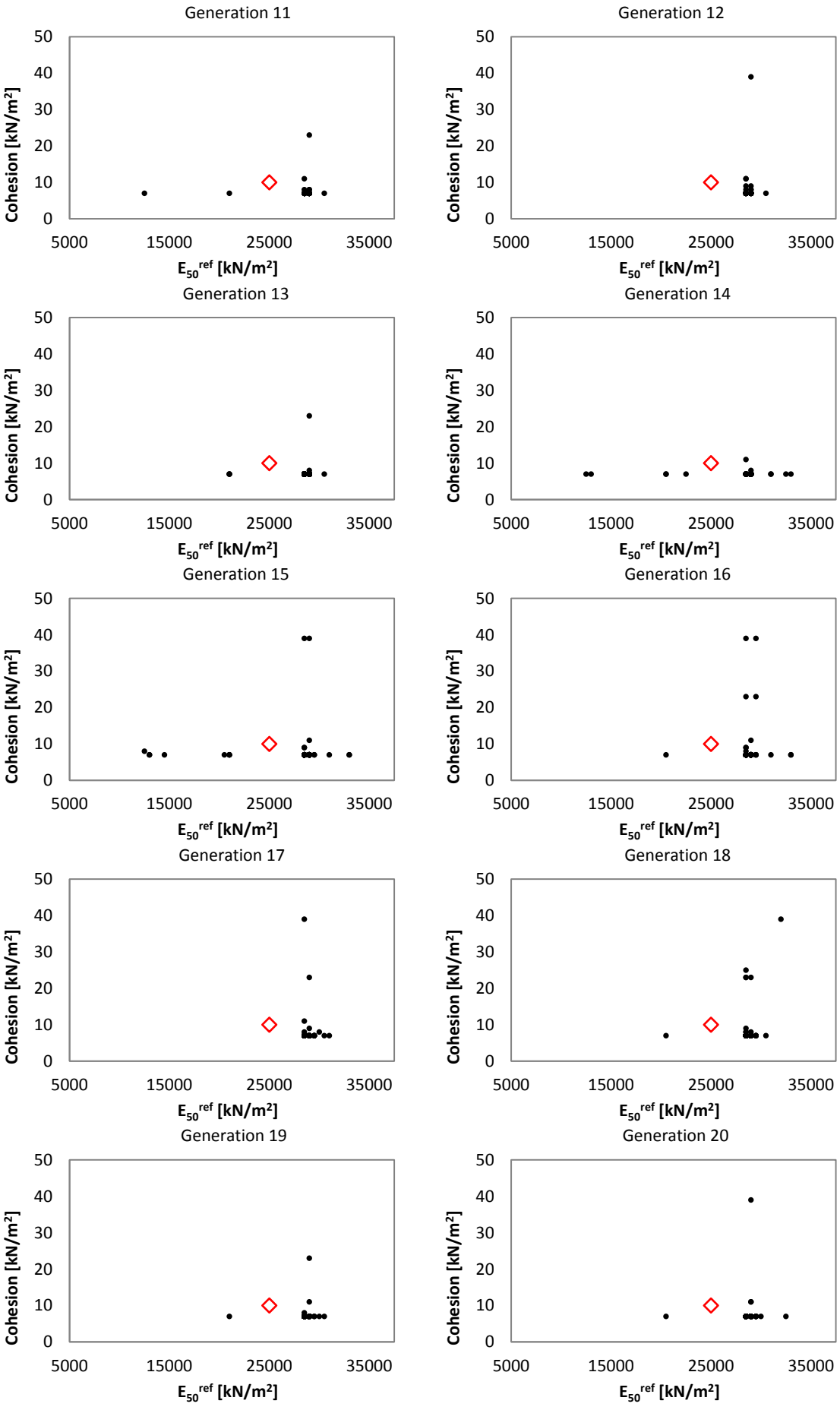
Generation 11
Generation 12
Generation 13
Generation 14
Generation 15
Generation 16
Generation 17
Generation 18
Generation 19
Generation 20
Cohesion [kN/m²]
E50ref [kN/m²]
0
10
20
30
40
50
5000
15000
25000
35000

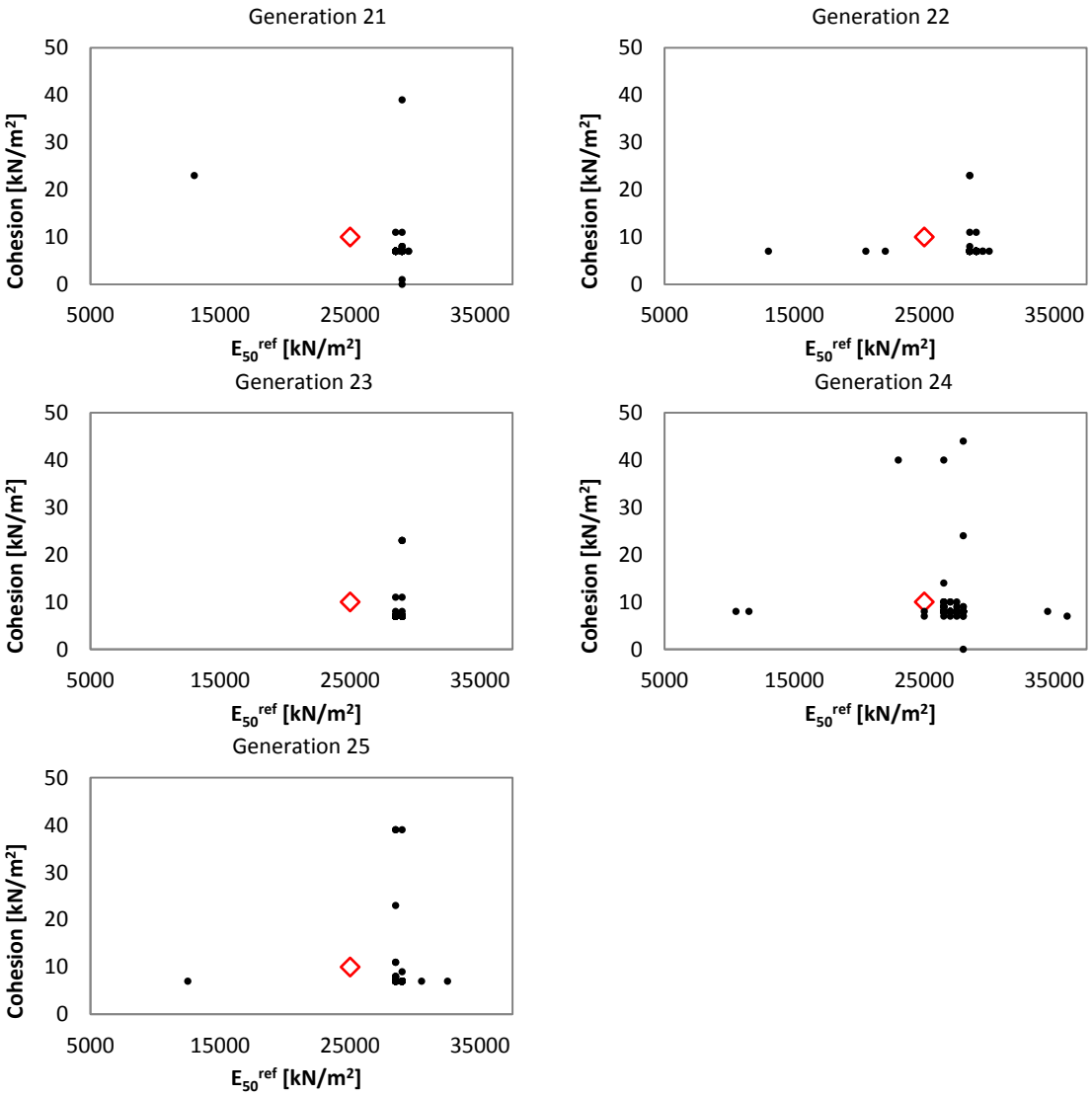

Figure 5.51. Evolution of the population over 25 generations using a SGA, with exact data, no fitness limit and a population size of 101 individuals.

As figure 5.51 shows, there has been no substantial exploration capable to drive the algorithm into the minimum after generation 3. As a result, it can be concluded that in cases where the objective function presents a steep narrow domain close to the minimum, the need of keeping a diverse population is vital for the good performance of the algorithm.

A summary of the results is shown in table 5.10 where the computational cost is also presented.

Case	Identified Value		Computational Cost
	E_{50}^{ref} [kN/m^2]	c [kN/m^2]	[Plaxis evaluations]
SGA (exact data with no fitness limit and population size of 101 individuals)	29000	7	219

Table 5.10. Results of the case of simple genetic algorithms, with exact data, no fitness limit and population size of 101 individuals.

5.3.4.2.2 Noisy Data Case Results

The results of the soil parameters identification using a simple genetic algorithm, with noisy data, and looking for the best individual, are presented in this section.

In figure 5.52 the initial population, represented together with the surface of the objective function, is shown, while figure 5.53 shows the population after 25 generations.

For this case, the best individual after 25 generations is represented by E_{50}^{ref} = 26500 kN/m^2 and c = 9 kN/m^2, when the actual values are E_{50}^{ref} = 25000 kN/m^2 and c = 10 kN/m^2. However, due to the introduction of noise and the domain discretization used to defined all possible solutions, the values of E_{50}^{ref} = 26500 kN/m^2 and c = 9 kN/m^2 have associated a smaller error (objective function) than the one associated with the real minimum, located in E_{50}^{ref} = 25000 kN/m^2 and c = 10 kN/m^2. In fact, from table 5.11, where the value of the best five individuals of all generations are shown, it can be noticed that the individual associated with the real minimum is not the individual with the smallest objective function.

Therefore, the concentration of individuals in the last generation, slightly deviated to the right of the minimum, is not due to misbehavior of the algorithm it is rather a consequence of the introduction of noise and the domain discretization. Therefore, the algorithm has found the best possible individual defined in the search space.

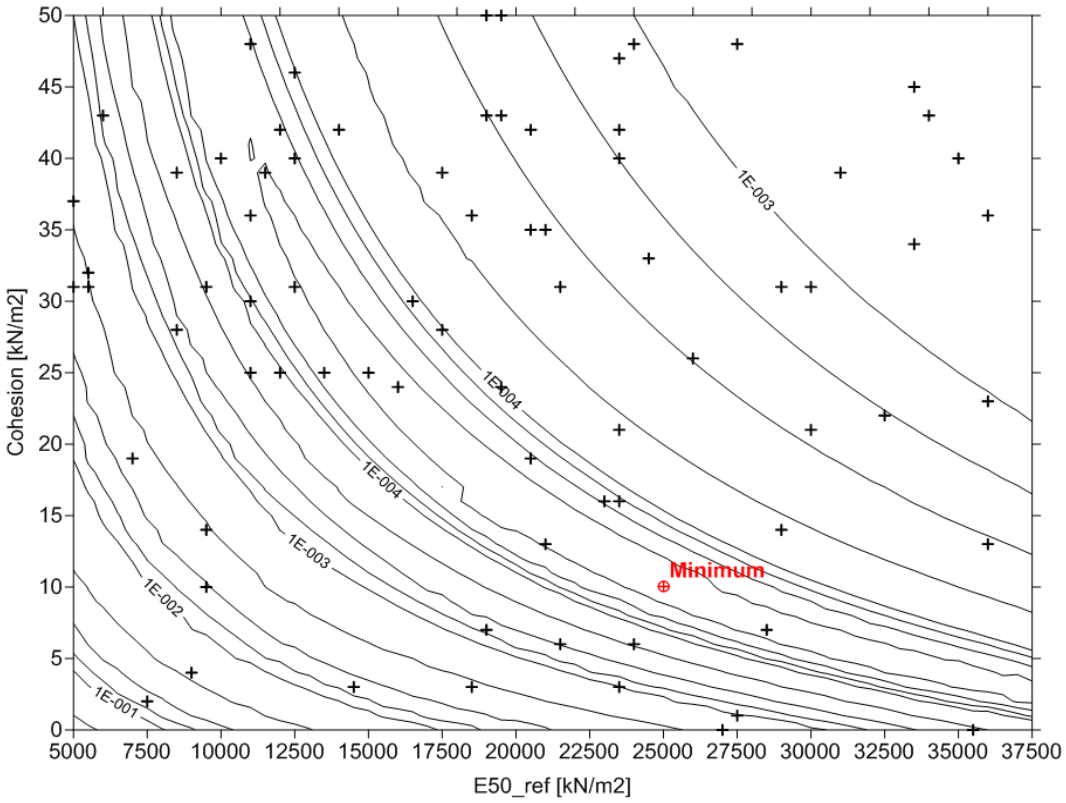

Figure 5.52. Initial population of 101 individuals randomly generated - Objective function [m^2]. The black crosses represent the individuals (SGA / looking for the best individual / noisy data).

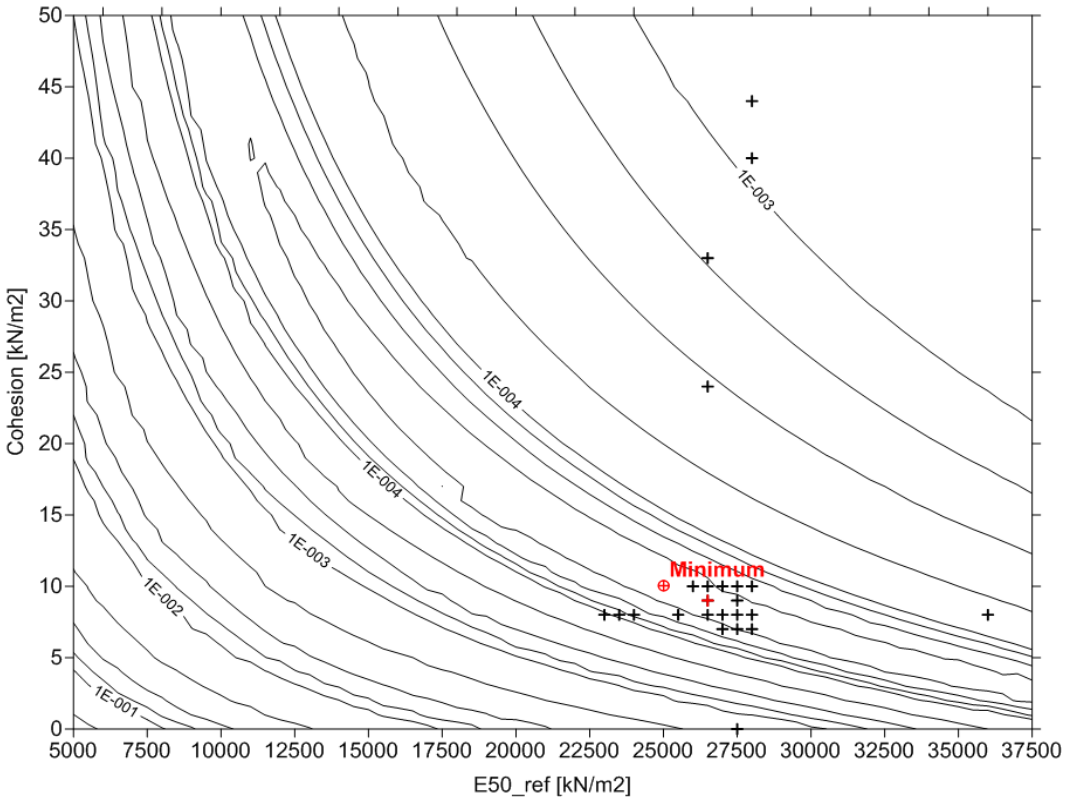

Figure 5.53. Population after 25 generations (last generation) - Objective function [m^2]. The black crosses represent the individuals of the last generation and the red cross represents the best individual of the generation (SGA / looking for the best individual / noisy data).

Individual	E_{50}^{ref} [kN/m^2]	c [kN/m^2]	Objective Function [m^2]
A	26500	9	$1.232 \cdot 10^{-5}$
B	27500	8	$1.259 \cdot 10^{-5}$
C	25000	10	$1.260 \cdot 10^{-5}$
D	28000	8	$1.265 \cdot 10^{-5}$
E	29000	7	$1.267 \cdot 10^{-5}$

Table 5.11. Parameter values and objective function values of the best five individuals of all generations (SGA / looking for the best individual / noisy data).

In contrast to what happened in the previous case (exact data), where diversity was lost just after three generations; herein, thanks to the use of a proper sensitive analysis (the sensitive analysis was carried out with the same type of data (noisy data) as the current analysis), the population size of 101 individuals and the non-application of the fitness limit, has led the algorithm to keep a good level of diversity over the generations.

In order to illustrate it, figure 5.54 shows the evolution of the standard population diversity, where it can be noticed that even after ten generations the value of SPD is still relatively high. Moreover, it can be also noticed, especially if it is compared with the previous case (exact data), that the percentage of new individual per generations is higher when using noisy data rather compared to the exact data case.

As mentioned before, the flattening effect of introducing noise into the data, has indirectly caused a lowering of the selection pressure that in this case has been beneficial to the analysis.

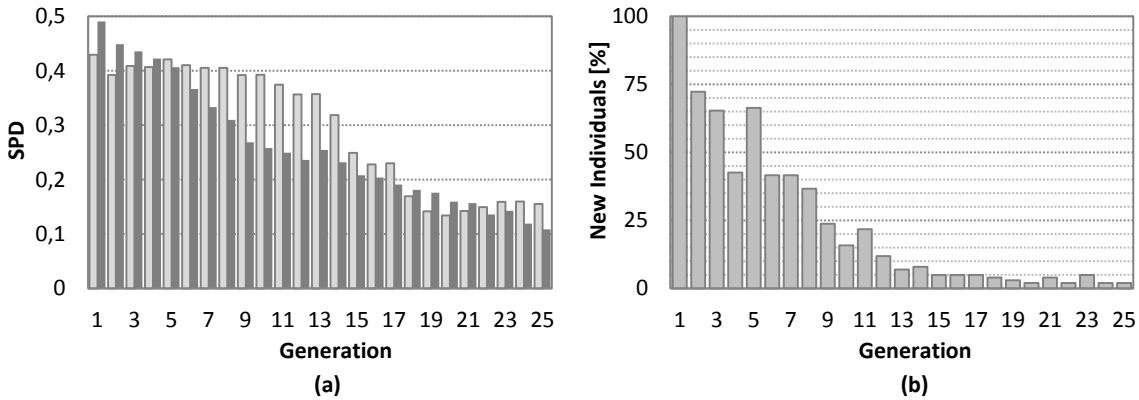

Figure 5.54. (a) evolution of the Standard Population Diversity (SPD), and (b) evolution of the percentage of new individuals in the population (SGA / looking for the best individual / noisy data).

The evolution, in terms of objective function value, is shown in figure 5.55, where the large difference between the best individual and the general population, presented in the case of exact data, has been significantly reduced. In some way, the reduction of this difference has caused a lower selection pressure and subsequently a higher individuals' diversity, leading to a better performance of the genetic algorithm.

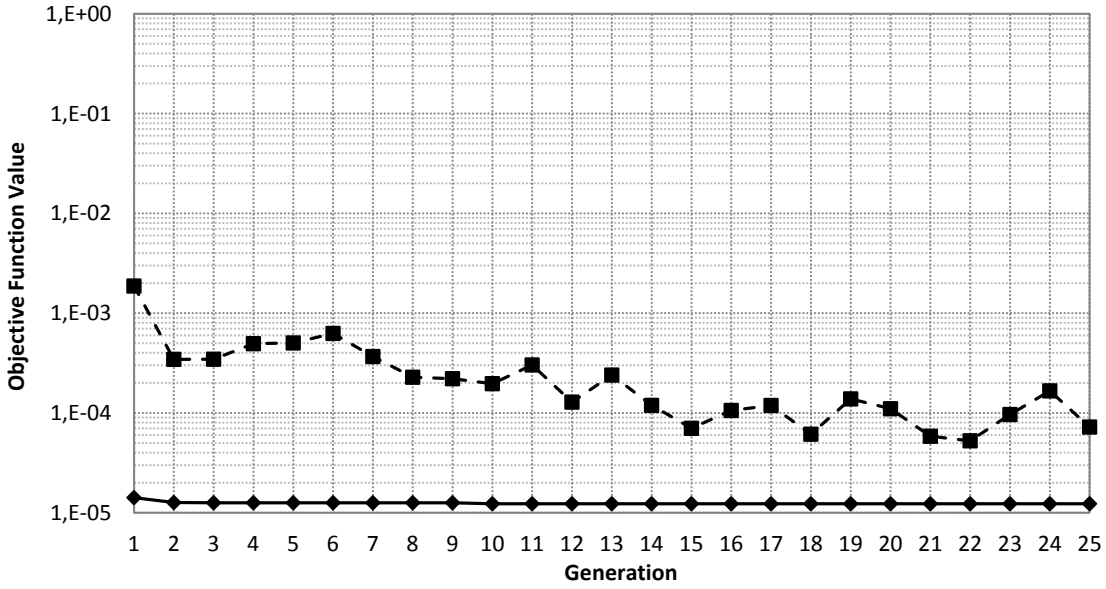

Figure 5.55. Evolution of the objective function. The solid line with diamonds represents the value of the best individual and the dashed line with squares represents the average value of the population (SGA / looking for the best individual / noisy data).

Similarly, and contrary to the previous case, figure 5.56 and figure 5.57 illustrate the good evolution of the best individual, where the best individual has been improving over the generations.

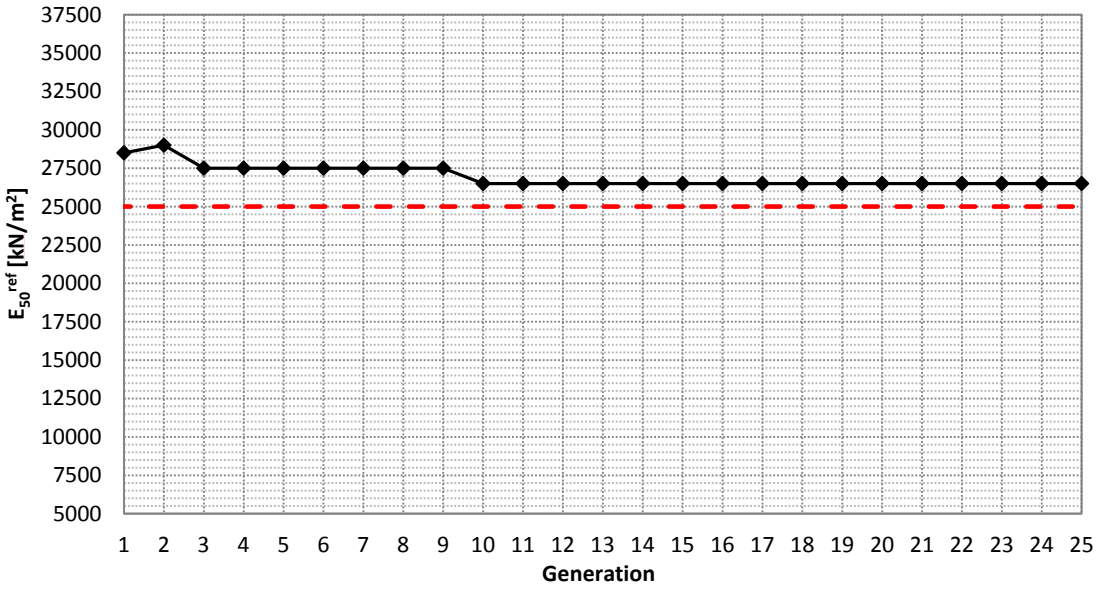

Figure 5.56. Evolution of the E_{50}^{ref} value (SGA / looking for the best individual / noisy data).

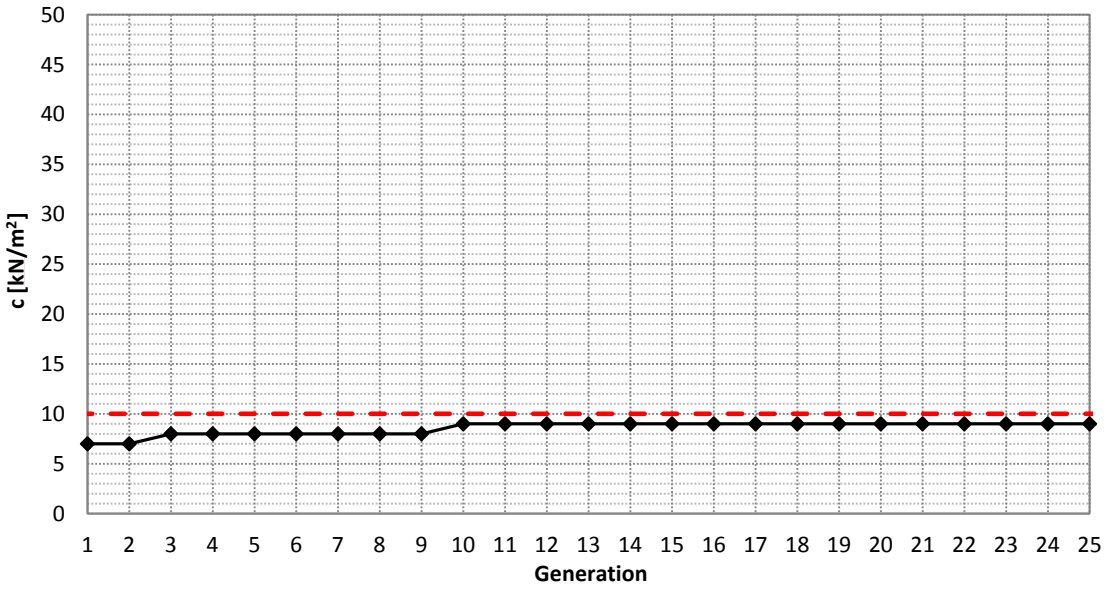

Figure 5.57. Evolution of the cohesion value (SGA / looking for the best individual / noisy data).

The entire evolution of the population, generation after generation, is shown in figure 5.58, where in generation 7 it can be noticed that the individual, associated to the real minimum, was created for the first time. Nevertheless, the algorithm was driven slightly more to the right of the minimum, due to the introduction of noise that has caused that the best individual, in terms of fitness, is the one with E_{50}^{ref} = 26500 kN/m^2 and c = 9 kN/m^2 , rather than the real one (E_{50}^{ref} = 25000 kN/m^2 and c = 10 kN/m^2) .

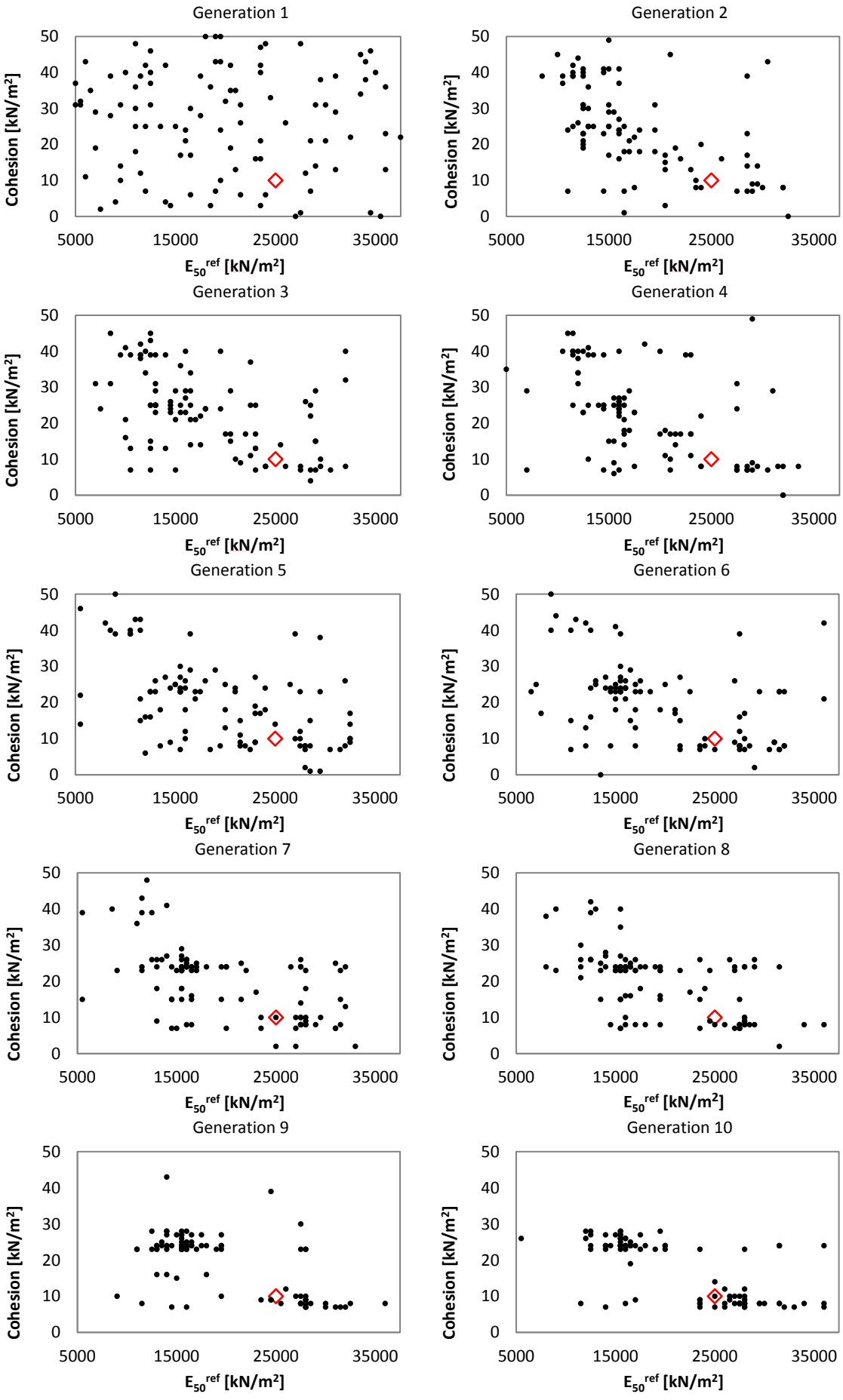
Generation 1
Generation 2
Generation 3
Generation 4
Generation 5
Generation 6
Generation 7
Generation 8
Generation 9
Generation 10
Cohesion [kN/m²]
E50ref [kN/m²]
0
10
20
30
40
50
5000
15000
25000
35000

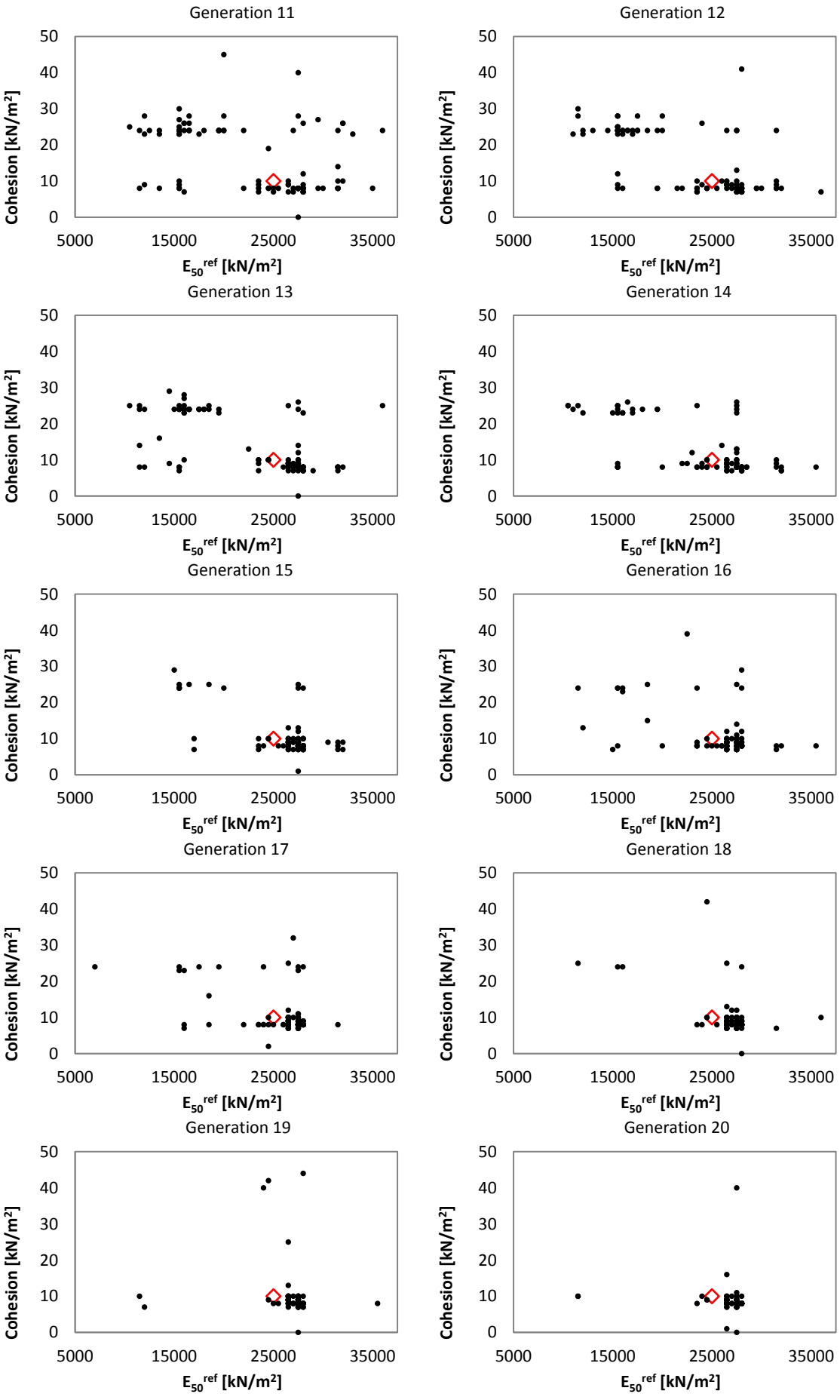
Generation 11
Generation 12
Generation 13
Generation 14
Generation 15
Generation 16
Generation 17
Generation 18
Generation 19
Generation 20
Cohesion [kN/m²]
E50ref [kN/m²]
0
10
20
30
40
50
5000
15000
25000
35000

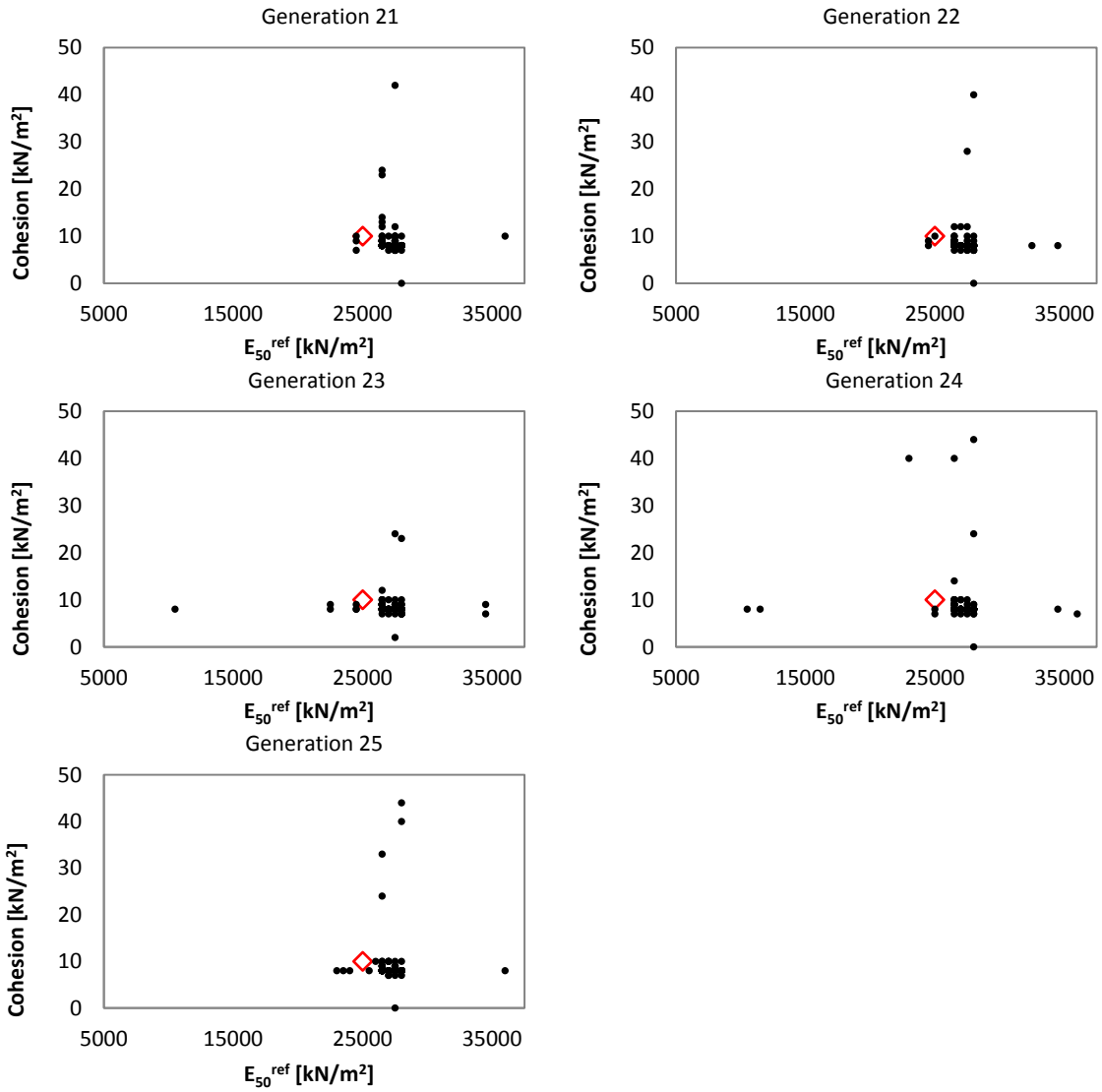

Figure 5.58. Evolution of the population over 25 generations using a SGA, with noisy data, no fitness limit and a population size of 101 individuals.

From the results presented herein, it can be stated that, in cases where the presence of noise flattens the surroundings of the minimum (as it has happen here), the algorithm works with an implicit lower selection pressure derived from the low variance of the objective function near the minimum, and that makes the algorithm, for this particular case, more robust.

A summary of the results is shown in table 5.12 where the computational cost is also presented.

Case	Identified Value		Computational Cost
	E_{50}^{ref} [kN/m^2]	c [kN/m^2]	[Plaxis evaluations]
SGA (noisy data with no fitness limit and population size of 101 individuals)	26500 ± 561.4	9 ± 0.015	599

Table 5.12. Results of the case of simple genetic algorithms with noisy data, no fitness limit and population size of 101 individuals.

5.3.4.3 Looking for the Best Set of Individuals

Rather than looking for the best possible individual, here, a restricted domain defined by a set of good individuals, which are considered a satisfactory solution of problem, is looked for. Therefore, the search is focused on finding enough good individuals to be capable to define a kind of frontier between good and bad individuals. The method to define the restricted domain is based on a principal component analysis (PCA), which is fully described in section 3.3.5.

Because of that focus on good individuals, the majority of the results here in this section are presented in terms of satisfactory individuals all along the generations, rather than individuals per generation that is, all individuals with an objective function value smaller than the frontier value are kept generation after generation to finally being involved in the PCA. Nonetheless, the results related to the individuals' diversity are referred to the entire population of good and bad individuals in each generation.

The frontier value used to separate the good individuals from the bad individuals (satisfactory or not satisfactory) was set to $2.5 \cdot 10^{-5}$ m^2, which is associated with equation (3.31) to an average standard deviation of the measurements of approximately 1 mm.

The main characteristics and parameters needed to fully define the problem of parameters estimation presented in this section are shown in table 5.13.

Optimization Algorithm	
Type of algorithm	SGA + Elitism
Selection type	Roulette Wheel (with fitness limit = frontier value)
GAP	1
Probability of applying crossover (P_c)	0.95
Probability of applying mutation (P_m)	0.01
Population size	101
Search Space Discretization	
$E_{50\ min}^{ref}$ [kN/m^2]	5000
$E_{50\ max}^{ref}$ [kN/m^2]	37500
$E_{50\ step\ size}^{ref}$ [kN/m^2]	500
c_{min} [kN/m^2]	0
c_{max} [kN/m^2]	50
$c_{step\ size}$ [kN/m^2]	1
Objective Function	
Type of objective function	Least-Squares Method
Measurements	
Type of measurement	Vertical Displacements (20 measurement points)

Figure 5.13. Main characteristics and parameters of the problem of parameters estimation (SGA / Looking for the best set of individual).

5.3.4.3.1 Exact Data Case Results

The results of the parameters estimation using a simple genetic algorithm, with exact data, and looking for the best set of individuals, are presented in this section.

Figure 5.59 shows the initial population plotted all together with the objective function surface, while figure 5.60 shows all the good individuals that have been found after 25 generations and the ellipse defined by the PCA.

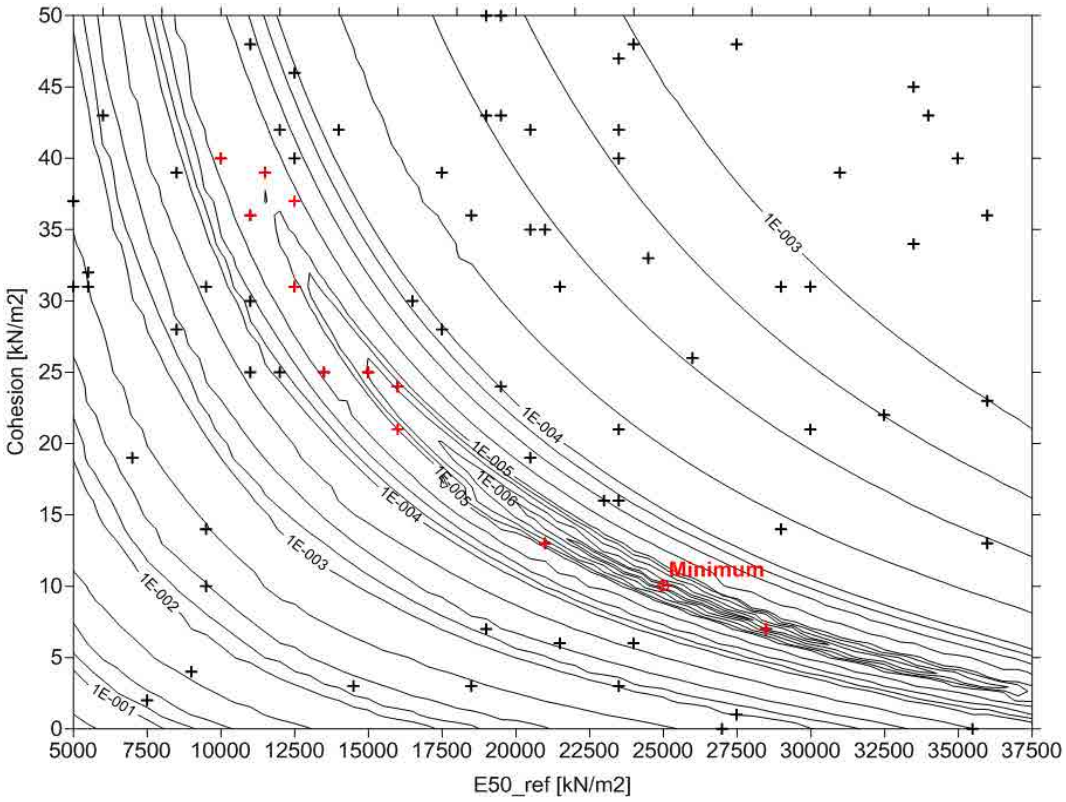

Figure 5.59. Initial population of 101 individuals randomly generated - Objective function [m^2]. The black crosses represent all individuals, while the red ones represent just the good individuals of the initial population (SGA / looking for the best set of individuals / exact data).

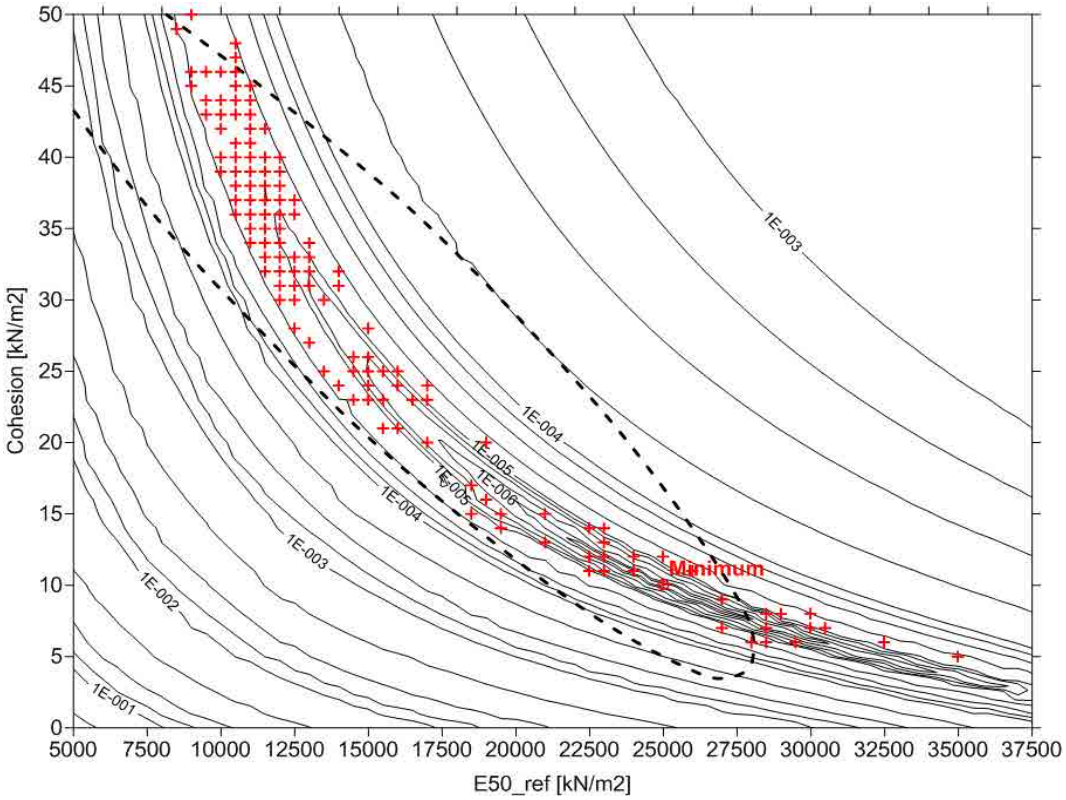

Figure 5.60. Set of good individuals after 25 generations - Objective function [m^2]. The red crosses represent the good individuals, while the dashed line represents the PCA ellipse (SGA / looking for the best set of individuals / exact data).

Part of the good representation of the individuals with respect to the objective function zone, associated with values of J<2.5·10^{-5} m^2, is due to the high diverse population that has been kept along the generations.

The evolution of the standard population diversity (SPD) and the percentage of new individuals generated in each generation is presented in figure 5.61.

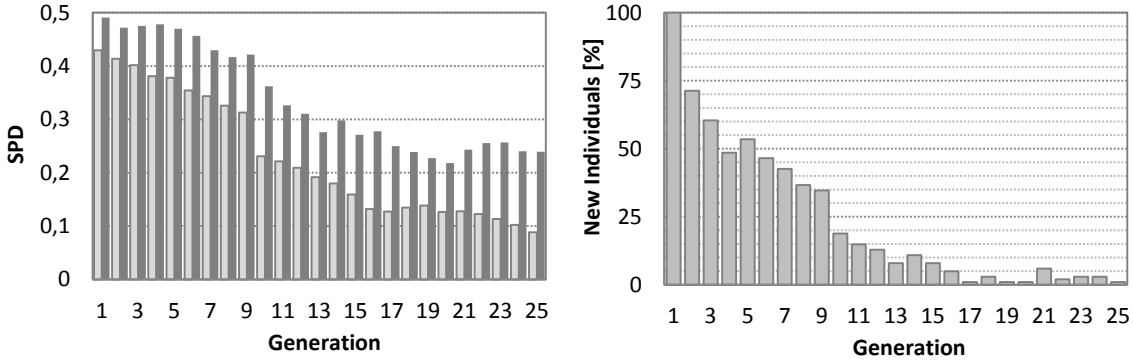

Figure 5.61. (a) evolution of the Standard Population Diversity (SPD), and (b) evolution of the percentage of new individuals in the population (SGA / looking for the best set of individuals / exact data).

Unfortunately, even though the good individuals are good enough to be representative to the domain, defined by J<2.5·10^{-5}m, the ellipse obtained from the PCA is not capable of matching the shape of the objective function. This incapability makes the solution of the problem, in the space $E_{50}^{ref} - c$, unsatisfactory.

Apart from the visual inspection of the representativeness of the PCA ellipse (looking directly at figure 5.60), only applicable when no more than three parameters are identified, an alternative method valid for n-parameters, presented in section 3.3.5.2, is used to illustrate its applicability as an inspection technique. The basis of this technique is comparing the objective function at the extreme of the ellipse axes with the objective function value defined as frontier value. In cases where the extreme of the axes are out of the search space, the point of intersection between the axes and the boundaries of the search space are used to compare with the frontier value.

The general idea of this technique is to check numerically that the shape of the objective function can be captured by an ellipse, or in the case of having more than 2 parameters, by an ellipsoid of n-dimensions.

Figure 5.62 shows the points that were used to verify the representativeness of the ellipse, while their numerical values and the frontier value are presented in table 5.14.

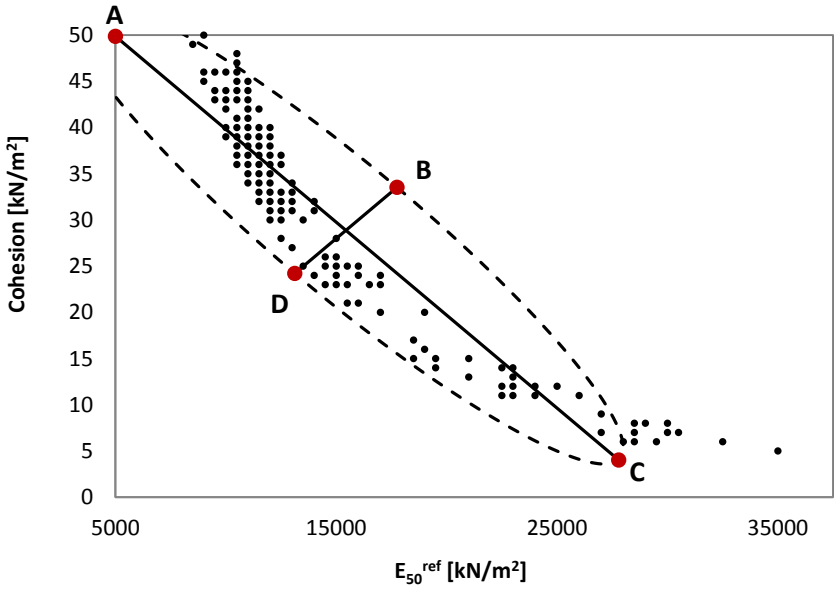

Figure 5.62. Verification points. The red points represent the verification points, the black points are the individuals involved in the PCA, the dashed line represents the PCA ellipse, and the solid lines represent the ellipse axes (SGA / looking for the best set of individuals / exact data).

Point	E_{50}^{ref} [kN/m^2]	c [kN/m^2]	J_{axis} [m^2]	$J_{frontier}$ [m^2]
A	5000	49.86	$9.51 \cdot 10^{-4}$	$2.5 \cdot 10^{-5}$
B	17751.48	33.53	$2.46 \cdot 10^{-4}$	$2.5 \cdot 10^{-5}$
C	27789.38	4.01	$1.66 \cdot 10^{-4}$	$2.5 \cdot 10^{-5}$
D	13120.52	24.21	$4.21 \cdot 10^{-5}$	$2.5 \cdot 10^{-5}$

Table 5.14. Numerical value to verify the representativeness of the PCA ellipse (SGA / looking for the best set of individuals / exact data).

Setting the value of the tolerance to 1, and comparing it with the error (eq. 3.32) between each verification point and the frontier value; just the point D satisfies the tolerance condition. Consequently, the ellipse is considered as not satisfactory, and the domain defined by the ellipse is not a proper solution of the problem.

After checking the representativeness of the ellipse and obtaining a negative response, there are two different methods to proceed in order to get a satisfactory result. The first method is reducing the ellipse until it matches the objective function, taking into account the standard deviation of the measurements associated with this reduction. The reduction of the ellipse is carried out by a new PCA imposing a smaller frontier value. However, in the limit of reduction, the method reduces the concept of working with a set of good individuals to finding an individual, changing completely the approach of the problem for which it was designed for (looking for the best set of individuals).

The other method is based on transforming some original variables, in this case E_{50}^{ref} or c, to make the ellipse capable to capture the objective function shape.

For this particular case, the representation of the objective function in the space $E_{50}^{ref} - c$ was transformed into the space $1/E_{50}^{ref} - c$ (similar approach was proposed in Levasseur et al., 2010) The new objective function representation in the space $1/E_{50}^{ref} - c$, all together with the new PCA ellipse are presented in figure 5.63.

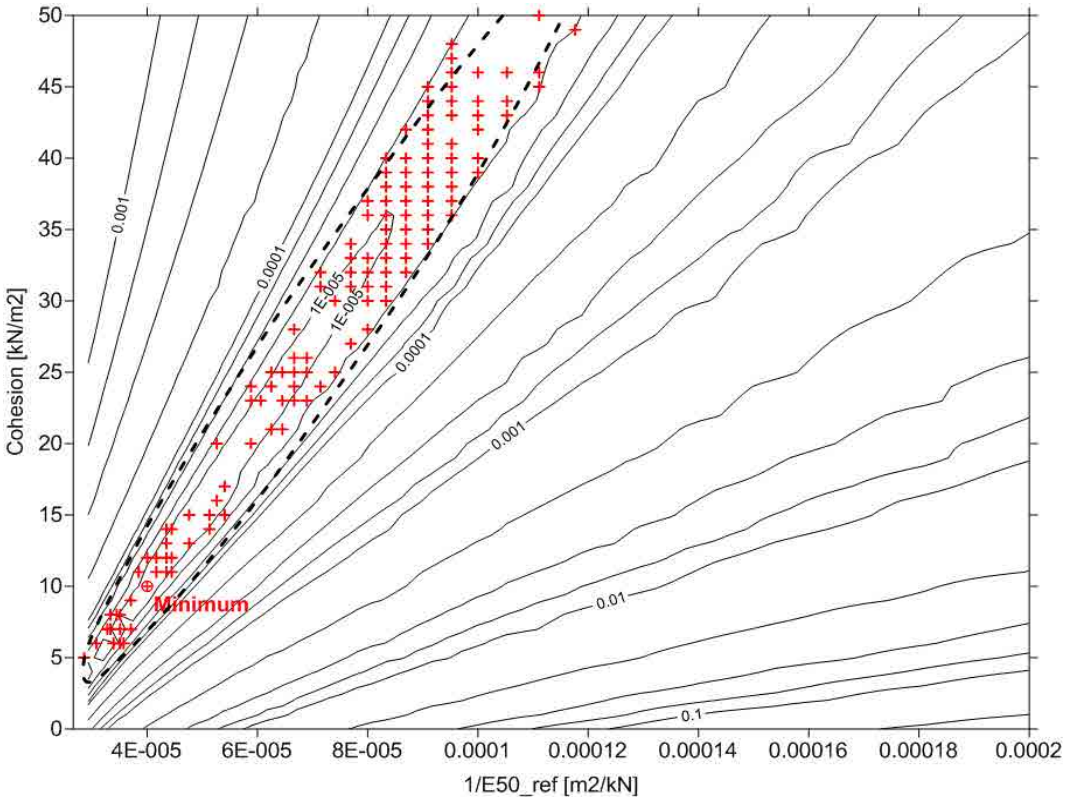

Figure 5.63. Representation of the objective function [m^{-2}] in the transformed space of $1/E_{50}^{ref} - c$. The red crosses represent the good individuals involved in the PCA, while the dashed line represents the PCA ellipse (SGA / looking for the best set of individuals / exact data).

Just by looking at figure 5.63, the matched of the PCA ellipse to the objective function shape can be clearly noticed. Moreover, if the representativeness is numerically checked by the proposed methodology, it can be corroborated that the new representation of the solution is actually a satisfactory solution of the problem (see table 5.15).

Point	$1/E_{50}^{ref}$ [m^2/kN]	c [kN/m^2]	J_{axis} [m^2]	$J_{frontier}$ [m^2]
A	$1.109 \cdot 10^{-4}$	50	$1.67 \cdot 10^{-5}$	$2.5 \cdot 10^{-5}$
B	$2.877 \cdot 10^{-5}$	3.74	$2.89 \cdot 10^{-6}$	$2.5 \cdot 10^{-5}$
C	$6.844 \cdot 10^{-5}$	31.66	$3.57 \cdot 10^{-5}$	$2.5 \cdot 10^{-5}$
D	$7.836 \cdot 10^{-5}$	26.07	$3.09 \cdot 10^{-5}$	$2.5 \cdot 10^{-5}$

Figure 5.15. Numerical value to verify the representativeness of the transformed PCA ellipse (SGA / looking for the best set of individuals / exact data).

Setting the value of the tolerance to 1, and comparing it with the error (eq. 3.32) between each verification point and the frontier value; all verification points satisfy the tolerance condition. Consequently, the ellipse is considered as satisfactory, and the domain defined by the ellipse is a proper solution of the problem.

Formally, every combination of parameters (individual) that satisfies equation 5.5 is a solution of the problem.

$$\frac{x^2}{a^2} + \frac{y^2}{b^2} \leq AF^2 \tag{5.5}$$

where x and y are the values of the parameters represented in terms of principal components, AF is an amplifier factor of the standard deviation, and a and b are the major and minor principal axes, which are the square root of the eigenvalues of the correlation matrix.

The reason for defining AF is to force the ellipse to enclose an expected specific percentage of individuals. If AF=1, then 68.2 % of the individuals involved in the PCA are expected to be enclosed in the ellipse, while if AF=2, the percentage increases to 95.4 %; this relationship is only valid if the individuals involved in the PCA are normally distributed in the search space.

In table 5.16, the results of the PCA and some relevant information involved in the analysis are shown.

Description	Values
Relevant information involved in the analysis	
Computational cost [Plaxis evaluations]	595
Number of individuals involved in the PCA	125
Mean of $1/E_{50}^{ref}$ [m^2/kN]	$7.3396 \cdot 10^{-5}$
Mean of c [kN/m^2]	28.872
Standard deviation of $1/E_{50}^{ref}$ [m^2/kN]	$2.2449 \cdot 10^{-5}$
Standard deviation of c [kN/m^2]	12.643
AF (amplifier factor of the standard deviation)	2
PCA results	
Correlation matrix	$\begin{bmatrix} 1 & 0.9755 \\ 0.9755 & 1 \end{bmatrix}$
Eigenvector (associated to the first principal component)	$[0.7071 \quad 0.7071]$
Eigenvector (associated to the second principal component)	$[-0.7071 \quad 0.7071]$
Eigenvalue (associated to the first principal component)	1.9755
Eigenvalue (associated to the second principal component)	0.0245

Table 5.16. PCA results and some relevant information involved in the analysis (SGA / looking for the best set of individuals / exact data).

Unfortunately, in some cases where the principal axes of the ellipse are too large, the solution of the optimization problem is not good enough to properly define a solution in terms of geotechnical values, meaning by that that there are too many diverse combinations of parameters that satisfy the optimization criteria, so it is not possible to define a representative geomaterial for all those combinations. In those cases, it would be necessary the introduction of extra information to finally defined the solution. The extra information, usually called previous information in the field of backanalysis (Ledesma, 1987 and Gens et al., 1988), is represented by parameter values obtained from different sources like laboratory tests.

5.3.4.3.2 Noisy Data Case Results

The results of the parameters estimation using a simple genetic algorithm, with noisy data, and looking for the best set of individuals, are presented in this section.

Figure 5.64 shows the initial population plotted all together with the objective function surface, while figure 5.65 shows all the good individuals that have been found after 25 generations and the ellipse defined by the PCA.

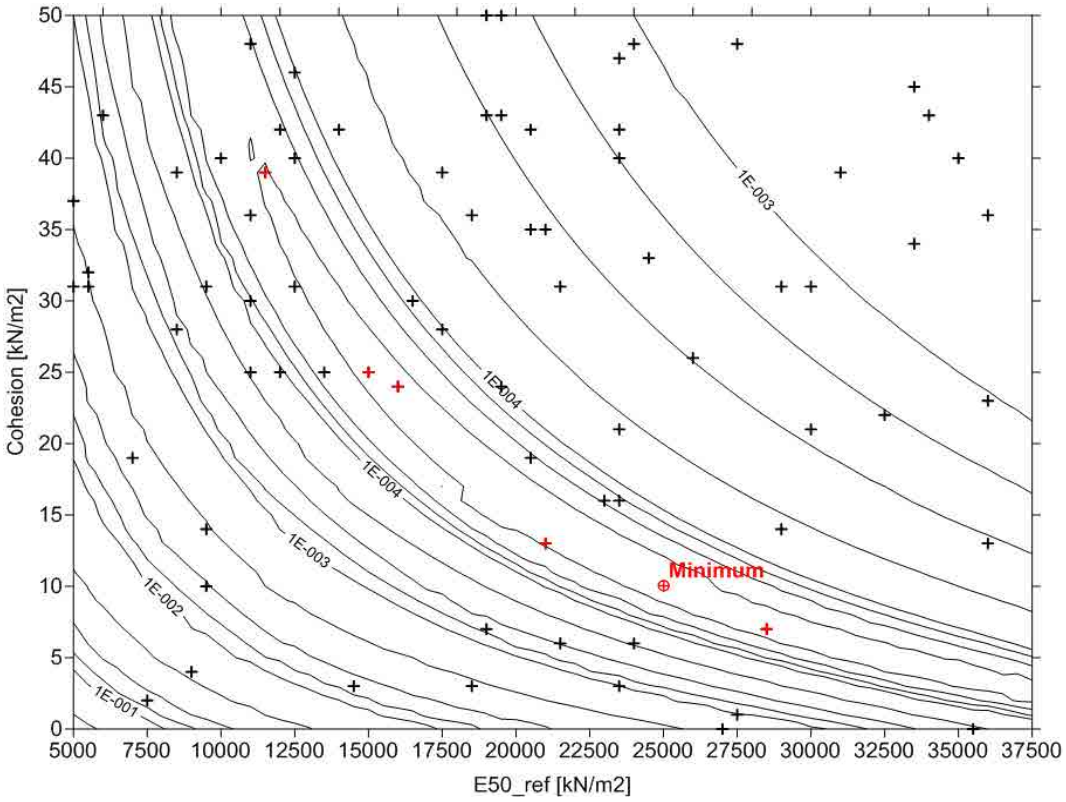

Figure 5.64. Initial population of 101 individuals randomly generated - Objective function [m^2]. The black crosses represent all individuals, while the red ones represent just the good individuals of the initial population (SGA / looking for the best set of individuals / noisy data).

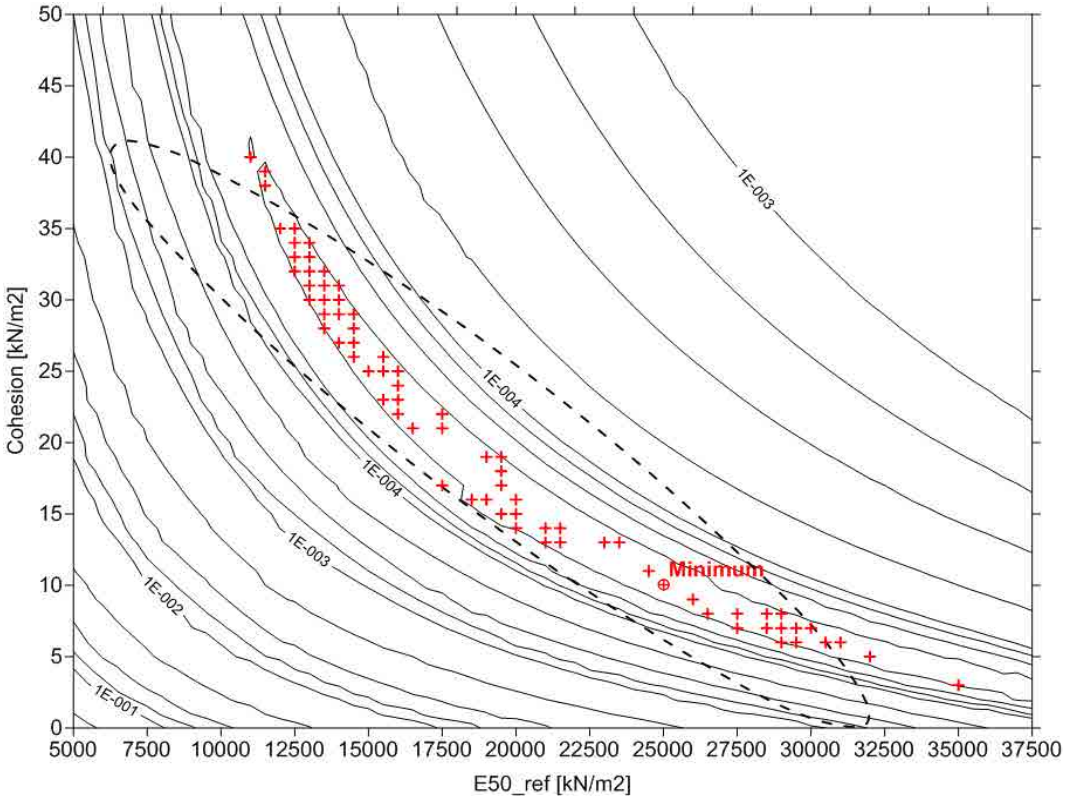

Figure 5.65. Set of good individuals after 25 generations - Objective function [m^2]. The red crosses represent the individuals, while the dashed line represents the PCA ellipse (SGA / looking for the best set of individuals / noisy data).

In terms of the representativeness of the good individuals with respect to objective function domain, defined by J<2.5·10^{-5} m^2, this case of noisy data shows a good representativeness. Therefore, it can be pointed out that the genetic algorithm has succeeded in capturing the shape of the objective function. However, as in the case of exact data, even having a good representativeness of the good individuals, thanks in part to the capability of the algorithm to keep a high diversity (see figure 5.66), the ellipse obtained from the PCA does not match the narrow banana shape valley defined by the objective function. Consequently, it was applied the same transformation on the original variables, from $E_{50}^{ref} - c$ to $1/E_{50}^{ref} - c$, to try to make the PCA ellipse more representative.

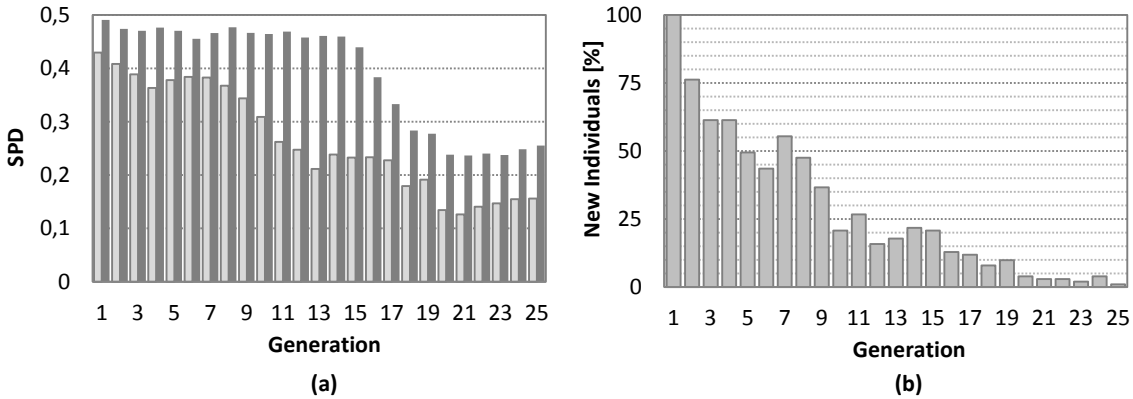

Figure 5.66. (a) evolution of the Standard Population Diversity (SPD), and (b) evolution of the percentage of new individuals in the population (SGA / looking for the best set of individuals / noisy data).

Figure 5.67 shows the new objective function representation in the space $1/E_{50}^{ref} - c$, all together with the new PCA ellipse.

Thanks to the transformation, the PCA ellipse has become a proper frontier between individuals considered solution of the problem and the ones that are not; as it can be noticed in figure 5.67.

In table 5.17, the results of the PCA and some relevant information involved in the analysis are shown.

Unfortunately, as in the previous case, due to the long length of one of the principal axes of the PCA ellipse, the results of the optimization problem are not good enough, in terms of geotechnical parameter values (it is not possible to define a representative soil material having such high parameters deviation), and it would be necessary to introduce previous information to finally get a suitable geotechnical solution of the parameters identification problem.

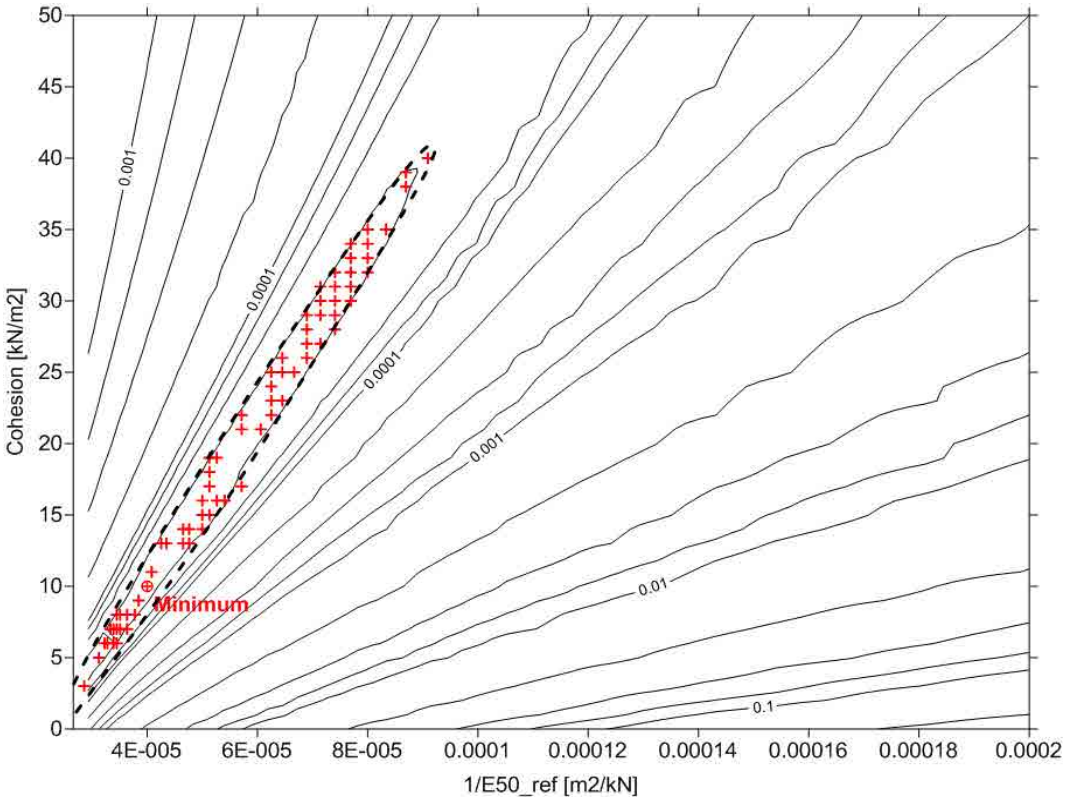

Figure 5.67. Representation of the objective function [m^{-2}] in the transformed space of $1/E_{50}^{ref} - c$. The red crosses represent the good individuals involved in the PCA, while the dashed line represents the PCA ellipse (SGA / looking for the best set of individuals / noisy data).

Description	Values
Relevant information involved in the analysis	
Computational cost [Plaxis evaluations]	722
Number of individuals involved in the PCA	71
Mean of $1/E_{50}^{ref}$ [m^2/kN]	$5.781 \cdot 10^{-5}$
Mean of c [kN/m^2]	20.577
Standard deviation of $1/E_{50}^{ref}$ [m^2/kN]	$1.718 \cdot 10^{-5}$
Standard deviation of c [kN/m^2]	10.242
AF (amplifier factor of the standard deviation)	2
PCA results	
Correlation matrix	$\begin{bmatrix} 1 & 0.9927 \\ 0.9927 & 1 \end{bmatrix}$
Eigenvector (associated to the first principal component)	$[0.7071 \quad 0.7071]$
Eigenvector (associated to the second principal component)	$[-0.7071 \quad 0.7071]$
Eigenvalue (associated to the first principal component)	1.9927
Eigenvalue (associated to the second principal component)	0.0073

Table 5.17. PCA results and some relevant information involved in the analysis (SGA / looking for the best set of individuals / noisy data).

5.3.5 Using an Adaptive Genetic Algorithm (AGA)

5.3.5.1 Previous Sensitivity Analysis (Population Size and Selection Pressure)

In this section, the same type of sensitivity analysis that was firstly presented in detail in section 5.3.4.1, has been used in order to show the effect of changing the population size and

the selection pressure, in terms of diversity and computational cost, on an adaptive genetic algorithm.

Figure 5.68 illustrates the evolution of the standard population diversity (SPD) for all different scenarios of population size and selection pressure (application or non-application of a fitness limit).

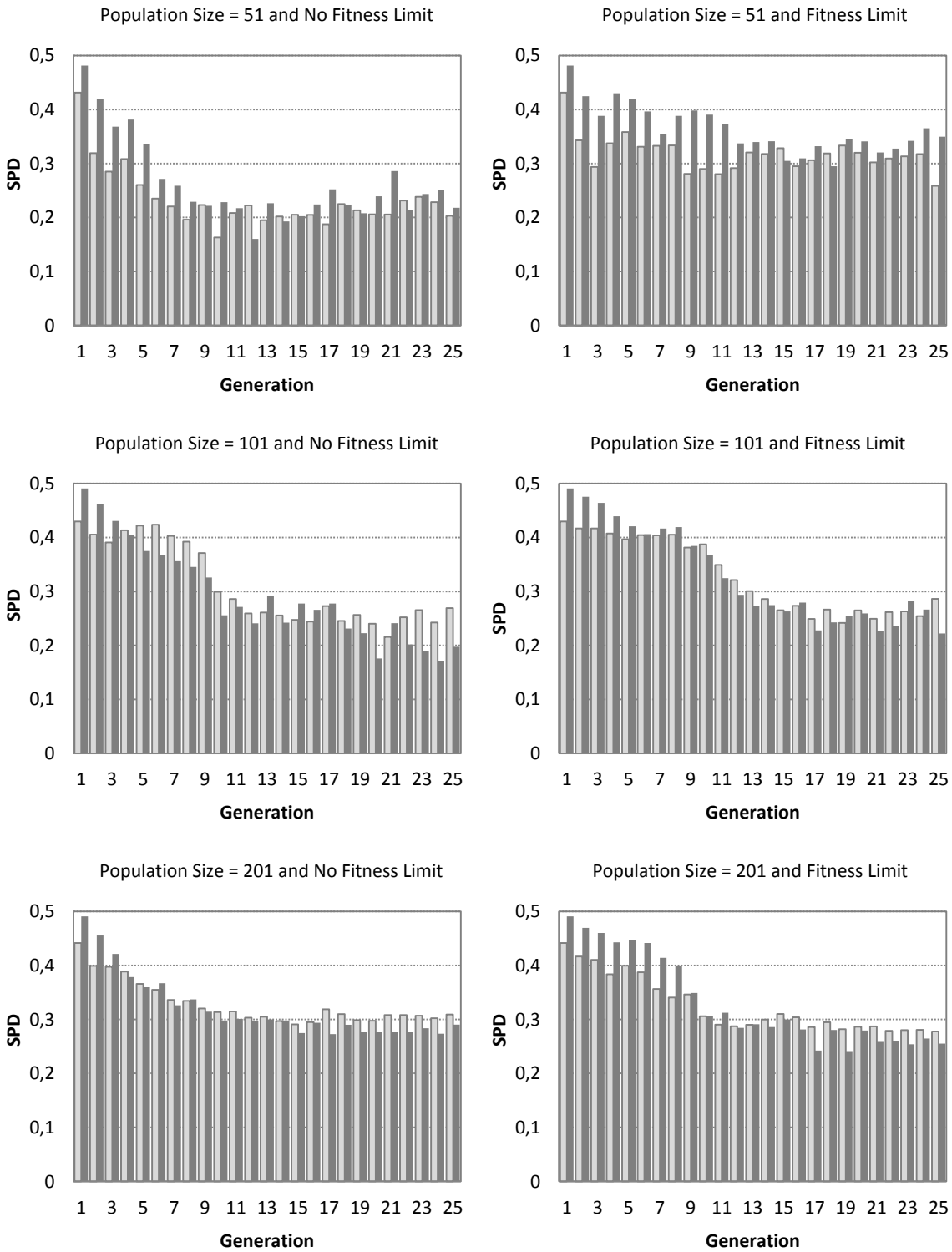

Figure 5.68. Evolution of the standard population diversity (SPD) using an AGA with noisy data. The light grey bars represent the SPD of the E_{50}^{ref} while the dark grey bars represent the SPD of the cohesion.

Due to the application of an adaptive crossover and mutation probability, the effect on the SPD with respect to the population size and the selection pressure has been significantly reduced in comparison to the case when using a simple genetic algorithm. The same happens with the generation of new individuals along the procedure (see figure 5.69).

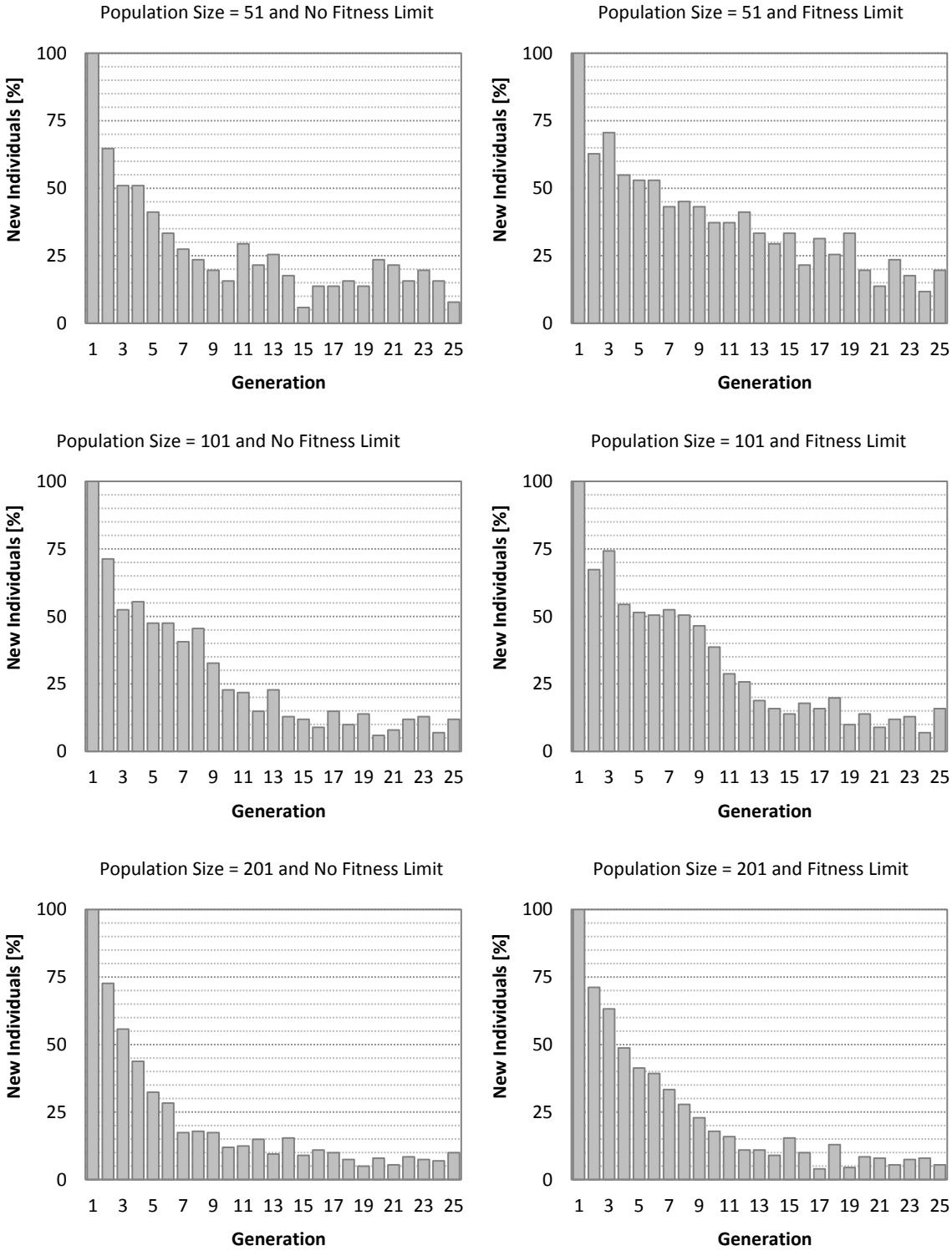

Figure 5.69. Evolution of the percentage of new individuals per generation using an AGA with noisy data.

As expected, the introduction of a genetic algorithm capable of self adapting the balance between exploitation and exploration, has made the algorithm less dependent on its internal parameters, and subsequently more robust. Moreover, comparing the case with highest exploitation focus (population size = 51 and no fitness limit) and the case with highest exploration focus (population size = 201 and fitness limit), it can be noticed that even having strongly different computational cost (351 direct calculations for the exploitation focus and 1210 direct calculations for the exploration focus) the individuals' diversity remains relatively high and steady in both cases. Therefore, it can be pointed out that when using an adaptive genetic algorithm, the role of population size and selection pressure, in terms of diversity, is taken up, to a large extent, by the adaptive nature of the algorithm itself.

However, in terms of representativeness of the individuals involved in the PCA, the application or non-application of a fitness limit still has some effect, as it can be seen in figure 5.70, where in the case with no fitness limit and a population size of 51 individuals, the calculated PCA ellipse does not match the theoretical PCA ellipse, whereas in the case with fitness limit and the same population size (51 individuals) there is a good match between the calculated and the theoretical ellipse.

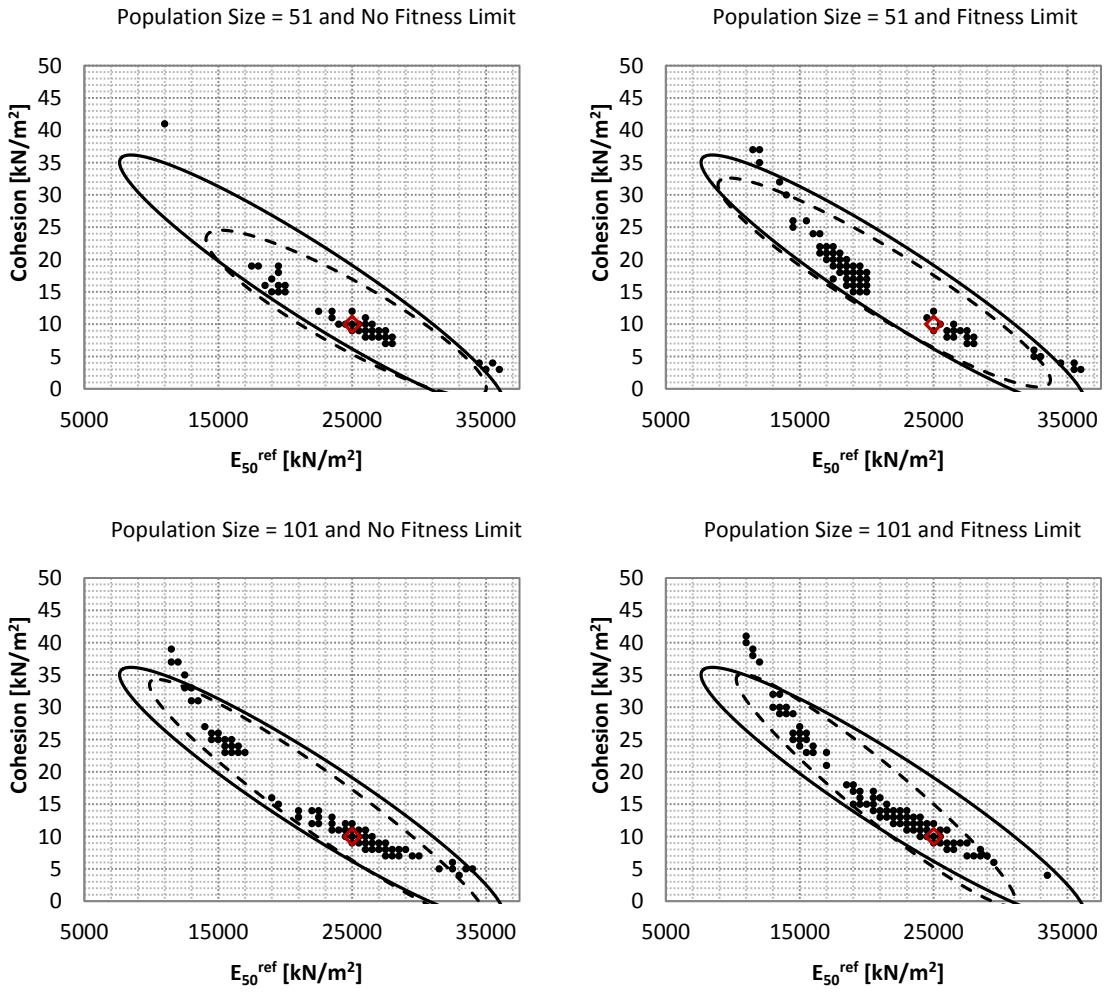

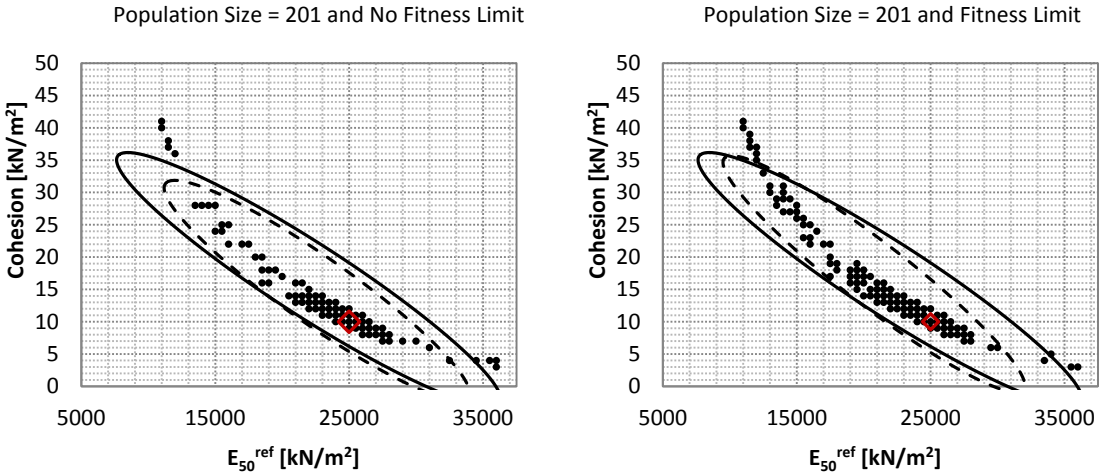

Figure 5.70. Representativeness of the individuals involved in the PCA using an AGA with noisy data (theoretical PCA ellipse versus calculated PCA ellipse). The solid line represents the theoretical PCA ellipse, the dashed line represents the calculated PCA ellipse, the black points are the individuals involved in the PCA and the red diamond is the individual that represents the solution of the problem.

Thanks to the results presented in this section, some specifications with respect to the population size and the application or non-application of the fitness limit, can be made.

On the one hand, when looking for the best individual, rather than the best set of individuals, an adaptive genetic algorithm without a fitness limit and a population size of 51 individuals was considered appropriate for trying to find this best individual, keeping a sufficient population's diversity with a reasonable computational cost. On the other hand, when looking for the best set of individuals, rather than the unique best individual, an adaptive genetic algorithm with a fitness limit and a population of 51 individuals was considered appropriate.

It is really important to mention that these recommendations are only valid for the case study presented herein. Therefore, if other problem is going to be solved, a new sensitivity analysis would be required. However, in the absence of any sensitivity analysis, it is recommended to use a fitness limit (low selection pressure) and the biggest possible populations, taking into account the computational cost of the problem.

5.3.5.2 Looking for the Best Individual

As mentioned before, genetic algorithm can be focused on just finding a good solution, represented by the best individual of all generations, or defining a solution domain, in this case represented by individuals considered good enough to represent the solution.

In this section, the problem is focused on trying to find the best individual represented in the search space.

The main characteristics and parameters needed to fully define the problem of parameters estimation, presented in this section, are shown in table 5.18.

Optimization Algorithm	
Type of algorithm	AGA + Elitism
Selection type	Roulette Wheel (without fitness limit)
GAP	1
Maximum probability of applying crossover (P_{c_max})	0.95
Minimum probability of applying crossover ($P_{c\ min}$)	0.50

Maximum probability of applying mutation (P_{m_max})	0.40
Minimum probability of applying mutation (P_{m_min})	0.01
Population size	101
Search Space Discretization	
$E_{50}^{ref}{}_{min}$ [kN/m^2]	5000
$E_{50}^{ref}{}_{max}$ [kN/m^2]	37500
$E_{50}^{ref}{}_{step\ size}$ [kN/m^2]	500
c_{min} [kN/m^2]	0
c_{max} [kN/m^2]	50
$c_{step\ size}$ [kN/m^2]	1
Objective Function	
Type of objective function	Least-Squares Method
Measurements	
Type of measurement	Vertical Displacements (20 measurement points)

Figure 5.18. Main characteristics and parameters of the problem of parameters estimation (AGA / Looking for the best individual).

5.3.5.2.1 Exact Data Case Results

The results of the parameters estimation using an adaptive genetic algorithm, with exact data, and looking for the best individual, are presented in this section.

In figure 5.71, the initial population of 51 individual all together with the objective function is shown, while figure 5.72 shows the final population after 25 generations.

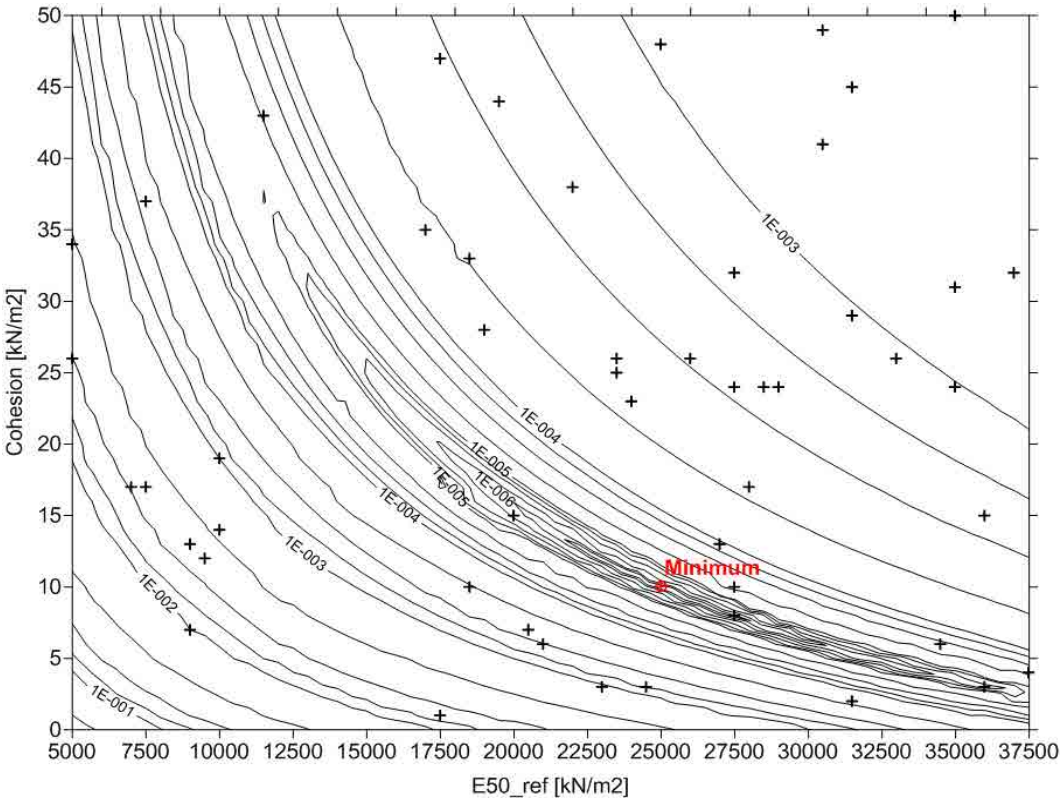

Figure 5.71. Initial population of 51 individuals randomly generated - Objective function [m^2]. The black crosses represent the individuals (AGA / looking for the best individual / exact data).

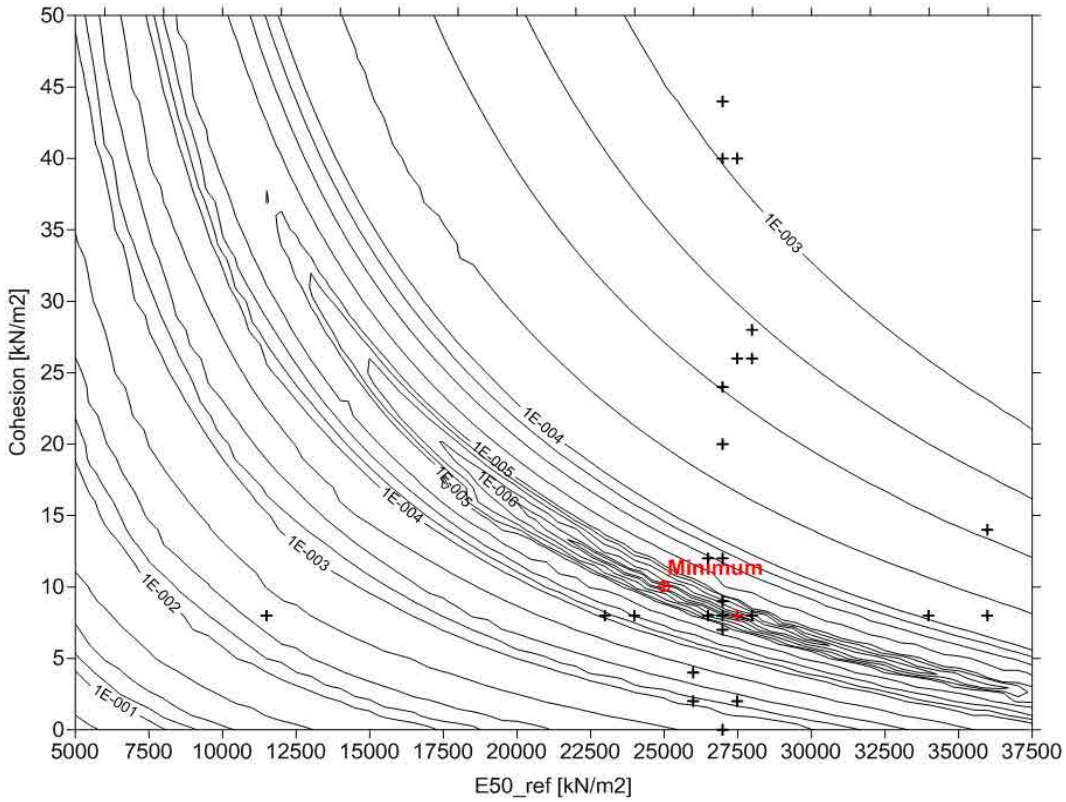

Figure 5.72. Population after 25 generations (last generation) - Objective function [m^2]. The black crosses represent the individuals of the last generation and the red cross represents the best individual of the generation (AGA / looking for the best individual / exact data).

Unfortunately, even using an adaptive genetic algorithm, the best individual found after 25 generations, does not represent the global minimum (E_{50}^{ref} = 25000 kN/m^2 and c = 10 kN/m^2). As in the other case when using the simple genetic algorithm, the definition of the population size and the application or non-application of a fitness limit, based on a sensitivity analysis using noisy data, instead of exact data, as it is the current case, has caused certain premature convergence. The main reason for this misbehavior of the algorithm is due to the large deviation of the objective function value between a group of relatively good individuals (around E_{50}^{ref} = 27500 kN/m^2 and c = 8 kN/m^2), and the average of the population. That has caused the algorithm to work with too much selection pressure, and consequently individuals' diversity has been reduced (see figure 5.73).

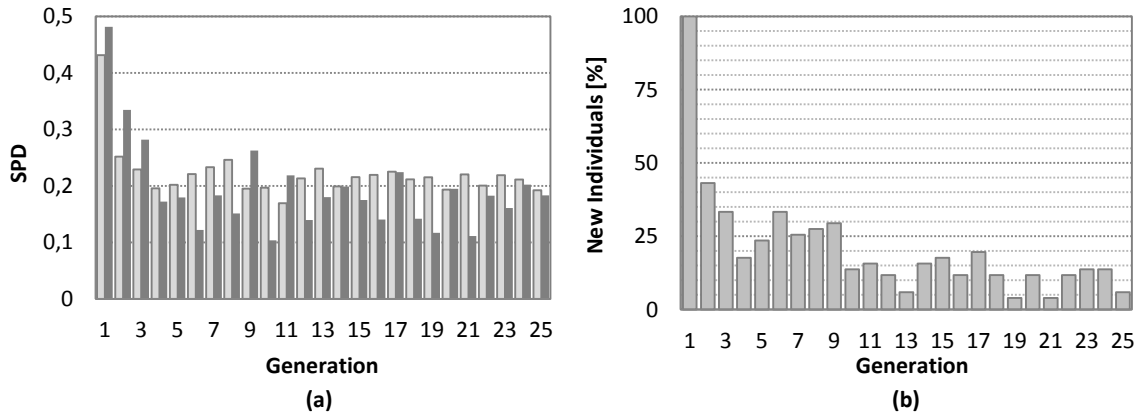

Figure 5.73. (a) evolution of the Standard Population Diversity (SPD), and (b) evolution of the percentage of new individuals in the population (AGA / looking for the best individual / exact data).

Figure 5.74 shows the evolution of the objective function of the best individual and the average of the population.

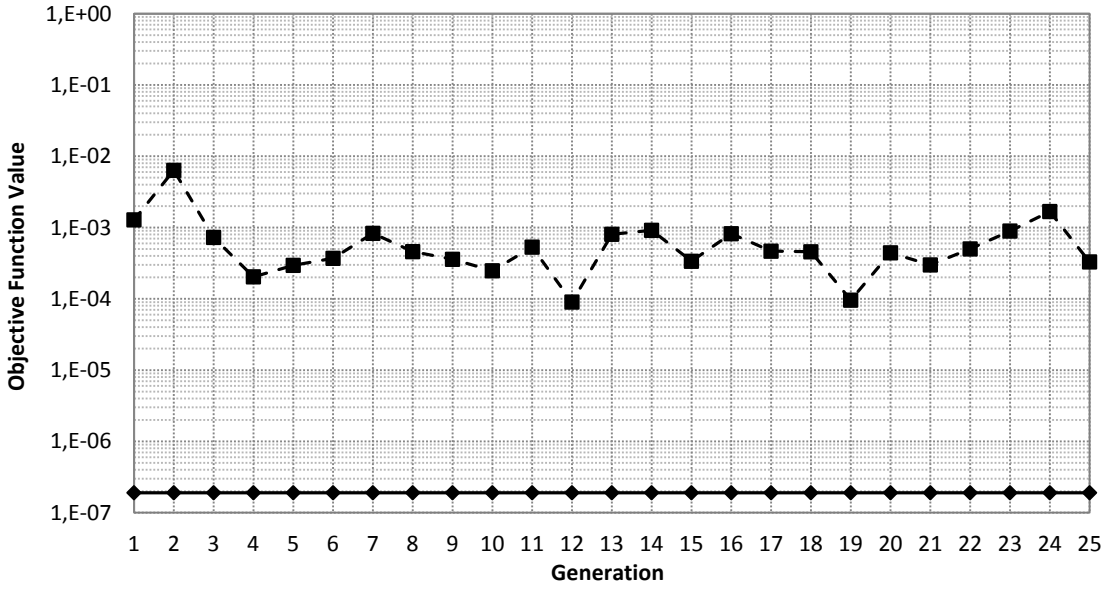

Figure 5.74. Evolution of the objective function. The solid line with diamonds represents the value of the best individual and the dashed line with squares represents the average value of the population (AGA / looking for the best individual / exact data).

The evolution of the parameters are shown in figure 5.75 and figure 5.76, where it is illustrated how that relatively good individual, created in the initial population, has remained as the best individual over all generations; causing no evolution.

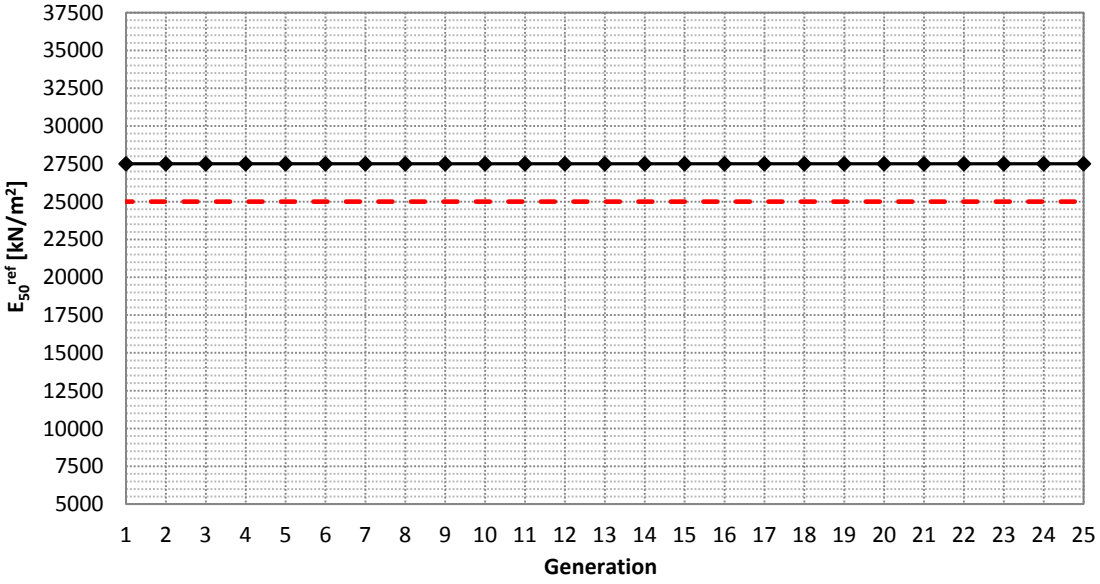

Figure 5.75. Evolution of the E_{50}^{ref} value (AGA / looking for the best individual / exact data).

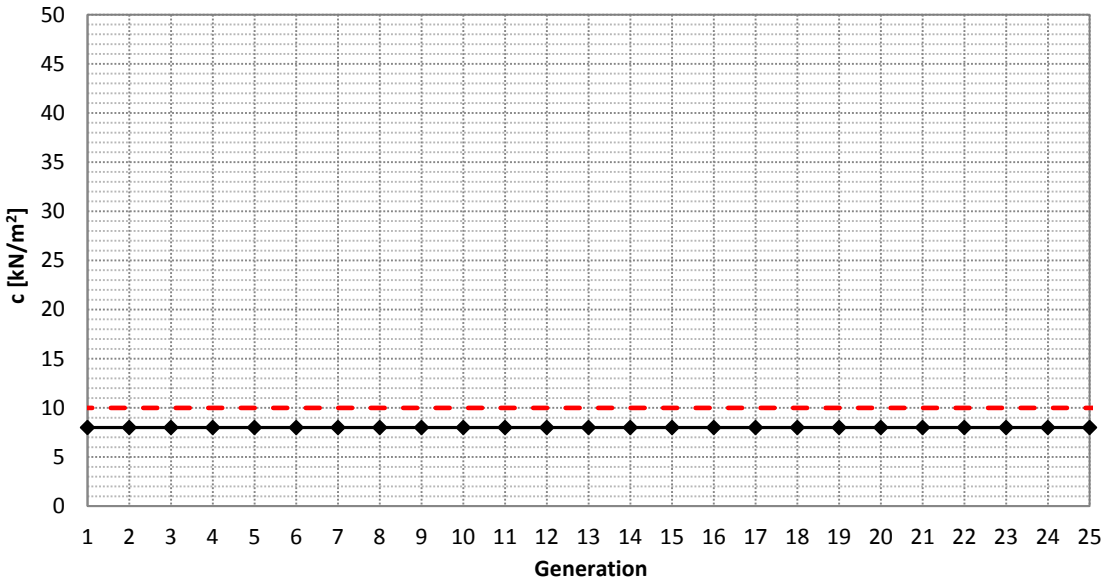

Figure 5.76. Evolution of the cohesion value (AGA / looking for the best individual / exact data).

Apart from that non-evolution of the best individual, the population has been evolving over the generations, and this evolution is fully illustrated in figure 5.77. Nonetheless, from the very beginning, the majority of the individuals and their offspring has been forced by themselves to drive the search in a high exploitation mode.

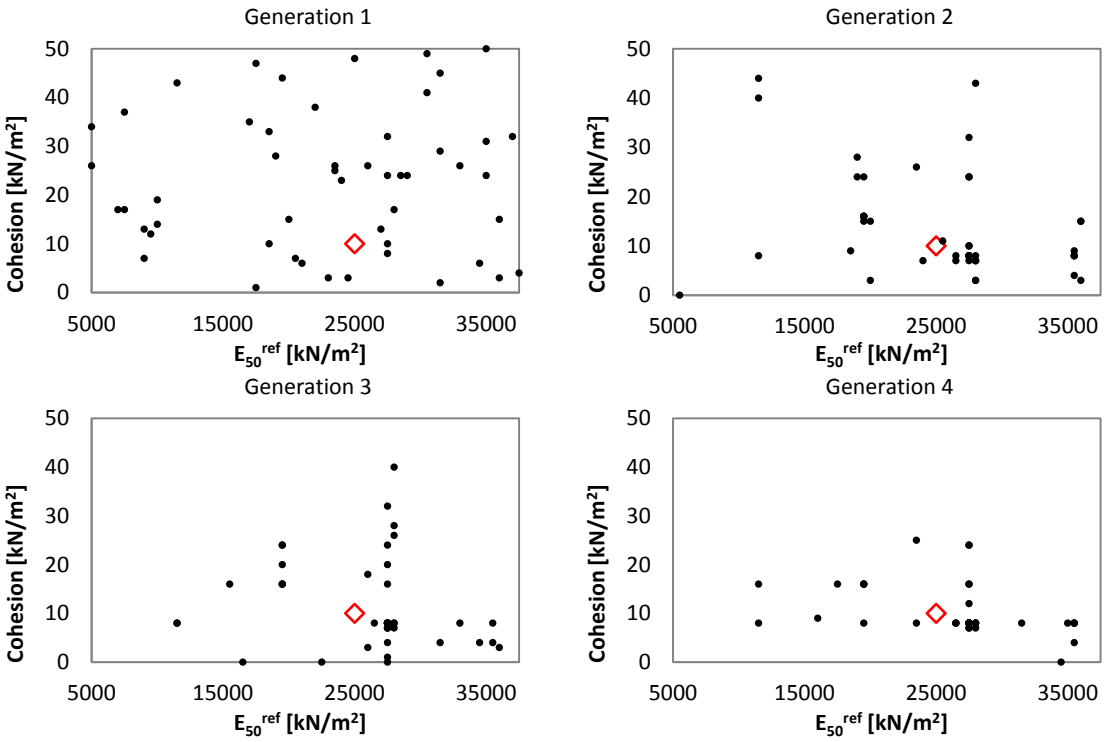

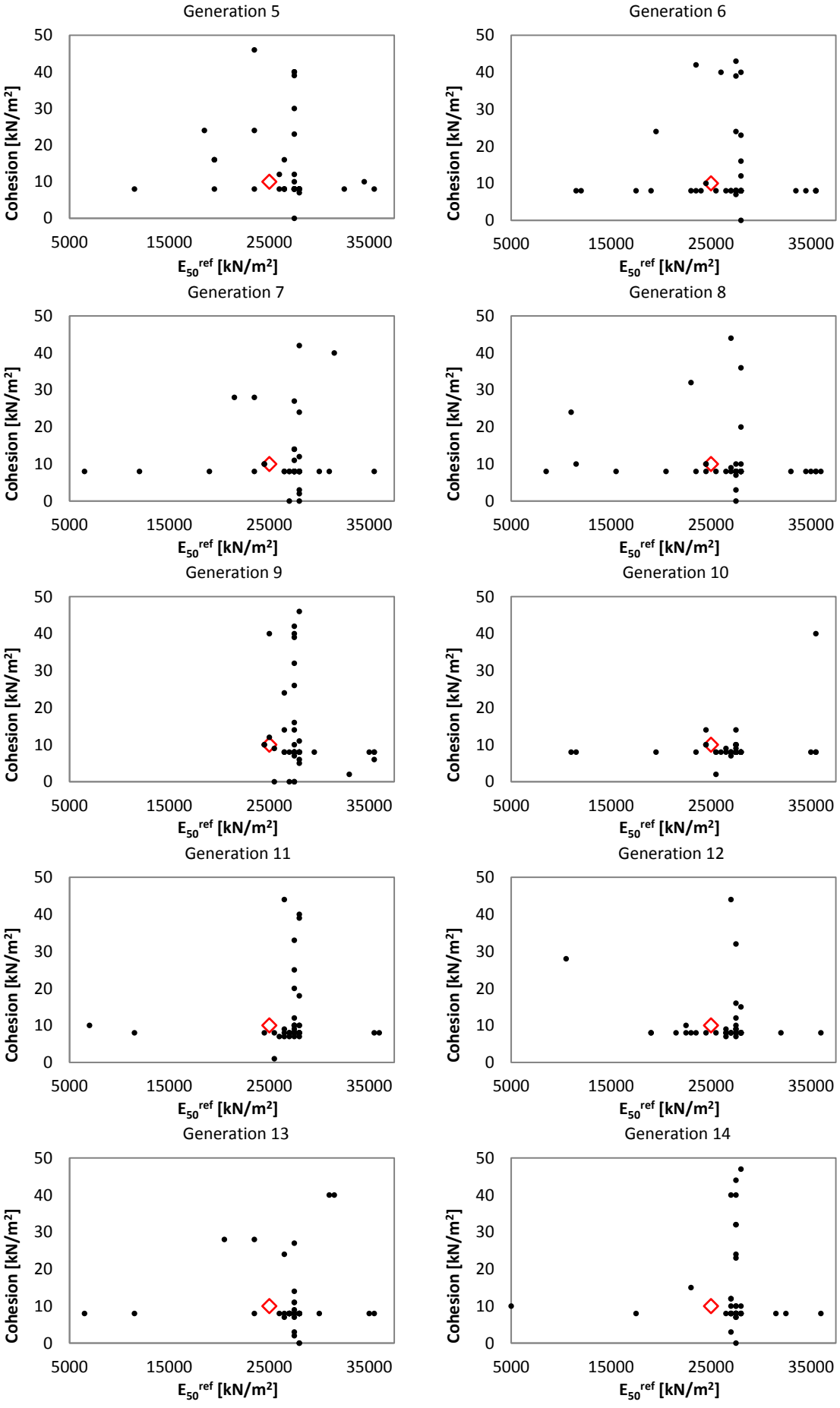
Generation 5
Generation 6
Generation 7
Generation 8
Generation 9
Generation 10
Generation 11
Generation 12
Generation 13
Generation 14
Cohesion [kN/m²]
E50ref [kN/m²]
0
10
20
30
40
50
5000
15000
25000
35000

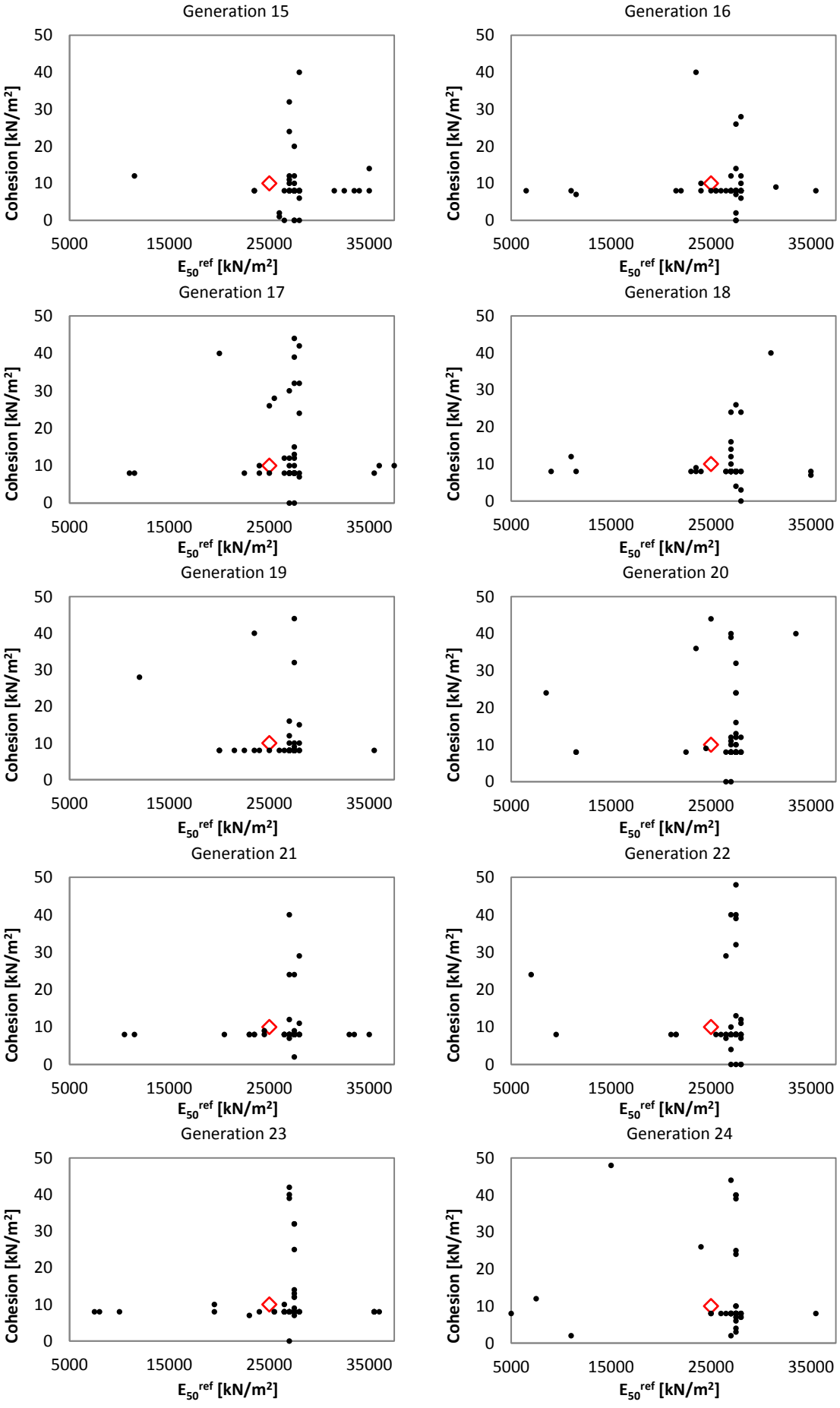
Generation 15
Generation 16
Generation 17
Generation 18
Generation 19
Generation 20
Generation 21
Generation 22
Generation 23
Generation 24
Cohesion [kN/m²]
E50ref [kN/m²]
0
10
20
30
40
50
5000
15000
25000
35000

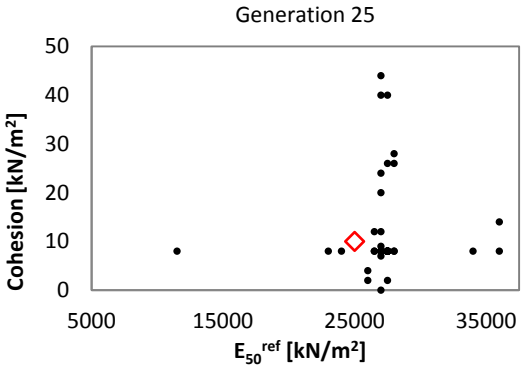

Figure 5.77. Evolution of the population over 25 generations using an AGA, with exact data, no fitness limit and a population size of 51 individuals.

Finally, the parameters associated with the best individual and the computational cost of the search, are presented in table 5.19, where in terms of geotechnics, the results can be considered a suitable solution of the problem.

Case	Identified Value		Computational Cost
	E_{50}^{ref} [kN/m^2]	c [kN/m^2]	[Plaxis evaluations]
AGA (exact data with no fitness limit and population size of 51 individuals)	26500	9	266

Table 5.19. Results of the case of adaptive genetic algorithms with exact data, no fitness limit and population size of 51 individuals.

5.3.5.2.2 Noisy Data Case Results

The results of the parameters estimation using an adaptive genetic algorithm, with noisy data, and looking for the best individual, are presented in this section.

In figure 5.78, the initial population of 51 individual all together with the objective function is shown, while figure 5.79 shows the final population after 25 generations.

From figure 5.79, it can be seen how the majority of the individuals are concentrated around the individual E_{50}^{ref}=26500 kN/m^2 and c=9 kN/m^2 (red cross), which in fact it is the best possible individual defined in the entire search space. Moreover, it also can be noted how well surrounded the best individual is; in part due to the high diversity of the first five generations (see figure 5.80).

Figure 5.81 shows the evolution of the objective function of the best individual and the average of the population.

The evolution in terms of parameter values for the best individual are shown in figure 5.82 and figure 5.83.

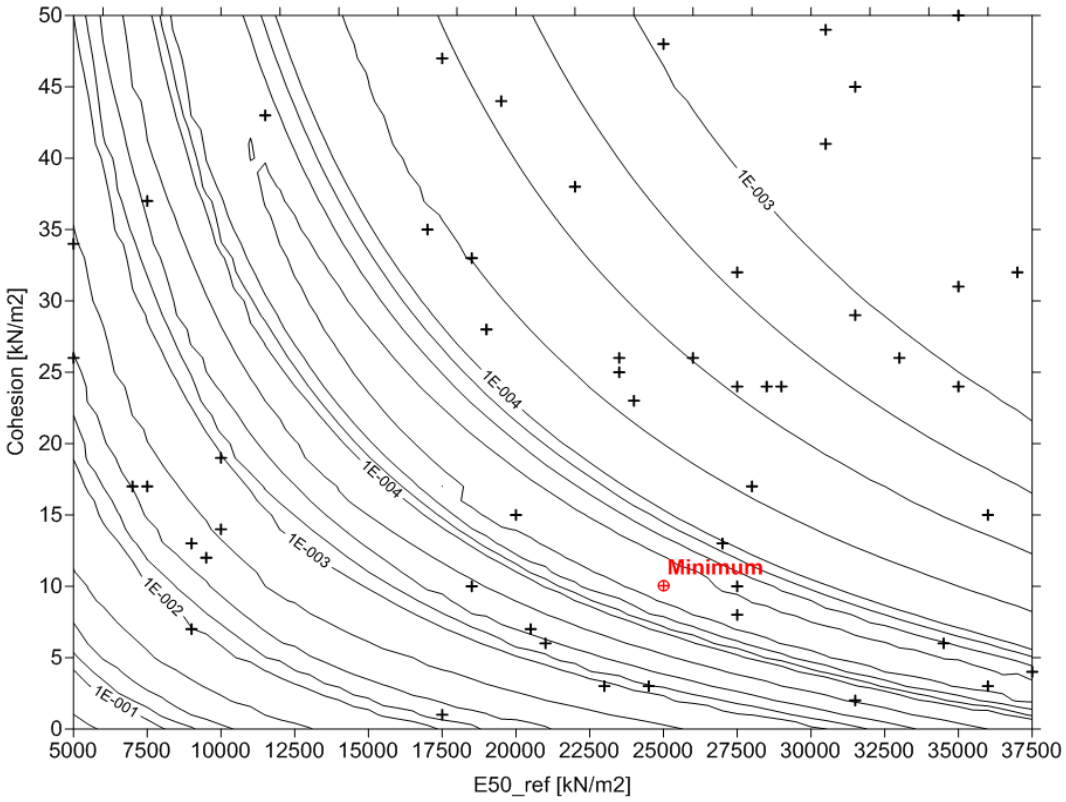

Figure 5.78. Initial population of 51 individuals randomly generated - Objective function [m^2]. The black crosses represent the individuals (AGA / looking for the best individual / noisy data).

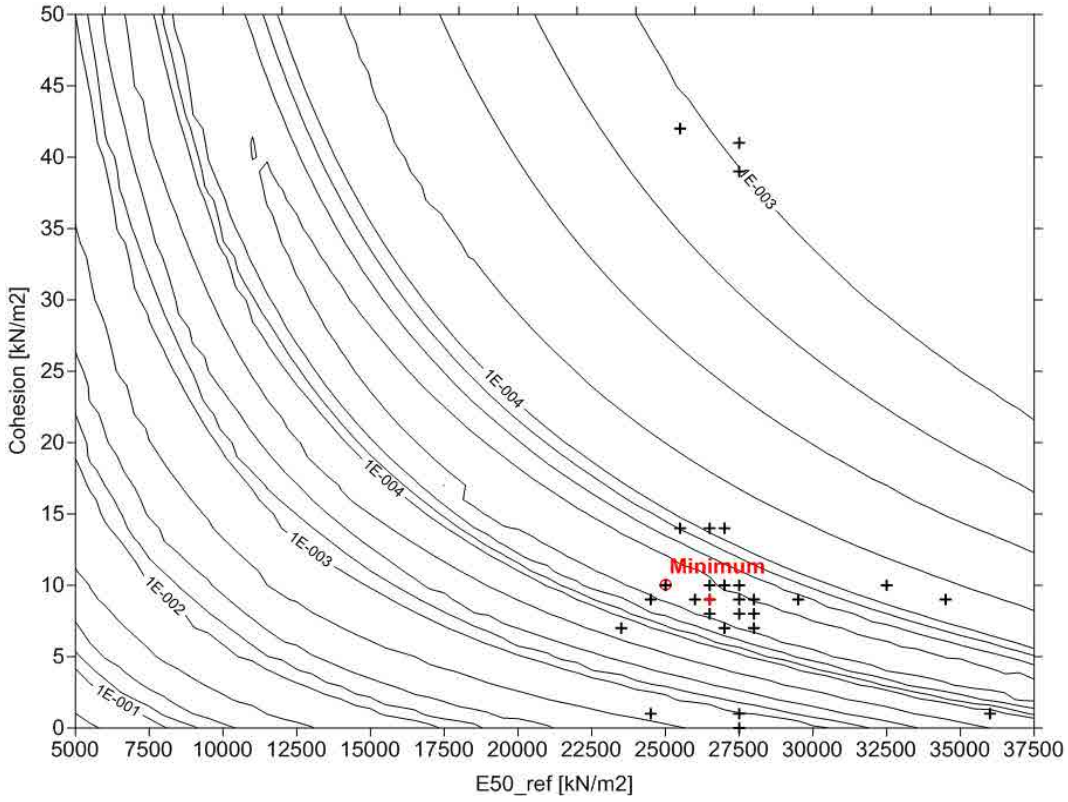

Figure 5.79. Population after 25 generations (last generation) - Objective function [m^2]. The black crosses represent the individuals of the last generation and the red cross represents the best individual of the generation (AGA / looking for the best individual / noisy data).

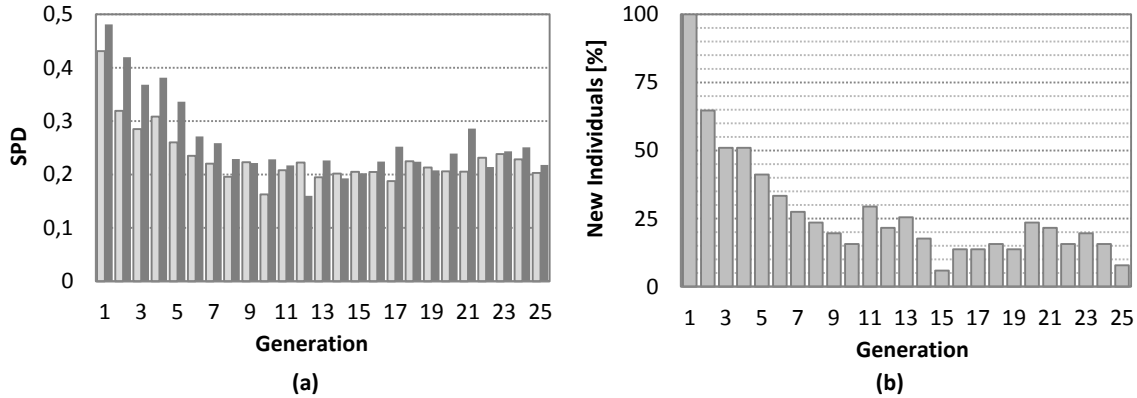

Figure 5.80. (a) evolution of the Standard Population Diversity (SPD), and (b) evolution of the percentage of new individuals in the population (AGA / looking for the best individual / noisy data).

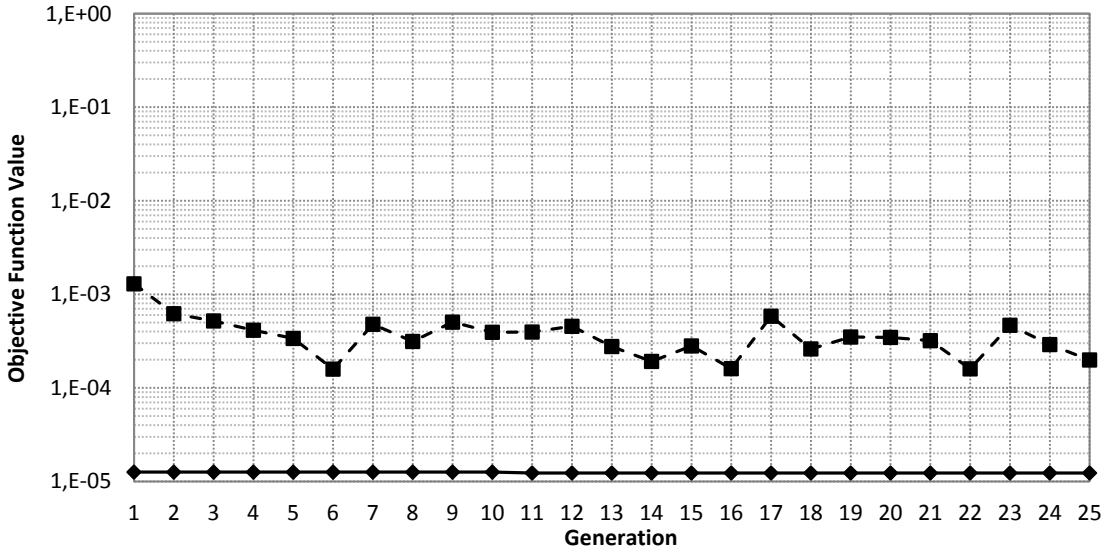

Figure 5.81. Evolution of the objective function. The solid line with diamonds represents the value of the best individual and the dashed line with squares represents the average value of the population (AGA / looking for the best individual / noisy data).

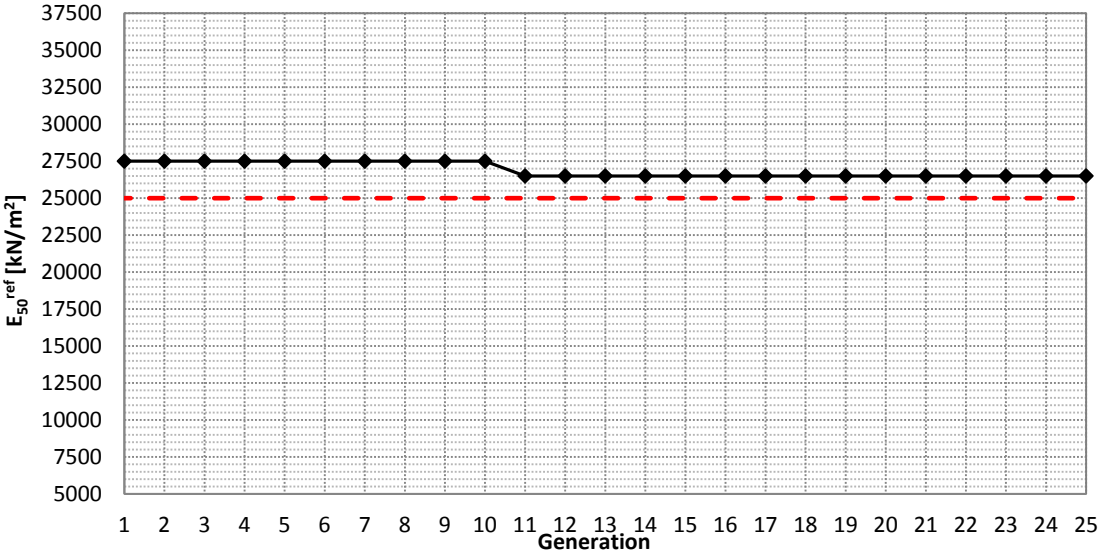

Figure 5.82. Evolution of the E_{50}^{ref} value (AGA / looking for the best individual / noisy data).

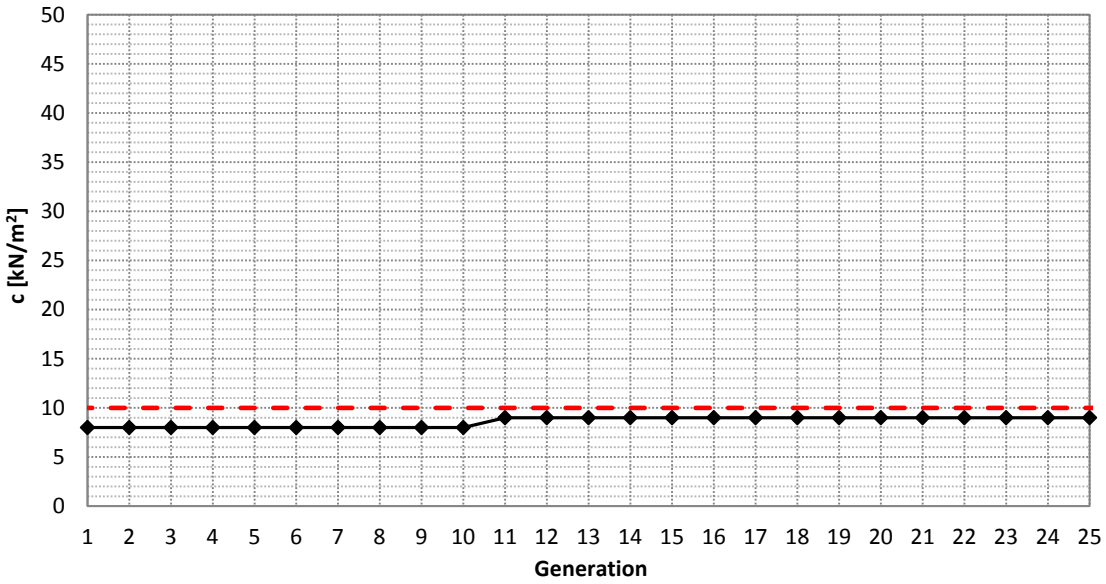

Figure 5.83. Evolution of the cohesion value (AGA / looking for the best individual / noisy data).

As mentioned before, even not having a high evolution of the best individual over the generations, does not strictly mean that the algorithm would have been improperly searching for the minimum.

From figure 5.84, it can be noticed how powerful the search has been, where initially the algorithm has been capable to capture the narrow banana shape valley, to later focus on the surroundings of the best individual defined for the noisy case (E_{50}^{ref}=26500 kN/m^2 and c=9 kN/m^2).

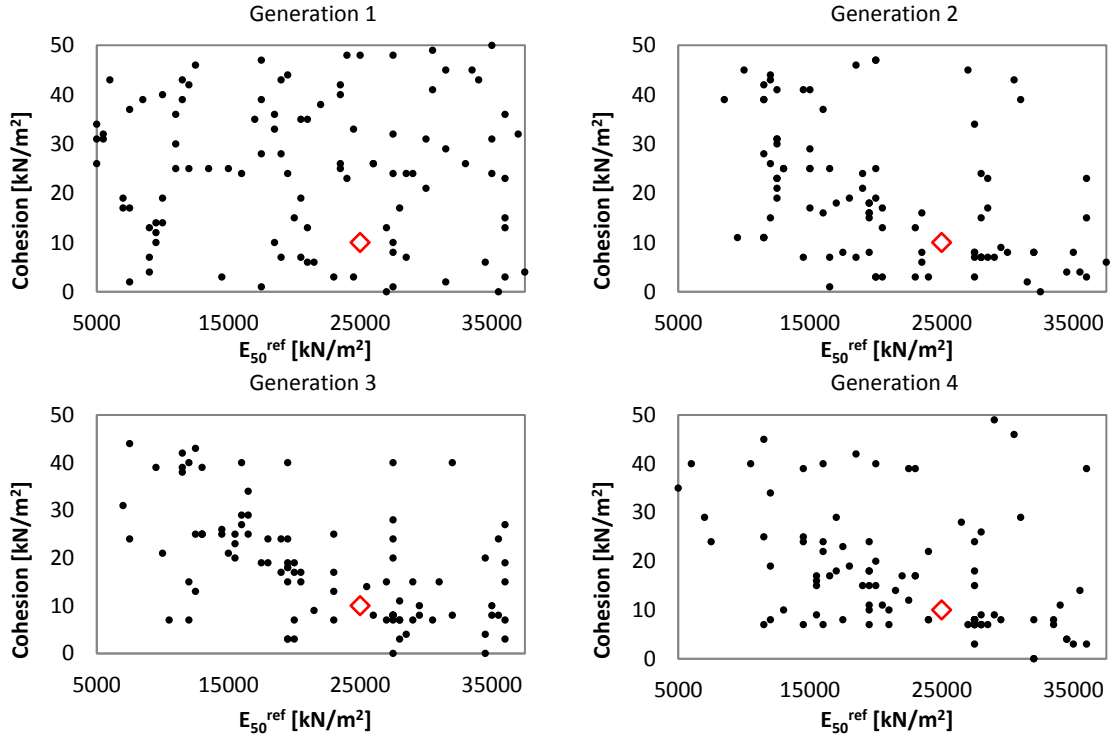

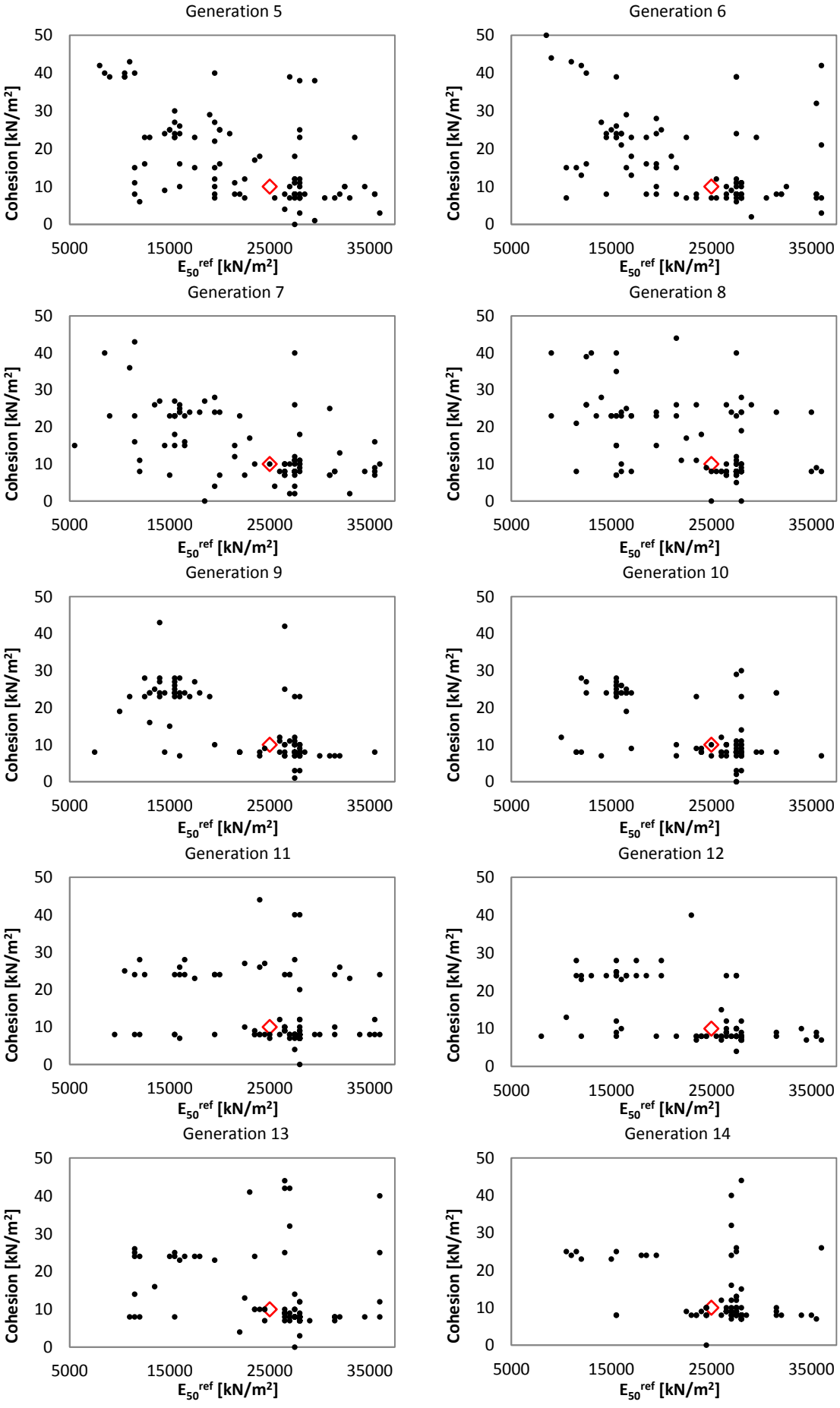
Generation 5
Generation 6
Generation 7
Generation 8
Generation 9
Generation 10
Generation 11
Generation 12
Generation 13
Generation 14
Cohesion [kN/m²]
E50ref [kN/m²]
0
10
20
30
40
50
5000
15000
25000
35000

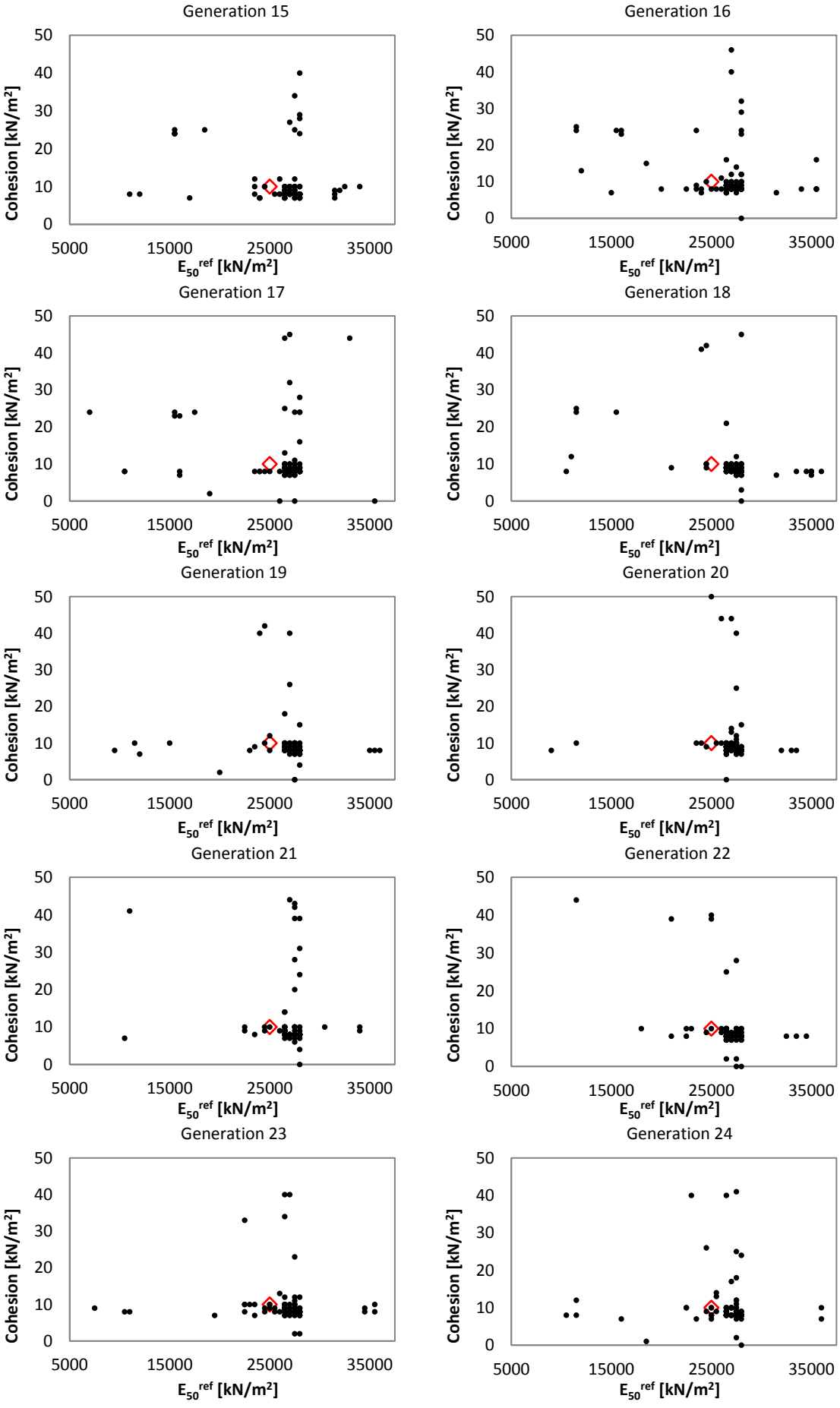
Generation 15
Generation 16
Generation 17
Generation 18
Generation 19
Generation 20
Generation 21
Generation 22
Generation 23
Generation 24
Cohesion [kN/m²]
E50ref [kN/m²]
0
10
20
30
40
50
5000
15000
25000
35000

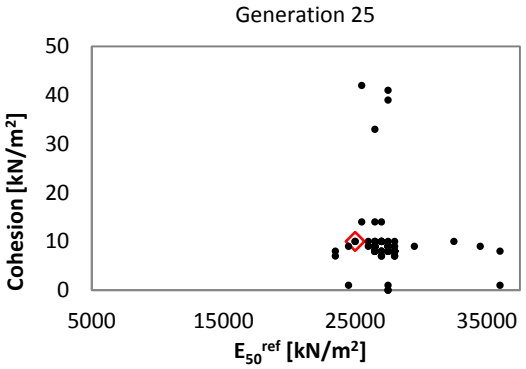

Figure 5.84. Evolution of the population all along 25 generations using AGA with noisy data, no fitness limit and a population size of 51 individuals.

Finally, the parameters associated with the best individual, and the computational cost are presented in table 5.20. The solution obtained can be considered satisfactory.

Case	Identified Value		Computational Cost
	E_{50}^{ref} [kN/m^2]	c [kN/m^2]	[Plaxis evaluations]
AGA (noisy data with no fitness limit and population size of 51 individuals)	26500 ± 561.4	9 ± 0.015	351

Table 5.20. Results of the case of adaptive genetic algorithms with noisy data, no fitness limit and population size of 51 individuals.

5.3.5.3 Looking for the Best Set of Individuals

The same procedure that was presented in section 5.3.4.3 has been followed herein to define the best set of individuals that are solution of the problem.

The main characteristics and parameters needed to fully define the problem are shown in table 5.21.

Optimization Algorithm	
Type of algorithm	AGA + Elitism
Selection type	Roulette Wheel (with fitness limit = frontier value)
GAP	1
Maximum probability of applying crossover (P_{c_max})	0.95
Minimum probability of applying crossover (P_{c_min})	0.50
Maximum probability of applying mutation (P_{m_max})	0.40
Minimum probability of applying mutation (P_{m_min})	0.01
Population size	51
Search Space Discretization	
$E_{50}^{ref}{}_{min}$ [kN/m^2]	5000
$E_{50}^{ref}{}_{max}$ [kN/m^2]	37500
$E_{50}^{ref}{}_{step\ size}$ [kN/m^2]	500
c_{min} [kN/m^2]	0
c_{max} [kN/m^2]	50
$c_{step\ size}$ [kN/m^2]	1
Objective Function	
Type of objective function	Least-Squares Method
Measurements	
Type of measurement	Vertical Displacements (20 measurement points)

Figure 5.21. Main characteristics and parameters of the problem of parameters estimation (AGA / Looking for the best set of individuals).

5.3.5.3.1 Exact Data Case Results

The results of the parameters estimation using an adaptive genetic algorithm, with exact data, and looking for the best set of individuals, are presented in this section.

Figure 5.85 illustrates the initial population of 51 individuals all together with the objective function, while in figure 5.86 all good individuals after 25 generations are shown.

Unfortunately, as it has occurred in all cases presented in this chapter, where the search has been focused on defining the best set of individuals, even the good representation of the individuals and their high diversity over the generations (see figure 5.87), the ellipse obtained from the PCA has not been capable to match the objective function shape. Consequently, the same variable transformation, which was applied in section 5.3.4.3, has been used to make the PCA ellipse capable to match the objective function (see figure 5.88). However, even the good match between the transformed PCA ellipse and the objective function shape, the high deviation of the parameters, enclosed in the ellipse has made difficult to associate the results to a unique soil material. In cases like this, it would be necessary to introduce previous information, usually parameter values obtained from different sources like laboratory tests, to better restrict the individuals that define the solution of the problem.

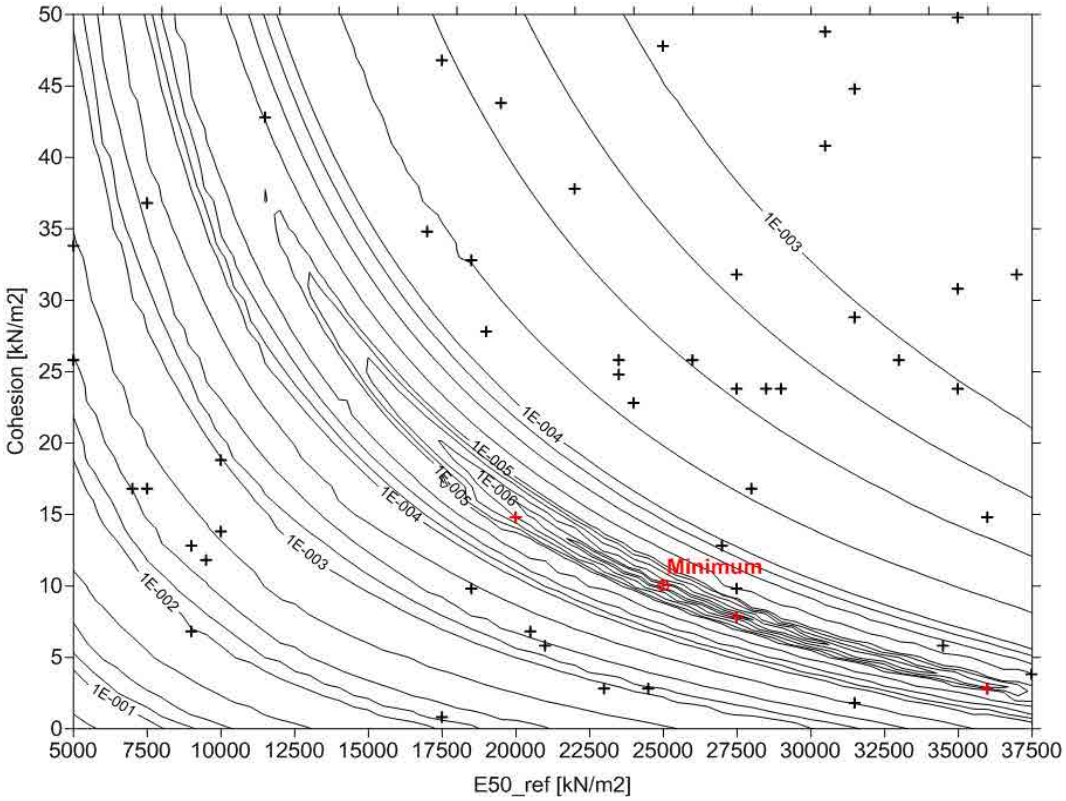

Figure 5.85. Initial population of 51 individuals randomly generated - Objective function [m^2]. The black crosses represent all individuals and the red ones represent just the good individuals of the initial population (AGA / looking for the best set of individuals / exact data).

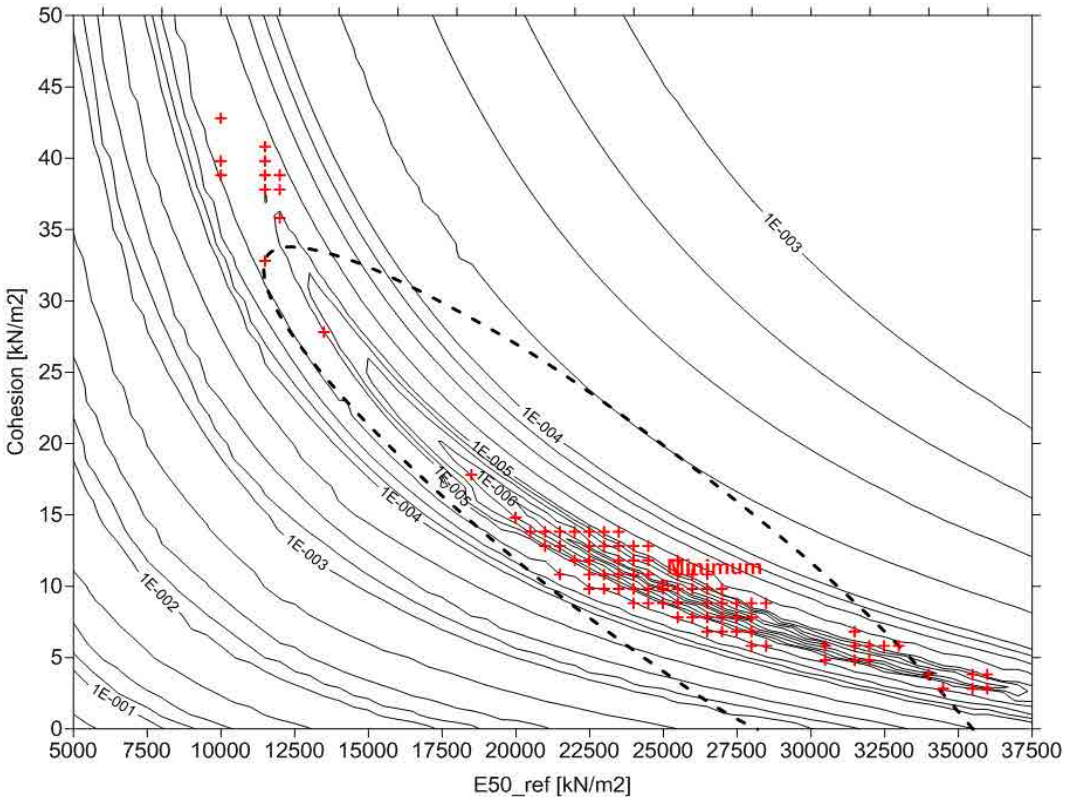

Figure 5.86. Set of good individuals after 25 generations - Objective function [m^2]. The red crosses represent the individuals and the dashed line represents the PCA ellipse (AGA / looking for the best set of individuals / exact data).

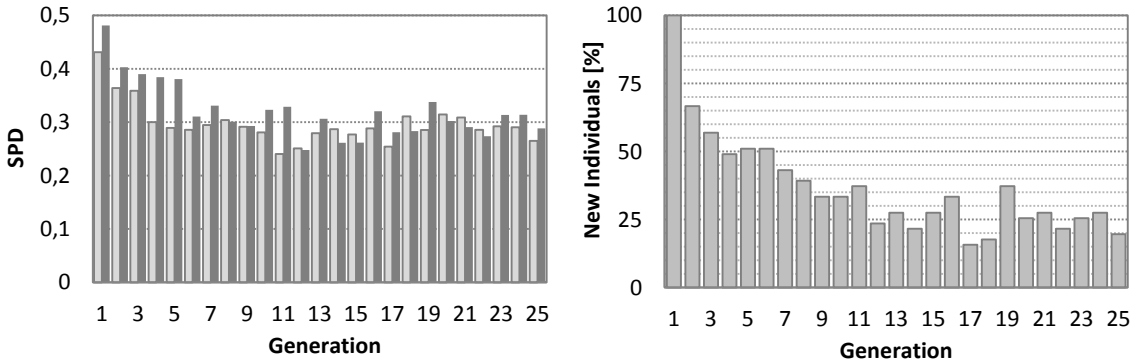

Figure 5.87. (a) evolution of the Standard Population Diversity (SPD), and (b) evolution of the percentage of new individuals in the population (AGA / looking for the best set of individuals / exact data).

Finally, the most relevant information involved in the analysis, as well as the results from the PCA, are shown in table 5.22.

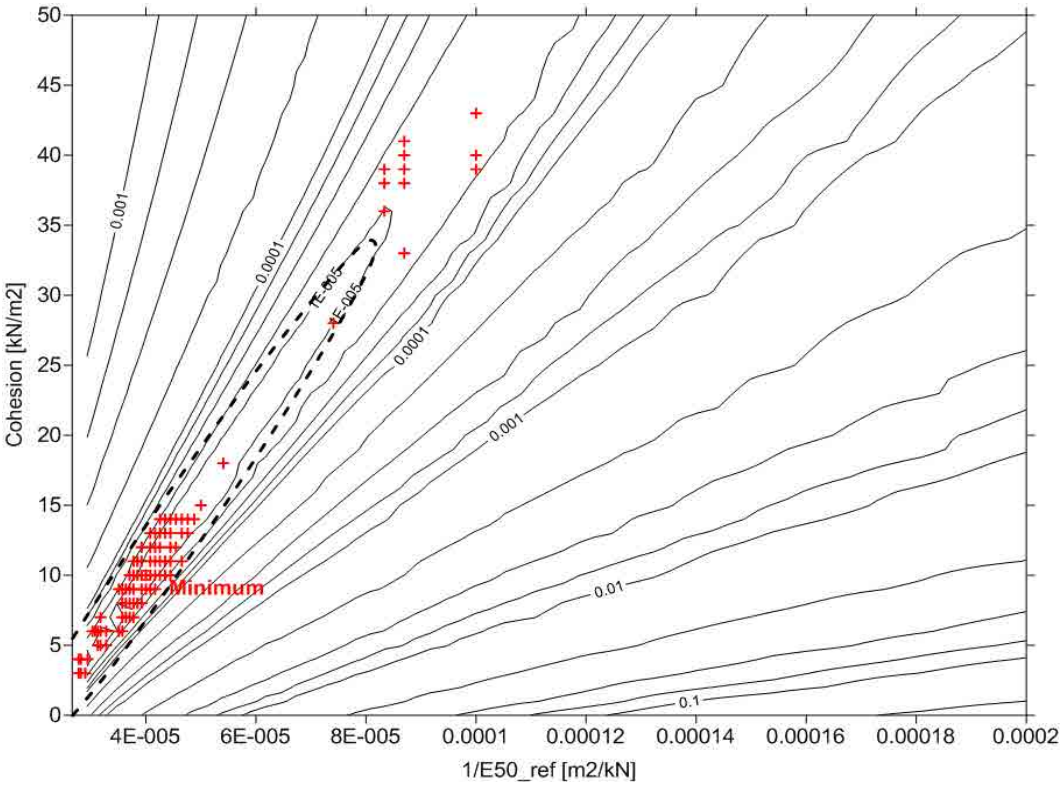

Figure 5.88. Representation of the objective function [m^{-2}] in the transformed space of $1/E_{50}^{ref} - c$. The red crosses represent the good individuals involved in the PCA and the dashed line represents the PCA ellipse (AGA / looking for the best set of individuals / exact data).

Description	Values
Relevant information involved in the analysis	
Computational cost [Plaxis evaluations]	465
Number of individuals involved in the PCA	89
Mean of $1/E_{50}^{ref}$ [m^2/kN]	$4.566 \cdot 10^{-5}$
Mean of c [kN/m^2]	13.359
Standard deviation of $1/E_{50}^{ref}$ [m^2/kN]	$1.794 \cdot 10^{-5}$
Standard deviation of c [kN/m^2]	10.270
AF (amplifier factor of the standard deviation)	2
PCA results	
Correlation matrix	$\begin{bmatrix} 1 & 0.9864 \\ 0.9864 & 1 \end{bmatrix}$
Eigenvector (associated to the first principal component)	$[0.7071 \quad 0.7071]$
Eigenvector (associated to the second principal component)	$[-0.7071 \quad 0.7071]$
Eigenvalue (associated to the first principal component)	1.9864
Eigenvalue (associated to the second principal component)	0.0135

Table 5.22. PCA results and some relevant information involved in the analysis (AGA / looking for the best set of individuals / exact data).

5.3.5.3.2 Noisy Data Case Results

The results of the parameter estimation using an adaptive genetic algorithm, with noisy data, and looking for the best set of individuals, are presented in this section.

Figure 5.89 illustrates the initial population of 51 individuals all together with the objective function, while in figure 5.90 the all good individuals after 25 generations are shown.

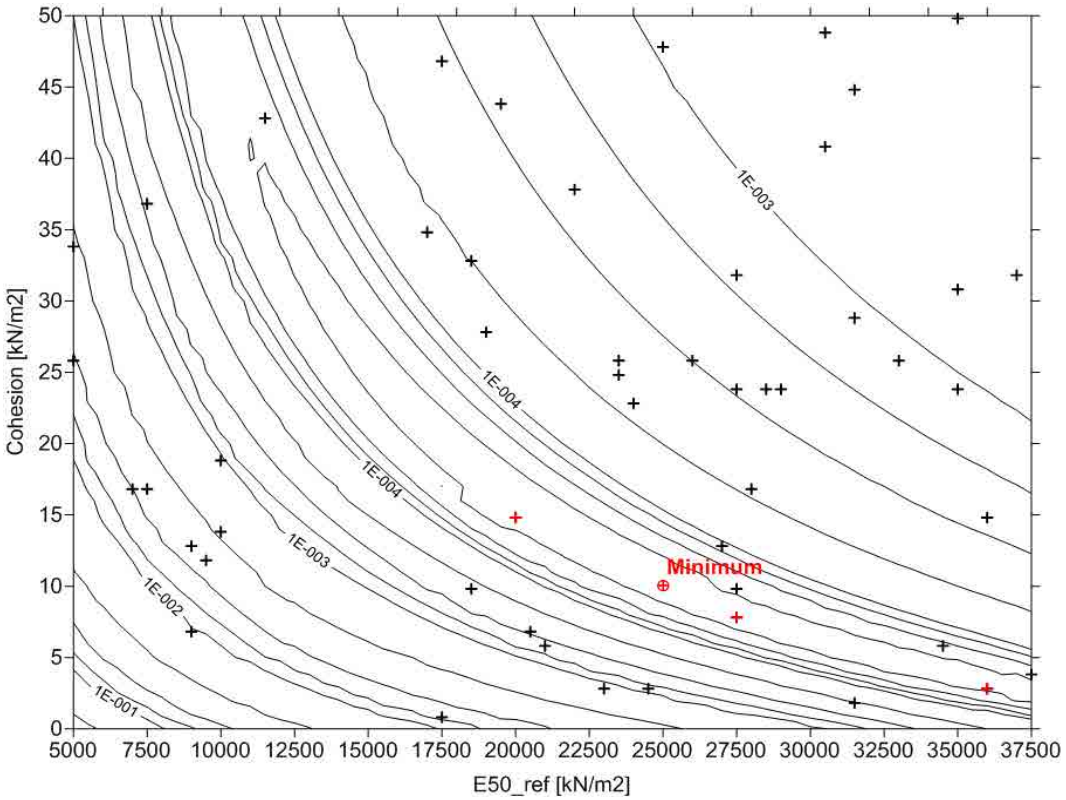

Figure 5.89. Initial population of 51 individuals randomly generated - Objective function [m^2]. The black crosses represent all individuals and the red ones represent just the good individuals of the initial population (AGA / looking for the best set of individuals / noisy data).

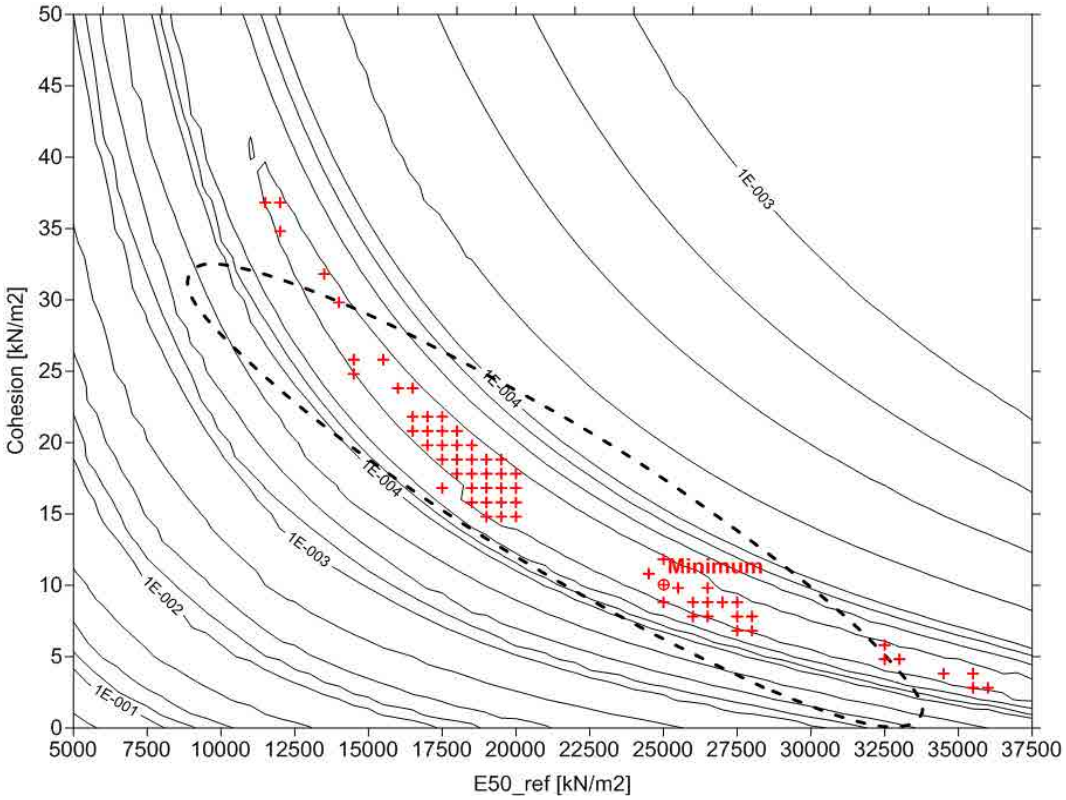

Figure 5.90. Set of good individuals after 25 generations - Objective function [m^2]. The red crosses represent the individuals and the dashed line represents the PCA ellipse (AGA / looking for the best set of individuals / noisy data).

No significant difference has been obtained from using noisy data instead of exact data (while looking for the best set of individuals). The higher robustness of the adaptive genetic algorithm, compared to the simple genetic algorithm, has partially reduced the effect of the introduction of noise, which highly affected the performance on previous analysis, especially in terms of imposing indirectly a high selection pressure.

Apart from the similar results already presented in figure 5.90, the rest of the results, presented in figures 5.91 and 5.92, are also very similar to the ones presented in the previous section. Therefore, it would be also necessary to introduce previous information to better restrict the individuals that defined the solution of the problem.

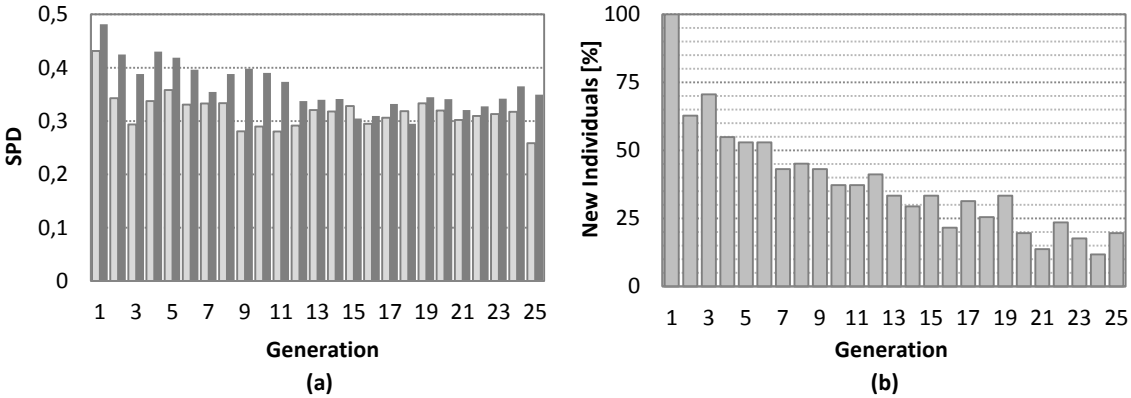

Figure 5.91. (a) evolution of the Standard Population Diversity (SPD), and (b) evolution of the percentage of new individuals in the population (AGA / looking for the best set of individuals / noisy data).

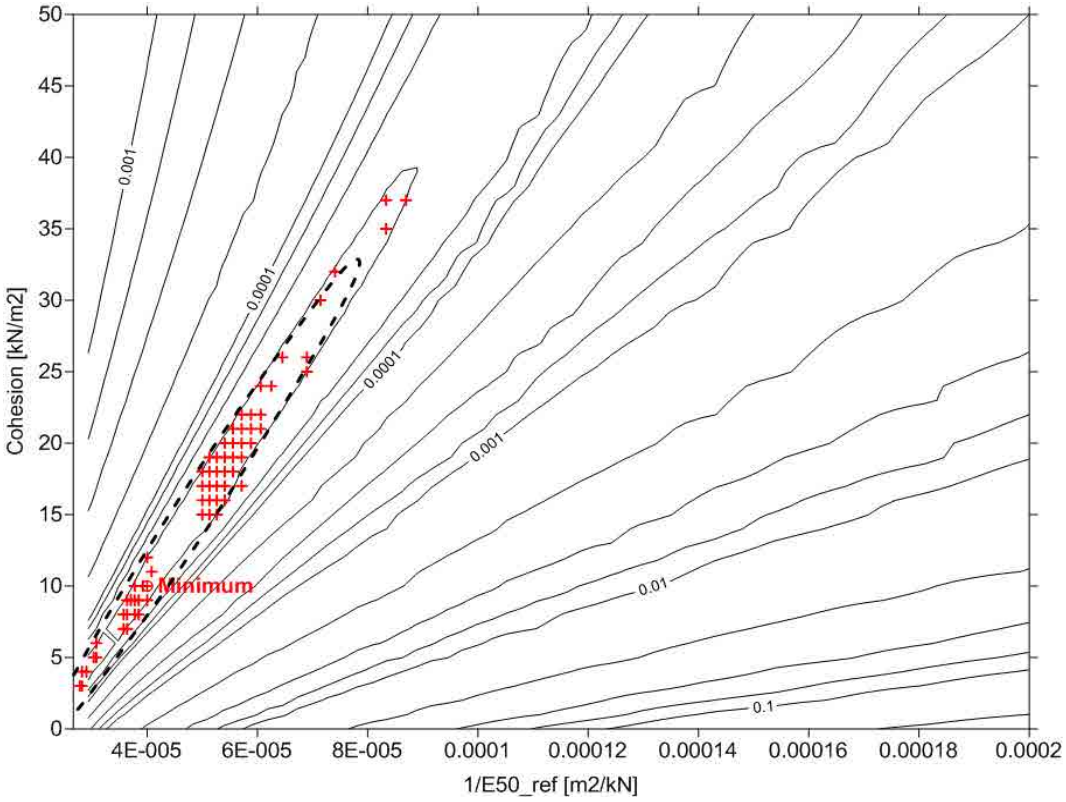

Figure 5.92. Representation of the objective function [m^{-2}] in the transformed space of $1/E_{50}^{ref} - c$. The red crosses represent the good individuals involved in the PCA and the dashed line represents the PCA ellipse (AGA / looking for the best set of individuals / noisy data).

Finally, the most relevant information involved in the analysis, as well as the results from the PCA, are shown in table 5.23.

Description	Values
Relevant information involved in the analysis	
Computational cost [Plaxis evaluations]	487
Number of individuals involved in the PCA	65
Mean of $1/E_{50}^{ref}$ [m^2/kN]	$5.065 \cdot 10^{-5}$
Mean of c [kN/m^2]	16.446
Standard deviation of $1/E_{50}^{ref}$ [m^2/kN]	$1.370 \cdot 10^{-5}$
Standard deviation of c [kN/m^2]	8.081
AF (amplifier factor of the standard deviation)	2
PCA results	
Correlation matrix	$\begin{bmatrix} 1 & 0.9883 \\ 0.9883 & 1 \end{bmatrix}$
Eigenvector (associated to the first principal component)	$[0.7071 \quad 0.7071]$
Eigenvector (associated to the second principal component)	$[-0.7071 \quad 0.7071]$
Eigenvalue (associated to the first principal component)	1.9883
Eigenvalue (associated to the second principal component)	0.0116

Table 5.23. PCA results and some relevant information involved in the analysis (AGA / looking for the best set of individuals / noisy data).

5.3.6 Using a Hybrid Method

Due to the fact that the hybrid method, defined in this thesis, is based on combining in serial form genetic algorithms with gradient based methods, multiple types of hybrid algorithms can be defined in terms of what kind of genetic algorithm is used, as well as what gradient based method is combined with. The final definition will depend on the problem.

Here, because of the extensive analysis that has been carried out using different algorithms (genetic algorithms and gradient based methods), it was considered appropriate to proceed with the analysis using the hybrid method, combining the adaptive genetic algorithm and the Gauss-Newton method (AGA + Gauss-Newton).

Thanks to the previous analysis, where the algorithm was permitted to run 25 consecutive generations, it was possible to study the point where no significant increase on the representativity of the PCA ellipse was obtained from letting the algorithm generating more new generations. Consequently, the switching point, from genetic algorithm to gradient based method, has been defined using the percentage of new individuals created per generation, which is strongly related to the representativity of the PCA ellipse and the efficiency of the algorithm in terms of computational cost. A value of 50% on the generation of new individuals was considered appropriate. Therefore, the switch from genetic algorithm to gradient based method occurred after the genetic algorithm is incapable to generate more than 50% of new individuals. For the stop criteria of the second stage of the algorithm (gradient based method), a fixed number of iterations was set up (10 iterations for the exact data case and 15 iterations for the noisy data case).

The main characteristics and parameters needed to fully define the hybrid method are shown in table 5.24.

Genetic Algorithm	
Optimization Algorithm	
Type of algorithm	AGA + Elitism
Selection type	Roulette Wheel (with fitness limit = frontier value)
GAP	1
Maximum probability of applying crossover (P_{c_max})	0.95
Minimum probability of applying crossover (P_{c_min})	0.50
Maximum probability of applying mutation (P_{m_max})	0.40
Minimum probability of applying mutation (P_{m_min})	0.01
Population size	51
Stop Criteria (switching point)	Less than 50% of new individuals
Search Space Discretization	
$E_{50}^{ref}{}_{min}$ [kN/m^2]	5000
$E_{50}^{ref}{}_{max}$ [kN/m^2]	37500
$E_{50}^{ref}{}_{step\ size}$ [kN/m^2]	500
c_{min} [kN/m^2]	0
c_{max} [kN/m^2]	50
$c_{step\ size}$ [kN/m^2]	1
Principal Component Analysis (PCA)	
Frontier Value	$2.5 \cdot 10^{-5}$m^2
AF (amplifier factor of the standard deviation)	2
Gradient Based Method	
Type of algorithm	Gauss-Newton
Stop Criteria	fixed number of iterations (exact data => 10 iterations / noisy data => 15 iterations)
Objective Function	
Type of objective function	Least-Squares Method
Measurements	
Type of measurement	Vertical Displacements (20 measurement points)

Table 5.24. Main characteristics and parameters of the Hybrid Method.

5.3.6.1 Exact Data Case Results

The results of the parameter estimation using the hybrid method with exact data are presented in this section.

In figure 5.93, it is presented the evolution of the number of new individuals generated per generation until reaching the bottom line of 50%.

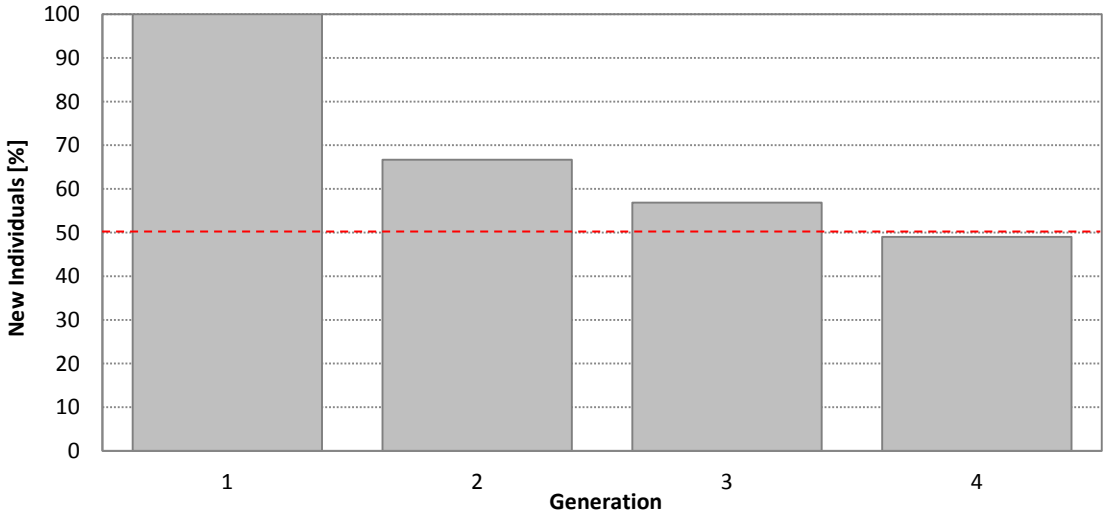

Figure 5.93. Evolution of the number of new individuals generated per generation. The red dashed line represents the percentage used as stop criteria (hybrid method / noisy data).

For this particular case, three generations were used to create the individuals involved in the PCA. The full evolution of the population and their good individuals are shown in figure 5.94.

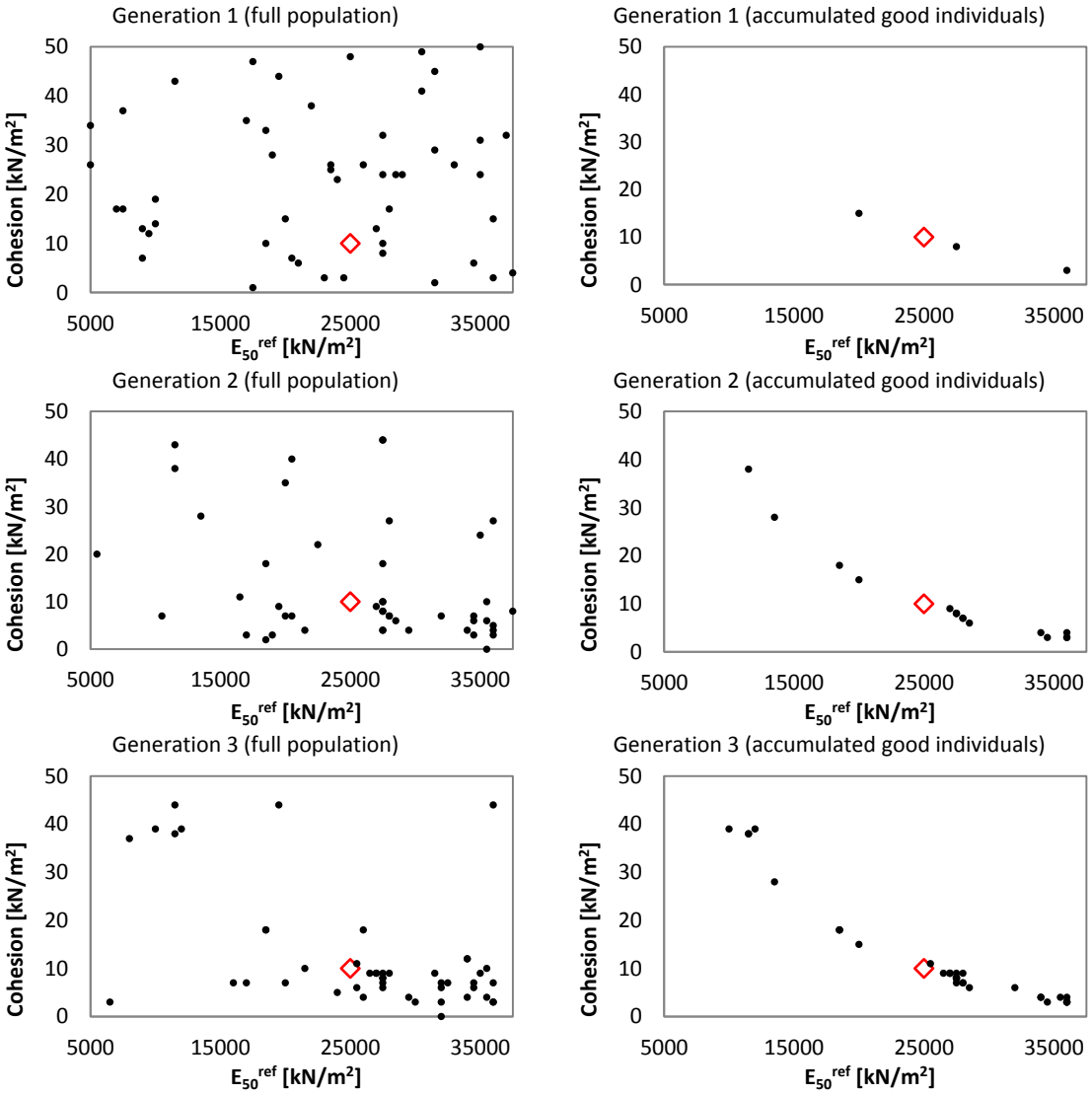

Figure 5.94. Full evolution of the population and their good individuals. The left column (full population) represents the evolution of the entire population where there are good and bad individuals. The right column (accumulated good individuals) represents the accumulated evolution of the good individuals over the generations. In both columns the black rhombuses represent the individuals while the red one represents the location of the minimum (hybrid method / exact data).

After three iterations and 114 individuals evaluated, 21 good individuals were generated and subsequently used in the principal component analysis to reduce and redefine the search space.

The most relevant information related to the PCA and the values of the eigenvectors and eigenvalues used to mathematically define the ellipse, are presented in table 5.25.

Description	Values
Mean of E_{50}^{ref} [kN/m^2]	25690.48
Mean of c [kN/m^2]	13.14
Standard deviation of E_{50}^{ref} [kN/m^2]	8347.86
Standard deviation of c [kN/m^2]	12.11
Correlation matrix	$\begin{bmatrix} 1 & -0.9481 \\ -0.9481 & 1 \end{bmatrix}$

Eigenvector (associated to the first principal component)	$[-0.7071 \quad 0.7071]$
Eigenvector (associated to the second principal component)	$[-0.7071 \quad -0.7071]$
Eigenvalue (associated to the first principal component)	1.9480
Eigenvalue (associated to the second principal component)	0.0519

Table 5.25. Principal Component Analysis (hybrid method / exact data).

In figure 5.95, the new search space defined by the PCA is graphically represented.

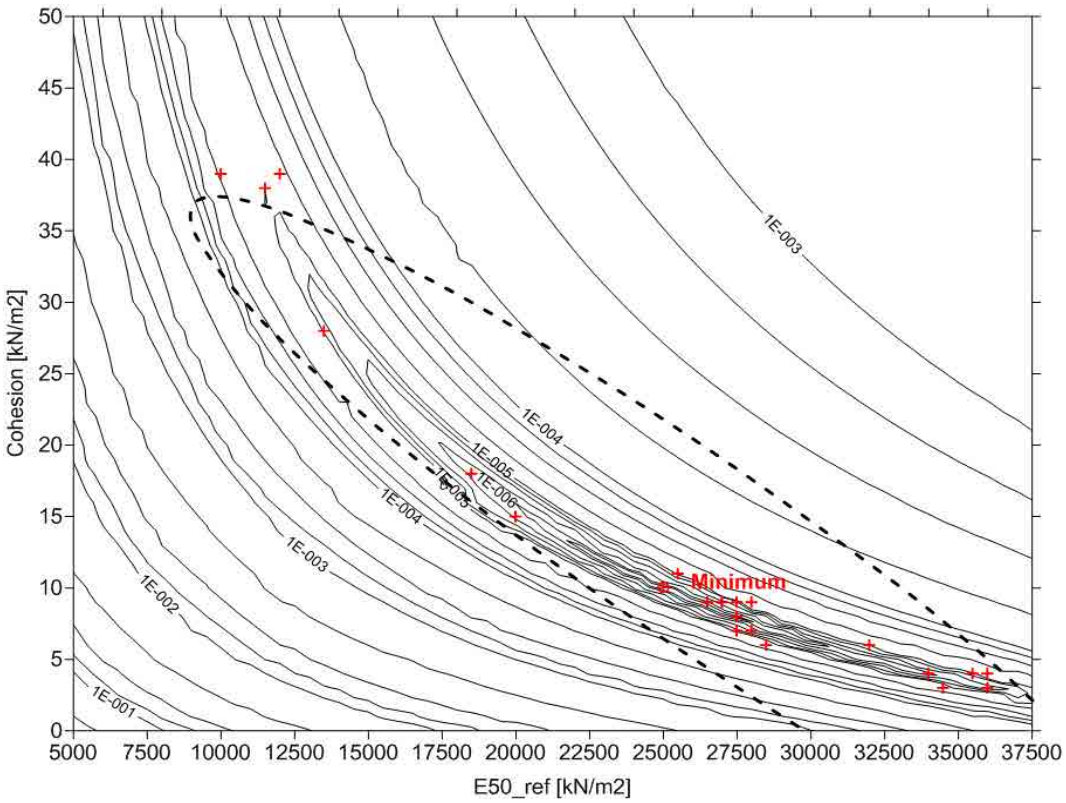

Figure 5.95. PCA ellipse - Objective function [m^2]. The dashed line represents the frontier of the new search space defined by the PCA and the red crosses represent the good individuals involved in the analysis (hybrid method / exact data).

As it occurred when using just genetic algorithms, the ellipse does not match the actual shape of the objective function. However, instead of applying the PCA to finally define a set of individuals as solution of the problem, in this case, the PCA is just being used to reduce the search space and defining the starting point for the gradient based method. Consequently, the mismatch between the PCA ellipse and the objective function shape does not require any transformation to force the match between them.

The path followed by the gradient based method is shown in figure 5.96, where the starting point is located in the center of the PCA ellipse.

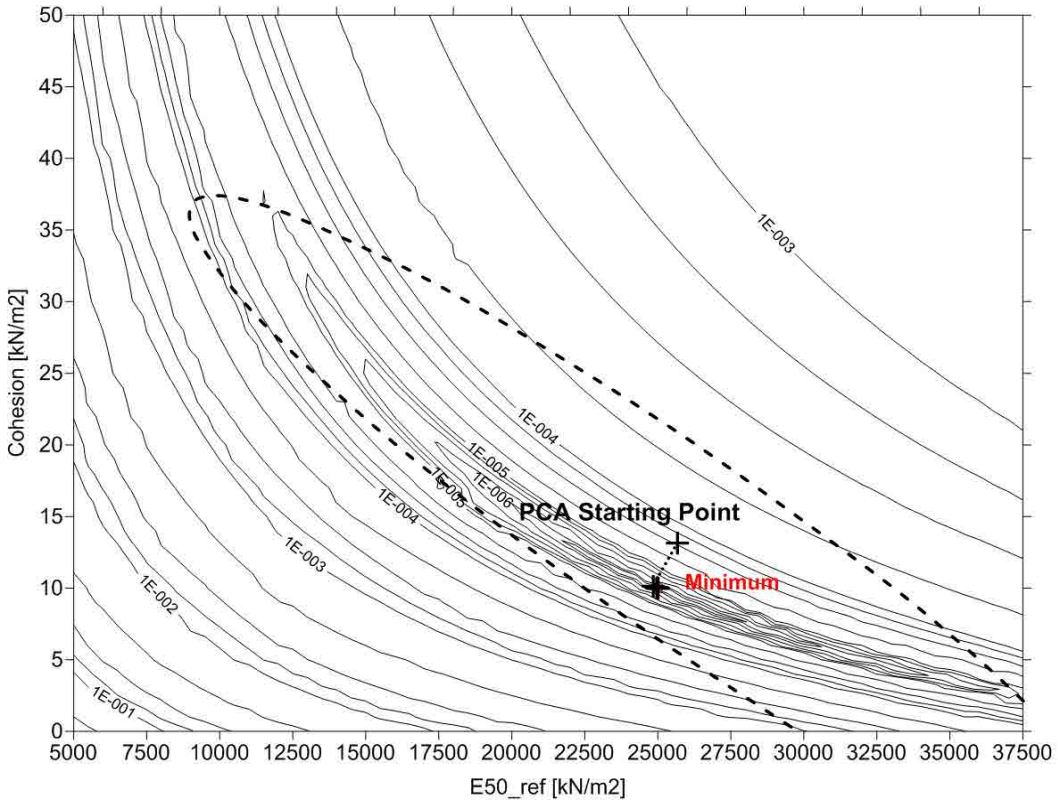

Figure 5.96. Gradient based method path starting from the center of the PCA ellipse - Objective function [m^2] (hybrid method / exact data).

In order to visualize in more detail the path followed by the gradient based method, the evolution in terms of objective function and parameters values are shown in figures 5.97, 5.98 and 5.99.

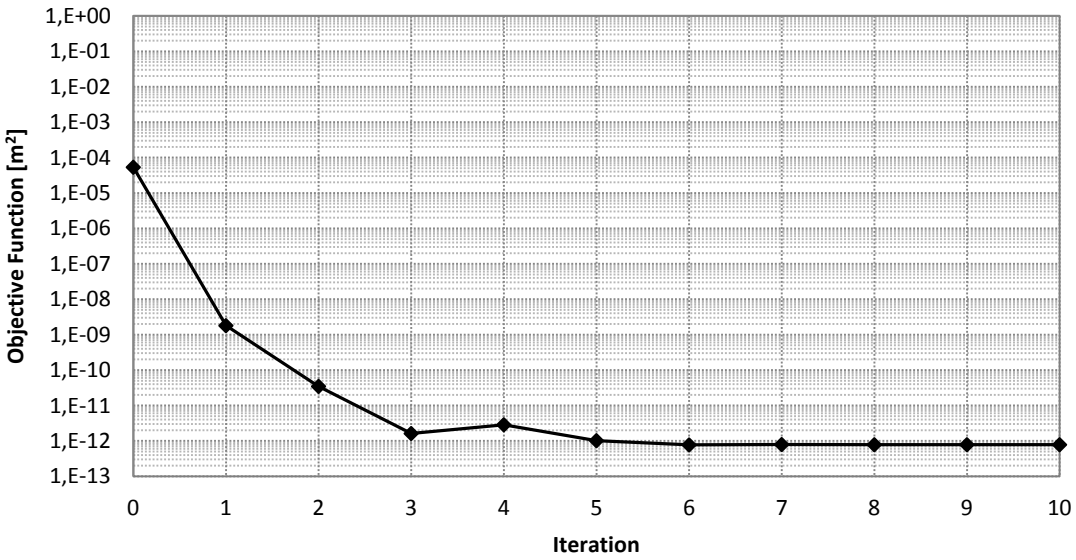

Figure 5.97. Evolution of the objective function using the Gauss-Newton method in the second stage of the hybrid method (hybrid method / exact data).

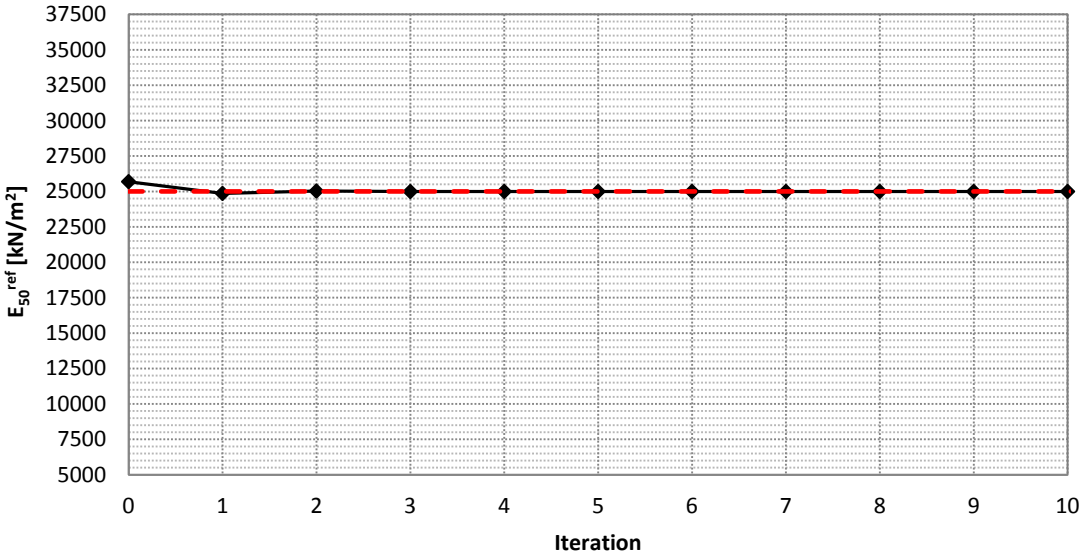

Figure 5.98. Evolution of the E_{50}^{ref} value using the Gauss-Newton method in the second stage of the hybrid method (hybrid method / exact data).

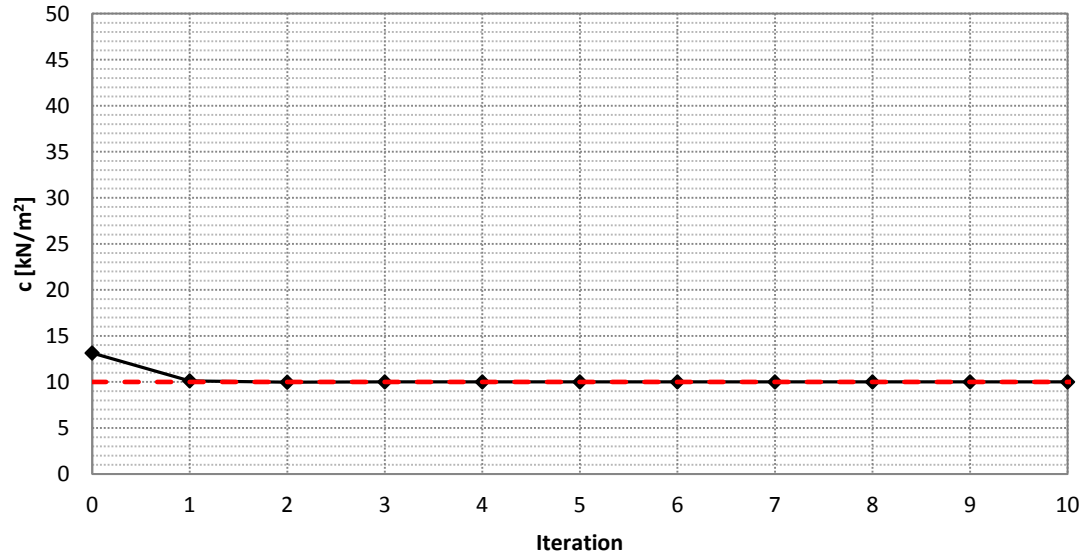

Figure 5.99. Evolution of the cohesion value using the Gauss-Newton method in the second stage of the hybrid method (hybrid method / exact data).

From this particular case, the use of the hybrid method has contributed to reduce the computational cost, compared with the isolated use of genetic algorithms, and increased the robustness of the gradient based method by selecting a suitable starting point and reducing the search space.

A summary of the results is shown in table 5.26.

Stage 1 (AGA + PCA)	
Number of generations	3
Computational cost [Plaxis evaluations]	114
Center of the PCA Ellipse	E_{50}^{ref} = 25690.48kN/m^2 and c = 13.14kN/m^2

Stage 2 (Gradient Based Method)	
Number of iterations	10
Computational cost [Plaxis evaluations]	30
Final values	E_{50}^{ref} = 24995.98kN/m^2 c = 10.00kN/m^2

Table 5.26. Results summary using the hybrid method with exact data. Plaxis evaluations is referred to the number of direct problems solved by the geotechnical program Plaxis.

5.3.6.2 Noisy Data Case Results

The results of the parameter estimation using the hybrid method with noisy data are presented in this section.

In figure 5.100, it is presented the evolution of the number of new individuals generated per generation until reaching the bottom line of 50%. As expected, the introduction of noise has increased the diversity of the population and consequently the potential of the algorithm to generate more new individuals.

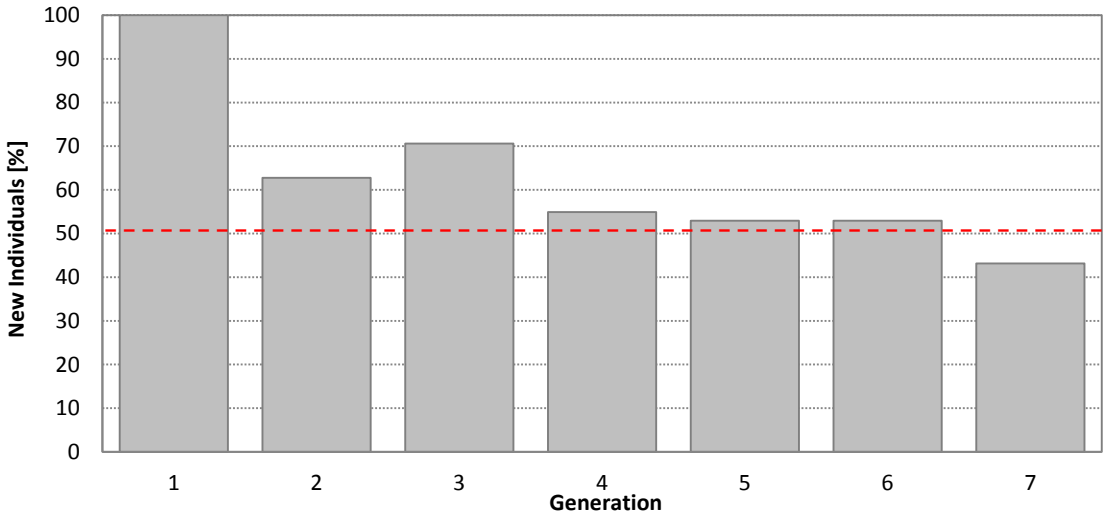

Figure 5.100. Evolution of the number of new individuals generated per generation. The red dashed line represents the percentage used as stop criteria (hybrid method / noisy data).

For this particular case, six generations were used to create the good individuals involved in the PCA. After those six generations, the algorithm evaluated 201 different individuals and a total of 28 of them were considered good individuals and subsequently used in the PCA.

The full evolution of the population and their good individuals are shown in figure 5.101, while the most relevant information related to the PCA and the values of the eigenvectors and eigenvalues used to mathematically define the ellipse, are presented in table 5.27. The graphical representation of the ellipse is shown in figure 5.102, where its shape does not matches the objective function shape. However, as previously explained, in the case of using the genetic algorithm as a part of a hybrid algorithm, the mismatch between the PCA ellipse and the objective function does not implicate any major problem on the identification procedure. Consequently, no transformation in the search space representation is required to force the match.

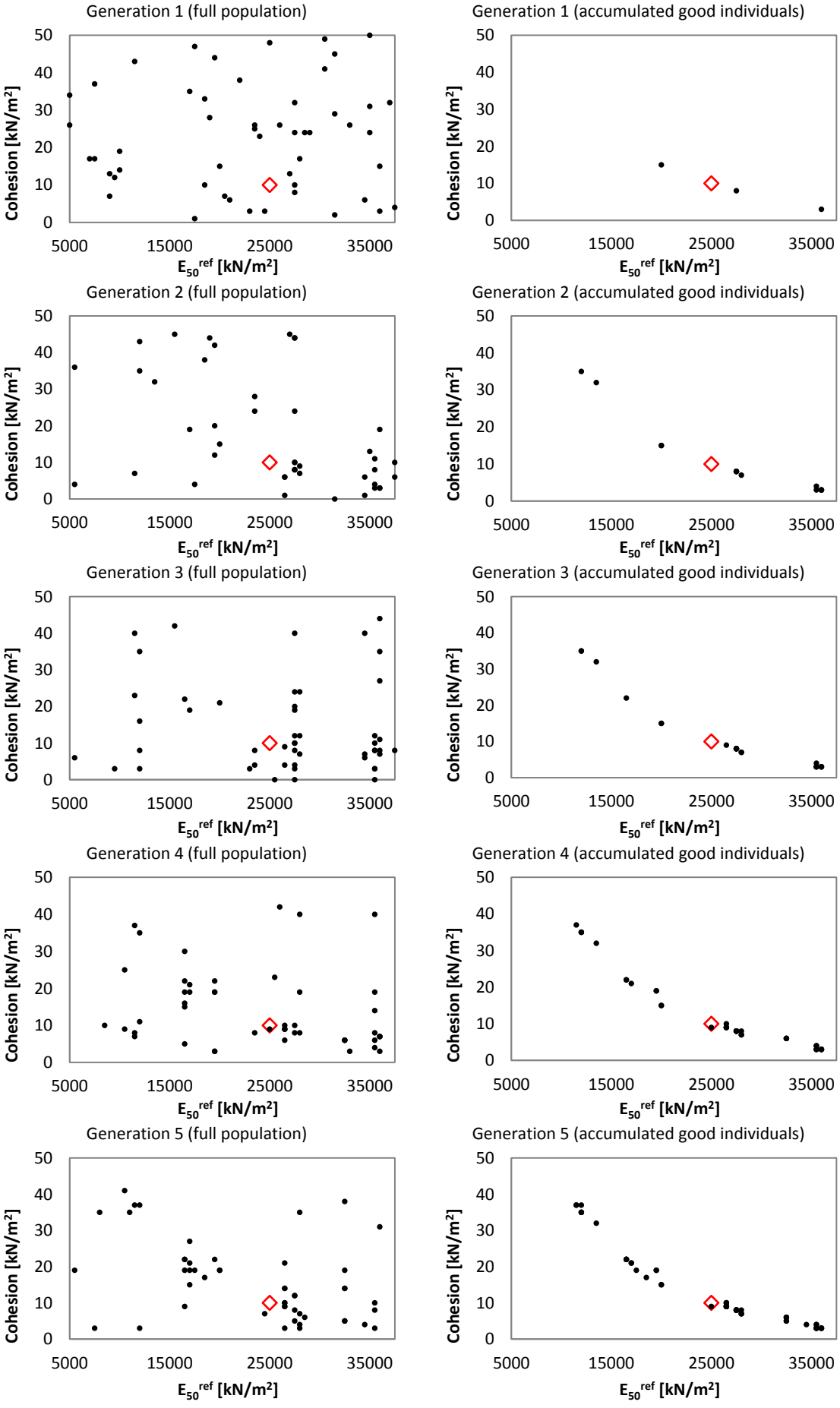
Generation 1 (full population)
Generation 1 (accumulated good individuals)
Generation 2 (full population)
Generation 2 (accumulated good individuals)
Generation 3 (full population)
Generation 3 (accumulated good individuals)
Generation 4 (full population)
Generation 4 (accumulated good individuals)
Generation 5 (full population)
Generation 5 (accumulated good individuals)
Cohesion [kN/m²]
E50ref [kN/m²]
0
10
20
30
40
50
5000
15000
25000
35000

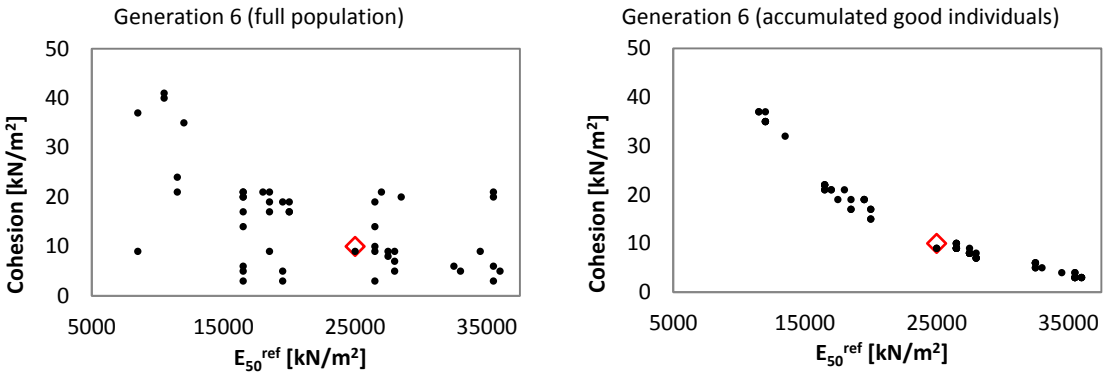

Figure 5.101. Full evolution of the population and their good individuals. The left column (full population) represents the evolution of the entire population where there are good and bad individuals. The right column (accumulated good individuals) represents the accumulated evolution of the good individuals over the generations. In both columns the black rhombuses represent the individuals while the red one represents the location of the minimum (hybrid method / noisy data).

Description	Values
Mean of E_{50}^{ref} [kN/m^2]	23553.57
Mean of c [kN/m^2]	15.07
Standard deviation of E_{50}^{ref} [kN/m^2]	7971.40
Standard deviation of c [kN/m^2]	10.49
Correlation matrix	$\begin{bmatrix} 1 & -0.9433 \\ -0.9433 & 1 \end{bmatrix}$
Eigenvector (associated to the first principal component)	$[-0.7071 \quad 0.7071]$
Eigenvector (associated to the second principal component)	$[-0.7071 \quad -0.7071]$
Eigenvalue (associated to the first principal component)	1.9433
Eigenvalue (associated to the second principal component)	0.0566

Table 5.27. Principal Component Analysis (hybrid method / noisy data).

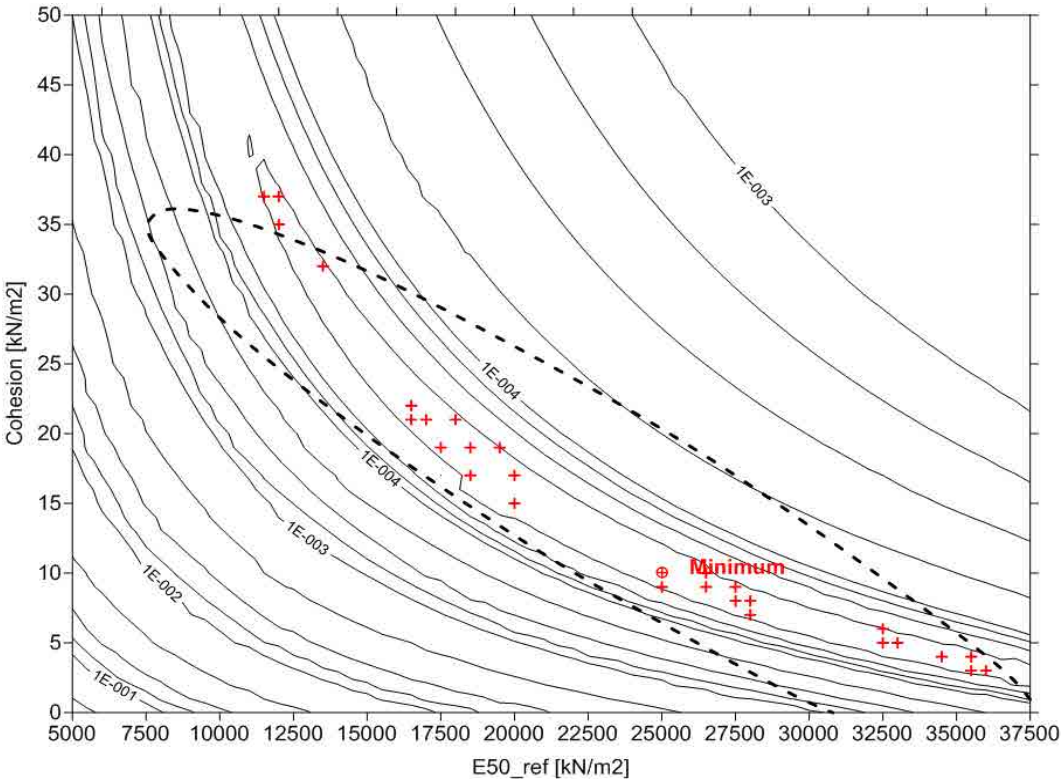

Figure 5.102. PCA ellipse - Objective function [m^2]. The dashed line represents the frontier of the new search space defined by the PCA and the red crosses represent the good individuals involved in the analysis (hybrid method / noisy data).

After defining the new search space, the Gauss-Newton method was initiated from the center of the PCA ellipse until reaching a value relatively close to the global minimum. The path followed by the algorithm is illustrated in figure 5.103. As in the other cases when using noisy data, the algorithm has been jumping around the minimum until reaching a value near the minimum.

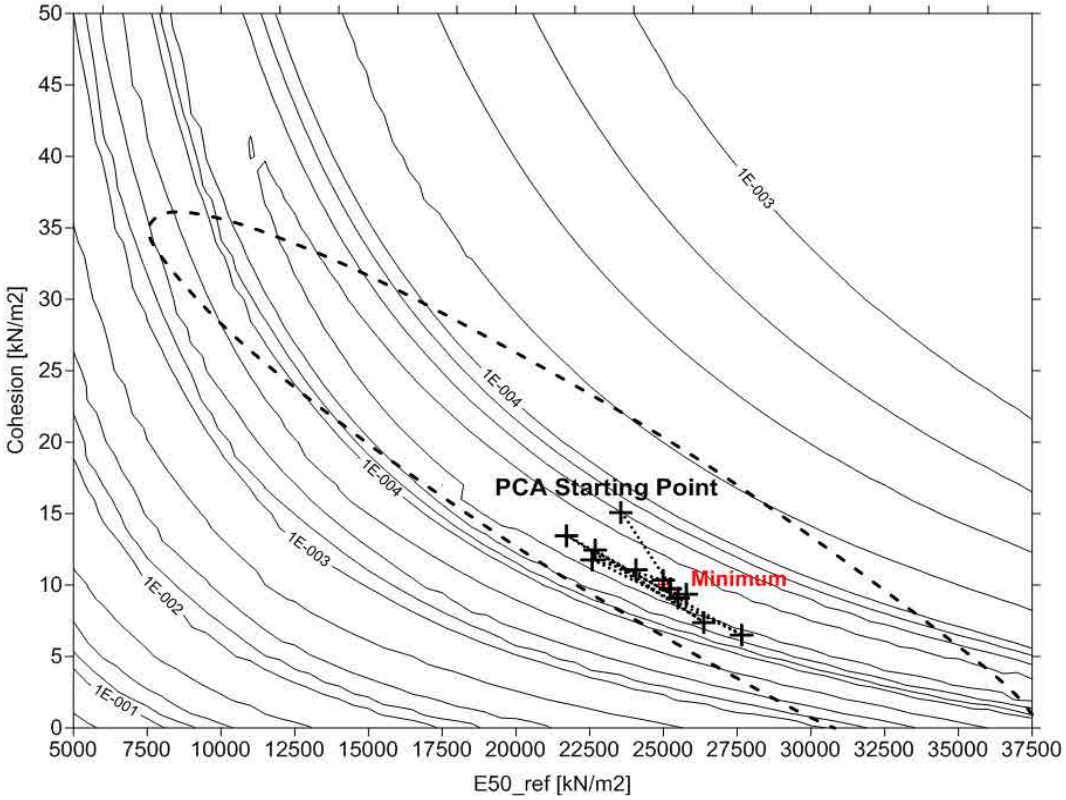

Figure 5.103. Gradient based method path starting from the center of the PCA ellipse - Objective function [m^2] (hybrid method / noisy data).

In order to see clearer the different iterations of the algorithm, the evolution, in terms of objective function and parameter values, are separately represented in figures 5.104, 5.105 and 5.106.

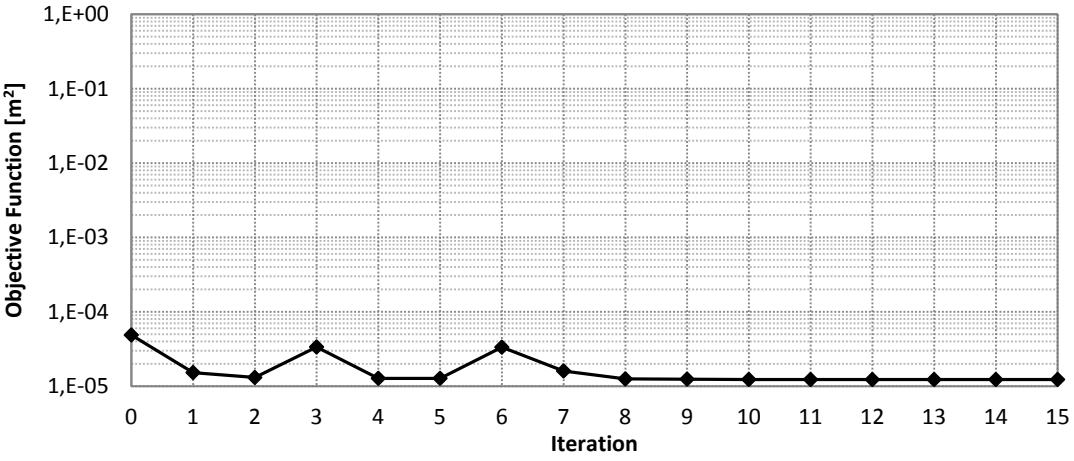

Figure 5.104. Evolution of the objective function using the Gauss-Newton method in the second stage of the hybrid method (hybrid method / noisy data).

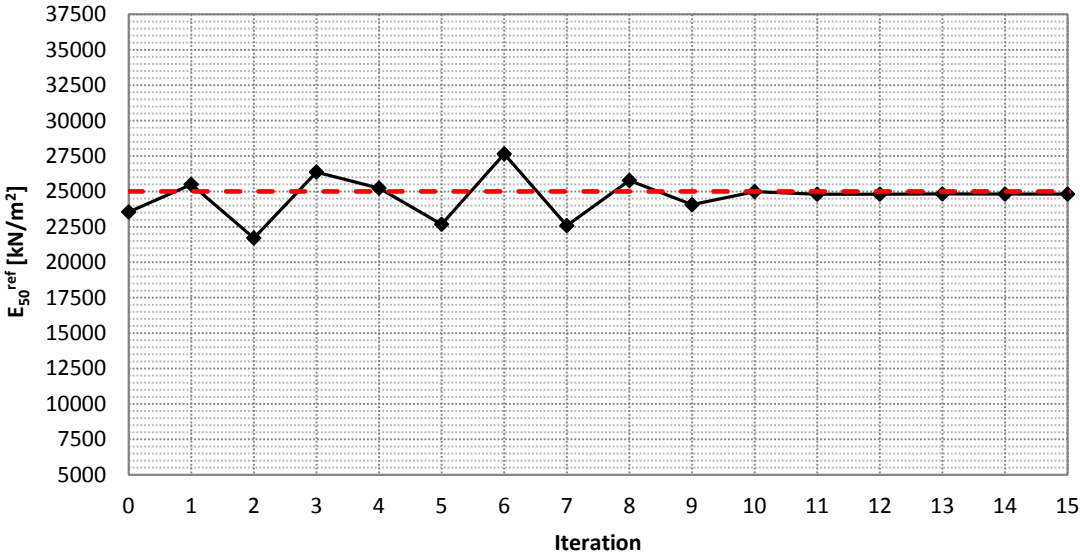

Figure 5.105. Evolution of the E_{50}^{ref} value using the Gauss-Newton method in the second stage of the hybrid method (hybrid method / noisy data).

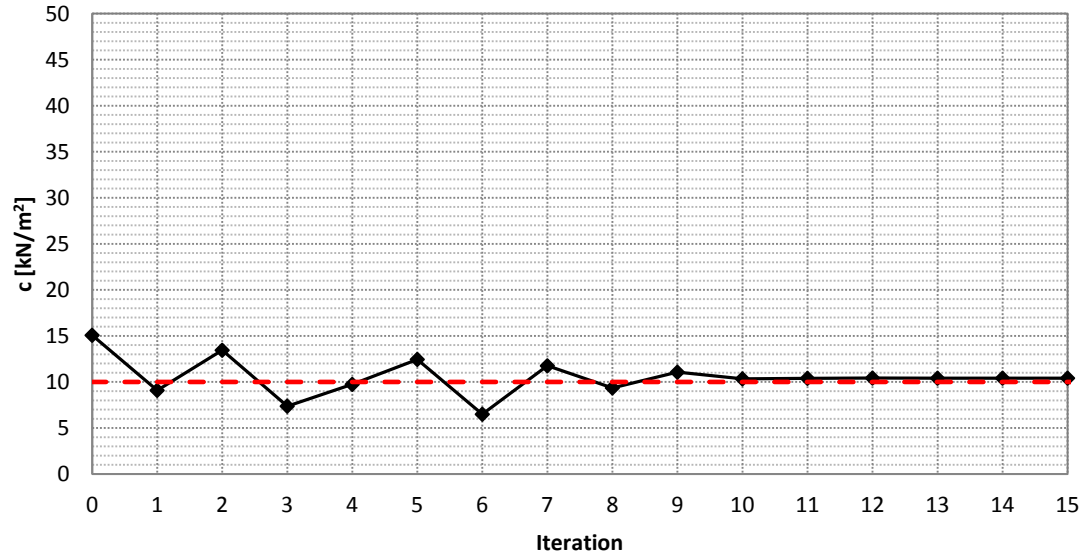

Figure 5.106. Evolution of the cohesion value using the Gauss-Newton method in the second stage of the hybrid method (hybrid method / noisy data).

As in the case of exact data, the hybrid method applied in a case with noisy data has reduced the computational cost, with respect to the cases where the genetic algorithm were applied, and increased the robustness of the gradient based method.

A summary of the results is shown in table 5.28.

Stage 1 (AGA + PCA)	
Number of generations	6
Computational cost [Plaxis evaluations]	201
Center of the PCA Ellipse	E_{50}^{ref} = 23553.57kN/m^2 and c = 15.07kN/m^2
Stage 2 (Gradient Based Method)	
Number of iterations	15

Computational cost [Plaxis evaluations]	44
Final values	E_{50}^{ref} = 24813.69±1820.3kN/m^2 c = 10.41±1.47kN/m^2

Table 5.28. Results summary using the hybrid method with noisy data. Plaxis evaluations is referred to the number of direct problems solved by the geotechnical program Plaxis.

5.3.7 Concluding Remarks from the Two Parameters Identification Case

After identifying the secant stiffness in standard drained triaxial test (E_{50}^{ref}) and the cohesion (c), using different optimization algorithms; several concluding remarks can be derived. A summary of global results is presented in table 5.29 to facilitate the comparison among the different methodologies, and consequently, to make easier the understanding of the concluding remarks presented here.

Case	Type of data	E_{50}^{ref} [kN/m^2]	c [kN/m^2]	Computational Cost [Plaxis evaluations]
		Gauss-Newton		
Starting Point 1	Exact	24995.99	10.00	30
Starting Point 2	Exact	24996.00	10.00	30
Starting Point 3	Exact	24996.00	10.00	30
Starting Point 1	Noisy	24803.57 ± 1805.4	10.42 ± 1.47	44
Starting Point 2	Noisy	24830.15 ± 1817.0	10.41 ± 1.47	44
Starting Point 3	Noisy	24813.70 ± 1820.3	10.41 ± 1.47	44
		Marquardt		
Starting Point 1	Exact	24995.99	10.00	30
Starting Point 2	Exact	24995.98	10.00	33
Starting Point 3	Exact	24995.99	10.00	78
Starting Point 1	Noisy	26301.64 ± 2089.6	9.09 ± 1.82	93
Starting Point 2	Noisy	21104.67 ± 1978.6	14.69 ± 2.66	120
Starting Point 3	Noisy	22827.13 ±1133.8	13.24 ± 1.50	87
		Simple Genetic Algorithm		
The best individual	Exact	29000	7	219
The best individual	Noisy	26500 ± 561.4	9 ± 0.015	599
The best set of individuals	Exact	See PCA ellipse in section 5.3.4.3.1		595
The best set of individuals	Noisy	See PCA ellipse in section 5.3.4.3.2		722
		Adaptive Genetic Algorithm		
The best individual	Exact	26500	9	266
The best individual	Noisy	26500 ± 561.4	9 ± 0.015	351
The best set of individuals	Exact	See PCA ellipse in section 5.3.5.3.1		465
The best set of individuals	Noisy	See PCA ellipse in section 5.3.5.3.2		487
		Hybrid Algorithm		
AGA + Gauss-Newton	Exact	24995.98	10.00	144
AGA + Gauss-Newton	Noisy	24813.69 ± 1820.3	10.41 ± 1.47	245

Table 5.29. Global Parameters Identification Results Summary (Two Parameters Identification Case).

For this particular synthetic case of two parameters identification, the best results, in terms of the balance between parameter values and computational cost, has been obtained from the Gauss-Newton method. However, it has to be pointed out that using a so really simple case with just two parameters to be identified, is the most appropriate scenario for the Gauss-Newton success. Therefore, it is not expected to get so good results when applying the method to real complex cases with a large number of parameters to be identified.

Having a narrow banana shape valley defining the surroundings of the minimum has made the Marquardt method face severe difficulties (see section 5.3.3). The restriction of the method to step forward if the new iteration has associated a higher error than the previous one has caused serious problems to the algorithm when moving through the narrow valley and finally

reach the minimum. Moreover, the significant difference in the magnitude between the values of E_{50}^{ref} and c, has made it difficult to find a suitable value of μ_0 and ρ that fits both parameters. Consequently, worse results were obtained by using the Marquardt method, which theoretically is an improvement of the Gauss-Newton method.

A good definition of μ_0 and ρ become fundamental, and they are problem dependent.

When looking for the best individual using simple genetic algorithms, the right choice of the population size and the selection pressure has a major impact on the performance of the algorithm, especially if there is a huge difference between the fitness of the good individuals and the average of the population. This situation usually causes premature convergence due to a fast loss of diversity. Whereas, when using an adaptive genetic algorithm, the self-adaptive system of the algorithm enforces to keep a certain level of diversity that facilitates a better performance, and makes the algorithm less dependent on population size and selection pressure.

On the other hand, when looking for the best set of individuals rather than the best individual, it has been noticed that even having a good match between the PCA ellipse and the objective function (satisfactory result in terms of optimization problem), geotechnically speaking, if the individuals enclosed in the PCA ellipse are not capable to be defined as a specific soil material, the final results of the backanalysis cannot be considered satisfactory. In those cases, it would be necessary the introduction of prior information to redefine and limit the individuals that represent the final solution.

Finally, when using a hybrid method that combines genetic algorithms with gradient based methods, it can be point out that a good balance between robustness and efficiency has been achieved. However, for this simple synthetic case, the hybrid algorithm is still less efficient than the Gauss-Newton method. Nonetheless, for complex real cases with a large number of parameters, it is expected that the hybrid algorithm will become more competitive than any gradient based method.

5.4 Optimal In Situ Instrumentation Layout (Two Parameters Identification Case)

Because of the primary objective of strictly studying the behavior and the performance of the different optimization algorithms presented in this thesis, it was not considered necessary, until now, to study the influence of the measurement points that usually are used to define a standard control section in a tunnel construction scenario. Supposing the tunnel problem as symmetric, a standard control section is usually defined by a sliding micrometer, located close to the tunnel crown, an inclinometer, located 2 meters from the side of the tunnel, and several vertical displacements surface points.

Two different tunnel scenarios were defined to carry out the analysis. The first scenario, named "Far From Collapse", is exactly the same one that has been used in section 5.3, while the second scenario, named "Close To Collapse", is geometrically and parametrically equal than the other scenario (Far From Collapse), with the difference that this new scenario has been forced to reach a state close to collapse.

The procedure to force the system to reach a state close to collapse was performed by imposing a value of ΣMStage=0.32, which causes a volume loss around 7% and displacements of decimeters.

From figure 5.107, the different regimes of the stress points can be seen, and subsequently compared with figure 5.4, which illustrates the regimes for the case defined as "far from collapse". Especially interesting is to compare figure 5.107b and figure 5.4b, which correspond to the construction phase where the majority of displacements occur, and where can be clearly observed the difference between a stable scenario far from collapse and a near collapse scenario with a significant domain in Mohr-Coulomb regime.

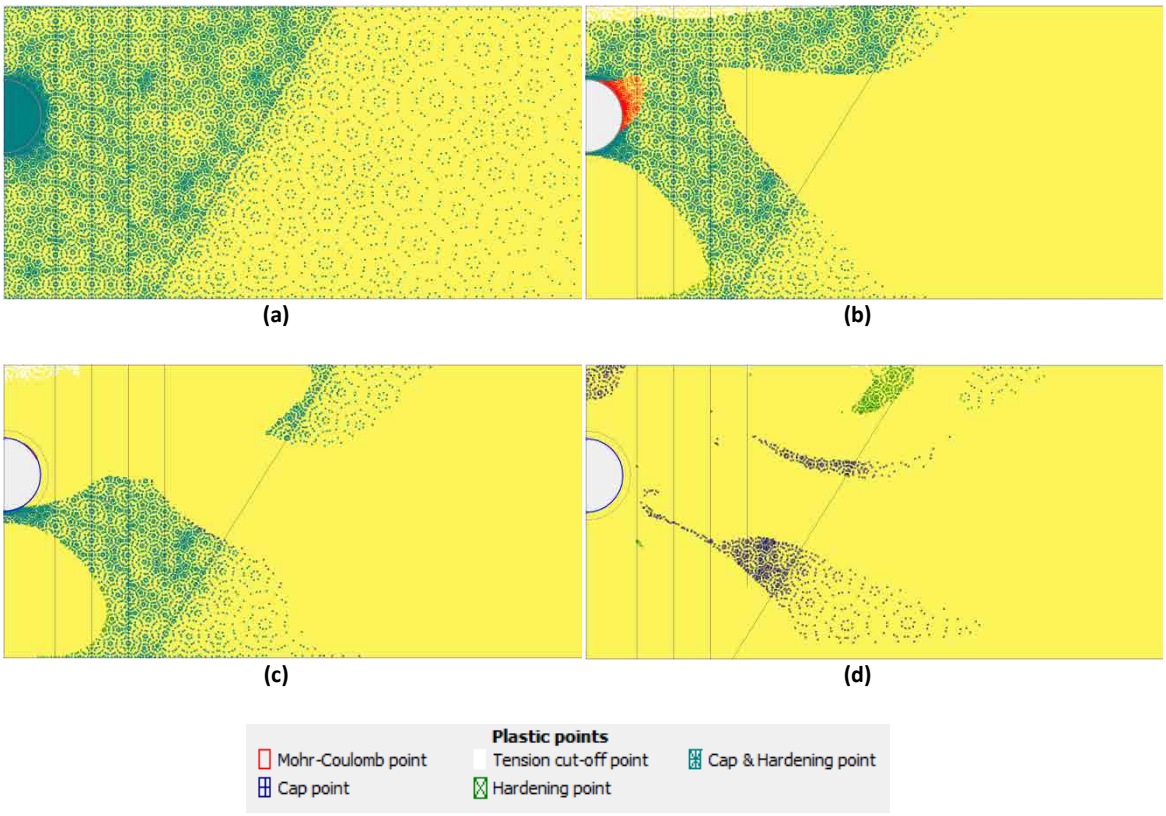

Figure 5.107. Plastic points of the scenario Close To Collapse. (a) shows the plastic points from the calculation phase 0, (b) shows the plastic points from the calculation phase 1, (c) shows the plastic points from the calculation phase 2 and (d) shows the plastic points from the calculation phase 3.

Before addressing the influence of the instruments separately; a similar analysis to the ones done by Murakami & Hasegawa (1988) and Shoji et al (1990) has been adapted to the problem of a tunnel construction of two parameters identification to illustrate the sensitivity of the vertical and horizontal displacements with respect to E_{50}^{ref} and c in the minimum. It has to be understood that the results and conclusions presented in this section are completely illustrative due to the fact that the sensitivity is evaluated at the minimum, which is something that is not known in practice. Moreover, depending on the values of the parameters, the results of the sensitivity can be significantly different, and trying to extrapolate the results from a particular case to the general scenario can be misleading. Nonetheless, using the kind of results extracted from this type of analysis can be really useful as an initial step to better define the optimal layout of the instrumentation.

The derivatives of the vertical and horizontal displacements with respect to E_{50}^{ref} are illustrated in figure 5.108.

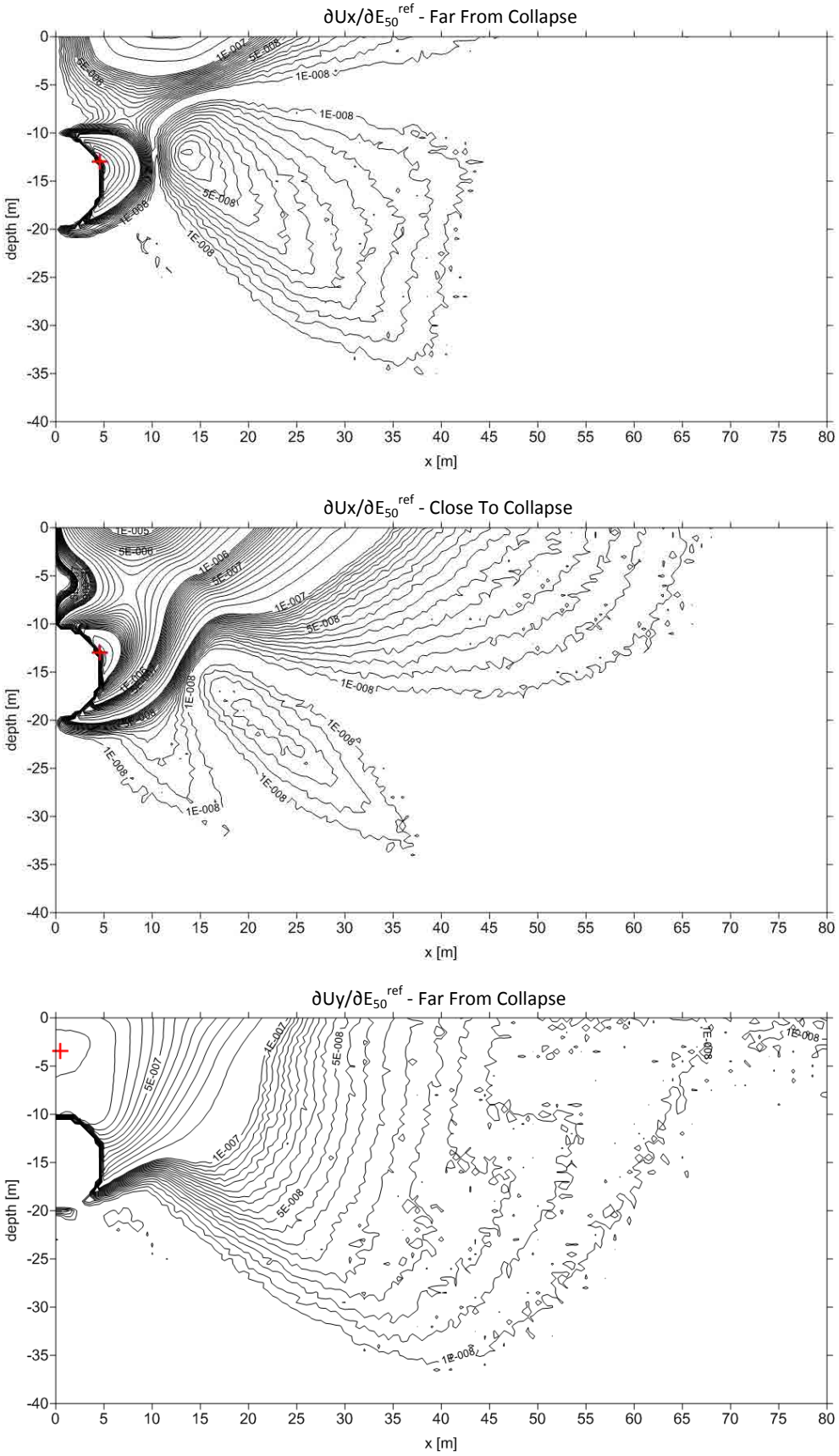

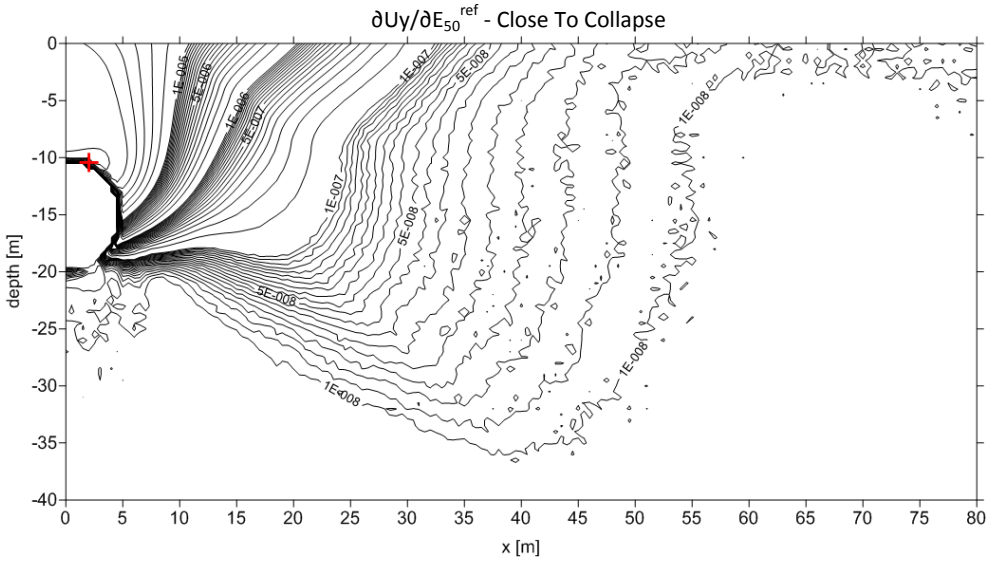

Table 5.108. Derivatives of the vertical (Uy) and horizontal (Ux) displacements with respect to E_{50}^{ref} in the minimum. The red cross represents the most sensitive point in the domain.

Independently from what kind of measurement the derivatives are defined (Ux or Uy), figure 5.108 points out that in general, the zones where the values of the derivatives are high, correspond with zones with large displacements. Therefore, it could be thought that: the higher the displacements are, the more sensitive the measurements are with respect to the parameter. However, as shown later, this tendency cannot be guaranteed in all the domain.

In terms of the morphology of the distribution of sensitivity, when using horizontal displacements, apart from the magnitude of the sensitivity, no significant difference exists between being far or close to collapse. In both scenarios, the most sensitive measurement point remains located in the same place. However, when using vertical displacements, even having a similar morphology of the distribution of sensitivity, the most sensitive measurement point has moved from the center, between the tunnel crown and the surface, to the tunnel crown. This phenomenon points out that when being far from collapse, the measurements, located in the middle between the tunnel crown and the surface, are more suitable (higher quality) than the ones next to the tunnel crown, to identify E_{50}^{ref}; and the opposite occurs when being close to collapse.

Similar results were obtained with respect to cohesion (see figure 5.109), where no significant difference was appreciated between the two scenarios; neither morphologically nor in terms of the most sensitive measurement location.

Theoretically, if the derivatives were constant, which is not true in this case, the type of maps illustrated in figure 5.108 and figure 5.109, would be directly used to define the optimal layout of the instrumentation. Therefore, as it has been exposed before, the use of this kind of analysis can be considered useful to initially define the layout of the instrumentation or as a simple guideline.

∂Ux/∂c - Far From Collapse

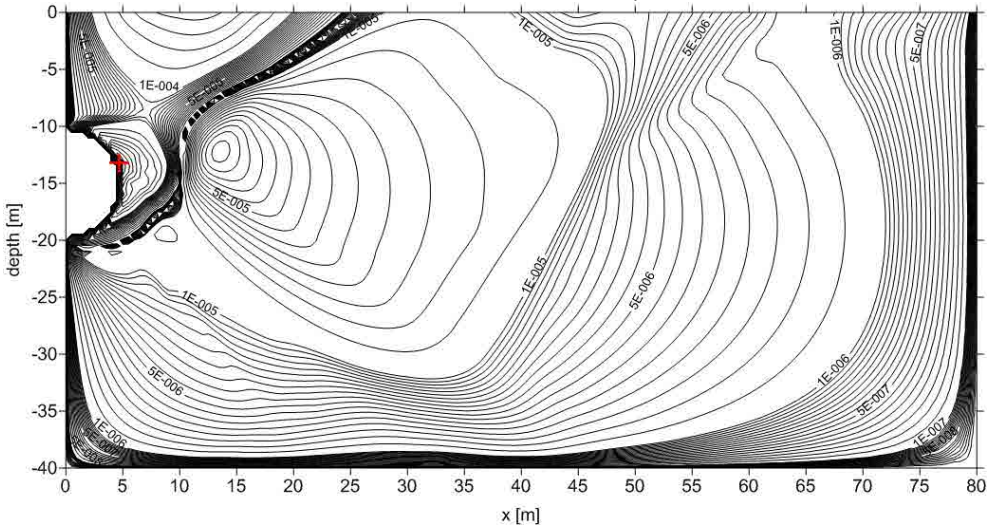

∂Ux/∂c - Close To Collapse

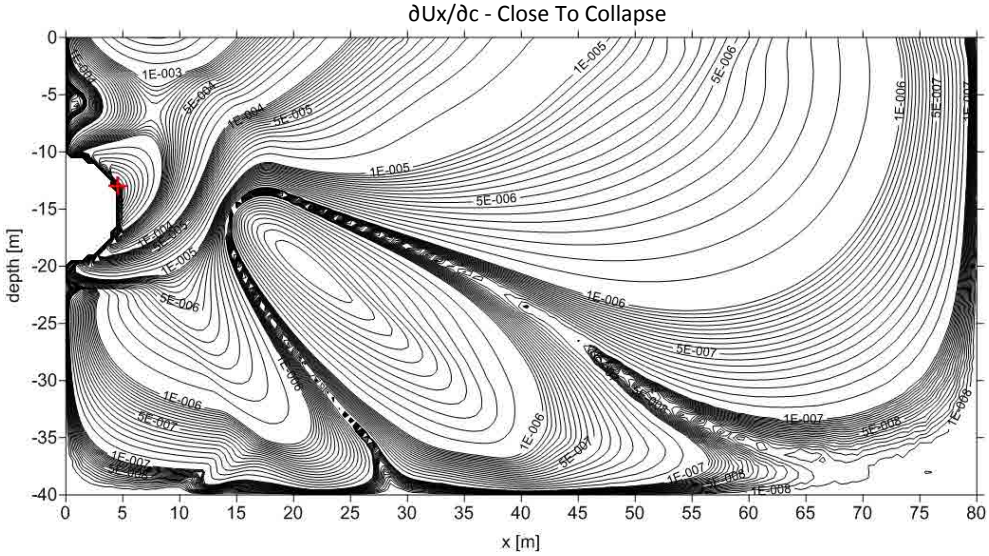

∂Uy/∂c - Far From Collapse

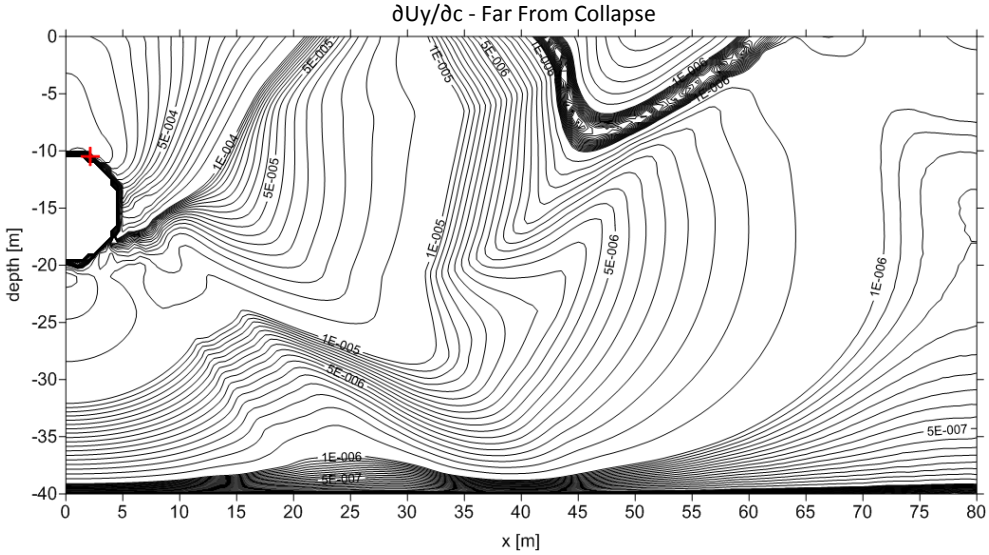

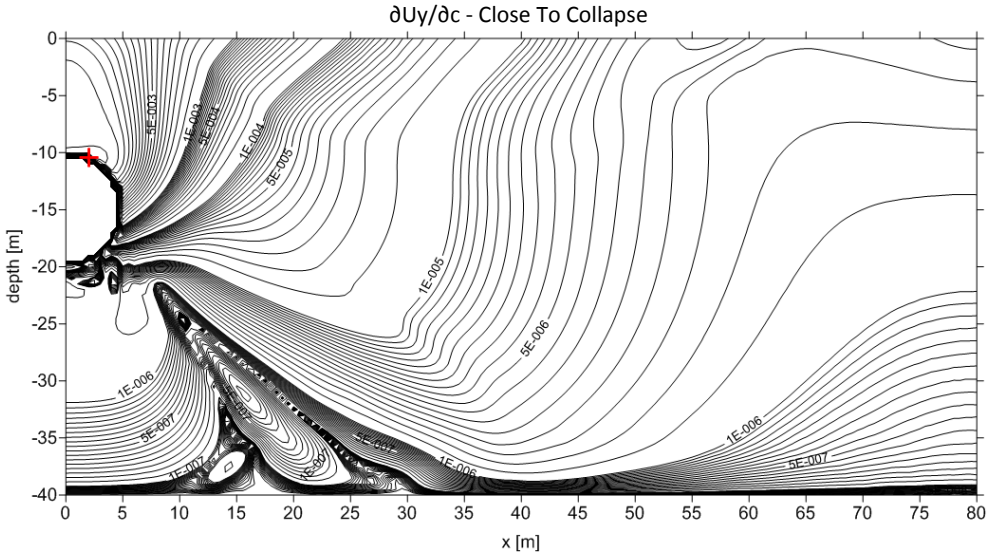

Table 5.109. Derivatives of the vertical (Uy) and horizontal (Ux) displacements with respect to c in the minimum. The red cross represents the most sensitive point in the domain.

In order to extrapolate the general guidelines that have been already presented to the field of in situ instrumentation, the sensitivity and displacements of the measurements of a standard control section have been studied.

The sensitivity and vertical displacements derived from a sliding micrometer, located above the tunnel crown (see figure 5.3.a), are illustrated in figure 5.110 and figure 5.111.

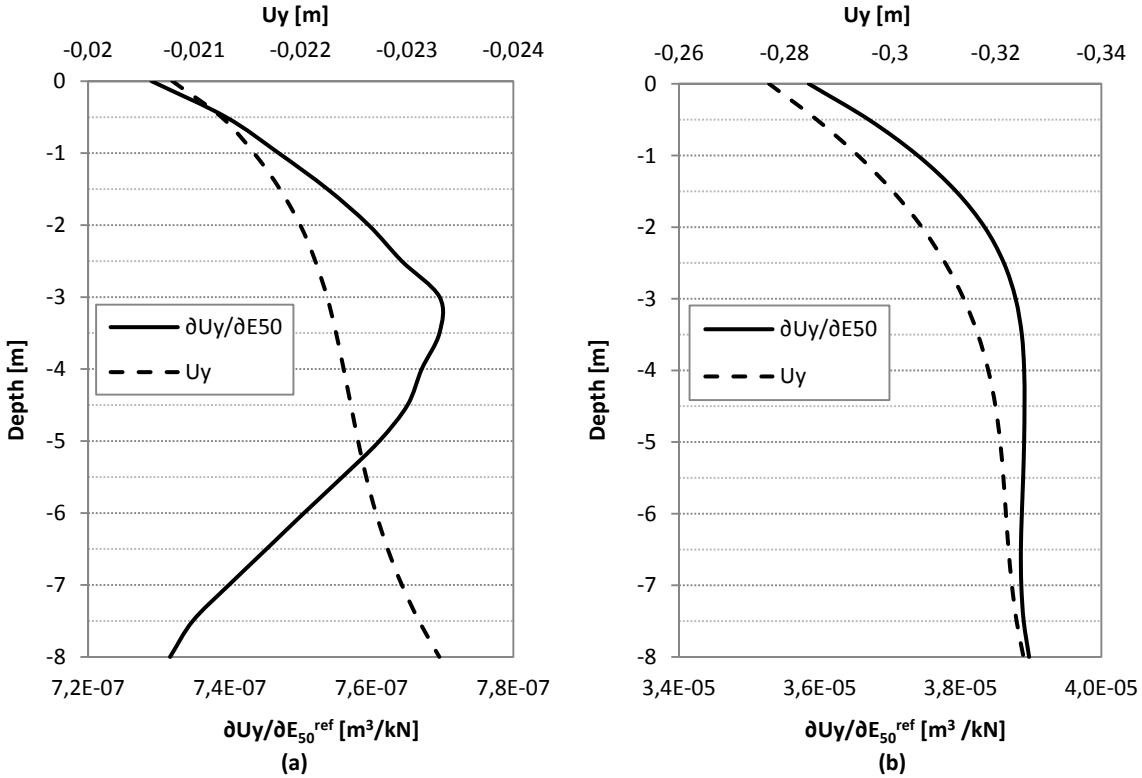

Figure 5.110. Vertical displacement derivative with respect to E_{50}^{ref} versus vertical displacement derived from a sliding micrometer located above the tunnel crown. (a) Far From Collapse. (b) Close To Collapse.

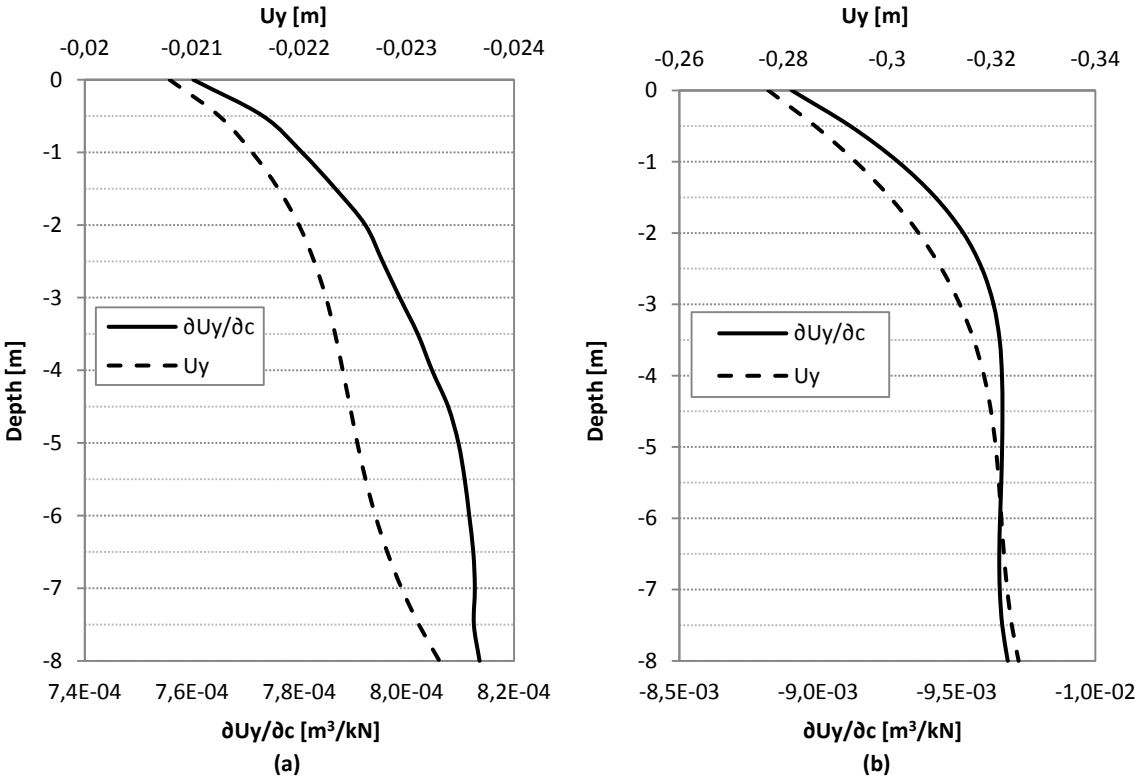

Figure 5.111. Vertical displacement derivative with respect to c versus vertical displacement derived from a sliding micrometer located above the tunnel crown. (a) Far From Collapse. (b) Close To Collapse.

As mentioned before, it cannot always be generally guaranteed that the higher the measurement is, the more sensitive it is. From figure 5.110a, it can be observed how the location of the most sensitive measurement (around 3 meters deep) does not match the location of the highest vertical displacement (8 meters deep). Nonetheless, as a general rule, it can be extrapolated that the higher the measurement is, the more sensitive the measurement is likely to be.

The mismatch between the vertical displacements and the derivatives of the vertical displacements with respect to E_{50}^{ref} is attributed to the different contributions of each construction stage towards the sensitivity distribution. As figure 5.112 shows, the distributions of the sensitivity along the sliding micrometer are completely opposite when comparing the values obtained from the tunnel excavation stage (phase1) and the consolidation stage (phase 3). Consequently, using the final accumulated displacements to define the derivatives makes that the most sensitive point is located approximately in the middle of the sliding micrometer.

The opposite sensitivity distribution between phase 1 and phase 3 are consequence of the initial stress state and the stress path associated with the different constructions phases. Being selected two different stress points, one close to the tunnel crown and the other 3 meters deep, it can be illustrated how the initial stress and the stress path are in control of defining the regime of the stress point, and consequently, what parameters are going to be potentially involved in (more involvement => more sensitivity).

As figure 5.113 shows, due to the tunnel excavation phase a noticeable decrease on q occurrs; this placed the stress point into the elastic zone. Then, after phase 2 (tunnel lining construction), which does not affect too much to the stress state, an increase on p' occurred

on the consolidation phase, which depending on the previous stress state can cause the movement of the compression hardening yield surface, and consequently, making the point more sensitive with respect E_{50}^{ref} (in this case study E_{50}^{ref} is linked to E_{oed}^{ref} by $0.8E_{50}^{ref} = E_{oed}^{ref}$).

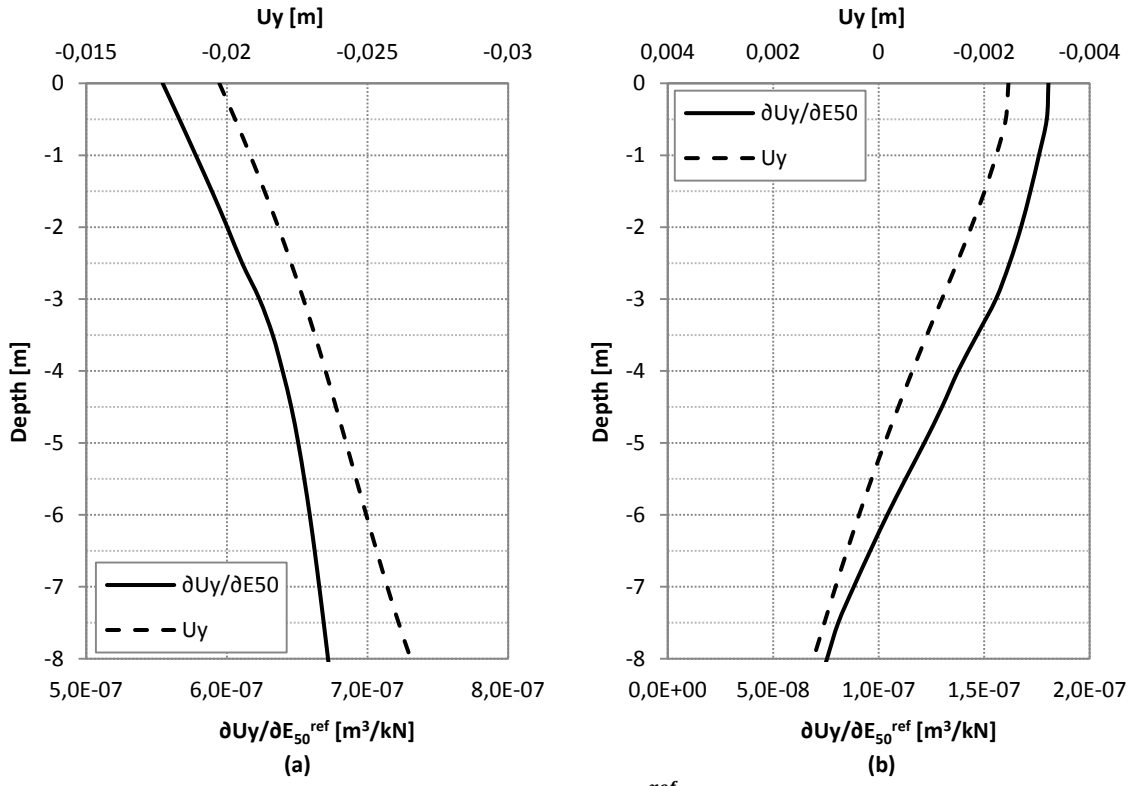

Figure 5.112. Vertical displacement derivative with respect to E_{50}^{ref} versus vertical displacement derived from a sliding micrometer located above the tunnel crown. (a) From tunnel excavation phase. (b) From consolidation phase.

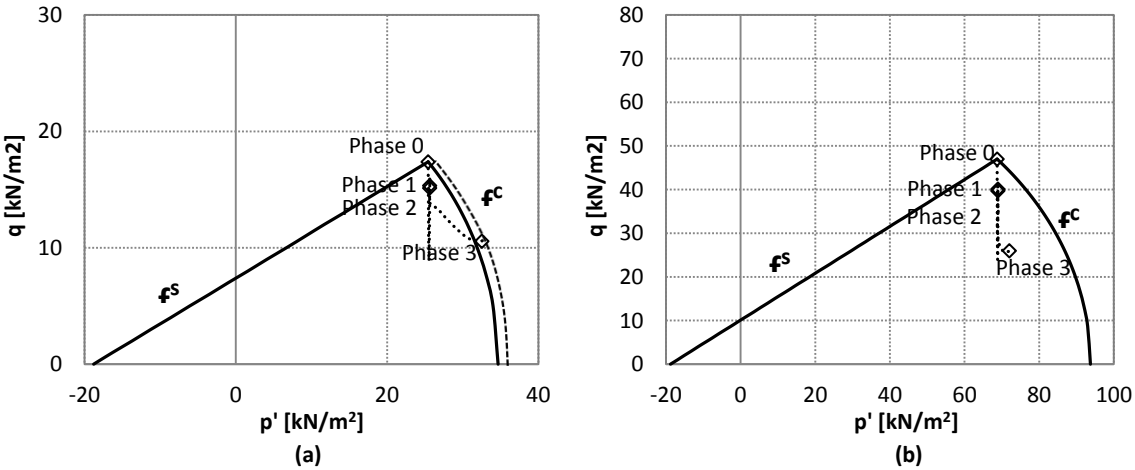

Figure 5.113. Stress path of two points located along the sliding micrometer (Far From Collapse). (a) Stress point located around 3 meters deep. (b) Stress point located 2 meters from the tunnel crown. f^s: Shear Hardening yield surface. f^c: Compression Hardening yield surface.

From the other types of in situ instruments (inclinometer and vertical displacement surface points) the sensitivity distribution matches the displacement profile for both scenarios, far and close to collapse (see figures 5.114, 5.115, 5.116 and 5.117).

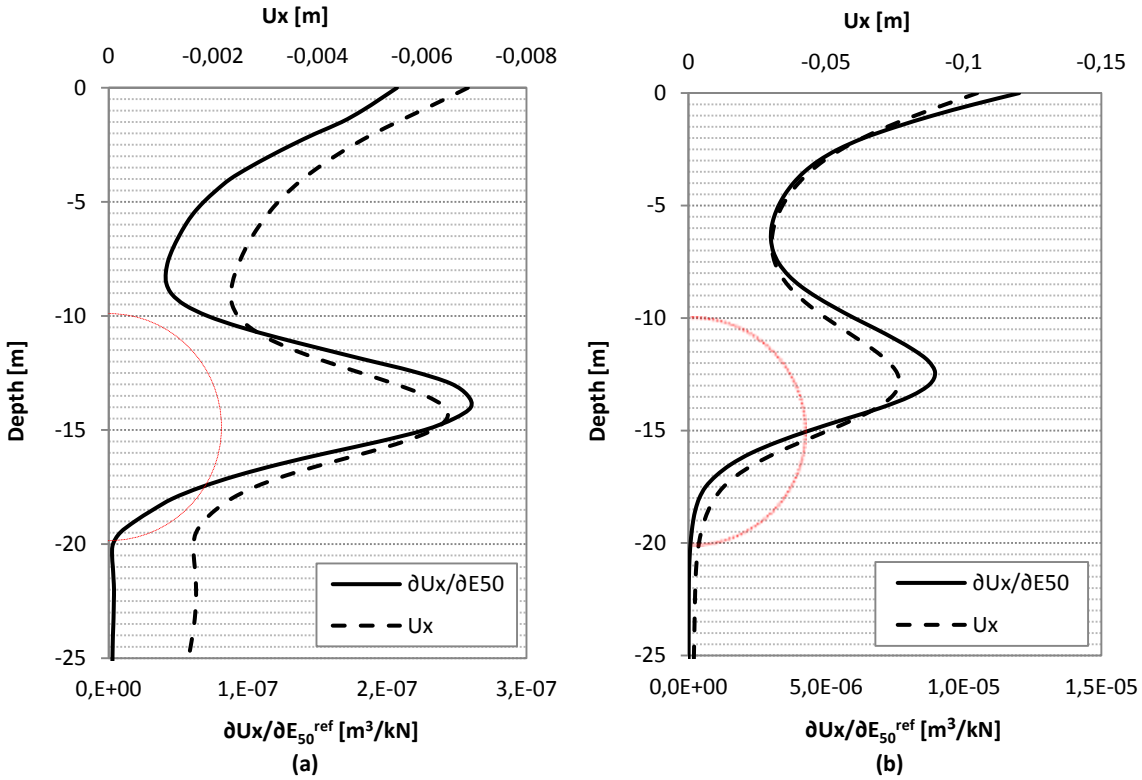

Figure 5.114. Vertical displacement derivative with respect to E_{50}^{ref} versus vertical displacement derived from an inclinometer. (a) Far From Collapse. (b) Close To Collapse. The red dashed line represents the tunnel contour.

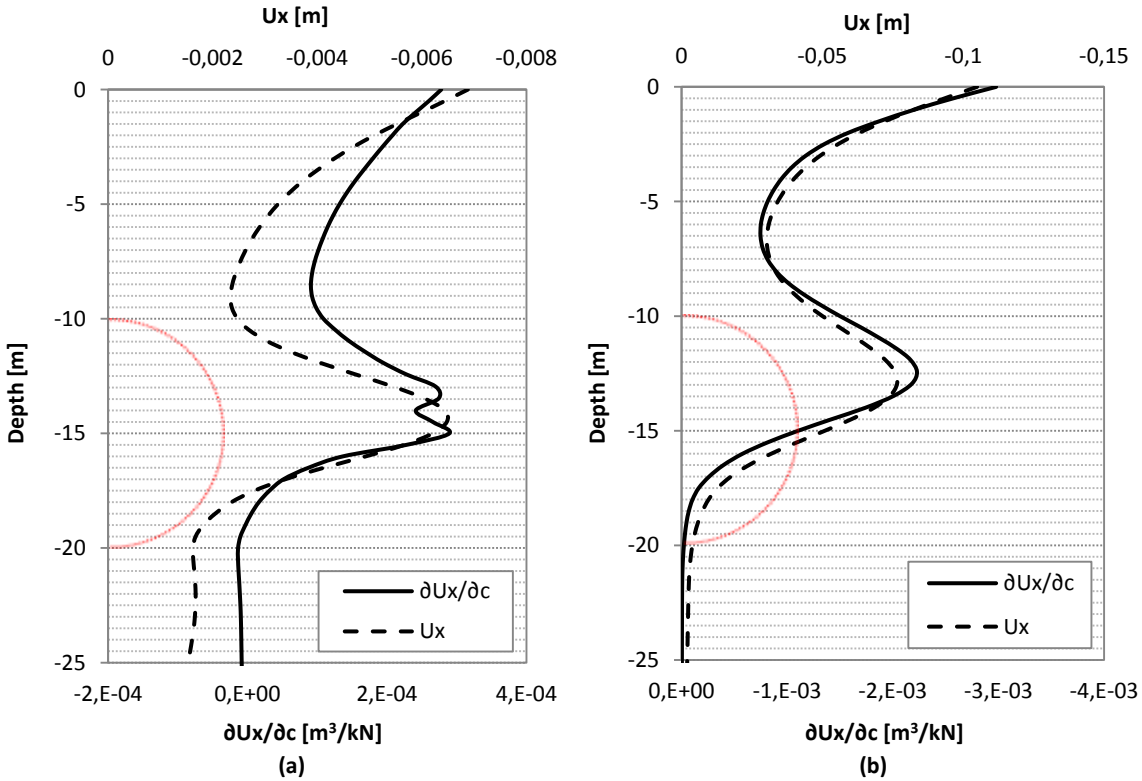

Figure 5.115. Vertical displacement derivative with respect to c versus vertical displacement derived from an inclinometer. (a) Far From Collapse. (b) Close To Collapse. The red dashed line represents the tunnel contour.

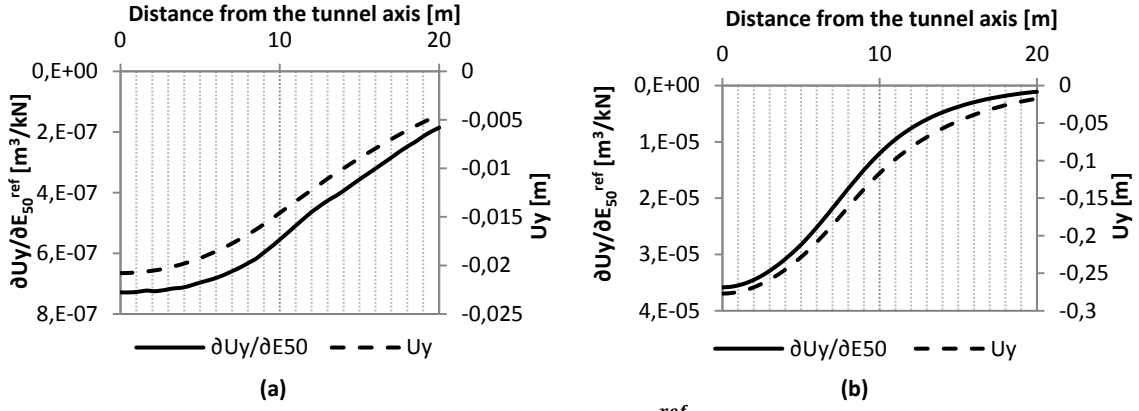

Figure 5.116. Vertical displacement derivative with respect to E_{50}^{ref} versus vertical displacement derived from vertical displacement surface points. (a) Far From Collapse. (b) Close To Collapse.

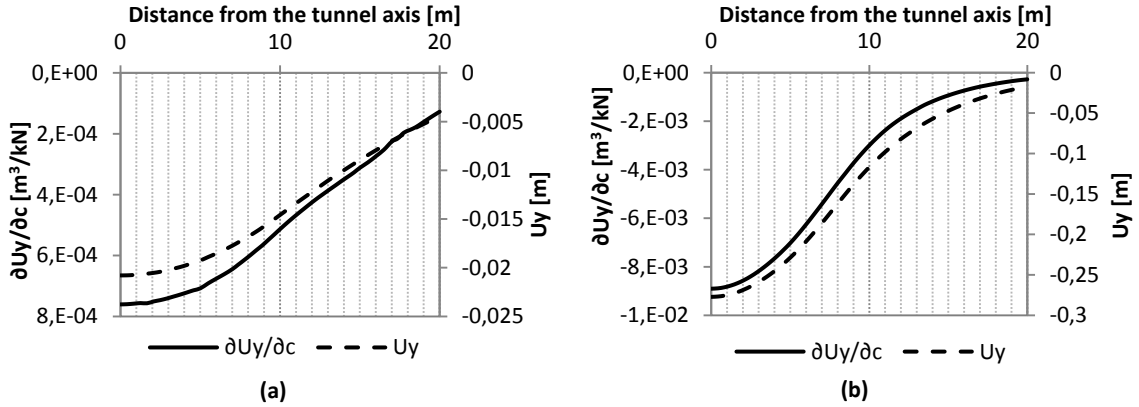

Figure 5.117. Vertical displacement derivative with respect to *c* versus vertical displacement derived from vertical displacement surface points. (a) Far From Collapse. (b) Close To Collapse.

Another approach to the problem of optimal instrumentation layout is studying the influence of the measurements over the objective function. This approach, as it is presented herein, is only applicable in cases where no more than two parameters are being identified and when it is feasible for the objective function to be graphically represented. As explained in section 5.3.1, the relationship between parameters and their sensitivity with respect to the measurements can be partially extrapolated from the morphology of the objective function shape.

In the following figures (5.118, 5.119, 5.120, 5.121, 5.122, 5.123, 5.124 and 5.125), the objective functions obtained from the different type of in situ instruments are shown. A total of 8 different objective function maps have been plotted by combining the two tunnel scenarios (far from collapse and close to collapse) with the instruments measurements (sliding micrometer, inclinometer, vertical displacement surface points and a full control section combining all the instruments).

From those figures, it can be pointed out that for this particular case study the measurements that provide a more propitious objective function shape for an easier identification of E_{50}^{ref} and *c* are the ones extracted from the inclinometer. The less narrow valley defined by the inclinometer measurements makes it easier for the gradient based methods to find the minimum.

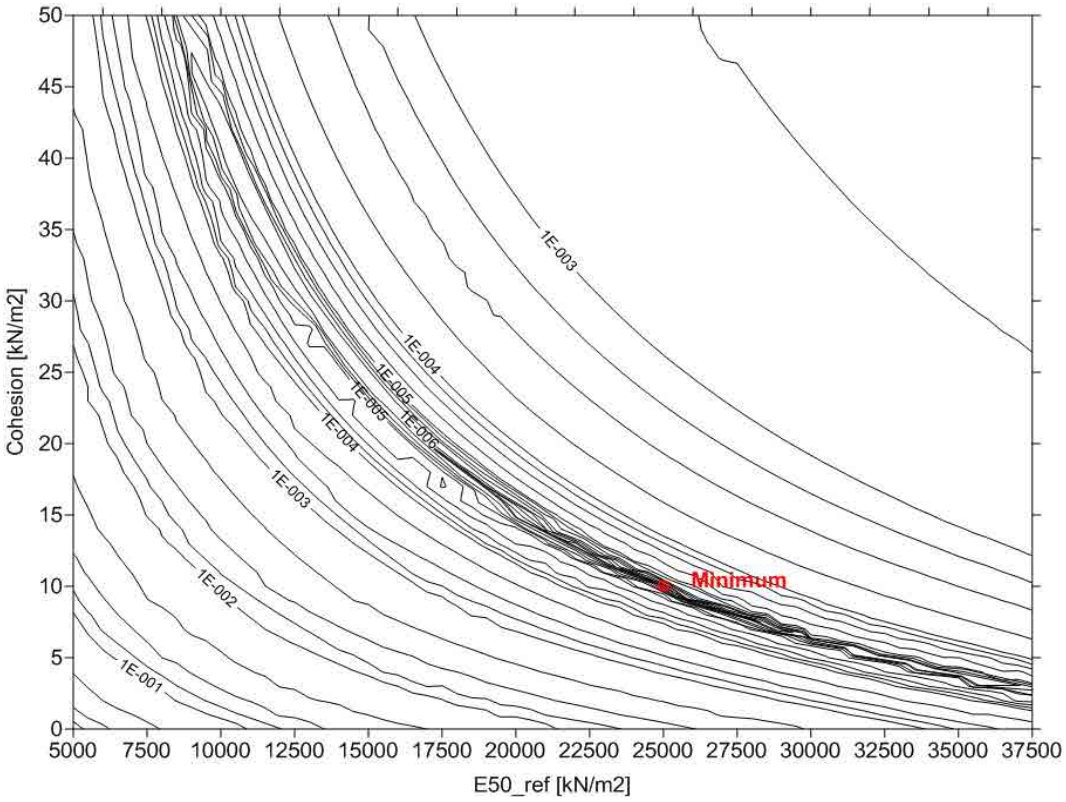

Figure 5.118. Mapping of the objective function [m^2] defined by using the measurements of a sliding micrometer with exact data (Far From Collapse).

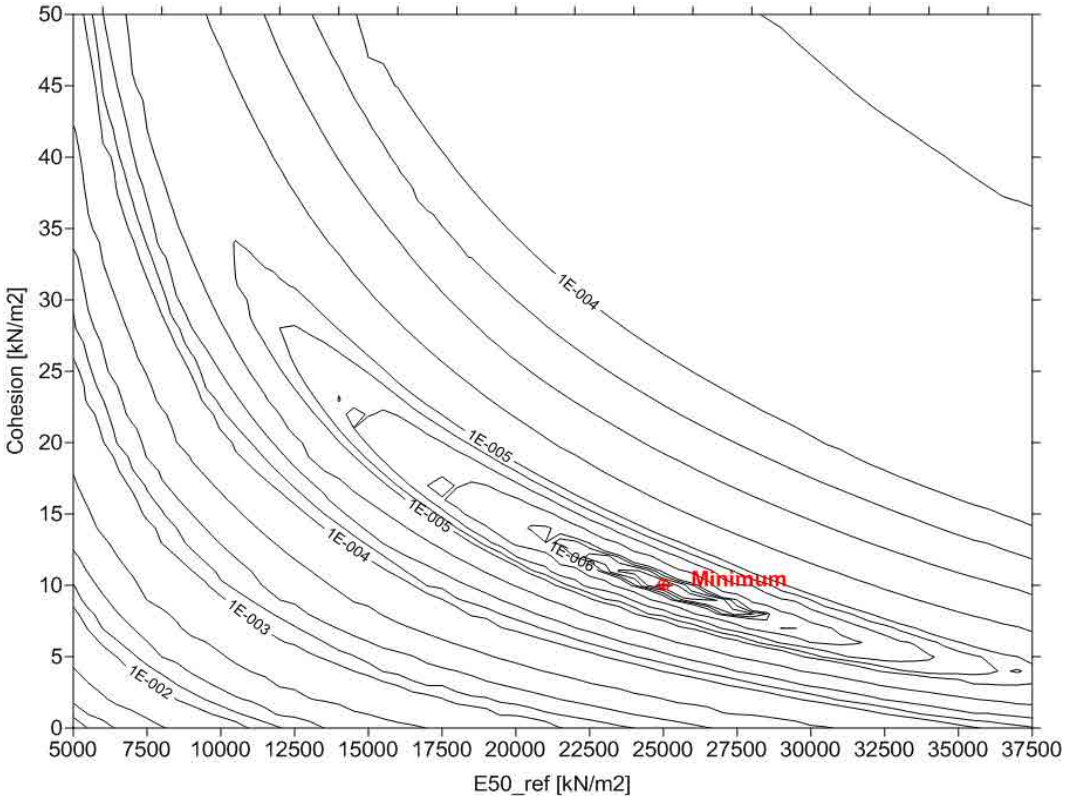

Figure 5.119. Mapping of the objective function [m^2] defined by using the measurements of an inclinometer with exact data (Far From Collapse).

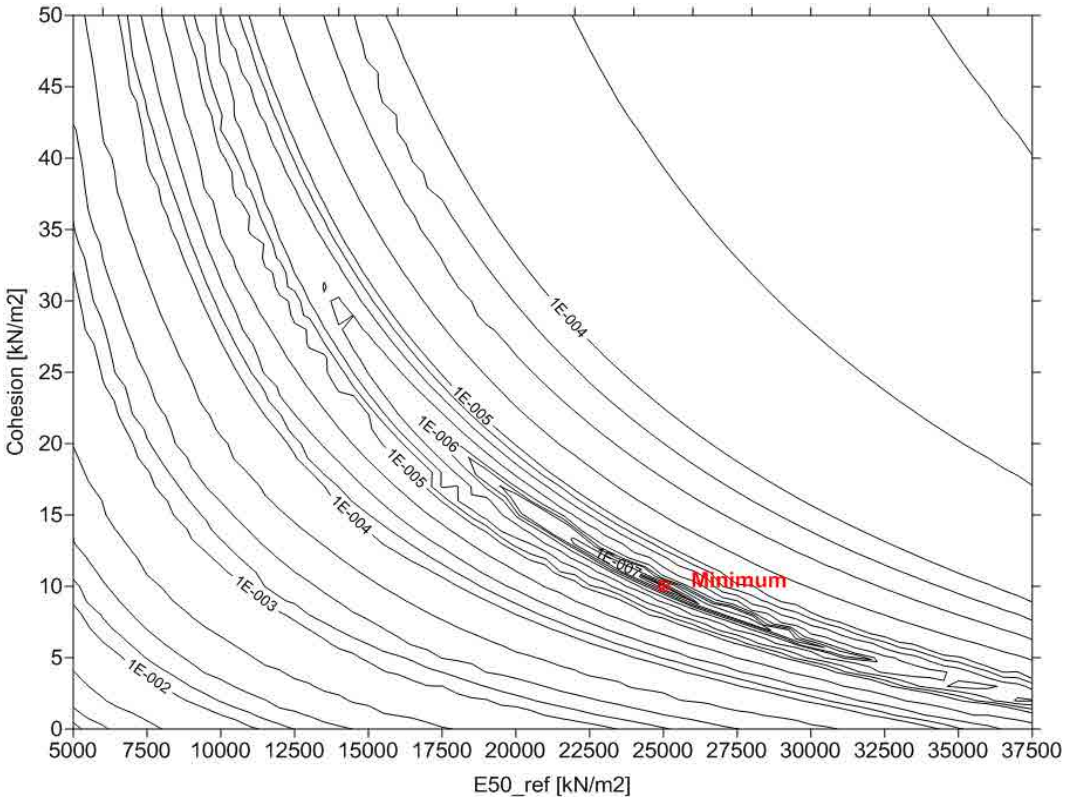

Figure 5.120. Mapping of the objective function [m^2] defined by using the measurements of several vertical displacement surface points with exact data (Far From Collapse).

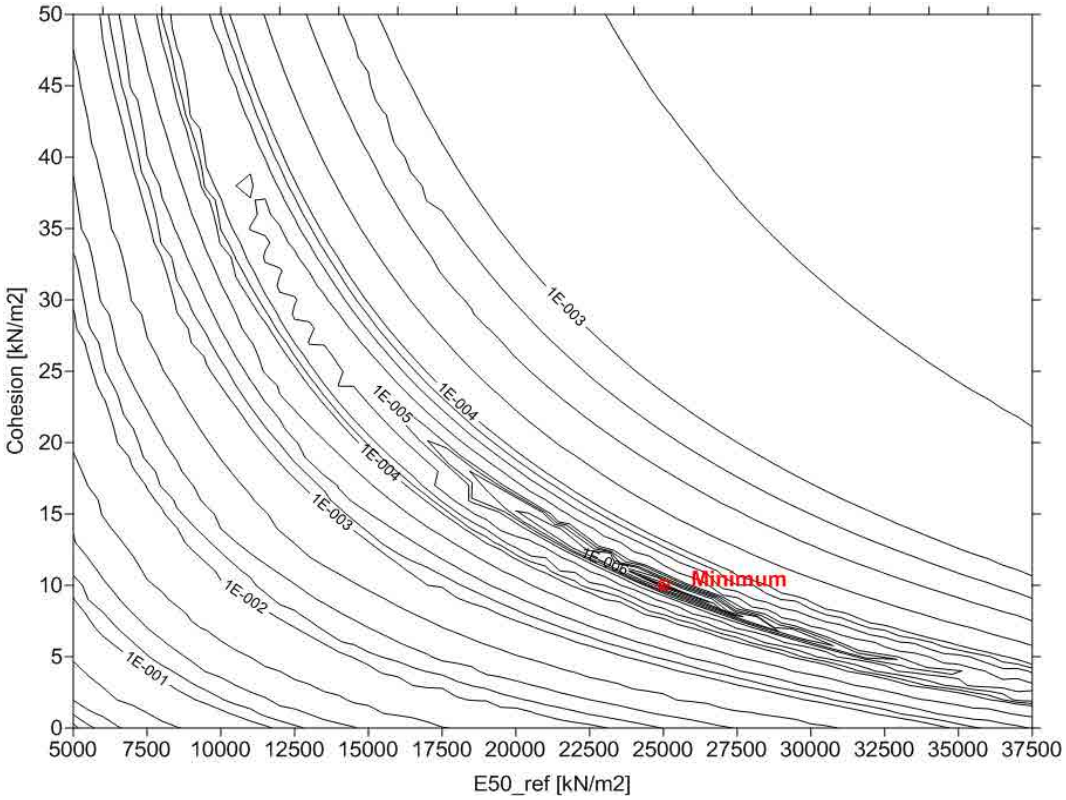

Figure 5.121. Mapping of the objective function [m^2] defined by using the measurements of a full control section with exact data (Far From Collapse).

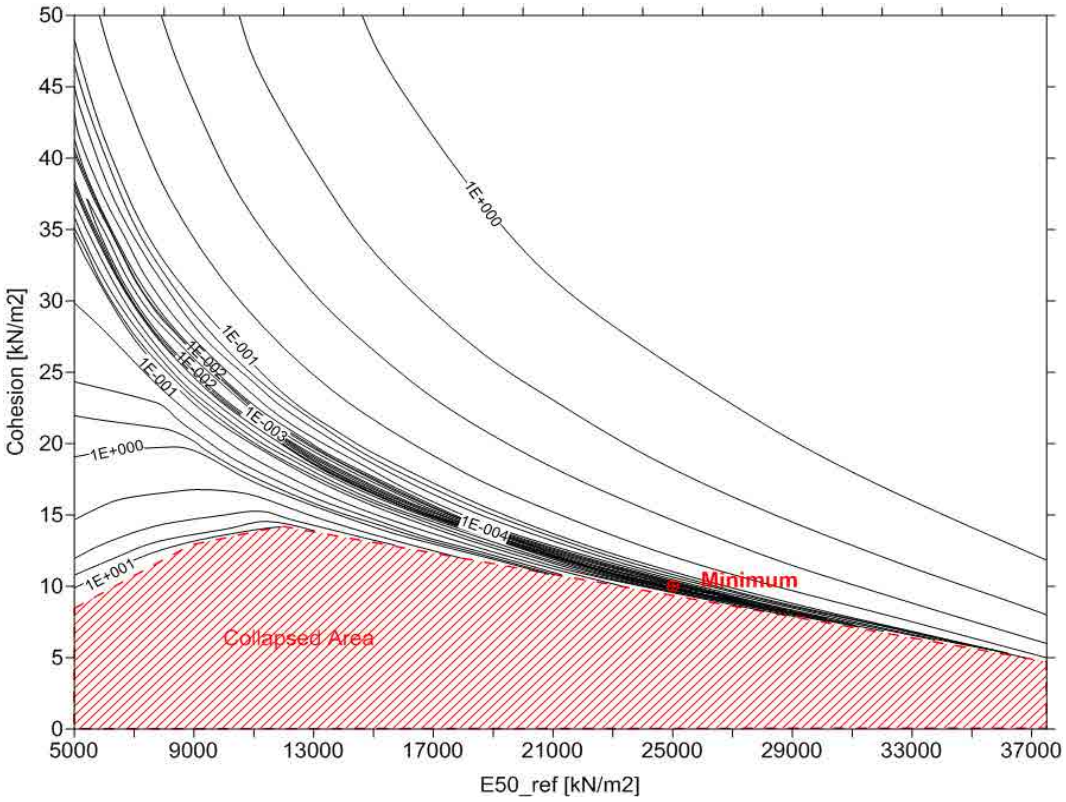

Figure 5.122. Mapping of the objective function [m^2] defined by using the measurements of a sliding micrometer with exact data (Close To Collapse).

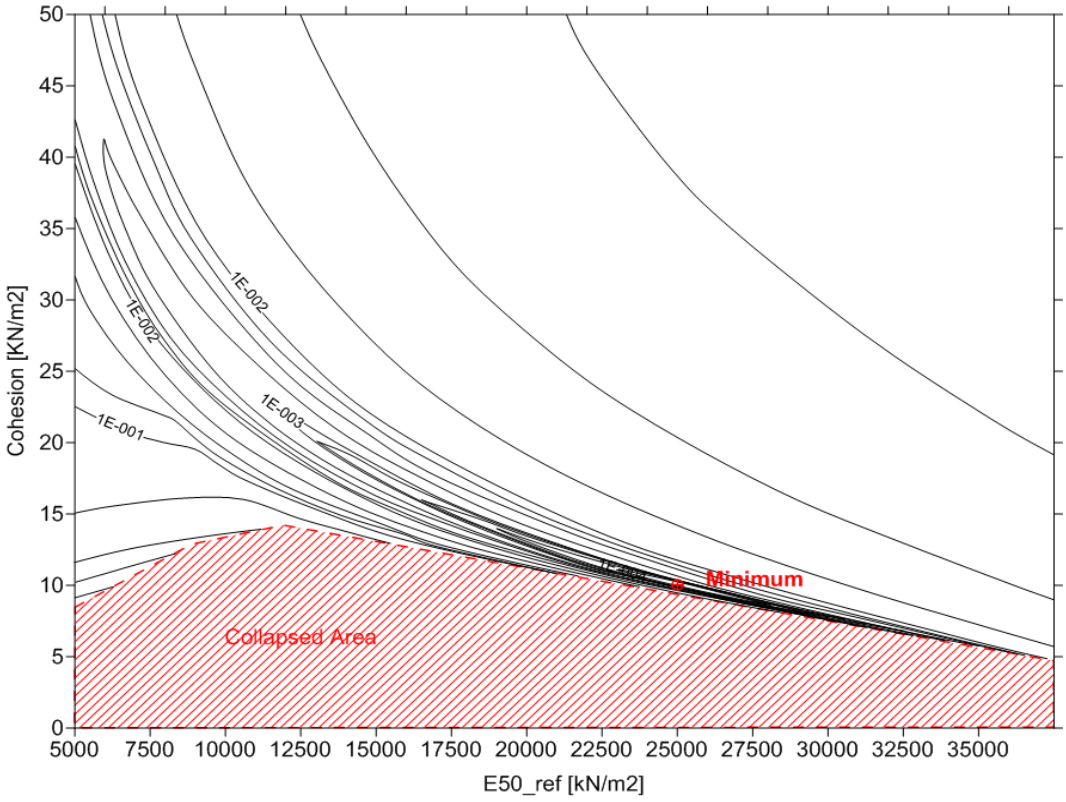

Figure 5.123. Mapping of the objective function [m^2] defined by using the measurements of an inclinometer with exact data (Close To Collapse).

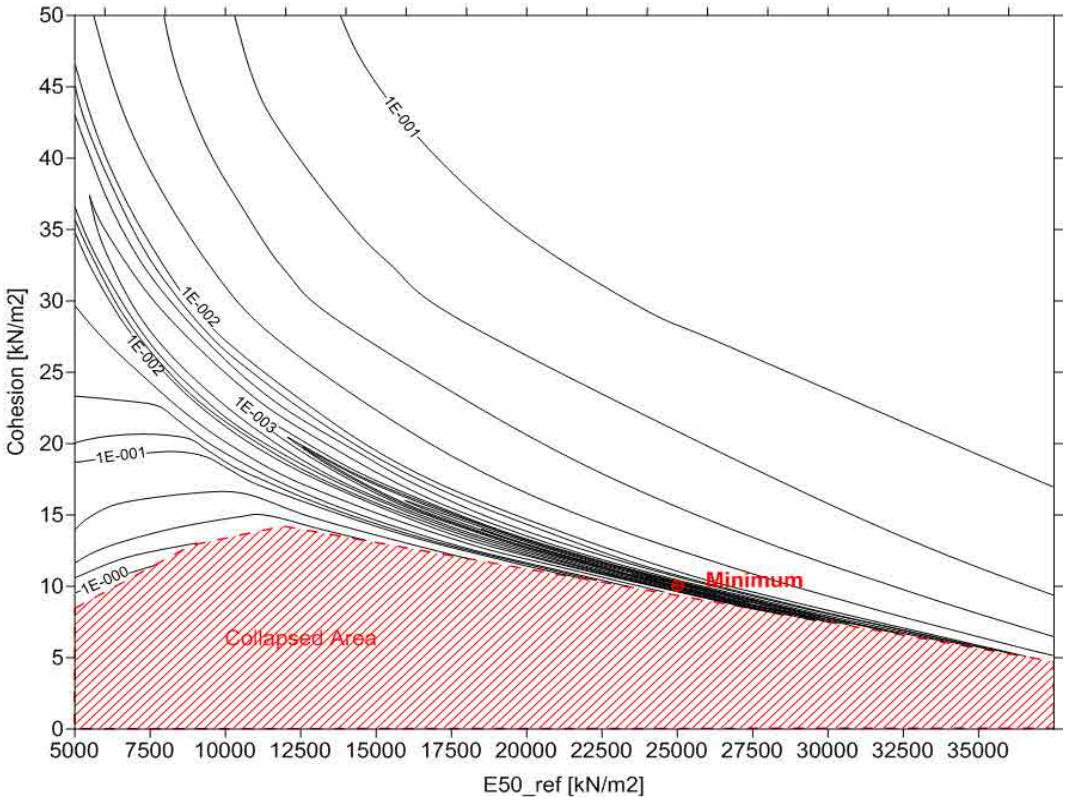

Figure 5.124. Mapping of the objective function [m^2] defined by using the measurements of several vertical displacement surface points with exact data (Close To Collapse).

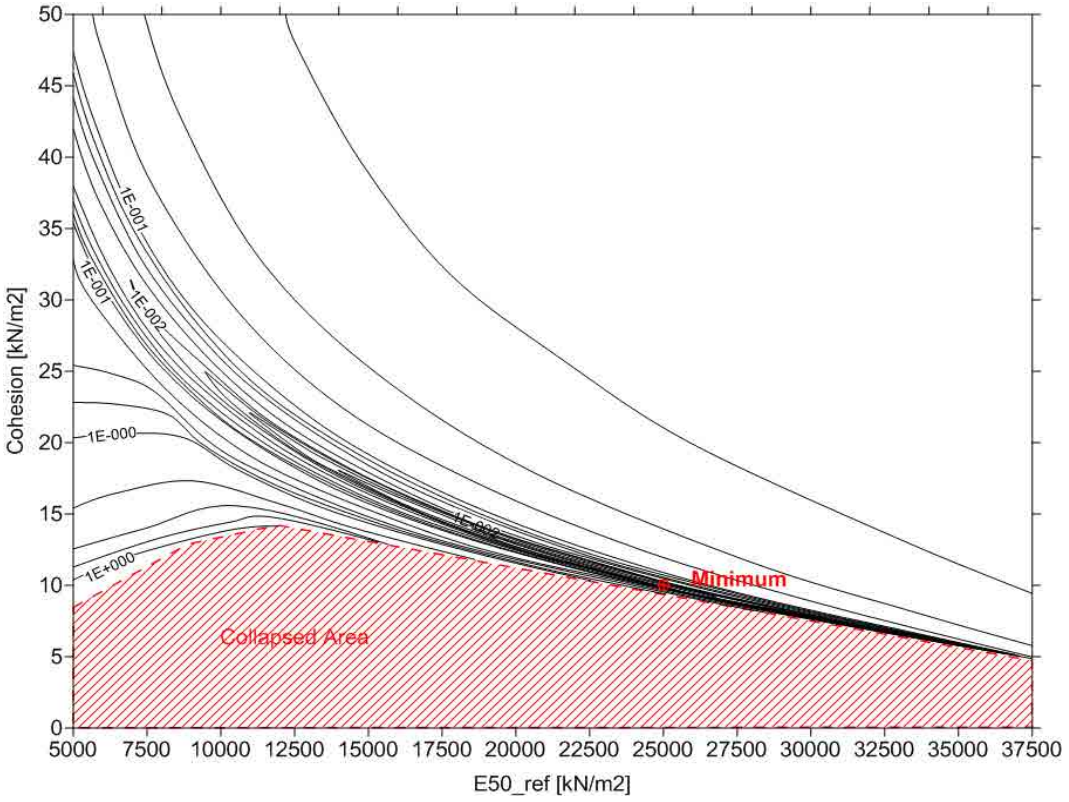

Figure 5.125. Mapping of the objective function [m^2] defined by using the measurements of a full control section with exact data (Close To Collapse).

It can be noticed, as it was expected, that for the case close to collapse the valley of the minimum is almost parallel to the E_{50}^{ref} axis, showing that the scenario close to collapse is more adequate to be used when cohesion has to be identified.

5.5 Four Parameters Identification Case (E_{50}^{ref}, E_{ur}^{ref}, φ and c)

5.5.1 Introduction

In this section four parameters, the reference secant stiffness in standard drained triaxial test (E_{50}^{ref}), the reference unloading-reloading stiffness (E_{ur}^{ref}), the effective angle of internal friction (φ), and the effective cohesion (c), have been identified by applying the hybrid method presented before. For this particular case, the hybrid algorithm has been defined by combining an adaptive genetic algorithm (AGA) with the Gauss-Newton method.

The measurements used for the analysis are the ones altered by the introduction of noise (Noisy Data) that were used in the case of two parameters identification.

Due to the conclusions derived from the section 3.3.8, where it was pointed out the influence of the stress-strain state, and also because of the introduction of two more parameters into the analysis, it was considered useful to analyze the soil parameters identification problem from both scenarios, close and far from collapse.

As a consequence of the significant difference on the magnitude of the measurements between scenarios, millimeters for the scenario far from collapse and decimeters for the scenario close to collapse, two different frontier values were defined to limit the selection pressure and to carry out the PCA. The two frontier values were proportionally defined between scenarios through their coefficients of variation.

Moreover, due to the increase of the problem complexity, from two parameters to four parameters, and especially for the case close to collapse, it was needed to use higher values of AF (amplifier factor of the standard deviation) to define the PCA ellipsoids. The fact of losing normal distribution requires increasing the value of AF to guarantee that 90% of the PCA individuals will be enclosed inside the ellipsoid to make it representative of the group of good individuals found by the genetic algorithm.

From figures 5.126 and 5.127, it can be appreciated what has been already mentioned about the loss of normal distribution. Using the good individuals obtained by the genetic algorithm for the case close to collapse (see section 5.4.2.2), the histograms and the "Detrended" normal Q-Q plot of the variables were plotted to formally confirm that the good individuals do not follow a normal distribution, which makes more difficult the resolution of the problem. The *IBM SPSS Statistics* software was used to obtain the histograms and the "Detrended" normal Q-Q plots presented in this thesis.

Finally, the main characteristics of the algorithm used to identify E_{50}^{ref}, E_{ur}^{ref}, φ and c, are shown in table 5.30, which are extrapolated from the results obtained from the exhaustive two parameter identification case presented in section 5.3.

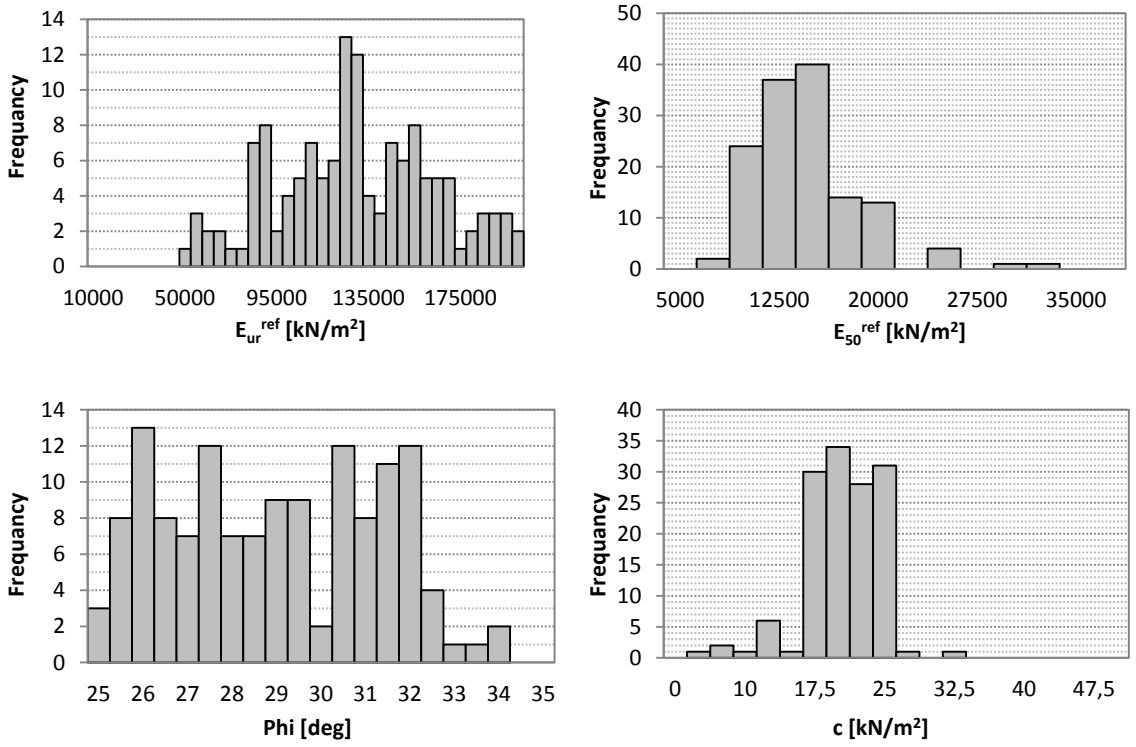

Figure 5.126. Histograms of the parameters values extracted from the good individuals involved in the PCA for the case close to collapse.

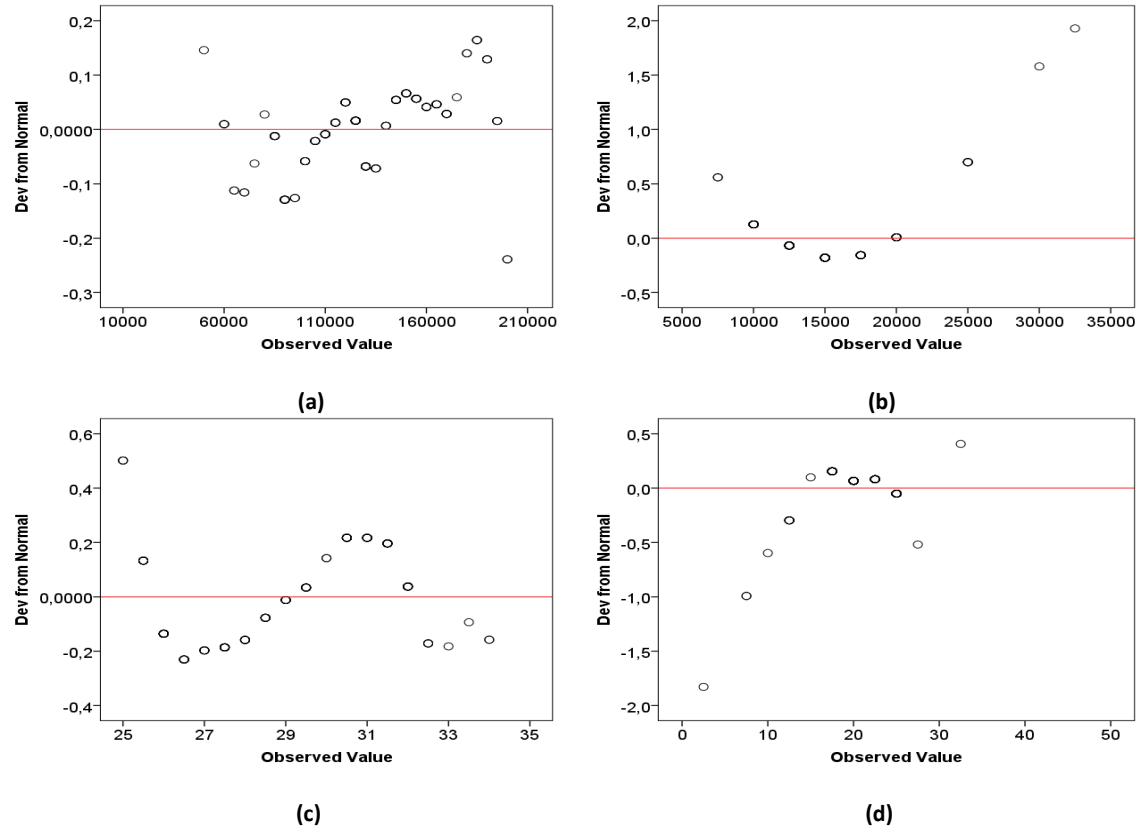

Figure 5.127. "Detrended" normal Q-Q plot of the parameters values extracted from the good individuals involved in the PCA for the case close to collapse. ("Q" stands for *quantile*). (a) Observed Value corresponds to E_{ur}^{ref}. (b) Observed Value corresponds to E_{50}^{ref}. (c) Observed Value corresponds to internal friction angle. (d) Observed Value corresponds to cohesion.

Genetic Algorithm	
Optimization Algorithm	
Type of algorithm	AGA + Elitism
Selection type	Roulette Wheel (with fitness limit = frontier value)
GAP	1
Maximum probability of applying crossover (P_{c_max})	0.95
Minimum probability of applying crossover (P_{c_min})	0.50
Maximum probability of applying mutation (P_{m_max})	0.40
Minimum probability of applying mutation (P_{m_min})	0.01
Population size	1001
Stop Criteria (switching point)	Less than 50% of new individuals
Search Space Discretization	
$E_{ur\ min}^{ref}$ [kN/m^2]	10000
$E_{ur\ max}^{ref}$ [kN/m^2]	200000
$E_{ur\ step\ size}^{ref}$ [kN/m^2]	5000
$E_{50\ min}^{ref}$ [kN/m^2]	5000
$E_{50\ max}^{ref}$ [kN/m^2]	37500
$E_{50\ step\ size}^{ref}$ [kN/m^2]	2500
φ_{min} [deg]	25
φ_{max} [deg]	35
$\varphi_{step\ size}$ [deg]	0.5
c_{min} [kN/m^2]	0
c_{max} [kN/m^2]	50
$c_{step\ size}$ [kN/m^2]	2.5
Principal Component Analysis (PCA)	
Far From Collapse	
Frontier Value	$2.22 \cdot 10^{-5}$m^2
AF (amplifier factor of the standard deviation)	2.8
Close To Collapse	
Frontier Value	$2.77 \cdot 10^{-3}$m^2
AF (amplifier factor of the standard deviation)	4.1
Gradient Based Method	
Type of algorithm	Gauss-Newton
Stop Criteria	fixed number of iterations (10 iterations)
Objective Function	
Type of objective function	Least-Squares Method
Measurements	
Type of measurement	Vertical Displacements (20 measurement points)

Table 5.30. Main characteristics and parameters of the Hybrid Method.

5.5.2 Results

The fact of identifying four parameters has made more difficult the visual study of the genetic algorithm evolution. However, different representations of the evolution have been defined in order to keep visual the understanding of the genetic algorithm behavior.

5.5.2.1 Far From Collapse

The results of the parameters estimation using the hybrid method with noisy data in a scenario far from collapse are presented in this section.

The distribution of the parameters values associated with the individuals of the initial generation and the last generation is shown in figure 5.128. A total of eight generations were created by the algorithm until reaching the limit value of 50% of new individuals per generation. As can be noticed in the figures, the dispersion among the individuals decreases considerably from the initial generation to the last one, except for the internal friction angle.

Unfortunately, only the values of E_{ur}^{ref} seem to converge towards the value associated with the minimum (E_{ur}^{ref} = 75000kN/m^2), while for E_{50}^{ref} and c, the convergence values deviate slightly from the minimum (E_{50}^{ref} = 25000kN/m^2 and c = 10kN/m^2).

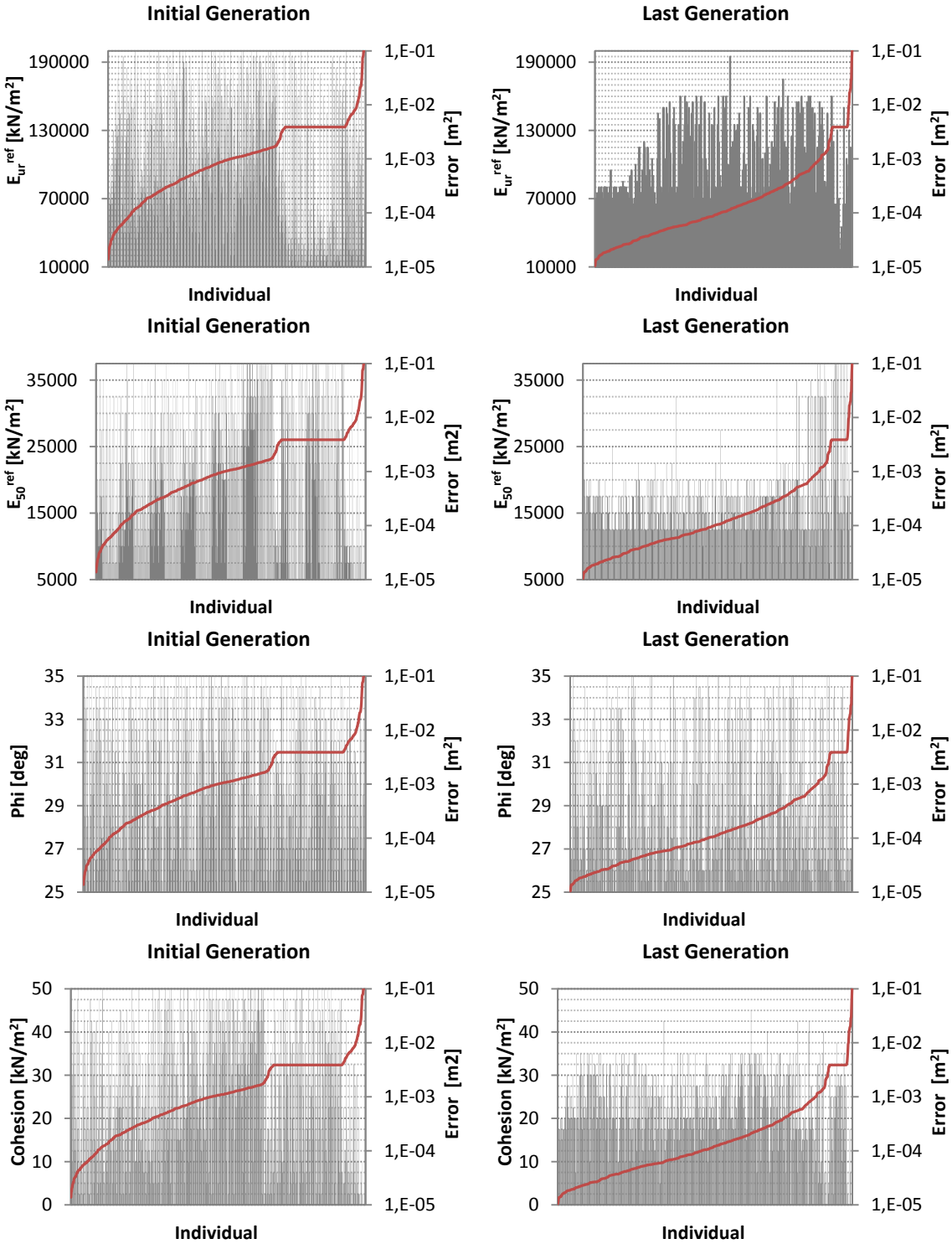

Figure 5.128. Parameters values associated to the individuals of the initial generation and the last generation. The gray bars represent the parameter values of the individuals while the red line represents the error associated to the individual. (hybrid method / noisy data / far from collapse).

The full evolution of the algorithm, taking into account the limitations associated with working with four parameters, can be visualized from figure 5.129. As figure 5.128 firstly pointed out, there is a deviation on the convergence towards the minimum, which from figure 5.129 and the error associated with the individuals, can be explained by the effect of having different combinations of parameters with lower error than the one used to generate the measurements; in part due to the introduction of noise in the measurements, and also because of the existence of complex relationships among the parameters that defined the Hardening soil model (see section 2.6). This phenomenon points out the difficulties associated with the identification of soil parameters while using sophisticated constitutive models.

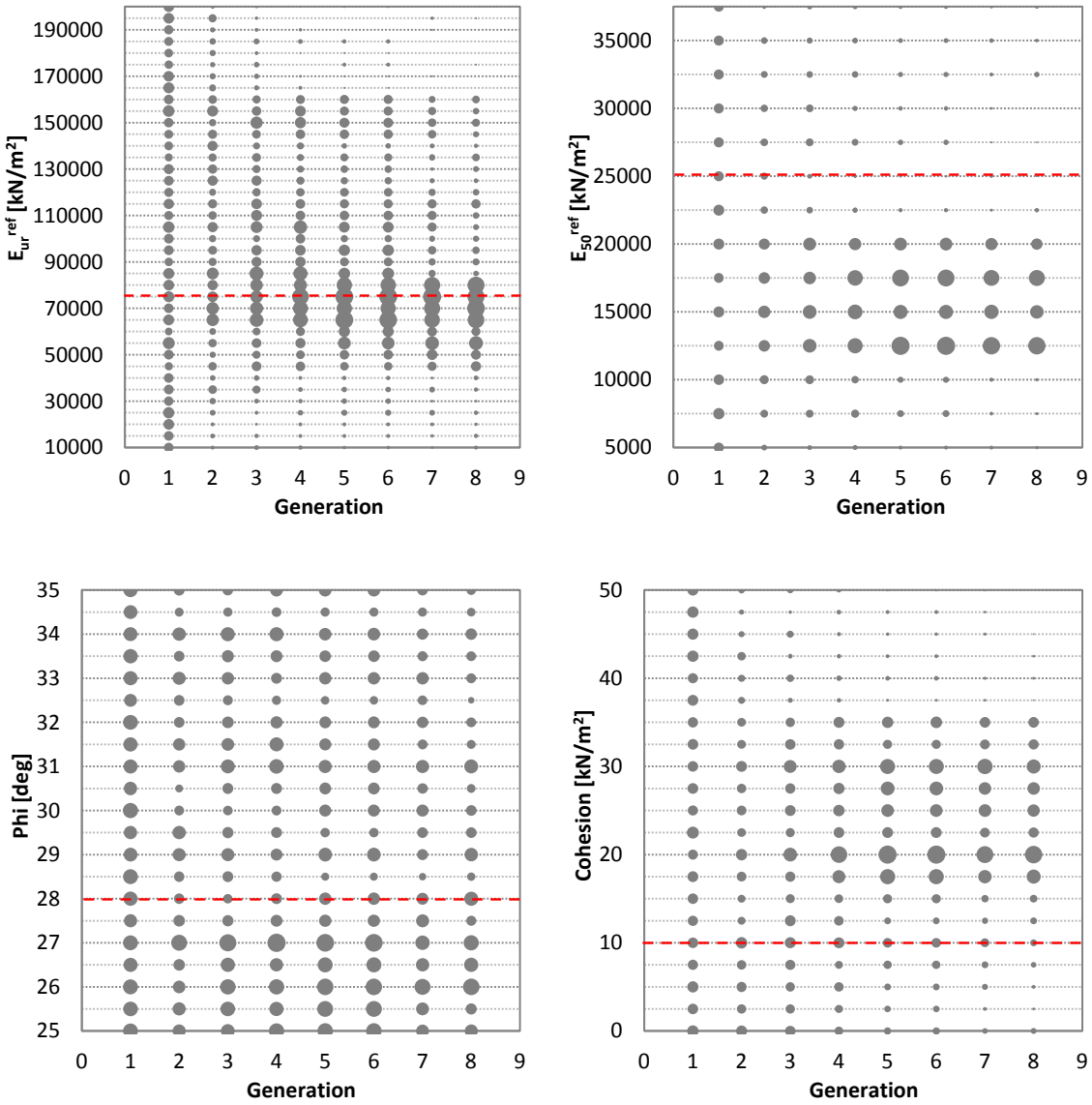

Figure 5.129. Full evolution of the parameters associated with the individuals. The size of the bubble is directly related to the number of individuals that share that specific parameter value. The red dashed line represents the value associated with the global minimum. (hybrid method / noisy data / far from collapse).

After 8 generations and a total of 5422 individuals evaluated, the principal component analysis (PCA) was conducted using 167 good individuals. The most relevant information related to the PCA is presented in table 5.31.

Description	Values
Mean of E_{ur}^{ref} [kN/m^2]	70898.20
Mean of E_{50}^{ref} [kN/m^2]	16811.37
Mean of φ [deg]	30.29
Mean of c [kN/m^2]	20.85
Standard deviation of E_{ur}^{ref} [kN/m^2]	9204.91
Standard deviation of E_{50}^{ref} [kN/m^2]	3584.86
Standard deviation of φ [deg]	2.81
Standard deviation of c [kN/m^2]	6.74
Correlation matrix	$\begin{bmatrix} 1 & 0.187 & -0.058 & -0.235 \\ 0.187 & 1 & -0.267 & -0.863 \\ -0.058 & -0.267 & 1 & -0.095 \\ -0.235 & -0.863 & -0.095 & 1 \end{bmatrix}$
Eigenvector (associated with the first principal component)	$[-0.2976 \quad -0.6776 \quad 0.1397 \quad 0.6578]$
Eigenvector (associated with the second principal component)	$[-0.0233 \quad -0.0802 \quad 0.9517 \quad -0.2953]$
Eigenvector (associated with the third principal component)	$[0.9531 \quad -0.2484 \quad 0.0532 \quad 0.1640]$
Eigenvector (associated with the fourth principal component)	$[0.0483 \quad 0.6875 \quad 0.2680 \quad 0.6731]$
Eigenvalue (associated with the first principal component)	1.9758
Eigenvalue (associated with the second principal component)	1.0535
Eigenvalue (associated with the third principal component)	0.9072
Eigenvalue (associated with the fourth principal component)	0.0633
Major principal axis length projected into the space of E_{ur}^{ref} [kN/m^2]	23399.87
Major principal axis length projected into the space of E_{50}^{ref} [kN/m^2]	9560.90
Major principal axis length projected into the space of φ [deg]	7.69
Major principal axis length projected into the space of c [kN/m^2]	17.45

Table 5.31. Principal Component Analysis (Hybrid Algorithm / Noisy Data / Far From Collapse).

Adapting equation 5.5 to four dimensions, it was checked that the global minimum was enclosed in the new search space defined by the PCA ellipsoid.

The evolution of the algorithm, once the switch from AGA to gradient based method was applied, is illustrated in figures 5.130, 5.131, 5.132, 5.133 and 5.134.

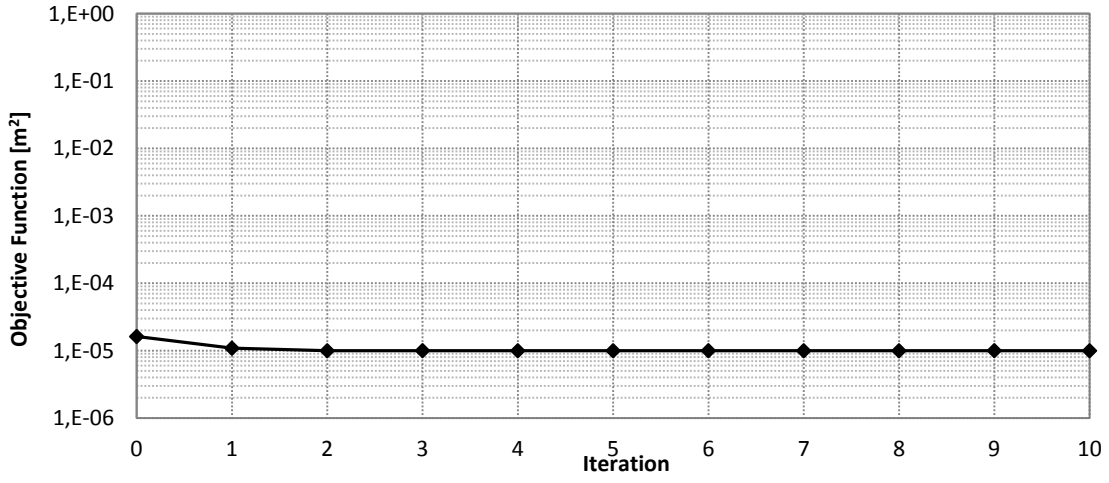

Figure 5.130. Evolution of the objective function using the Gauss-Newton method in the second stage of the hybrid method (hybrid method / noisy data / far from collapse).

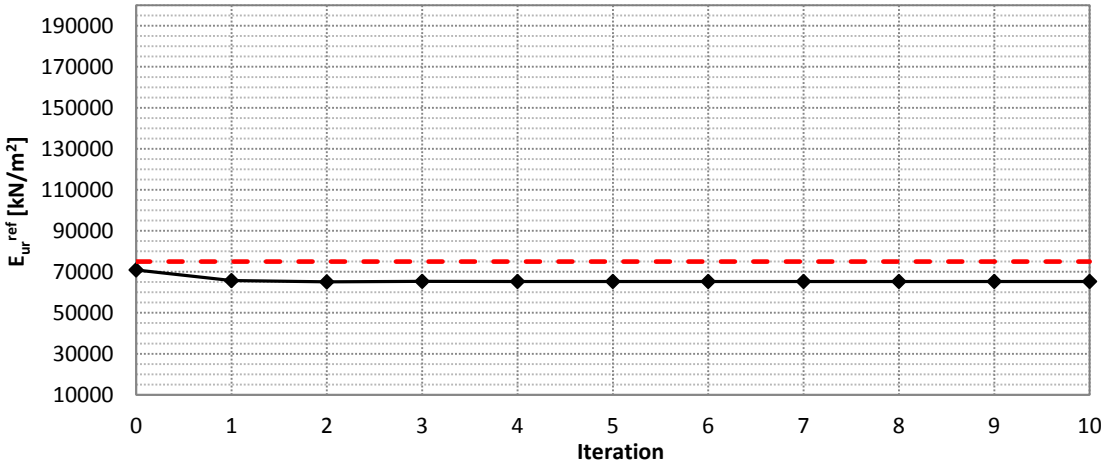

Figure 5.131. Evolution of the E_{ur}^{ref} value using the Gauss-Newton method in the second stage of the hybrid method (hybrid method / noisy data / far from collapse).

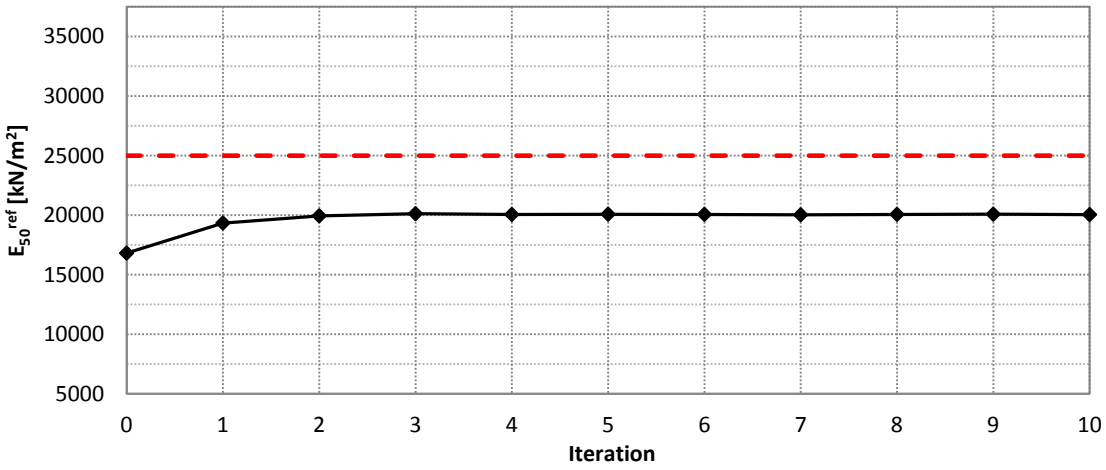

Figure 5.132. Evolution of the E_{50}^{ref} value using the Gauss-Newton method in the second stage of the hybrid method (hybrid method / noisy data / far from collapse).

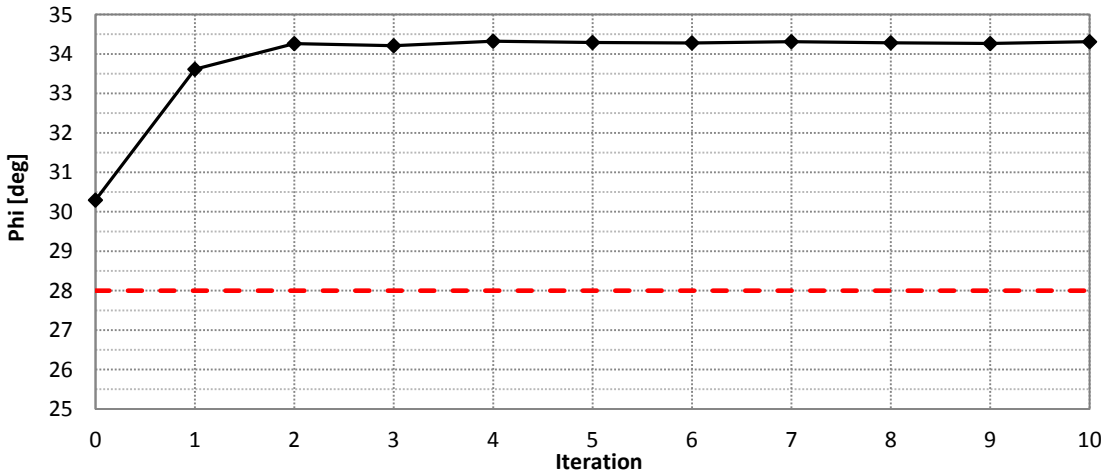

Figure 5.133. Evolution of the φ value using the Gauss-Newton method in the second stage of the hybrid method (hybrid method / noisy data / far from collapse).

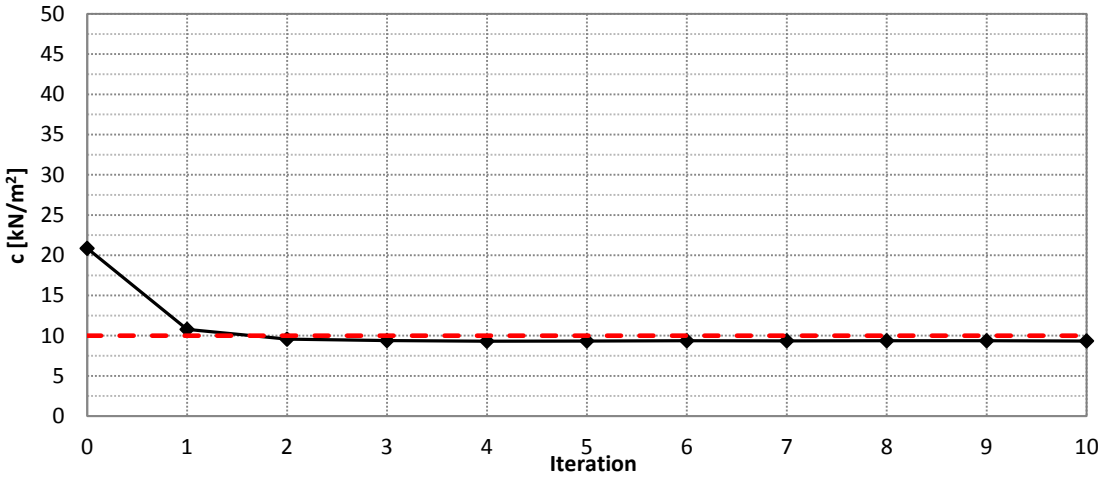

Figure 5.134. Evolution of the cohesion value using the Gauss-Newton method in the second stage of the hybrid method (hybrid method / noisy data / far from collapse).

Even though figures 5.131, 5.132, 5.133 and 5.134 show that the final results do not match the parameters used to generate the measurements, the value of the error associated with the solution obtained by the algorithm is lower than the one derived from the actual real soil parameters values ($9.96 \cdot 10^{-6} m^2$ vs. $1.126 \cdot 10^{-5} m^2$). Therefore, on the one hand, in terms of optimization, the algorithm has found the solution of the problem, while on the other hand, in terms of geotechnics, the solution is not fully satisfactory. However, no better results in terms of parameter values can be obtained without introducing more information into the analysis, such as parameters previous information extracted from other methodologies (e.g. laboratory tests, in situ tests, literature ...).

The comparison between the displacement measurements and the results obtained from the numerical model associated with the parameters obtained from the current backanalysis is illustrated in figure 5.135. Even though, in terms of parameters values, not all of them are close to the actual value, the displacements look quite similar.

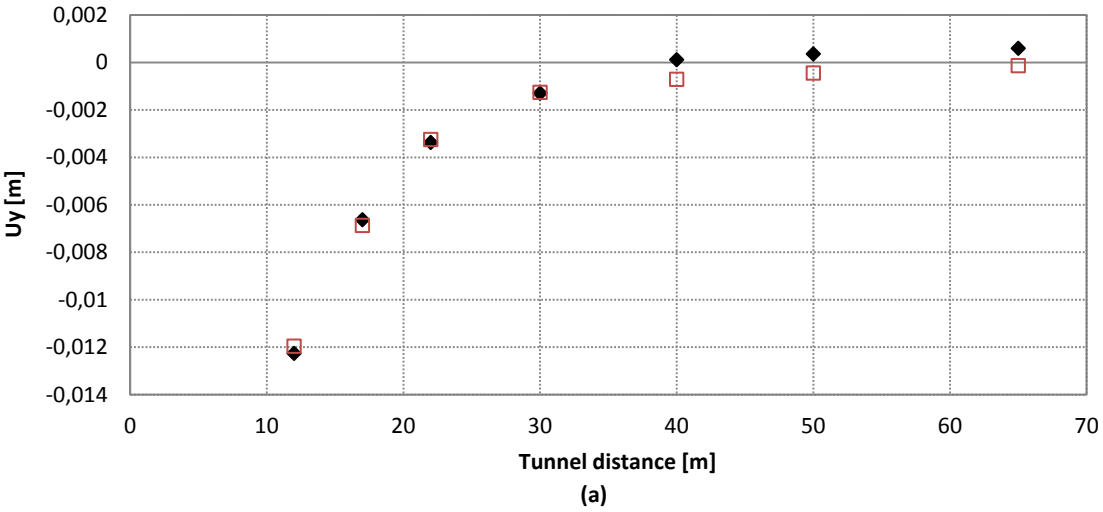

(a)

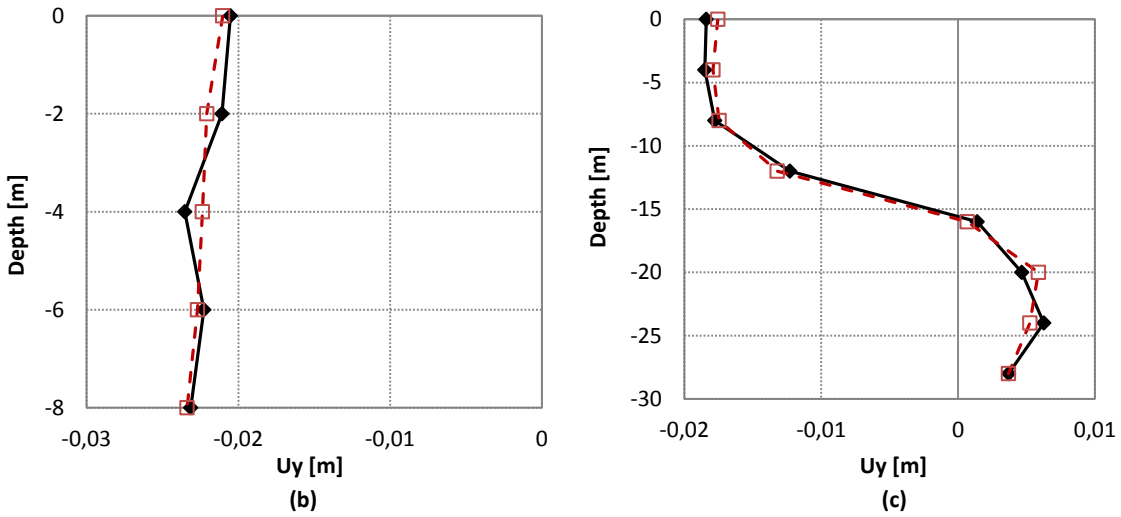

Figure 5.135. Measurements vs. Calculations (the black rhombuses represent the measurements while the red empty squares represent the Plaxis calculations associated with the parameters obtained from the current backanalysis). (a) Vertical displacements on the surface. (b) Vertical displacements representing a sliding micrometer located along the vertical tunnel axis. (c) Vertical displacements representing a sliding micrometer located two meters away from the tunnel side. (hybrid method / noisy data / far from collapse).

A summary of the results is shown in table 5.32.

Stage 1 (AGA + PCA)	
Number of generations	8
Computational cost [Plaxis evaluations]	5422
Center of the PCA Ellipse	E_{ur}^{ref} = 70898.20 kN/m^2 E_{50}^{ref} = 16811.37 kN/m^2 φ = 30.29^o c = 20.85 kN/m^2
Stage 2 (Gradient Based Method)	
Number of iterations	10
Computational cost [Plaxis evaluations]	49
Final values	E_{ur}^{ref} = 65270.20±1031.1 kN/m^2 E_{50}^{ref} = 20043.22±1816.9 kN/m^2 φ = 34.31±1.06^o c = 9.34±2.9 kN/m^2

Table 5.32. Results summary using the hybrid method with noisy data for a tunnel scenario far from collapse. Plaxis evaluations is referred to the number of direct problems solved by the geotechnical program Plaxis.

5.5.2.2 Close To Collapse

The results of the parameters estimation using the hybrid method with noisy data in a scenario close to collapse are presented in this section.

For this particular case, within 5 generations the adaptive genetic algorithm has not been able to generate more than 50% of new individuals, in part due to the restrictions derived from the instability of the scenario, where combinations of parameters really close to the solution makes the tunnel collapse, causing consequently a plunge of the number of individuals.

The evolution of the population from the initial generation to the last one (generation 5) is shown in figure 5.136. As in other cases, the algorithm seems to converge; however, this convergence does not match exactly the solution of the problem.

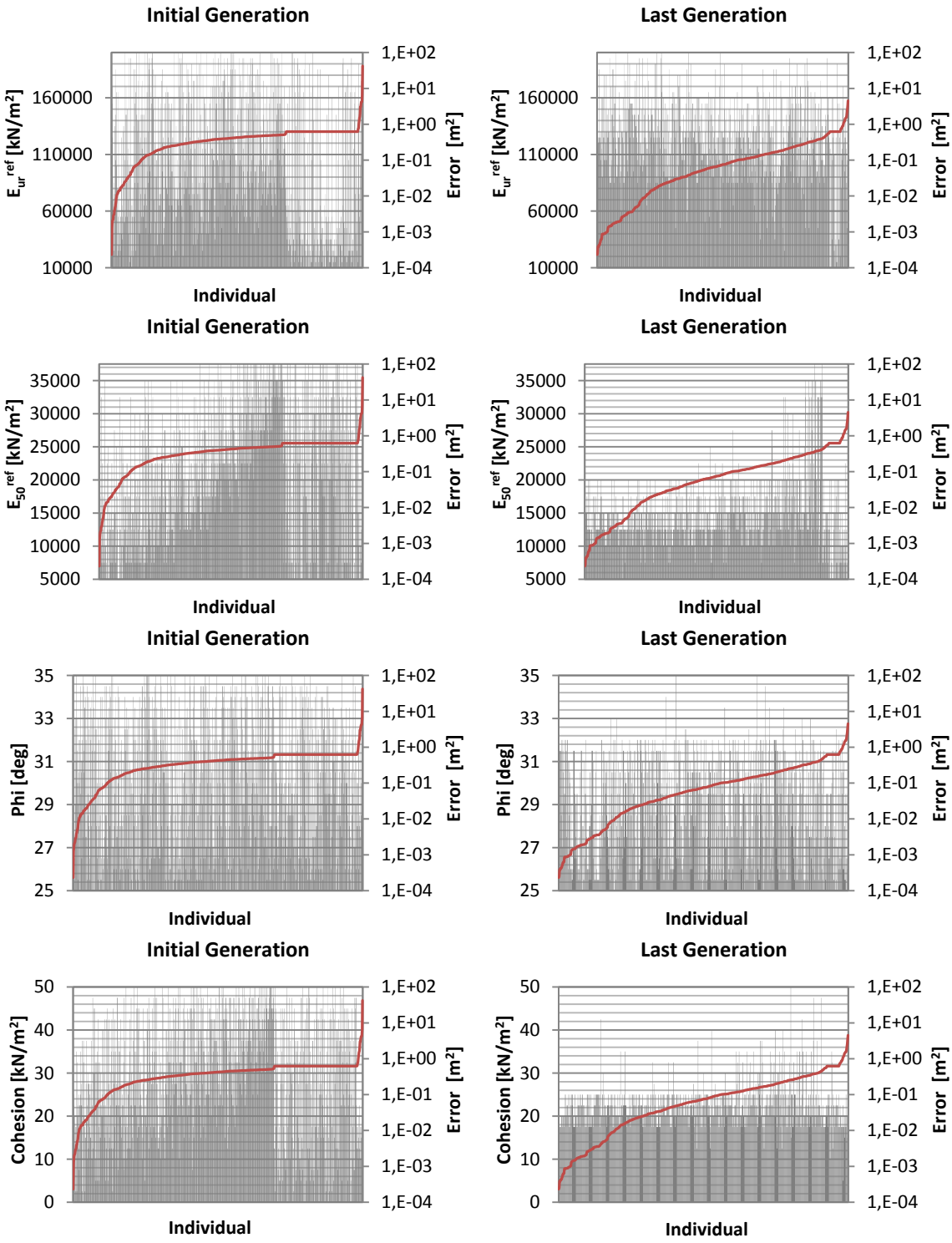

Figure 5.136. Parameters values associated to the individuals of the initial generation and the last generation. The gray bars represent the parameter values of the individuals while the red line represents the error associated to the individual. (hybrid method / noisy data / close to collapse).

In order to visualize the evolution of the algorithm more globally, in figure 5.137 the results of the adaptive genetic algorithm have also been shown as they were presented in the previous section (figure 5.129). Unfortunately, it corroborates what figure 5.136 previously showed; the population does not converge to the global minimum.

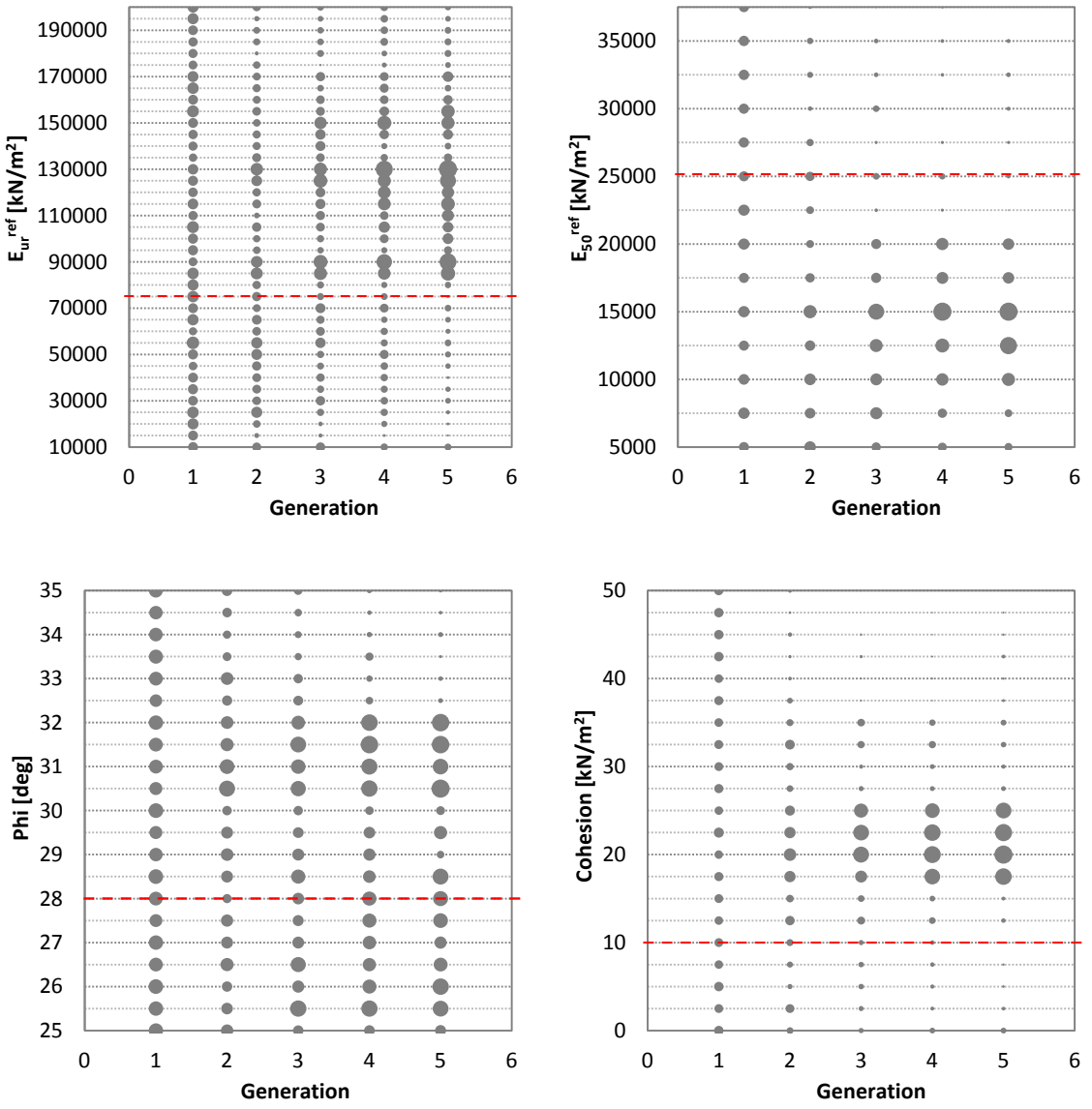

Figure 5.137. Full evolution of the parameters associated with the individuals. The size of the bubble is directly related to the number of individuals that share that specific parameter value. The red dashed line represents the value associated with the global minimum. (hybrid method / noisy data / close to collapse).

The most relevant information related to the PCA is presented in table 5.33, which was obtained after five generations, 4375 Plaxis evaluations and 136 good individuals.

Description	Values
Mean of E_{ur}^{ref} [kN/m^2]	129191.20
Mean of E_{50}^{ref} [kN/m^2]	14595.59
Mean of φ [deg]	28.96
Mean of c [kN/m^2]	20.49
Standard deviation of E_{ur}^{ref} [kN/m^2]	34486.82
Standard deviation of E_{50}^{ref} [kN/m^2]	4096.30
Standard deviation of φ [deg]	2.35
Standard deviation of c [kN/m^2]	4.21
Correlation matrix	$\begin{bmatrix} 1 & 0.155 & -0.180 & 0.302 \\ 0.155 & 1 & -0.124 & -0.741 \\ -0.180 & -0.124 & 1 & -0.377 \\ 0.302 & -0.741 & -0.377 & 1 \end{bmatrix}$
Eigenvector (associated with the first principal component)	$[0.2255 \quad -0.5703 \quad -0.2978 \quad 0.7315]$

Eigenvector (associated with the second principal component)	$[-0.6118 \quad -0.5422 \quad 0.5763 \quad 0.0004]$
Eigenvector (associated with the third principal component)	$[-0.7125 \quad 0.0605 \quad -0.6987 \quad -0.0176]$
Eigenvector (associated with the fourth principal component)	$[0.2600 \quad -0.6140 \quad -0.3012 \quad -0.6815]$
Eigenvalue (associated with the first principal component)	1.8251
Eigenvalue (associated with the second principal component)	1.3080
Eigenvalue (associated with the third principal component)	0.8171
Eigenvalue (associated with the fourth principal component)	0.0496
Major principal axis length projected into the space of E_{ur}^{ref} [kN/m^2]	98869.71
Major principal axis length projected into the space of E_{50}^{ref} [kN/m^2]	12940.97
Major principal axis length projected into the space of φ [deg]	6.37
Major principal axis length projected into the space of c [kN/m^2]	17.07

Table 5.33. Principal Component Analysis (Hybrid Algorithm / Noisy Data / Close To Collapse).

Adapting equation 5.5 to four dimensions, it was checked that the global minimum was enclosed in the new search space defined by the PCA ellipsoid.

The evolution of the algorithm, once the switch from AGA to gradient based method was applied, is illustrated in figures 5.138, 5.139, 5.140, 5.141 and 5.142.

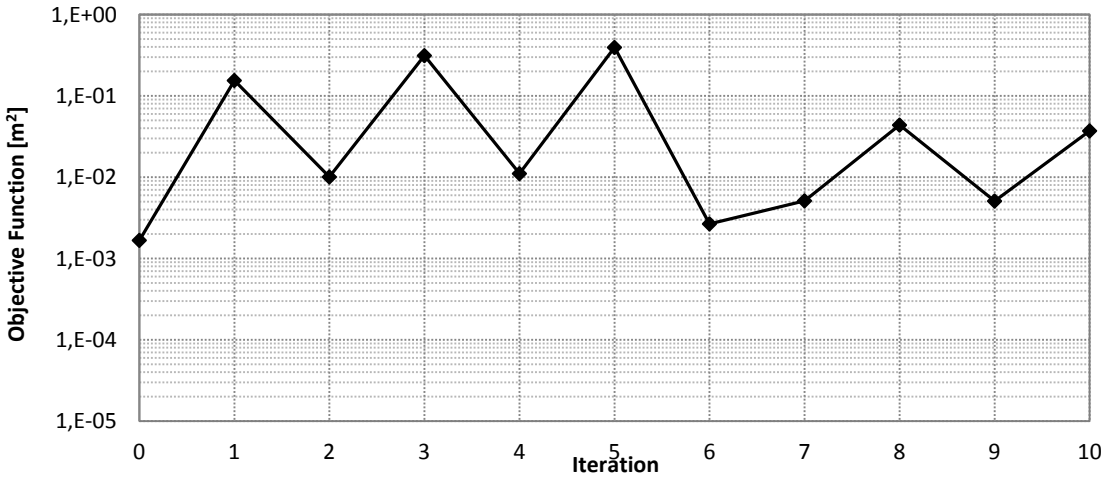

Figure 5.138. Evolution of the objective function using the Gauss-Newton method in the second stage of the hybrid method (hybrid method / noisy data / close to collapse).

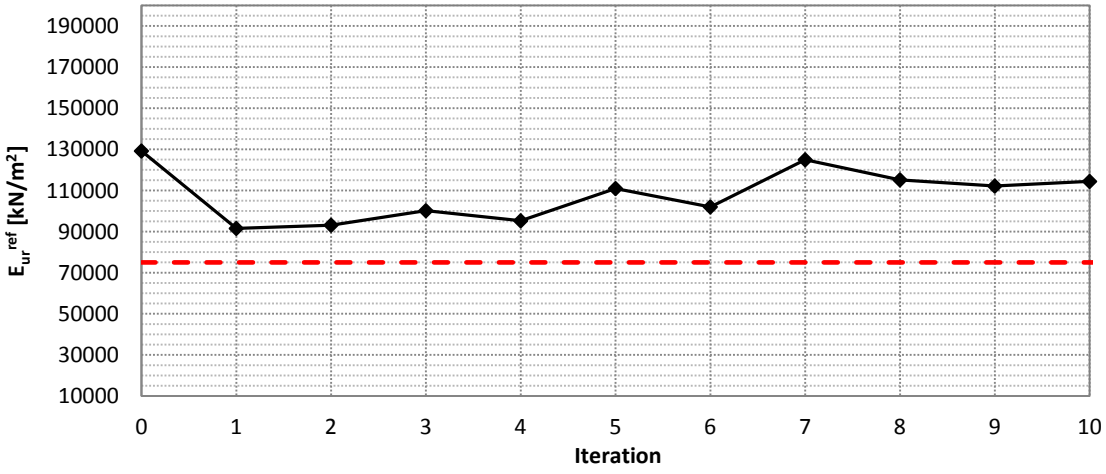

Figure 5.139. Evolution of the E_{ur}^{ref} value using the Gauss-Newton method in the second stage of the hybrid method (hybrid method / noisy data / close to collapse).

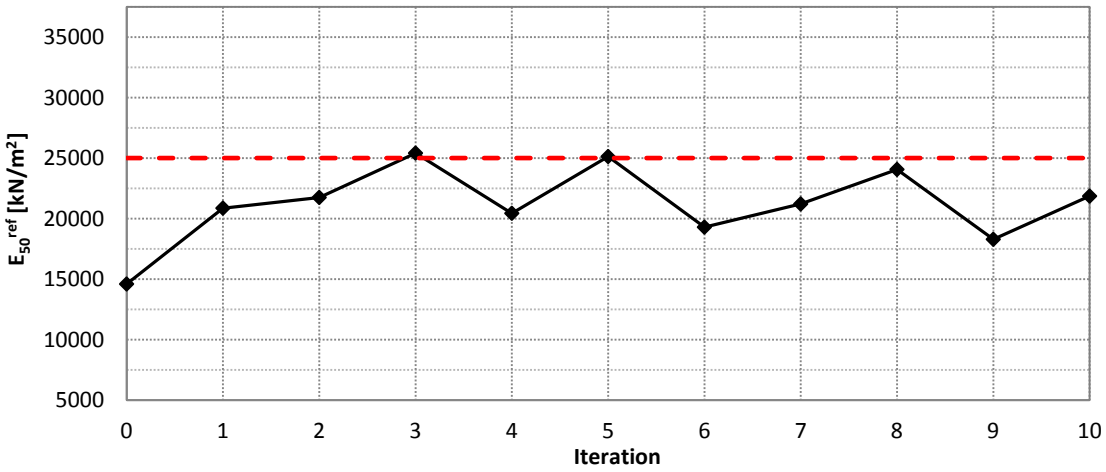

Figure 5.140. Evolution of the E_{50}^{ref} value using the Gauss-Newton method in the second stage of the hybrid method (hybrid method / noisy data / close to collapse).

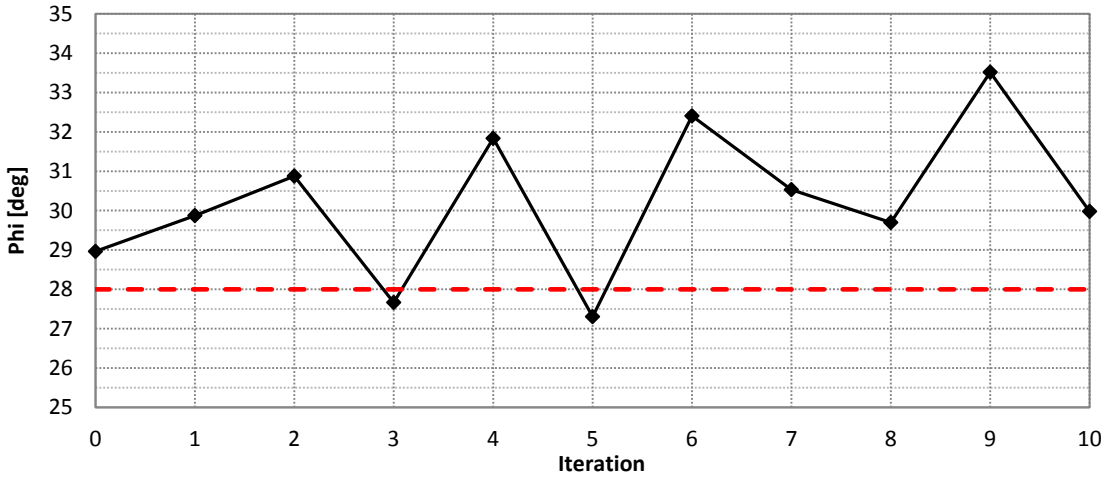

Figure 5.141. Evolution of the φ value using the Gauss-Newton method in the second stage of the hybrid method (hybrid method / noisy data / close to collapse).

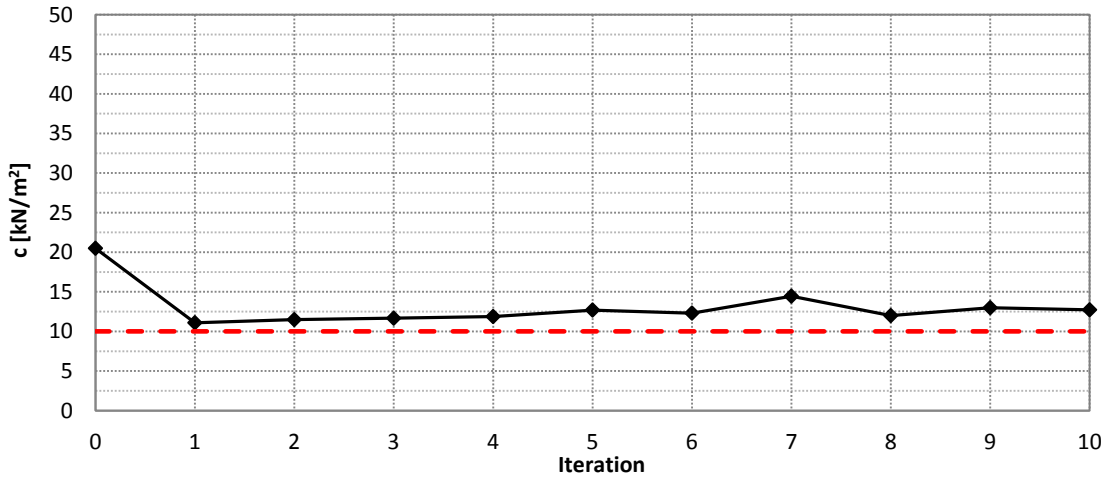

Figure 5.142. Evolution of the cohesion value using the Gauss-Newton method in the second stage of the hybrid method (hybrid method / noisy data / close to collapse).

Contrary to the case far from collapse, where the algorithm converges to a solution that does not match the global minimum, in terms of parameter values, but it does find an even better solution in terms of objective function value, the case close to collapse seems to try to converge to the minimum, in terms of parameters, but with a worse value of the objective function. In addition, it shows an unstable behavior in terms of objective function and parameter values (except for cohesion).

In order to tackle this instability of the Gauss-Newton method, the second stage of the hybrid algorithm was recalculated using the Marquardt method instead of the Gauss-Newton. However, althogh getting a stable behavior of the objective function, forced by the definition of the Marquardt method (see figure 5.143), it was not possible to drive the search into the global minimum (neither in terms of parameter values nor in terms of objective function value).

After ten iterations using the Marquardt method, the parameters obtained from the analysis were: E_{ur}^{ref} = 186716 kN/m^2, E_{50}^{ref} = 12454 kN/m^2, φ = 34.15^0 and c = 20.54 kN/m^2, while the ones associated with the global minimum are: E_{ur}^{ref} = 75000 kN/m^2, E_{50}^{ref} = 25000 kN/m^2, φ = 28^0 and c = 10 kN/m^2. Moreover, the value of the objective function obtained in the analysis was 2.213·10^{-4} m^2, while the one associated with the global minimum is 1.47·10^{-5} m^2. Nonetheless, if the displacements obtained from the calculations are compared with the measurements, the match between them is quite good (see figure 5.144), which highlights the difficulty of the parameters identification problem, especially derived from the none-uniqueness nature of complex geotechnical scenarios.

Another aspect that has been studied in this section is the reasons why the case close to collapse has exhibited more difficulty than the one far from collapse, when it was expected to be easier due to its higher sensitivity, as shown in section 5.3.8.

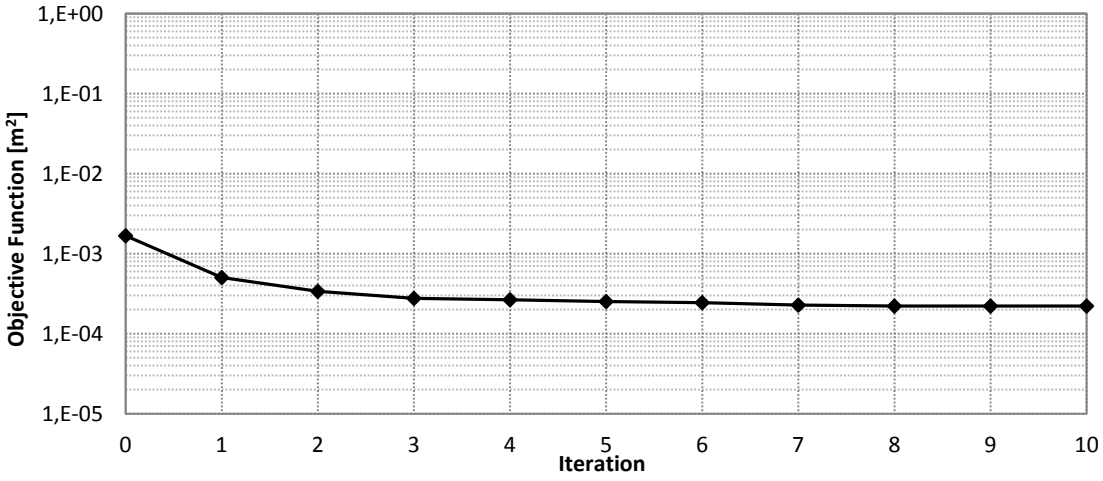

Figure 5.143. Evolution of the objective function using the Marquardt method in the second stage of the hybrid method (hybrid method / noisy data / close to collapse).

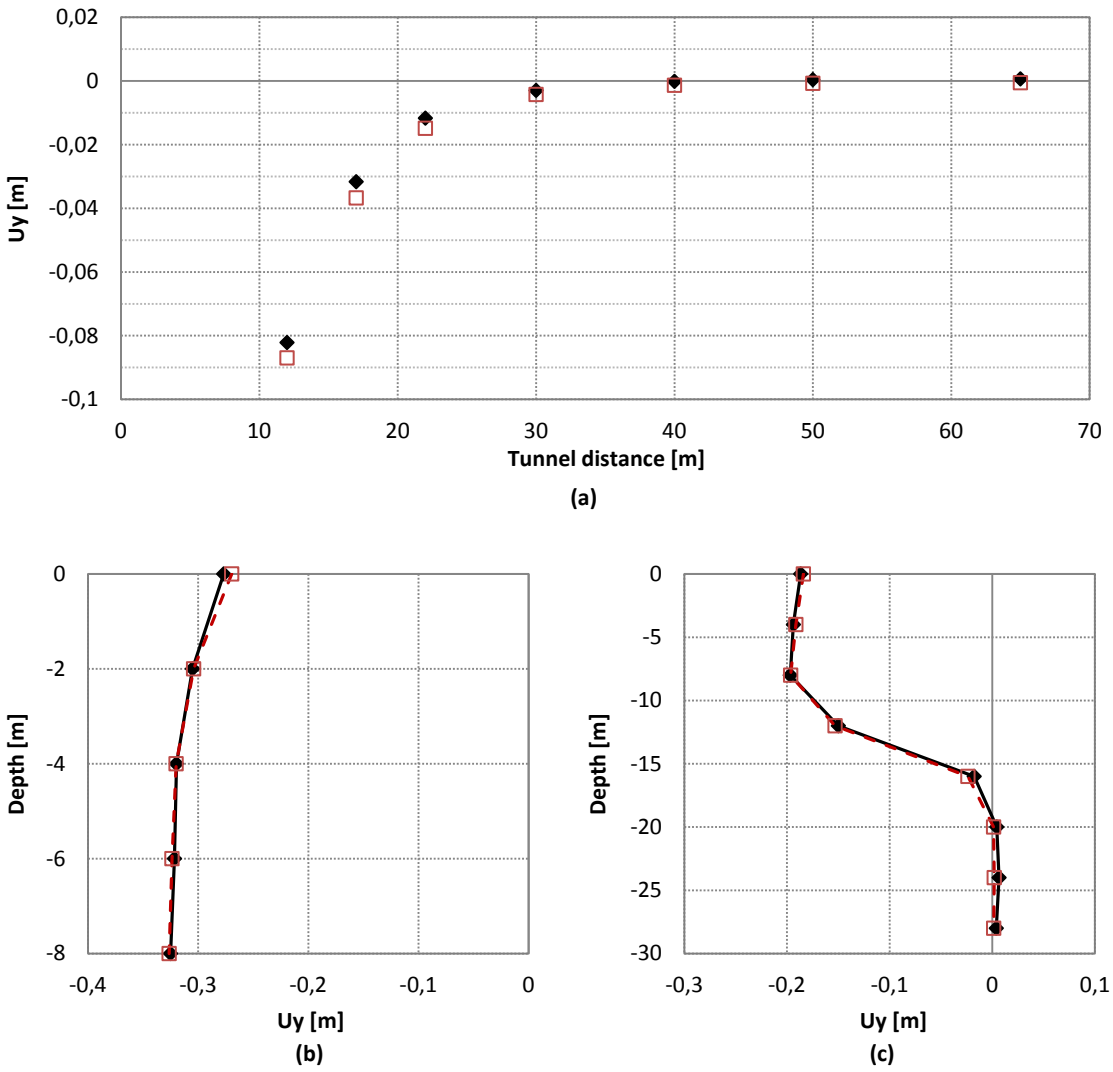

Figure 5.144. Measurements vs. Calculations (the black rhombuses represent the measurements while the red empty squares represent the Plaxis calculations associated with the parameters obtained from the current backanalysis). (a) Vertical displacements on the surface. (b) Vertical displacements representing a sliding micrometer located along the vertical tunnel axis. (c) Vertical displacements representing a sliding micrometer located two meters away from the tunnel side. (hybrid method / noisy data / close to collapse).

The additional difficulty of the case close to collapse is associated with new restricted boundary conditions derived from the parameters combinations that causes the tunnel to collapse, which in this case study makes the solution to be closely surrounded by the boundaries. In fact, if all parameters, except the cohesion, are fixed with the values associated with the minimum and the value of cohesion is changed as it is defined in the search space discretization (see table 5.30), it can be appreciated, as shown in figure 5.145, that the solution of the problem is located close to a boundary.

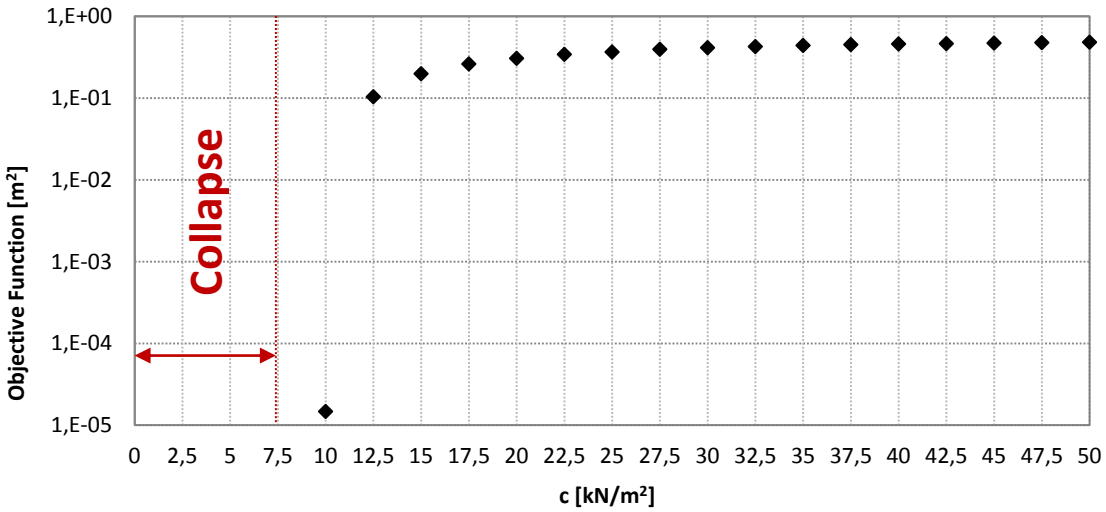

Figure 5.145. Objective Function vs. Cohesion. The rest of parameters are fixed with the values associated with the minimum. The red zone represents the cohesion values that cause the tunnel to collapse. (hybrid method / noisy data / close to collapse).

Unfortunately, this situation makes more difficult for genetic algorithms and gradient based methods to find the solution; especially for genetic algorithms, which base the majority of the search on the fitness of the individuals and their recombination (selection and crossover). Supposing that two individuals are selected to generate two new offsprings, and none of the parents are located on the boundary, it is not possible to create a new individual out of the space defined by the hyperplanes associated with the line connecting both parents, and consequently no new individuals will be located on the boundary, unless the mutation operator creates it, which statistically is highly unlikely using the standard values of mutation probability that are used in most cases.

Therefore, in order to confirm that better results would be obtained in the case close to collapse due to the higher on the sensitivity of the measurements, a new less restricted scenario close to collapse was defined. The new scenario, named Relatively Close To Collapse, was defined by setting the value of ΣMStage to 0.305 instead of 0.32 that was used in the previous case.

The reduction of the value of ΣMStage, which seems not highly significant, has permitted to extend the boundaries around the minimum, and consequently, getting the results that were expected for a case relatively close to collapse.

The difference between both cases (close to collapse vs. relatively close to collapse), in terms of plastic points evolution, can be illustrated by comparing figures 5.107 and 5.146, especially if comparing (b), which corresponds to the soil relaxation due to the tunnel excavation, and where it can be noticed a significant reduction in the number of Mohr-Coulomb plastic points. However, due to the large displacements that also occurred in the relatively close to collapse case (larger than a decimeter), it is still reasonable to consider the new case study as a representative case for a tunnel close to collapse.

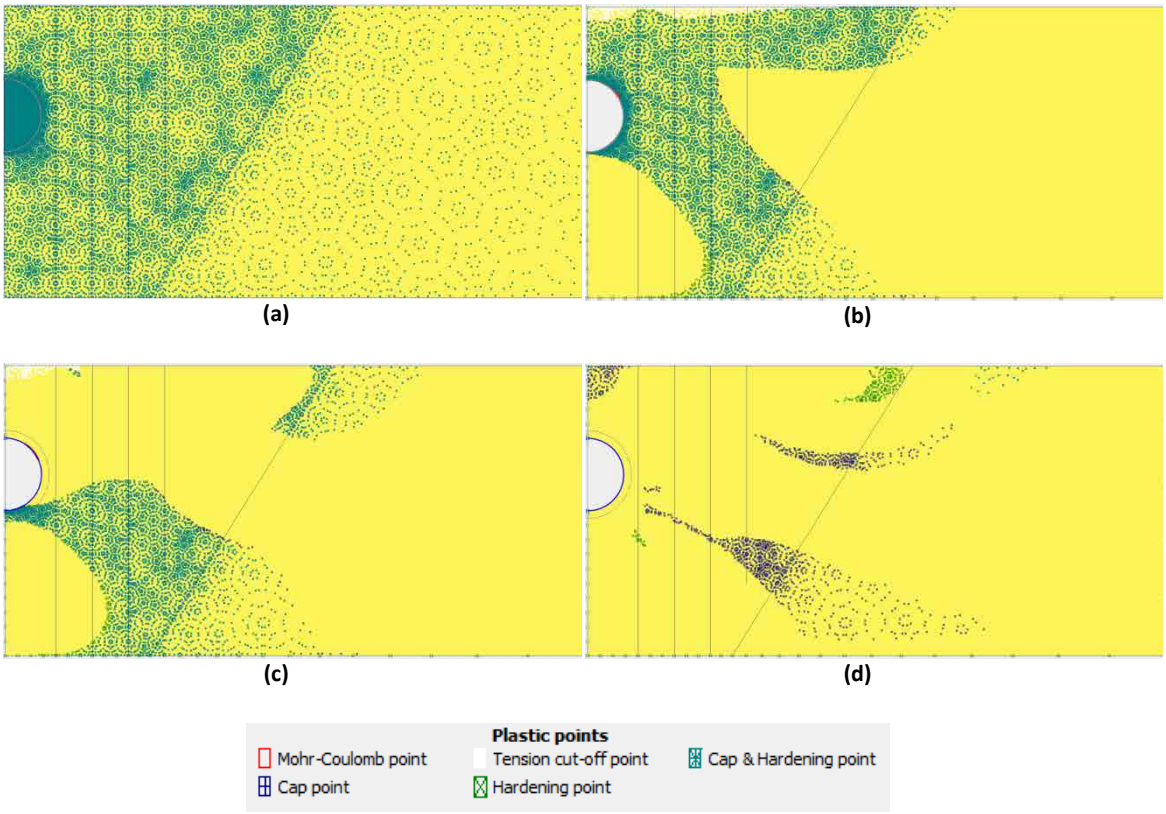

Figure 5.146. Plastic points of the scenario Relatively Close To Collapse. (a) shows the plastic points from the calculation phase 0, (b) shows the plastic points from the calculation phase 1, (c) shows the plastic points from the calculation phase 2 and (d) shows the plastic points from the calculation phase 3.

After four generations, 3185 Plaxis evaluations and 125 good individuals involved in the principal component analysis (PCA), it was defined a new search space containing the global minimum. The most relevant information related to the PCA is presented in table 5.34.

Description	Values
Frontier Value	$9.307 \cdot 10^{-4}$ m^2
AF (amplifier factor of the standard deviation)	2.7
Mean of E_{ur}^{ref} [kN/m^2]	114320
Mean of E_{50}^{ref} [kN/m^2]	15520
Mean of φ [deg]	30.20
Mean of c [kN/m^2]	19.72
Standard deviation of E_{ur}^{ref} [kN/m^2]	44388.06
Standard deviation of E_{50}^{ref} [kN/m^2]	6232.2
Standard deviation of φ [deg]	3.12
Standard deviation of c [kN/m^2]	8.00
Correlation matrix	$\begin{bmatrix} 1 & 0.186 & -0.181 & 0.333 \\ 0.186 & 1 & -0.064 & -0.679 \\ -0.181 & -0.064 & 1 & -0.453 \\ 0.333 & -0.679 & -0.453 & 1 \end{bmatrix}$
Eigenvector (associated with the first principal component)	$[0.2648 \quad -0.4922 \quad -0.4081 \quad 0.7218]$
Eigenvector (associated with the second principal component)	$[-0.6280 \quad -0.6323 \quad 0.4503 \quad 0.0538]$
Eigenvector (associated with the third principal component)	$[-0.6670 \quad 0.1374 \quad -0.7285 \quad -0.0734]$
Eigenvector (associated with the fourth principal component)	$[0.300 \quad -0.5821 \quad -0.3160 \quad -0.6860]$
Eigenvalue (associated with the first principal component)	1.8422
Eigenvalue (associated with the second principal component)	1.2889
Eigenvalue (associated with the third principal component)	0.8006
Eigenvalue (associated with the fourth principal component)	0.0681
Major principal axis length projected into the space of E_{ur}^{ref} [kN/m^2]	85448.93

Major principal axis length projected into the space of E_{50}^{ref} [kN/m^2]	12080.9
Major principal axis length projected into the space of φ [deg]	5.50
Major principal axis length projected into the space of c [kN/m^2]	21.16

Table 5.34. Principal Component Analysis (Hybrid Algorithm / Noisy Data / Relatively Close To Collapse).

The evolution of the algorithm, once the switch from genetic algorithm to gradient based method is performed, is illustrated in figures 5.147, 5.148, 5.149, 5.150 and 5.151. They show how the gradient based method, in this particular case the Gauss-Newton method, finds a good solution after few iterations.

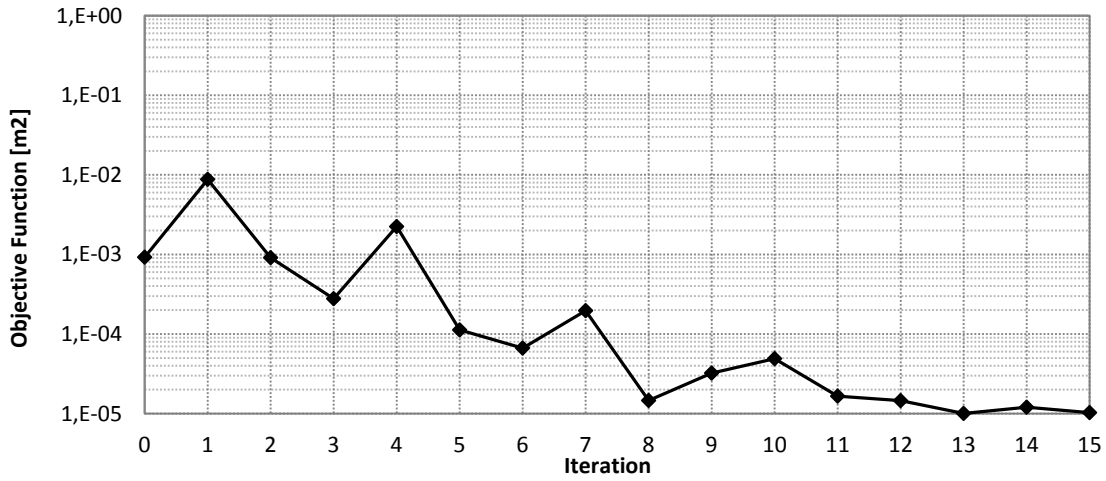

Figure 5.147. Evolution of the objective function using the Gauss-Newton method in the second stage of the hybrid method (hybrid method / noisy data / relatively close to collapse).

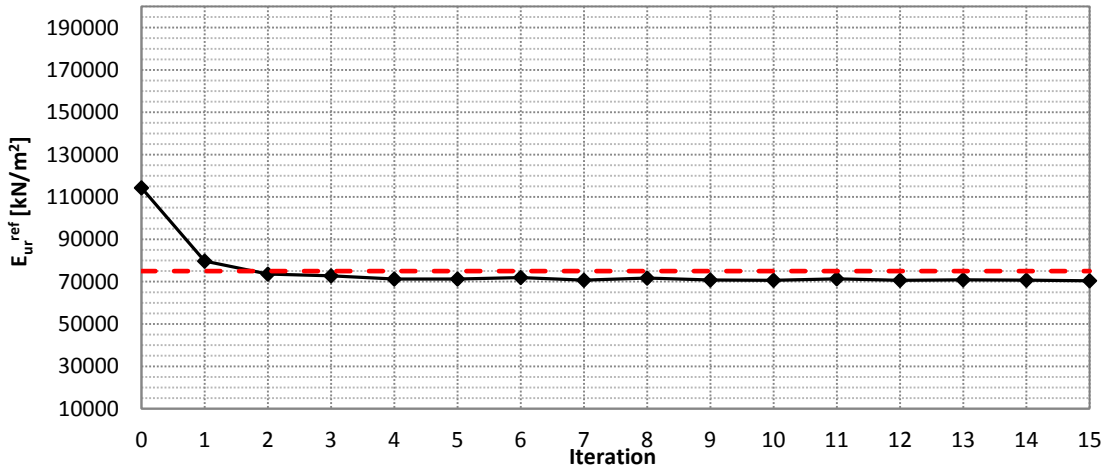

Figure 5.148. Evolution of the E_{ur}^{ref} value using the Gauss-Newton method in the second stage of the hybrid method (hybrid method / noisy data / relatively close to collapse).

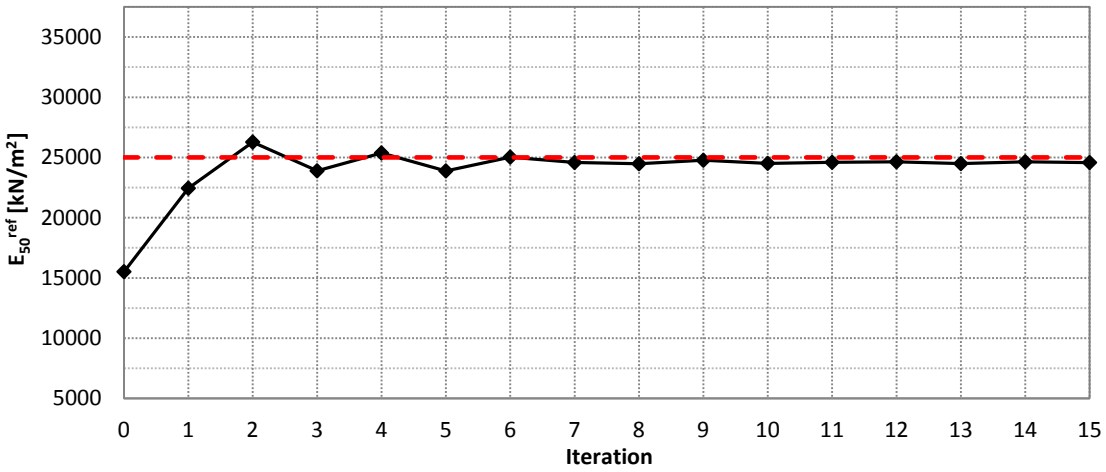

Figure 5.149. Evolution of the E_{50}^{ref} value using the Gauss-Newton method in the second stage of the hybrid method (hybrid method / noisy data / relatively close to collapse).

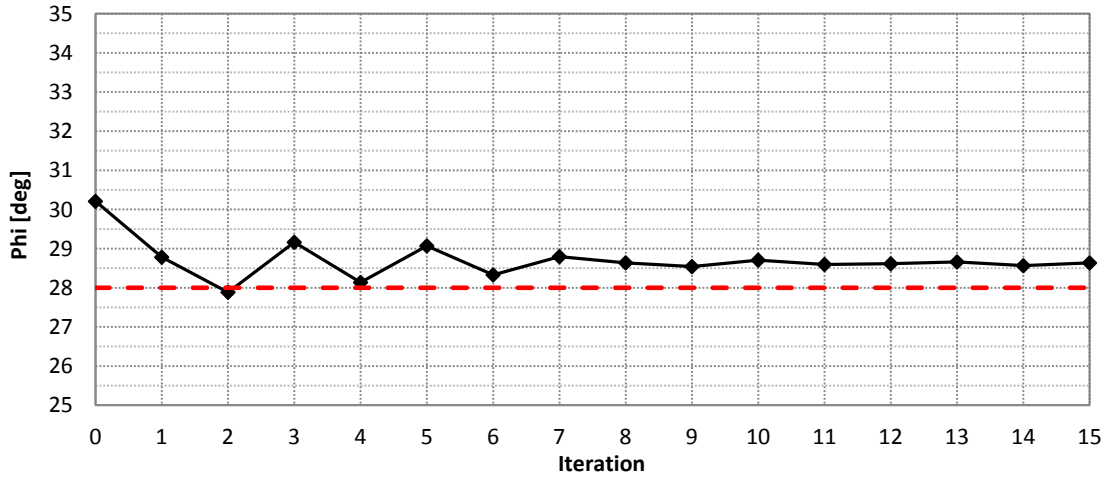

Figure 5.150. Evolution of the φ value using the Gauss-Newton method in the second stage of the hybrid method (hybrid method / noisy data / relatively close to collapse).

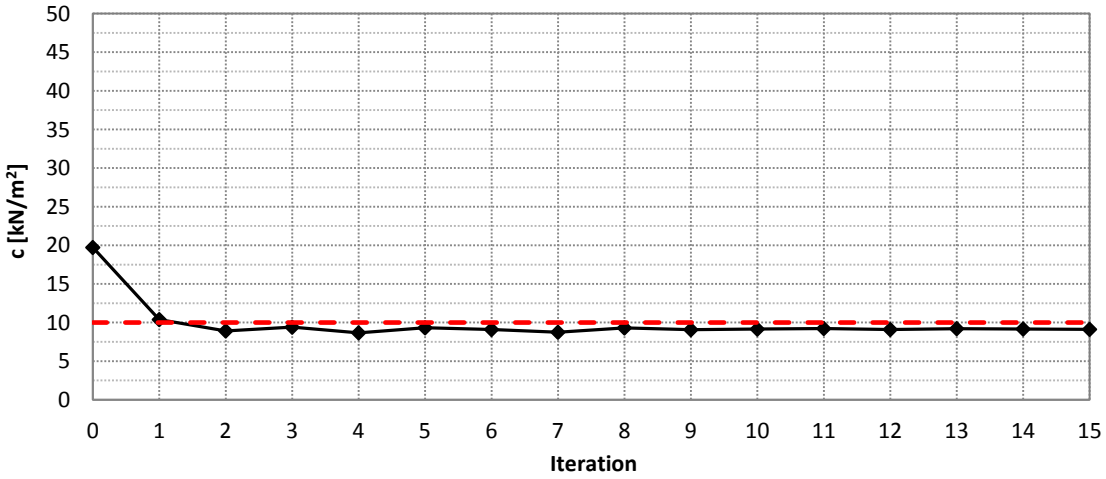

Figure 5.151. Evolution of the cohesion value using the Gauss-Newton method in the second stage of the hybrid method (hybrid method / noisy data / relatively close to collapse).

The slight discrepancy between the parameters obtained from the analysis and the ones used to define the measurements, as it was explained before, is caused by the introduction of noise. In terms of objective function, the value obtained by the algorithm is lower than the one derived from the real global minimum ($1.028 \cdot 10^{-5}$ m^2 vs. $1.306 \cdot 10^{-5}$ m^2). Therefore, the results obtained from this analysis can be considered as solution of the problem. Moreover, in terms of displacements, it can be seen in figure 5.152 the excellent match between measurements and calculations.

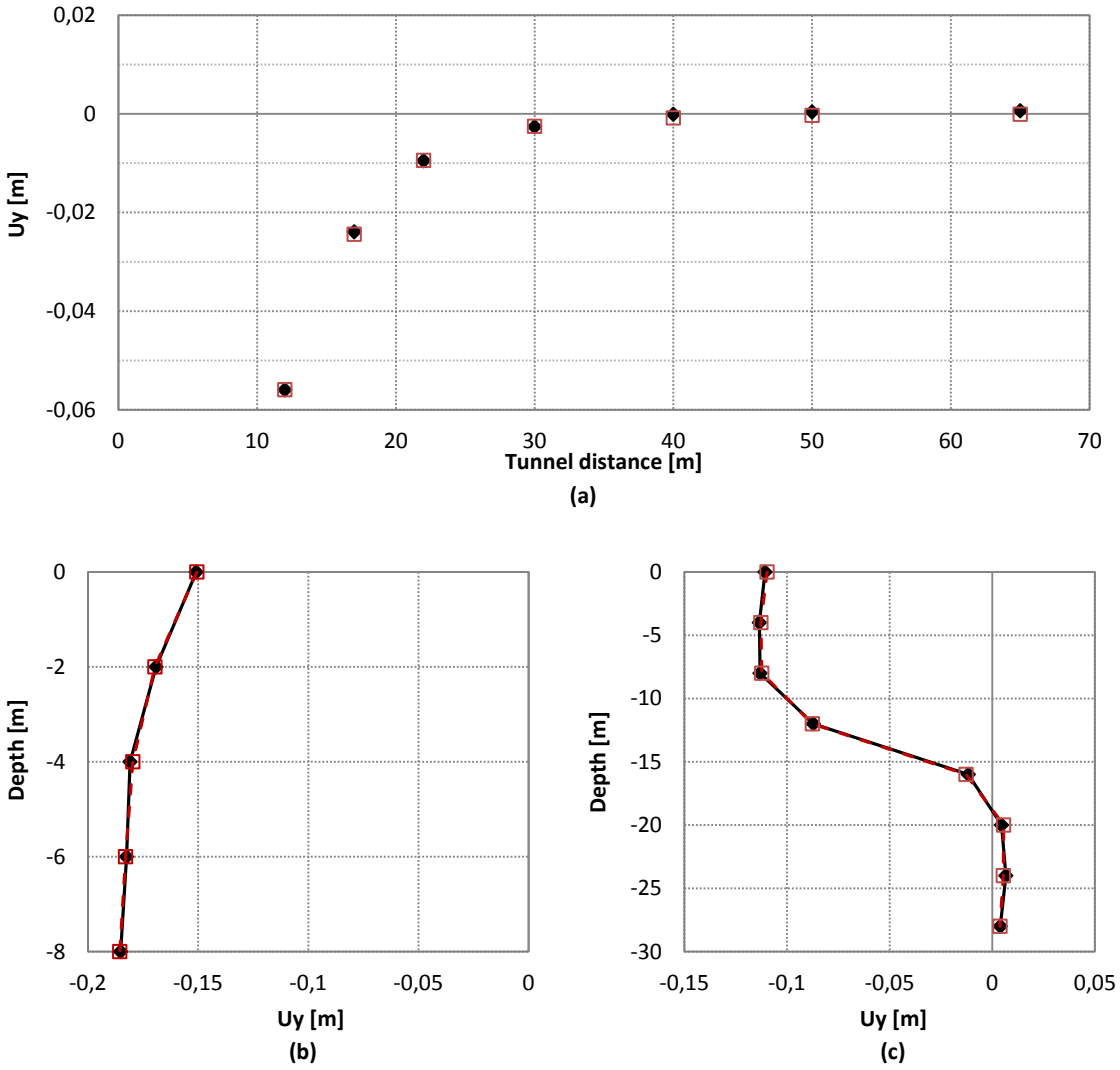

Figure 5.152. Measurements vs. Calculations (the black rhombuses represent the measurements while the red empty squares represent the Plaxis calculations associated with the parameters obtained from the current backanalysis). (a) Vertical displacements on the surface. (b) Vertical displacements representing a sliding micrometer located along the vertical tunnel axis. (c) Vertical displacements representing a sliding micrometer located two meters away from the tunnel side. (hybrid method / noisy data / relatively close to collapse).

A summary of the results is shown in table 5.35.

	Stage 1 (AGA + PCA)
Number of generations	4
Computational cost [Plaxis evaluations]	3185
Center of the PCA Ellipse	E_{ur}^{ref} = 114320 kN/m^2 E_{50}^{ref} = 15520 kN/m^2 φ = 30.20^o

	c = 19.72 kN/m^2
Stage 2 (Gradient Based Method)	
Number of iterations	10
Computational cost [Plaxis evaluations]	49
Final values	E_{ur}^{ref} = 70438.38±563.2 kN/m^2
	E_{50}^{ref} = 24580.15±567.8 kN/m^2
	φ = 28.63±0.32^o
	c = 9.12±0.3 kN/m^2

Table 5.35. Results summary using the hybrid method with noisy data for a tunnel scenario relatively close to collapse. Plaxis evaluations is referred to the number of direct problems solved by the geotechnical program Plaxis.

5.5.3 Concluding Remarks from the Four Parameters Identification Case

After carrying out an exhaustive backanalysis to identify the reference secant stiffness in standard drained triaxial test (E_{50}^{ref}), the reference unloading-reloading stiffness (E_{ur}^{ref}), the effective angle of internal friction (φ), and the effective cohesion (c) of a shallow tunnel, several conclusions can be drawn.

The hybrid algorithm used in this section (AGA + Gauss-Newton) has shown a high robustness facing the identification of four parameter in two different scenarios (far from collapse and close to collapse). Even having some problems, as there were in the case close to collapse, the structure of the algorithm and the information that is stored during the analysis led to understand why problems occurred, and consequently being capable to take the measures required to cope with them.

Using sophisticated constitutive models as the Hardening Soil Model implemented in Plaxis, where many of their parameters are interconnected among them, makes more likely to have none-uniqueness solutions. In these cases, it is highly recommended the introduction of prior information into the analysis.

While using synthetic cases, the introduction of noise into the measurements can caused the drift of the minimum and the appearance of local minima.

Backanalyzing geotechnical problems extremely close to collapse can cause the contraction of the boundary conditions until forcing the minimum to be located on the boundary, which increases significantly the challenge of finding the minimum by genetic algorithms and gradient based methods.

As it has been shown when analyzing the relatively close to collapse case, where the tunnel collapse does not severely penalize the boundary conditions (solution extremely close to the boundaries), better results were obtained due to the higher sensitivity of the measurements to parameter changes.

5.6 Concluding Remarks of the Methodology

After all results and conclusions presented so far in this chapter, it can be pointed out some general concluding remarks of the geotechnical backanalysis methodology described in this thesis.

A flexible, efficient and robust backanalysis methodology has been defined in this thesis, which can be adapted as required by the specific problem. The adaptive nature of the algorithm is based on the type of optimization method applied to the problem (Gauss-Newton method, Marquardt method, Simple Genetic Algorithm, Adaptive Genetic Algorithm and Hybrid Method).

For simple synthetic cases with few parameters to identify, the Gauss-Newton method has shown itself as the most balanced algorithm between obtaining correct parameter values and computational cost. However, it is not expected to get so good results when applying it to real complex cases with a large number of parameters to identify.

Even though the Marquardt method is an improvement of the Gauss-Newton method, in cases where large differences in the magnitudes of the parameters values exist, it can be challenging to find suitable values of μ_0 and ρ that fit all parameters. Consequently, worse results can be obtained when using the Marquardt method.

When looking for the best individual using simple genetic algorithms, the right choice of the population size and the selection pressure has a major impact on the performance of the algorithm, especially if there is a large difference between the fitness of the good individuals and the average of the population. This situation usually causes premature convergence due to the fast loss of diversity. Whereas, when using an adaptive genetic algorithm, the self-adaptive system of the algorithm enforces to keep a certain level of diversity that facilitates a better performance, and makes the algorithm less dependent on population size and selection pressure.

On the other hand, when looking for the best set of individuals rather than the best individual, it has been noticed that even having a good match between the PCA ellipse and the objective function (satisfactory result in terms of optimization problem), in geotechnical terms, if the individuals enclosed in the PCA ellipse are not capable to be defined as a specific soil material, the final results of the backanalysis cannot be considered satisfactory. In those cases, it would be necessary the introduction of prior information to redefine and limit the individuals that represent the final solution.

The hybrid method has shown a significant balance between robustness and efficiency. However, for the synthetic cases that have been studied in this thesis, the hybrid method is still less competitive than the simple Gauss-Newton method. Nonetheless, for complex real problems with a large number of parameters, it is expected that the hybrid method will become more competitive than any gradient based method.

Finally, in terms of suitable type of optimization algorithm, it is concluded that it does not exist any specific algorithm that performs always better than the others. The highly problem dependent nature of backanalysis makes it impossible to define a unique algorithm capable of overcoming every specific problem. However, what it has been possible to do was to develop a flexible and robust backanalysis methodology that is potentially expected to be capable to obtain competitive results in a wide range of geotechnical problems.

Using sophisticated constitutive models, which may contain complex parameters interconnections, makes it more likely to have none-unique solutions. The introduction of parameters prior information seems the most adequate procedure to redefine the problem to deal with the challenge of none-uniqueness.

Constitutive models that do not have interrelations among parameters are expected to be more suitable for geotechnical backanalysis.

The more sensitive the measurements are, the more likely it is to obtained satisfactory results. Even though the general knowledge points out that the higher the measurements are, the more sensitive they can be, it was shown here that this is not always the case. Nonetheless, as a general rule, it can be extrapolated that in most cases the higher the measurements are, the more sensitive they are likely to be.

Backanalyzing geotechnical problems extremely close to collapse can cause the contraction of the boundary conditions until forcing the minimum to be located on the boundary, which increases significantly the challenge of finding the minimum by genetic algorithms and gradient based methods.

Chapter 6

Case Study 1: Barcelona Metro Tunnel (Line 9)

6.1 Introduction

The main goal of a geotechnical backanalysis is to identify the soil parameters that match the mathematical model predictions with the measurements. However, in addition to that, in this chapter, the influence of the tunnel construction procedure, the type of measurements involved in the analysis, and the use or not use of the instruments error structure has been also studied.

In order to achieve those objectives, a simplified backanalysis (preliminary backanalysis, section 6.4) was defined to study the influence of different tunnel construction procedures and different types of measurements. For this preliminary backanalysis, it was considered appropriate, for the sake of simplicity, to identify just one soil parameter. Subsequently, a sophisticated backanalysis was defined to effectively identify various soil parameters, and to study the influence of the instruments error structure on their identification. Nonetheless, in both backanalyses the same numerical model and measurements were used to analyze a real tunnel construction.

6.2 Barcelona Metro Tunnel (Line 9)

The new Barcelona metro line 9, temporally on construction stand-by, will be the largest European metro line with a total of 47.8 km and 52 stations (see figure 6.1). The new line will connect the two sides of the city, from the Llobregat's river side to the Besos' river side (from

south to north), and more important, it will finally connect the Barcelona Airport with the city of Barcelona by metro.

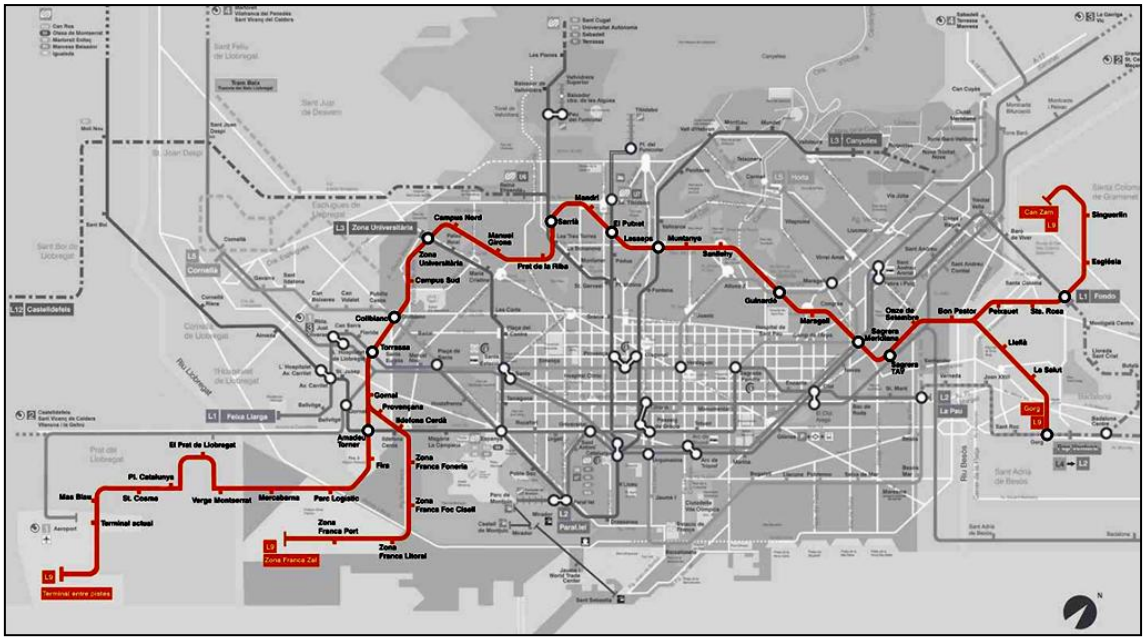

Figure 6.1. Barcelona metro line 9.

In terms of tunnel construction, 90% of the tunnel has been already finished, whereas in terms of stations construction less work has been completed; with only the north part of the line, between the stations of Can Zam and Onze de Setembre, under operation (9 stations and 7.8 km of line).

The majority of the excavation of the tunnel has been conducted by three Tunnel Boring Machines (TBM); a 12 meter diameter Earth Pressure Balance shield (EPB), two 9.4 meter diameter EPBs, and a 12 meter diameter Mix shield. From figure 6.2, it can be seen the cutting wheel and the back-up of the 9.4m EPB.

(a) **(b)**

Figure 6.2. 9.4 meters diameter EPB shield used to excavate part of the tunnel of the new Line 9 of the Barcelona Metro. (a) cutting wheel of the EPB. (b) back-up of the EPB.

The construction of the metro has faced many challenges related to the complexity of the geology of Barcelona (see figure 6.3), which includes a variety of soft deltaic deposits materials, and a huge block of granite that presents different levels of weathering, from intact rock to an almost soil behavior.

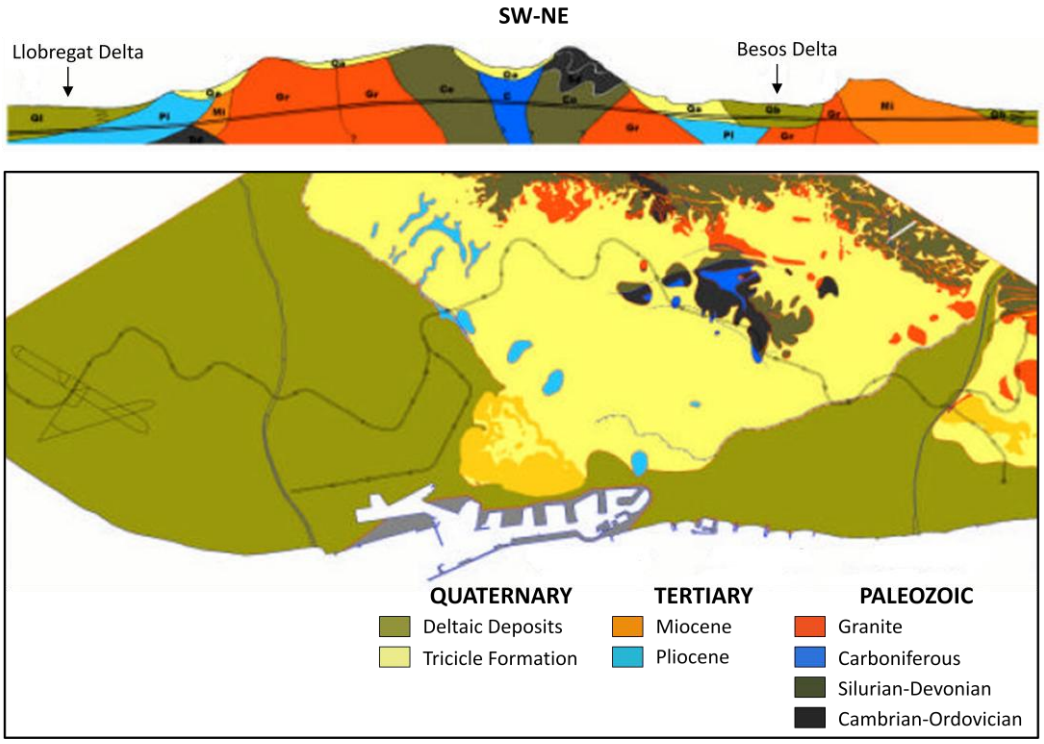

Figure 6.3. Longitudinal geological cross-section of the Barcelona Metro L9, and geological map of the Barcelona area (M. Filbà, 2006).

Because of the geotechnical and technical difficulties, associated with the construction of the tunnel, an extensive manual and automatic control system was implemented to keep track of movements caused by the tunnel construction. Furthermore, several highly instrumented cross-sections were placed along the tunnel to fully monitor surface and deep soil displacements, plus water table variations.

6.3 Analyzed Cross-Section

6.3.1 Introduction

A highly instrumented cross-section was selected to carry out the study presented in this chapter. The analyzed cross-section, named CP-IV, is located between the future stations of Mas Blau and St. Cosme (see figure 6.4).

The tunnel in this part of the line was excavated by means of the 9.4m EPB. In order to reduce the movements induced by the tunnel construction, three different pressures were systematically applied to the ground: the face pressure, the bentonite pressure, and the grouting pressure. All of these pressures are usually referred to them as TBM driving parameters, and they have been extensively studied to determine their actual influence on a tunnel construction. Some relevant results on that field can be seen in Wongsaroj et al. (2006), Di Mariano et al. (2009), and Gens et al. (2009).

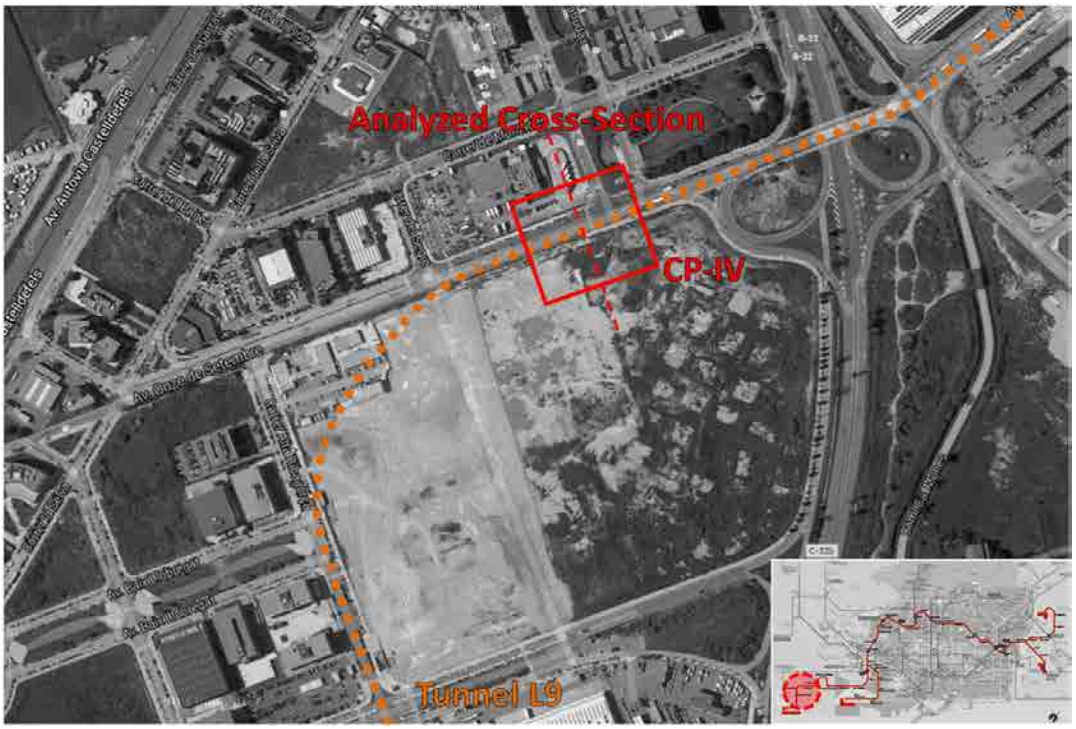

Figure 6.4. Location of the Analyzed Cross-Section (between Mas Blau station and St. Cosme station). (Image extracted from Google Maps).

The geological profile of the CP-VI is defined, from top to bottom, by 1m of man-made fill (Fill), 3m of brown fine silts (Ql1), 11m of gray fine sands with some gravels inclusions (Ql2), 20m of a gray mixture (Ql3) of silty clays with some interlayered sands, sandy silts, clay and silts, and 3m of sandy silts (Ql3s). Except for the fill layer, which has a man-made origin, all soil materials presented in CP-IV were deposited by the Llobregat River during the Quaternary age. The water table is nearly horizontal and is located 4 meters above sea level (see figure 6.5).

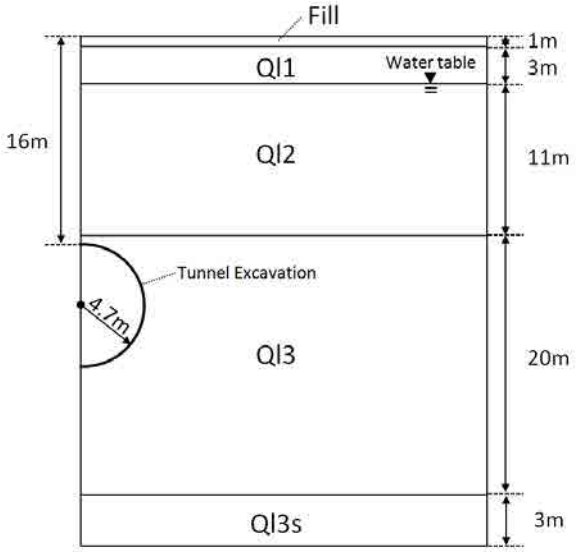

Figure 6.5. Geological profile of the Analyzed Cross-Section CP-IV.

The running tunnel was lined with 8.43m inner diameter pre-cast segment concrete rings. The rings are formed by segments of 1.5m length and 0.32m thick (6 segments + 1 key per ring). The tunnel crown in CP-IV is located at 16m depth.

In figure 6.6, a scheme and a picture of the tunnel lining is shown.

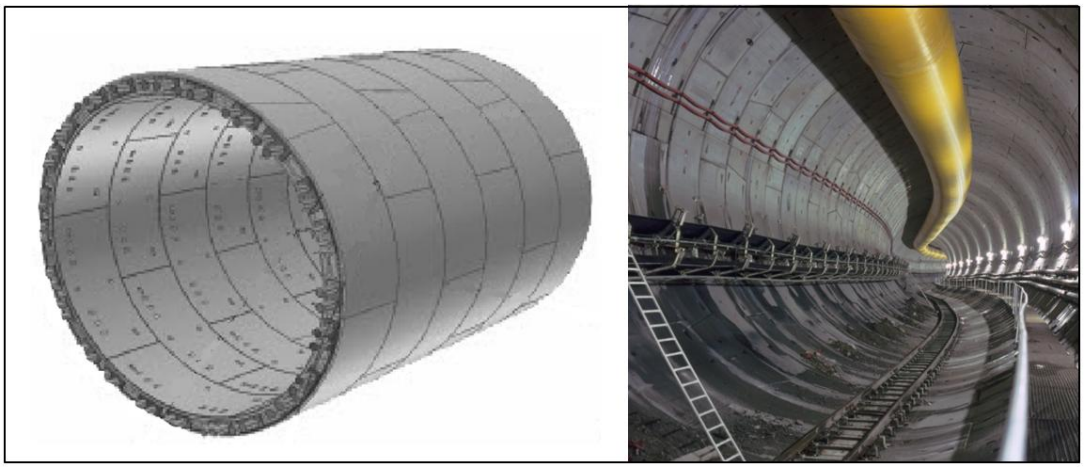

Figure 6.6. Scheme and picture of the tunnel lining of the Barcelona Metro L9 (tunnel excavated by the 9.4m EPB).

6.3.2 In Situ Measurements

The in situ measurements used to carry ou the backanalysis were extracted from the instrumentation placed on the cross-section CP-IV. Around 20 instruments were installed in CP-IV: 6 combined surface points (horizontal and vertical displacements), 6 vertical surface points, 2 inclinometers, 4 sliding micrometers, and 4 piezometers. However, due to the uncertanties related to the measurement process, it was considerd more apropriate to use only some of the measurements that have been studied in more depth (Gens et al., 2009, and Yubero, 2015). In figure 6.7, the location of all the instruments are shown (the ones that were used and also the ones that were not used in the analysis).

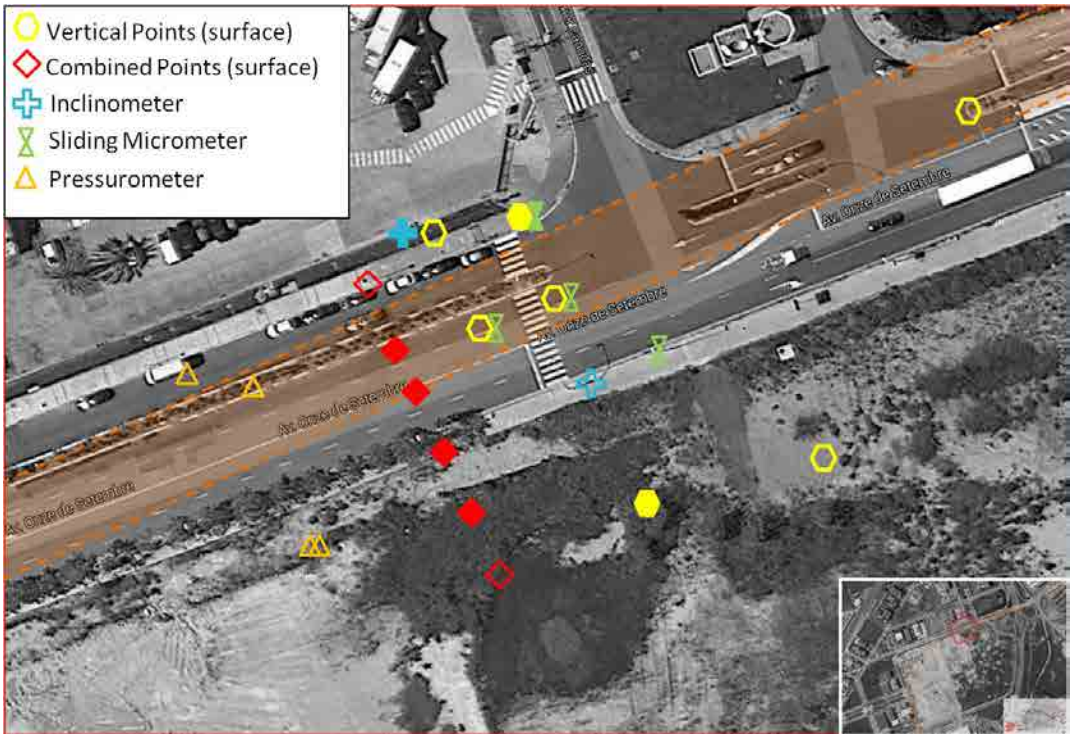

Figure 6.7. CP-IV instrumentation. Only the instruments with filled symbol labels were used. (Image extracted from Google Maps).

Even though the instruments were not located in the same precisely cross-section, the instruments used for the analysis (4 combined surface points, 2 vertical surface points, 1 inclinometer, and 1 sliding micrometer) were supposed to be located in the same cross-section (analyzed cross-section, see figure 6.4). Moreover, the problem was considered symmetric. Therefore, displacements equal to those obtained from the sliding micrometer and the inclinometer, located in the opposite side to where the combined points were placed, were assumed to occur on the other side.

Two different set of measurements were used to describe the short term and the long term behavior. The short term measurements were associated with the movements that had occurred three days after the excavation with the EPB face about 75m away from the analyzed cross-section. The rest of the movements were associated with the long term behavior of excess pore water dissipation (consolidation). A total of 58 measurements for each case (short and long term) were used to carry out the backanalysis. The measurements are shown in figure 6.8.

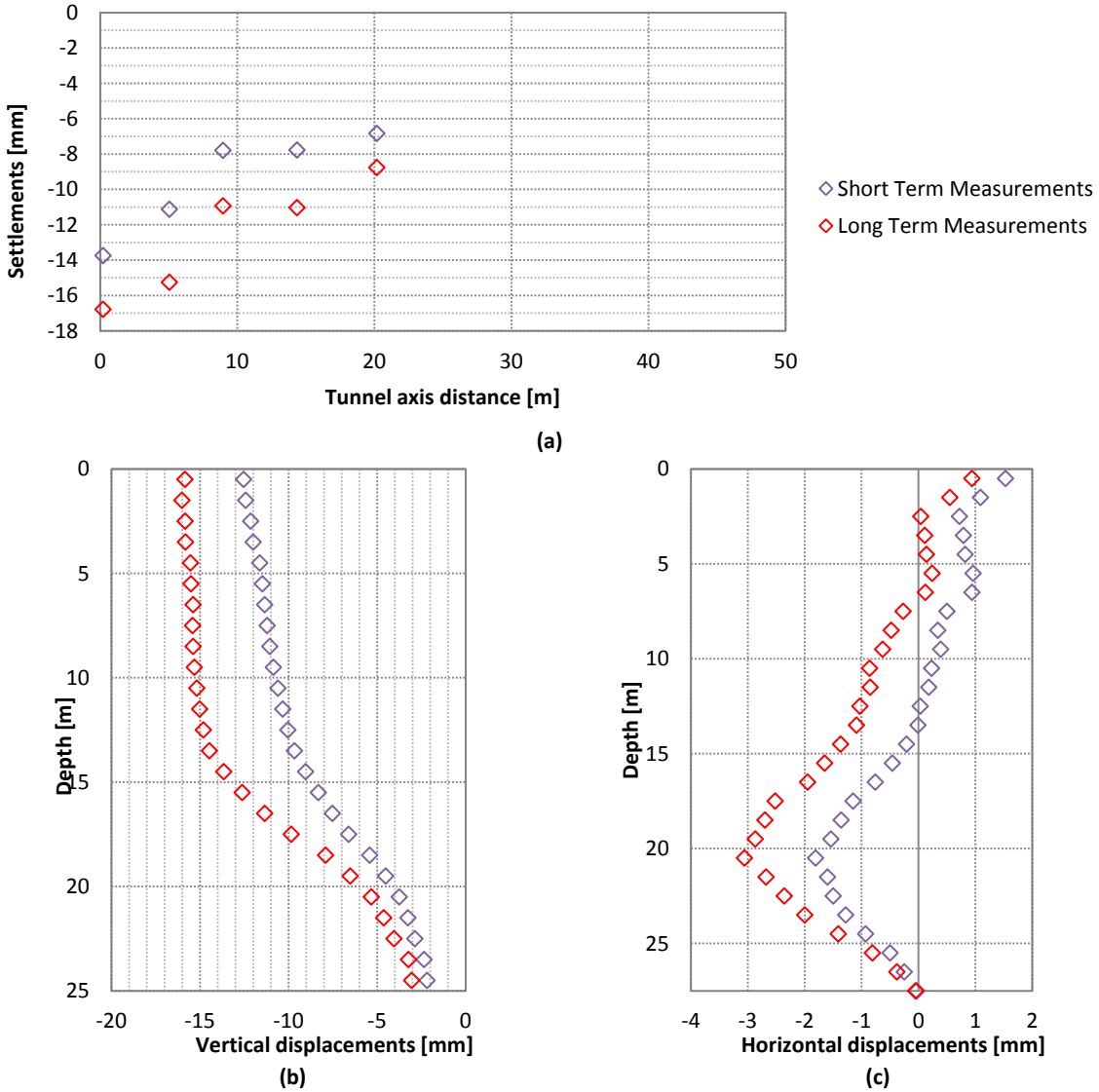

Figure 6.8. In situ measurements of CP-IV. (a) settlements extracted from the combined and the vertical points. (b) vertical displacements extracted from the sliding micrometer. (c) horizontal displacements extracted from the inclinometer.

6.4 Numerical model

The commercial geotechnical software Plaxis 2D (version 9) was used to build a two-dimensional numerical model of the cross-section CP-IV. The hypotheses of plane strain and symmetric behavior were adopted. The model is 100 meters wide and 40 meters high. The rest of the geometrical aspects, such as the geological layers and the tunnel excavation, are presented in figure 6.5. 1013 15-node triangle elements were used to discretize the geometry of the problem; consequently, 8408 nodes and 12156 stress points were generated (see figure 6.9).

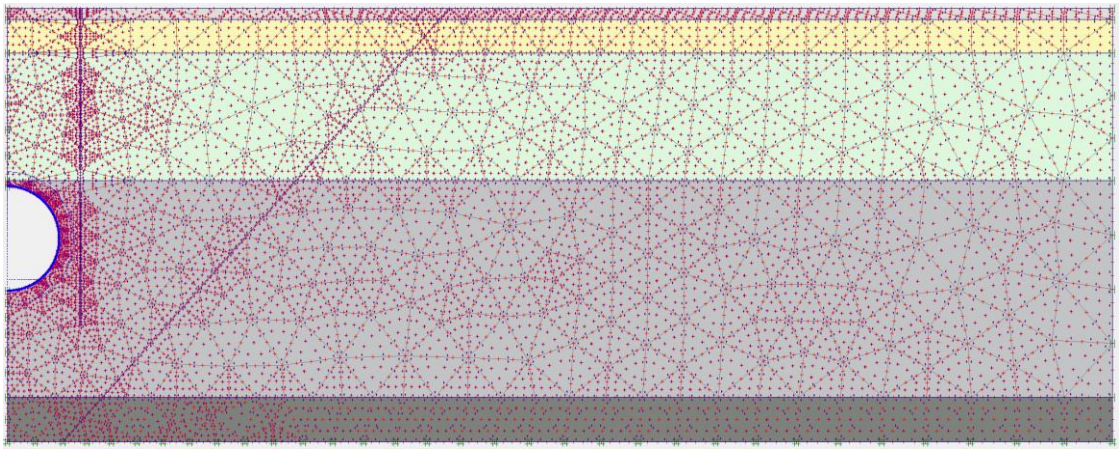

Figure 6.9. Numerical model of cross-section CP-IV. The red and purple dots represent the nodes and the stress points respectively.

The soil parameters used in the study, presented in table 6.1, were directly extracted from Gens et al. (2009), except the internal friction angle and the stiffness moduli of Ql3, which were considered as the unknowns of the backanalysis problem.

The tunnel dimensions correspond to those of the EPB cutting wheel (9.4m) and it was considered impervious, not letting the water flow though the lining. In order to simulate the soil-structure interaction, an interface was defined adjacent to the outer side of the tunnel. The structural properties of the lining are shown in table 6.2.

Parameter	Fill	Ql1	Ql2	Ql3	Ql3s
Constitutive Model	M-C	Hardening	Hardening	Hardening	Hardening
Soil Type	Undrained	Undrained	Drained	Undrained	Undrained
γ_{unsat} [kN/m^3]	17.5	14.7	17.5	13.8	14.7
γ_{sat} [kN/m^3]	17.5	19.5	21.3	18.8	19
k_x [m/day]	-	8.6E-4	8.64	8.6E-4	8.6E-4
k_y [m/day]	-	8.6E-4	8.64	8.6E-4	8.6E-4
E [kN/m^2]	10000	-	-	-	-
E_{50}^{ref} [kN/m^2]	-	19300	22500	unknown	14900
E_{oed}^{ref} [kN/m^2]	-	17000	19200	$E_{oed}^{ref} = 0.8E_{50}^{ref}$	14300
E_{ur}^{ref} [kN/m^2]	-	57900	67500	unknown	44700
m [-]	-	0.9	0.5	0.9	0.6
c [kN/m^2]	0.1	1	1	1	0.2
φ [deg]	26	29	32	unknown	28
ψ [deg]	0	0	0	0	0
ν [-]	0.3	-	-	-	-
ν_{ur} [-]	-	0.2	0.2	0.2	0.2
p^{ref} [kN/m^2]	-	100	100	100	100
K_0^{NC} [-]	-	$1 - \sin\varphi$	$1 - \sin\varphi$	$1 - \sin\varphi$	$1 - \sin\varphi$

R_f [-]	0.9	0.9	0.9	0.9	0.9
$\sigma_{tension}$ [kN/m^2]	0	0	0	0	0
$c_{increment}$ [kN/m^2/m]	0	0	0	0	0
R_{inter} [-]	1	0.6	0.6	0.6	0.6

Table 6.1. Soil parameters used to define the numerical model of cross-section CP-IV (Gens et al., 2009).). γ_{unsat}: unsaturated soil weight, γ_{sat}: saturated soil weight, k_x and k_y: horizontal and vertical permeability, E: Young's modulus, E_{50}^{ref}: secant stiffness in standard drained triaxial test, E_{oed}^{ref}: tangent stiffness for primary oedometer loading, E_{ur}^{ref}: unloading/reloading stiffness, m: power for stress-level dependency of stiffness, c: effective cohesion, φ: effective angle of internal friction, ψ: angle of dilatancy, ν: Poisson's ratio, ν_{ur}: Poisson's ratio for unloading/reloading, p^{ref}: Reference stress for stiffnesses, K_0^{NC}: coefficient of lateral earth pressure for normal consolidation, R_f: Failure ratio, $\sigma_{tension}$: Tensile strength, $c_{increment}$: cohesion increment with depth, and R_{inter}: strength reduction factor for interfaces.

Parameter	Description	Value
Material type	Constitutive model	elastic
EA	Axial stiffness	1.216·10^7 [kN/m]
EI	Flexural rigidity	1.0376·10^5 [kNm^2/m]
d_{eq}	Equivalent thickness	0.32 [m]
w	Weight	8 [kN/m/m]
ν	Poisson's ratio	0.2 [-]

Table 6.2. Structural properties of the tunnel lining. EA: axial stiffness; EI: flexural rigidity; w: weight; v: Poisson's ratio.

As previously mentioned, different tunnel construction procedures have been studied to determine the one that better suits the problem. Therefore, the different construction phases are not presented in this section, due to the fact that each procedure has a different scheme, and it was not considered as a general intrinsic aspect of the model but rather a specific manner to define the problem.

6.5 Preliminary Backanalysis: Tunnel Construction Procedures (Plaxis 2D)

6.5.1 Introduction

It is well known that a tunnel excavation by means of an EPB is a three-dimensional problem, and it should be strictly tackled three-dimensionally. However, even with the increase of computers capability, the time consumption for carrying out a three-dimensional numerical analysis nowadays is still too high. That computational cost makes the 3D backanalysis approach not feasible for a day to day basis. Therefore, in the last three decades, many methodologies have been presented to extrapolate the three-dimensional approach to a simpler and less expensive computational cost two-dimensional one.

In Möller (2006) and Möller & Vermeer (2008), a brief review of the aspects of such two-dimensional approaches is presented, as well as the definition of a new one. Traditionally, the different approaches have been classified by their nature, which can be based on prescribed displacements or any type of stress modification around the excavation. The most common approaches for stress modification are the stress reduction method and the grout pressure method. Consequently, the classification that nowadays is being generally accepted is constituted by three different types of methods:

- Prescribed Displacements Methods.

- Stress Reduction Methods.

- Grout Pressure Methods.

In the following sections (6.5.2, 6.5.3 and 6.5.4), three different tunnel construction procedures have been chosen to study their influence on the framework of backanalysis. A modified tunnel lining contraction method has been defined to represent the prescribed displacements methods. To represent the stress reduction methods, the popular ΣMStage method (also known as *β-Method*) has been selected, while the grout pressure method presented by Möller (2006) has also been adopted to finally consider all types of methods.

Moreover, apart from the strictly tunnel construction procedure analysis, the influence of using short and long term measurements has been also studied, as well as the type of instruments used to extract the measurements.

6.5.2 Definition

The preliminary backanalysis has focused on studying the morphology of the objective function shape. Depending on the tunnel construction procedure and the type of measurements, different objective functions shapes are obtained. Therefore, by studying their morphology and the differences among them, it is expected to determine the most suitable tunnel construction procedure, and the influence of the measurements.

For the sake of simplicity, and especially in terms of graphical representation, it was considered appropriate to link the three stiffness moduli of Ql3, and treat them as a unique parameter to identify. The Plaxis recommended relationship was used to link them ($E_{oed}^{ref} = 0.8 \cdot E_{50}^{ref}$ and $E_{ur}^{ref} = 3 \cdot E_{50}^{ref}$). Moreover, the contraction, the ΣMStage, and the grout pressure were also considered as parameters to identify. However, for this preliminary backanalysis, the internal friction angle was not implemented as a parameter to identify; and the value of 27.5^0, proposed by Gens et al. (2009), was used.

Therefore, in order to graphically represent the objective function, and subsequently study its morphology, a few thousands direct problems were evaluated. Specifically, 1300 combinations of E_{50}^{ref} (from 5000kN/m^2 to 125000kN/m^2, in increments of 100kN/m^2) and Lining Contraction (from 0.3 to 0.6, in increments of 0.025), 1100 combinations of E_{50}^{ref} (from 5000kN/m^2 to 125000kN/m^2, in increments of 100kN/m^2) and ΣMStage (from 0.05 to 0.3, in increments of 0.025), and 900 combinations of E_{50}^{ref} (from 5000kN/m^2 to 125000kN/m^2, in increments of 100kN/m^2) and Grout Pressure (1.5, 1.75, 2, 2.125, 2.25, 2.375, 2.5, 2.75 and 3bars) were defined for that purpose. The simple Least-Squares method was used to define the objective function (eq. 2.1).

Due to the parameters values discretization (many more values of E_{50}^{ref} than tunnel construction parameters) and the gridding method used to plot the objective function, the results presented in the following sections (6.5.3, 6.5.4 and 6.5.5) can locally present some graphical misrepresentation of the objective function shape. Nonetheless, its general morphology can be considered fully valid.

A sensitivity analysis was carried out to determine the most suited gridding method to better represent the shape of the objective function. Among the different options that the contouring

and surface modeling software *Surfer 10* offers, the Kriging method seemed to yield the best results.

6.5.3 The Modified Tunnel Lining Contraction Method

The modified tunnel lining construction method is based on the original contraction method defined by Vermeer & Brinkgreve (1993), where the ground loss is simulated by a certain tunnel contraction. As pointed out in Möller (2006), the original contraction method tends to generate a homogeneous radial displacement distribution towards the center of the tunnel. The reason of that homogeneous distribution is due to the large stiffness difference between the lining and the ground. This causes unrealistic ground loss distributions and subsequently unrealistic results for both surface settlements and deep ground movements too. Therefore, here, the basic idea of the GAP method, presented by Rowe et al. (1983), has been adopted and combined with the original approach to overcome the intrinsic limitation of applying an almost homogeneous prescribed displacements distribution. In the GAP method, the ground loss is considered in terms of a vertical gap between the tunnel lining and the actual excavation, assuming that the gap is located at the crown of the lining, thus generating more realistic ground movement distributions.

The implementation of the modified tunnel lining contraction method on Plaxis is carried out by means of prescribing some displacements at the bottom of the tunnel and applying a lining contraction. The objective of prescribing displacements at the bottom of the tunnel is to restrict the displacements on that part of the tunnel and subsequently to force the lining contraction to concentrate the displacements on the crown. Both prescribed displacements and lining contraction are applied in the same calculation phase. The definition of the magnitude of the prescribed displacements is based on geometrical aspects related to the excavation and the equipment used to excavate it. For this particular case study, the prescribed displacements were set to 5mm.

In figure 6.10, the comparison between the original contraction method, described by Vermeer & Brinkgreve (1993), and the modified tunnel lining construction method defined here is illustrated.

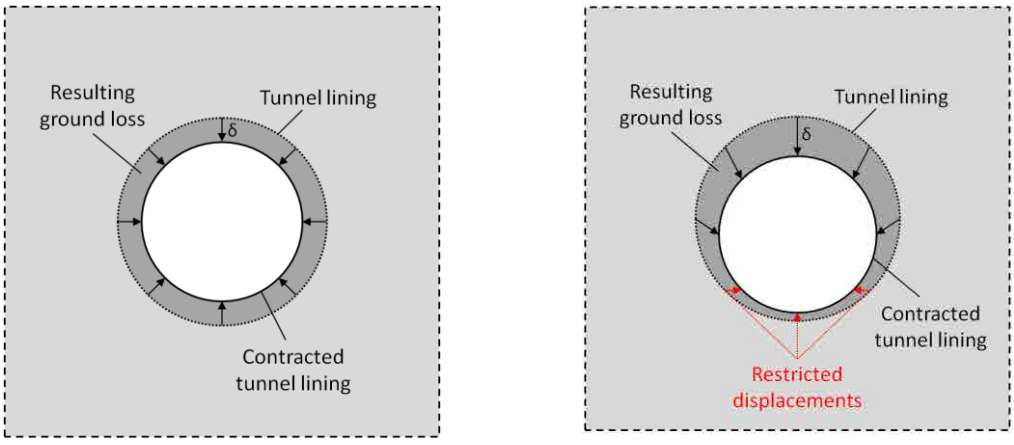

Figure 6.10. (a) Original contraction method. (b) Modified tunnel lining contraction method.

Finally, the full tunnel construction procedure is presented in table 6.3.

Plaxis phase (stage)	Description
0	Initial stress generation => K_0 method.
1	Tunnel construction by means of the modified tunnel lining contraction => Application of the Plaxis tunnel contraction while restricting the vertical displacements of some points located on the bottom of the tunnel lining (5mm). The water inside the tunnel is removed (dry cluster).
2	Consolidation => All excess water pore pressure is dissipated (t=365days)

Table 6.3. Tunnel construction stages defined in the numerical model (Plaxis). Case: Modified Tunnel Lining Contraction Method.

6.5.3.1 Results

The different objective functions shapes, obtained from using simultaneously all instruments in full, short, and long term (full term = short term + long term), are illustrated in the following figures (figure 6.11, 6.12 and 6.13).

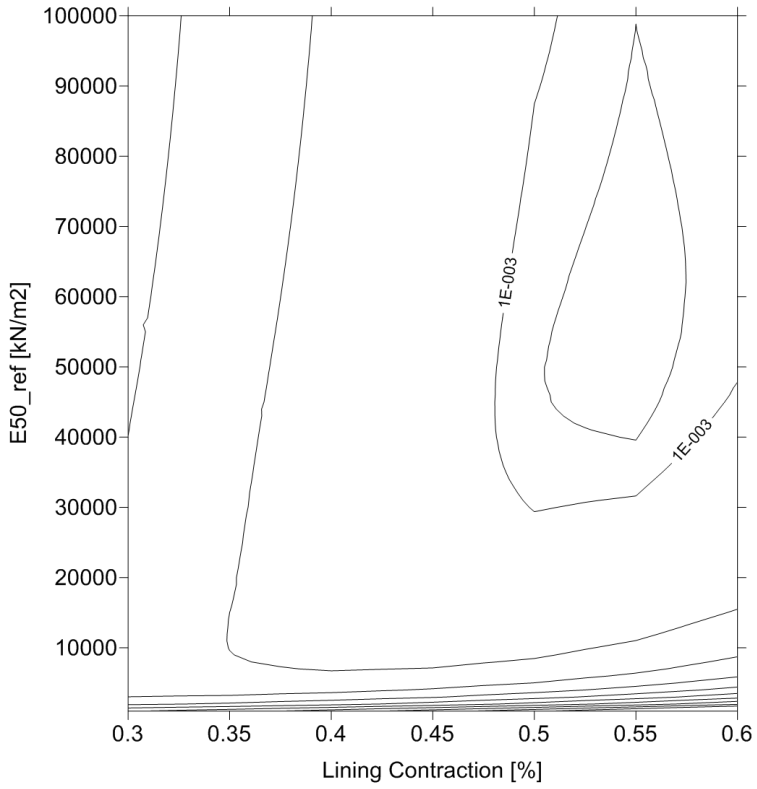

Figure 6.11. Mapping of the objective function [m^2] for full term behavior and all instruments measurements (Modified Tunnel Lining Contraction Method).

As figure 6.11 shows, even having a morphology capable of describing a global minimum, the large distance between contour lines leads to a wide range of different combinations of E_{50}^{ref} and lining contraction that have similar value of objective function. Therefore, no promising results are expected to obtain while using simultaneously short and long term measurements from all instruments. However, by studying the difference between the results obtained from short and long term behavior (figure 6.12 and figure 6.13), a better understanding of what is happening can be obtained.

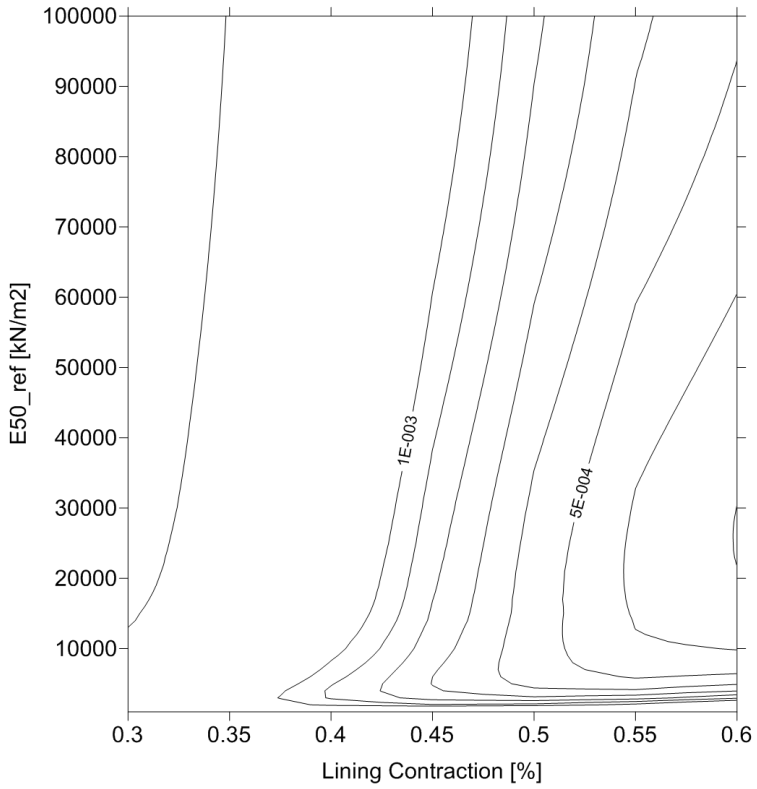

Figure 6.12. Mapping of the objective function [m^2] for short term behavior and all instruments measurements (Modified Tunnel Lining Contraction Method).

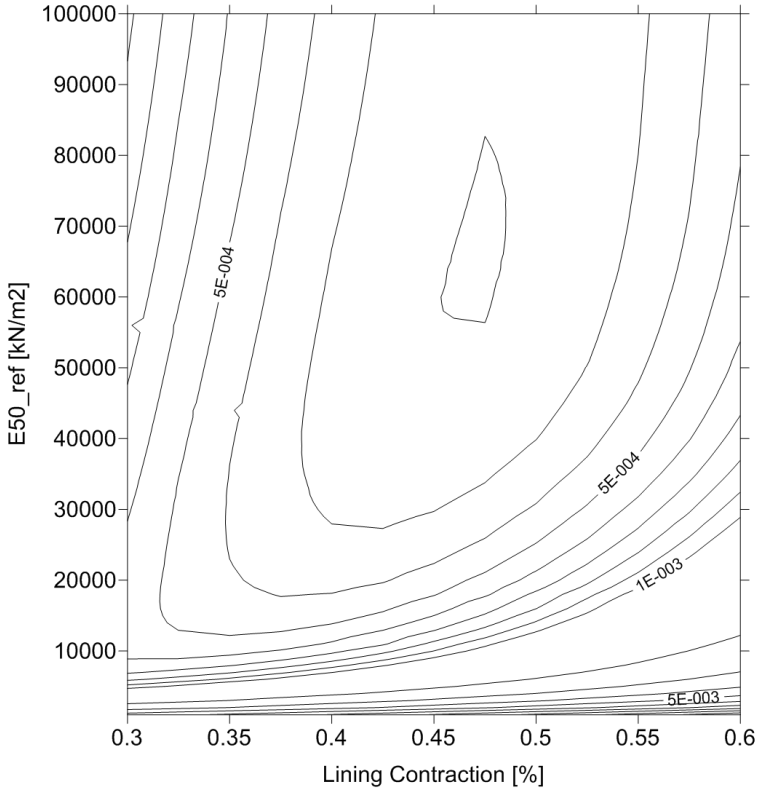

Figure 6.13. Mapping of the objective function [m^2] for long term behavior and all instruments measurements (Modified Tunnel Lining Contraction Method).

Surprisingly, the results obtained from long term behavior have significantly improved the morphology of the objective function in terms of delimiting a narrower global minimum and surroundings, which helps to identify the parameters. A certain improvement was expected due to the effect of the consolidation, but not as much as it was obtained.

On the other hand, figure 6.12 indicates that the measurements from short term behavior are little sensitive to soil stiffness. A similar conclusion was presented in Sagaseta (1987) for incompressible material, where it was stated that the strain field is independent from the soil stiffness.

Unfortunately, different solutions of the same problem have been obtained when using short, long, and full term measurements. Assuming that the model was correct, and the measurements had the same error uncertainties, no differences among solutions should be expected.

Strictly focusing on the value of the error between measurements and calculations, the use of long term measurements has provided the better solution of the problem (see table 6.4).

Measurements		Contraction [%]	E_{50}^{ref} [kN/m^2]	Error [m^2]
Time	**Instruments**			
Full Term	All instruments (116 measurements)	0.55	58000	$8.42 \cdot 10^{-4}$
Short Term	All instruments (58 measurements)	0.60	26000	$2.97 \cdot 10^{-4}$
Long Term	All instruments (58 measurements)	0.475	66000	$1.94 \cdot 10^{-4}$

Table 6.4. Best combinations of tunnel lining contraction and E_{50}^{ref}, while using the modified tunnel contraction method.

The same happens If the results are graphically compared in terms of displacements (see figure 6.14, 6.15 and 6.16).

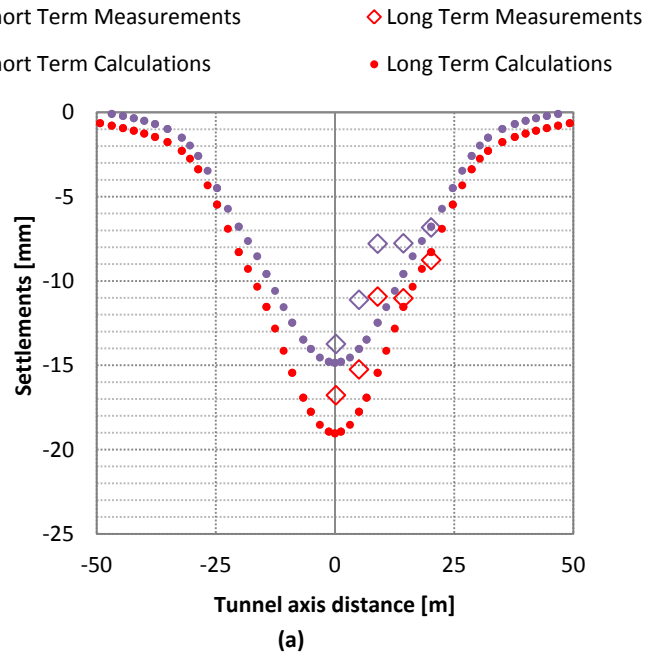

(a)

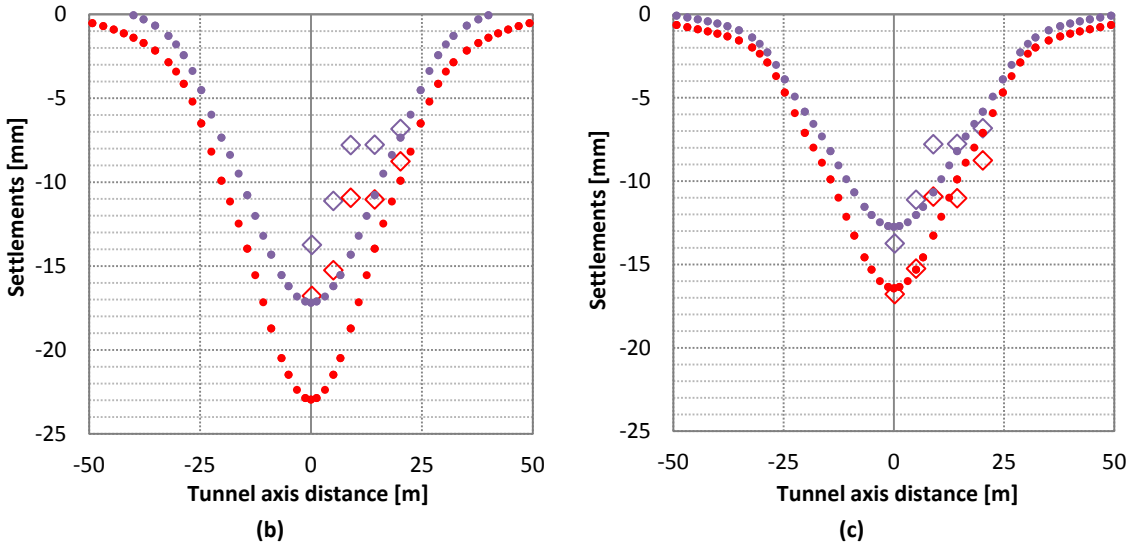

Figure 6.14. Comparison between measured and calculated settlements. (a) Best combination of tunnel lining contraction and E_{50}^{ref} using full term measurements. (b) Best combination of tunnel lining contraction and E_{50}^{ref} using short term measurements. (c) Best combination of tunnel lining contraction and E_{50}^{ref} using long term measurements. (Modified Tunnel Lining Contraction Method).

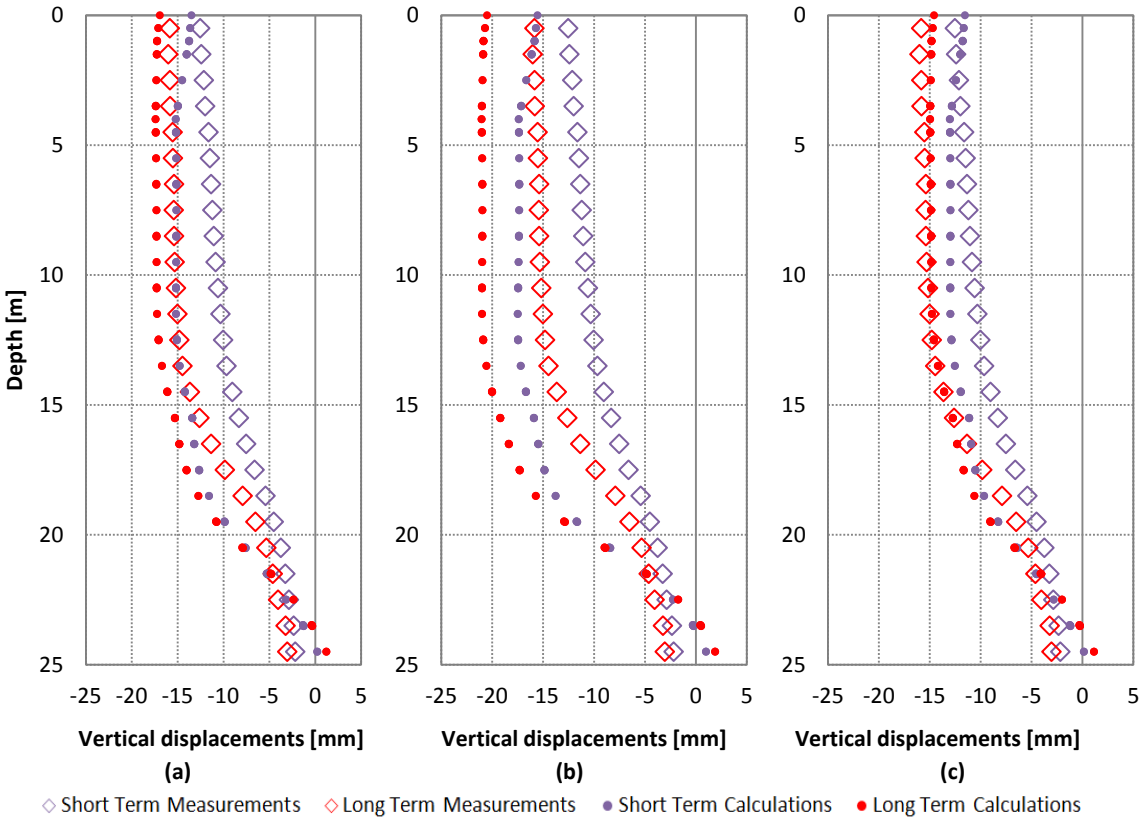

Figure 6.15. Comparison between measured and calculated vertical displacements (Sliding Micrometer). (a) Best combination of tunnel lining contraction and E_{50}^{ref} using full term measurements. (b) Best combination of tunnel lining contraction and E_{50}^{ref} using short term measurements. (c) Best combination of tunnel lining contraction and E_{50}^{ref} using long term measurements. (Modified Tunnel Lining Contraction Method).

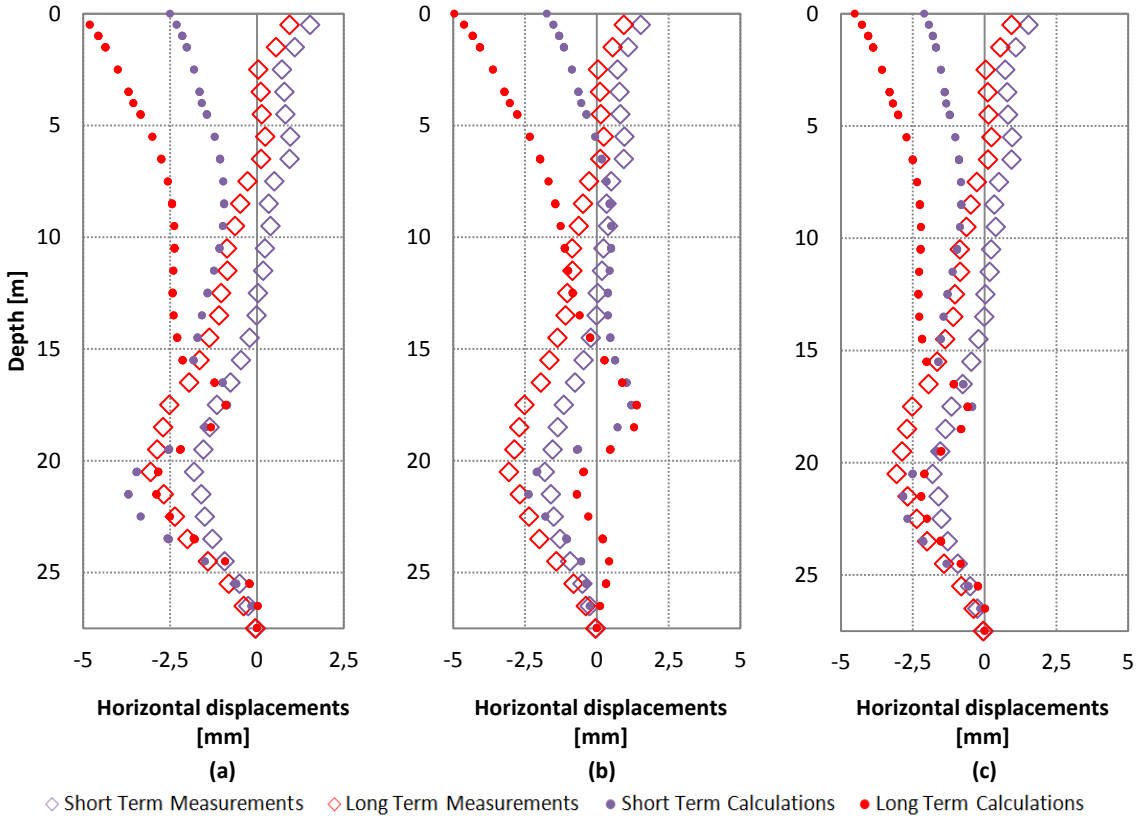

Figure 6.16. Comparison between measured and calculated horizontal displacements (Inclinometer). (a) Best combination of tunnel lining contraction and E_{50}^{ref} using full term measurements. (b) Best combination of tunnel lining contraction and E_{50}^{ref} using short term measurements. (c) Best combination of tunnel lining contraction and E_{50}^{ref} using long term measurements. (Modified Tunnel Lining Contraction Method).

In Appendix A, the objective functions defined by means of each type of instrument are presented for further analyses.

6.5.4 The ΣMStage Method (also known as *β-Method*)

Initially, the ΣMStage method was intended to be applied when simulating conventional tunnel constructions, where the stress ground relaxation and the load sharing between lining and ground are naturally addressed by the method. However, Muir (1975) extended that idea to shield tunnelling, where nowadays it is quite often used.

The method is based on reducing the initial ground pressure (σ_0), which is acting on the inside of the excavation, by 1 - ΣMStage, with 0 < ΣMStage < 1, and then installing the lining to finally support the ground (see figure 6.17). Unfortunately, the proper value of the ΣMStage is not easy to determine, in part, due to the fact that it just not only represents one geotechnical phenomenon or property, but a combination of several of them suggesting that ΣMStage can be considered as a parameter to identify.

In table 6.5, the different calculation phases defined in Plaxis are presented.

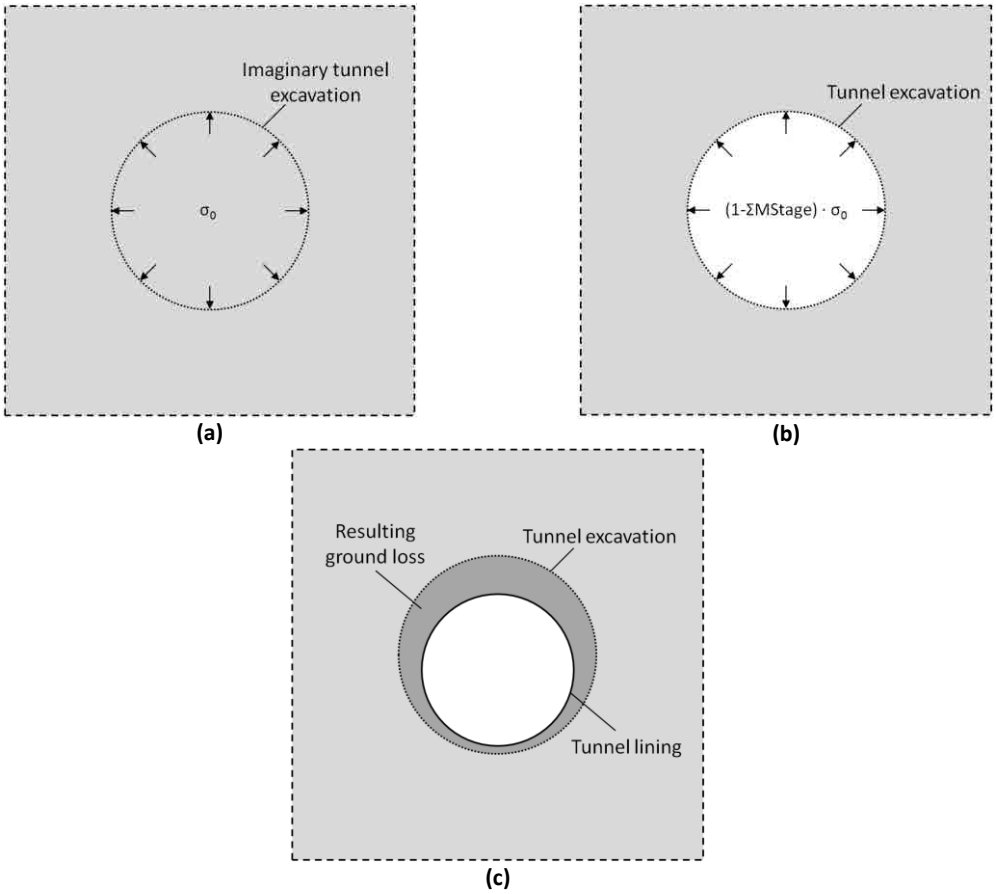

Figure 6.17. ΣMStage tunnel construction procedure scheme. (a) Initial stress state. (b) Ground relaxation. (c) Tunnel lining installation.

Plaxis phase (stage)	Description
0	Initial stress generation => K_0 method.
1	Tunnel excavation => Deactivation of the soil inside the excavation, and application of a ΣMStage<1. The water inside the tunnel is removed (dry cluster).
2	Tunnel lining installation => Activation of the lining (at the end of the Phase => ΣMStage = 1)
3	Consolidation => All excess water pore pressure is dissipated (t=365days)

Table 6.5. Tunnel construction stages defined in the numerical model (Plaxis). Case: ΣMStage Method.

6.5.4.1 Results

The different objective functions shapes, obtained from using simultaneously all instruments in full, short, and long term, are illustrated in the following figures (figure 6.18, 6.19 and 6.20).

At first glance, similar objective function morphologies can be appreciated in figures 6.18, 6.19 and 6.20. However, differences between the locations of the minima can also be observed. The differences are associated with the measurements uncertainties, especially those derived from the difficulty of determining the exact moment to extract the short term measurements, and the impossibility of the numerical model to fully capture the full term behavior.

Strictly focusing on the value of the error between measurements and calculations, the use of long term measurements has provided the better solution to the problem (see table 6.6).

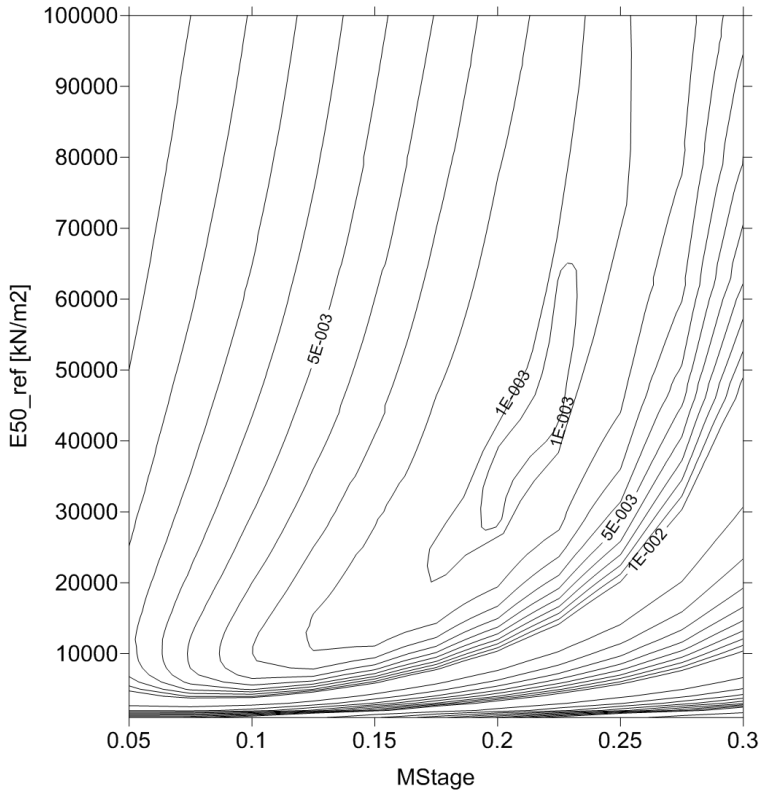

Figure 6.18. Mapping of the objective function [m^2] for full term behavior and all instruments measurements (ΣMStage Method).

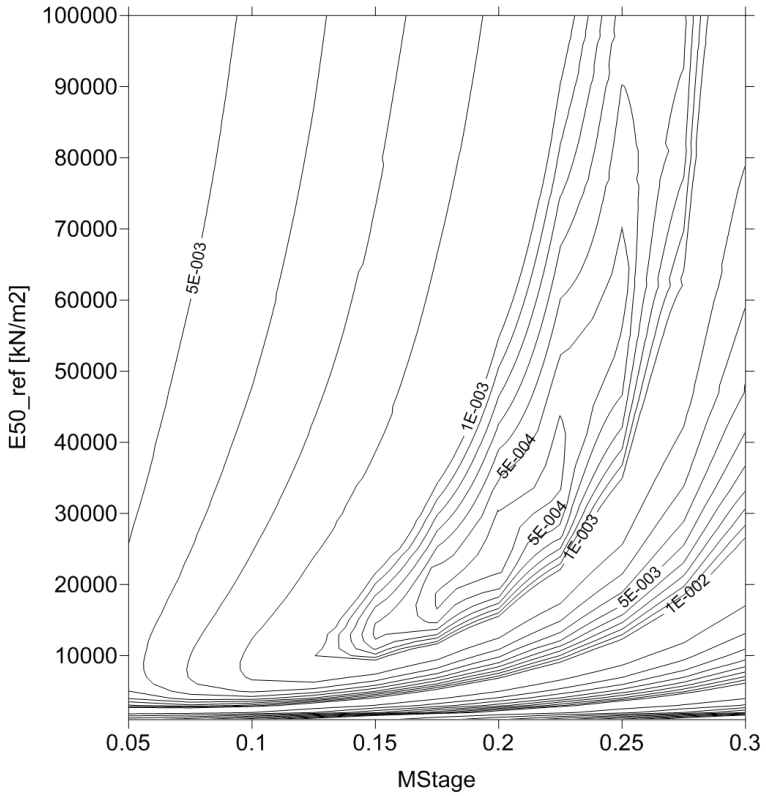

Figure 6.19. Mapping of the objective function [m^2] for short term behavior and all instruments measurements (ΣMStage Method).

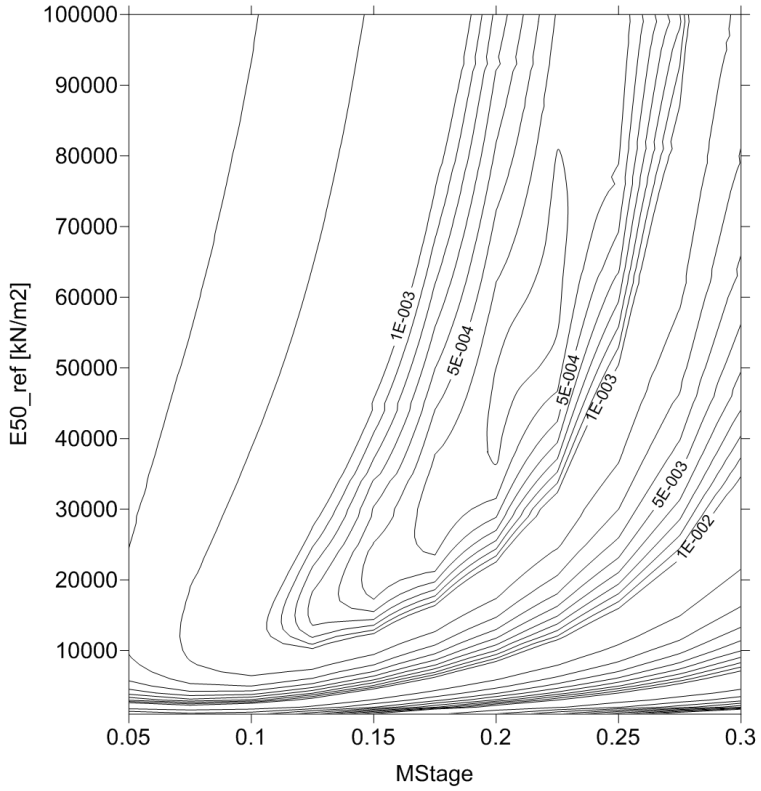

Figure 6.20. Mapping of the objective function [m^2] for long term behavior and all instruments measurements (ΣMStage Method).

Measurements		ΣMStage	E_{50}^{ref} [kN/m^2]	Error [m^2]
Time	**Instruments**			
Full Term	All instruments (116 measurements)	0.200	33000	$8.10 \cdot 10^{-4}$
Short Term	All instruments (58 measurements)	0.200	25000	$3.36 \cdot 10^{-4}$
Long Term	All instruments (58 measurements)	0.225	66000	$2.64 \cdot 10^{-4}$

Table 6.6. Best combinations of tunnel lining contraction and E_{50}^{ref}, while using the ΣMStage method.

Unfortunately, even having a relatively good objective function morphology, slightly variations of ΣMStage, close to the minimum, causes significant variations of E_{50}^{ref}. For instance, if for long term measurements the ΣMStage is set to 0.200, the value of E_{50}^{ref} reduces to 43000kN/m^2, with an associated error of $2.69 \cdot 10^{-4} m^2$, which is almost the same value obtained while using ΣMStage=0.225 (see table 6.6). The same happened for short and full term measurements.

The graphical comparison between measurements and calculations associated with the values of table 6.6 are sown in figures 6.21, 6.22 and 6.23.

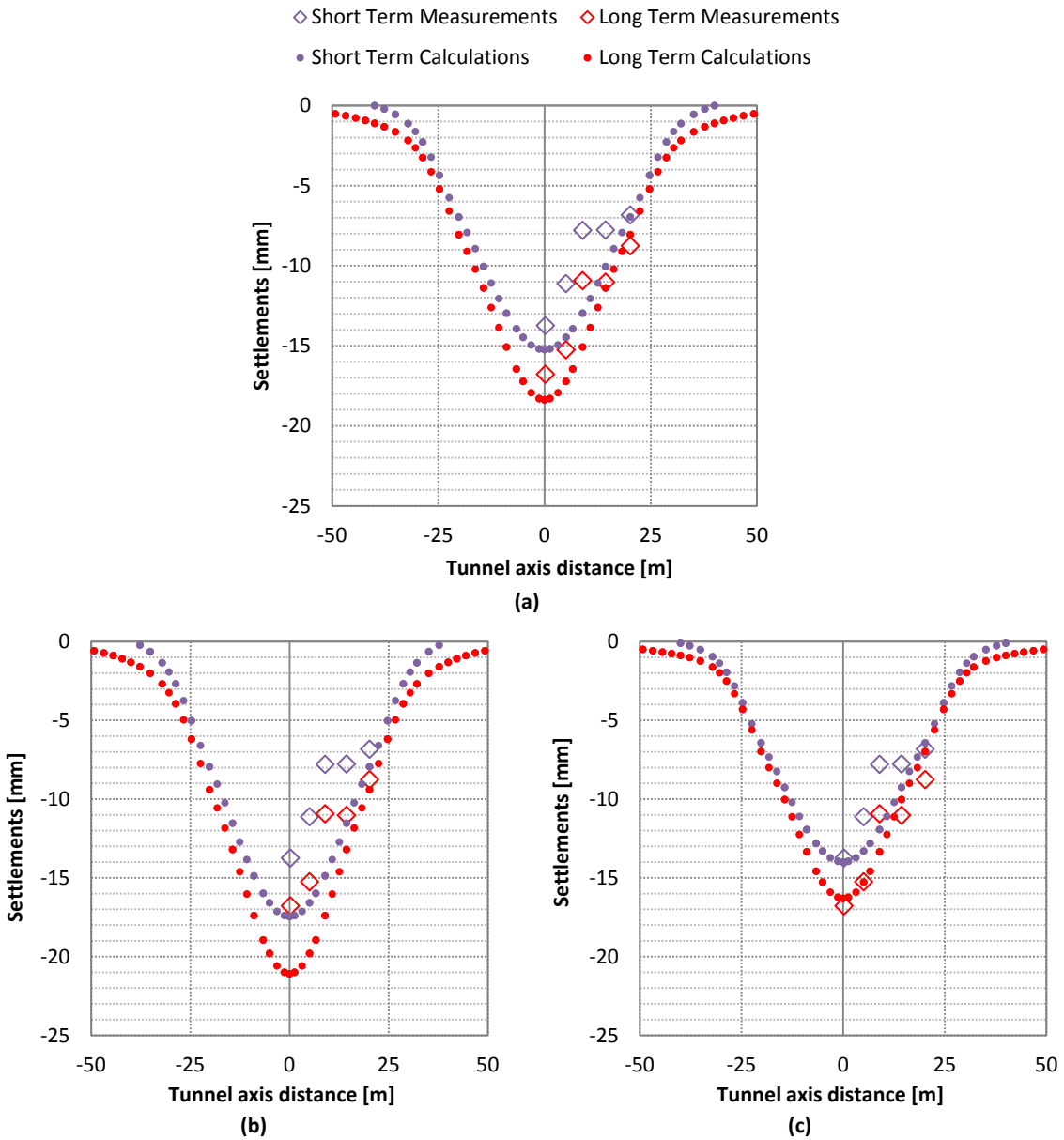

Figure 6.21. Comparison between measured and calculated settlements. (a) Best combination of ΣMStage and E_{50}^{ref} using full term measurements. (b) Best combination of ΣMStage and E_{50}^{ref} using short term measurements. (c) Best combination of ΣMStage and E_{50}^{ref} using long term measurements. (ΣMStage Method).

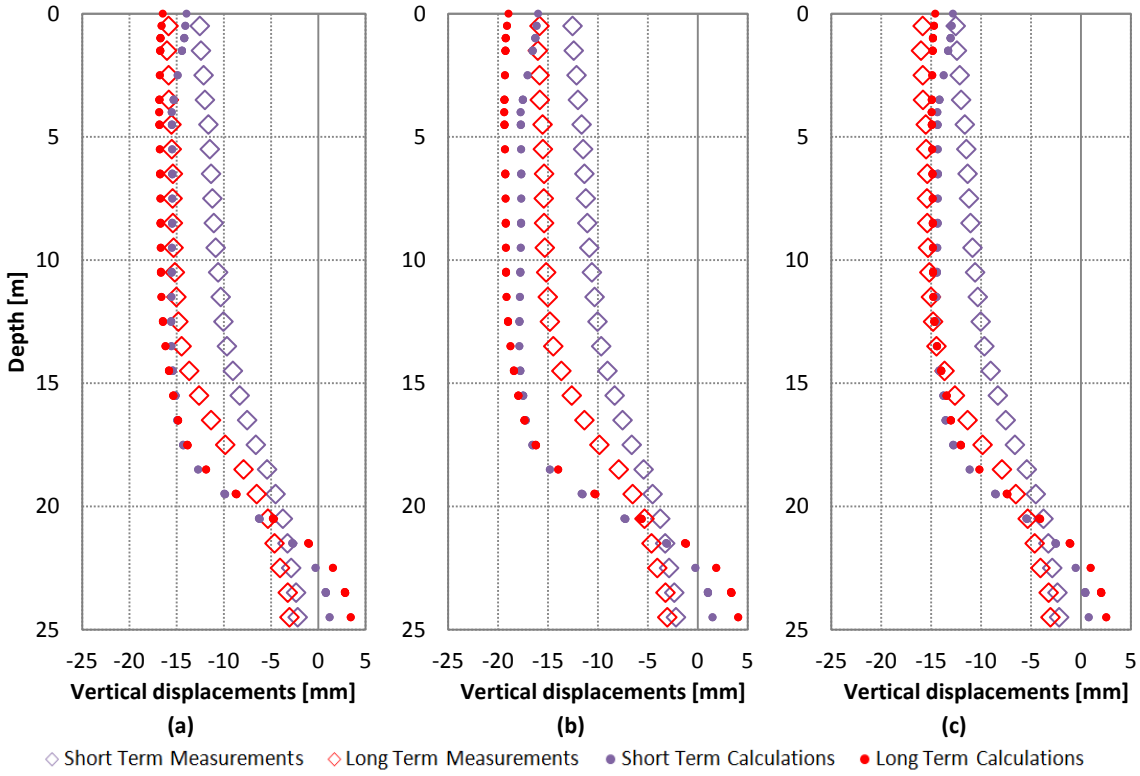

Figure 6.22. Comparison between measured and calculated vertical displacements (Sliding Micrometer). (a) Best combination of ΣMStage and E_{50}^{ref} using full term measurements. (b) Best combination of tunnel ΣMStage and E_{50}^{ref} using short term measurements. (c) Best combination of ΣMStage and E_{50}^{ref} using long term measurements. (ΣMStage Method).

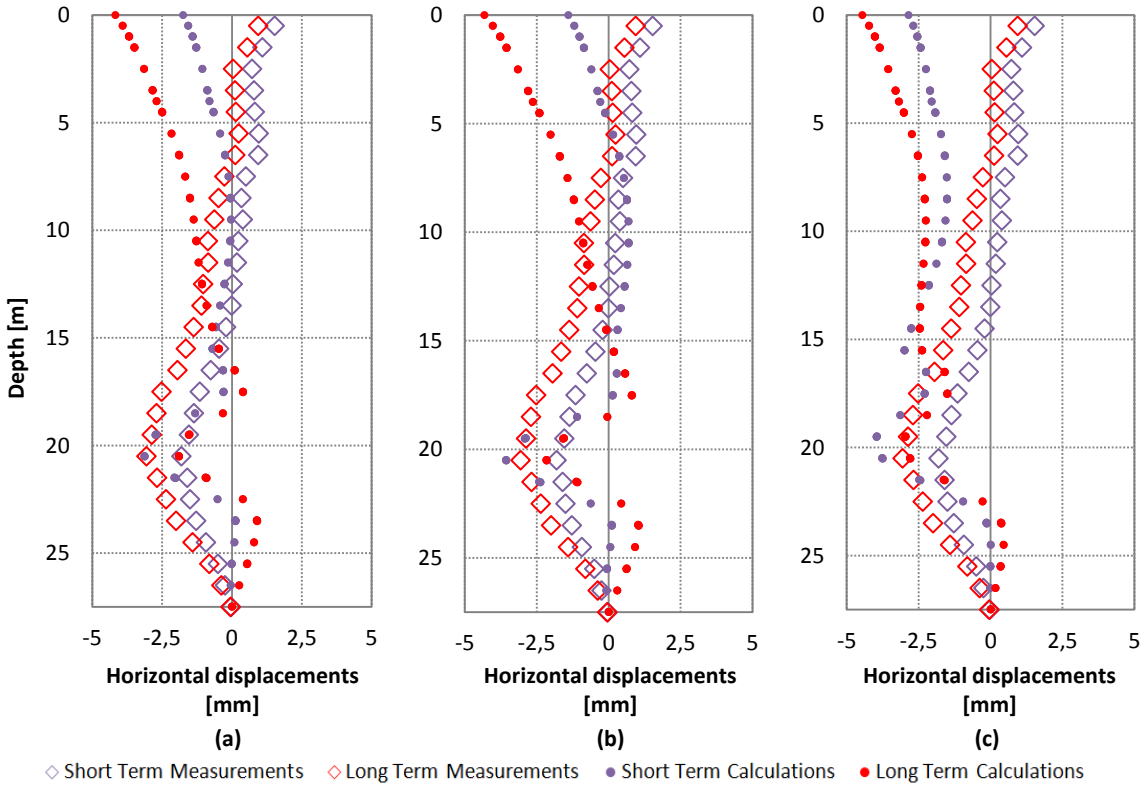

Figure 6.23. Comparison between measured and calculated horizontal displacements (Inclinometer). (a) Best combination of ΣMStage and E_{50}^{ref} using full term measurements. (b) Best combination of ΣMStage and E_{50}^{ref} using short term measurements. (c) Best combination of ΣMStage and E_{50}^{ref} using long term measurements. (ΣMStage Method).

In order to study separately the influence of the measurements obtained from each type of instrument, new maps of the objective function have been defined by using only one type of instrument at a time (see figures 6.24, 6.25, 6.26, 6.27, 6.28 and 6.29). For this analysis, only short and long term measurements have been used separately.

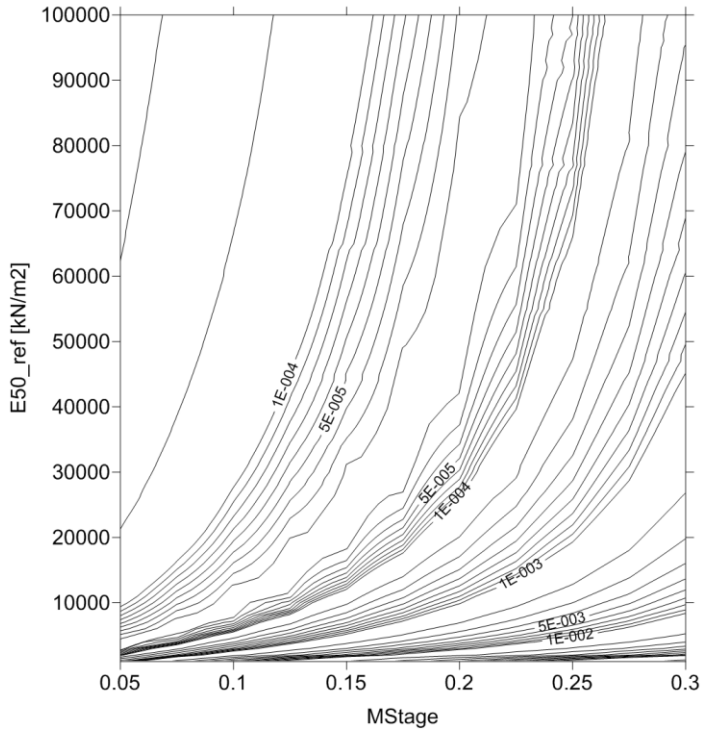

Figure 6.24. Mapping of the objective function [m^2] for short term behavior and surface measurements (ΣMStage Method).

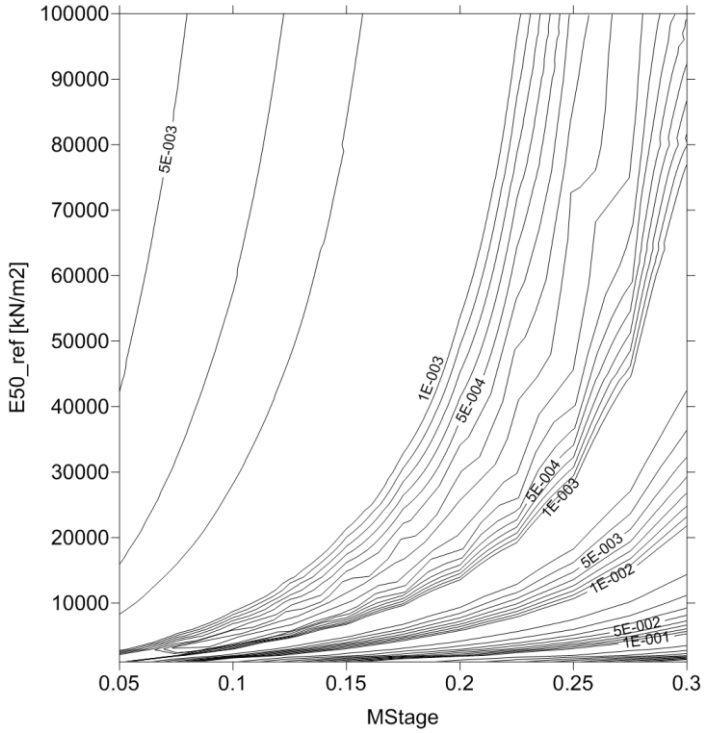

Figure 6.25. Mapping of the objective function [m^2] for short term behavior and sliding micrometer measurements (ΣMStage Method).

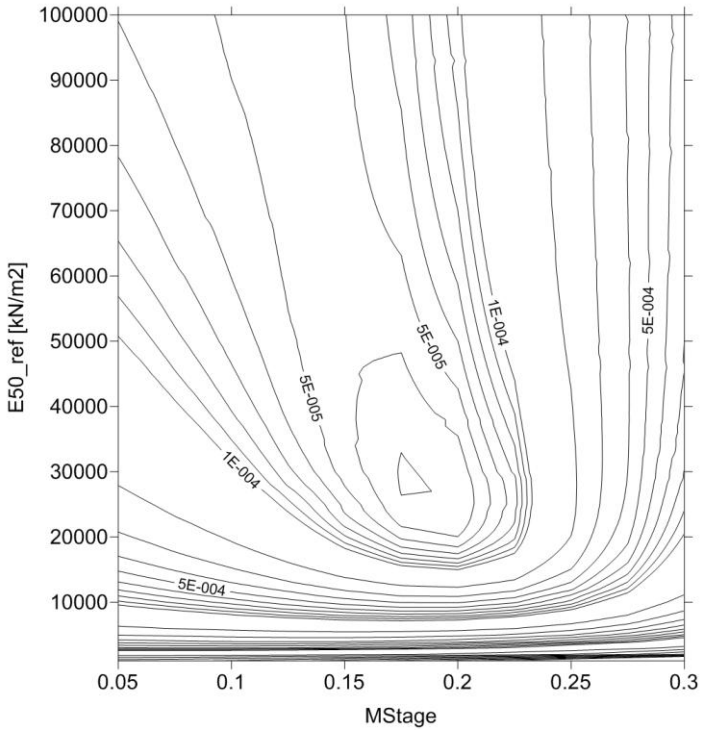

Figure 6.26. Mapping of the objective function [m^2] for short term behavior and inclinometer measurements (ΣMStage Method).

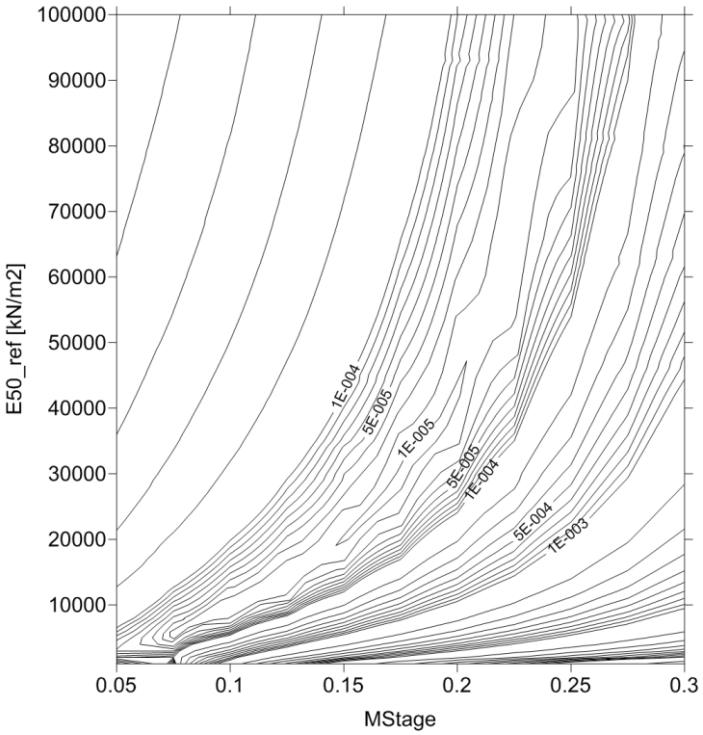

Figure 6.27. Mapping of the objective function [m^2] for long term behavior and surface measurements (ΣMStage Method).

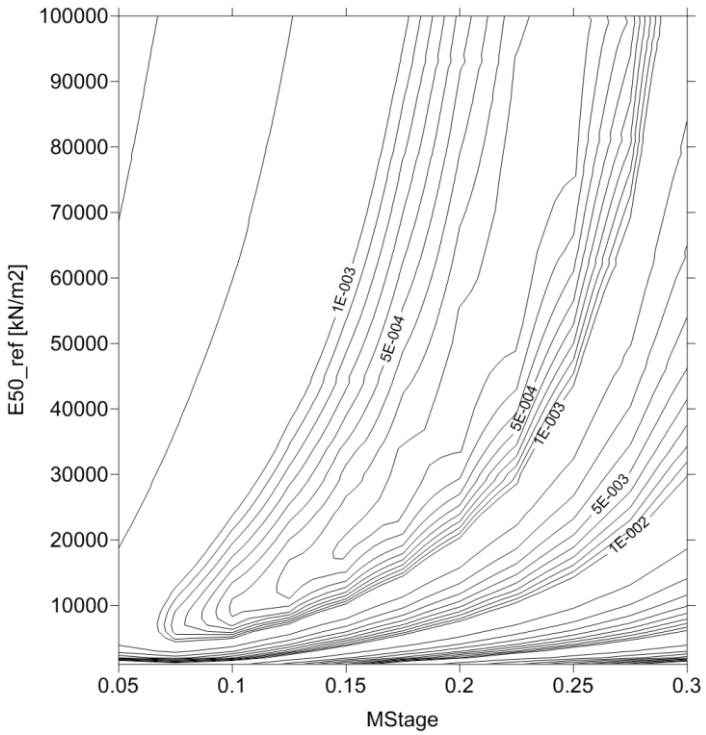

Figure 6.28. Mapping of the objective function [m^2] for long term behavior and sliding micrometer measurements (ΣMStage Method).

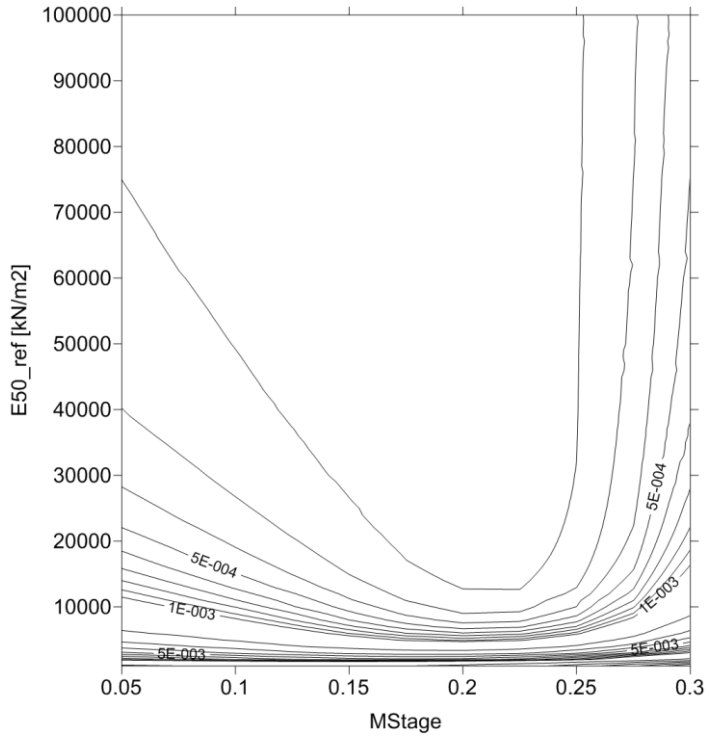

Figure 6.29. Mapping of the objective function [m^2] for long term behavior and inclinometer measurements (ΣMStage Method).

By comparing these figures (6.24, 6.25, 6.26, 6.27, 6.28 and 6.29), it can be pointed out that: while using the short term measurements, it seems that all measurements are required to properly define a minimum that narrows the area considered as solution of the problem. As figures 6.24 and 6.25 show, the use of only vertical displacements (surface points and/or

sliding micrometer measurements) describes a long banana shape minimum that goes almost from side to side of the search space. However, on the other hand, when using long term measurements, it seems that the measurements extracted from the inclinometer are not required to describe a proper minimum. From figure 6.29, it is clear that the horizontal displacements measured by the inclinometer during consolidation are not very sensitive to E_{50}^{ref} and the ΣMStage value.

6.5.5 The Grout Pressure Method

The grout pressure method that has been applied in this section is based on that described in Möller (2006) and Möller & Vermeer (2008), where this tunnel construction procedure was firstly presented.

Similar to the ΣMStage method, the grout pressure method also prescribes a new stress boundary condition along the tunnel excavation. But unlike the ΣMStage method, which uses stress reduction to set the new stress boundary conditions, the grout pressure method directly replaces the initial stress condition by a given grout pressure distribution. In practice, while using the geotechnical software Plaxis 2D (version 9), the grout pressure method is defined by two different stages (see figure 6.30). The first one, which is used to simulate the actual grout pressure, is defined by prescribing a hydrostatical pressure increasing with depth. The grout pressure profile is directly prescribed in the Plaxis cluster pore pressure distribution window (User defined pore pressure distribution). In the second stage, the grout pressure is deactivated and the tunnel lining is installed.

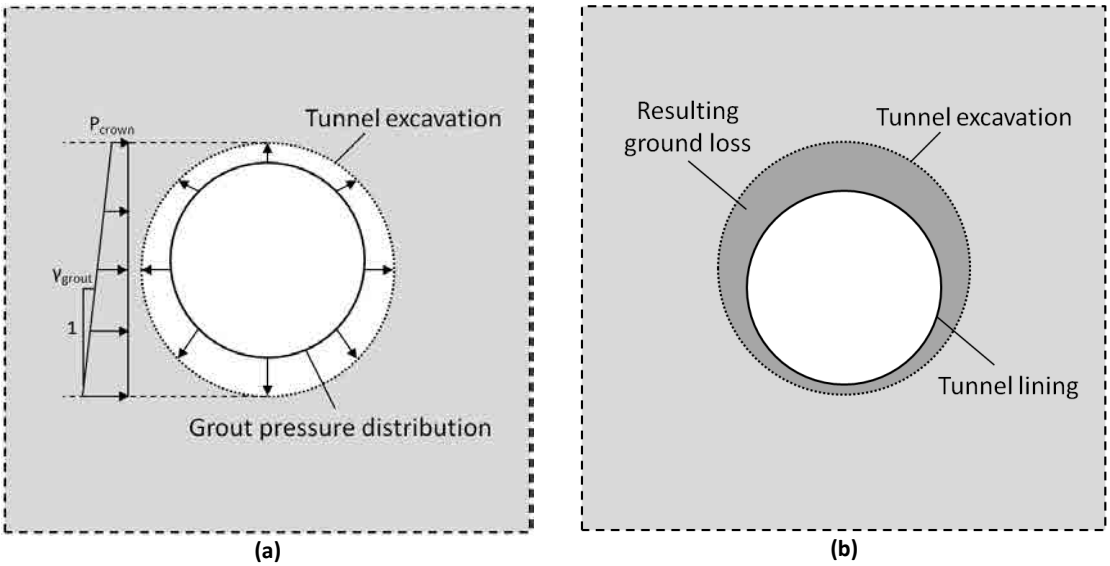

Figure 6.30. Grout Pressure Method scheme. (a) Stage 1: grout pressure application. (b) Stage 2: tunnel lining installation.

For this particular case study, the grout pressure values were set between 1.5bars and 3.0bars.

Finally, the full tunnel construction procedure is presented in table 6.7.

Note that only a stress normal to the boundary is applied to the tunnel excavated surface.

Plaxis phase (stage)	Description
0	Initial stress generation => K_0 method.
1	Tunnel excavation => Deactivation of the soil inside the excavation, and application of the grout pressure (user defined pore pressure distribution).
2	Tunnel lining installation => Activation of the lining and deactivation of the grout pressure.
3	Consolidation => All excess water pore pressure is dissipated (t=365days)

Table 6.7. Tunnel construction stages defined in the numerical model (Plaxis). Case: Grout Pressure Method.

6.5.5.1 Results

The different objective functions shapes, obtained from using simultaneously all instruments in full, short, and long term, are illustrated in the following figures (figure 6.31, 6.32 and 6.33).

Unfortunately, even the high sensitivity of the model with respect to the grout pressure, the grout pressure method has not been capable of defining a promising objective function morphology. The almost parallel contour lines to the stiffness module axis makes the measurements not sensitive to E_{50}^{ref}. Moreover, if the results illustrated in figures 6.31, 6.32 and 6.33 are compared with the ones obtained from the other tunnel construction procedures, it can be noticed that, apart from the morphology of the objective function, the absolute value of the objective function is significantly higher (the error between measurements and calculations are higher). As explained later, essentially, the reason of that increase in the error is caused by the limitation of the method to capture the horizontal displacements for this particular case study.

The best combinations of E_{50}^{ref} and grout pressure for short, long and full term behavior are presented in table 6.8.

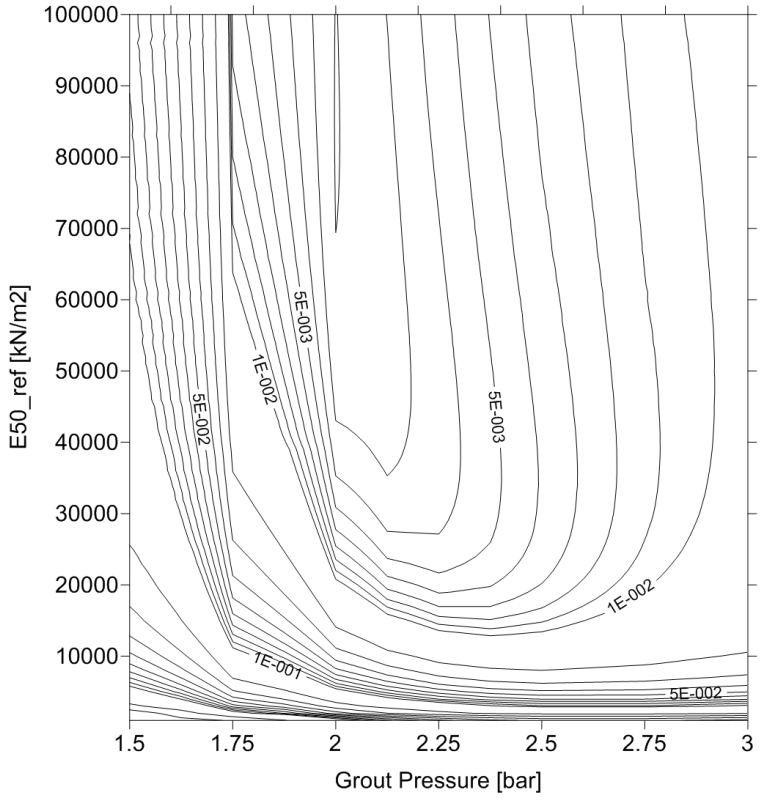

Figure 6.31. Mapping of the objective function [m^2] for full term behavior and all instruments measurements (Grout Pressure Method).

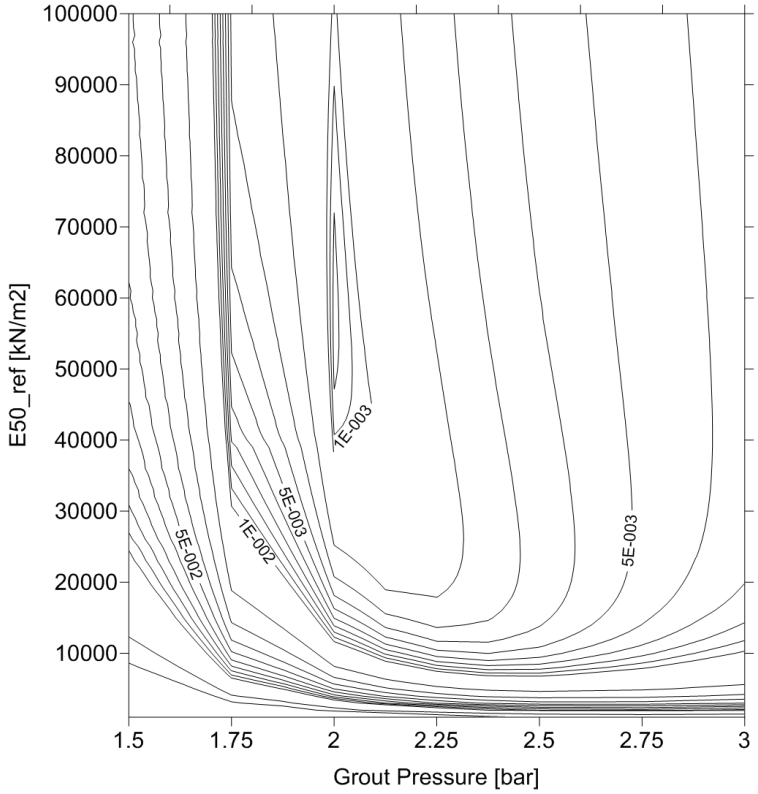

Figure 6.32. Mapping of the objective function [m^2] for short term behavior and all instruments measurements (Grout Pressure Method).

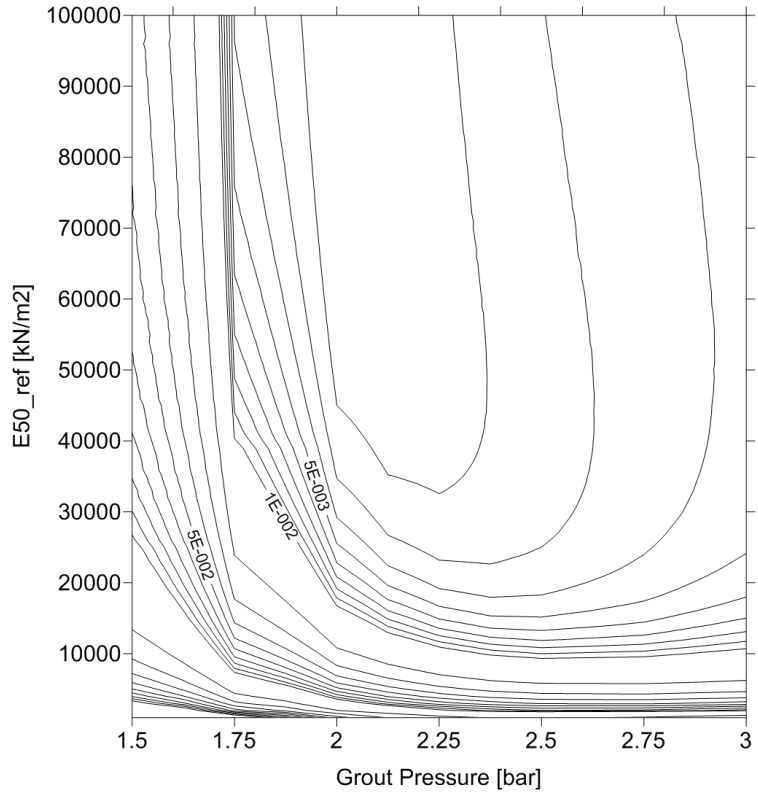

Figure 6.33. Mapping of the objective function [m^2] for long term behavior and all instruments measurements (Grout Pressure Method).

Measurements		Grout Pressure [bar]	E_{50}^{ref} [kN/m^2]	Error [m^2]
Time	Instruments			
Full Term	All instruments (116 measurements)	2	84000	$1.93 \cdot 10^{-3}$
Short Term	All instruments (58 measurements)	2	58000	$7.58 \cdot 10^{-4}$
Long Term	All instruments (58 measurements)	2	100000	$1.004 \cdot 10^{-3}$

Table 6.8. Best combinations of grout pressure and E_{50}^{ref}, while using the Grout Pressure method.

The graphical comparison between measurements and calculations associated with the values of table 6.8, are sown in figures 6.34, 6.35 and 6.36.

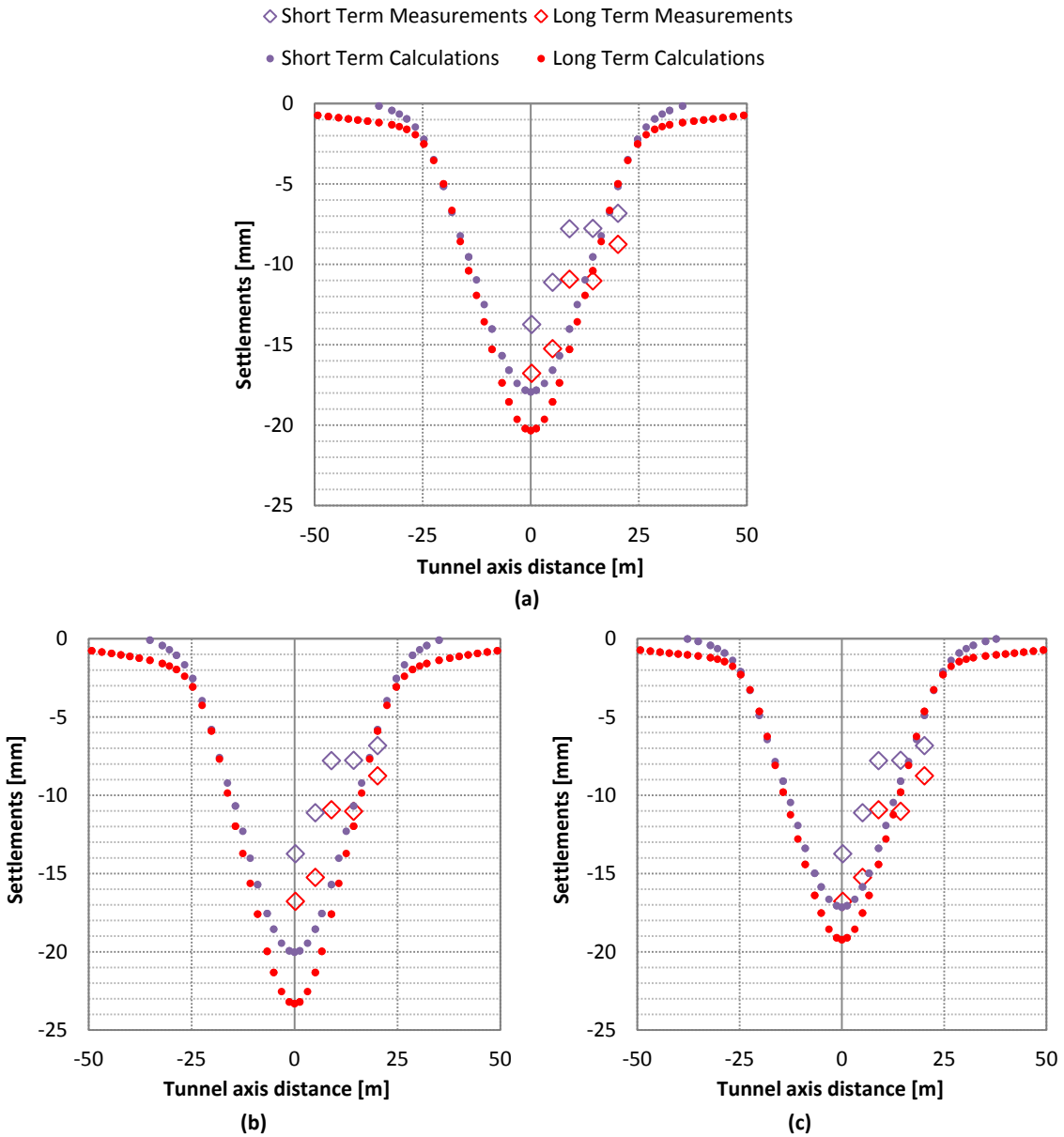

Figure 6.34. Comparison between measured and calculated settlements. (a) Best combination of grout pressure and E_{50}^{ref} using full term measurements. (b) Best combination of grout pressure and E_{50}^{ref} using short term measurements. (c) Best combination of grout pressure and E_{50}^{ref} using long term measurements. (Grout Pressure Method).

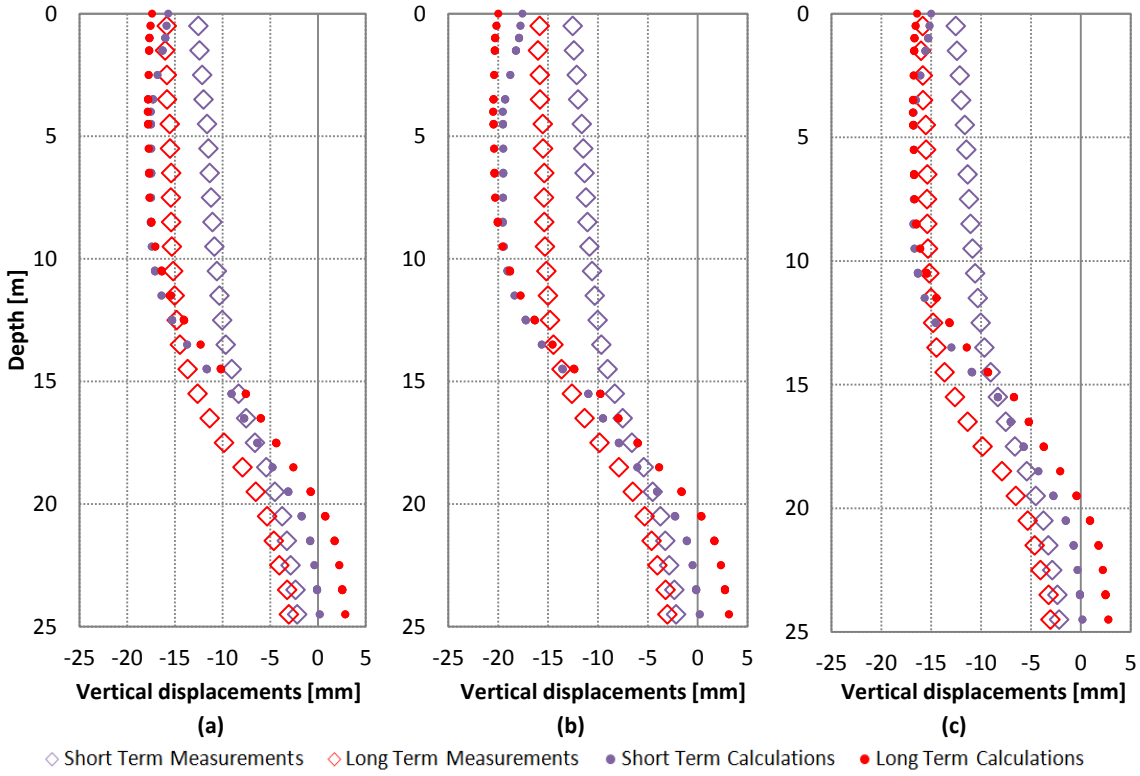

Figure 6.35. Comparison between measured and calculated vertical displacements (Sliding Micrometer). (a) Best combination of grout pressure and E_{50}^{ref} using full term measurements. (b) Best combination of tunnel grout pressure and E_{50}^{ref} using short term measurements. (c) Best combination of grout pressure and E_{50}^{ref} using long term measurements. (Grout Pressure Method).

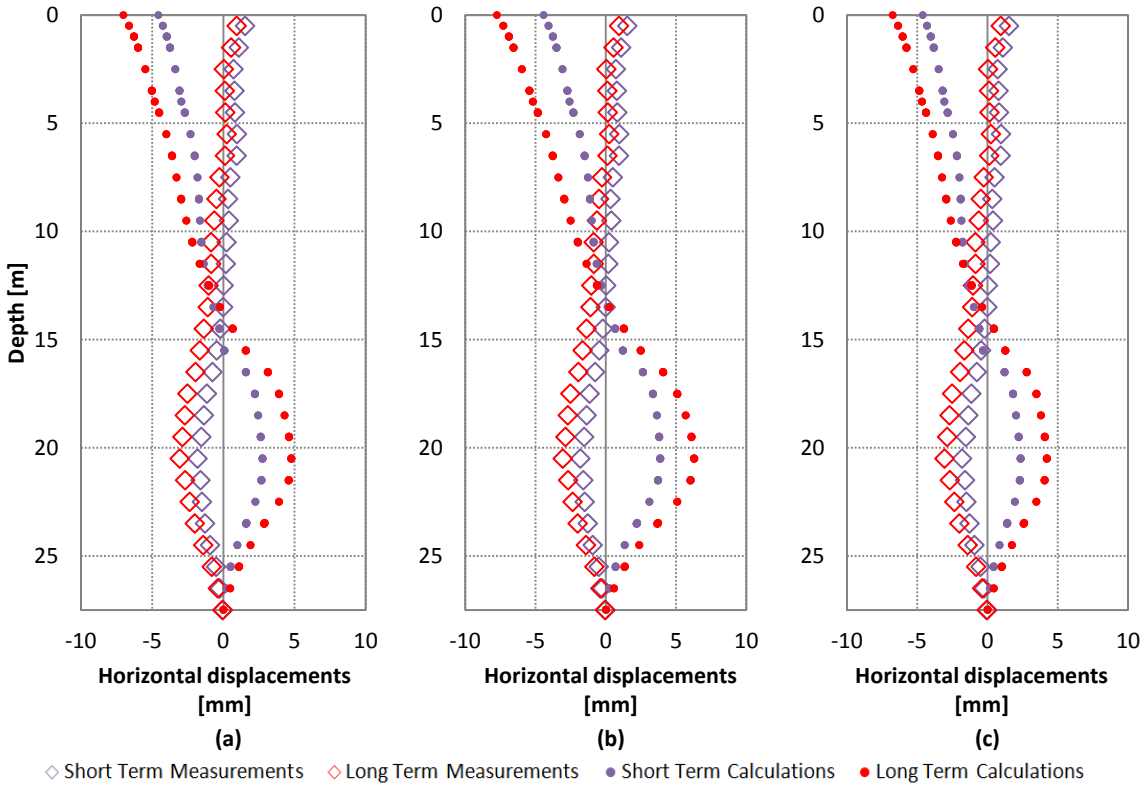

Figure 6.36. Comparison between measured and calculated horizontal displacements (Inclinometer). (a) Best combination of grout pressure and E_{50}^{ref} using full term measurements. (b) Best combination of grout pressure and E_{50}^{ref} using short term measurements. (c) Best combination of grout pressure and E_{50}^{ref} using long term measurements. (Grout Pressure Method).

Apart from the general mismatch between measurements and calculations, figure 6.36, shows that the numerical model predicts horizontal displacements in opposite direction to the measured ones. This causes that the horizontal displacements reduce substantially the contribution of the vertical displacements on the objective function. In general, the introduction of more measurements tends towards a better definition of the problem; however, in cases, such as the one presented in this section, where some measurements seem to be contradictory from the numerical model point of view (the model is supposed to be perfect and any discrepancy between measurements and calculations are associated with measurements errors), the introduction of more measurements makes more difficult the resolution of the problem of parameters identification.

As illustrated in figures 6.10, 6.17 and 6.30, the expected resulting ground loss is usually represented by a non-homogeneous contraction of the excavation cavity towards the center of the tunnel. However, as shown in figure 6.37, directly extracted from Möller (2006), while applying the grout pressure method, the resulting ground loss distribution is strongly controlled by the grout pressure and the value K_0, which can cause, for some combinations of grout pressure and K_0, displacements towards the outside of the tunnel (Grout pressure > σ_0). Strictly speaking, there is no reason for not accepting displacements towards the outside of the tunnel, in fact, if the EPB is driven at high pressure, displacements towards the outside of the tunnel are expected. However, it is more common to have combinations of grout pressure and initial stresses that causes displacements toward the center of the tunnel.

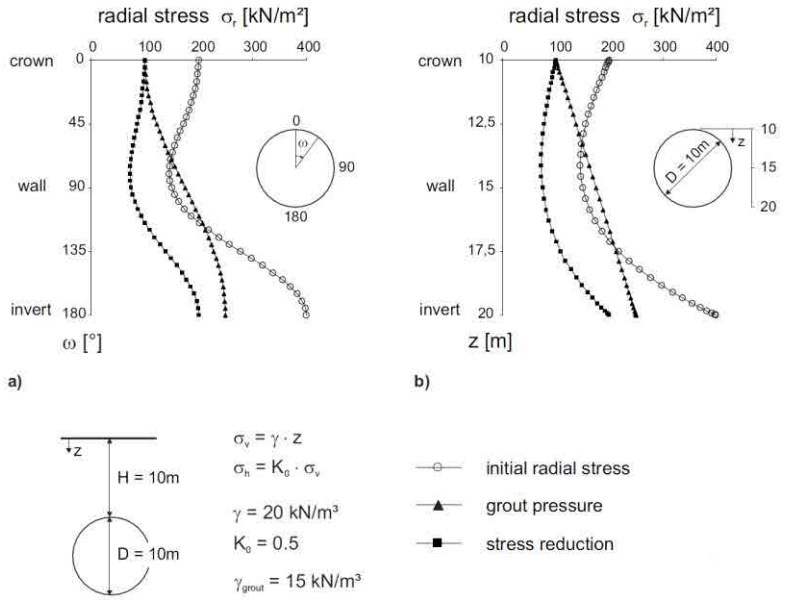

Figure 6.37. Difference in pressure distribution of stress reduction (equivalent to the ΣMStage method presented in this thesis) and grout pressure methods. Display of radial stresses: a) as a function of rotation angle ω, b) as a function of depth z. (Möller, 2006).

For a better understanding of what has been discussed here about the relative influence of the horizontal displacements (sliding micrometer) and the vertical displacements (surface points and inclinometer) on the objective function morphology, see Appendix A where the maps of all objective functions obtained using the grout pressure method are presented.

6.5.6 Concluding Remarks of the Preliminary Backanalysis

As shown in the previous sections (6.5.3, 6.5.4 and 6.5.5), significant different results have been obtained using different tunnel construction procedures and different type of measurements (see table 6.9). Some recommendations and guidelines can drawn.

Time	Measurements Instruments	Contraction [%]	E_{50}^{ref} [kN/m^2]	Error [m^2]
Full Term	All instruments (116 measurements)	0.55	58000	$8.42 \cdot 10^{-4}$
Short Term	All instruments (58 measurements)	0.60	26000	$2.97 \cdot 10^{-4}$
Long Term	All instruments (58 measurements)	0.475	66000	$1.94 \cdot 10^{-4}$
Time	**Measurements Instruments**	**ΣMStage**	**E_{50}^{ref} [kN/m^2]**	**Error [m^2]**
Full Term	All instruments (116 measurements)	0.200	33000	$8.10 \cdot 10^{-4}$
Short Term	All instruments (58 measurements)	0.200	25000	$3.36 \cdot 10^{-4}$
Long Term	All instruments (58 measurements)	0.225	66000	$2.64 \cdot 10^{-4}$
Time	**Measurements Instruments**	**Grout Pressure [bar]**	**E_{50}^{ref} [kN/m^2]**	**Error [m^2]**
Full Term	All instruments (116 measurements)	2	84000	$1.93 \cdot 10^{-3}$
Short Term	All instruments (58 measurements)	2	58000	$7.58 \cdot 10^{-4}$
Long Term	All instruments (58 measurements)	2	100000	$1.004 \cdot 10^{-3}$

Table 6.9. Summary of results when using short, long and full term measurements for the three different tunnel construction procedures presented in this thesis.

The Modified Tunnel Lining Contraction Method (or any prescribed displacement method) should not be used to identify soil stiffness, especially using short term measurements, due to the low sensitivity of the computed measurements to soil stiffness as already anticipated by Sagaseta (1987) for incompressible materials. However, the Modified Tunnel Lining Contraction Method seems a good methodology to capture the soil behavior once the soil parameters are known.

Even having differences about the precise location of the minimum, depending on the type of measurements, the ΣMStage Method has proved itself as the best method to identify the soil stiffness. Part of that discrepancy is associated with the uncertainties to determine the moment when to define the frontier between short and long term, and the limitations of the model to capture the full term behavior. Therefore, the application of the ΣMStage Method using long term measurements seems the most adequate procedure to identify the soil stiffness. However, if only short term measurements are available, it is recommended to combined vertical and horizontal displacements measurements. That need for both types of displacements are not required for long term, since the model seems unable to capture the long term horizontal displacements.

The high dependency on grout pressure and K_0 makes of the Grout Pressure Method a limited approach, especially when horizontal displacements have a substantial role on the problem. Therefore, the application of the Grout Pressure Method is only recommended for cases

where the combination of grout pressure and K_0 is expected to generate a stress imbalance (Grout Pressure ≈ $\sigma_0 = \sigma_v \cdot K_0$) that is likely to occur in the excavation of the tunnel.

As mentioned before, geotechnical backanalyses are strongly problem dependent. Therefore, the guidelines and recommendations presented in this section are expected to be only valid for similar case studies. Any kind of extrapolation should require further analyses.

6.6 Backanalysis (E_{50}^{ref}, E_{ur}^{ref} and φ)

In this final part of Chapter 6, a full backanalysis intended to identify E_{50}^{ref}, E_{ur}^{ref} and φ is presented. However, apart from the soil parameters identification the effect of the instruments error structure on the backanalysis has been also studied.

6.6.1 Definition

Initially, the recommendations extracted from the preliminary backanalysis have been adopted in this backanalysis. However, any required modification will be noted as needed. Therefore, the ΣMStage Method and the long term measurements were used to define the problem. Moreover, as in the preliminary backanalysis, several analyses were conducted varying the value of the ΣMStage. For this particular case, four different values of ΣMStage were used (ΣMStage = 0.175, 0.200, 0.225 and 0.250).

Firstly, an adaptive genetic algorithm (AGA) was used to define four different backanalyses (one backanalysis for each different value of ΣMStage) focused on determine the proper value of ΣMStage. Then, considering the proper value of ΣMStage the one associated with lowest value of the error, a gradient based method was applied to finally find the best parameters (having fixed ΣMStage). The Gauss-Newton method was combined with the AGA and a Principal Component Analysis (PCA) to formally represent the hybrid method presented in section 3.4.

When not using the instruments error structure the Least-Squares method was adopted to define the objective function (eq. 2.2), whereas when using the instruments error structure the Maximum Likelihood method was adopted (eq. 2.8) to fully take into account the effect of the instruments error. In order to strictly study the influence of the error structure, rather than the precision of the instrument itself, the measurements covariance matrix ($\boldsymbol{C}_x$) was directly defined by the instruments error structure ($\boldsymbol{E}_x$) (see section 2.4). For the $\boldsymbol{E}_x$ used for this particular case study see Appendix A.

The main characteristics and parameters needed to fully define the backanalysis procedure are shown in table 6.10.

Genetic Algorithm	
Optimization Algorithm	
Type of algorithm	AGA + Elitism
Selection type	Roulette Wheel (with NO fitness limit)
GAP	1
Maximum probability of applying crossover (P_{c_max})	0.95
Minimum probability of applying crossover (P_{c_min})	0.50
Maximum probability of applying mutation (P_{m_max})	0.40
Minimum probability of applying mutation (P_{m_min})	0.01

Population size	101
Initial Population (equal for all analyses presented in this chapter)	Randomly generated
Stop Criteria (switching point)	20 generations
Search Space Discretization	
$E_{50}^{ref}{}_{min}$ [kN/m^2]	5000
$E_{50}^{ref}{}_{max}$ [kN/m^2]	100000
$E_{50}^{ref}{}_{step\ size}$ [kN/m^2]	1000
$E_{ur}^{ref}{}_{min}$ [kN/m^2]	10000
$E_{ur}^{ref}{}_{max}$ [kN/m^2]	500000
$E_{ur}^{ref}{}_{step\ size}$ [kN/m^2]	2500
φ_{min} [deg]	25
φ_{max} [deg]	35
$\varphi_{step\ size}$ [deg]	0.5
Principal Component Analysis (PCA)	
NOT Using the Instruments Error Structure	
Frontier Value	$2.8 \cdot 10^{-4}$m^2 (equivalent to 2.25mm of average standard deviation)
AF (amplifier factor of the standard deviation)	2
Using the Instruments Error Structure	
Frontier Value	10% of the best individuals from all generations
AF (amplifier factor of the standard deviation)	2
Gradient Based Method	
Type of algorithm	Gauss-Newton
Stop Criteria	fixed number of iterations (10 iterations)
Objective Function	
NOT Using the Instruments Error Structure	
Type of objective function	Least-Squares Method
Using the Instruments Error Structure	
Type of objective function	Maximum Likelihood
Measurements	
Type of measurement	Vertical and Horizontal Displacements from Long Term behavior (5 surface points, 1 sliding micrometer and 1 inclinometer => 58 measurement points)

Table 6.10. Main characteristics and parameters of the backanalysis.

6.6.2 Results

6.6.2.1 Not Using the Instruments Error Structure

In figures 6.38 and 6.39, the distribution of the initial population and the final distribution after 20 generations are illustrated.

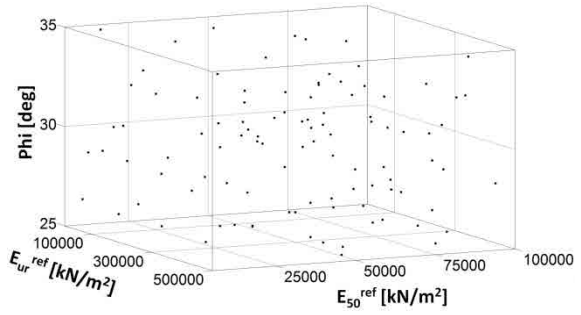

Figure 6.38. Initial Population (the same randomly generated population was used for all cases presented in this chapter)

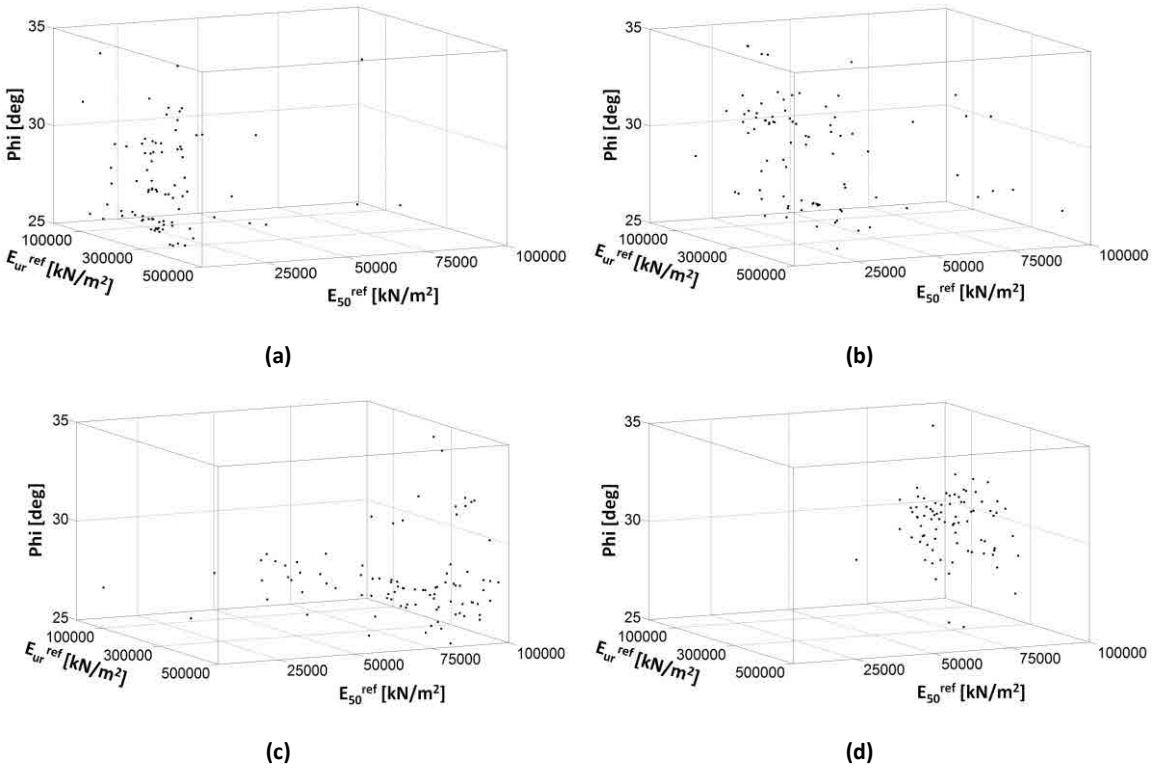

Figure 6.39. Final Population after 20 consecutive generations. (a) ΣMStage=0.175. (b) ΣMStage=0.200. (c) ΣMStage=0.225. (d) ΣMStage=0.250.

In terms of parameters combinations, it is clear that depending on the value of the ΣMStage the population converges to different domains of the search space. However, in terms of the objective function value of the best individual (error), there is practically no difference between them (see table 6.11), which makes the parameters identification more complex. The same happens if the results, associated with the values of the table 6.11, are graphically compared (see figures 6.40, 6.41 and 6.42). It should be noticed that although the short term behavior is represented in the figures, it has not been used to carry out the backanalysis. However, it was considered interesting to plot it altogether with the long term behavior results to achieve a better global understanding of the problem.

ΣMStage	E_{50}^{ref} [kN/m^2]	E_{ur}^{ref} [kN/m^2]	φ [deg]	Error [m^2]
0.175	12000	227500	30	$2.539 \cdot 10^{-4}$
0.200	16000	227500	35	$2.479 \cdot 10^{-4}$
0.225	62000	170000	28	$2.597 \cdot 10^{-4}$
0.250	72000	152500	29.5	$2.591 \cdot 10^{-4}$

Table 6.11. Best individual for each value of ΣMStage after 20 generations. The error represents the objective function value.

As in the preliminary backanalysis, the measurements extracted from the inclinometer are not properly captured by the model, especially if short and long term measurements are compared with the calculations at the same time; neither the magnitude nor the evolution of the movements are matched. However, the vertical displacements seem to be well captured by the model. Moreover, unlike the preliminary backanalysis, if the short and long term vertical displacements, extracted from the sliding micrometer, are compared, it can be noticed that for some combinations of ΣMStage and soil parameters, the difference between short and long term behavior can be reproduced by the model.

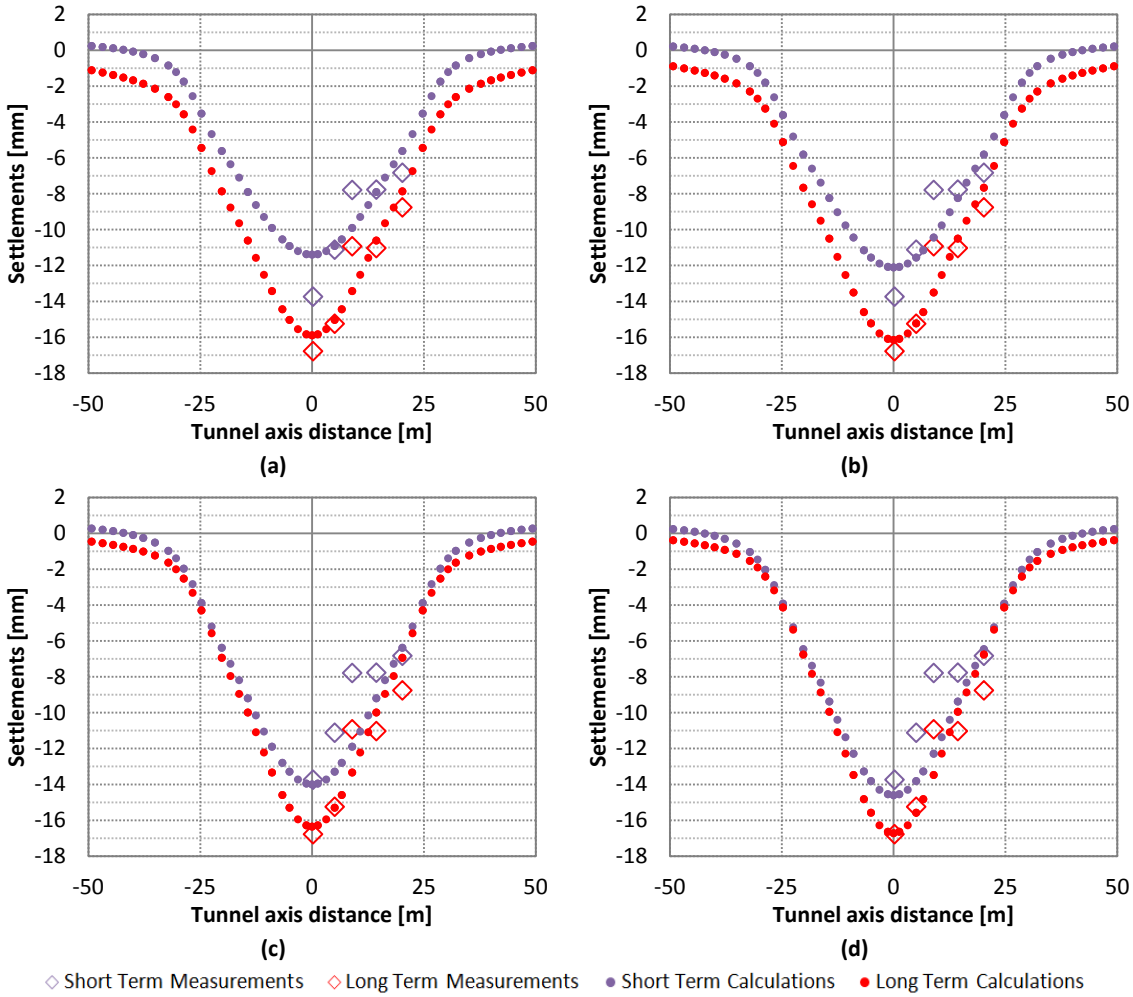

Figure 6.40. Comparison between measured and calculated settlements. (a) ΣMStage=0.175. (b) ΣMStage=0.200. (c) ΣMStage=0.225. (d) ΣMStage=0.250.

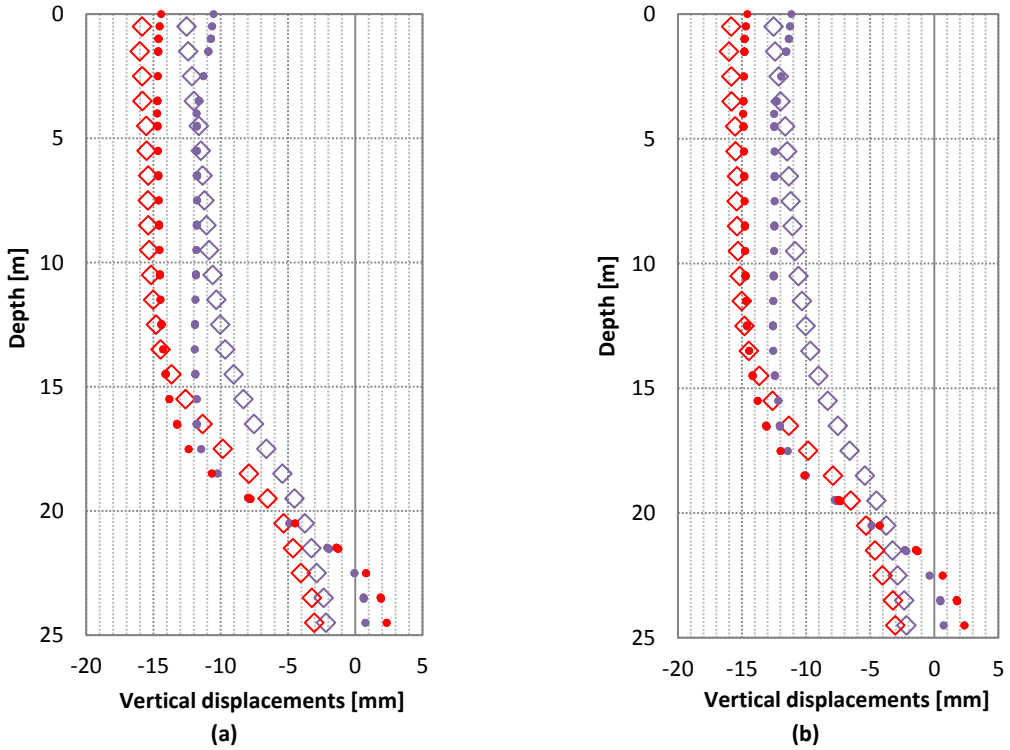

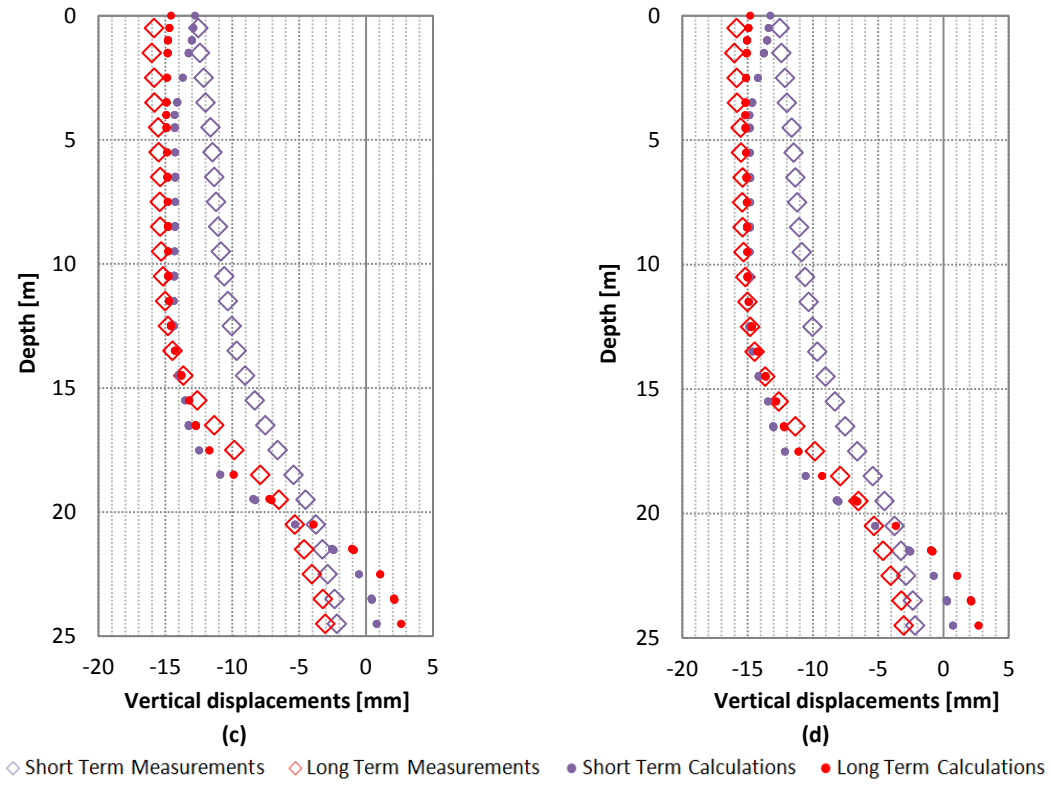

Figure 6.41. Comparison between measured and calculated vertical displacements (Sliding Micrometer). (a) ΣMStage=0.175. (b) ΣMStage=0.200. (c) ΣMStage=0.225. (d) ΣMStage=0.250.

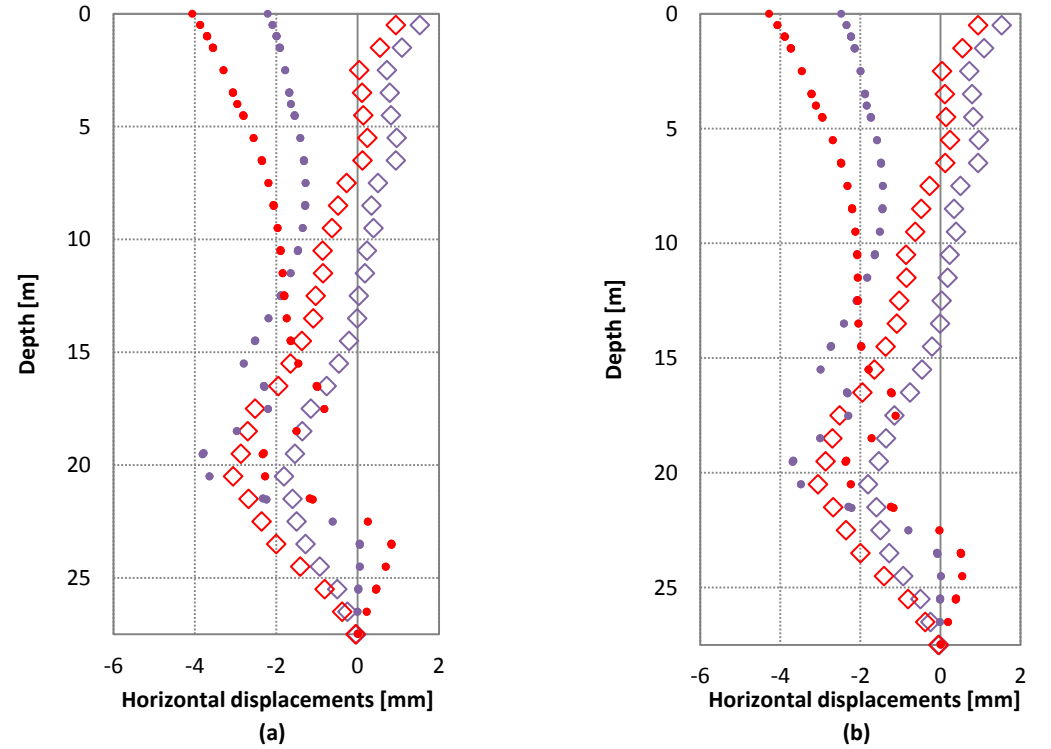

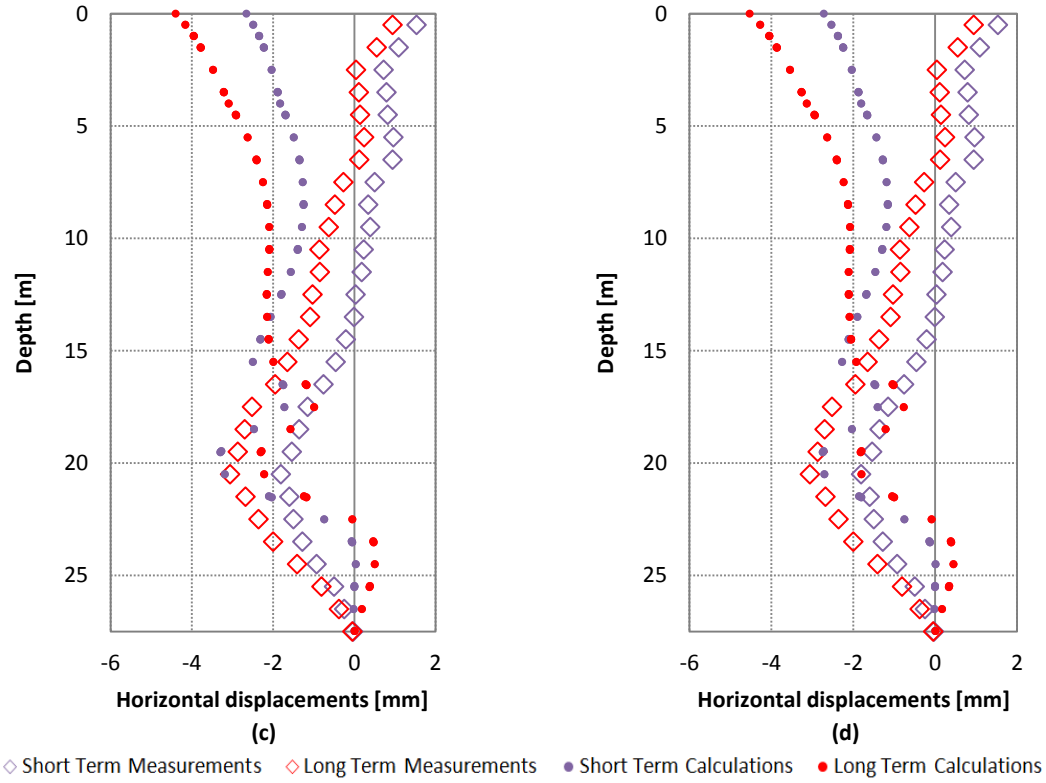

Figure 6.42. Comparison between measured and calculated horizontal displacements (Inclinometer). (a) ΣMStage=0.175. (b) ΣMStage=0.200. (c) ΣMStage=0.225. (d) ΣMStage=0.250.

Furthermore, the PCA (see figure 6.43), also indicates that there are different combinations of soil parameters and ΣMStage that have similar objective function values (no intersection among the different PCA ellipsoids defined with the same frontier value). However, the number of good individuals depending on the value of ΣMStage is significant different between low (0.175 and 0.200) and high (0.225 and 0.250) values of ΣMStage (279 good individuals for ΣMStage=0.175, 241 good individuals for ΣMStage=0.200, 85 good individuals for ΣMStage=0.225, and 131 good individuals for ΣMStage=0.250).

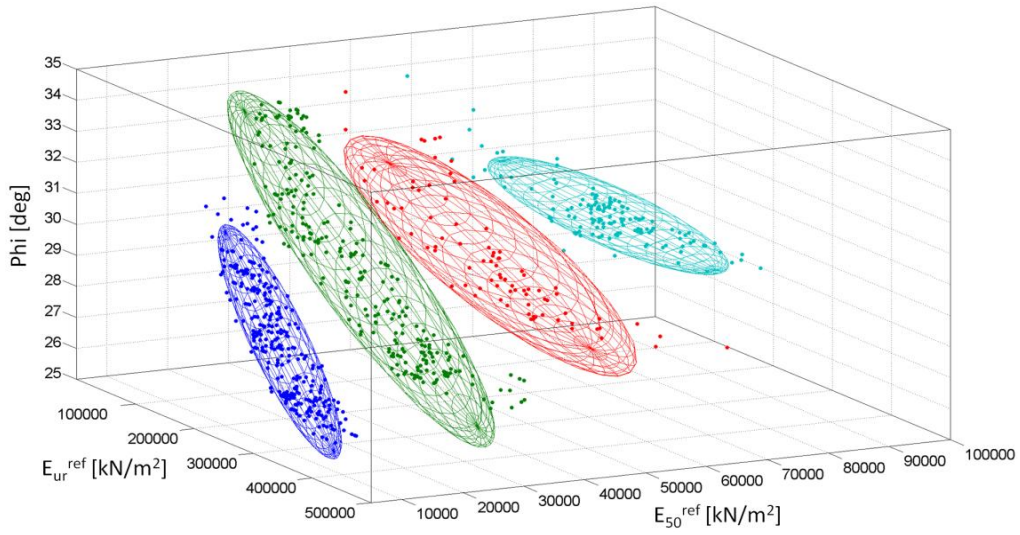

Figure 6.43. Graphical representation of the Principal Component Analysis results. The blue points and the blue ellipsoid are associated with ΣMStage=0.175. The green points and the green ellipsoid are associated with ΣMStage=0.200. The red points and the red ellipsoid are associated with ΣMStage=0.225. The turquoise points and the turquoise ellipsoid are associated with ΣMStage=0.250.

Not surprisingly, the higher the ΣMStage is, the higher the soil stiffness is, and vice versa. Moreover, if figure 6.43 is plotted in the space $\varphi - E_{50}^{ref}$ (see figure 6.44), the strong relationship between φ and E_{50}^{ref} can be observed, where the higher the φ is, the lower the E_{50}^{ref} is. Nothing similar occurs with the rest of parameters (see figure 6.45 and 6.46)

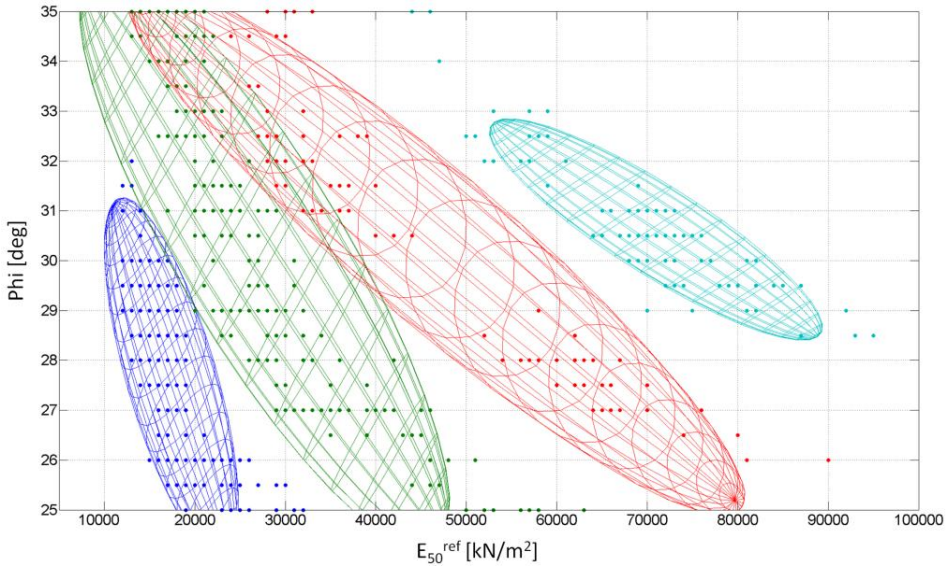

Figure 6.44. Side view of the PCA ellipsoids in the space $\varphi - E_{50}^{ref}$. The blue points and the blue ellipsoid are associated with ΣMStage=0.175. The green points and the green ellipsoid are associated with ΣMStage=0.200. The red points and the red ellipsoid are associated with ΣMStage=0.225. The turquoise points and the turquoise ellipsoid are associated with ΣMStage=0.250.

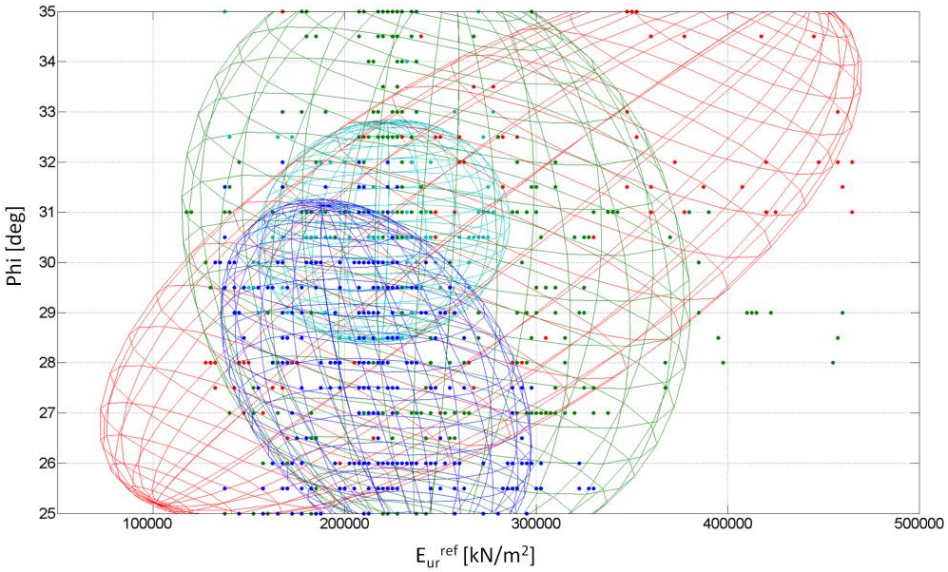

Figure 6.45. Side view of the PCA ellipsoids in the space $\varphi - E_{ur}^{ref}$. The blue points and the blue ellipsoid are associated with ΣMStage=0.175. The green points and the green ellipsoid are associated with ΣMStage=0.200. The red points and the red ellipsoid are associated with ΣMStage=0.225. The turquoise points and the turquoise ellipsoid are associated with ΣMStage=0.250.

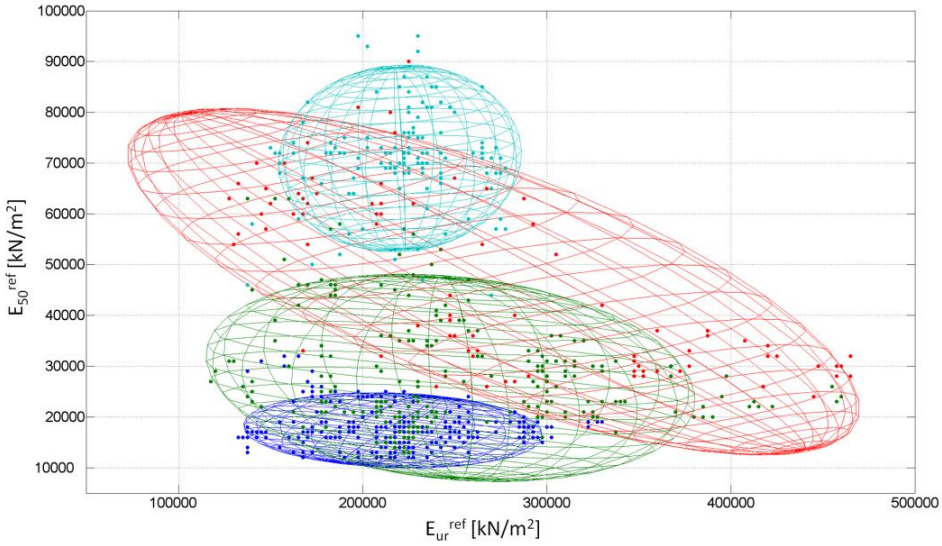

Figure 6.46. Side view of the PCA ellipsoids in the space $E_{50}^{ref} - E_{ur}^{ref}$. The blue points and the blue ellipsoid are associated with ΣMStage=0.175. The green points and the green ellipsoid are associated with ΣMStage=0.200. The red points and the red ellipsoid are associated with ΣMStage=0.225. The turquoise points and the turquoise ellipsoid are associated with ΣMStage=0.250.

Unfortunately, the results presented so far in this section indicate that more information and restrictions are required to properly define the problem, before a reliable set of parameters can be obtained as a solution of the problem.

If the objective function is fed with short and long term measurements at the same time, the error associated with ΣMStage = 0.175 and ΣMStage = 0.200 (see table 6.12), for the combination of soil parameters presented in table 6.11, are significant lower than those associated with ΣMStage = 0.225 and ΣMStage = 0.250 (see table 6.12). Therefore, it seems that for this particular case, unlike the preliminary backanalysis, the use of short and long term measurements simultaneously are more appropriate than only using long term measurements.

ΣMStage	E_{50}^{ref} [kN/m^2]	E_{ur}^{ref} [kN/m^2]	φ [deg]	Error [m^2]
0.175	12000	227500	30	$5.174 \cdot 10^{-4}$
0.200	16000	227500	35	$5.414 \cdot 10^{-4}$
0.225	62000	170000	28	$7.118 \cdot 10^{-4}$
0.250	72000	152500	29.5	$7.395 \cdot 10^{-4}$

Table 6.12. Best individual extracted from the backanalysis where only long term measurements were used to drive the optimization procedure. However, the error shown in this table is defined by using short and long term measurements.

Consequently, it was considered necessary to repeat the full backanalysis using both types of measurements simultaneously.

Starting from the same initial population as the previous backanalysis (see figure 6.38), figure 6.47 illustrates the distribution of the population after 20 generations; whereas table 6.13 shows the soil parameter values and the errors associated with the best individuals. As shown in table 6.13, the best match is associated with the ΣMStage value of 0.175, which is the lowest value that was evaluated. Therefore, it was considered appropriate to evaluate a lower value of ΣMStage to check whether or not the error keeps decreasing while reducing the ΣMStage. For ΣMStage = 0.150, the best individual obtained after 20 generations has an error of $4.584 \cdot 10^{-4}$m^2; making ΣMStage = 0.175 the most suitable value for this particular case.

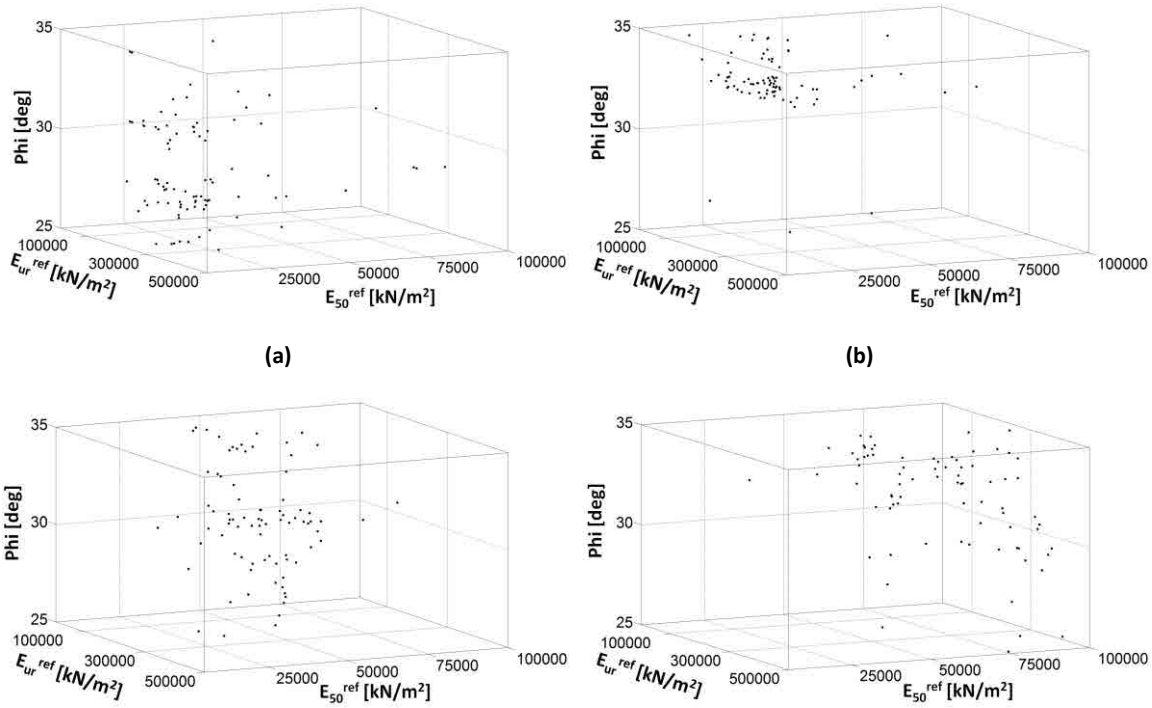

Figure 6.47. Final Population after 20 consecutive generations. (a) ΣMStage=0.175. (b) ΣMStage=0.200. (c) ΣMStage=0.225. (d) ΣMStage=0.250. (Using simultaneously both short and long term measurements).

ΣMStage	E_{50}^{ref} [kN/m^2]	E_{ur}^{ref} [kN/m^2]	φ [deg]	Error [m^2]
0.175	12000	167500	34.5	$4.463 \cdot 10^{-4}$
0.200	24000	145000	35	$4.698 \cdot 10^{-4}$
0.225	41000	127500	35	$5.043 \cdot 10^{-4}$
0.250	60000	152500	34.5	$5.405 \cdot 10^{-4}$

Table 6.13. Best individual for each value of ΣMStage after 20 generations. The error represents the objective function value using short and long term measurements.

Figures 6.48, 6.49 and 6.50 illustrate the comparison between measurements and calculations.

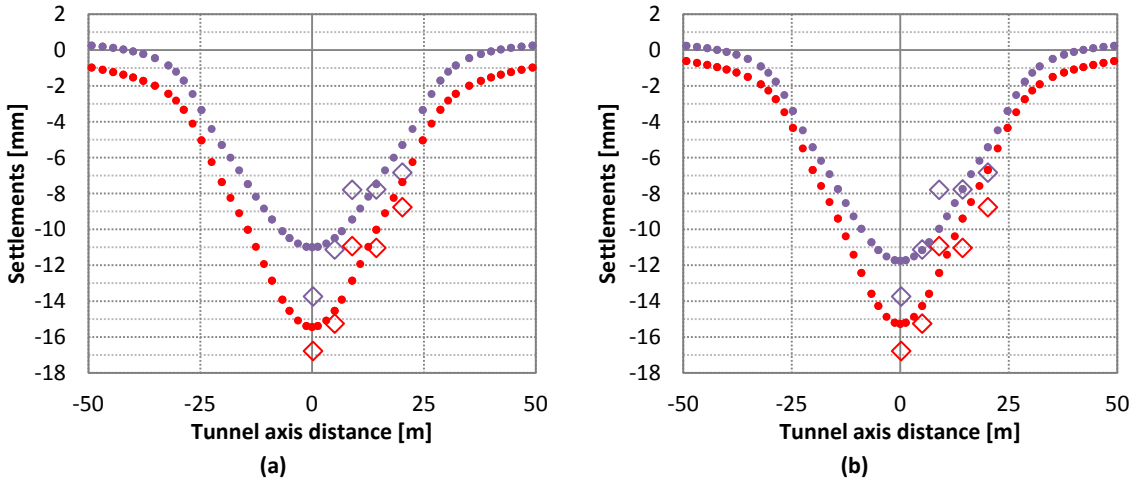

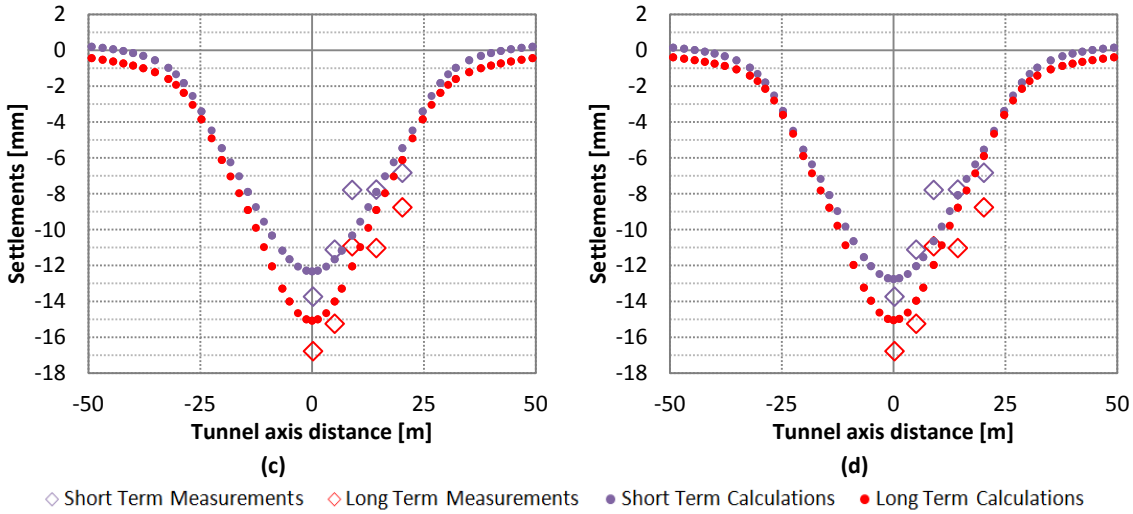

Figure 6.48. Comparison between measured and calculated settlements. (a) ΣMStage=0.175. (b) ΣMStage=0.200. (c) ΣMStage=0.225. (d) ΣMStage=0.250. (Using short and long term measurements)

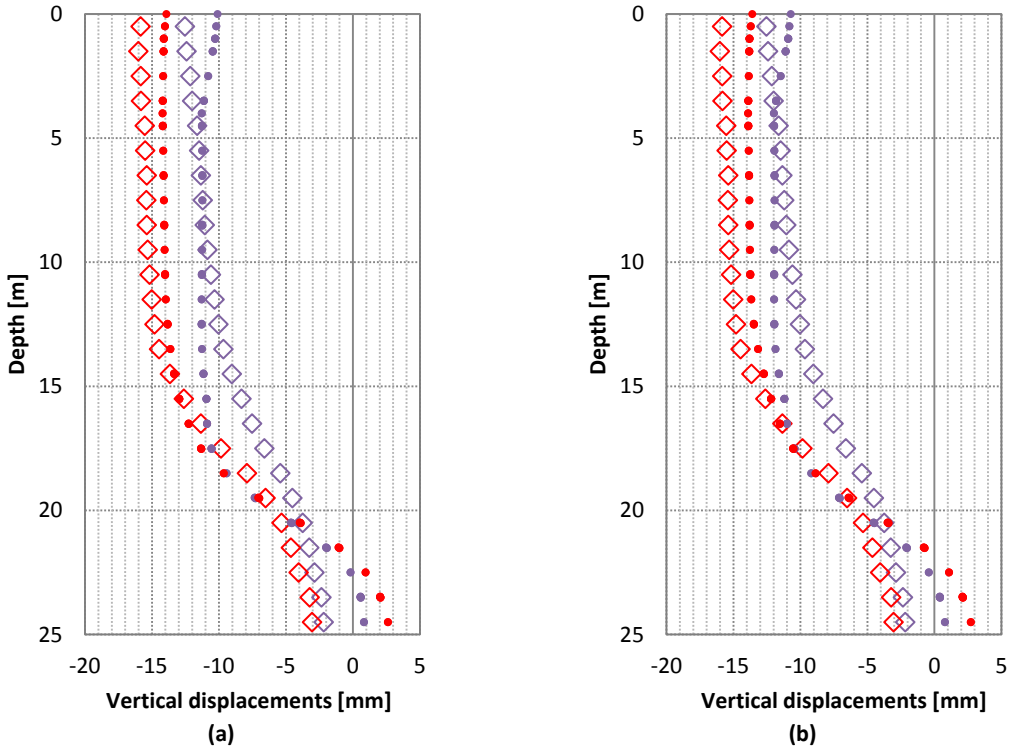

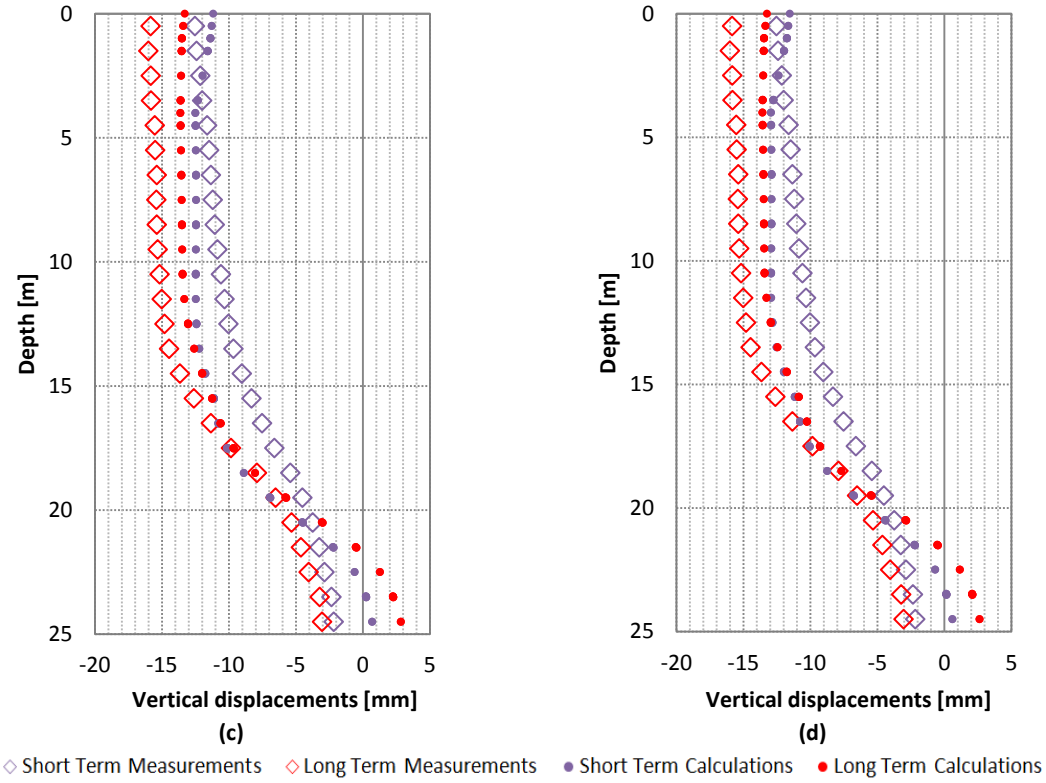

Figure 6.49. Comparison between measured and calculated vertical displacements (Sliding Micrometer). (a) ΣMStage=0.175. (b) ΣMStage=0.200. (c) ΣMStage=0.225. (d) ΣMStage=0.250. (Using short and long term measurements).

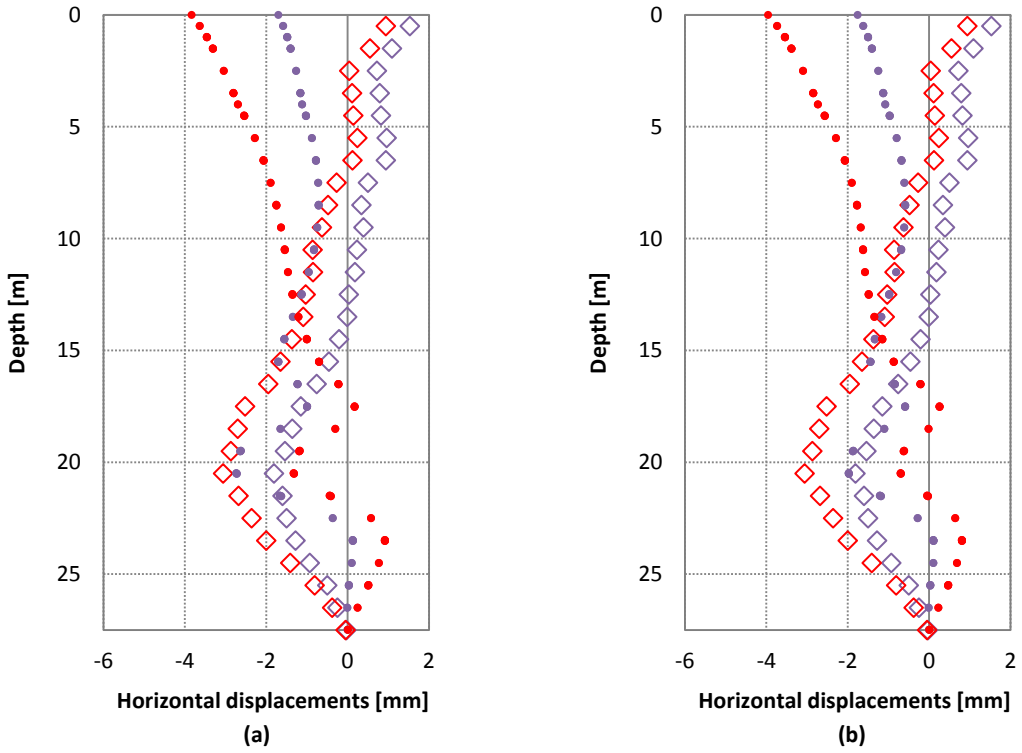

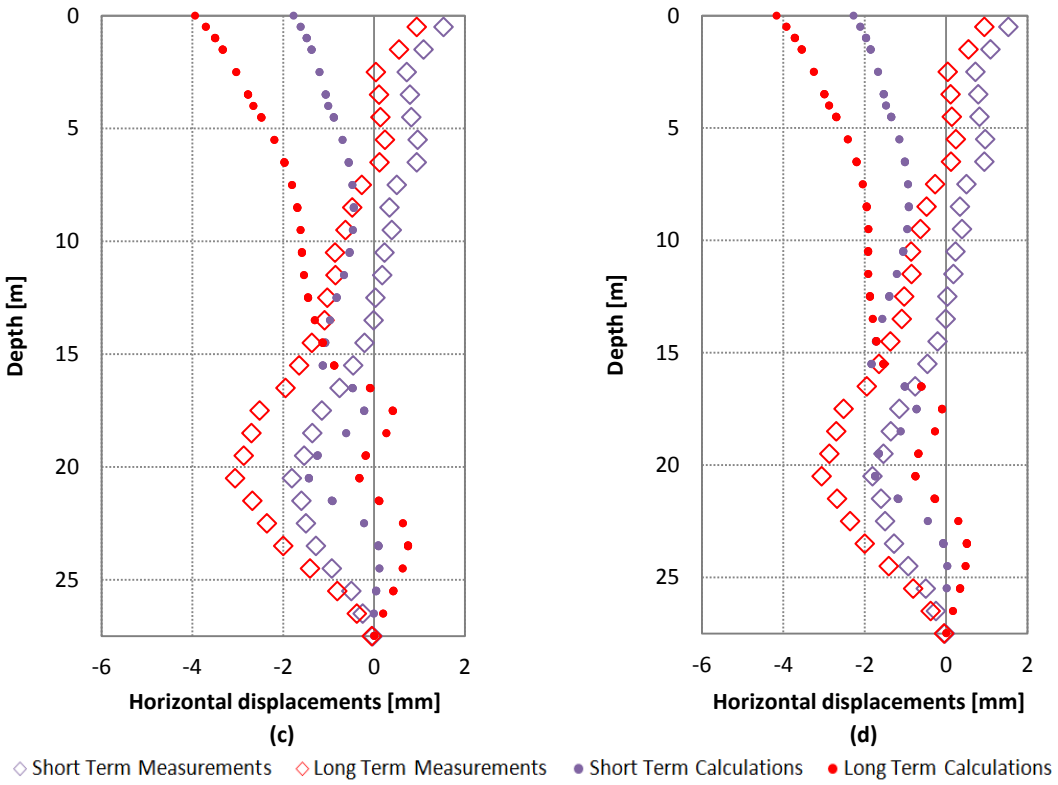

Figure 6.50. Comparison between measured and calculated horizontal displacements (Inclinometer). (a) ΣMStage=0.175. (b) ΣMStage=0.200. (c) ΣMStage=0.225. (d) ΣMStage=0.250. (Using short and long term measurements).

As in the previous backanalysis, combinations of a low value of ΣMStage and E_{50}^{ref} have made the model capable of reproducing part of the movements caused during consolidation, especially the ones associated with the sliding micrometer. The fact of having linked E_{50}^{ref} with E_{oed}^{ref} (E_{oed}^{ref} = 0.8·E_{50}^{ref}) has caused E_{50}^{ref} to control indirectly the plastic volumetric strains that are mainly controlled by E_{oed}^{ref}. Consequently, the plastic volumetric strains generated during consolidation can be simulated; except for values of E_{50}^{ref} higher than 30000kN/m^2.

Then, using the results associated with ΣMStage=0.175 as a solution of the adaptive genetic algorithm (see table 6.13), the PCA was conducted. The most relevant information related to the PCA is presented in table 6.14.

Description	Values
Frontier Value	$5.72 \cdot 10^{-4}$ m^2
AF (amplifier factor of the standard deviation)	2
Mean of E_{ur}^{ref} [kN/m^2]	186518.29
Mean of E_{50}^{ref} [kN/m^2]	23039.02
Mean of φ [deg]	28.58
Standard deviation of E_{ur}^{ref} [kN/m^2]	42269.76
Standard deviation of E_{50}^{ref} [kN/m^2]	6744.26
Standard deviation of φ [deg]	2.34
Correlation matrix	$\begin{bmatrix} 1 & -0.219 & -0.251 \\ -0.219 & 1 & -0.684 \\ -0.251 & -0.684 & 1 \end{bmatrix}$
Eigenvector (associated with the first principal component)	$[-0.04 \quad -0.70 \quad 0.71]$
Eigenvector (associated with the second principal component)	$[0.93 \quad -0.29 \quad -0.24]$
Eigenvector (associated with the third principal component)	$[-0.38 \quad -0.65 \quad -0.66]$

Eigenvalue (associated with the first principal component)	1.68
Eigenvalue (associated with the second principal component)	1.13
Eigenvalue (associated with the third principal component)	0.18

Table 6.14. Principal Component Analysis. (Using short and long term measurements / Not Using the Instruments Error Structure).

After defining the PCA ellipsoid, the Gauss-Newton method, starting from the center of the ellipsoid, was applied to finally find the best set of parameters. Unfortunately, no better solution was found by the gradient based method, in part due to the fact that the best individual obtained by the AGA was located outside the ellipsoid, and the algorithm got stuck at the border of the ellipsoid after a few iterations (see figure 6.51).

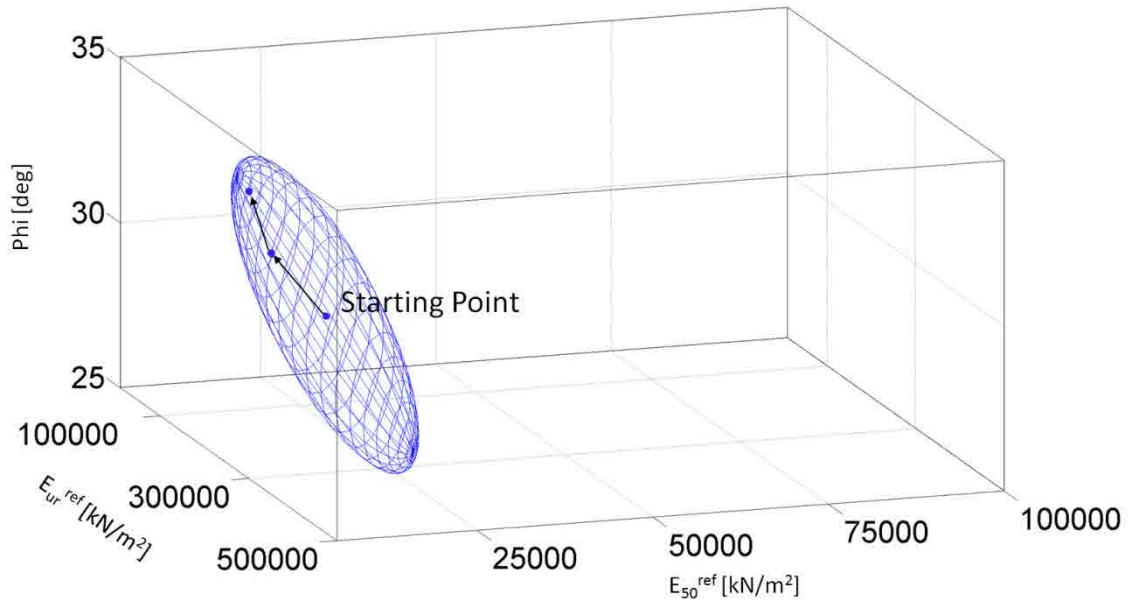

Figure 6.51. Gauss-Newton iterative procedure. The PCA ellipsoid (*AF*=2) defines the new search space and its center is used as starting point. (ΣMStage=0.175).

Even starting from the center of the ellipsoid where the error is $5.12 \cdot 10^{-4} m^2$ and finishing with a set of parameters with an error of $4.653 \cdot 10^{-4} m^2$, this error of $4.653 \cdot 10^{-4} m^2$ is still higher than the one associated with the best individual found by the AGA ($4.463 \cdot 10^{-4} m^2$), which does not let to consider the result as a solution of the problem. The parameter values after applying the Gauss-Newton method are shown in table 6.15.

ΣMStage	E_{50}^{ref} [kN/m^2]	E_{ur}^{ref} [kN/m^2]	φ [deg]	Error [m^2]
0.175	11081.2	206464.2	32.6	$4.653 \cdot 10^{-4}$

Figure 6.15. Soil parameters results after applying the Gauss-Newton Method - *AF*=2 (Using short and long term measurements / Not Using the instruments error structure).

In order to avoid the algorithm getting stuck on the border of the ellipsoid, it was considered appropriate to expand the PCA ellipsoid by applying a larger amplifier factor (*AF*) of the standard deviation (AF = 2.85). With this value of AF, it was guaranteed the presence of the best AGA individual inside the ellipsoid. However, the algorithm got stuck at the border of the expanded PCA ellipsoid again (see figure 6.52 and table 6.16). Therefore, an ultimate case without ellipsoid border restriction was defined. Unfortunately, the same occurred in this case where the algorithm got stuck at the border of the original parameters search space (see figure 6.53 and table 6.17).

It seems that close to the borders of the search space, the gradient based methods are less suitable for backanalysis.

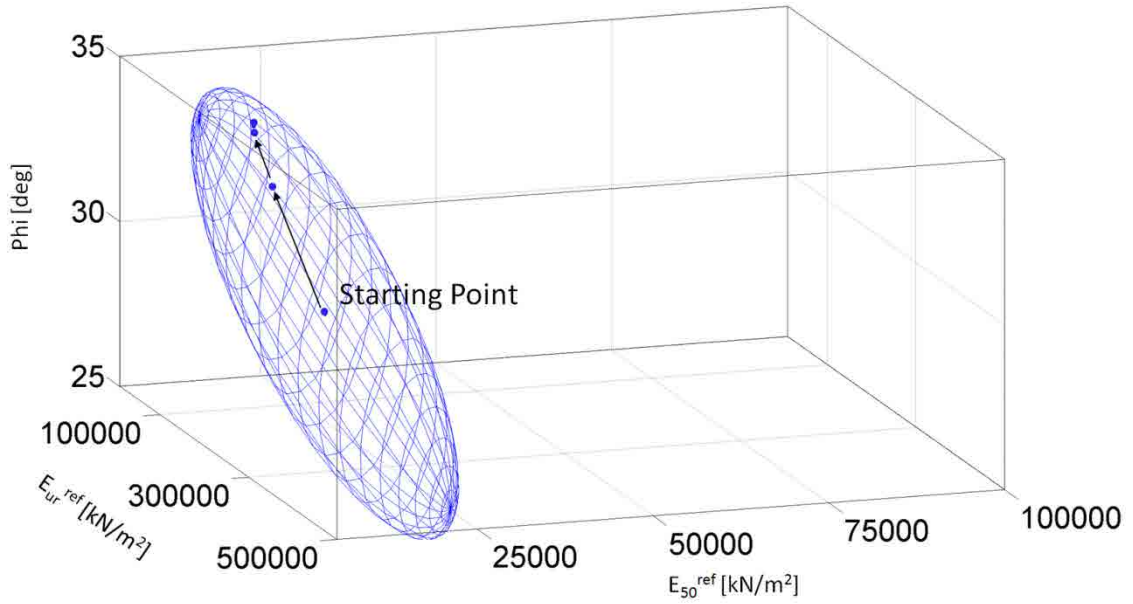

Figure 6.52. Gauss-Newton iterative procedure. The PCA ellipsoid (*AF*=2.85) defines the new search space and its center is used as starting point. (ΣMStage=0.175).

ΣMStage	E_{50}^{ref} [kN/m^2]	E_{ur}^{ref} [kN/m^2]	φ [deg]	Error [m^2]
0.175	12041.7	200066.1	34.6	$4.68 \cdot 10^{-4}$

Figure 6.16. Soil parameters results after applying the Gauss-Newton Method - *AF*=2.85 (Using short and long term measurements / Not Using the instruments error structure).

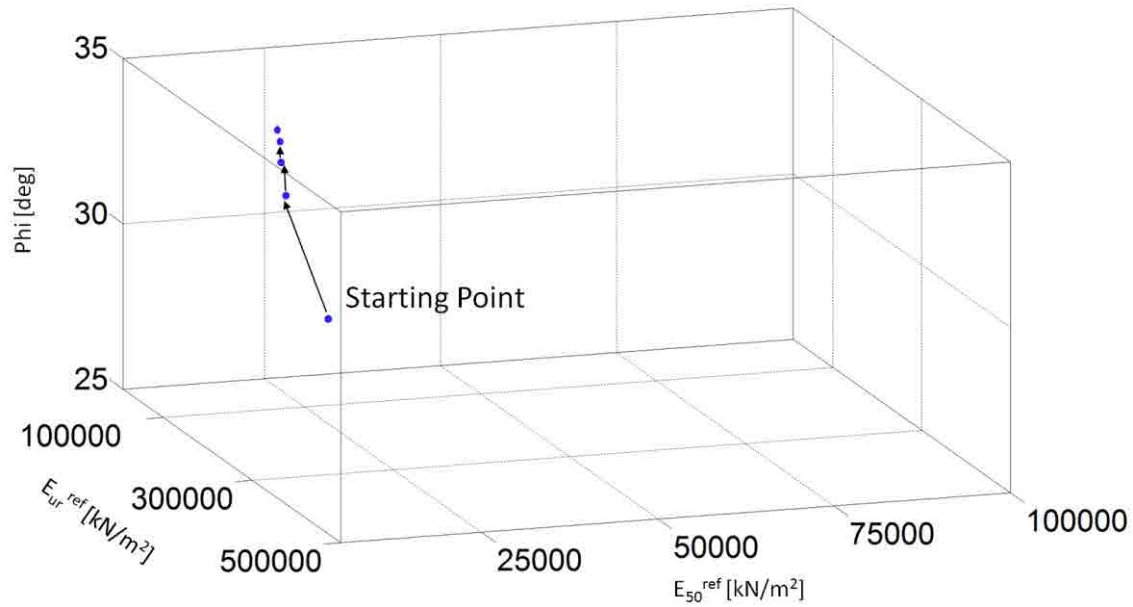

Figure 6.53. Gauss-Newton iterative procedure. Without the PCA ellipsoid border restrictions but using the PCA ellipsoid center as starting point. (ΣMStage=0.175).

ΣMStage	E_{50}^{ref} [kN/m^2]	E_{ur}^{ref} [kN/m^2]	φ [deg]	Error [m^2]
0.175	12161.4	243197.9	35	$5.11 \cdot 10^{-4}$

Figure 6.17. Soil parameters results after applying the Gauss-Newton Method - Without PCA ellipsoid border restrictions (Using short and long term measurements / Not Using the instruments error structure).

6.6.2.2 Using the Instruments Error Structure

As in the previous analysis (not using the instruments error structure), different values of ΣMStage were evaluated (0.150, 0.175, 0.200, 0.225 and 0.250). However, here in this section only the results obtained from using ΣMStage = 0.175 are shown. The instruments error structure was incorporated in the analysis as described in Section 2.4. The set of parameters obtained from using ΣMStage = 0.175 were the ones that best matched the measurements and the calculations.

In figure 6.54, the distribution of the initial population and the final distributions after 20 generations are illustrated.

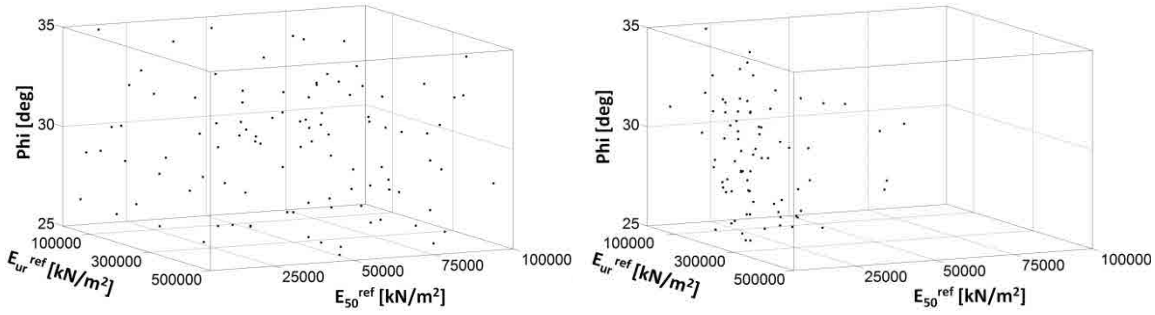

Figure 6.54. (a) Initial Population (the same population used in the previous analyses). (b) Final Population after 20 consecutive generations. (ΣMStage=0.175)

The parameters and the error associated with the best individual are shown in table 6.18.

ΣMStage	E_{50}^{ref} [kN/m^2]	E_{ur}^{ref} [kN/m^2]	φ [deg]	Error [-]
0.175	19000	57500	35	$5.48 \cdot 10^{-5}$

Figure 6.18. Best individual after 20 generations. The error represents the objective function value using short and long term measurements with the instruments error structure.

The comparison between measurements and calculations is illustrated in figure 6.55.

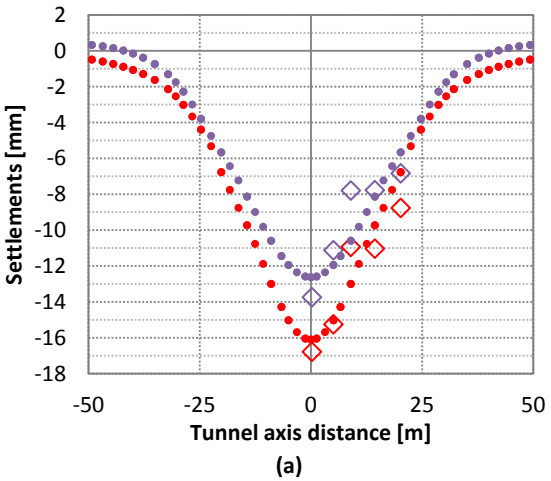

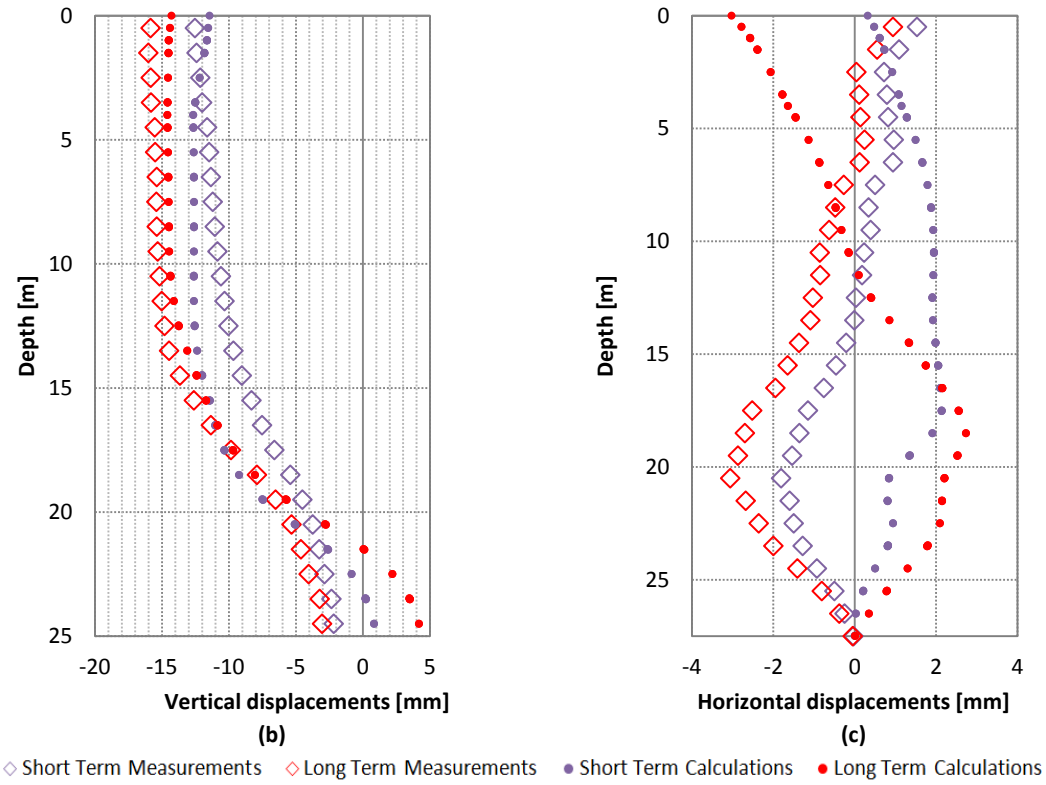

Figure 6.55. Comparison between measurements and calculations. (a) Settlements. (b) Vertical displacements - Sliding micrometer. (c) Horizontal displacements - Inclinometer.

From figure 6.55, the effect of the instrument error structure can be noticed, especially from figure 6.55.c, where the calculations do not match the measurements due to the penalty action caused by the instrument error structure matrix (see Appendix A). As mentioned before, the incremental instruments propagate their error from their origin point of measurement forward. Therefore, less weight is associated with those measurements. In contrast, relatively high weight is applied to the measurements associated with non-incremental instruments, such as the settlement measurements. If figures 6.55.a and 6.48.a are compared, it can be noticed how in figure 6.55.a (Using the Instruments Error Structure) the calculations match better the settlements measurements than in figure 6.48.a (Not Using the Instruments Error Structure). In those cases where the instruments error structure is not taken into account, the magnitude and the number of measurements of each instrument define their importance on the backanalysis.

The results of the PCA are shown in table 6.19, whereas the good individuals involved in the PCA and the PCA ellipsoid are illustrated in figure 6.56.

Description	Values
Frontier Value	Best 10% of the individuals
AF (amplifier factor of the standard deviation)	2
Mean of E_{ur}^{ref} [kN/m^2]	123620.69
Mean of E_{50}^{ref} [kN/m^2]	15896.55
Mean of φ [deg]	32.49
Standard deviation of E_{ur}^{ref} [kN/m^2]	37510.34
Standard deviation of E_{50}^{ref} [kN/m^2]	3052.15
Standard deviation of φ [deg]	1.76

Correlation matrix	$\begin{bmatrix} 1 & -0.505 & -0.597 \\ -0.505 & 1 & -0.208 \\ -0.597 & -0.208 & 1 \end{bmatrix}$
Eigenvector (associated with the first principal component)	$[0.75 \quad -0.39 \quad -0.53]$
Eigenvector (associated with the second principal component)	$[-0.05 \quad 0.77 \quad -0.64]$
Eigenvector (associated with the third principal component)	$[-0.66 \quad -0.50 \quad -0.56]$
Eigenvalue (associated with the first principal component)	1.69
Eigenvalue (associated with the second principal component)	1.20
Eigenvalue (associated with the third principal component)	0.11

Table 6.19. Principal Component Analysis. (Using short and long term measurements / Using the Instruments Error Structure).

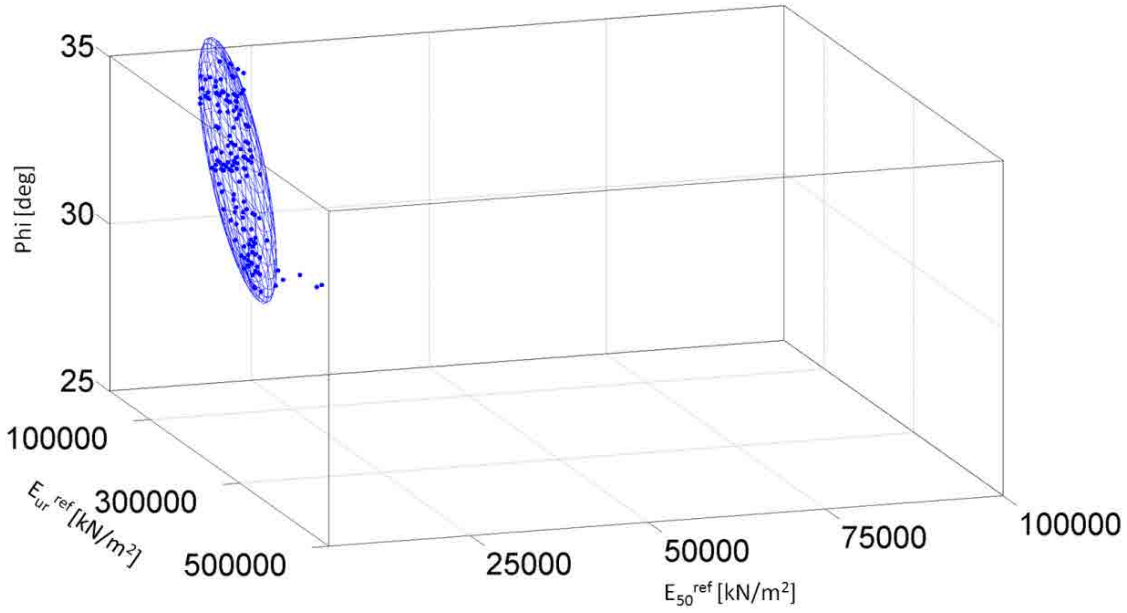

Figure 6.56. Graphical representation of the Principal Component Analysis results (ΣMStage = 0.175 / Using the Instruments Error Structure).

Starting from the center of the PCA ellipsoid, the Gauss-Newton method was finally applied to find the best set of parameters (see figure 6.57). Unfortunately, as occurred when "Not Using the Instruments Error Structure", no better solution was found by the gradient based method, which also got stuck at the border.

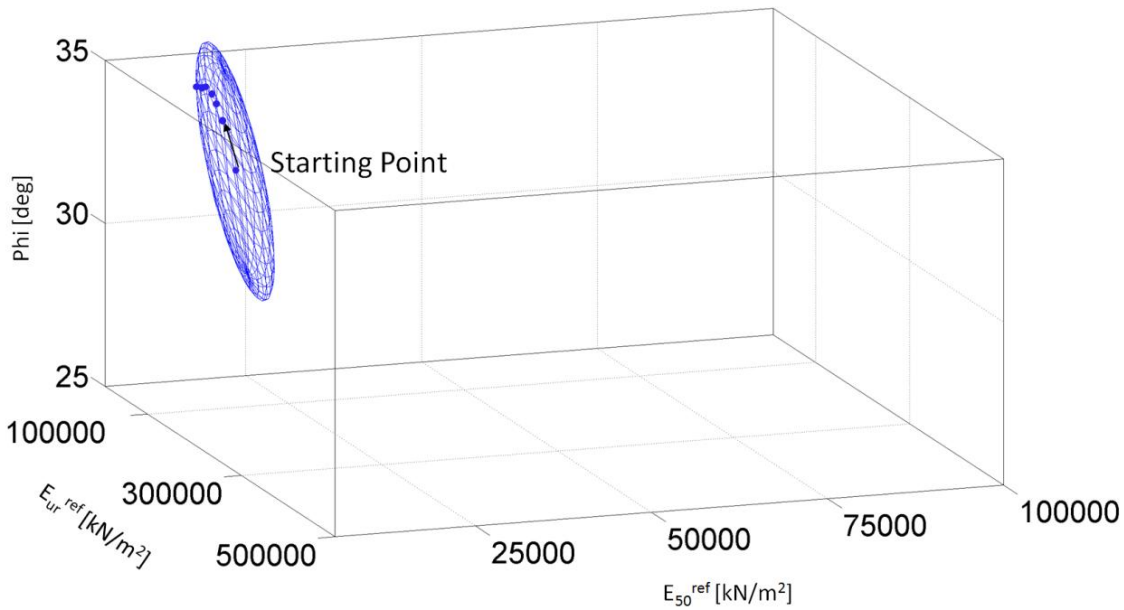

Figure 5.57. Gauss-Newton iterative procedure. The PCA ellipsoid (*AF*=2.85) defines the new search space and its center is used as starting point. (ΣMStage=0.175).

The parameters associated with the last Gauss-Newton iteration are shown in table 6.20.

ΣMStage	E_{50}^{ref} [kN/m^2]	E_{ur}^{ref} [kN/m^2]	φ [deg]	Error [-]
0.175	11546.81	106104.3	35	$6.75 \cdot 10^{-5}$

Figure 6.20. Parameters associated with the last Gauss-Newton iteration. The error represents the objective function value using short and long term measurements with the instruments error structure.

6.6.3 Analysis of the Results

From both analyses (using and not using the instruments error structure), no improvement was obtained from using a gradient based method after an AGA. That highlights the limitation of the local gradient based methods for complex problems with noisy measurements. Moreover, due to the use of the Hardening Soil Model, where many of their parameters are interrelated among them, the proper definition of the global boundary conditions, as well as the ones derived from the PCA ellipsoid, is extremely difficult to guarantee, which is crucial for the proper functioning of a gradient based method. Figure 6.44 illustrates, assuming that the value range of φ is geotechnically appropriate (25^0-35^0), how different good combinations (good individuals) of φ and E_{50}^{ref} with similar objective function value are spread along all the range of the φ axis; making it highly likely that the algorithm will reach the boundary and subsequently gets stuck on it. In contrast, genetic algorithms, not only are better at dealing with this feature, but they also provide valuable information to illustrate this phenomenon.

Independently from the optimization technique used, the difficulty or even the inconsistency of trying to identify the internal friction angle when being far from collapse can be noted. As mentioned before, even being far from collapse, the internal friction angle affects the soil behavior due to the nature of its formulation (see section 2.6.1). This causes that some geotechnically inconsistent solutions are obtained. As figures 5.58 and 5.59 have shown, no Mohr-Coulomb plastic points appeared on the model, except in the man-made fill material (fill) located at the top of the geological profile, which indicates in some way that the tunnel

construction is still far from collapse. Consequently, the influence of φ on the backanalysis is mainly due to its indirect effect over the stiffness moduli rather than its role controlling failure. Therefore, it seems more appropriate not to involve φ in the analysis for those cases.

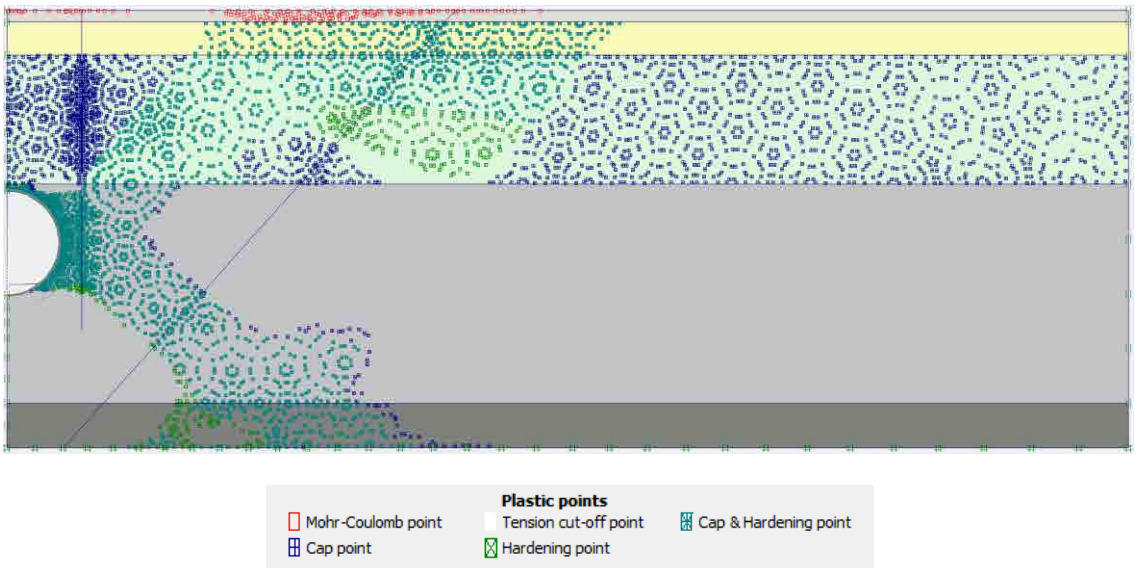

Figure 6.58. Plastic points at the end of the Plaxis phase 1 (tunnel excavation) from the best individual not using the instruments error structure (E_{50}^{ref}=12000kN/m^2, E_{ur}^{ref}=167500kN/m^2 and φ=34.5^0).

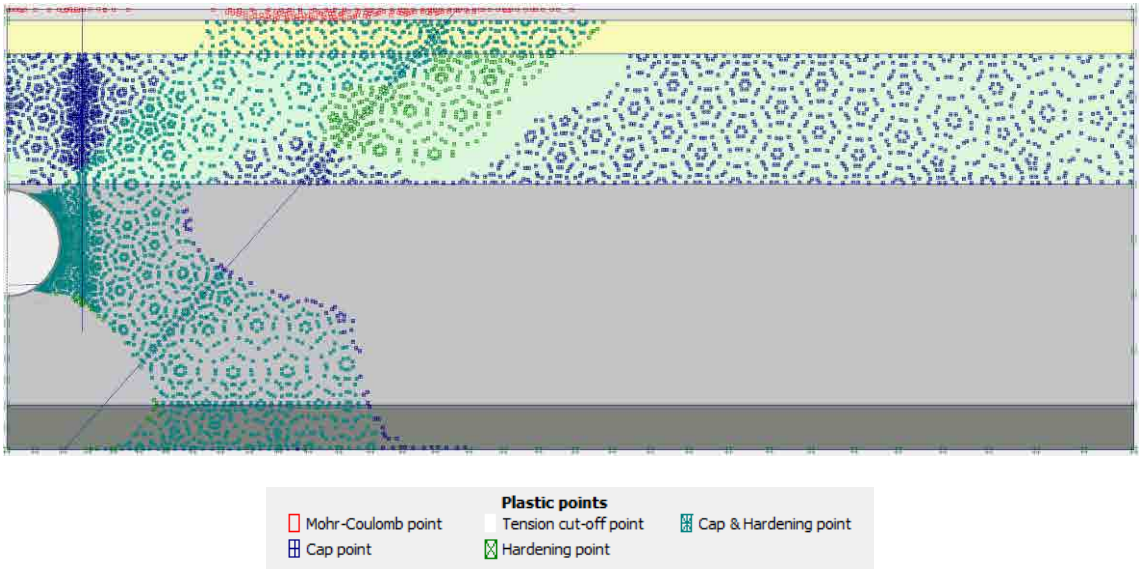

Figure 6.59. Plastic points at the end of the Plaxis phase 1 (tunnel excavation) from the best individual using the instruments error structure (E_{50}^{ref}=19000kN/m^2, E_{ur}^{ref}=57500kN/m^2 and φ=35^0).

In terms of matching measurements and calculations, the results derived from the best individual (using and not using the instruments error structure) are reasonably satisfactory, except for the inclinometer (compare figure 6.48.a vs. 6.55.a, 6.49.a vs. 6.55.b and 6.50.a vs. 6.55.c). The mismatch of the top 15 meters of the inclinometer, corresponding to the soil layers not backanalyzed, is mainly due to the input soil parameters used in the analysis (table 6.1) and the little influence of the backanalyzed soil layer (Ql3) over the horizontal

displacements of the above materials. However, the discrepancies between the measurements and the calculations at the bottom part of the inclinometer (corresponding to the soil layer backanalyzed) are mainly attributed to the numerical model limitations and the way that the backanalysis has been defined in terms of objective function (using and not using the instruments error structure).

Independently of using or not using the instruments error structure, similar calculated settlements and vertical displacements (sliding micrometer) were obtained from both analyses. However, significant different results were obtained in terms of calculated horizontal displacements (inclinometer). As mentioned before, the effect of using the instruments error structure, as been defined in this thesis, has caused that the measurements of horizontal displacements to have low weights, and consequently, low influence on the soil parameters identification process. Therefore, in terms of soil parameters values, different values have been obtained. If the parameters values associated with the best individual obtained from both analyses are compared (see tables 6.13 and 6.17), it can be noticed a large difference between the values of E_{ur}^{ref} (167500kN/m^2 vs. 57500kN/m^2). That difference subsequently causes different displacements fields. As figures 6.60, 6.61, 6.62 shown, having a lower E_{ur}^{ref} produces larger displacements. For this particular case study, due to the higher stiffness of the tunnel lining with respect to the soil, the difference between the vertical displacements at the bottom of the tunnel obtained from both analyses (using and not using the instruments error structure) is transmitted by the lining to the side of the tunnel; causing the large discrepancy between calculated horizontal displacements (compare figure 6.50.a vs. 6.55.c).

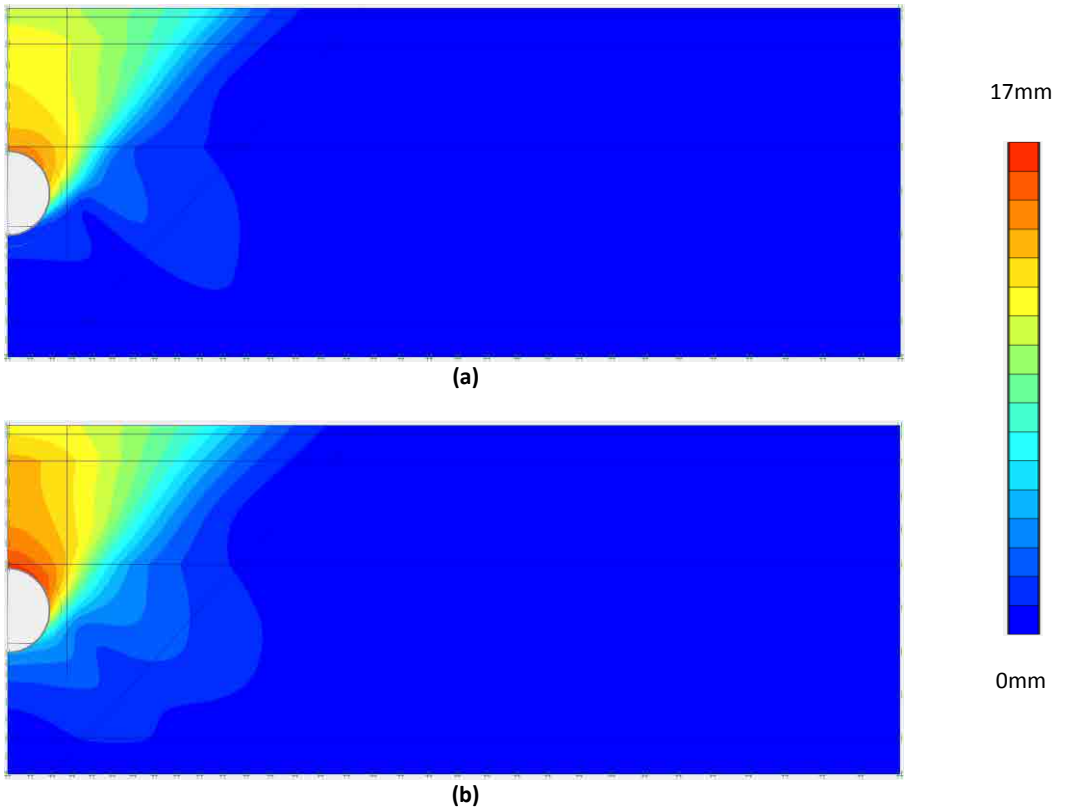

Figure 6.60. Phase total displacements (tunnel excavation). (a) Not using the instruments error structure. (b) Using the instruments error structure.

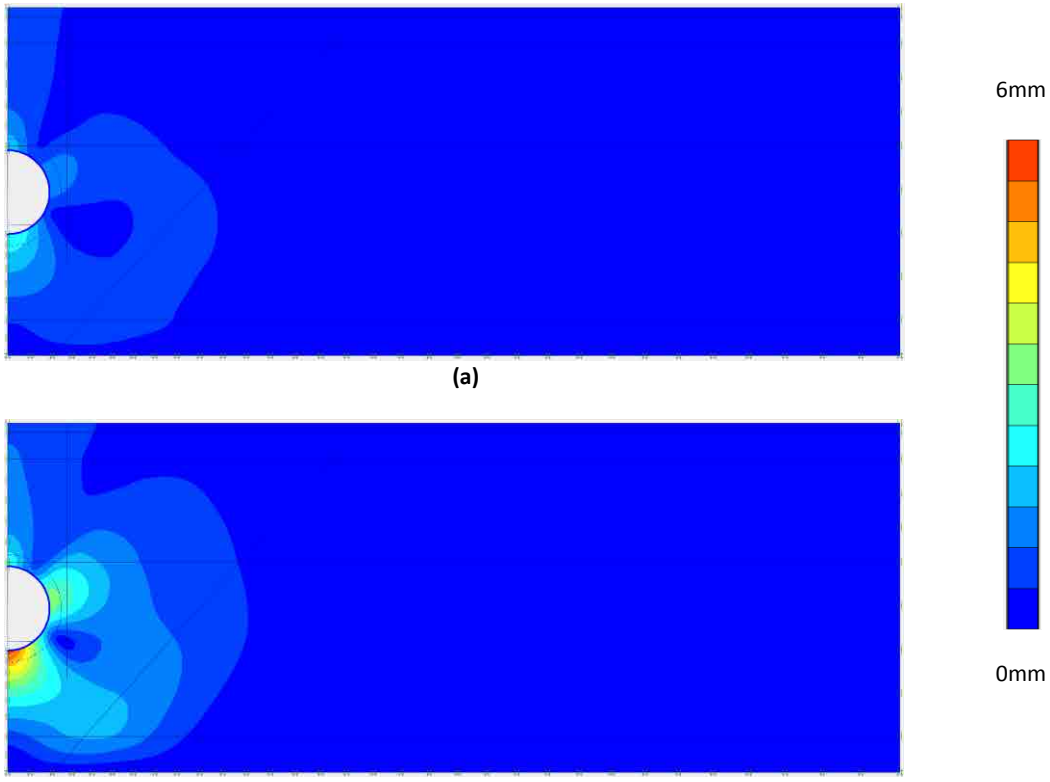

(a)

(b)

Figure 6.61. Phase total displacements (tunnel lining installation). (a) Not using the instruments error structure. (b) Using the instruments error structure.

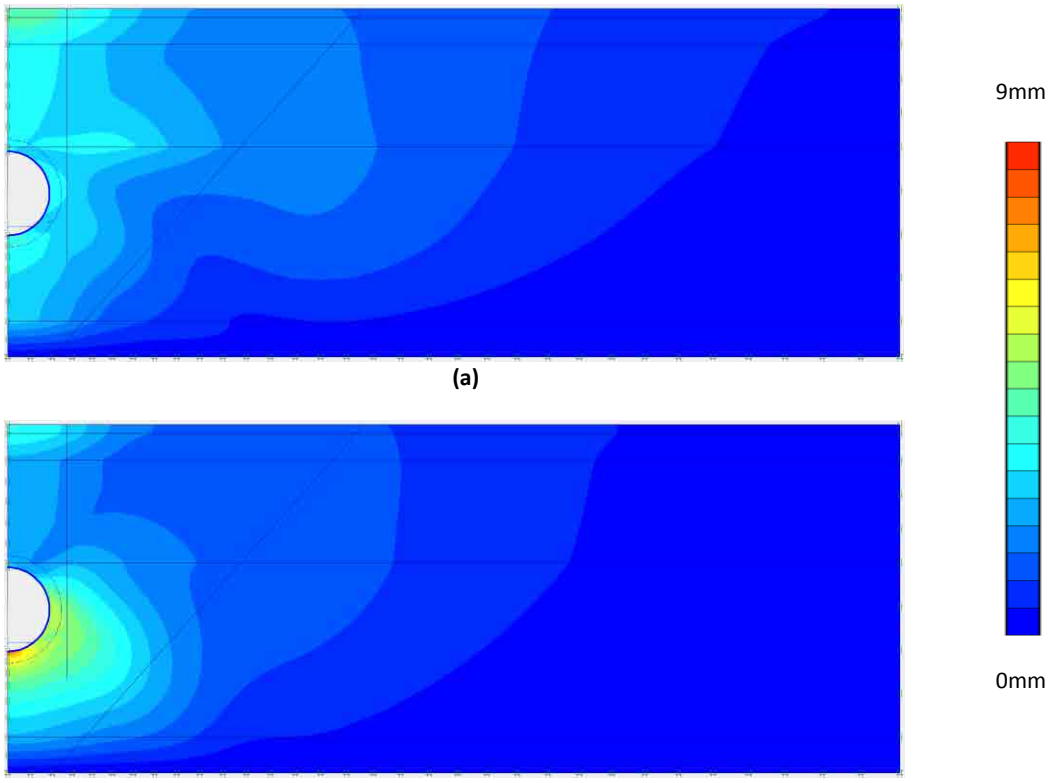

(a)

(b)

Figure 6.62. Phase total displacements (consolidation). (a) Not using the instruments error structure. (b) Using the instruments error structure.

6.6.3 Concluding Remarks of the Backanalysis

After the backanalysis presented in this section (6.6), several concluding remarks can be pointed out.

Very similar solutions in terms of objective function can be obtained from different combinations of soil parameters and ΣMStage. Therefore, more information was required to properly define the solution. Consequently, in contrast to the preliminary backanalysis (section 6.5), both short and long term measurements were introduced into the backanalysis.

Thanks to the introduction of both sets of measurements into the backanalysis, the numerical model was capable of capturing short and long term behavior, which consequently facilitated the definition of a better solution.

In terms of optimization algorithms, the adaptive genetic algorithm has shown a better behavior than the gradient based method that has struggled to cope with the boundaries of the search space.

For this particular case study where the tunnel construction is far from collapse, the identification by backanalysis of the internal friction angle does not seem adequate due to the fact that the friction angles should be more directly related to failure. Moreover, a strong relationship exists between φ and E_{50}^{ref} that subsequently makes more difficult to identify a proper value of E_{50}^{ref}. The higher the φ is, the lower E_{50}^{ref} is.

When settlements, vertical displacements extracted from sliding micrometers and horizontal displacements extracted from inclinometers are used as measurements simultaneously, better results were obtained when not using the instruments error structure.

Finally, as a consequence of what has been mentioned above, the value of φ was considered fixed and set to 27.5^0 (the same that was proposed by Gens et al., 2009). Consequently, the solution of the problem was defined by the best individual (with φ = 27.5^0) obtained from the adaptive genetic algorithm with "not using the instruments error structure". By forcing the value of φ, the effect of φ over the identification of E_{50}^{ref} and E_{ur}^{ref}, especially over E_{50}^{ref}, was eliminated. Table 6.21 shows the set of parameters considered as solution of the soil parameters identification problem presented in this chapter.

ΣMStage	E_{50}^{ref} [kN/m^2]	E_{ur}^{ref} [kN/m^2]	φ [deg]	Error [m^2]
0.175	23000	172500	27.5	$5.11 \cdot 10^{-4}$

Table 6.21. Solution of the soil parameters identification problem (QI3). The error represents the objective function value using short and long term measurements with no instruments error structure.

Chapter 7

Case Study 2: Girona High-Speed Railway Station

7.1 Introduction

As previously mentioned in the thesis, one of the main goals of backanalyzing a problem is identifying the parameters that make the conceptual model capable of predicting the soil behavior in a reliable manner. However, apart from having a well calibrated model, what is also really important is to be able to use the model to corroborate the validity of the hypotheses used in design; and if necessary or possible, to modify them in order to optimize the design.

The large excavation of the Girona High-Speed Railway Station, excavated in different stages, was considered a suitable scenario to test the methodology proposed in this thesis, and to illustrate the concept of adaptive design by backanalysis to optimize the construction in real time. Meaning by adaptive design by backanalysis, the evolution of the design caused by the update of the soil parameters values. That evolution is governed by feeding the backanalysis with new available measurements that permits recalibrating the model. By using this technique, it is expected to: 1) Identify the soil parameters in the early stages, 2) Validate the design hypotheses, and 3) Check the robustness of the model by controlling the soil parameters evolution.

An extensive analysis was conducted to identify the reference secant stiffness in standard drained triaxial test (E_{50}^{ref}), and the reference unloading-reloading stiffness (E_{ur}^{ref}); as well as

studying the applicability of the adaptive design concept in a complex real case. As all cases presented in the thesis, the numerical models used to proceed with the backanalyses have been defined by means of the Plaxis 2D code. However, for this particular case study, where some construction stages had a strong three-dimensional nature, it was considered useful to define a 3D model (Plaxis 3D) to finally reproduce the soil behavior (but not to backanalyze the problem).

7.2 Girona High-Speed Railway Station

A large underground station, along the new Spanish high-speed railway line, connecting Barcelona and the French border, was successfully built in the downtown of Girona. Both the project and the construction of the station was an outstanding challenge for all engineers involved in it, due to the magnitude of the excavation, the severe hydraulic conditions, and the preexisting infrastructures surrounding the station (including a railway bridge).

The new Girona High-Speed Railway Station is a large diaphragm wall enclosure about 600m long, 55m wide and 25m deep (see figure 7.1). The station is formed by an outer diaphragm wall perimeter, an inner mixed pile-diaphragm wall corridor, three intermediate slabs, the upper slab and three inverted arches at the bottom (see figure 7.2). The outer diaphragm wall was built by means of a hydromill equipment in order to ensure a good contact between panels (1.2m x 2.4m) and make the lateral perimeter of the excavation as water tight as possible. The interior walls are a combination of isolated diaphragm panels (1.2m x 2.4m) between pile walls ($Ø_{pile}$=1.2m). The reason of building mixed pile-diaphragm walls in the interior of the station was because of: 1) The need of intermediate supporting points for the slabs. The diaphragm panels were the ones used as supporting points. 2) Timing: The pass of the tunnel boring machine (TBM) through the station was planned to occur before finishing the excavation. As a consequence, a provisional inner excavation, using the mixed walls as retaining structures, was designed to allow the TBM to pass through. 3) Increasing the resistance against uplift. The piles were design to provide extra resistance to the global stability of the station against uplift.

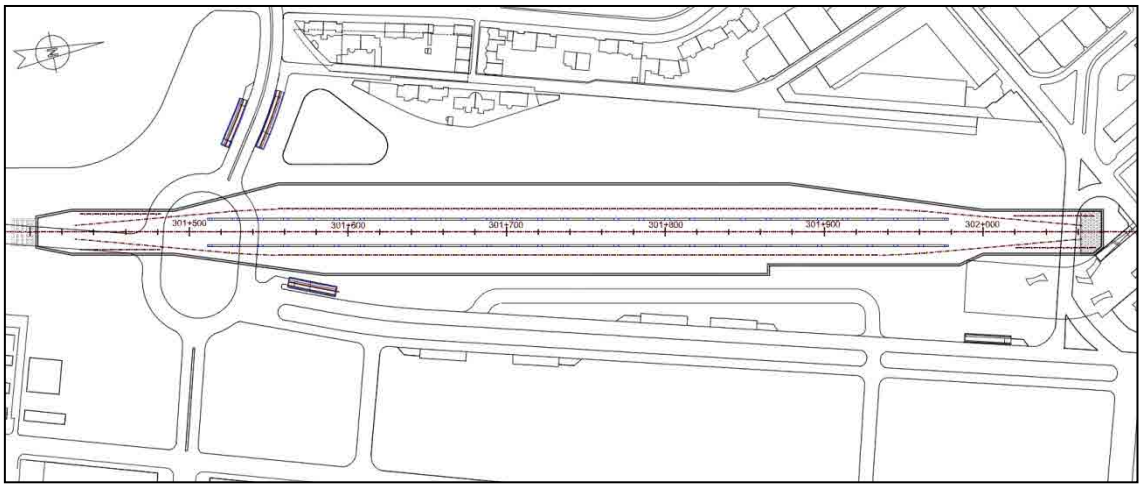

Figure 7.1. Girona High-Speed Railway Station.

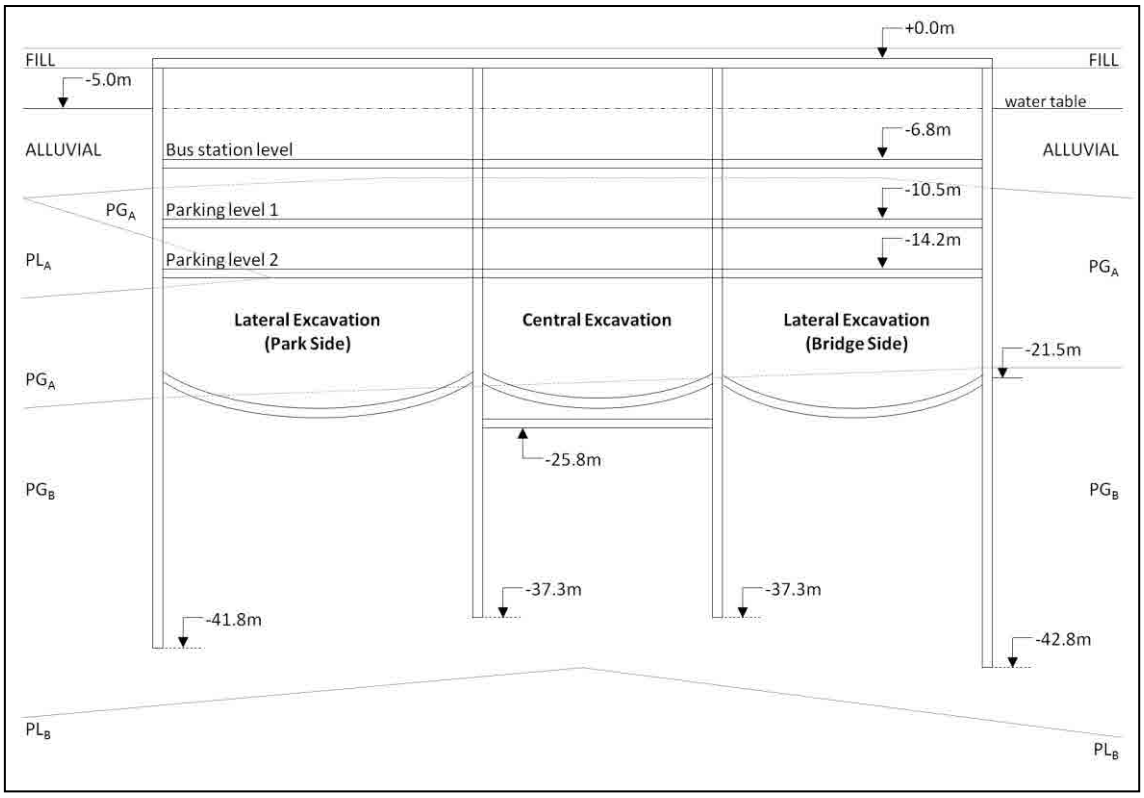

Figure 7.2. Structural and geological cross-section of the Girona High-Speed Railway Station (central part of the station). PL_A: shallow cohesive Pliocene. PG_A: shallow granular Pliocene. PL_B: deep cohesive Pliocene. PG_B: deep granular Pliocene.

The geological profile is schematically defined, from top to bottom, by 1.5m of man-made fill, 6-8m of alluvial sandy gravel and more than 50m of alternating layers of cohesive (silty clay) and granular material (sandy gravel), both from Pliocene origin (see figure 7.2). The Pliocene stratum was divided into two different subgroups based on soil stiffness; shallow Pliocene formed by cohesive Pliocene (PL_A) and granular Pliocene (PG_A), and deep Pliocene formed by cohesive Pliocene (PL_B) and granular Pliocene (PG_B).

Initially, the soil parameters values were obtained from several soil characterization campaigns, where an extensive number of laboratory tests, Cross-Hole tests and pressuremeter tests (Mènard type) were conducted. The values that were initially used to define the numerical model during design are shown in table 7.1.

Parameter	Fill	Alluvial	PL_A	PG_A	PL_B	PG_B
Constitutive Model	M-C	M-C	Hardening	Hardening	Hardening	Hardening
γ_{unsat} [kN/m^3]	18	18	19	19	19	19
γ_{sat} [kN/m^3]	20	20	21	21	21	21
$k_x = k_y$ [m/day]	0.514	0.514	0.026	0.321	0.026	0.321
E [kN/m^2]	20000	50000	-	-	-	-
E_{50}^{ref} [kN/m^2]	-	-	25000	25000	50000	50000
E_{oed}^{ref} [kN/m^2]	-	-	25000	25000	50000	50000
E_{ur}^{ref} [kN/m^2]	-	-	87500	87500	175000	175000
m [-]	-	-	1	1	1	1
c [kN/m^2]	10	0	10	5	10	5
φ [deg]	28	40	28	35	28	35
ψ [deg]	0	0	0	0	0	0
ν [-]	0.3	0.3	-	-	-	-
ν_{ur} [-]	-	-	0.2	0.2	0.2	0.2

p^{ref} [kN/m^2]	-	-	100	100	100	100
K_0^{NC} [-]	-	-	$1-\sin\varphi$	$1-\sin\varphi$	$1-\sin\varphi$	$1-\sin\varphi$
R_f [-]	0.9	0.9	0.9	0.9	0.9	0.9
$\sigma_{tension}$ [kN/m^2]	0	0	0	0	0	0
$c_{increment}$ [kN/m^2/m]	0	0	0	0	0	0
R_{inter} [-]	0.6	0.6	0.6	0.6	0.6	0.6

Table 7.1. Design soil parameter values adapted to be used in the numerical model (Plaxis 2D). γ_{unsat}: unsaturated soil weight, γ_{sat}: saturated soil weight, k_x and k_y: horizontal and vertical permeability, E: Young's modulus, E_{50}^{ref}: secant stiffness in standard drained triaxial test, E_{oed}^{ref}: tangent stiffness for primary oedometer loading, E_{ur}^{ref}: unloading/reloading stiffness, m: power for stress-level dependency of stiffness, c: effective cohesion, φ: effective angle of internal friction, ψ: angle of dilatancy, ν: Poisson's ratio, ν_{ur}: Poisson's ratio for unloading/reloading, p^{ref}: Reference stress for stiffnesses, K_0^{NC}: coefficient of lateral earth pressure for normal consolidation, R_f: Failure ratio, $\sigma_{tension}$: Tensile strength, $c_{increment}$: cohesion increment with depth, and R_{inter}: strength reduction factor for interfaces.

The station construction procedure was adapted to the need of the TBM passing through the station before finishing all the excavation. A series of consecutive stages of excavation and slab construction were followed (see figure 7.3). During the excavation the water table inside the excavation was set 3 m below the maximum excavation level and its initial position was not recovered until the station was finished.

Some of the construction stages shown in figure 7.3 are illustrated in the pictures shown in figures 7.4, 7.5, 7.6, 7.7, 7.8. The platform of the station just before and after its full completion is also shown (see figures 7.9 and 7.10).

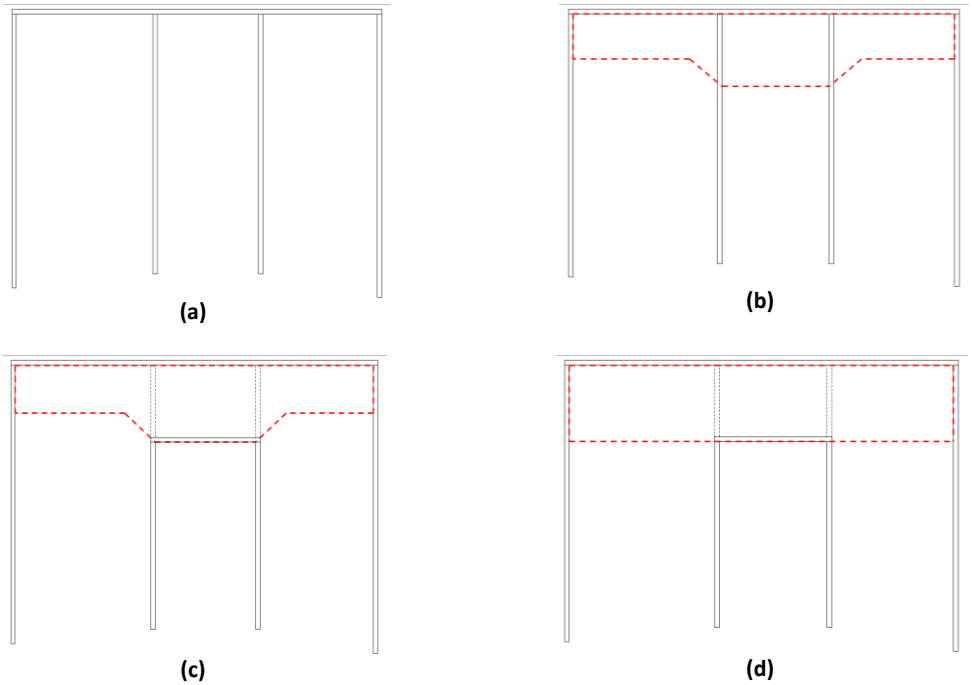

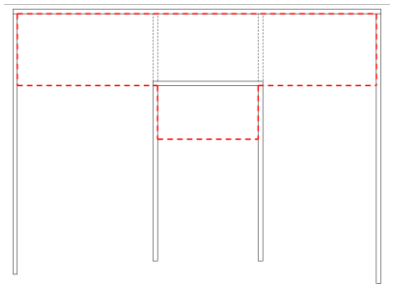

(e)

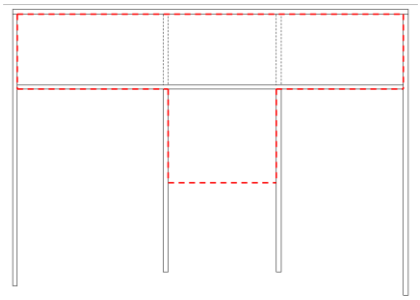

(f)

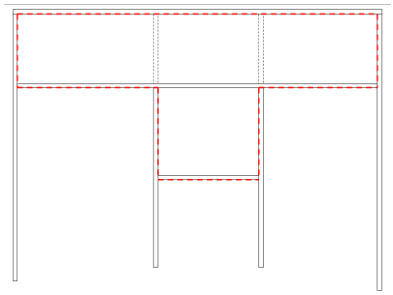

(g)

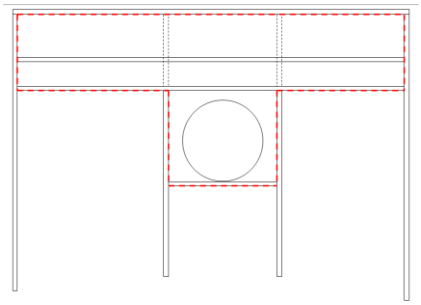

(h)

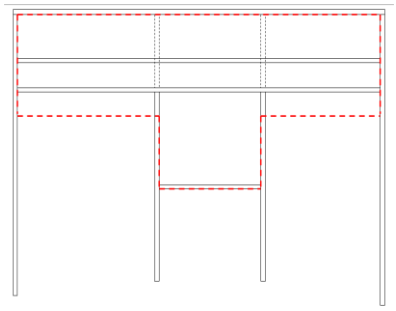

(i)

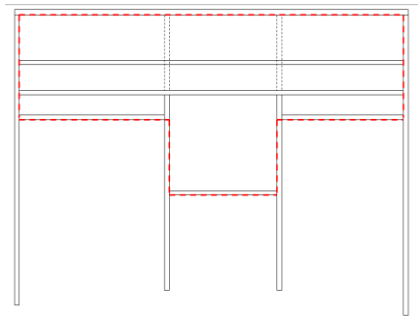

(j)

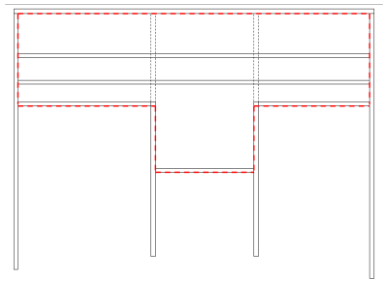

(k)

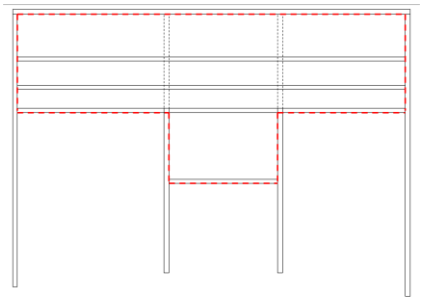

(l)

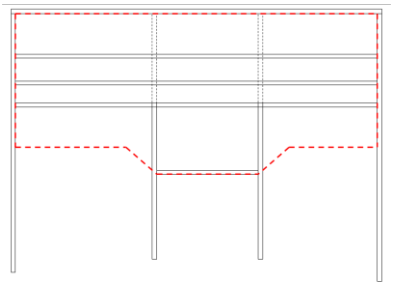

(m)

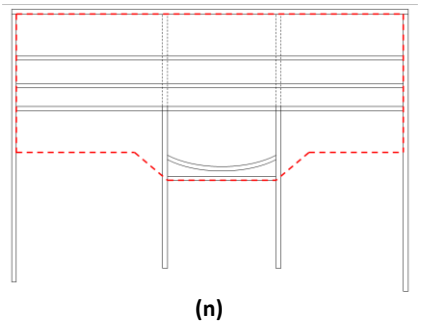

(n)

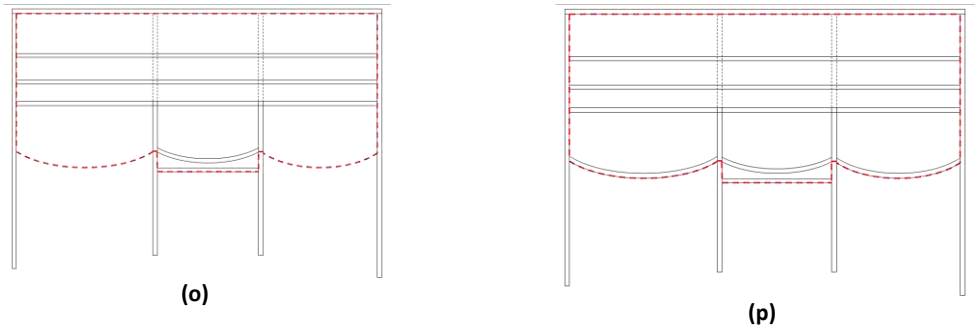

Figure 7.3. Girona High-Speed Railway Station construction procedure. The dashed red line represents the excavation level. (a) Construction of the external diaphragm walls, the internal mixed pile-diaphragm wall corridor and the upper slab. (b) Central excavation to parking level 1 and lateral excavation to bus station level. (c) Piles demolition between upper slab and parking level 1, central construction of the parking level 1. (d) Lateral excavation to parking level 1. (e) 7.285m of central excavation. (f) Lateral construction of the parking level 1 and central excavation to maximum excavation level. (g) Construction of the central bottom slab. (h) Construction of the bus station slab and pass of the tunnel boring machine through the station. (i) Lateral excavation to parking level 2. (j) Lateral construction of the parking level 2. (k) Piles demolition between parking level 1 and parking level 2. (l) Central construction of the parking level 2. (m) 6.785m of lateral excavation. (n) Construction of the central inverted arch. (o) Lateral excavation to maximum excavation level. In this phase the excavation was carried out by sequences of 12m length to avoid excessive displacements. (p) Construction of the laterals inverted arches in sequences of 12m length. (o) and (p) were alternated until completing the full length of the station.

Figure 7.4. Picture of the interior of the station under construction. Construction stage corresponding to that shown in figure 7.3.c (Piles demolition between upper slab and parking level 1).

Figure 7.5. Picture of the interior of the station under construction. Construction stage corresponding to that shown in figure 7.3.e (7.285m of central excavation).

Figure 7.6. Picture of the interior of the station under construction. Construction stage corresponding to that shown in figure 7.3.h (Construction of the bus station slab and passing of the tunnel boring machine through the station).

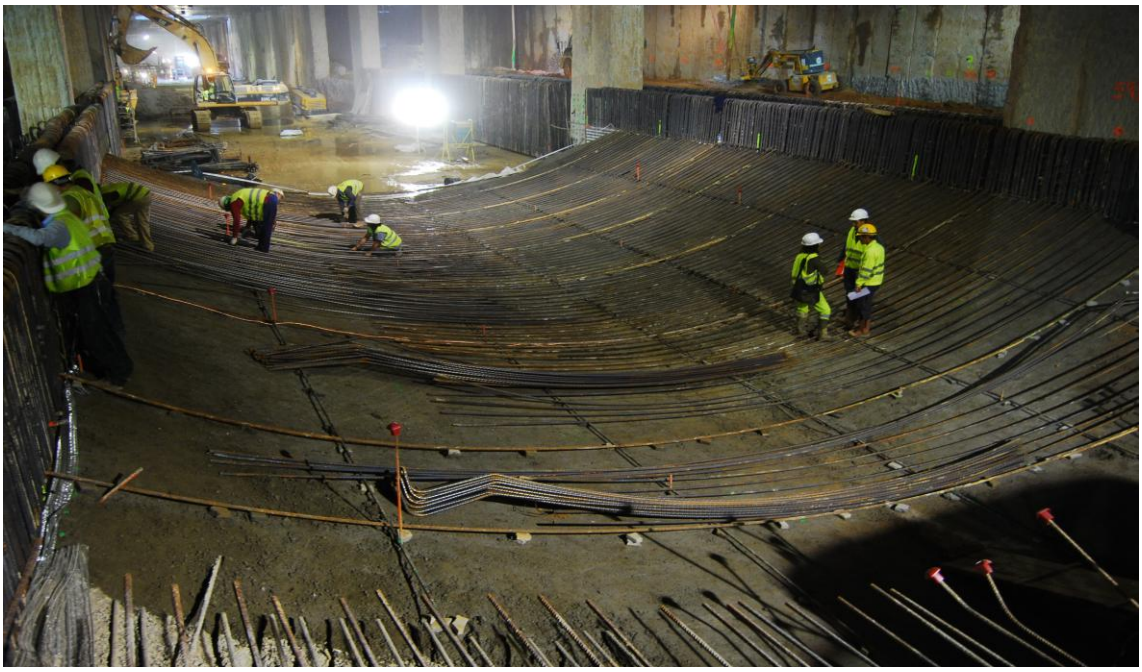

Figure 7.7. Picture of the interior of the station under construction. Construction stage corresponding to that shown in figure 7.3.n (Construction of the central inverted arch).

Figure 7.8. Picture of the interior of the station under construction. Construction stage corresponding to that shown in figure 7.3.o and 7.3.p (Lateral excavation to maximum excavation level and construction of the laterals inverted arches).

Figure 7.9. Picture of the station platform just before its full completion.

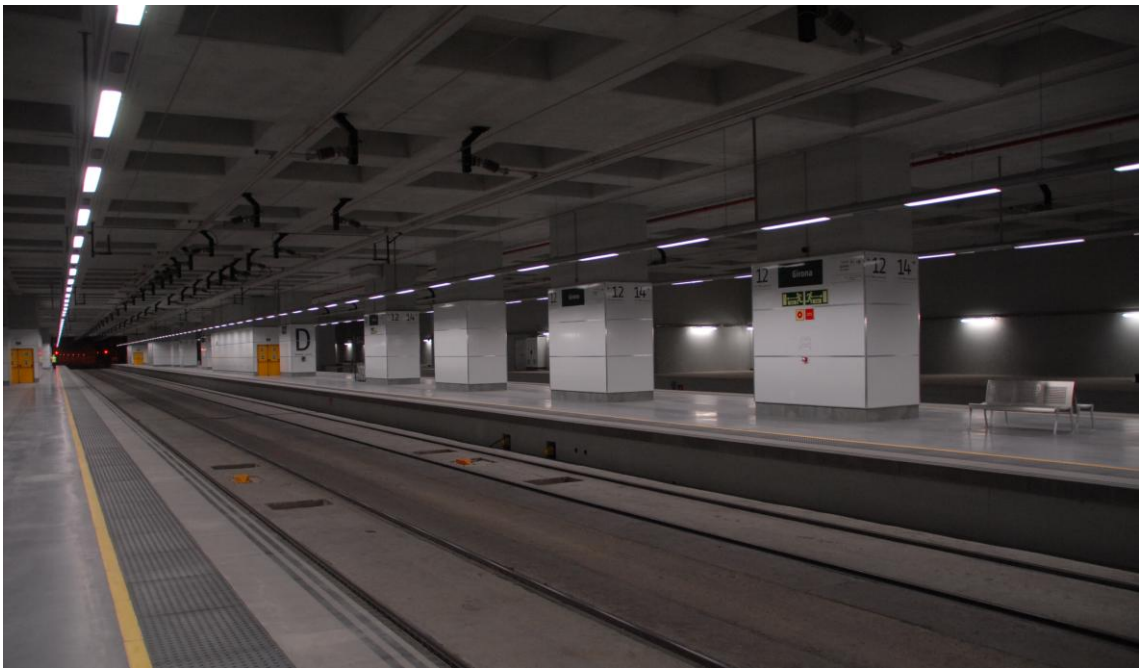

Figure 7.10. Picture of the station platform just after its full completion.

7.3 Numerical Model (Backanalysis 2D Model)

The commercial geotechnical software Plaxis V9 was used to build a two-dimensional numerical model of the central part of the station (the widest section). The station was simulated assuming plane-strain conditions. The soil stratigraphy was assumed non-uniform across the site (see figure 7.2). Six different soil materials were considered: A man-made fill material (Fill), an alluvial sandy gravel (Alluvial), two Pliocene sandy gravels (PG_A and PG_B) and

two Pliocene silty clays (PL_A and PL_B). The same constitutive models and soil parameter values that were used in the design analyses were adopted to carry out the backanalysis; with the exception of the stiffness moduli of PL_A, PL_B, PG_A and PG_B, which were the parameters to identify; and their permeabilities that were redefined after further analyses (see table 7.2). The water table was set 5 meters depth from the top surface of the model. Figure 7.11 shows the geometry and the mesh of the model (model formed by 3600 elements of 15 nodes).

Parameter	Fill	Alluvial	PL_A	PG_A	PL_B	PG_B
Constitutive Model	M-C	M-C	Hardening	Hardening	Hardening	Hardening
γ_{unsat} [kN/m^3]	18	18	19	19	19	19
γ_{sat} [kN/m^3]	20	20	21	21	21	21
k_x [m/day]	0.514	0.514	0.05	2.5	0.2	2.5
k_y [m/day]	0.514	0.514	0.001	2.5	0.2	2.5
E [kN/m^2]	20000	50000	-	-	-	-
E_{50}^{ref} [kN/m^2]	-	-	unknown	unknown	unknown	unknown
E_{oed}^{ref} [kN/m^2]	-	-	$E_{oed}^{ref} = E_{50}^{ref}$	$E_{oed}^{ref} = E_{50}^{ref}$	$E_{oed}^{ref} = E_{50}^{ref}$	$E_{oed}^{ref} = E_{50}^{ref}$
E_{ur}^{ref} [kN/m^2]	-	-	unknown	unknown	unknown	unknown
m [-]	-	-	1	1	1	1
c [kN/m^2]	10	0	10	5	10	5
φ [deg]	28	40	28	35	28	35
ψ [deg]	0	0	0	0	0	0
ν [-]	0.3	0.3	-	-	-	-
ν_{ur} [-]	-	-	0.2	0.2	0.2	0.2
p^{ref} [kN/m^2]	-	-	100	100	100	100
K_0^{NC} [-]	-	-	$1 - \sin\varphi$	$1 - \sin\varphi$	$1 - \sin\varphi$	$1 - \sin\varphi$
R_f [-]	0.9	0.9	0.9	0.9	0.9	0.9
$\sigma_{tension}$ [kN/m^2]	0	0	0	0	0	0
$c_{increment}$ [kN/m^2/m]	0	0	0	0	0	0
R_{inter} [-]	0.6	0.6	0.6	0.6	0.6	0.6

Table 7.2. Soil parameters values used to defined the Plaxis model applied for carrying out the backanalysis. γ_{unsat}: unsaturated soil weight, γ_{sat}: saturated soil weight, k_x and k_y: horizontal and vertical permeability, E: Young's modulus, E_{50}^{ref}: secant stiffness in standard drained triaxial test, E_{oed}^{ref}: tangent stiffness for primary oedometer loading, E_{ur}^{ref}: unloading/reloading stiffness, m: power for stress-level dependency of stiffness, c: effective cohesion, φ: effective angle of internal friction, ψ: angle of dilatancy, ν: Poisson's ratio, ν_{ur}: Poisson's ratio for unloading/reloading, p^{ref}: Reference stress for stiffnesses, K_0^{NC}: coefficient of lateral earth pressure for normal consolidation, R_f: Failure ratio, $\sigma_{tension}$: Tensile strength, $c_{increment}$: cohesion increment with depth, and R_{inter}: strength reduction factor for interfaces.

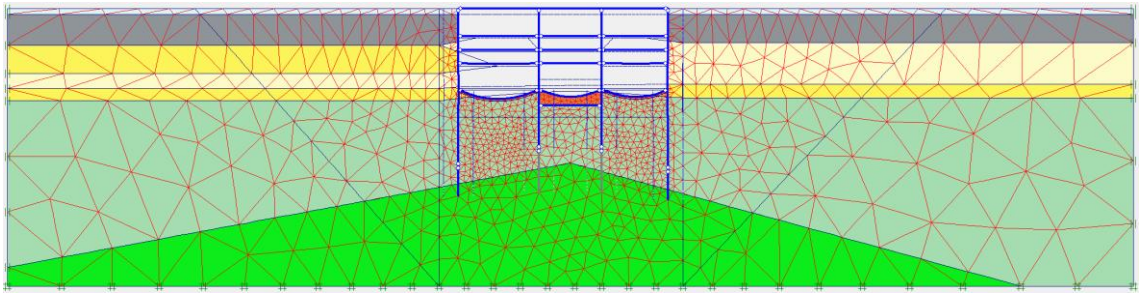

Figure 7.11. Numerical model of the central part of the Girona High-Speed Railway Station (300 m x 73.785 m).

From figure 7.12, it can be seen the match between water pressures, obtained from in situ measurements, and the ones given by the numerical model once the water pumping of the interior of the station was carried out. The water pumping condition was defined by prescribing, at 3 meters below the maximum excavation level, a water pressure equal to zero.

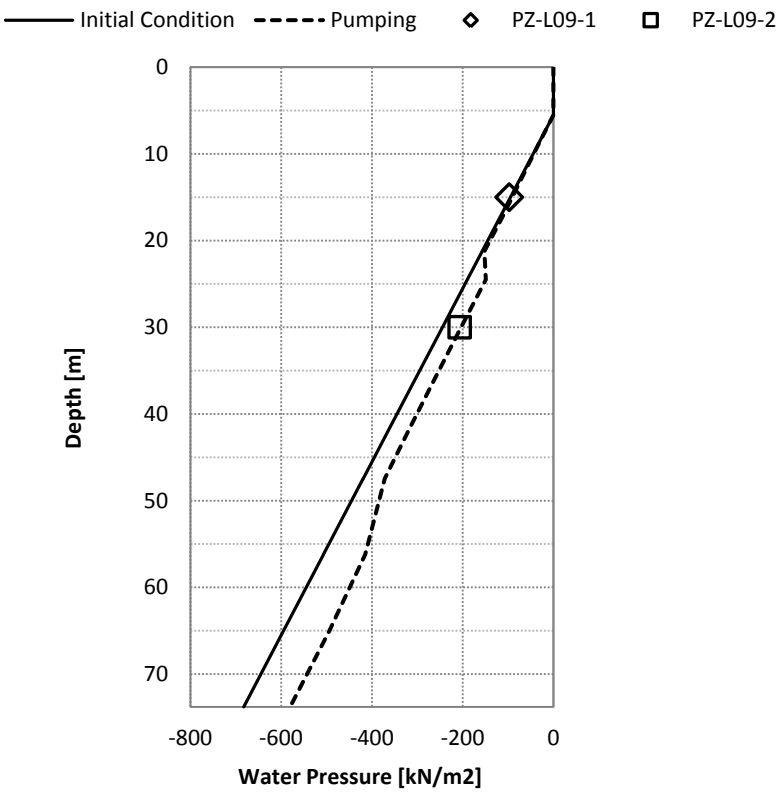

Figure 7.12. Water pressure behind the exterior diaphragm wall perimeter. The solid and dashed lines represent the values obtained from the numerical model, before and after pumping the water inside the excavation, while the square and the diamond represent the values extracted from two piezometers after pumping the water inside the excavation.

The diaphragm walls, piles and all slabs were simulated as beam elements (plates). The values that were implemented in the model are shown in table 7.3.

Structure	EA [kN/m]	EI [kNm^2/m]	w [kN/m^2]	v [-]
Upper slab	$1.52 \cdot 10^7$	$2.10 \cdot 10^6$	21.8	0.2
Bus station level slab	$1.33 \cdot 10^7$	$1.24 \cdot 10^6$	18.4	0.2
Parking level 1 slab	$1.33 \cdot 10^7$	$1.24 \cdot 10^6$	18.4	0.2
Parking level 2 slab	$1.28 \cdot 10^7$	$6.48 \cdot 10^5$	15.7	0.2
Inverted arches	$3.43 \cdot 10^7$	$4.12 \cdot 10^6$	30.0	0.2
Central bottom slab	$1.43 \cdot 10^7$	$2.98 \cdot 10^5$	12.5	0.2
Exterior diaphragm walls	$3.43 \cdot 10^7$	$4.12 \cdot 10^6$	30.0	0.2
Interior mixed pile-diaphragm walls	$2.23 \cdot 10^7$	$1.39 \cdot 10^6$	19.5	0.2
Interior pile demolished walls	$5.46 \cdot 10^6$	$1.65 \cdot 10^4$	4.8	0.2

Table 7.3. Structures properties. EA: axial stiffness; EI: flexural rigidity; w: weight; v: Poisson's ratio.

Interfaces were introduced in order to simulate the soil-structure interaction. Because of the morphology of the slab-diaphragm wall connection, the contact between slabs and diaphragm walls were defined by free rotation springs, which were not allowed to transmit moments from the slabs to the diaphragm walls.

Several construction stages were defined in order to reproduce the actual real construction process. The stages were based on the scheme presented in figure 7.3 with a slight modification with respect to the timing related to the construction of the lateral parts of the parking level 1 slab. The stages implemented in Plaxis are summarized in table 7.4.

Plaxis phase (stage)	Description
0	Initial stress generation (gravity loading method).
1	Construction of the exterior diaphragm walls, the interior mixed pile-diaphragm walls and the upper slab. Reset displacements to zero at the beginning of the phase.
2	Dewatering the interior of the excavation. The water table in the interior of the excavation was set 3 m below the maximum excavation level. Water conditions generated by groundwater calculation.
3	Central excavation to parking level 1 and lateral excavation to bus station level.
4	Pile demolition between upper slab and parking level 1. Central construction of the parking level 1. Lateral excavation to parking level 1.
5	7.285 m of central excavation.
6	Central excavation to maximum excavation level.
7	Lateral construction of the parking level 1. Construction of the central bottom slab and the bus station slab. Lateral excavation to parking level 2.
8	Construction of the parking level 2 and pile demolition between parking level 1 and parking level 2. 6.785 m of lateral excavation.
9	Construction of the central inverted arch and gap fill (gap between the central bottom slab and the inverted arch). Lateral excavation to maximum excavation level.
10	Construction of the lateral inverted arches. Pile demolition between the parking level 2 and the inverted arches.

Table 7.4. Construction stages defined in the numerical model (Plaxis).

7.4 In Situ Measurements

Even the dense instrumentation network installed on the station, only the closest and more representative instrument of the central part of the station was used to extract the measurements involved in the analysis. 18 horizontal displacements points were extracted from an inclinometer embedded in the outer diaphragm wall. Seven different sets of measurements were extracted from the seven different excavation stages (equivalent to Plaxis phases 3, 4, 5, 6, 7, 8 and 9). In order to clarify the nomenclature of the excavation stages, new labels were used; where Plaxis phase 3 becomes Exc_1, phase 4 becomes Exc_2, phase 5 becomes Exc_3, phase 6 becomes Exc_4, phase 7 becomes Exc_5, phase 8 becomes Exc_6 and phase 9 becomes Exc_7. Table 7.5 shows the numerical values of the measurements.

Depth [m]	Exc_1 [mm]	Exc_2 [mm]	Exc_3 [mm]	Exc_4 [mm]	Exc_5 [mm]	Exc_6 [mm]	Exc_7 [mm]
0	1.03	3.25	5.18	4.48	0.61	0.61	0.61
2	1.12	3.52	4.85	5.57	4.5	4.35	5.15
4	1.45	4.15	5.11	7.54	8.36	8.36	9.6
6	1.54	4.69	5.66	9.98	12.38	12.51	13.77
10	2.1	6.32	7.51	15.31	17.18	17.53	19.21
12	1.37	5.42	5.98	13.41	16.38	17.01	18.81
14	0.6	3.9	3.84	10.01	15.31	16.81	18.1
16	0.87	3.59	3.31	8.68	15.08	17.88	16.15
18	1.27	3.37	3.2	8.57	13.6	17.57	19.2
20	0.98	2.5	2.41	6.66	10.84	15.24	16.38
26	0.24	1.19	1.23	3.03	3.93	5.08	5.65
28	-0.06	0.65	0.76	2.46	2.76	3.19	3.81
30	-0.46	0.22	0.4	1.82	2	2.22	2.61
32	-0.4	0.08	0.5	1.65	1.75	1.8	2.3
34	-0.67	-0.35	0.24	1.24	1.22	1.22	1.67
36	-0.49	-0.26	0.49	1.04	1.24	1.34	1.63
38	-0.47	-0.35	0.32	0.82	0.85	0.92	1.26
40	0	0.03	0.05	0.05	0.18	0.23	0.35

Table 7.5. Horizontal displacements extracted from an inclinometer embedded in the exterior diaphragm wall. Positive values indicate movements towards the interior of the station. Negative values indicate movements towards the exterior of the station.

In figure 7.13, it is illustrated the evolution of the horizontal displacements along all the length of the inclinometer.

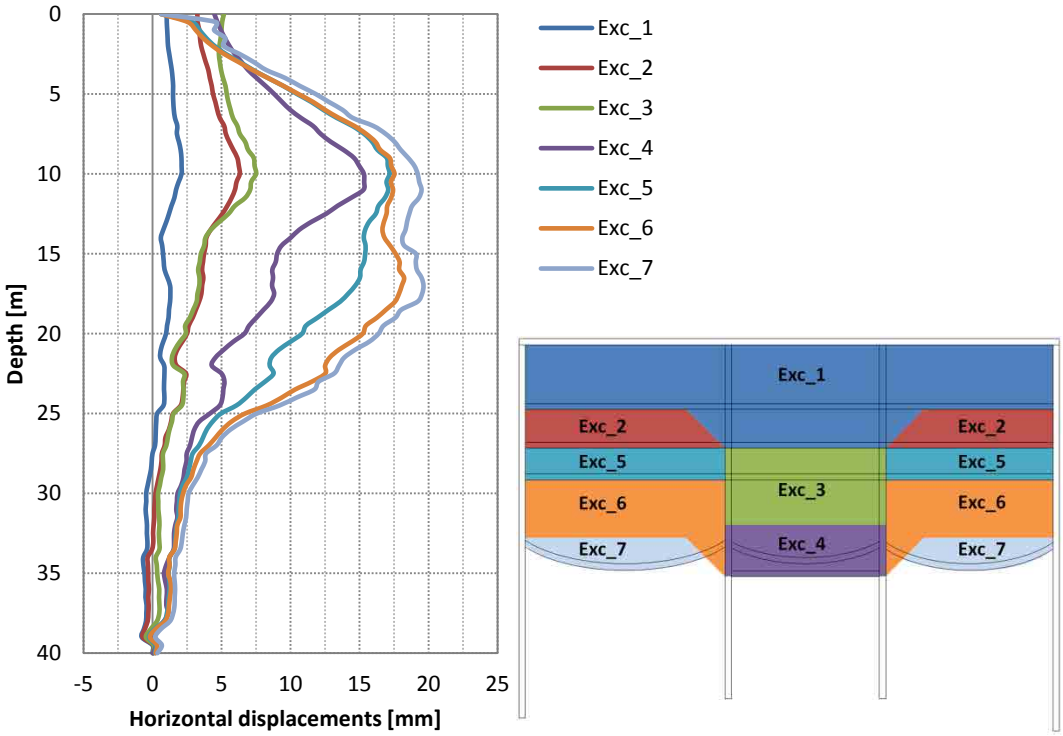

Figure 7.13. Evolution of the horizontal displacement measurements (extracted from an inclinometer embedded in the exterior diaphragm wall).

7.5 Soil Parameters (E_{50}^{ref} and E_{ur}^{ref})

Usually, as important as using the proper optimization algorithm is to choose the parameters that are going to be identified. Not all parameters can always be identified for any specific geotechnical scenario. And not all parameters can be simultaneously identified with the guaranty of not losing uniqueness. Obviously, a certain level of parameters sensitivity to measurements is required. However, many times, especially when using sophisticated constitutive models, it is not easy to be certain about how much sensitivity is required to identify a parameter, or which parameters can be simultaneously identified.

For this particular case study, it was expected that the excavation was far from collapse; consequently, a more relevant role was expected from the stiffness moduli than from cohesion and internal friction angle. Moreover, the fact that better results of cohesion and internal friction angle are usually obtained from laboratory tests, made it reasonable to focus the backanalysis on parameters that are more difficult to be obtained from laboratory tests, such as the stiffness moduli, which require an extensive and difficult stress-strain control to properly obtain their values. Therefore, E_{50}^{ref} and E_{ur}^{ref} were the parameters selected to be identified.

However, in order to corroborate what has been already mentioned, the stress path of several points close to the excavation (extracted from the Plaxis 2D model with the soil parameters obtained from the backanalysis, see section 7.7) were examined.

The location of those points are shown on figure 7.14, whereas the stress paths are plotted in figure 7.15.

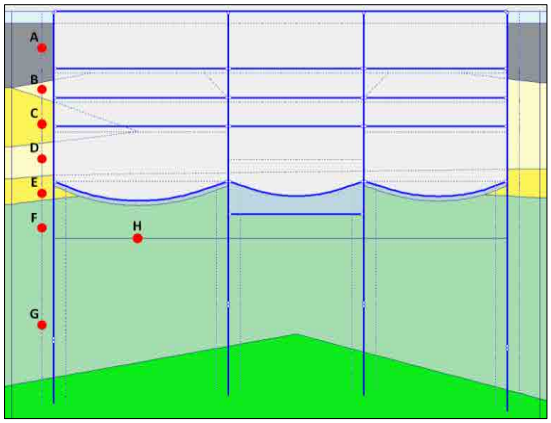

Figure 7.14.Control stress points location.

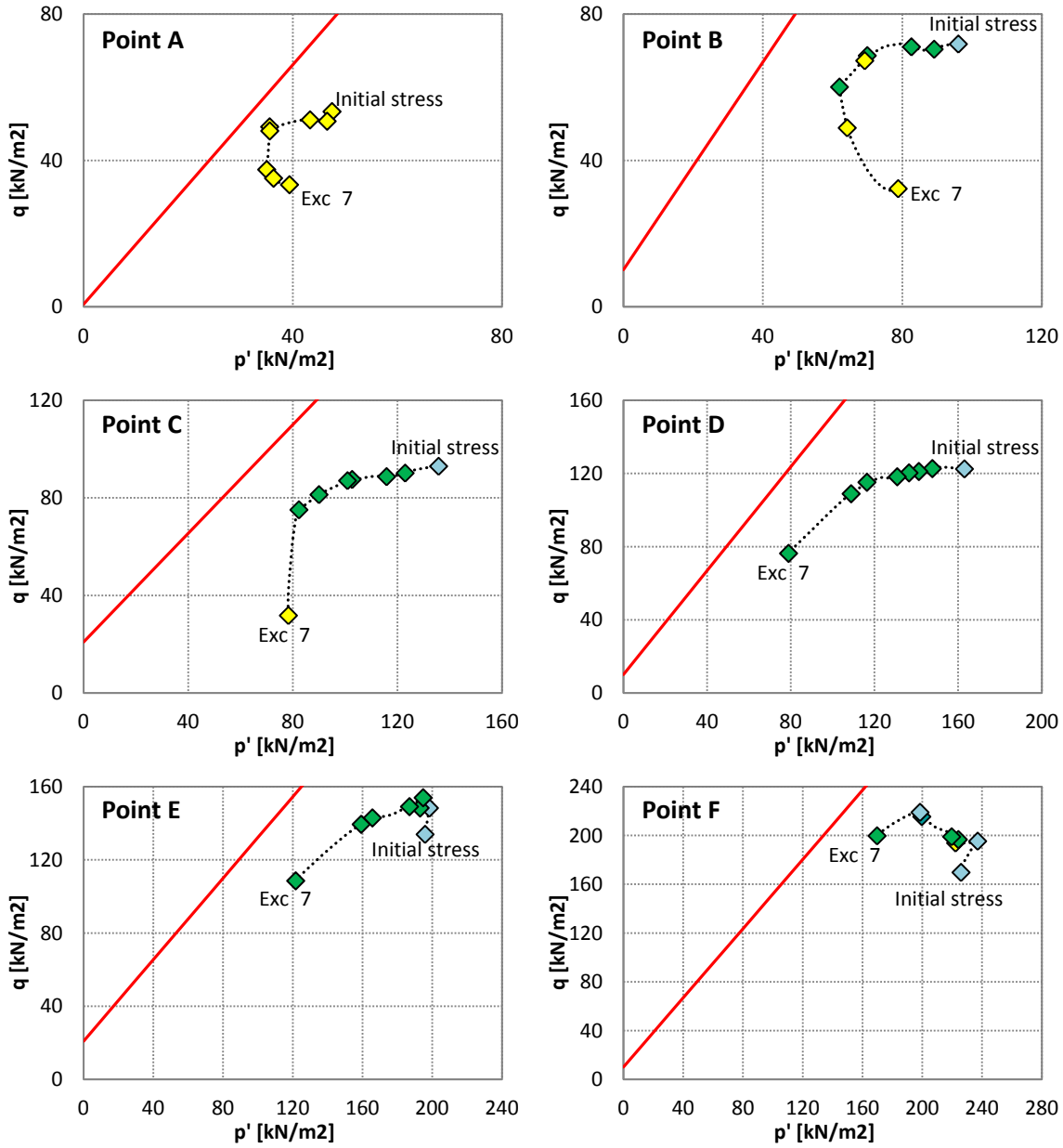

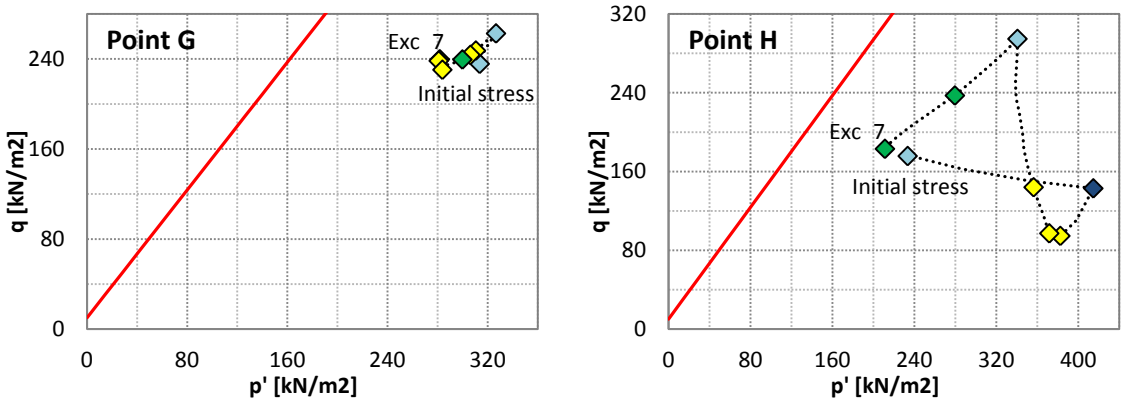

Figure 7.15. Stress paths around the station. The solid red line represents the Mohr-Coulomb failure line. The diamonds represent the stress state of the different stages. The color of the diamonds indicates the regime of the point: yellow represents Elastic regime, bright blue represents Cap & Hardening regime, dark blue represents Cap regime, and green represents Hardening regime.

Because of the definition of the soil as normal consolidated, all points start from a Cap & Hardening regime, except point A that was associated with a soil material defined by the Mohr-Coulomb constitutive model. Then, different stress paths were followed by the points, but none of them reached the Mohr-Coulomb failure line. Therefore, as mentioned before, it was not expected that cohesion and internal friction angle had a main role on the soil behavior, apart from that derived from the parameters interaction caused by the nature of the Hardening Soil model implemented in Plaxis (see section 2.6.1).

Finally, in order to simplify the problem, it was assigned the same value of stiffness moduli for the two shallow Pliocene materials of group A (PL_A and PG_A) and the two deep Pliocene materials of group B (PL_B and PG_B). Moreover, the stiffness moduli of the shallow and deep Pliocene were directly related to ($5E^{ref}_{50\_A}=E^{ref}_{50\_B}$, $5E^{ref}_{oed\_A}=E^{ref}_{oed\_B}$ and $5E^{ref}_{ur\_A}=E^{ref}_{ur\_B}$). Several preliminary backanalyses were carried out to determine the proper relationship between shallow and deep Pliocene materials. Six different values of A-B materials stiffness relationship (stiffness relationship of 1.5, 2, 3, 4, 5 and 6) were used in those preliminary backanalyses, where the A-B relationship of 5 caused the best match between measurements and calculations.

7.6 Analysis of the influence of the different excavation stages measurements

7.6.1 Definition

The first analysis, presented in this chapter, was designed to study: the influence of the magnitude and the number of measurements on the parameters reliability, its influence on the methodology, and the potential of continuously feeding the backanalysis with results extracted from previous stages.

Firstly, six different backanalyses were carried out with each set of measurements, except the set of measurements from Exc_7 that was considered as an excavation stage too three-dimensional to be analyzed with a two-dimensional model.

Secondly, it was conducted a backanalysis with all set of measurements implemented simultaneously (except Exc_7).

Finally, five backanalyses with continuous feeding were carried out. That continuous feeding of the backanalysis was defined by restricting the individuals involved in the PCA. The restriction is based on the intersection of PCA ellipses obtained from previous backanalysis where earlier stages measurements were used.

In order to accomplish those objectives, the application of an adaptive genetic algorithm (AGA) focused on finding the best set of individuals was considered the most adequate scheme.

The main characteristics of the backanalyses presented in this section are shown in table 7.6

Optimization Algorithm	
Type of algorithm	AGA + Elitism
Selection type	Roulette Wheel (with fitness limit = $2.5 \cdot 10^{-5} m^2$)
GAP	1
Maximum probability of applying crossover (P_{c_max})	0.95
Minimum probability of applying crossover (P_{c_min})	0.50
Maximum probability of applying mutation (P_{m_max})	0.40
Minimum probability of applying mutation (P_{m_min})	0.01
Population size	51
Maximum number of generations	25
Search Space Discretization	
$E_{50\ min}^{ref}$ [kN/m^2]	25000
$E_{50\ max}^{ref}$ [kN/m^2]	125000
$E_{50\ step\ size}^{ref}$ [kN/m^2]	5000
$E_{ur\ min}^{ref}$ [kN/m^2]	75000
$E_{ur\ max}^{ref}$ [kN/m^2]	750000
$E_{ur\ step\ size}^{ref}$ [kN/m^2]	5000
Principal Component Analysis (PCA)	
Frontier Value [m^2]	$1.125 \cdot 10^{-4}$ => one set of measurements / $5 \cdot 10^{-4}$ all measurements
AF (amplifier factor of the standard deviation)	2
Objective Function	
Type of objective function	Least-Squares Method
Measurements	
Type of measurement	Exc_1 => Horizontal Displacements (18 measurement points)
	Exc_2 => Horizontal Displacements (18 measurement points)
	Exc_3 => Horizontal Displacements (18 measurement points)
	Exc_4 => Horizontal Displacements (18 measurement points)
	Exc_5 => Horizontal Displacements (18 measurement points)
	Exc_6 => Horizontal Displacements (18 measurement points)
	Full => Horizontal Displacements (108 measurement points)

Table 7.6. Main characteristics of the backanalyses presented in section 7.6.

7.6.2 Results

The results of the backanalyses, represented by the PCA ellipses and the individuals involved in the PCA, after 25 generations, are illustrated in figure 7.16.

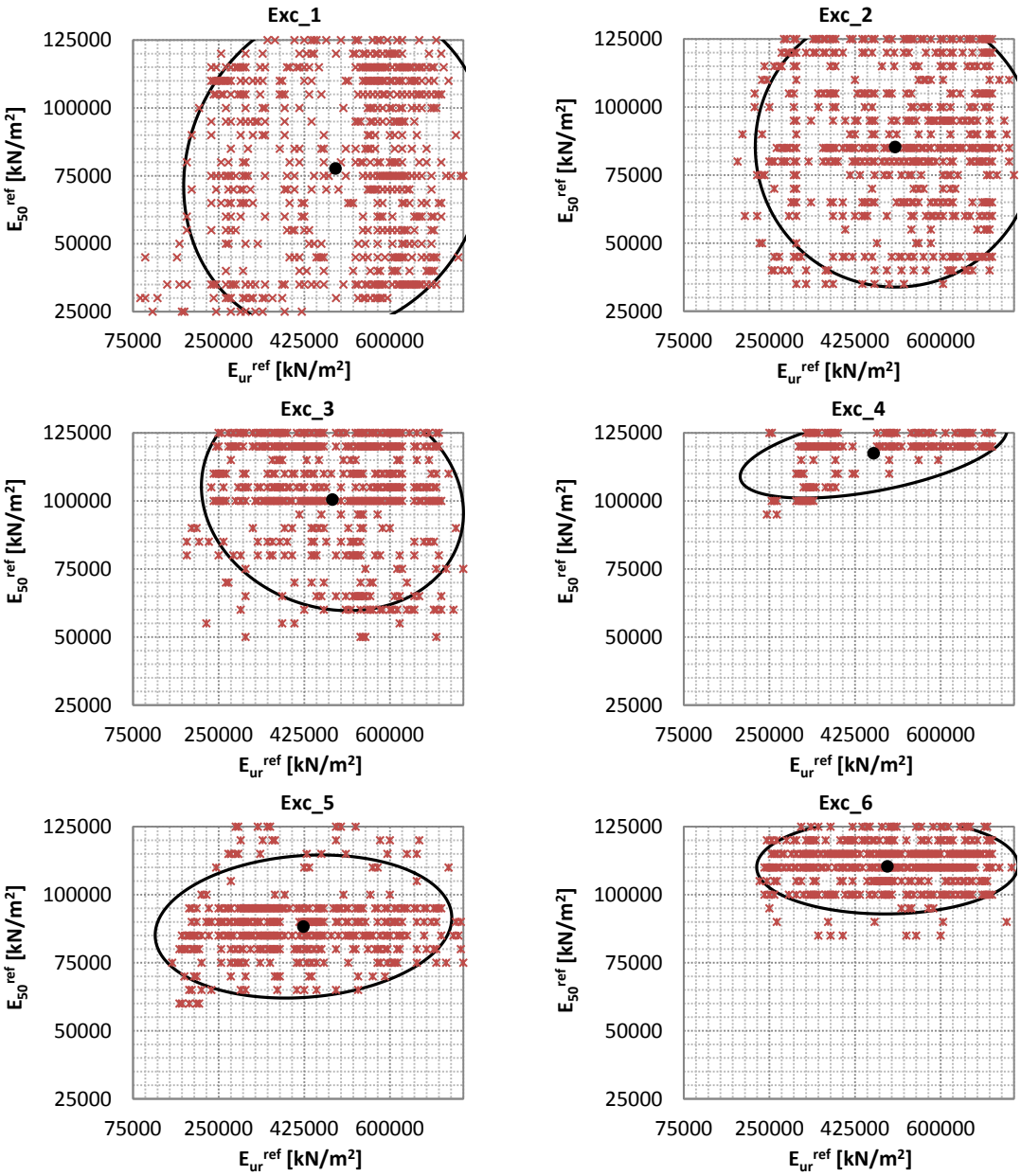

Figure 7.16. PCA ellipses after 25 generations using only measurements from one excavation stage at a time. The red crosses represent the good individuals involved in the PCA (good individuals are individuals with a fitness value inferior to $1.125 \cdot 10^{-4} m^2$, which is equivalent to 2.5mm of standard deviation associated with the measurements). The solid black line represents the PCA ellipse, and the black point represents the center of the ellipse. (only represented the results of the shallow Pliocene materials, PL_A and PG_A).

Because of using the same frontier value, to distinguish between good and bad individuals, and also because of increasing the magnitude of the measurements from Exc_1 to Exc_6, it was not surprising that the PCA ellipses tend to be smaller as the excavation progresses. However, the fact that the location of the centers of the ellipses remained relatively static for all different stages, which helps to obtain the parameters from the early stages, was something not obvious.

Figure 7.17 shows the evolution of E_{50}^{ref} and E_{ur}^{ref}, associated with the centers of the ellipses, and the evolution of the standard deviation of the individuals included in the PCA. The decrease of the standard deviation indicates that the final solution domain is more restricted, and consequently, the solution has a higher quality.

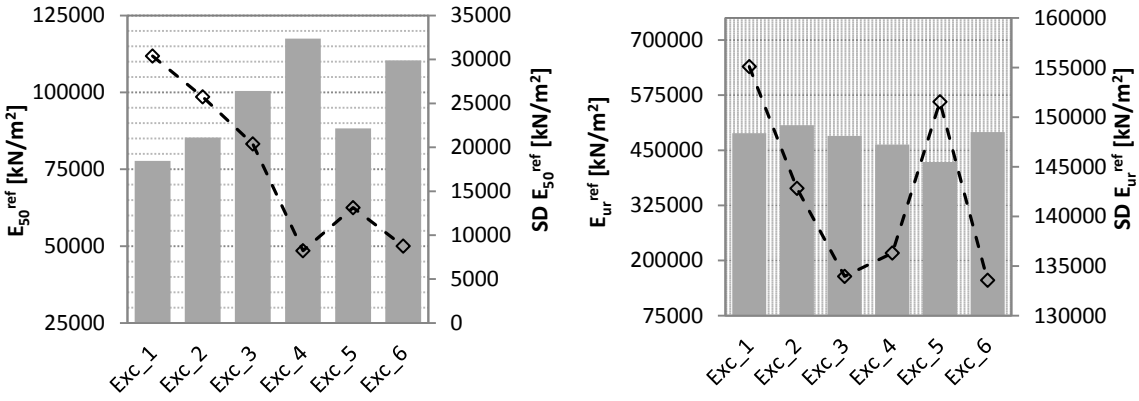

Figure 7.17. Evolution of the PCA ellipse center location and the standard deviation associated with the individuals involved in the PCA. The bars represent the parameter value associated with the center of the PCA ellipse and the diamonds represent the standard deviation of the PCA ellipse (only represented the results of the shallow Pliocene materials, PL_A and PG_A).

The comparison between the measurements and the calculation, associated with the combination of E_{50}^{ref} and E_{ur}^{ref} derived from the center of the PCA ellipse, are illustrated in figure 7.18, whereas the numerical error associated with is shown in table 7.7.

Using only Exc_1	Using only Exc_2	Using only Exc_3	Using only Exc_4	Using only Exc_5	Using only Exc_6
$5.63 \cdot 10^{-4} m^2$	$3.65 \cdot 10^{-4} m^2$	$2.38 \cdot 10^{-4} m^2$	$2.16 \cdot 10^{-4} m^2$	$2.99 \cdot 10^{-4} m^2$	$2.17 \cdot 10^{-4} m^2$

Table 7.7. Error between measurements and calculations. Even though, only one set of measurement at a time was used to drive the search, all set of measurements were simultaneously used to defined the error presented in this table.

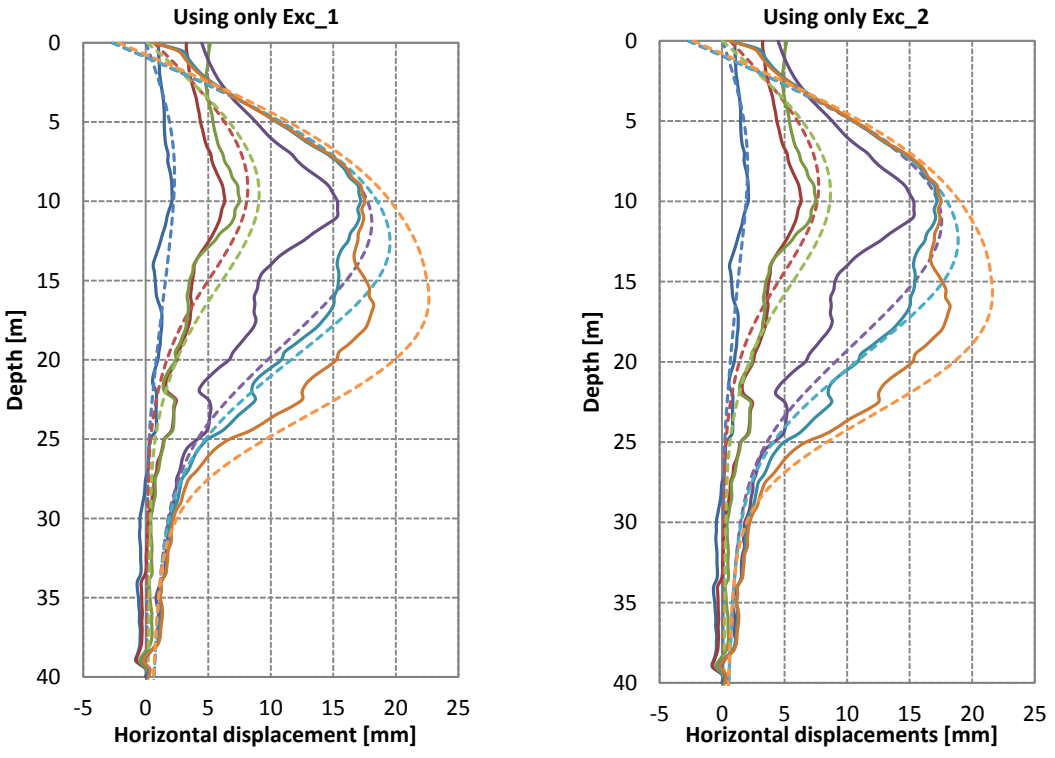

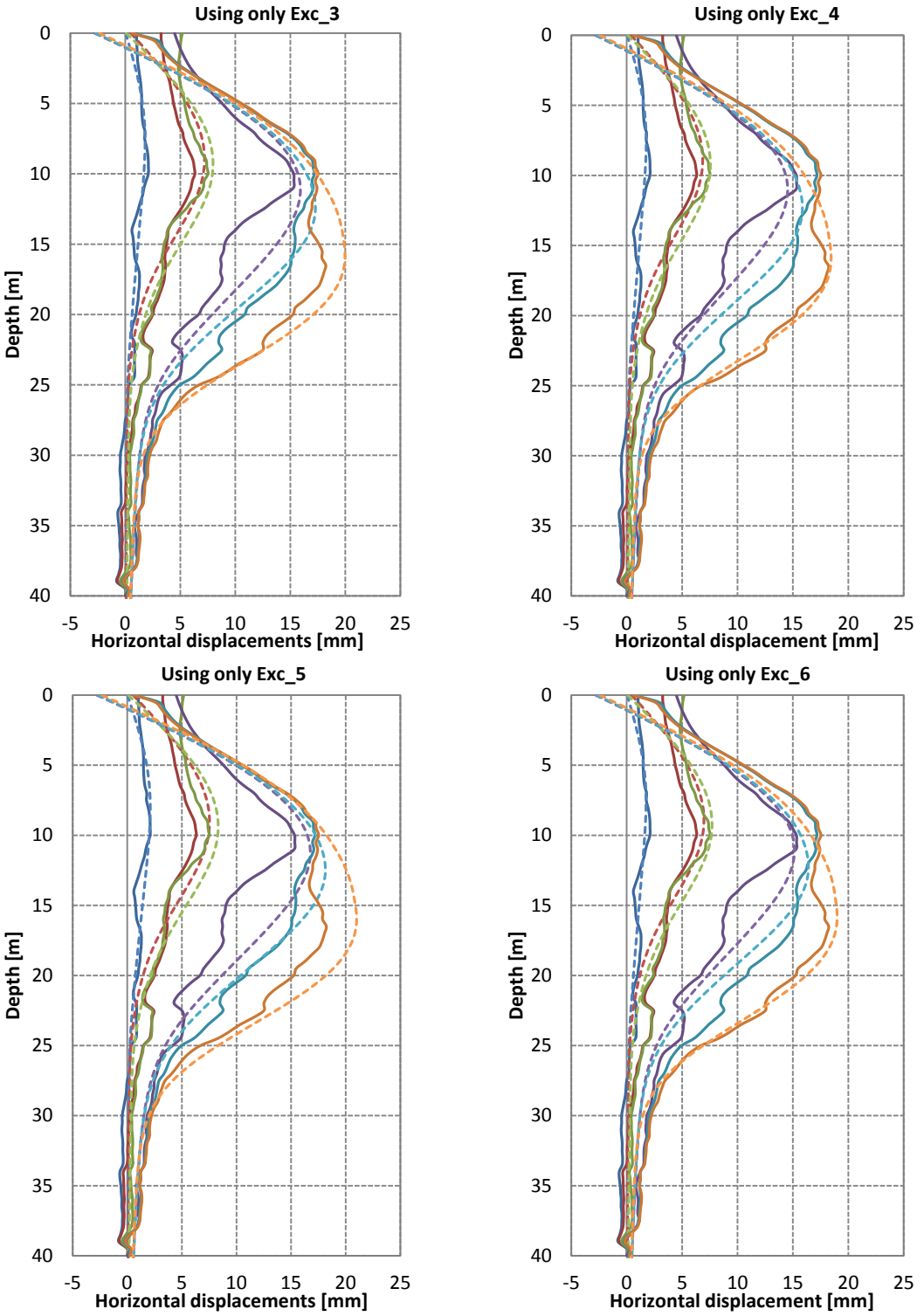

Figure 7.18. Comparison between horizontal displacements extracted from the inclinometer and the ones extracted from the numerical model (Plaxis 2D). The solid lines represent the displacements from the instrument and the dashed lines represent the displacements from the numerical model. Exc_1 (blue), Exc_2 (red), Exc_3 (green), Exc_4 (purple), Exc_5 (bright blue), and Exc_6 (yellow).

The case where all measurements, from stage Exc_1 to stage Exc_6, were simultaneously used to backanalyze the Girona station was also studied. The PCA ellipse obtained after 25 generations is presented in figure 7.19.

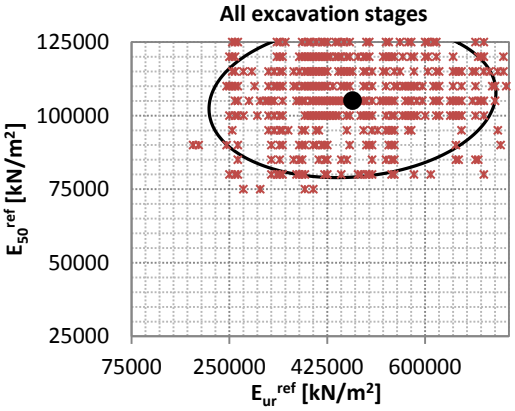

Figure 7.19. PCA ellipse after 25 generations using simultaneously all measurements (from Exc_1 to Exc_6). The red crosses represent the good individuals involved in the PCA (good individuals are individuals with a fitness value inferior to $5 \cdot 10^{-4} m^2$, which is equivalent to 2.5mm of standard deviation associated with the measurements). The solid black line represents the PCA ellipse, and the black point represents the center of the ellipse. (only represented the results of the shallow Pliocene materials, PL_A and PG_A).

In figure 7.20, it is illustrated the comparison between the measurements and the calculations extracted from the backanalysis where all measurements (from Exc_1 to Exc_6) were involved.

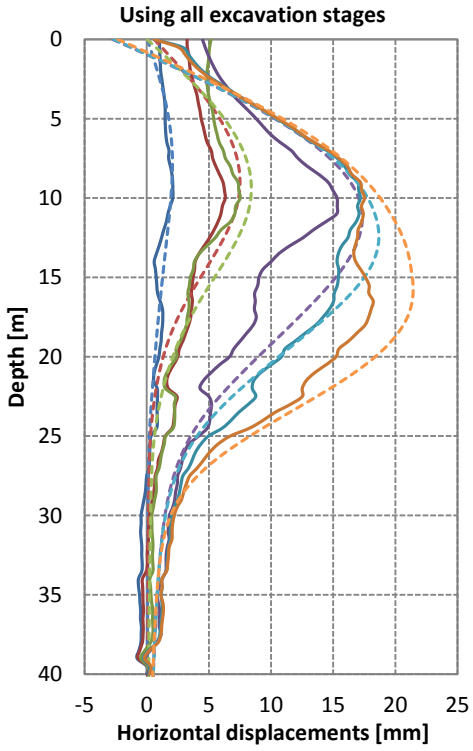

Figure 7.20. Comparison between horizontal displacements extracted from the inclinometer and the ones extracted from the numerical model using all excavation stages (Plaxis 2D). The solid lines represent the displacements from the instrument and the dashed lines represent the displacements from the numerical model. Exc_1 (blue), Exc_2 (red), Exc_3 (green), Exc_4 (purple), Exc_5 (bright blue), and Exc_6 (yellow).

Unfortunately, no improvement in terms of match between measurements and calculations has been noticed by using more sets of measurements (error = $2.23 \cdot 10^{-4} m^2$) . However, what it has been noticed is an increase in time consumption. As previously explained in Chapter 4, extracting the displacements from the results general file increases considerably the time consumption of the methodology. For this particular case, the time consumption to extract the

results has been six times higher than in the cases with just one set of measurements; and in those cases were the computational cost of evaluating the numerical model is not very high, such as the two-dimensional Girona station model, the results extraction can represent a significant amount of time of the backanalysis.

Finally, figure 7.21 shows the evolution of the PCA ellipses obtained while feeding the analysis with previous results. The feeding is carried out by means of a continuous intersection of previous PCA ellipses obtained from backanalyses where earlier stages measurements were used. Those previous PCA ellipses were defined by just using one set of measurements at a time. Strictly speaking, no combination of set of measurements is introduced in the objective function; they are only used to define and restrict the good individuals involved in the PCA.

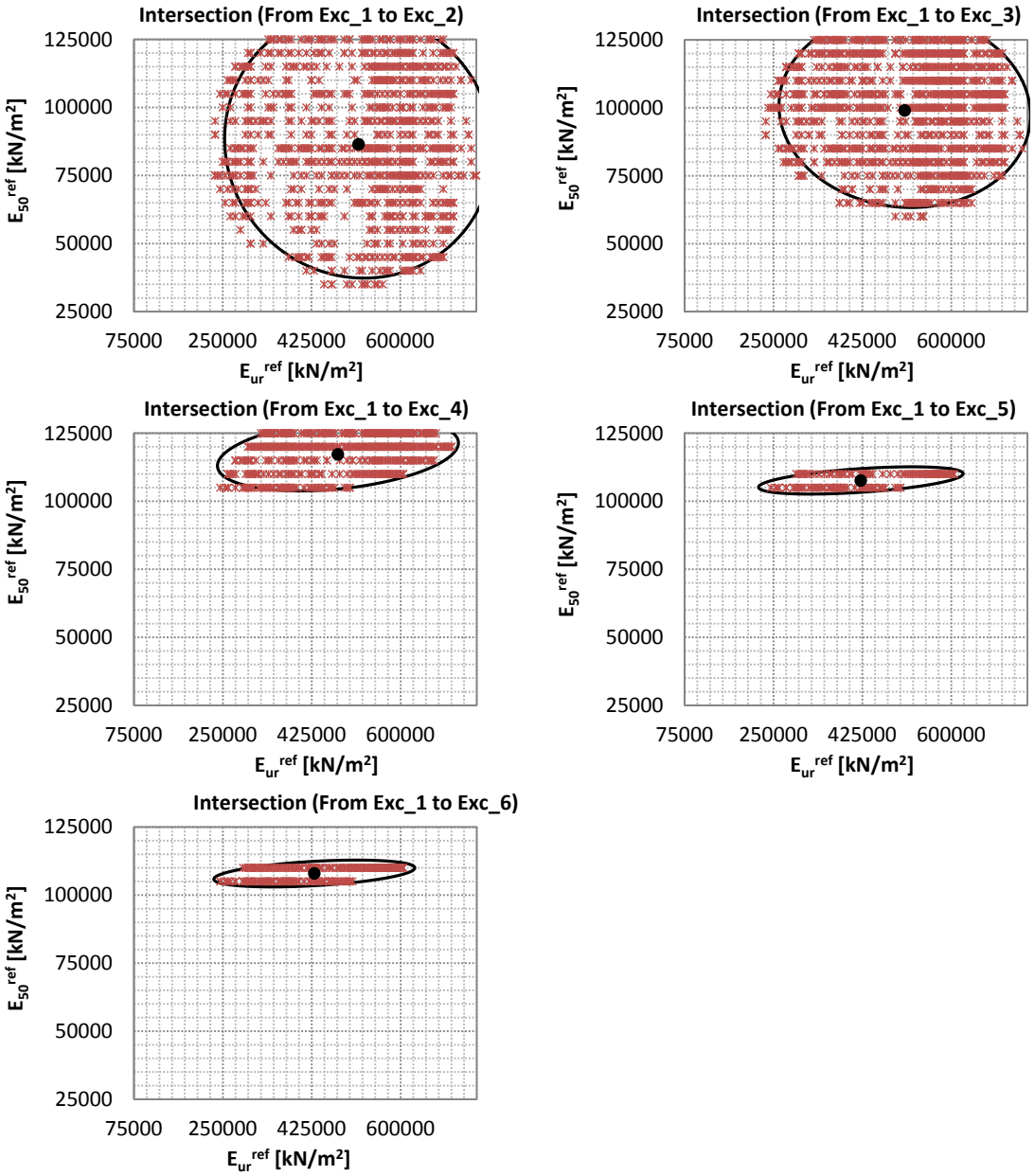

Figure 7.21. Evolving PCA ellipses defined by intersection. The red crosses represent the good individuals involved in the PCA (meaning by good individuals individuals with a fitness value equivalent to 2.5mm of standard deviation associated with the measurements). The solid black line represents the PCA ellipse, and the black point represents the center of the ellipse. (only represented the results of the shallow Pliocene materials, PL_A and PG_A).

As it can be appreciated in figure 7.21, the final results, in terms of parameter values (center of the ellipse), are relatively similar to the ones extracted from the previous analyses, where no intersection was applied. However, the lengths of the principal axes have been significantly reduced for the cases of *From Exc_1 to Exc_5* and *From Exc_1 to Exc_6*, which generates a more restricted solution domain, and consequently, a better solution of the problem.

The comparison between measurements and calculations obtained from the evolutionary method is illustrated in figure 7.22.

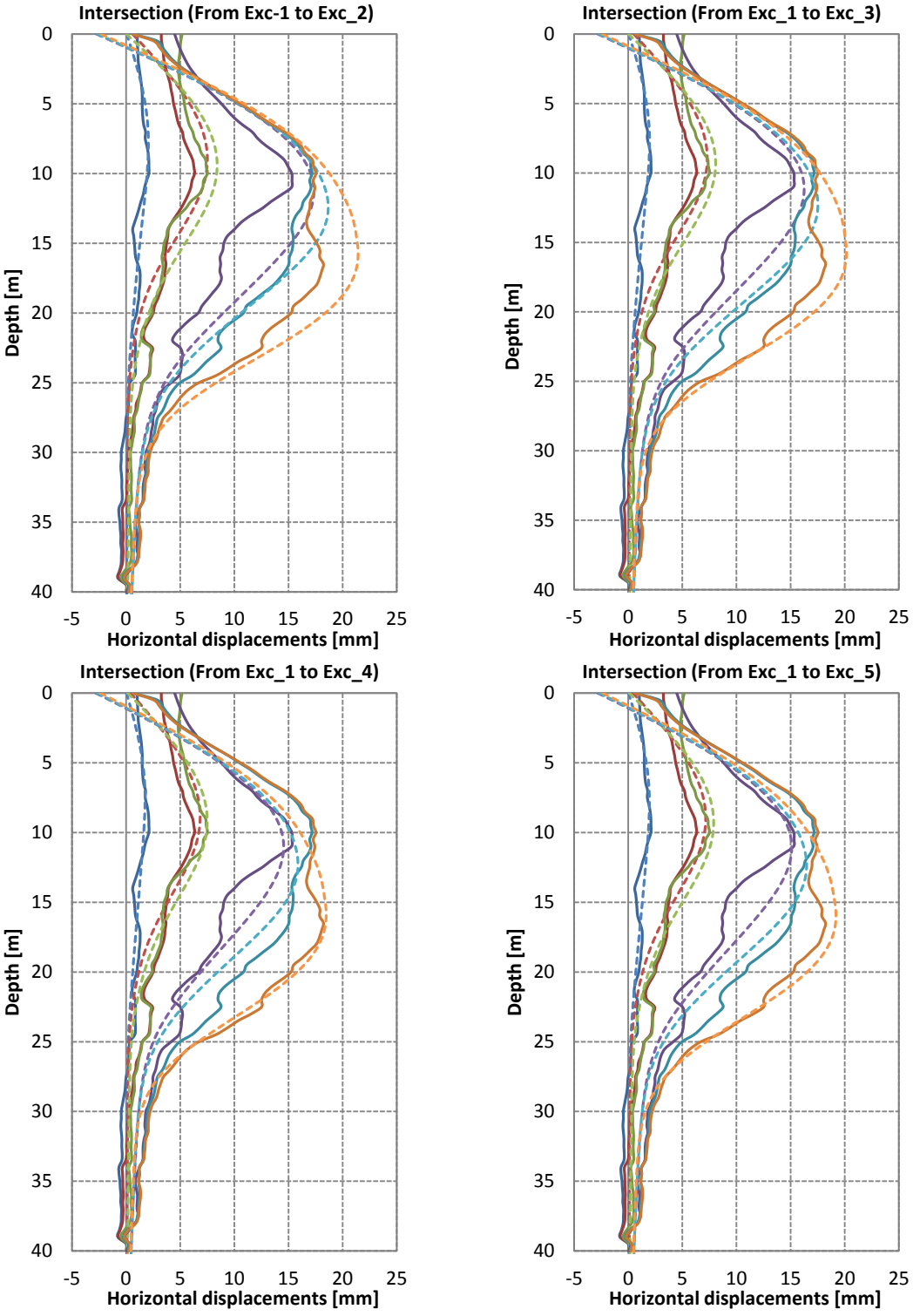

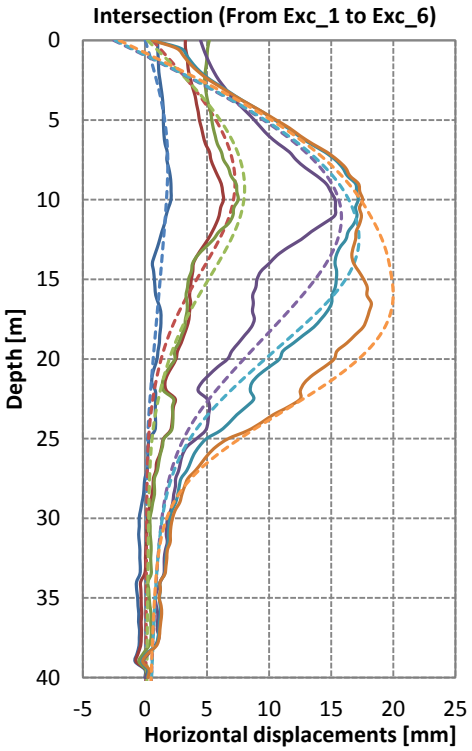

Figure 7.22 Comparison between horizontal displacements extracted from the inclinometer and the ones extracted from the numerical model using all excavation stages (Plaxis 2D). The solid lines represent the displacements from the instrument and the dashed lines represent the displacements from the numerical model. Exc_1 (blue), Exc_2 (red), Exc_3 (green), Exc_4 (purple), Exc_5 (bright blue), and Exc_6 (yellow).

A summary of the results derived from the analyses presented in this section is shown in table 7.8. The parameters in that table correspond to the center of the ellipses shown in figures 7.16, 7.19 and 7.21.

Case	$E_{50\_A}^{ref}$ [kN/m^2]	$E_{ur\_A}^{ref}$ [kN/m^2]	SD $E_{50\_A}^{ref}$ [kN/m^2]	SD $E_{ur\_A}^{ref}$ [kN/m^2]
Using only Exc_1	77723.13	788788.71	30398.93	155104.56
Using only Exc_2	85335.43	507012.58	25749.13	142829.80
Using only Exc_3	100489.26	482517.90	20392.37	133955.45
Using only Exc_4	117500.00	462916.67	8230.92	136309.09
Using only Exc_5	88288.69	423244.05	13134.32	151555.75
Using only Exc_6	110424.24	491196.97	8758.95	133565.24
Using all measurements	105095.63	470136.61	13087.86	128272.97
From Exc_1 to Exc_2 (intersection)	86462.43	518000.00	24579.21	132152.72
From Exc_1 to Exc_3 (intersection)	99020.98	508416.58	17837.90	123753.85
From Exc_1 to Exc_4 (intersection)	117220.00	476490.00	6720.26	118616.90
From Exc_1 to Exc_5 (intersection)	107611.94	421940.30	2506.86	100663.05
From Exc_1 to Exc_6 (intersection)	107941.18	430122.55	2466.82	98903.40

Table 7.8. Results summary derived from the analyses presented in section 7.6. The parameter values correspond to the values associated with the centers of the PCA ellipses. SD stands for standard deviation of the individuals involved in the PCA.

7.6.3 Concluding Remarks

When looking for the best set of individuals, better solutions were obtained when the construction progresses involving larger displacements. This higher quality is reflected in a smaller PCA ellipse size.

In those cases where the final solution of the problem is defined in terms of the PCA ellipse, the fact that the center of the ellipse remains static while updating the measurements, makes the soil parameters susceptible to be identified in the early stages.

When feeding constantly the analysis with results from previous stages (intersection of PCA ellipses), better results were obtained when looking for the best set of individuals.

7.7 Backanalysis

7.7.1 Definition

Here in this section, a backanalysis procedure is presented with the only purpose of identifying the best values of E_{50}^{ref} and E_{ur}^{ref} with a reasonable computational cost.

The hybrid algorithm was used as optimization technique. Only the measurements from Exc_6 were used. The main characteristics of the backanalysis are shown in table 7.9.

Genetic Algorithm	
Optimization Algorithm	
Type of algorithm	AGA + Elitism
Selection type	Roulette Wheel (with fitness limit = $2.5 \cdot 10^{-5} m^2$)
GAP	1
Maximum probability of applying crossover (P_{c_max})	0.95
Minimum probability of applying crossover (P_{c_min})	0.50
Maximum probability of applying mutation (P_{m_max})	0.40
Minimum probability of applying mutation (P_{m_min})	0.01
Population size	51
Stop Criteria (switching point)	Less than 50% of new individuals
Search Space Discretization	
$E_{50\ min}^{ref}$ [kN/m^2]	25000
$E_{50\ max}^{ref}$ [kN/m^2]	125000
$E_{50\ step\ size}^{ref}$ [kN/m^2]	5000
$E_{ur\ min}^{ref}$ [kN/m^2]	75000
$E_{ur\ max}^{ref}$ [kN/m^2]	750000
$E_{ur\ step\ size}^{ref}$ [kN/m^2]	5000
Principal Component Analysis (PCA)	
Frontier Value [m^2]	$1.125 \cdot 10^{-4}$
AF (amplifier factor of the standard deviation)	2
Gradient Based Method	
Type of algorithm	Gauss-Newton
Stop Criteria	fixed number of iterations (25 iterations)
Objective Function	
Type of objective function	Least-Squares Method
Measurements	
Type of measurement	Exc_6 => horizontal displacements (18 measurement points)

Table 7.9. Main characteristics of the backanalysis presented in section 7.7.

7.7.2 Results

Two generations were created until crossing the bottom line of 50% of new individuals per generation. A total of 80 individuals were evaluated and 46 of them were considered good enough to be involved in the PCA. The evolution of the population, in terms of parameters values and objective function, is illustrated in figure 7.23.

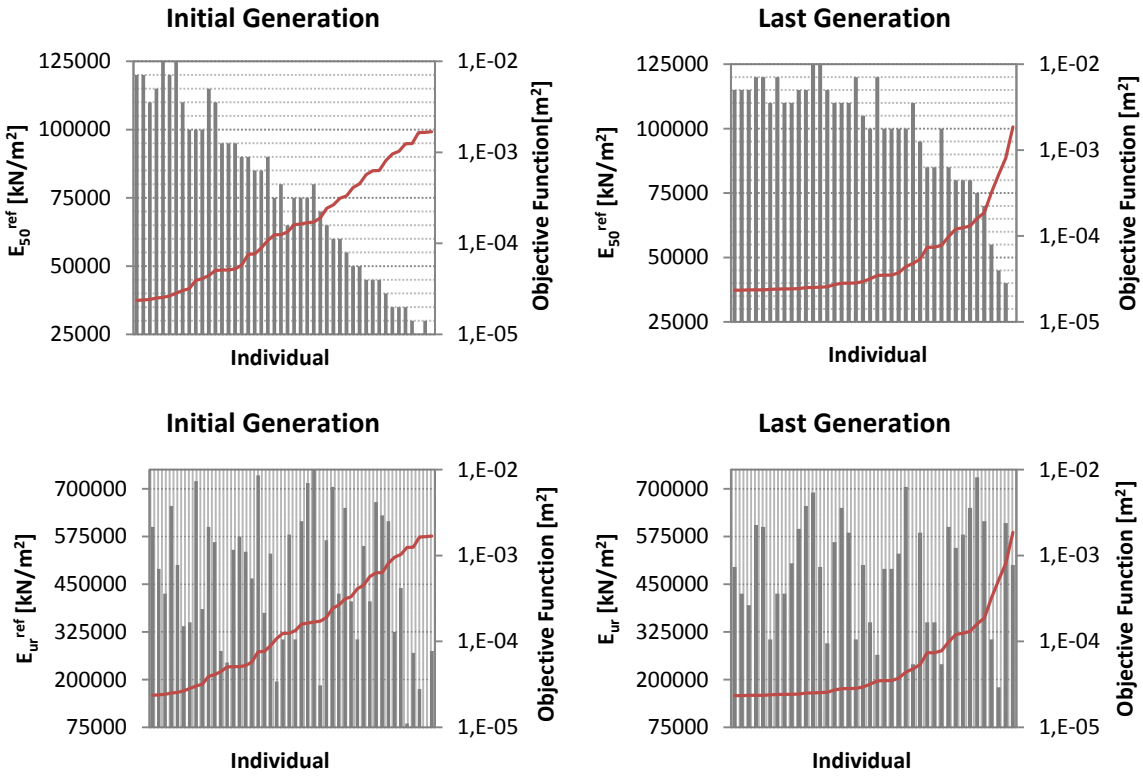

Figure 7.23. Parameters values associated with the individuals of the initial generation and the last generation. The gray bars represent the parameter values of the individuals, and the red line represents the objective function value. (only represented the results of the shallow Pliocene materials, PL_A and PG_A).

As it is shown in figure 7.23, a strong relationship between the value of E_{50}^{ref} and the objective function value exists (following the clear trend: the higher the value of E_{50}^{ref} is, the higher the objective function is), which indicates that the measurements are highly sensitive to E_{50}^{ref}. Unfortunately, for E_{ur}^{ref} there is not such strong relationship. That difference of sensitivities is also reflected on the shape of the PCA ellipse, the higher the sensitivity is, the shorter the axis is (see figure 7.24 and table 7.10).

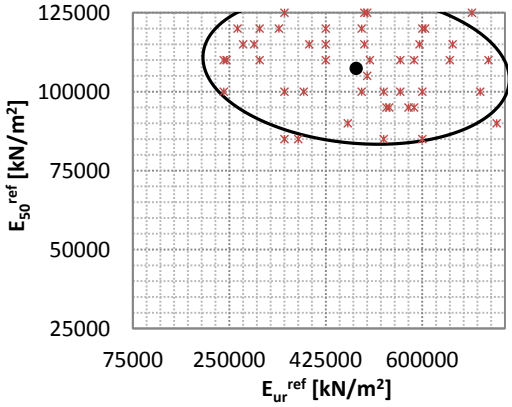

Figure 7.24. PCA ellipse after 2 generations using only measurements from Exc_6. The red crosses represent the good individuals involved in the PCA (good individuals are individuals with a fitness value inferior to $1.125 \cdot 10^{-4} m^2$, which is equivalent to 2.5mm of standard deviation associated with the measurements). The solid black line represents the PCA ellipse, and the black point represents the center of the ellipse. (only represented the results of the shallow Pliocene materials, PL_A and PG_A).

Description	Values
Relevant information involved in the analysis	
Computational cost [Plaxis evaluations]	80
Number of individuals involved in the PCA	46
Mean of E_{50}^{ref} [m^2/kN]	107391.30
Mean of E_{ur}^{ref} [kN/m^2]	480108.69
Standard deviation of E_{50}^{ref} [m^2/kN]	12006.44
Standard deviation of E_{ur}^{ref} [kN/m^2]	138846.40
AF (amplifier factor of the standard deviation)	2
PCA results	
Correlation matrix	$\begin{bmatrix} 1 & -0.1451 \\ -0.1451 & 1 \end{bmatrix}$
Eigenvector (associated to the first principal component)	$[-0.7071 \quad 0.7071]$
Eigenvector (associated to the second principal component)	$[-0.7071 \quad -0.7071]$
Eigenvalue (associated to the first principal component)	1.1451
Eigenvalue (associated to the second principal component)	0.8548
Ellipse projected into the space of E_{50}^{ref} [kN/m^2]	24013.30
Ellipse projected into the space of E_{ur}^{ref} [kN/m^2]	277565.77

Table 7.10. Principal Component Analysis.

From the center of the ellipse, the Gauss-Newton method was used to look for the minimum. The evolution of the Gauss-Newton method is illustrated in figures 7.25.

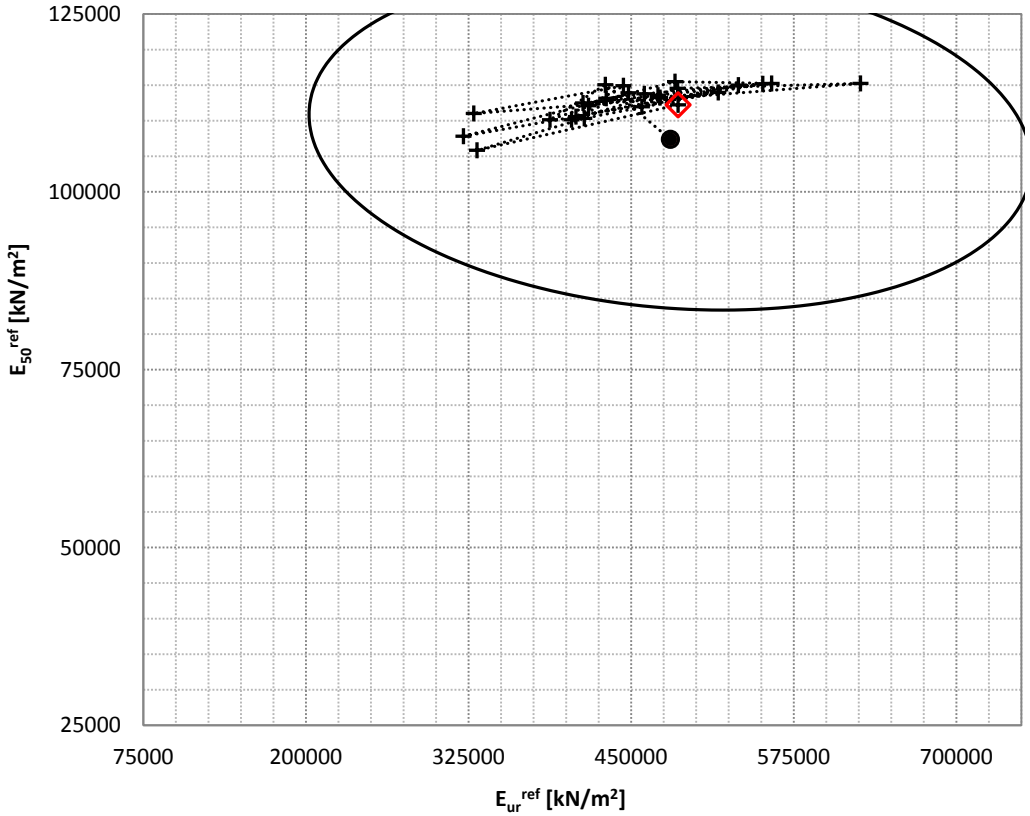

Figure 7.25. Gauss-Newton evolution. The black point represents the starting point (center of the ellipse). The black crosses represent the iterations, and the red rhombus represents the iteration associated with the lowest error (error = 2.05·10^{-5}m^2 on iteration 24 => E_{50}^{ref}= 112230.82 kN/m^2 and E_{ur}^{ref}= 486117.39KN/m^2). (only represented the results of the shallow Pliocene materials, PL_A and PG_A).

Due to the low influence of the E_{ur}^{ref} the search has fluctuated along the E_{ur}^{ref} axis. Therefore, in order to control the fluctuation, it was considered appropriated to apply the Marquardt

method instead of the Gauss-Newton method. However, even getting a search with no fluctuations, the final results, in terms of objective function, were not better than the one obtained from the Gauss-Newton method. Consequently, the results obtained from the Gauss-Newton method were considered as solution of the problem (see table 7.11).

Parameter	PL_A	PG_A	PL_B	PG_B
E_{50}^{ref} [kN/m^2]	112230.82	112230.82	561154.10	561154.10
E_{ur}^{ref} [kN/m^2]	486117.39	486117.39	2430586.95	2430586.95

Table 7.11. Final results of the backanalysis (Hybrid Method => AGA + Gauss-Newton).

The comparison between the measurements and the calculations obtained by using the soil parameters shown in table 7.11 is illustrated in figure 7.26.

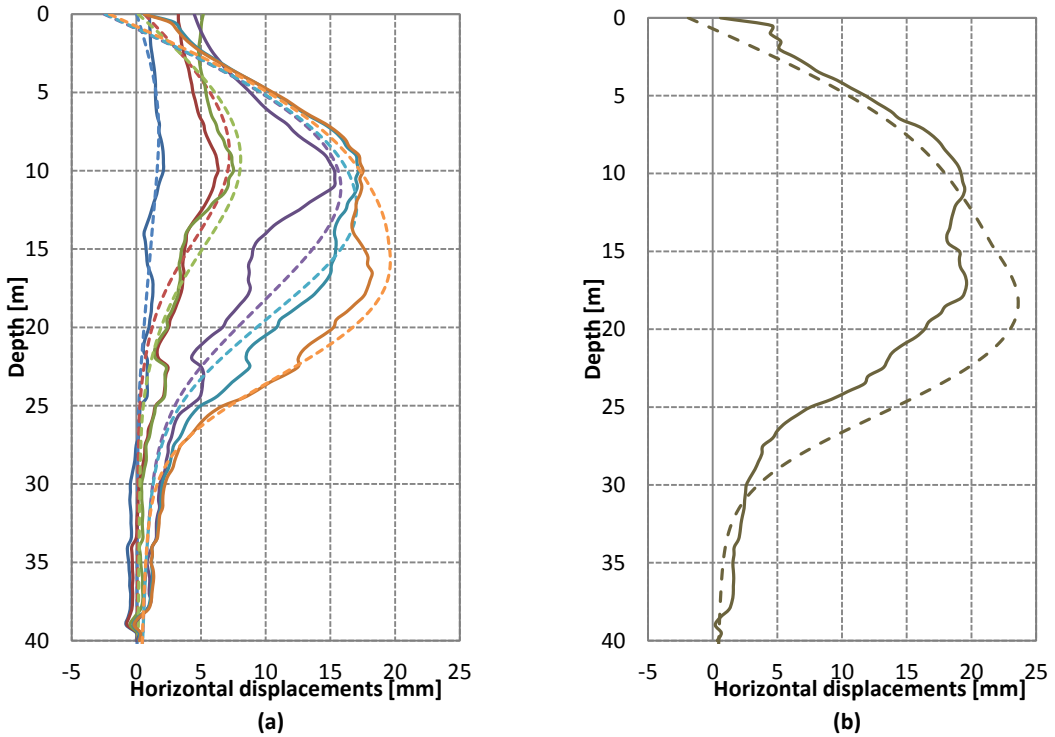

Figure 7.26. Comparison between horizontal displacements extracted from the inclinometer and the ones extracted from the numerical model using the soil parameters shown in table 7.10 (Plaxis 2D). (a) Two-dimensional construction stages => Exc_1, Exc_2, Exc_3, Exc_4, Exc_5 and Exc_6. (b) Three-dimensional construction stage => Exc_7. The solid lines represent the displacements from the instrument and the dashed lines represent the displacements from the numerical model. Exc_1 (blue), Exc_2 (red), Exc_3 (green), Exc_4 (purple), Exc_5 (bright blue), Exc_6 (yellow), and Exc_7 (dark green).

As it is shown in figure 7.26.a, the numerical model matches the measurements relatively well. Therefore, it can be pointed out that the hybrid methodology applied in this case study seems to work properly. However, no match was obtained when the last excavation stage (Exc_7) was simulated (see figure 7.26.b). Nonetheless, after identifying the soil parameters from previous stages (using the 2D model), it is possible to introduce those parameters into a three-dimensional model to properly reproduce the soil behavior (see section 7.8).

7.7.3 Concluding Remarks

The hybrid method presented in this thesis has shown a good behavior facing a complex real case study, both in terms of robustness and computational cost.

Strong three-dimensional construction stages behavior cannot be captured with two-dimensional approaches.

As it is shown in table 7.10, higher values of E_{50}^{ref} and E_{ur}^{ref} were obtained by backanalysis, highlighting that the soil parameters used during design were underestimated (see table 7.1). Unfortunately, at the time that the station was being built, the backanalysis methodology presented in the thesis was not fully defined yet, therefore, it was not possible to optimize the design in an automatic manner.

7.8 Three-Dimensional Simulation

As previously mentioned, the construction of the Girona High-Speed Railway Station has involved some construction stages with a strong three-dimensional nature (see figure 7.3.o and figure 7.3.p), which were not realistic to reproduce by means of a two-dimensional model. Therefore, it was considered necessary and useful to define a new numerical model capable of capturing the real three-dimensional behavior.

7.8.1 Numerical Model (3D Model)

The new model was built using the geotechnical software Plaxis 3D (see figure 7.27 and figure 7.28).

In order to reduce the computational cost and the difficulty derived from generating a three-dimensional mesh, only half of the station was simulated. The wider side of the station, the park side, was the one that was simulated by the new three-dimensional model. Some discrepancies were expected from halving the geometry and changing the slab-diaphragm wall connections; from free rotational springs to rigid springs (Plaxis 3D cannot simulate free rotational springs between plates). However, as it will be shown later, similar results were obtained from both models (comparing stages that can be considerd 2D).

Moreover, thanks to the introduction of the third dimension, it was also possible to simulate the mixed pile-diaphragm wall separately, which was not possible while using a two-dimensional model.

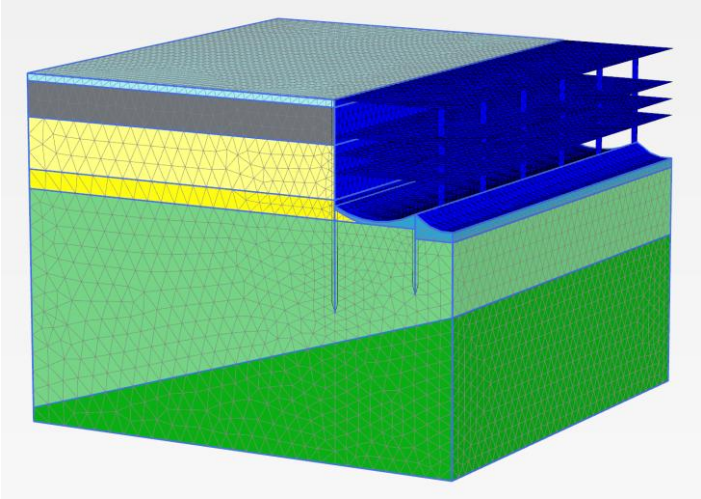

Figure 7.27. General view of the geometry and mesh of the Plaxis 3D model.

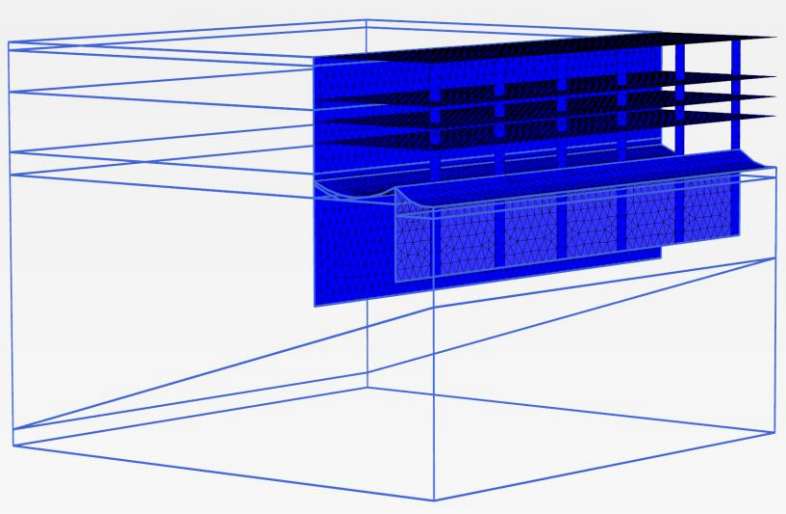

Figure 7.28. Structural geometry of the Girona High-Speed Railway Station of the Plaxis 3D model.

All structural and soil parameters values were derived from the two-dimensional model after carrying out the backanalysis. The Plaxis phases 9 and 10, implemented in the two-dimensional model (see table 7.4), were replaced by ten consecutive phases. In a particular phase, 12m length of the lateral corridor is excavated and the inverted arch of the previous excavated meters is built. Figure 7.29 illustrates the procedure.

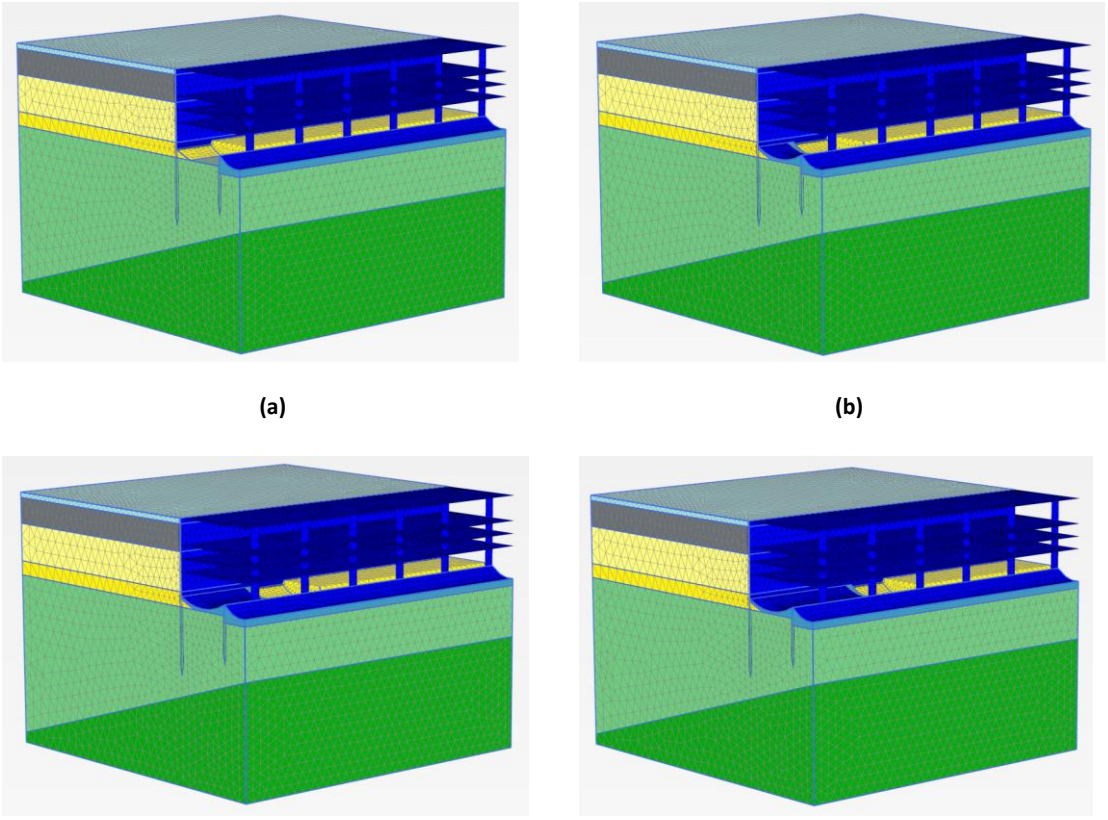

(a) **(b)**

(c) **(d)**

Figure 7.29. Sequence of excavation and inverted arches construction (12m length). From (a) to (d) until finishing the entire station.

7.8.2 2D vs. 3D

In figure 7.30, the comparison between measurements and calculation for both numerical models (2D and 3D) is shown. As mentioned before, while using the two-dimensional model, the calculation phase Exc_7 was not capable of capturing the soil response, whereas when using the three-dimensional model, the soil response corresponding to Exc_7 was properly captured.

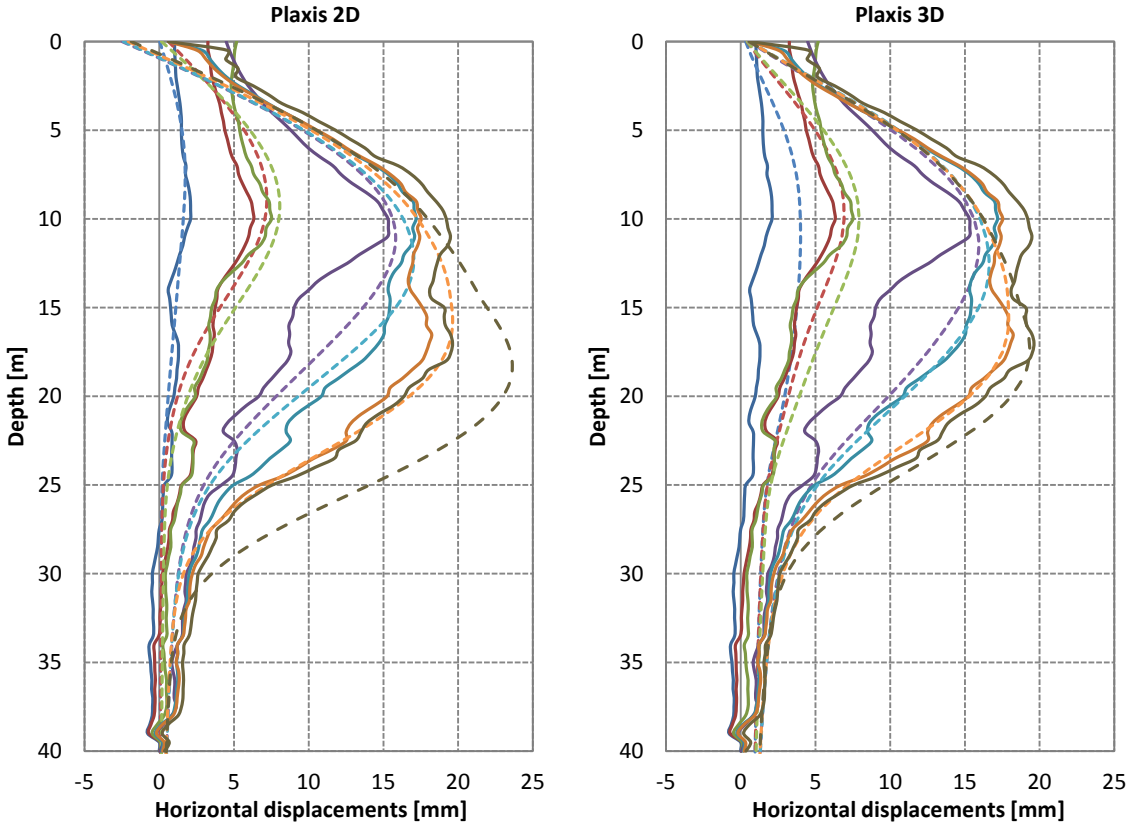

Figure 7.30. Comparison between horizontal displacements extracted from the inclinometer and the ones extracted from the numerical model using the soil parameters shown in table 7.10 (Plaxis 2D vs. Plaxis 3D). The solid lines represent the displacements from the instrument and the dashed lines represent the displacements from the numerical model. Exc_1 (blue), Exc_2 (red), Exc_3 (green), Exc_4 (purple), Exc_5 (bright blue), Exc_6 (yellow), and Exc_7 (dark green).

7.8.3 Concluding Remarks

For this particular case study, the identification of the soil parameters in the early stages, using a two-dimensional model, has let the definition of a "pre-calibrated" three-dimensional model to fully describe all construction stages.

Chapter 8

Case Study 3: Mars Surface Exploratory Rovers

8.1 Introduction

Apart from the application of the backanalysis methodology presented in this thesis to geotechnical works, such as tunnels and excavations (Chapter 6 and Chapter 7), its application to a less conventional geotechnical scenario was considered useful to confirm the applicability and robustness of the methodology. The operation of wheeled mobile robots to explore the surface of Mars were used with that purpose, where the interaction between the rovers' wheels and terrain allows some soil parameters to be identified.

From the mid 70's, several space missions have been carried out to land robots on the surface of Mars. The main objective of those missions was to conduct scientific experiments focused on understanding the planet's climate history, surface geology, and potential for past or present life. In 1976, the NASA landers Viking 1 and Viking 2 landed on Mars for the first time in human history (see figure 8.1.a). The Vikings used robotic arms to conduct soil trenching experiments to analyze Martial soil (Moore et al., 1977). In 1997, the NASA rover Sojourner (see figure 8.1.b) reached the surface of Mars as the first wheeled spacecraft to land on Mars. In this case, the rover used its wheels as a trenching device to identify soil cohesion and internal friction angle (Matijevic et al., 1997). In 2004, the NASA twin rovers Spirit and Opportunity also explored Mars (see figure 8.1.b). The rovers drove around more than 6 years while obtaining images before, during and after their drives; together with monitoring wheel turns and electric currents, suspension angles, and rover attitudes to evaluate mobility. They

also retrieved terrain and soil properties using basic terramechanics approaches. Finally, in 2012, the newest NASA rover Curiosity (see figure 8.1.b) landed on Mars, with the objective of continuing data acquisition, and expanding the knowledge to design the basis for a planned Mars 2020 rover mission.

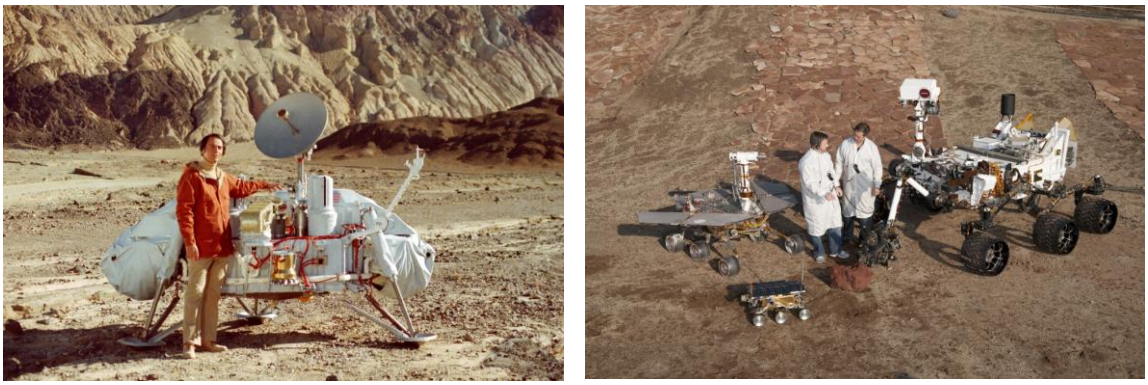

(a) **(b)**

Figure 8.1. NASA's Mars surface exploratory robots. (a) Model of the Viking lander. (b) Front and center is the flight spare for the Sojourner rover. On the left there is a working sibling to Spirit and Opportunity. On the right is a laboratory test rover of the Curiosity rover. Images Credit: NASA/JPL-Caltech.

As a result of the difficulties of mobile robots navigation over sloped, rocky, and deformable terrain, and partial difficulties derived from Earth-Mars communication time delays, a tremendous effort has been placed in studying online terrain parameter estimation. However, previous to the online analyses, several researchers, such as Nohse et al. (1991) and Shmulevich et al. (1996), have already studied terrain parameters estimation offline using dedicated testing equipment.

In Iagnemma et al. (2004), an online estimation method using on-board robot sensors was presented. The methodology relies on a simplified form of classical terramechanics equations and uses a linear-least squares method to compute terrain parameters in real time. Good results of soil cohesion and internal friction angle were obtained from the simulation. Sullivan et al. (2011) also obtained good results of soil cohesion and internal friction angles. In this case, to identify the soil parameters, the concept of electromechanical work was used in combination with the Mohr-Coulomb failure criterion. Their methodology was applied using wheel trenching and scuffing experiments data, collected from the Spirit and Opportunity Martial missions.

Apart from just identifying soil cohesion and internal friction angle, Ding et al. (2009) and Iagnemma et al. (2011) focused on fully defining the parameters of classical terramechanics models to predict the rover-soil interaction.

Most of the online analyses, using classical terramechanics theory, are based on the ideas introduced by Bekker (1969), who proposed a set of semi-empirical equations to predict different mobility aspects; such as compaction resistance, traction, sinkage, and driving torque. Further modifications of the original Bekker theory were done by Wong & Reece (1967a and 1967b) who not only applied correction factors to Bekker equations, but also expanded the Bekker methodology to calculate wheel performance through the predictions of stress distributions at the wheel-terrain interface. The model proposed by Wong and Reece has the merit of deriving all wheel performance metrics, such as torque, drawbar force and

sinkage, from the calculated stress distributions at the interface. In contrast, Bekker's original approach was based on a series of specific formulations intended to model each single aspect of the vehicle mobility independently.

Traditionally, the theory of terramechanics has been focused on studying the interaction between heavy vehicles and terrain. However, in recent years, the analysis of lightweight rovers' mobility has raised many questions regarding whether classical terramechanics theory is appropriate for reduced scale vehicles. In Senatore & Iagnemma (2014), a thorough analysis of stress distributions, under lightweight wheeled vehicles, was carried out to validate the extrapolation of the classical theory of therramechanics, from heavy vehicles, to lightweight vehicles; more commonly used in space exploratory missions. Additionally, an overview of the most significant work of lightweight vehicles was presented (Carrier, 1994; Richter et al., 2006; Ding et al., 2010; and Meirion-Griffith & Spenko, 2013). Senatore & Iagnemma (2014) concluded that the classical theory of terramechanics, as it was finally defined in Wong & Reece (1967a and 1967b), was in theory able to characterize the mobility performance of lightweight vehicles; pointing out the empirical nature of the method and its drawbacks. They also found that two coefficients c_1 and c_2 (see section 8.2) do not depend on vertical load, and consequently, the coefficients can be considered constant for a specific wheel-soil configuration. Moreover, the analysis of soil kinematics under the wheel, presented in their paper, showed that the hypotheses behind the shear stress formulation were not entirely valid: this explains why the shear modulus K_x, obtained from direct shear tests (or other shear tests), does not produce accurate results when using the Wong and Reece model.

8.2 Wheel-Terrain Interaction Model (Wong & Reece Model)

The Wong and Reece model is based on two fundamental relationships: the pressure-sinkage relationship, and the relationship between the shear stress and the shear deformation. The pressure-sinkage relationship controls the depth that a rover wheel will sink into the terrain, and consequently, the amount of resistance that it will have to overcome to move. The other fundamental relationship, the shear stress-shear displacement relationship, controls the magnitude of the traction generated by the rover and transmitted by the wheels during the drive, which represents how easy or difficult it will be to progress through terrain.

In figure 8.2, the most relevant actions acting on the wheel are schematically represented; where z is the wheel sinkage, θ_f is the front or entrance angle at which the wheel begins to contact the terrain, θ_r is the rear or exit angle at which the wheel looses contact with the terrain, θ_m is the angle of maximum stress ($\sigma_m = \sigma(\theta_m)$), T is the driving torque of the motor, DP is the resistance provided by forward movement, which is equal to the drawbar pull, W is the vertical load of the wheel, r is the wheel radius, v is the rover velocity, and ω is the angular velocity of the wheel. The wheel-terrain interaction defines a continuous normal stress ($\sigma(\theta)$) and shearing stress ($\tau(\theta)$), which are divided into a front part (σ_f, τ_f) and a rear part ((σ_r, τ_r).

The pressure-sinkage relationship was defined by Bekker (1956), relates the normal stress (σ) to sinkage through empirically-determined pressure-sinkage parameters k_c, k_φ and n as:

$$\sigma = \left(\frac{k_c}{b} + k_\varphi\right) z^n \tag{8.1}$$

where b is the wheel width, k_c and k_φ are the pressure-sinkage moduli, n is the sinkage exponent, and z is the sinkage. These parameters were traditionally obtained from the well-known bevameter technique that was proposed by Bekker (1956, 1960 and 1969).

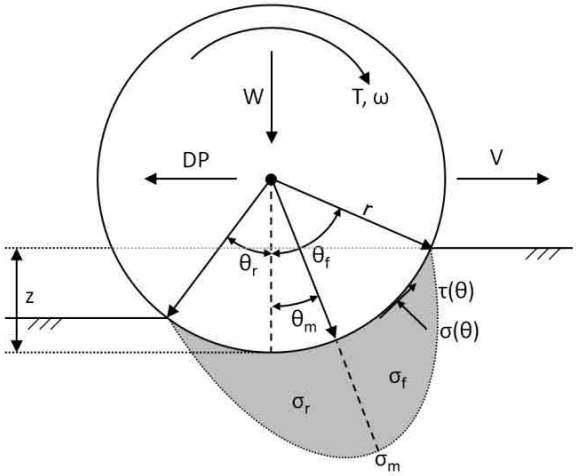

Figure 8.2. Schematic representation of wheel-terrain interaction for a rigid wheel on deformable terrain.

Normal stress on the interface between wheel and terrain can be easily evaluated by introducing a scaling function into Bekker's pressure-sinkage relationship to satisfy the zero-stress boundary conditions in the entry and exit contact between wheel and terrain.

$$\sigma(\theta) = \begin{cases} \sigma_f = \left(\frac{k_c}{b} + k_\varphi\right) z_f^n; & \theta_m < \theta < \theta_f \\ \sigma_r = \left(\frac{k_c}{b} + k_\varphi\right) z_r^n; & \theta_r < \theta < \theta_m \end{cases} \tag{8.2}$$

where z_f and z_r represent the wheel sinkage expressed as a function of the wheel angular location (θ).

$$z_f(\theta) = r\left(\cos\theta - \cos\theta_f\right) \tag{8.3}$$

$$z_r(\theta) = r\left(\cos\left(\theta_f - \frac{\theta-\theta_r}{\theta_m-\theta_r}\left(\theta_f - \theta_m\right)\right) - \cos\theta_f\right) \tag{8.4}$$

The location of the point of maximum stress can be defined as presented in equation 8.5, which was suggested by Wong & Reece (1967a).

$$\theta_m = (c_1 + c_2 i)\theta_f \tag{8.5}$$

where c_1 and c_2 are two empirical parameters to locate the maximum stress, and i is the slip ratio defined as:

$$i = 1 - \left(\frac{v}{r\cdot\omega}\right) \tag{8.6}$$

where v is the forward velocity and ω is the angular velocity.

The shear stress-shear displacement relationship is governed by the Mohr-Coulomb failure criterion, coupled with a modulation function proposed by Janosi & Hanamota (1961).

$$\tau(\theta) = (c + \sigma(\theta)\tan\varphi)\left(1 - e^{-\frac{j}{K_x}}\right) \tag{8.7}$$

where c is the soil cohesion, φ is the soil internal friction angle, K_x is a fitting constant labeled shear modulus (not to be confused with the shear modulus G popularly used in engineering), and j is the shear displacement.

Assuming only positive slip (to simplify the definition of j), the shear displacement can be defined as follows:

$$j = r\left[\theta_f - \theta - (1 - i)\left(\sin\theta_f - \sin\theta\right)\right] \tag{8.8}$$

The actions that balance the wheel-terrain interaction system (see figure 8.2) can be calculated as:

$$T = r^2 b \int_{\theta_r}^{\theta_f} \tau(\theta) d\theta \tag{8.9}$$

$$DP = rb\left(\int_{\theta_r}^{\theta_f} \tau(\theta)\cos\theta d\theta - \int_{\theta_r}^{\theta_f} \sigma(\theta)\sin\theta d\theta\right) \tag{8.10}$$

$$W = rb\left(\int_{\theta_r}^{\theta_f} \sigma(\theta)\cos\theta d\theta + \int_{\theta_r}^{\theta_f} \tau(\theta)\sin\theta d\theta\right) \tag{8.11}$$

The sinkage of the wheel (z) can be obtained by solving a vertical force equilibrium problem, which prescribes the fact that the force resisting wheel penetration into the terrain must be balanced by the vertical load acting on the wheel (W). Note that the balance of the vertical load must be the first equation to be solved in order to obtain θ_f, while keeping θ_r as a constant to fully define the problem, and subsequently solve equation 8.11 and later equation 8.9 and 8.10.

In terms of backanalysis or parameters identification, the more common parameters that are involved in the identification are the cohesion (c), the internal friction angle (φ), the pressure-sinkage moduli (k_c and k_φ), the pressure-sinkage exponent (n), and the shear modulus (K_x).

8.3 Backanalysis

Here in this section, the backanalysis intends to identify the majority of the parameters that defined the Wong and Reece wheel-terrain model ($c, \varphi, k_c, k_\varphi, n$ and K_x), and bringing the reliability of the model itself into question. A scenario similar to that a rover would find in a Martial surface exploratory mission has been used. Moreover, a modified optimization strategy has been defined in order to overcome some aspects related to the limitation of extrapolating the classic terramechanics theory, traditionally based on heavy vehicles (average ground pressure over 20kPa), to lightweight rovers. Those aspects have been highlighted and thoroughly studied by Senatore & Iagnemma (2011 and 2014) and Senatore et al (2012).

8.3.1 Definition

8.3.1.1 Data

A test bed, designed, manufactured and run by the Robotic Mobility Group at MIT, was used to generate a set of experimental data. The characteristics of the test bed were based on the

standard design described by Iagnemma et al (2005). The test bed was composed of a Lexan soil bin (0.9m long and 0.6m wide) surrounded by an aluminum frame where all the moving parts, actuators and sensors, were attached. Two low-friction rails were used to slide a carriage longitudinally where the wheel was attached (see figure 8.3). The wheel was able to rotate at a desired angular velocity, and free vertical displacements of the wheel mount were also permitted. This typical setup allows control of slip and vertical load by modifying the translational velocity of the carriage, the angular velocity of the wheel, and the applied load.

(a) **(b)**

Figure 8.3. MIT test bed. (a) CAD drawing of the terramechanics test bed showing the imager for particle image velocity (PIV). (b) Actual PIV setup with the high speed camera and two flood lights. Images Credit: Senatore et al 2012.

An average of 15 test bed experiments, for each pair of vertical load (W) and slip ratio (i), were conducted to extract the values of Torque (T), Drawbar Pull (DP) and Sinkage (z) to generate the set of data used in the backanalysis (see table 8.1 and figure 8.4). The data correspond to an average of the values of the different tests with their respective standard deviations. The description of the sensors that were used to extract the measurements is presented in Senatore & Iagnemma (2014).

W [N]	i	T [Nm]	DP [N]	z [mm]	σ_T [Nm]	σ_{DP} [N]	σ_z [mm]
70	0	1.52	3.33	6.67	0.281	1.689	9.425
70	0.1	3.24	16.05	6.93	0.234	1.128	10.941
70	0.3	4.06	21.06	7.72	0.308	1.819	10.735
70	0.5	5.54	30.95	8.75	1.024	0.827	2.295
70	0.7	6.37	35.28	10.34	1.069	0.772	1.719
100	0	2.83	8.06	8.39	0.250	1.870	5.237
100	0.1	4.96	23.72	8.71	0.777	2.644	5.811
100	0.3	6.00	29.54	9.69	0.497	2.433	3.708
100	0.5	7.87	41.59	10.95	0.926	1.510	3.464
100	0.7	8.78	45.43	12.94	1.374	3.918	3.441
150	0	5.59	19.18	10.83	0.314	1.892	5.806
150	0.1	8.10	37.17	11.25	0.896	2.487	5.599
150	0.3	9.36	43.24	12.50	0.298	2.541	3.207
150	0.5	11.75	57.67	14.10	4.222	3.229	2.029
150	0.7	12.75	59.87	16.66	0.008	2.855	3.634

Table 8.1. Test bed data. W: vertical load, i: slip ratio, T: torque, DP: drawbar pull, z: sinkage, σ_T: torque standard deviation, σ_{DP} : drawbar pull standard deviation, and σ_z: sinkage standard deviation. All the data presented in this table were facilitated by Senatore and Iagnemma from the Robotic Mobility Group at MIT.

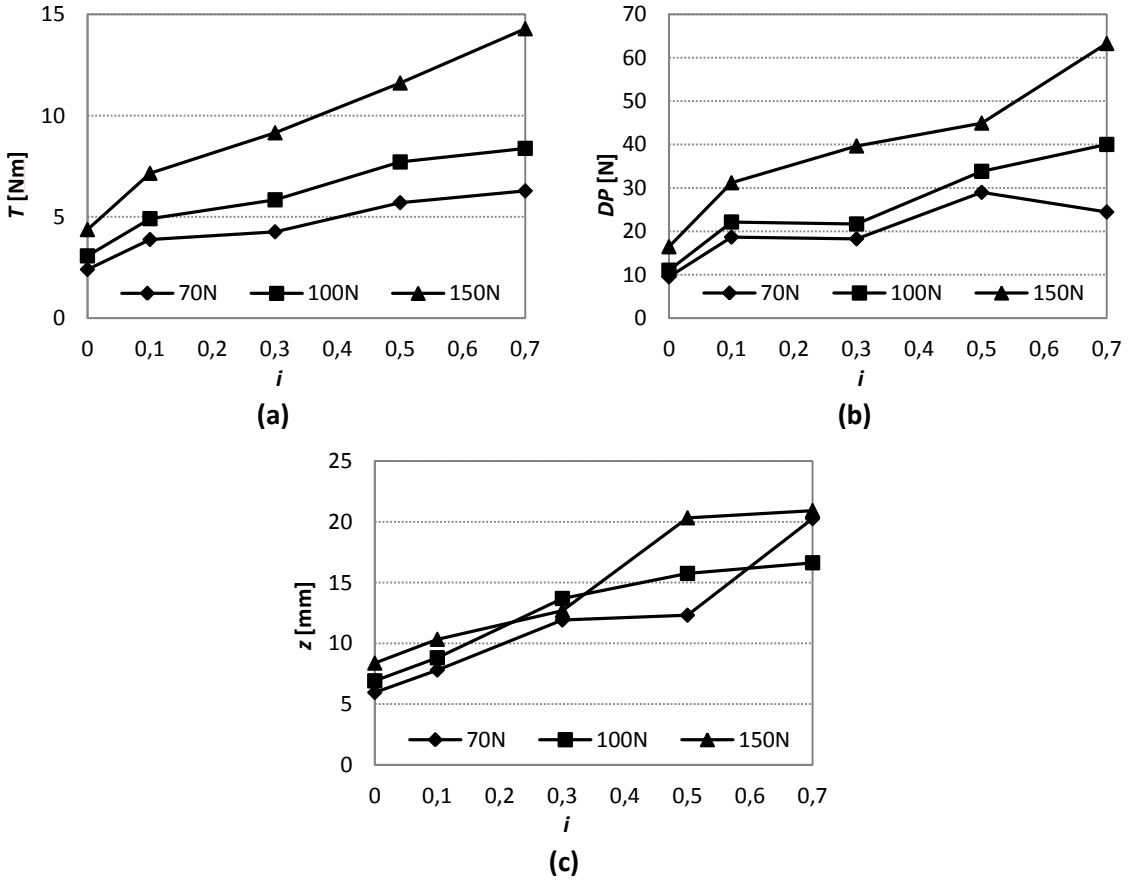

Figure 8.4. Graphical representation of the test bed data. (a) torque vs. slip ratio for W=70N, W=100N and W=150N. (b) drawbar pull vs. slip ratio for W=70N, W=100N and W=150N. (c) sinkage vs. slip ratio for W=70N, W=100N and W=150N.

8.3.1.2 Soil Description

The soil material that was placed inside the test bed was the Mojave Martian Simulant (MMS) defined in Beegle et al (2007) and Peters et al (2008). The MMS is a mixture of finely crushed and sorted granular basalt, with particle size distribution spanning from micron to millimeter scale, with 80% of particles above the 10 μm threshold. The material was intended to mimic both at chemical and mechanical level the Mars soil characteristics. The soil properties of the MMS, shown in table 8.2, were derived from several plate penetration tests and direct shear tests.

Parameter	Value
c [N/m^2]	600
φ [deg]	35
k_c [N/m^{n+1}]	846130
k_φ [N/m^{n+2}]	6708000
n	1.4
K_x [m]	0.0006

Table 8.2. Mojave Martian Simulant soil properties. Parameters extracted from Senatore & Iagnemma (2014).

8.3.1.3 Backanalysis Scheme

As previously mentioned, the extrapolation of the classical terramechanics theory, generally designed for heavy vehicles, to lightweight rovers, has highlighted the limitations of the shear stress-shear displacement relationship (equation 8.7) proposed by Janosi & Hanamota (1961). The relationship is based on two fundamental hypotheses of classical terramechanics:

1) The soil slip velocity corresponds to the wheel rim velocity.

2) The shear stress evolution at the wheel-terrain interface is similar to the shear-displacement relationship observed in direct shear tests.

Unfortunately, as mentioned by Senatore & Iagnemma (2011 and 2014), and Senatore et al (2012), hypothesis 1 and hypothesis 2 are not absolutely correct. Visual inspections of the soil kinematics under a rigid wheel showed that soil at the wheel interface typically remains attached to the wheel rim, and there is little or no relative motion between the soil and the wheel rim. Consequently, the true shear modulus (K_x) cannot be considered representative of soil shearing behavior under the wheel. They noted that shearing also depends on slip conditions, which causes K_x to be dependent on slip. Senatore and Iagnemma argued that the shear modulus should be viewed as an empirical parameter that governs the complex mapping between soil flow and shear stress at the wheel interface, rather than as a simple constant extracted from direct shear tests.

As a result of using genetic algorithms as principal optimization technique, the K_x modification of Senatore & Iagnemma (2014) was incorporated in the backanalysis scheme by extracting the shear modulus from the chromosome, and defining, for each different value of slip, a new optimization analysis for the shear modulus. Consequently, for each individual, with its chromosome representing the values of c, φ , k_c, k_φ and n, a vector of K_x values, with a length equal to the number of different values of slip, was used to define all parameters of the model.

In figure 8.5, the structure of the algorithm is illustrated, where the step associated with the shear modulus optimization can be seen in detail (to see in more detail the rest of the structure see figure 3.13).

Because of the high values of the standard deviation of the sinkage measurements (see table 8.1), and even having the possibility to fully define C_{x_cv2} (eq. 2.17) containing the three types of measurements (torque, drawbar pull and sinkage), and let the matrix to directly penalize the sinkage, the use of sinkage measurements was considered not appropriate. Several preliminary analyses were conducted to study the influence of the sinkage, and it was concluded that using sinkage measurements would contaminate the analysis rather than introducing valuable information into it. Moreover, in Senatore & Iagnemma (2014), and Zhou et al (2014), it was also pointed out how difficult it is to match the sinkage measurements for the wheel-terrain model, partly, because of the high inaccuracy of the measurements. Therefore, only torque and drawbar pull were used in the analysis and consequently C_{x_cv2} was only defined by torque and drawbar pull.

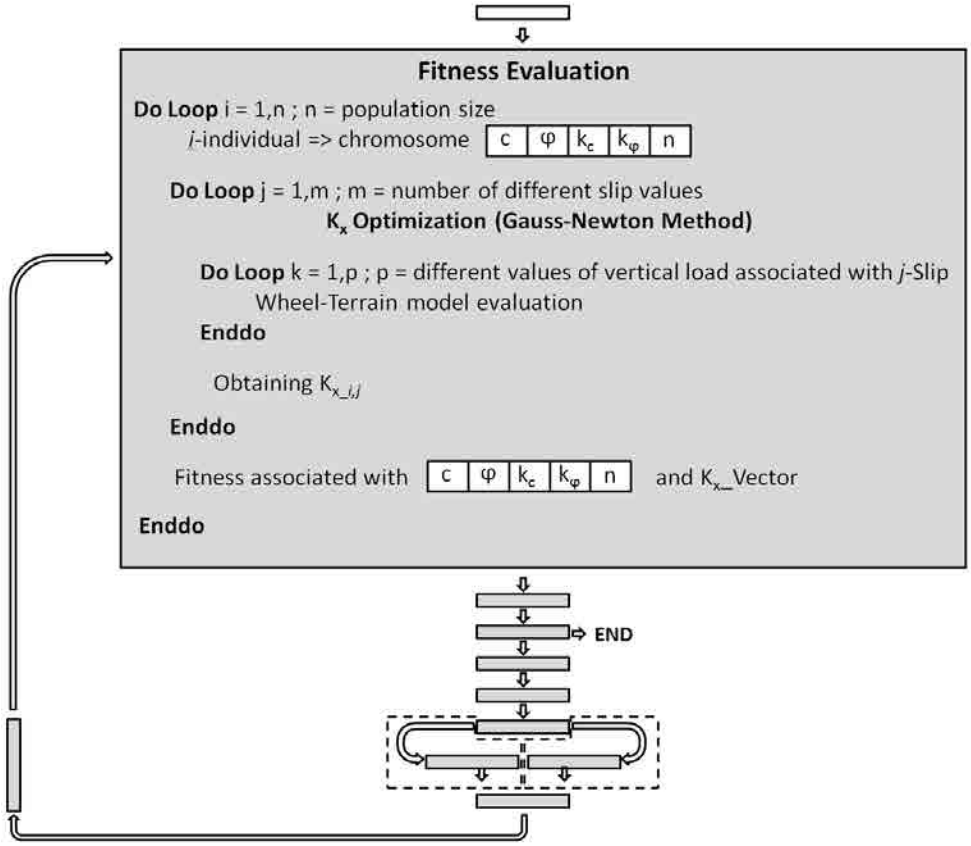

Figure 8.5. Optimization algorithm structure used for the Mars Rover problem. To see in more detail the rest of "boxes" represented in the figure, see figure 3.13

The main characteristics of the backanalysis are shown in table 8.3.

Identification of: c, φ, k_c, k_φ and n / Genetic Algorithm	
Optimization Algorithm	
Type of algorithm	AGA + Elitism
Selection type	Roulette Wheel
GAP	1
Maximum probability of applying crossover (P_{c_max})	0.95
Minimum probability of applying crossover (P_{c_min})	0.50
Maximum probability of applying mutation ($P_{m\ max}$)	0.40
Minimum probability of applying mutation ($P_{m\ min}$)	0.01
Population size	1001
Stop Criteria	25 generations
Search Space Discretization (total number of individuals = 3788154086)	
c_{min} [N/m^2]	0
c_{max} [N/m^2]	5000
$c_{step\ size}$ [N/m^2]	100
φ_{min} [deg]	20
φ_{max} [deg]	40
$\varphi_{step\ size}$ [deg]	0.5
k_{c_min} [N/m^{n+1}]	10000
k_{c_max} [N/m^{n+1}]	1000000
$k_{c_{step}size}$ [N/m^{n+1}]	1000
k_{φ_min} [N/m^{n+2}]	1000000
k_{φ_max} [N/m^{n+2}]	10000000
$k_{\varphi_{step}size}$ [N/m^{n+2}]	50000
n_{min} [-]	0.5
n_{max} [-]	1.5
$n_{step\ size}$ [-]	0.01

K_x Optimization / Gradient Based Method	
Type of algorithm	Gauss-Newton
Stop Criteria	fixed number of iterations (10 iterations)
K_x Domain	
K_{x_min} [m]	0.0005
K_{x_max} [m]	0.025
Objective Function	
Genetic Algorithm	
Type of objective function	Maximum Likelihood Method with relative error (eq.2.15)
Gradient Based Method	
Type of objective function	Least-Squares Method
Measurements	
Genetic Algorithm	
Type of measurement	Torque and Drawbar (15 measurements for each type)
Gradient Based Method	
Type of measurement	Torque and Drawbar (5 sets of measurements of 3 measurements of torque and 3 of drawbar)

Table 8.3. Main characteristics of the backanalysis.

For this particular case study, where the conceptual model was not represented by means of a Plaxis model, and where a new specific optimization strategy was also implemented (two levels of optimization: for K_x and the rest of the parameters), the HBCode was modified in order to tackle the new needs of the problem. As a result, the Mars-HBCode was created.

8.3.2 Results

After 25 generations and a total of 3411 different individuals evaluated, the best individual extracted from the analysis was constituted by:

c = 3000N/m^2

φ = 40^o

k_c = 72000N/m^{n+1}

k_φ = 4350000N/m^{n+2}

n = 1.42

$K_x(i = 0, i = 0.1, i = 0.3, i = 0.5, i = 0.7)$ = (0.0075, 0.013, 0.025, 0.025, 0.025m)

It can be noted that the parameters of the best individual do not match the parameters extracted from laboratory (see table 8.2). However, it was possible to obtain an acceptable match between the measurements and the calculations obtained from the best individual, except, naturally, for the sinkage values, which were not involved in the analysis (see figure 8.6).

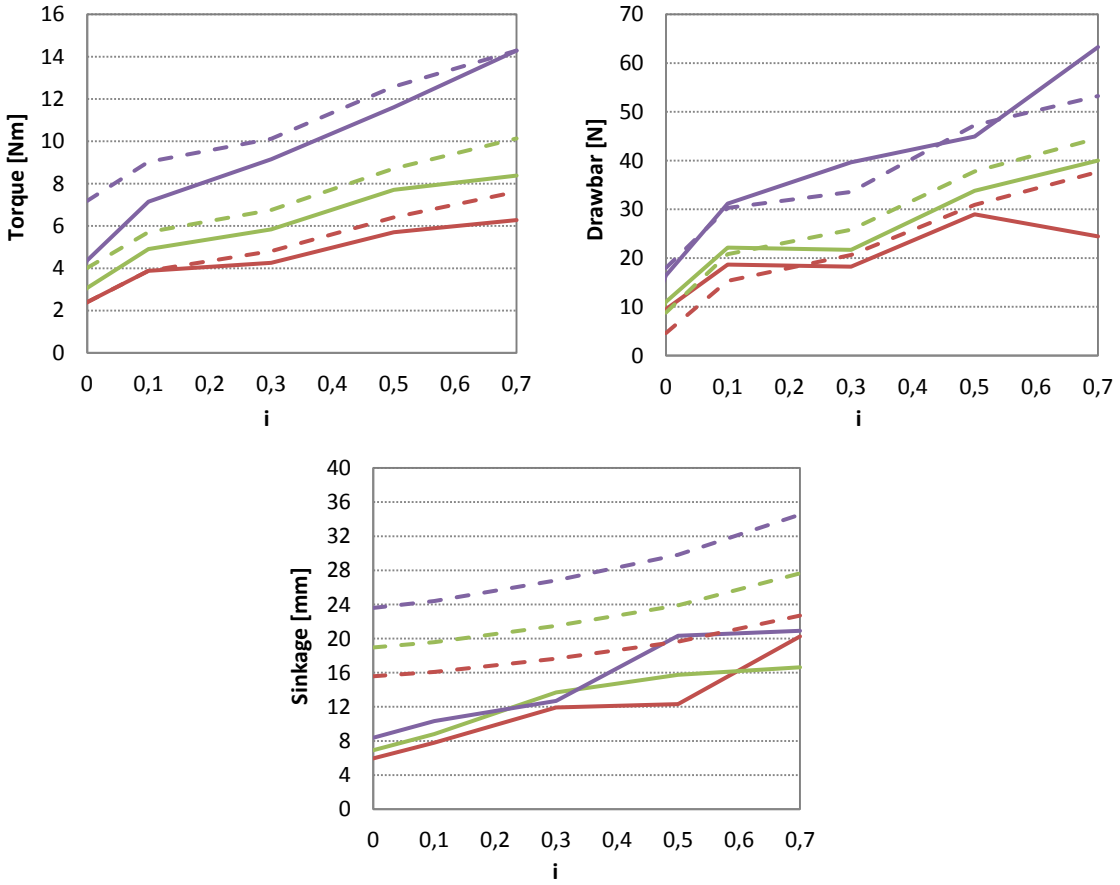

Figure 8.6. Comparison between measurements and calculations obtained from the best individual. The solid lines represent the measurements, and the dashed lines the calculations. Red => W=70N, Green => W=100N and Purple => W=150N.

Apart from studying the best individual as a solution of the problem, a Principal Component Analysis (PCA) was also conducted in order to study in more depth the morphology of the good individuals (and not only the best one). Approximately 2% of the individuals evaluated during the evolution were considered good enough to be involved in the PCA (a total of 71 individuals). The most relevant results of the PCA are shown in table 8.4.

Description	Values
Mean of c [N/m^2]	4185.92
Mean of φ [deg]	37.22
Mean of k_c [N/m^{n+1}]	243549.30
Mean of k_φ [N/m^{n+2}]	3640845.07
Mean of n [-]	1.38
Standard deviation of c [N/m^2]	536.47
Standard deviation of φ [deg]	2.72
Standard deviation of k_c [N/m^{n+1}]	169513.57
Standard deviation of k_φ [N/m^{n+2}]	1724804.54
Standard deviation of n [-]	0.08
Correlation matrix	$\begin{bmatrix} 1 & -0.11 & 0.18 & 0.16 & -0.35 \\ -0.11 & 1 & -0.39 & 0.34 & -0.61 \\ 0.18 & -0.39 & 1 & -0.51 & 0.54 \\ 0.16 & 0.34 & -0.51 & 1 & -0.04 \\ -0.35 & -0.61 & 0.54 & -0.04 & 1 \end{bmatrix}$
Eigenvector (associated with the first principal component)	$[-0.075 \quad -0.525 \quad 0.539 \quad -0.391 \quad 0.522]$
Eigenvector (associated with the second principal component)	$[-0.857 \quad 0.103 \quad -0.287 \quad 0.145 \quad 0.386]$
Eigenvector (associated with the third principal component)	$[-0.321 \quad 0.295 \quad 0.090 \quad -0.785 \quad -0.43]$

Eigenvector (associated with the fourth principal component)	$[-0.0004 \quad -0.7 \quad -0.644 \quad -0.224 \quad -0.27]$
Eigenvector (associated with the fifth principal component)	$[0.393 \quad 0.366 \quad -0.45 \quad -0.398 \quad 0.59]$
Eigenvalue (associated with the first principal component)	2.241
Eigenvalue (associated with the second principal component)	1.203
Eigenvalue (associated with the third principal component)	0.975
Eigenvalue (associated with the fourth principal component)	0.573
Eigenvalue (associated with the fifth principal component)	0.007

Table 8.4. Principal Component Analysis. Values corresponding to the 71 best individuals involved in the PCA.

In terms of parameter values, better results were obtained when defining the solution by PCA. However, if the ellipsoid is not capable of matching the objective function shape, even having apparently better results than only using the best individual, the solution cannot be considered satisfactory.

Unfortunately, 50% of the individuals involved in the PCA were not located inside the PCA ellipsoid, which indicates that the ellipsoid was not very representative to the objective function. Moreover, if more attention is placed on the distribution of the best individuals, it can be observed (figure 8.7) how the good individuals have significant different combinations of parameters values, which also makes more difficult to obtain a representative ellipsoid.

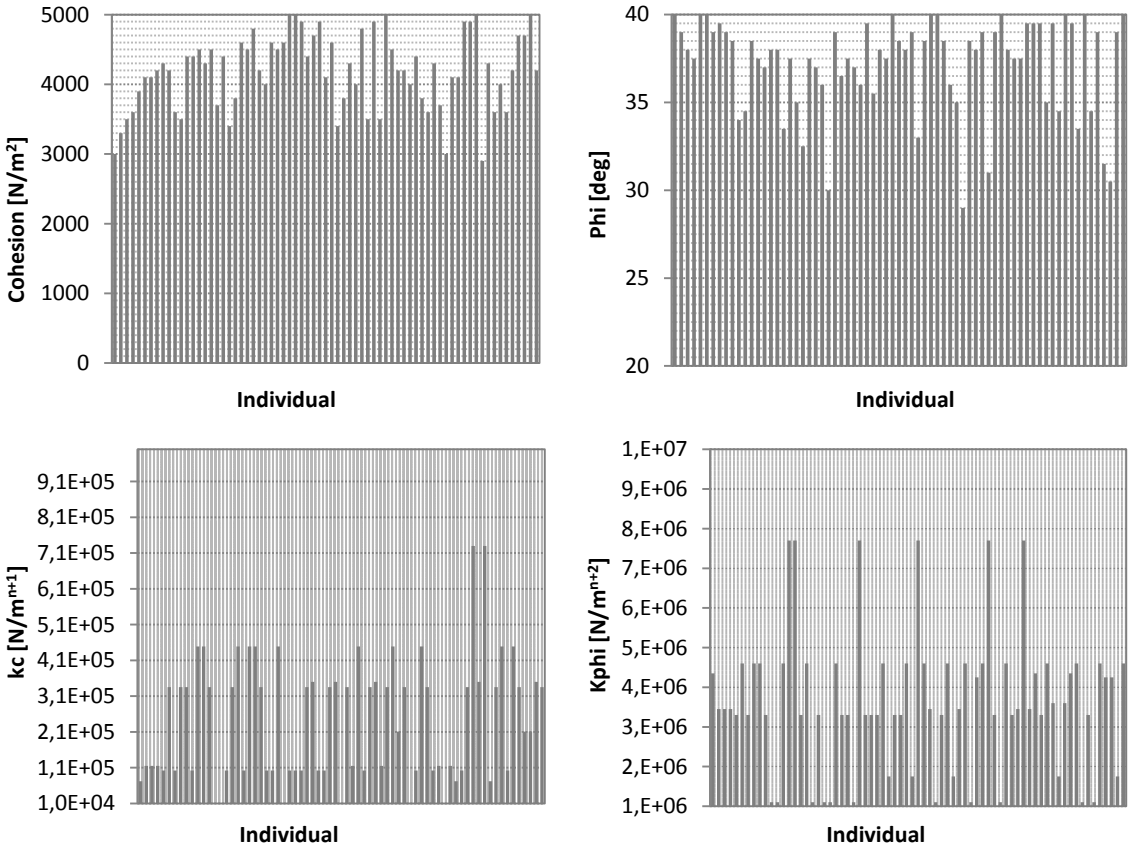

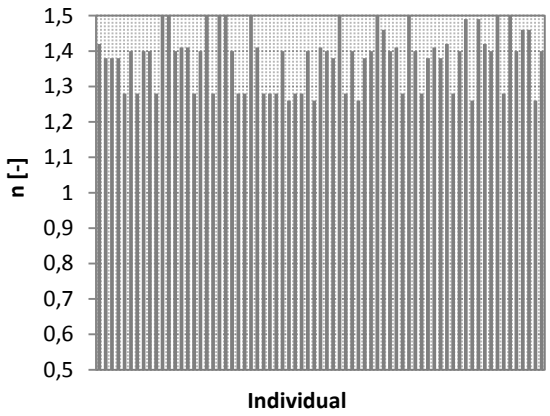

Figure 8.7. Parameters distribution associated with the individuals involved in the PCA (good individuals). The gray bars represent the parameter values of the individuals.

For this particular case, this phenomenon is statistically explained by the non-normal distribution of the good individuals that are used to define the surroundings of the minimum, and which reflect that many local minima are embedded in the objective function. Due to the fact that the axes of the ellipsoid are proportionally defined to the standard deviation of the parameters, represented into the space of factors, the property of enclosing a certain percentage of individuals, and subsequently quantifying the representativeness of the ellipsoid, are not guaranteed if a normal distribution is not followed. The property of the number of good individuals enclosed into the PCA ellipsoid is a necessary but not sufficient condition to describe the ellipsoid as representative to the objective function.

In figure 8.8, the histograms and the "Detrended" Normal Q-Q plots of the parameters are presented to formally illustrate the non-normal distribution of the good individuals.

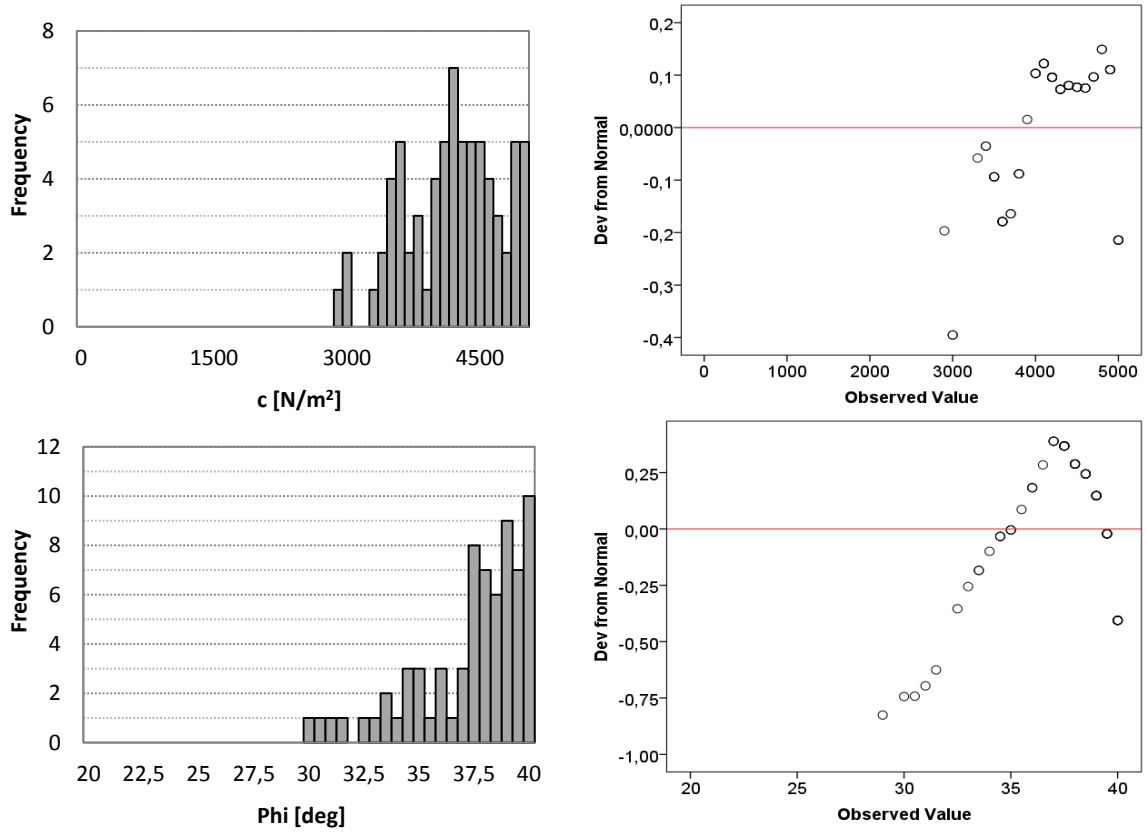

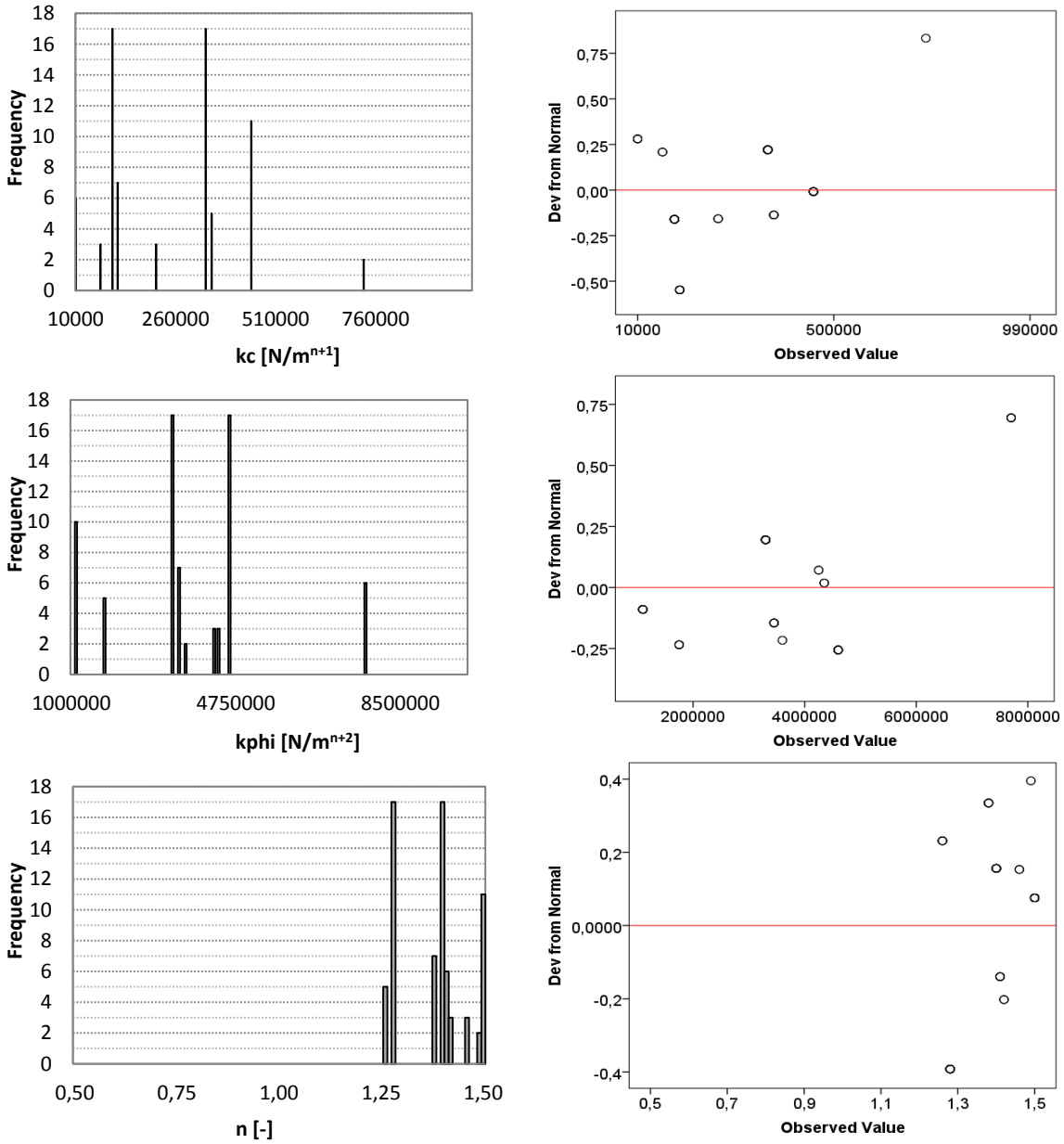

Figure 8.8. Histograms (on the left) and "Detrended" Normal Q-Q plots (on the right) of the good individuals.

Another effect of having non-unique solution is a sort of premature convergence of the genetic algorithm caused by initial concentrations of relatively good individuals. The fact of having significant different combinations of parameters, with similar fitness, caused that an initial concentration of similar good individuals has promoted the domain where they are located; overtaking the influence of the fitness on the selection stage by the number of similar relatively good individuals. From equation 3.15, the phenomenon already mentioned, can be mathematically seen, where $m(H,t)$ represents the similar good individuals, and $f(H)/\bar{f}$ represents the effect of the fitness on the selection stage.

In figures 8.9, 8.10, 8.11, 8.12 and 8.13, the full evolution of the population is illustrated, where even having a better individual in the population (the one named as the best individual), the algorithm is driven into another minimum due to a initial larger number of similar individuals with a relatively good fitness with respect to the best one.

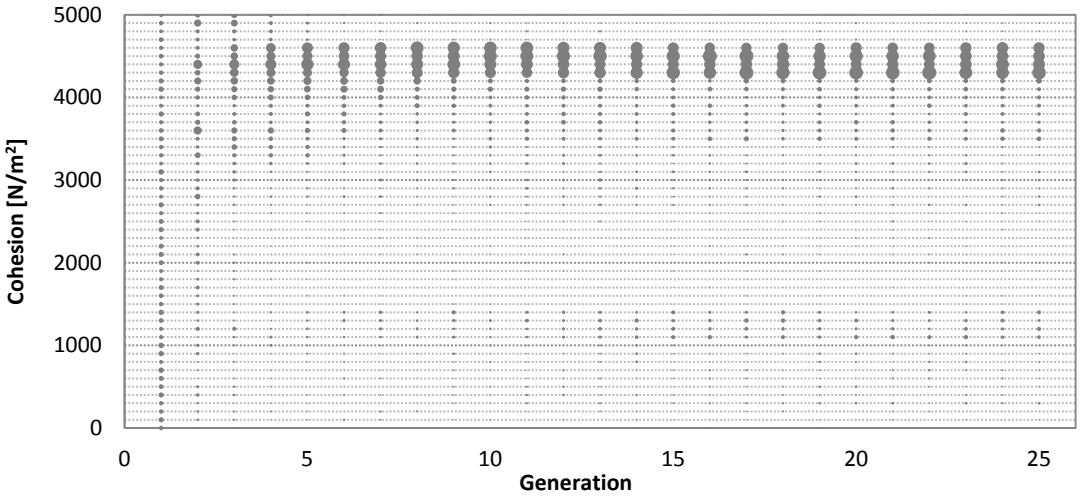

Figure 8.9. Full evolution of the cohesion. The sizes of the bubbles are directly related to the number of individuals that share that specific value.

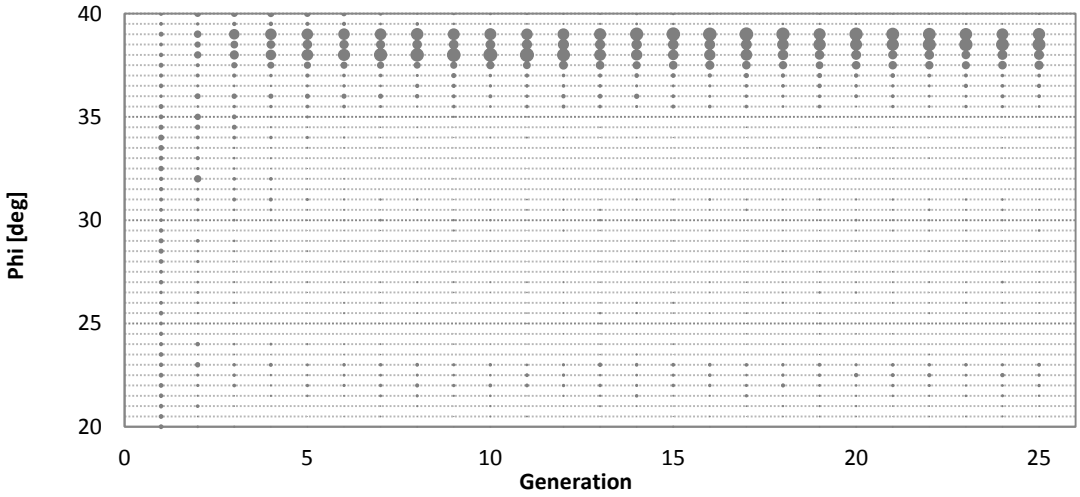

Figure 8.10. Full evolution of the internal friction angle. The sizes of the bubbles are directly related to the number of individuals that share that specific value.

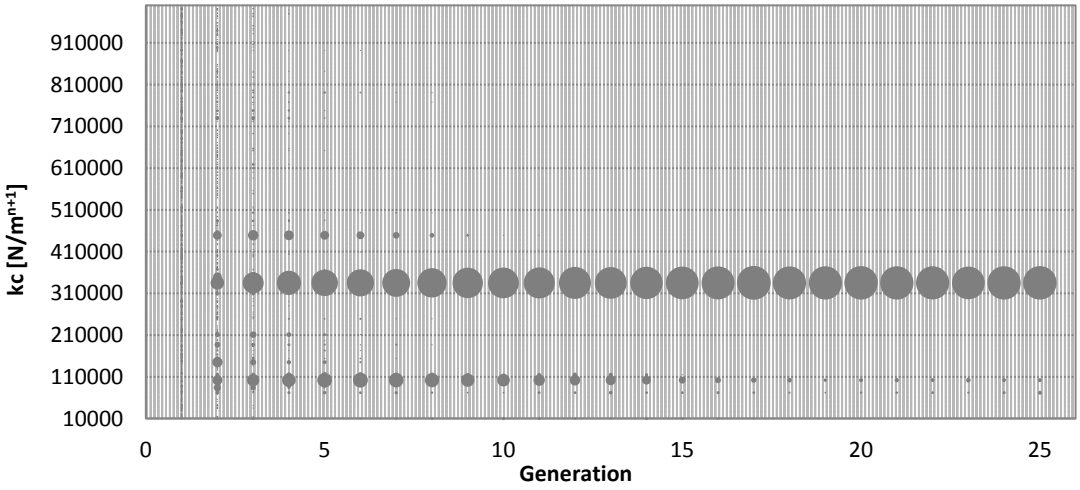

Figure 8.11. Full evolution of the Bekker's parameter k_c. The sizes of the bubbles are directly related to the number of individuals that share that specific value.

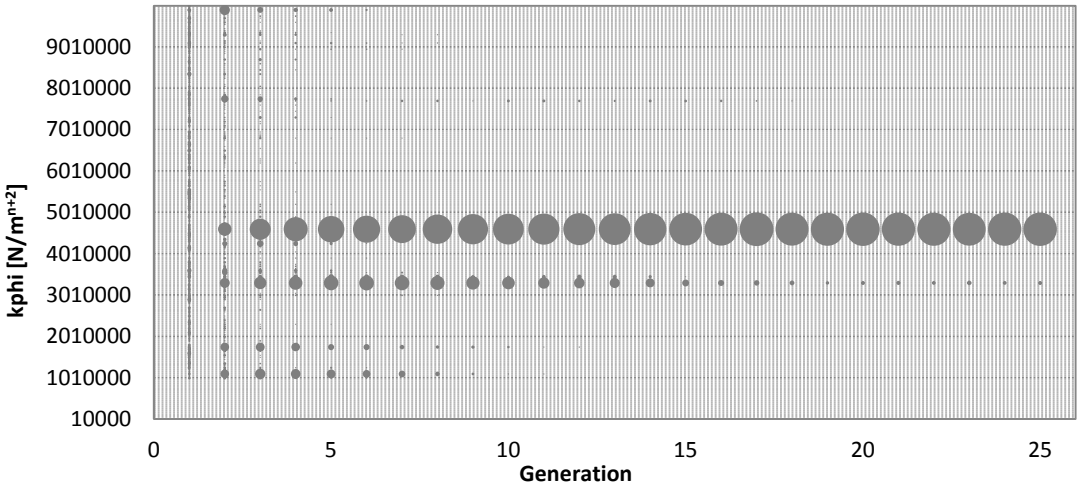

Figure 8.12. Full evolution of the Bekker's parameter k_{φ}. The sizes of the bubbles are directly related to the number of individuals that share that specific value.

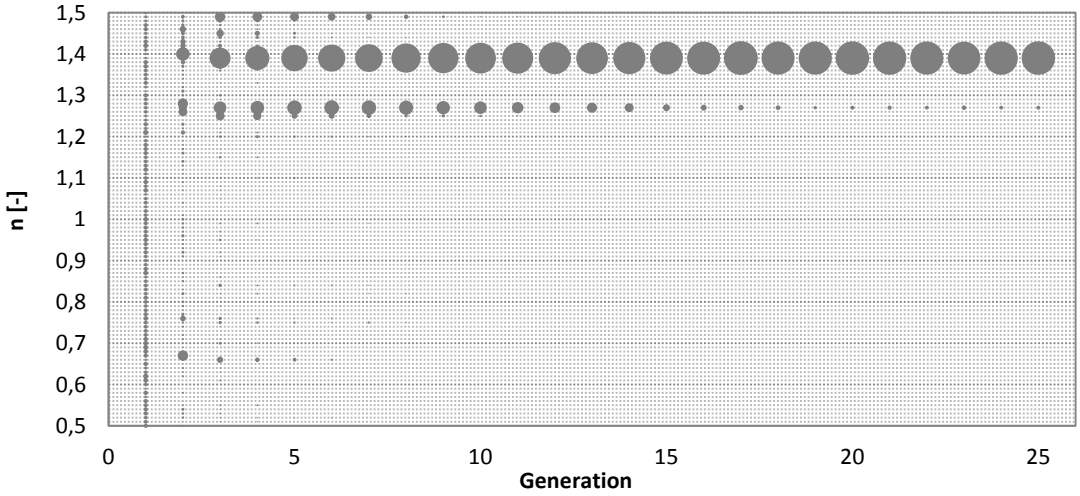

Figure 8.13. Full evolution of the sinkage exponent. The sizes of the bubbles are directly related to the number of individuals that share that specific value.

In order to understand the reasons for the high complexity of the objective function shape, it was considered useful to take a step back and carry out a simpler backanalysis. For that purpose, instead of using the C_{x_cv2} matrix to define the objective function, the identity matrix was used. By doing that it was expected to be able to directly compare the results obtained from the laboratory tests with the ones obtained from the backanalysis. Not surprisingly, although match between measurements and calculations obtained using the two sets of parameters is similar (see figure 8.14), the fitness associated with the combination of the parameters extracted from the "simple" backanalysis was 30% higher than the one associated with the parameters extracted from laboratory (see table 8.5). This indicates that the genetic algorithm was not the responsible for the mismatch between parameters, it appears that the mismatch is a consequence of the failure of the wheel-terrain model to define a unique solution.

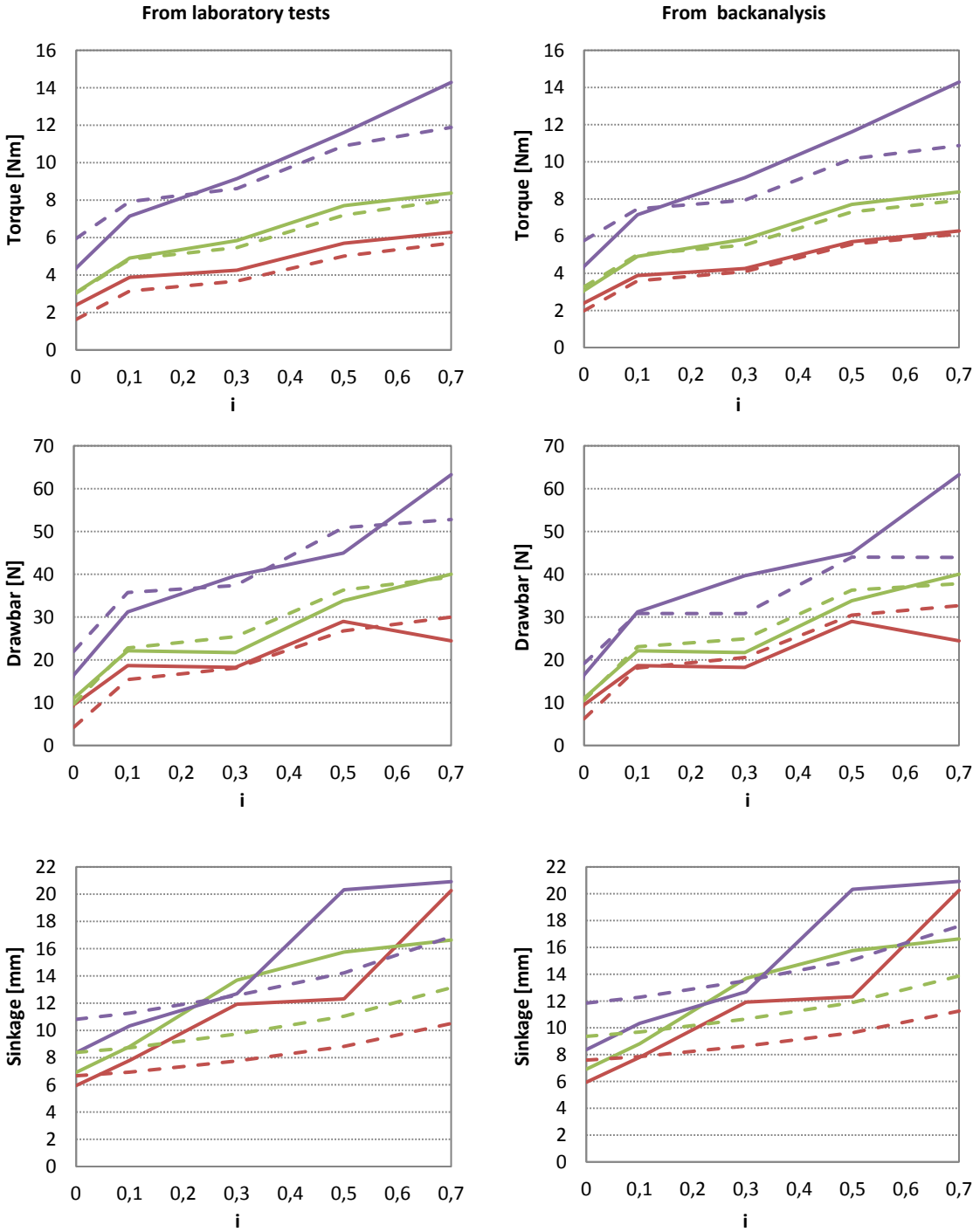

Figure 8.14. Comparison between measurements and wheel-terrain model calculations. The figures on the left side are associated with the parameters obtained from laboratory tests, and the ones on the right side are associated with the parameters obtained from the "simple" backanalysis. The solid lines represent the measurements, and the dashed lines the calculations. Red => W=70N, Green => W=100N and Purple => W=150N.

Parameter	From laboratory tests	From "Simple" backanalysis
c [N/m^2]	600	3400
φ [deg]	35	26
k_c [N/m^{n+1}]	846130	15000
k_φ [N/m^{n+2}]	6708000	9700000
n [-]	1.4	1.29
	From laboratory tests	**From "Simple" backanalysis**
Fitness	1.0039	1.4275

Table 8.5. Parameter values introduced in the wheel-terrain model, and their fitness associated with. From laboratory tests => Parameters extracted from Senatore & Iagnemma (2014).

8.4 Concluding Remarks

After examining the results presented in the previous section, several concluding remarks can be drawn.

Although good results were obtained in terms of fitness, it was not possible to match the soil parameters from the backanalysis with the values extracted from laboratory tests.

As a result of the extensive presence of local minima, the genetic algorithm was strongly governed by premature concentrations of relatively good individuals. The effect of that concentration makes the number of relatively good individuals to overtake the influence of the fitness during selection; making more difficult for the algorithm to find the global minimum.

The non-normal distribution of the good individuals invalidates the PCA ellipsoid to be considered as a solution of the problem. Consequently, only the best individual can be considered a proper solution of the problem.

Finally, it should be noted that in the backanalysis the wheel-terrain model was supposed to be exactly correct. Therefore, any discrepancy between the model and the measurements was implicitly assumed to be caused by measurement errors. Of course, some of the discrepancies between observations and computations must also be due to limitations of the wheel-terrain model. However, more important than the discrepancy between measurements and model, it is the effect of having none-uniqueness solution on the reliability of the model. That makes the model inadequate as a basis for the identification of the soil parameters. Therefore, in order to be able to define an efficient and robust backanalysis methodology for Mars surface exploratory rovers, the definition or the use of a more appropriate wheel-terrain model is crucial.

Chapter 9

Conclusions and Future Research

9.1 Conclusions

This thesis deals with Geotechnical backanalysis, presenting several procedures to identify parameters from field measurements. Those procedures are based on gradient based methods, genetic algorithms, particularly appropriate for large problems involving many parameters, and a combination of both of them (hybrid methods). The algorithms have been applied to several synthetic examples and real cases including tunneling, a large excavation and a case related to wheel-terrain interaction (Mars rover). From the work presented in previous chapters, and regarding the mathematical procedures to perform the backanalysis described in this thesis, the main conclusions are set out in this section.

From Chapter 5, where all the different optimizations algorithms presented in this thesis have been tested in a synthetic tunnel case study, the following conclusions can be extracted:

- A flexible, efficient and robust backanalysis methodology has been defined in this thesis, which can be adapted to specific needs of the problem. The adaptive nature of the methodology is based on the type of optimization method applied to the problem (Gauss-Newton method, Marquardt method, Simple Genetic Algorithms, Adaptive Genetic Algorithms and Hybrid Methods).

- The Gauss-Newton method has shown itself as the most balanced method in terms of parameters results and computational cost. However, for real complex problems with a large

number of parameters, it is not expected to obtain such good results. Therefore, in those cases it is anticipated that more robust methods, such as genetic algorithms, would obtain better results.

- When large differences in the magnitudes of the parameters involved in the analysis exist, the definition of μ_0 and ρ (parameters that control the Marquardt method) can be challenging. Consequently, in those cases, even though the Marquardt method is an improvement of the Gauss-Newton method, worse results can be obtained.

- The right choice of the population size and the selection pressure has a major impact on the performance of Simple Genetic Algorithms, especially if there is a large difference between the fitness of the good individuals and the average of the population. The combination of those factors can drive the algorithm into premature convergence due to the fast loss of diversity. However, when using Adaptive Genetic Algorithms, the adaptive nature of the algorithm forces the population to keep a certain level of diversity that makes the algorithm less dependent on population size and selection pressure, and consequently, less likely to end in premature convergence.

- After checking the match between the PCA ellipse (or ellipsoid) and the objective function, it is necessary to analyze if the combinations of soil parameters enclosed in the ellipse can be representative of a specific soil material in order to finally consider the solution geotechnicaly satisfactory. In the cases where the definition of a unique soil material is not possible, more information, such as prior information, should be introduced to redefine and limit the individuals (soil parameters combinations) that provide the solution.

- A good balance between robustness and efficiency was obtained when using the hybrid method. However, for a simple synthetic case, as the one presented in Chapter 5, the Gauss-Newton method is still more competitive than the hybrid method. Nonetheless, for complex real problems with a large number of parameters, the hybrid method is expected to surpass the performance of any gradient based method.

- Sophisticated constitutive models, such as the Hardening Soil Model, make the soil parameters identification extremely difficult due to the interconnection among some of their parameters. That interconnection makes it more likely to lead a none-unique solution. In those cases it is recommended to introduce prior information to restrict some of those undesired solutions that are geotechnicaly unsatisfactory.

- Constitutive models that do not have interconnections among parameters are expected to be more suitable for geotechnical backanalysis.

- From the results presented herein, it can be extrapolated that in most cases the higher the measurements are, the more sensitive to model parameters they are likely to be. Nonetheless, it must be pointed out that this is not always the case.

- For geotechnical scenarios extremely close to collapse, the parameters that constitute the solution to the backanalysis problem are probably found on the boundaries of the objective function, which makes it more challenging for the optimization algorithms presented in this thesis to find the solution due to their limitations to move around the boundaries.

From the first real case study (Barcelona Metro Tunnel - Chapter 6) the following conclusions can be drawn:

- In spite of the strong three-dimensional nature of a real tunnel construction by means of an EPB, a two-dimensional simulation can be used to define the problem obtaining still good results. However, some additional assumptions and hypotheses are required to reduce the real three-dimensional problem to a simplified two-dimensional one. That simplification can be archived by means of any of the three methods presented in this thesis (The Modified Tunnel Lining Contraction Method, The ΣMStage Method and The Grout Pressure Method). The selection of the method depends on the objective of the analysis and on the nature of the problem.

- For the particular case study where the final objective of the analysis, apart from studying the difference among the methods, was to determine the stiffness of the soil (preliminary backanalysis), the method that performed the best was the ΣMStage method. However, if the soil parameters are known and the analysis is strictly focused on displacements, the Modified Tunnel Lining Contraction method also gives good results (but it should never be used to identify soil parameters due to its lack of parameters sensitivity). No good results in terms of soil parameters and displacements were obtained by using the Grout Pressure method. As mentioned in Chapter 6, the Grout Pressure Method is only recommended for cases where the combination of grout pressure and K_0 is expected to generate a stress disequilibrium (Grout Pressure ≈ $\sigma_0 = \sigma_v \cdot K_0$) that is likely to occur in reality while excavating the tunnel.

- Very similar solutions in terms of objective function can be obtained from different combinations of soil parameters and ΣMStage. Therefore, more information is required to properly define the solution. Consequently, unlike in the preliminary backanalysis where the three stiffness moduli were linked among them ($E_{oed}^{ref} = 0.8E_{50}^{ref}$ and $E_{ur}^{ref} = 3E_{50}^{ref}$), in the full backanalysis E_{50}^{ref} and E_{ur}^{ref} were identified separately, short and long term measurements were introduced in the analysis in order to capture short and long term behavior in order to facilitate the definition of a better solution.

- For the particular case study where the tunnel construction is far from collapse, the identification by backanalysis of the internal friction angle seems inadequate due to the nature of φ (failure parameter). Moreover, a strong relationship was noted between φ and E_{50}^{ref} that made also more difficult to identify a proper value of E_{50}^{ref}. For a particular set of measurements, the higher the φ is, the lower E_{50}^{ref} is obtained.

- When using the instruments error structure as defined in section 2.4, the influence (weight) of the measurements extracted from the sliding micrometers and the inclinometers (incremental instruments) are reduced in comparison to the isolated measurements such as settlements.

Based on the results of the second real case study (Girona High-Speed Railway Station), the following conclusions can be pointed out:

- When defining the solution of the problem by the Principal Component Analysis ("best set of individual"), better solutions are obtained when the construction of the excavation progresses

and results in larger displacements. The reduction in the size of the PCA ellipse reflects the increase in the quality of the solution.

- The fact that the center of the ellipse remains stationary while updating the measurements, makes the soil parameters amenable to be identified in the early stages of construction.

- When feeding constantly the analysis with results from previous stages (intersection of PCA ellipses), better results are obtained in terms of principal components.

- The hybrid method has shown a good behavior in a complex real case study, both in terms of robustness and computational cost.

- For this particular case study, the identification of the soil parameters in the early stages, using a two-dimensional model, has allowed the definition of a "pre-calibrated" three-dimensional model to fully describe all construction stages, especially the last one (Exc_7) with a strong three-dimensional nature that was not possible to be captured by the two-dimensional model.

Derived from the results of the case study 3 (Mars Surface Exploratory Rover), the following conclusions can be drawn:

- Even when obtaining a good match between the measurements and the calculated values, it was not possible to match the soil parameters values extracted from laboratory tests.

- The extensive presence of local minima has caused early concentrations of relatively good individuals. Those concentrations has subsequently caused that the number of those good individuals overtake the influence of the fitness on the selection process.

- In the backanalysis the wheel-terrain model was supposed to be exactly correct. Therefore, any discrepancy between the model and the measurements was implicitly assumed to be caused by measurement errors. Of course, some of the discrepancies between observations and computations must also be due to limitations of the wheel-terrain model. However, more important than the discrepancy between measurements and model, it is the effect on the reliability of the model of having none-uniqueness solution. That makes the model inadequate as a basis for the identification of the soil parameters. Therefore, in order to be able to define an efficient and robust backanalysis methodology for the Mars surface exploratory rovers, the definition and use of a more appropriate wheel-terrain model is crucial.

Finally, as a general conclusion it must be highlighted the strongly problem dependent nature of geotechnical backanalyses, and the difficulty to devise general guidelines to enable the soil parameters identification. Nonetheless, the following scheme can be helpful to deal with the strong problem dependency:

- Use more than just one soil constitutive model (a simple and a complex one).

- Identify if the scenario is close or far from collapse (especially useful to reduce the number of potential parameters to be indentified if the scenario is far from collapse).

- Use more than just one optimization technique.

- Study the non-uniqueness of the problem if possible.

- Compare the results obtained from laboratory tests with the ones obtained from the backanalysis.

9.2 Future Research

Derived from the conclusions presented above, three different potential lines of future research are presented. They are related to:

- Optimization Algorithms.

- Constitutive Models.

- Strongly Problem Dependent Nature of Geotechnical Backanalyses.

Optimization Algorithms

As mentioned and discussed in this thesis, a unique optimization algorithm that can be considered as the most adequate one for all problems does not exist. In some cases, the robustness of an algorithm can cause unjustified computational cost, whereas in some other cases, highly efficient algorithms cannot cope with complex problems. However, taking into account the main objective of this thesis to define a methodology capable of being applied to a large number of geotechnical problems, the weakness of the gradient based methods presented in some cases suggests that more effort should be placed on improving them.

The main problems of the gradient based methods appeared when several parameters are simultaneously identified and the algorithm is driven to the borders of the search space. Those limitations are directly related to the difficulty of driving the search with the information extracted from the derivatives and the poor conditions of this type of algorithms to deal with states close to the boundary. Therefore, in order to overcome those situations where the gradient based method has shown a poor performance, the use of a direct algorithm (without the need of using the gradient of the function) with less computational cost than the genetic algorithms, such as the Simplex Method (Nelder & Mead, 1965), seems an adequate direction for future research.

Constitutive Models

Part of the difficulties that the optimization algorithms have is not caused by intrinsic limitations of them but by adoption of inappropriate soil constitutive models. The use of sophisticated constitutive models, such as the Hardening Soil Model, can generate non-unique solutions due to the strong relationship that exists among some parameters. Moreover, in some cases, those parameters do not have a physical geotechnical meaning; making it more difficult to find a proper solution of the soil parameters identification problem.

Several authors (Ghaboussi et al., 1991, Ellis et al., 1995, Ghaboussi & Sidarta, 1997 and Ghaboussi et al., 1998) worked on the idea of creating a methodology based on a self-adaptive constitutive model where a neural-network approach is used to define the constitutive model that captures the real soil behavior. Good results were obtained in Hashash et al. (2003 and

2006) and Finno & Hashash (2009), where a self-adaptive constitutive model was defined for a deep excavation. However, even the first impression about this methodology that seems perfect to deal with the limitations of the "traditional" constitutive models, it cannot be forgotten that behind this methodology there are several hidden layers of nodes that enclose the mathematical expressions that describe the stress-strain soil behavior in a form of a "black-box". Consequently, similar limitations as the ones presented by the "traditional" constitutive models are expected to appear.

Therefore, the use of complex constitutive model different from the one that has been used in this thesis, and the study in depth of the relationships among parameters that can generate non-unique solutions seems the most appropriate path to be followed for future research.

Strongly Problem Dependent Nature of Geotechnical Backanalyses

As shown throughout the thesis, it is extremely difficult to set up any general guidelines (what, where and when to measure in order to identify a specific soil parameter) to enable the soil parameters identification due to the strongly dependent nature of geotechnical backanalyses. Therefore, in order to find those guidelines that can help planning future backanalyses, the study of a large number of synthetics geotechnical scenarios seems a potential way to find those general guidelines that cannot be fully defined in this thesis, in part, due to the limited number of synthetic cases presented.

References

Affenzeller, M. and Wagner, S. (2005). *Offspring selection: A new self-adaptive selection scheme for genetic algorithms*. Proceeding of the International Conference on Adaptive and Natural Computational Algorithms, Coimbra, Portugal, 218-221.

Arai, K. Ohta, H. and Kojima, K. (1984). *Estimation of soil parameters based on monitored movement of subsoil under consolidation.* Soils and Foundations, 14, 95-108.

Arai, K. Ohta, H., Kojima, K. and Wakasugi, M. (1986). *Application of Back-analysis to several test embankments on Soft Clay Deposits.* Soils and Foundations, 26(2), 60-72.

Baram, Y. & Sandell, N.R. (1978). *An information theoretic approach to dynamical systems modelling and identification.* IEEE Transactions on Automatic Control, 23, 61-66.

Beck, J.V. & Woodbury, K.A. (1998). *Inverse problems and parameter estimation: integration of measurements and analysis.* Measurement Science and Technology, 9(6), 839-847.

Beegle, L.W., Peters G.H, Mungas, G.S., Bearman, G.H., Smith, J.A. and Anderson R.C. (2007). *Mojave martial simulant: a new martial soil simulant.* Proceeding of the Lunar and Planetary Institute Science Conference (abstracts).

Bekker, M. (1956). *Theory of land locomotion: The mechanics of vehicle mobility.* The University of Michigan Press, Ann Arbor, MI, USA.

Bekker, M. (1960). *Off-the-road locomotion; research and developments in terramechanics.* The University of Michigan Press, Ann Arbor, MI, USA.

Bekker, M. (1969). *Introduction to terrain-vehicle systems.* The University of Michigan Press, Ann Arbor, MI, USA.

Benz, T. (2007). *Small-Strain Stiffness of Soils and its Numerical Consequences.* Ph.D. thesis, University of Stuttgart, Stuttgart, Germany.

Brindle, A. (1981). *Genetic algorithms for function optimization*. Ph.D. thesis. University of Alberta. Edmonton, AB, Canada.

Brinkgreve, R.B.J. & Broere, W. (2008). *Plaxis, 2D - Version 9.0.* Plaxis b.v., The Netherlands.

Bury, K.V. (1975). *Statistical models in applied science*. John Wiley and Sons, New York, NY, USA.

Cancelli, A. & Cividini, A. (1984). *An embankment on soft clays with sand drains. Numerical characterization of the parameters from in-situ measurements.* Proceeding of the International Conference on Case Histories in Geotechnical Engineering. University of Missouri-Rolla, MO, USA, 2, 637-643.

Calvello, M. (2002). *Inverse Analysis of a Supported Excavation through Chicago Glacial Clay.* Ph.D. thesis. Northwestern University, Evanston, IL, USA.

Carrera, J. (1988). *State of the art of the inverse problem applied to the flow and solute transport equations.* Groundwater Flow and Quality Modelling, Reidel, Dordrecht, The Netherlands, 549-583.

Carrier, W.D. (1994). *Trafficability of lunar microrovers (part 1).* Technical Report: LGI TR94-02, Lunar Geotechnical Institute, Lakeland, FL, USA.

Chen, R.S., Lu, K.Y. and You, S.C. (2002). *A hybrid genetic algorithm approach on multi-objective of assembly planning problem.* Engineering Applications of Artificial Intelligence, 15, 447-457.

Chicone, C. (1999). *Ordinary differential equations with applications*. Springer, New York, USA.

Cividini, A., Jurina, L. and Gioda, G. (1981). *Some aspects of characterization problems in geomechanics.* International Journal of Rock Mechanics and Mining Sciences & Geomechanics Abstracts, 18(6), 487-503.

Cividini, A., Maier, G., and Nappi, A. (1983). *Parameter estimation of static geotechnical model using a Bayes' approach.* International Journal of Rock Mechanics and Mining Sciences & Geomechanics Abstracts, 20(5), 215-226.

Darwin, C.R. (1859). *On the Origin of Species by Means of Natural Selection or the Preservation of Favoured Races in the Struggle for Life*. John Murray, London, UK.

Davis, L. (1987). *Genetic Algorithms and Simulated Annealing*, Pitman, London, UK.

De Jong, K.A. (1975). *An analysis of the behavior of a class of genetic adaptive systems*. Ph.D. thesis. University of Michigan, Ann Arbor, MI, USA.

De Jong, K.A. and Spears, W.M. (1992). *A formal analysis of the role of multi-point crossover in genetic algorithms.* Annals of Mathematics and Artificial Intelligence, Springer, 5, 1-26.

de Santos, C., Ledesma, A. and Gens, A. (2014). *Hybrid minimization algorithm applied to tunnel backanaysis.* Proceeding of the 14th International Conference of the International Association for Computer Methods and Advances in Geomechanics, Kyoto, Japan.

Diaz-Gomez, P.A. and Hougen, D.F. (2007a). *Initial Population for Genetic Algorithms: A Metric Approach.* Proceeding of the International Conference on Genetic and Evolutionary Methods, Las Vegas, NV, USA, 43-49.

Diaz-Gomez, P.A. and Hougen, D.F. (2007b). *Empirical Study: Initial Population Diversity and Genetic Algorithm Performance*. Proceeding of the Conference on Artificial Intelligence and Pattern Recognition, Orlando, FL, USA, 334-341.

Diaz-Gomez, P.A. and Hougen, D.F. (2009). *Initial Population Diversity and Performance Independence*. Proceeding of the Conference on Artificial Intelligence and Pattern Recognition, Orlando, FL, USA, 64-69.

Di Mariano, A., Persio, R., Gens, A., Castellanza R. and Arroyo, M. (2009). *Influence of some EPB operation parameters on ground movements.* Proceeding of the 2nd International Conference on Computational Methods in Tunnelling, Bochum, Germany, 43-50.

Ding, L., Yoshida, K., Nagatani, K., Gao, H. and Deng, Z. (2009). *Parameter identification for planetary soil based on a decoupled analytical wheel-soil interaction terramechanics model.* Proceeding of the IEEE International Conference on Intelligent Robots and Systems, St. Louis, MO, USA, 4122-4127.

Ding, L., Gao, H., Deng, Z and Tao, J. (2010). *Wheel slip-sinkage and its prediction model of lunar rover.* Journal of Central South University Technology, 17(1), 129-135.

Duncan, J.M. & Chang, C.Y. (1970). *Nonlinear analysis of stress and strain in soil.* ASCE - Journal of the Soil Mechanics and Foundation Division, 96, 1629-1653.

Edwards, A.W.F. (1972). *Likelihood.* Cambridge University Press, Cambridge, United Kingdom.

Eiben, A., de Wilde, A. and Schut, M. (2006a). *Boosting genetic algorithms with self-adaptive selection.* Proceeding of the IEEE Conference on Evolutionary Computation, Vancouver, BC, Canada, 477-482.

Eiben, A., de Wilde, A. and Schut, M. (2006b). *Is self-adaptation of selection pressure and population size possible? A case study.* Proceeding of the 9th Parallel Problem Solving from Nature, Reykjavik, Iceland, 4193, 900-909.

Ellis, G.W., Yao, C., Zhao, R. and Penimadu, D. (1995). *Stress-Strain Modeling of Sands Using Artificial Neural Networks.* Journal of Engineering Mechanics Division, ASCE, 121, 429-435.

Engl, H.W., Hanke, M. and Neubauer, A. (1996). *Regularization of inverse problems.* Kluwert, Dordrecht, The Netherlands.

Eykhoff, P. (1974). *System identification. Parameter and state estimation.* John Wiley and Sons, Chichester, United Kingdom.

Filbà, M. (2006). *Estudio geotécnico de las obras de la nueva línea 9 del Metro de Barcelona* (in Spanish). Technical Report.

Finno, R.J. & Calvello, M. (2005). *Supported Excavations: Observational Method and Inverse Modeling.* Journal of Geotechnical and Geoenvironmental Engineering, 131(7), 826-836.

Finno, R.J. & Hashash, Y.M.A. (2009). *Integrated Tool for Predicting, Monitoring and Controlling Ground Movements due to Excavations.* Proceeding of NSF Engineering Research and Innovation Conference, Honolulu, HI, USA.

Fletcher, R. (1981). *Practical Methods of Optimization. Volume 1, Unconstrained optimization. Volume 2, Constrained optimization.* John Wiley and Sons, Chichester, United Kingdom.

Fogarty, T.C. (1989). *Varying the probability of mutation in genetic algorithms*. Proceeding of the 3rd International Conference on Genetic Algorithms, Morgan Kaufmann, San Francisco, CA, USA, 104-109.

Gens, A., Ledesma, A. and Alonso, E.E. (1988). *Backanalysis using prior information. Application to the staged excavation of a cavern in rock.* Proceeding of the 6th International Conference on Numerical Methods in Geomechanics, Innsbruck, Austria, 2009-2016.

Gens, A., Ledesma, A. and Alonso, E.E. (1996). *Estimation of Parameters in Geotechnical Backanalysis - II. Application to a Tunnel Excavation Problem.* Computers and Geotechnics, 18(1), 28-46.

Gens, A., Persio, R., Di Mariano, A., Castellanza, R. and Arroyo, M. (2009). *Relación entre parámetros de una tuneladora EPB y los movimientos del terreno* (in Spanish). Proceeding of the 3as Jornadas Hispano-Portuguesas de Geotecnia, Madrid, Spain, 433-441.

Ghaboussi, J., Garrett, J.H. and Wu, X. (1991). *Knowledge-Based Modeling of Material Behavior with Neural Networks.* Journal of Engineering Mechanics Division, ASCE, 117(1), 132-153.

Ghaboussi, J., Pecknold, D.A., Zhang, M. and Haj-Ali, R.H. (1998). *Autoprogressive Training of Neural Network Constitutive Models.* International Journal for Numerical Methods in Engineering, 42, 105-126.

Gioda, G. (1980). *Indirect identification of the average elastic characteristics of rock masses.* Proceeding of the International Conference on Structural Foundations on Rock, Sydney, Australia, 65-73.

Gioda, G. (1985). *Some remarks on back analysis and characterization problems.* Proceeding of the 5th International Conference on Numerical Methods in Geomechanics, Nagoya, Japan, 47-61.

Gioda, G. & Maier, G. (1980). *Direct search solution of an inverse problem in elastoplasticity: identification of cohesion, friction angle and in situ stress by pressure tunnel tests.* International Journal for Numerical Methods in Engineering, 15, 1823-1848.

Gioda, G. & Sakurai, S. (1987). *Back analysis procedures for the implementation on field measurements in geomechanics.* International Journal for Numerical and Analytical Methods in Geomechanics, 11, 555-583.

Glover, F. and Laguna, A. (1993). *Tabu Search*. Chapter 3 in Modern Heuristic Techniques for Combinatorial Problems, Blackwell Scientific Publications, Oxford, UK.

Goldberg, D.E. (1985). *Optimal initial population size for binary-coded genetic algorithms*. TCGA Report 85001, University of Alabama, Tuscaloosa, AL, USA.

Goldberg, D.E. (1989a). *Genetic Algorithms in Search, Optimization, and Machine Learning*. Addison-Wesley, MA, USA.

Goldberg, D.E. (1989b). *Sizing populations for serial and parallel genetic algorithms*. Proceeding of the 3rd International Conference on Genetic Algorithms, Morgan Kaufmann, San Francisco, CA, USA, 70-79.

Goldberg, D.E. and Deb, K. (1991). *A comparative analysis of selection schemes used in genetic algorithms*. Foundations of Genetic Algorithms, Morgan Kaufmann, San Francisco, CA, USA, 69-93.

Goldberg, D.E., Deb, K. and Clark, J.H. (1992). *Genetic algorithms, noise, and sizing of populations*. Complex Systems, 6, 333-362.

Grefenstette, J.J. (1986). *Optimization of control parameters for genetic algorithms*. IEEE Transactions on Systems, Man, and Cybernetics, 16, 122-128.

Haftka, R.T., Scott, E.P. and Cruz, J.R. (1998). *Optimization and experiments: A survey.* Applied Mechanics Reviews, 51(7), 435-448.

Hagras, H., Pounds-Cornish, A., Colley, M., Callaghan, V. and Clarke, G. (2004). *Evolving spiking neural network controllers for autonomous Robots.* Proceeding in the IEEE International Conference on Robotics and Automation, New Orleans, LA, USA, 5, 4620-4626.

Hashash, Y.M.A, Marulanda, C., Ghaboussi, J. and Jung, S. (2003). *Systematic update of a deep excavation model using field performance data.* Computer and Geotechnics, 30, 477-488.

Hashash, Y.M.A, Marulanda, C., Ghaboussi, J. and Jung, S. (2006). *Novel Approach to Integration of Numerical Modeling and Field Observations for Deep Excavations.* Journal of Geotechnical and Geoenvironmental Engineering, ASCE, 132, 1019-1031.

**Hashash, Y.M.A., Levasseur, S., Osouli, A., Finno, R. and Malécot, Y. (2010*). Comparison of two inverse analysis techniques for learning deep excavation response.* Computers and Geotechnics, 37, 323-333.

Hesser, J. and Männer, R. (1991). *Towards an Optimal Mutation Probability in Genetic Algorithms*. Proceeding of the 1st Parallel Problem Solving from Nature, Springer-Verlag, London, UK, 23-32.

Hesser, J. and Männer, R. (1992). *Investigation of the m-heuristic for optimal mutation probabilities*. Proceeding of the 2nd Parallel Problem Solving from Nature, Brussels, Belgium, 115-124.

Hisatake, M. & Ito, T. (1985). *Back analysis for tunnels by optimization method.* Proceeding of the 5th International Conference on Numerical Methods in Geomechanics, Nagoya, Japan, 1301-1307.

Holland, J.H. (1975). *Adaptive in Nature and Artificial Systems*. University of Michigan Press, Ann Arbor, MI, USA.

Iagnemma, K., Kang, S., Shibly, H. and Dubowsky, S. (2004). *On-Line terrain parameter estimation for planetary rovers.* IEEE Transactions on Robotics and Automation, 20(5), 921-927.

Iagnemma, K., Shibly, H. and Dubowsky, S. (2005). *A laboratory single wheel testbed for studying planetary rover wheel-terrain interaction*. Technical Report: 01-05-05, Field and Space Robotic Laboratory, Massachusetts Institute of Technology, Cambridge, MA, USA.

Iagnemma, K., Senatore, C., Trease, B., Arvidson, R. Shaw, A., Zhou, F., et al. (2011). *Terramechanics modeling of Mars surface exploration rovers for simulation and parameter estimation.* Proceeding of the International Design Engineering Technical Conferences & Computers and Information in Engineering Conferences, Washington, DC, USA, 28-31.

Janbu, N. (1963). *Soil compressibility as determined by oedometer and triaxial tests.* Proceeding of the 3rd European Conference on Soil Mechanics and Foundation Engineering, Wiesbanden, Germany, 1, 19-25.

Janosi, Z. and Hanamoto, B. (1961). *Analytical determination of drawbar pull as a function of slip for tracked vehicles in deformable soils.* Proceeding of the 1st International Conference on Terrain-Vehicle Systems, Turin, Italy.

Kasprzyk, G.P. and Jaskula, M. (2004). *Application of the hybrid genetic-simplex algorithm for deconvulution of electro-chemical responses in SDLSV method.* Journal of Electroanalytical Chemistry, 567, 39-66.

Kim, K.W., Baek, S.W., Kim, M.Y. and Ryou, H.S. (2004). *Estimation of emissivities in a two-dimensional irregular geometry by inverse radiation analysis using hybrid genetic algorithm.* Journal of Quantitative Spectroscopy and Radiative Transfer, 87, 1-14.

Kondner, R.L. & Zelasko, J.S. (1963). *A hyperbolic stress-strain formulation for sands.* Proceeding of the 2nd Pan-American Conference on Soil Mechanics and Foundations, Brazil, 1, 289-394.

Kovari, K. & Amstad, Ch. (1983). *Fundamentals of deformation measurements.* Proceeding of the International Symposium on Field Measurements in Geomechanics, Zurich, Switzerland, 1, 219-239.

Ledesma, A. (1987). *Parameter Identification in Geotechnics. Application in tunnel excavations.* (Spanish). Ph.D. thesis. Technical University of Catalonia - UPC- BarcelonaTech, Barcelona, Spain.

Ledesma, A., Gens, A. and Alonso, E.E. (1996). *Estimation of Parameters in Geotechnical Backanalysis - I. Maximum Likelihood Approach.* Computers and Geotechnics, 18(1), 1-27.

Ledesma, A. & Romero, E. (1997). *Systematic backanalysis in tunnel excavation problems as a monitoring technique.* Proceeding of the XIV International Conference on Soil Mechanics and Foundation Engineering, Hamburg, Germany, 1425-1428.

Lee, Y.H. and Lee, M.H. (2002). *A shape based block layout approach to facility layout problems using hybrid genetic algorithm.* Computers and Industrial Engineering, 42, 237-248.

Levasseur, S. (2007). *Inverse analysis in geotechnics: development of a method based on genetic algorithms.* (French). University Joseph Fourier - Grenoble I, Grenoble, France.

Levasseur, S. Malécot, Y., Boulon, M. and Flavigny, E. (2007). *Soil parameter identification using a genetic algorithm.* International Journal for Numerical and Analytical Methods in Geomechanics, 32, 189-213.

Levasseur, S. Malécot, Y., Boulon, M. and Flavigny, E. (2009*).* *Statistical inverse analysis based on genetic algorithm and principal component analysis: Method and developments using synthetic data.* International Journal for Numerical and Analytical Methods in Geomechanics, 33, 1485-1511.

Levasseur, S. Malécot, Y., Boulon, M. and Flavigny, E. (2010*).* *Statistical inverse analysis based on genetic algorithm and principal component analysis: Applications to excavation problems and pressuremeter tests.* International Journal for Numerical and Analytical Methods in Geomechanics, 34, 471-491.

Levenberg, K. (1944). A *Method for the Solution of Certain Non-Linear Problems in Least Squares.* The Quarterly of Applied Mathematics, 2, 164-168.

Liu, D. and Feng, S. (2004). *A novel adaptive genetic algorithm.* Proceeding in the International Conference on Machine Learning and Cybernetics, Shanghai, China, 1, 414-416.

Malécot, Y., Levasseur, S., Boulon, M. and Flavigny, E. (2004). *Inverse analysis of in-situ geotechnical measurements using a genetic algorithm.* Proceeding of the 9th International Symposium on Numerical Models in Geomechanics, Ottawa, Canada.

Marquardt, D.W. (1963). *An algorithm for least-squares estimation of nonlinear parameters.* Journal of the Society for Industrial and Applied Mathematics, 11(2), 431-441.

Matijevic et al. (Rover Team) (1997). *Characterization of Martial surface deposits by the Mars pathfinder rover, Sojourner.* Science, 278(5), 1765-1768.

Mc Ginley, B., Maher, J., O'Riordan, C. and Morgan, F. (2011). *Maintaining Healthy Population Diversity Using Adaptive Crossover, Mutation, and Selection.* IEEE Transactions on Evolutionary Computation, 15(5), 692-714.

Meirion-Griffith, G. and Spenko, M. (2013). *A pressure-sinkage model for small-diameter wheels on compactive, deformable terrain.* Journal of Terramechanics, 50(1), 37-44.

Mendel, G. (1865). *Experiments in Plant Hybridization*. Natural History Society Brno. Brno, Czech Republic.

Misevicius, A. (2004). *An improved genetic algorithm: new results for the quadratic assignment problem.* Knowledge Based Systems, 17, 65-73.

Möller, S.C. (2006). *Tunnel induced settlements and structural forces in linings.* Ph.D. thesis. Institute of Geotechnical Engineering, University of Stuttgart, Stuttgart, Germany.

Möller, S.C. and Vermeer, P.A. (2008). *On numerical simulation of tunnel installation.* Tunnelling and Underground Space Technology, 23, 461-475.

Moore, M., Hutton, R., Scott, R., Spitzer, C. and Shorthill, R. (1977). *Surface material of the Viking landing sites, Mars.* Journal of Geophysical Research, 82(28), 4497-4523.

Muir, A.M. (1975). *The circular tunnel in elastic ground.* Geotechnique, 25 (1), 115-127.

Murakami, A. & Hasegawa, T. (1988). *Back analysis using Kalman filter-finite elemens and optimal location of observed points.* Proceeding of the International Conference on Numerical Methods in Geomechanics, Innsbruck, Austria, 2051-2058.

Nohse, Y., Hashuguchi, K., Ueno, M., Shikanai, T, Izumi, H. and Koyama, F. (1991). *A measurement of basic mechanical quantities of off-the-road travelling performance.* Journal of Terramechanics, 28(4), 359-370.

Ohde, J. (1951). *Soil Mechanics.* (German). Hütter, Germany, 3.

Pearson, K. (1895). *Notes on regression and inheritance in the case of two parents.* Proceeding of the Royal Society of London, 58, 240-242.

Peters. G.H, Abbey, W., Bearman, G.H., Mungas, G.S., Smith, J.A., Anderson, R.C., Douglas, S. and Beegle, L.W. (2008). *Mojave mars simulant-characterization of a new geologic mars analog.* Icarus, 197(2), 361-377.

Rechea, C., Levasseur, S. and Finno, R. (2007). *Inverse analysis techniques for parameter identification in simulation of excavation support systems.* Computers and Geothecnics, 35, 331-345.

Richardson, Z., Palmer, M.R., Liepins, G. and Hilliard, M. (1989). *Some Guidelines for Genetic Algorithms with Penalty Functions.* Proceeding of the 3rd International Conference on Genetic Algorithms, Morgan Kaufmann, San Francisco, CA, USA, 191-197.

Richter, L, Ellery, A., Gao, Y., Michaud, S., Schmitz, N. and Weiβ, S. (2006). *A predictive wheel-soil interaction model for planetary rovers validated in testbeds and against mer rovers performance data.* Proceeding of 10th European regional conference of ISTVS, Budapest, Hungary.

Rowe, P.W. (1962). *The stress-dilatancy relation for static equilibrium of an assembly of particles in contact.* Proceeding of the Royal Society of London, Series A, Mathematical and Physical Sciences, 269, 500-527.

Rowe, R.K., Lo, K.Y. and Kack, G.J. (1983). *A method of estimating surface settlement above tunnels constructed in soft ground.* Canadian Geotechnical Journal, 20, 11-22.

Sagaseta, C. (1987). *Analysis of undrained soil deformation due to ground loss.* Geotechnique, 37 (3), 301-320.

Sakurai, S. (1983). *Displacement measurements associated with the design of underground openings.* Proceeding of the international Symposium on Field Measurements in Geomechanics, Zurich, Switzerland, 1163-1178.

Sakurai, S. & Takeuchi, K. (1983). *Back analysis of measured displacements of tunnels.* Rock Mechanics and Rock Engineering, 16, 173-180.

Scales, L.E. (1986). *Introduction to non-linear optimization.* Springer-Verlag. New York, USA.

Schaffer, J.D. and Morishma, A. (1987). *An adaptive crossover mechanism for genetic algorithms.* Proceeding of the 2nd International Conference on Genetic Algorithms. Morgan Kaufmann, San Francisco, CA, USA, 36-40.

Schaffer, J.D., Caruana, R.A., Eshelman, L.J. and Das, R. (1989). *A Study of Control Parameters Affecting Online Performance of Genetic Algorithms for Function Optimization*. Proceeding of the 3rd International Conference on Genetic Algorithms, Morgan Kaufmann, San Francisco, CA, USA, 51-60.

Schanz, T. (1998). *On the mechanical behavior of frictional material.* (German). Mitteilung 45 des Instituts für Geotechnik, University of Stuttgart, Stuttgart, Germany.

Schanz, T., Vermeer, P.A. and Bonnier, P.G. (1999). *The hardening soil model: Formulation and verification.* Beyond 200 in Computational Geotechnics - 10 Years of PLAXIS, Balkema, Rotterdam, Netherlands.

Senatore, C. and Iagnemma, K. (2011). *Direct shear behaviour of dry, granular soils subject to low normal stresses.* Proceeding of 17th International Symposium of the international Society of Terrain-Vehicle Systems, Blacksburg, VA, USA.

Senatore, C., Wulfmeier, M., MacLennan, J., Jayakumar, P. and Iagnemma, K. (2012). *Investigation of stress and failure in granular soils for lightweight robotic vehicle applications.* Proceeding of the NDIA ground vehicle systems engineering and technology symposium modeling & simulation, testing and validation (MSTV) mini-symposium. Troy, MI, USA.

Senatore, C. and Iagnemma, K. (2014). *Analysis of stress distribution under lightweight wheeled vehicles.* Journal of Terramechanics, 51, 1-17.

Shmulevich, I., Ronai, D. and Wolf, D. (1996). *A new field single wheel tester.* Journal of Terramechanics, 33(3), 133-141.

Shoji, M., Ohta, H., Arai, K., Matsumoto, T. and Takahashi, T. (1990). *Two-Dimensional Consolidation Back-Analysis.* Soils and Foundations, 30(2), 60-78.

Siedlecki, W. and Sklanski, J. (1989). *Constrained Genetic Optimization via Dynamic Reward-Penalty Balancing and Its Use in Pattern Recognition.* Proceeding of the 3rd International Conference on Genetic Algorithms, Morgan Kaufmann, San Francisco, CA, USA, 141-150.

Srinivas, M. and Parnaik, L. (1994). *Adaptive probabilities of crossover and mutation in genetic algorithms*. IEEE Transactions on Systems, Man, and Cybernetics, 24(4), 656-667.

Sullivan, R., Anderson, R., Biesiadecki, J., Bond, T. and Stewart, H. (2011). *Cohesions, friction angles, and other physical properties of Martial regolith from Mars Exploration Rover wheel trenches and wheel scuffs.* Journal of Geophysical Research, 116, 1-38.

Tarantola, A. (1987). *Inverse Problem Theory.* Elsevier, Amsterdam, The Netherlands.

Thierens, D. (2002). *Adaptive mutation rate control schemes in genetic algorithms*. Proceeding in the IEEE Congress on Evolutionary Computation, Honolulu, HI, USA, 980-985.

Tsai, F.T-C. (2002). *Inverse problem and parameter structure identification in groundnwater modeling.* Ph.D. thesis. Department of Civil and Environmental Engineering, University of California Los Angeles, Los Angeles, CA, USA.

Tsai, F.T-C., Sun, N-Z. and Yeh, W.W-G. (2003a). *Global-local optimization for parameter structure identification in three-dimensional groundwater modeling.* Water Resources Reserch, 39(2), 1043-1056.

Tsai, F.T-C., Sun, N-Z. and Yeh, W.W-G. (2003b). *A Combinatorial Optimization Scheme for Parameter Structure Identification in Ground Water Modeling.* Ground Water, 41(2), 156-169.

Venclik, P. (1994). *Development of an inverse back analysis code and its verification.* Proceeding of the Third European Conference on Numerical Methods in Geotechnical Engineering, Manchester, United Kingdom, 423-430.

Vermeer, P.A. (1978). *A double hardening model for sand.* Géotechnique, 28(4), 413-433.

Vermeer, P.A. and Brinkgreve, R. (1993). *Plaxis Version 5 Manual.* Balkema, Rotterdam, The Netherlands.

Wang, H.F. and Wu, K.Y. (2004). *Hybrid genetic algorithm for optimization problems with permutation property.* Computers and Operation Research, 31, 2453-2471.

Wiggins, R.A. (1972). *The General Linear Inverse Problem: Implication of Surface Waves and Free Oscillations for Earth Structure.* Reviews of Geophysics and Space Physics, 10(1), 251-285.

Wong, J. and Reece, A. (1967a). *Prediction of rigid wheel performance based on the analysis of soil-wheel stresses. Part I. Performance of driven rigid wheels.* Journal of Terramechanics, 4(1), 81-98.

Wong, J. and Reece, A. (1967b). *Prediction of rigid wheel performance based on the analysis of soil-wheel stresses. Part II. Performance of towed rigid wheels.* Journal of Terramechanics, 4(2), 7-25.

Wongsaroj, j., Borghi, F.X., Soga, K., Mair R.J., Sugiyama, T,m Hagiwara, T. and Bowers, K.H. (2006). *Effect of TBM driving parameters on ground surface movements: Channel Tunnel Rail Link Contract 220.* Geotechnical Aspects of Underground Construction in Soft Ground. Taylor & Francis, Rotterdam, The Netherlands, 335-341.

Xiang, Z., Swoboa, G. and Cen, Z. (2003). *Optimal Layout of Displacement Measurements for Parameter Identification Process in Geomechanics.* International Journal of Geomechanics, 3(2), 205-216.

Yang, Z., Hachino, T. and Tsuji, T. (1997). *On-line identification of continuous time-delay systems combining least-squares techniques with a genetic algorithm.* International Journal of Control, 66(1), 23-42.

Yubero, M.T. (2015). *Personal Communication.*

Zhou, F., Arvidson, R.E., Bennett, K., Trease, B., Lindemann, R., Bellutta, P., Iagnemma, K. and Senatore, C. (2014). *Simulations of Mars Rover Traverses.* Journal of Field Robotics, 31(1), 141-160.

Zhu, K. (2003). *A diversity-controlling adaptive genetic algorithm for the vehicle routing problem with time windows*. Proceeding of the 15th IEEE International Conference on Tools with Artificial Intelligence, Sacramento, CA, USA, 173-183.

Appendix A: Additional Results and Information of the Case Study 1 (Chapter 6)

Here in this appendix, additional results and information of the Case Study 1 is presented as follows:

- Additional results of the preliminary backanalysis - Modified Tunnel Lining Contraction Method.
- Additional results of the preliminary backanalysis - ΣMStage Method.
- Additional results of the preliminary backanalysis - Grout Pressure Method.
- Additional information of the backanalysis - Using the Instruments Error Structure.

Additional results of the preliminary backanalysis - Modified Tunnel Lining Contraction Method

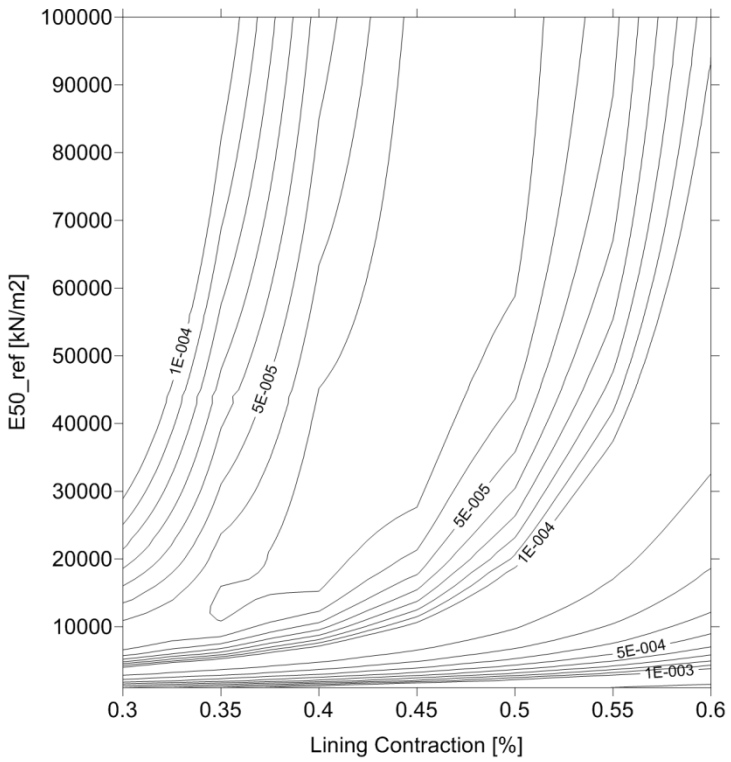

Figure A.1. Mapping of the objective function for full term behavior and surface measurements (Modified Tunnel Lining Contraction Method).

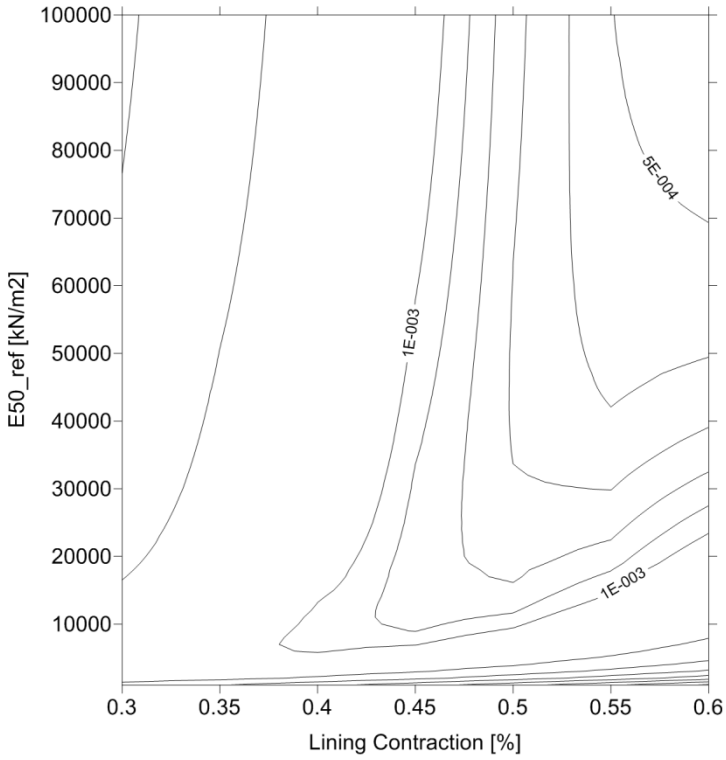

Figure A.2. Mapping of the objective function for full term behavior and sliding micrometer measurements (Modified Tunnel Lining Contraction Method).

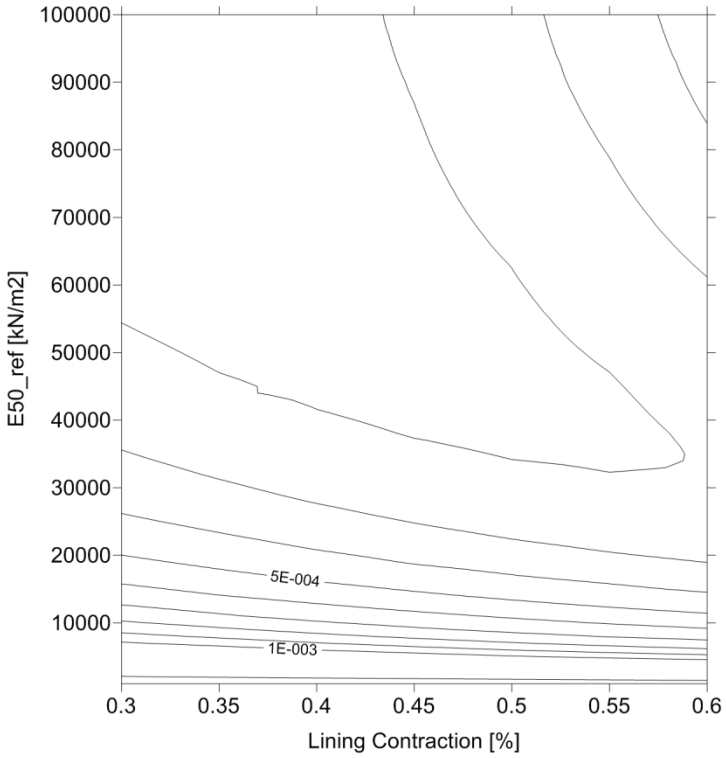

Figure A.3. Mapping of the objective function for full term behavior and inclinometer measurements (Modified Tunnel Lining Contraction Method).

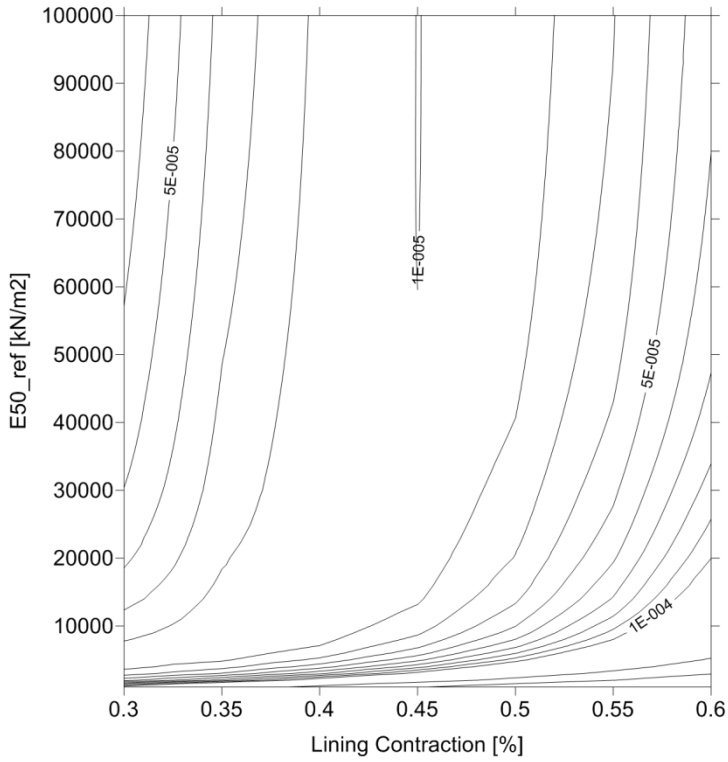

Figure A.4. Mapping of the objective function for short term behavior and surface measurements (Modified Tunnel Lining Contraction Method).

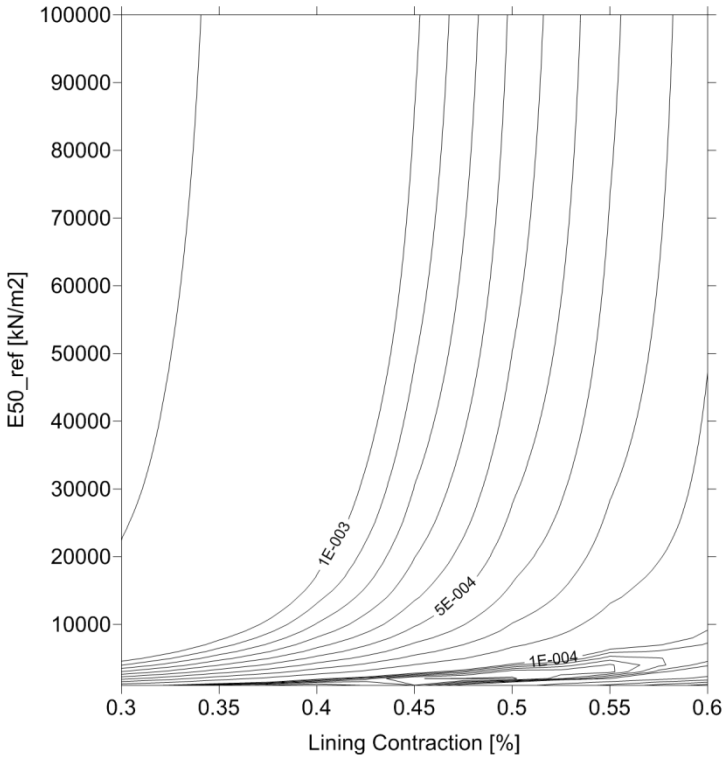

Figure A.5. Mapping of the objective function for short term behavior and sliding micrometer measurements (Modified Tunnel Lining Contraction Method).

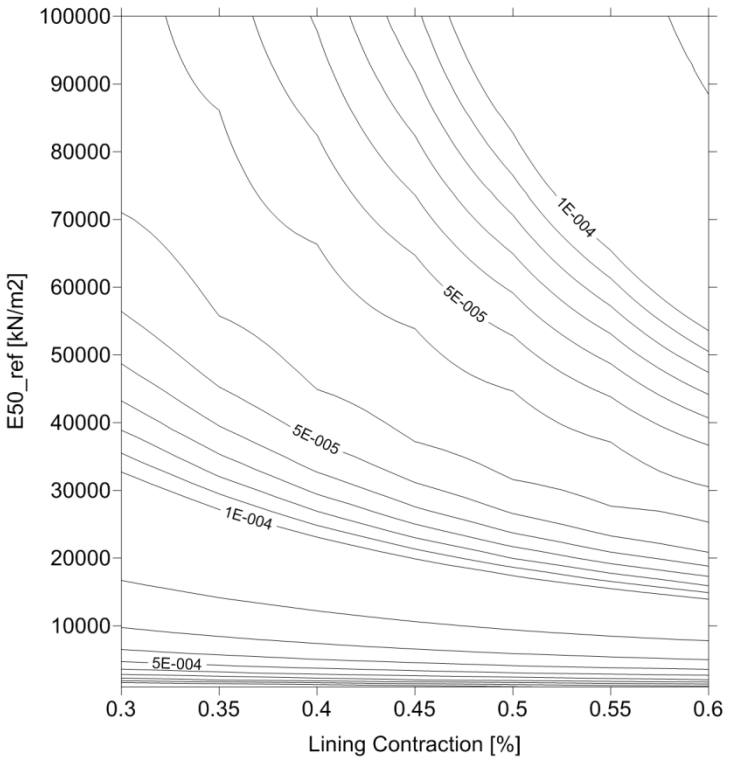

Figure A.6. Mapping of the objective function for short term behavior and inclinometer measurements (Modified Tunnel Lining Contraction Method).

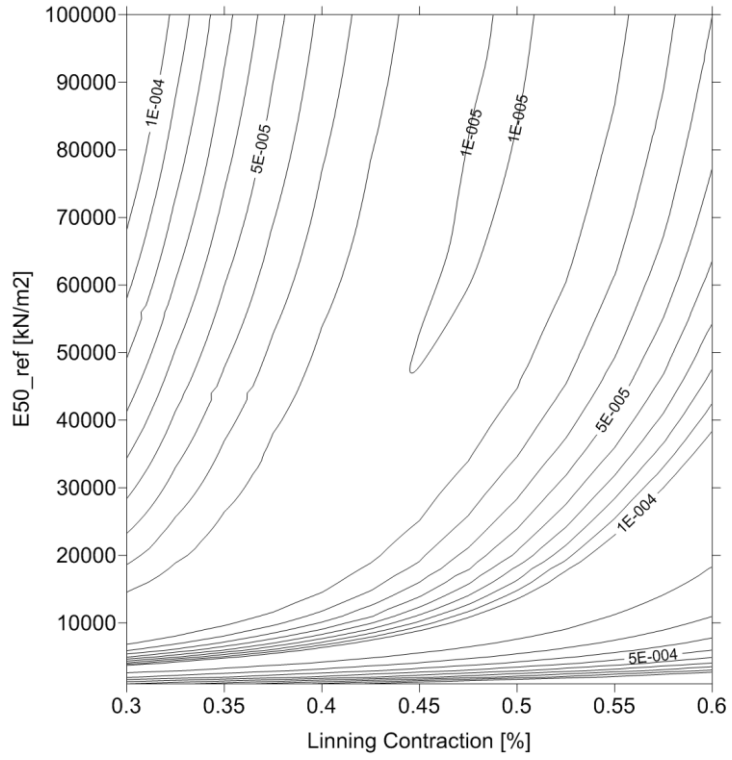

Figure A.7. Mapping of the objective function for long term behavior and surface measurements (Modified Tunnel Lining Contraction Method).

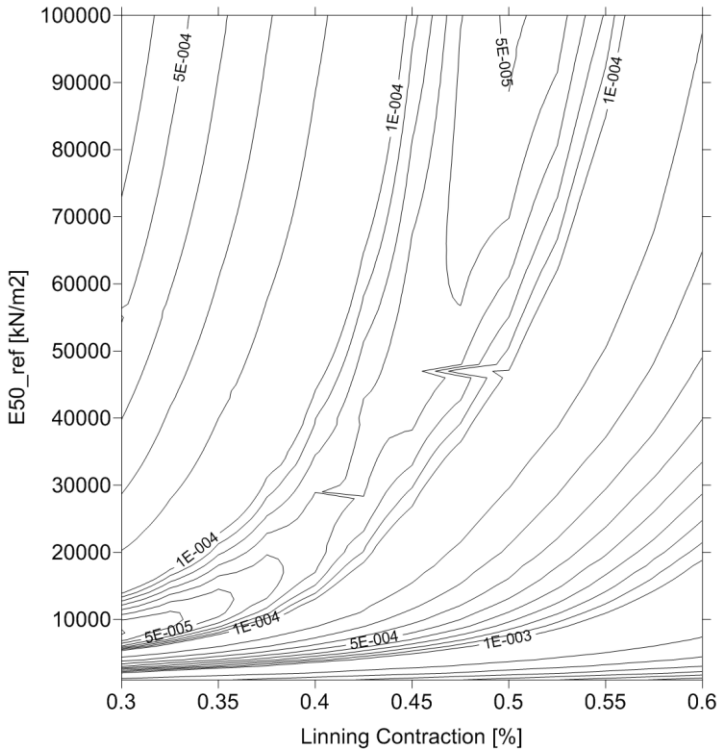

Figure A.8. Mapping of the objective function for long term behavior and sliding micrometer measurements (Modified Tunnel Lining Contraction Method).

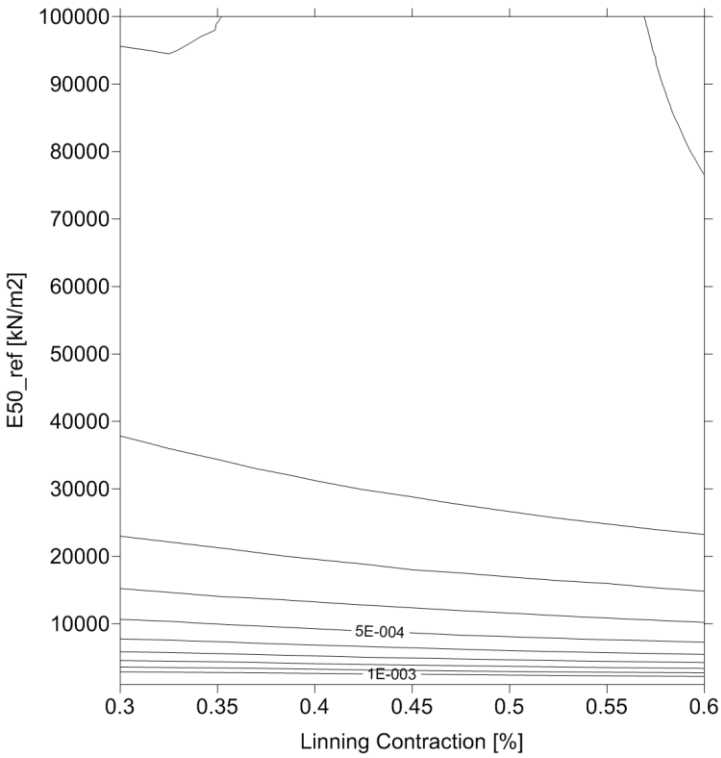

Figure A.9. Mapping of the objective function for long term behavior and inclinometer measurements (Modified Tunnel Lining Contraction Method).

Additional results of the preliminary backanalysis - ΣMStage Method

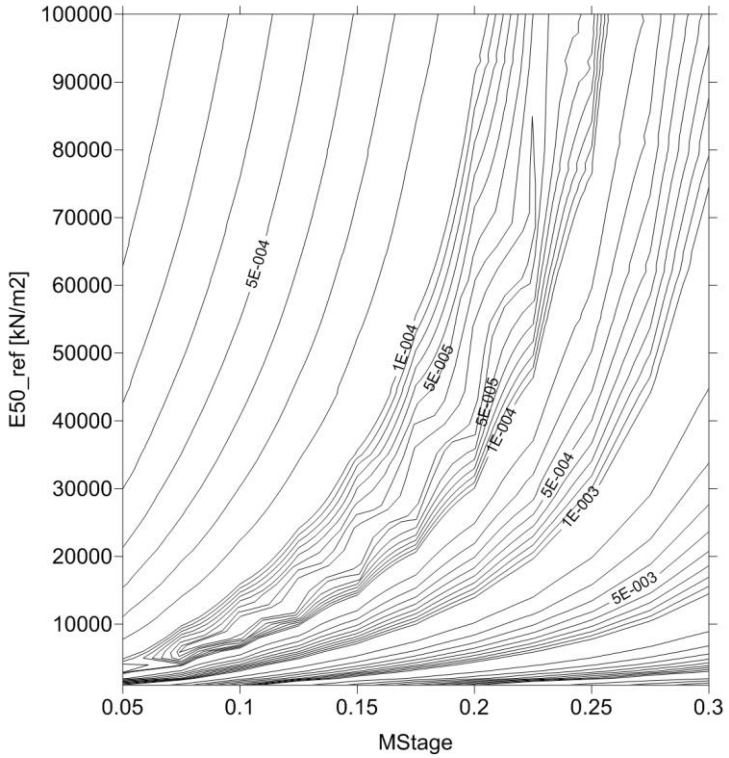

Figure A.10. Mapping of the objective function for full term behavior and surface measurements (ΣMStage Method).

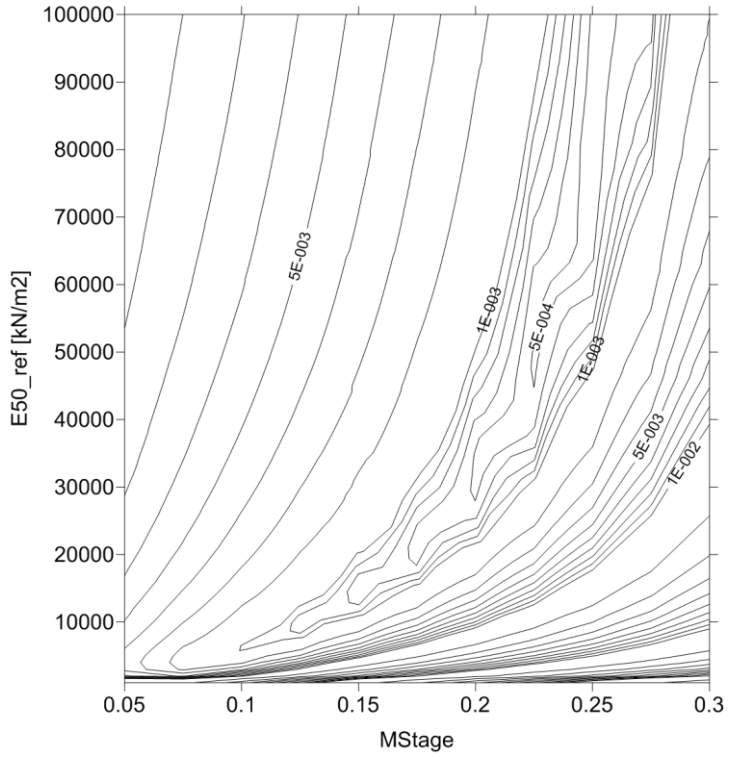

Figure A.11. Mapping of the objective function for full term behavior and sliding micrometer measurements (ΣMStage Method).

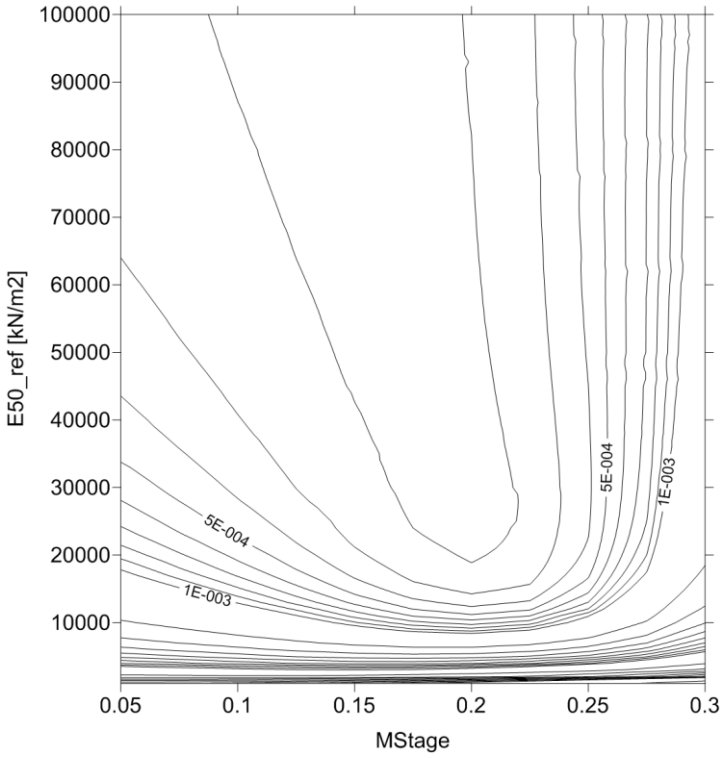

Figure A.12. Mapping of the objective function for full term behavior and inclinometer measurements (ΣMStage Method).

Additional results for the preliminary backanalysis - Grout Pressure Method

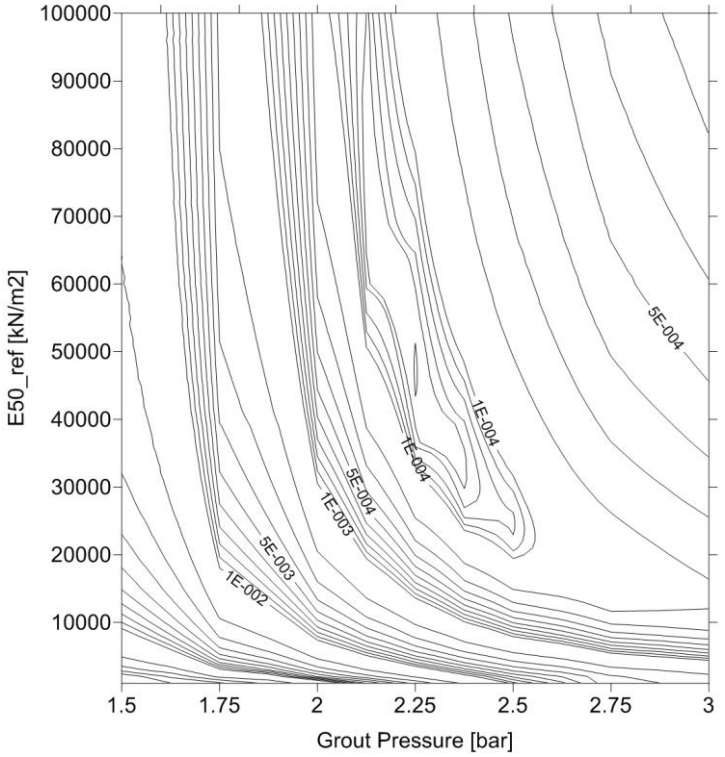

Figure A.13. Mapping of the objective function for full term behavior and surface measurements (Grout Pressure Method).

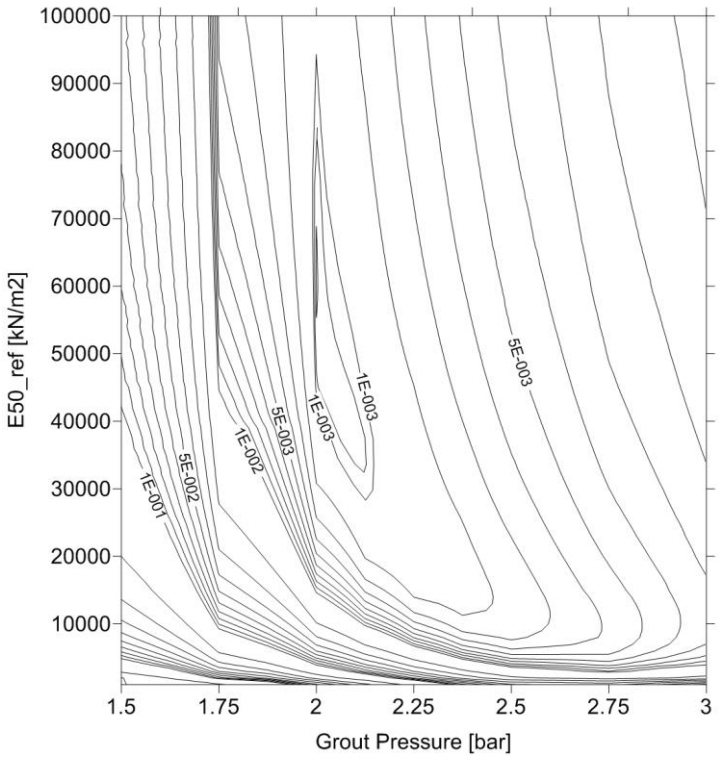

Figure A.14. Mapping of the objective function for full term behavior and sliding micrometer measurements (Grout Pressure Method).

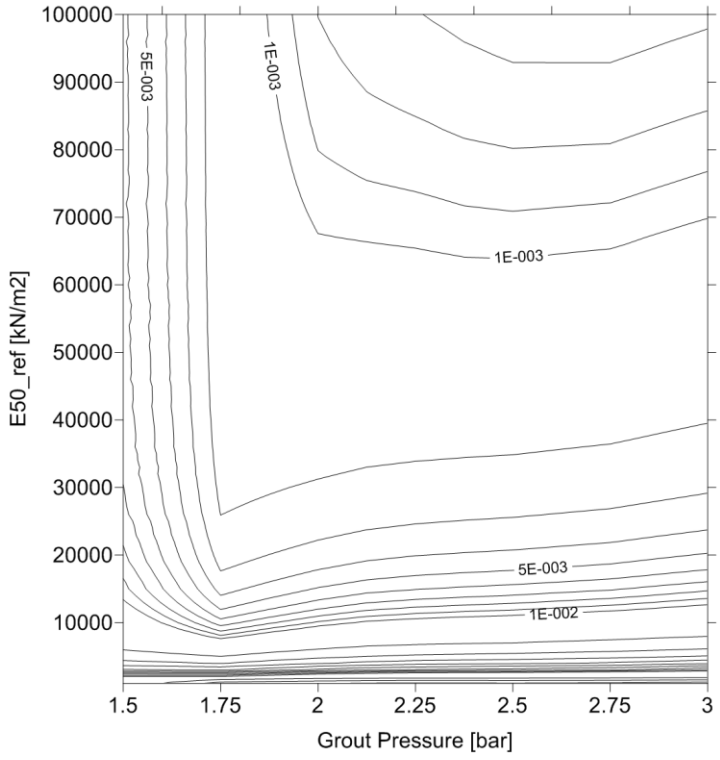

Figure A.15. Mapping of the objective function for full term behavior and inclinometer measurements (Grout Pressure Method).

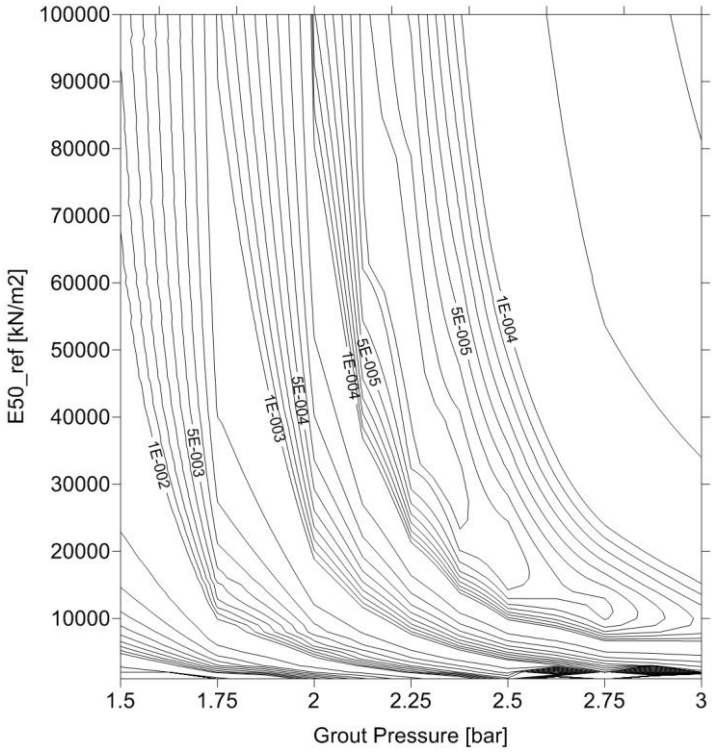

Figure A.16. Mapping of the objective function for short term behavior and surface measurements (Grout Pressure Method).

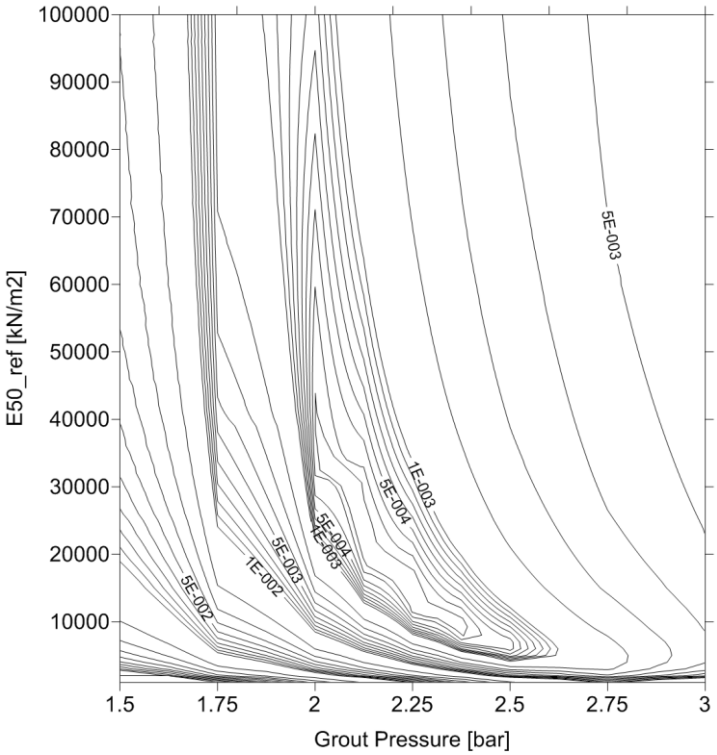

Figure A.17. Mapping of the objective function for short term behavior and sliding micrometer measurements (Grout Pressure Method).

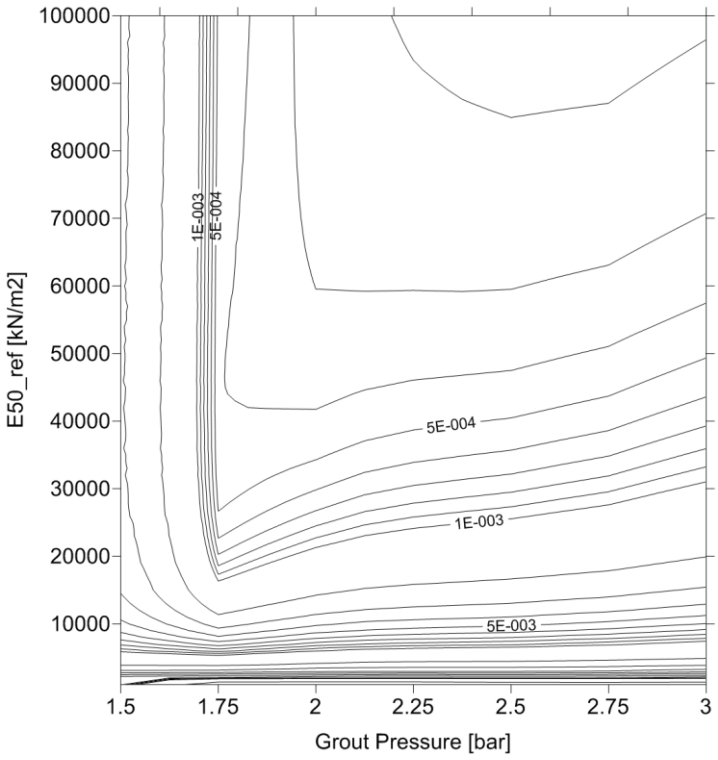

Figure A.18. Mapping of the objective function for short term behavior and inclinometer measurements (Grout Pressure Method).

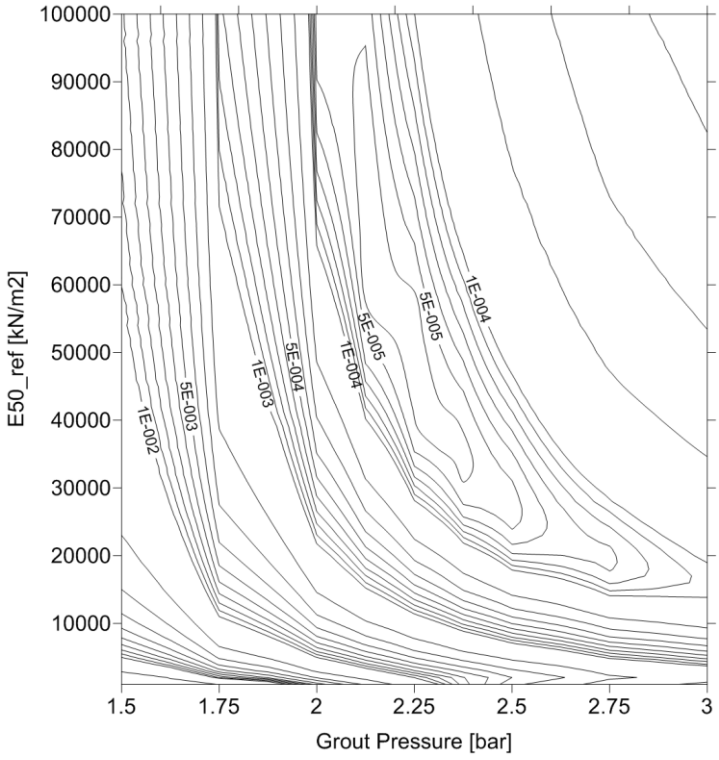

Figure A.19. Mapping of the objective function for long term behavior and surface measurements (Grout Pressure Method).

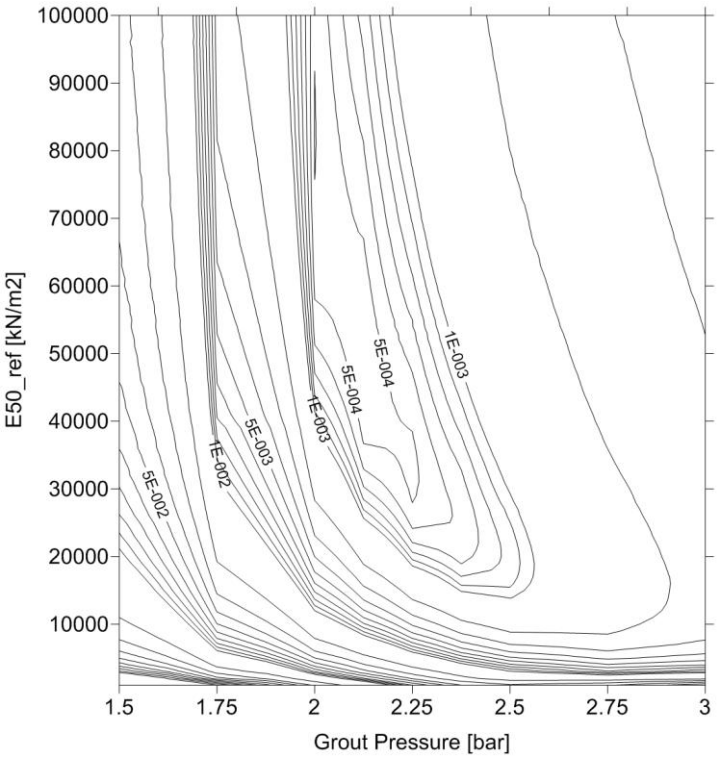

Figure A.20. Mapping of the objective function for long term behavior and sliding micrometer measurements (Grout Pressure Method).

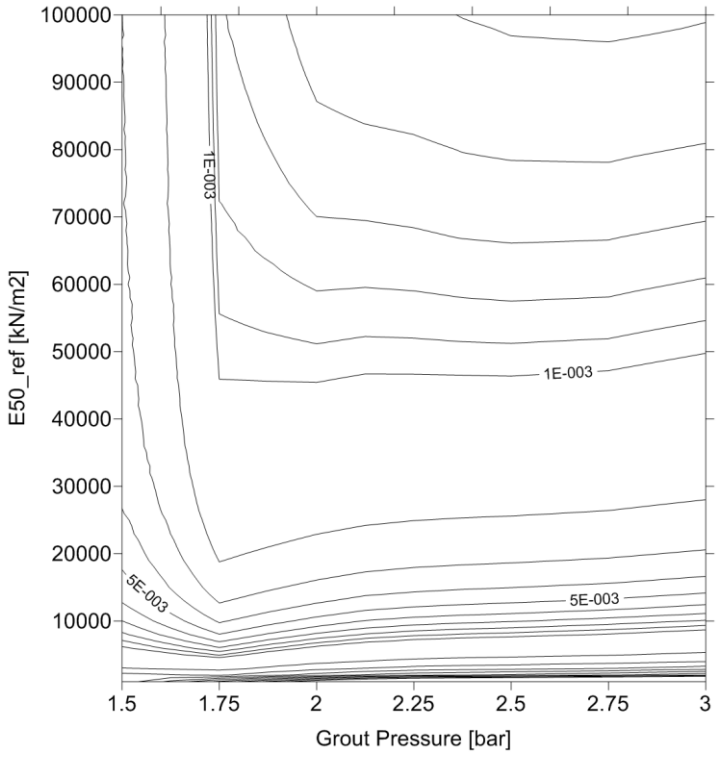

Figure A.21. Mapping of the objective function for long term behavior and inclinometer measurements (Grout Pressure Method).

Additional information of the backanalysis - Using the Instruments Error Structure

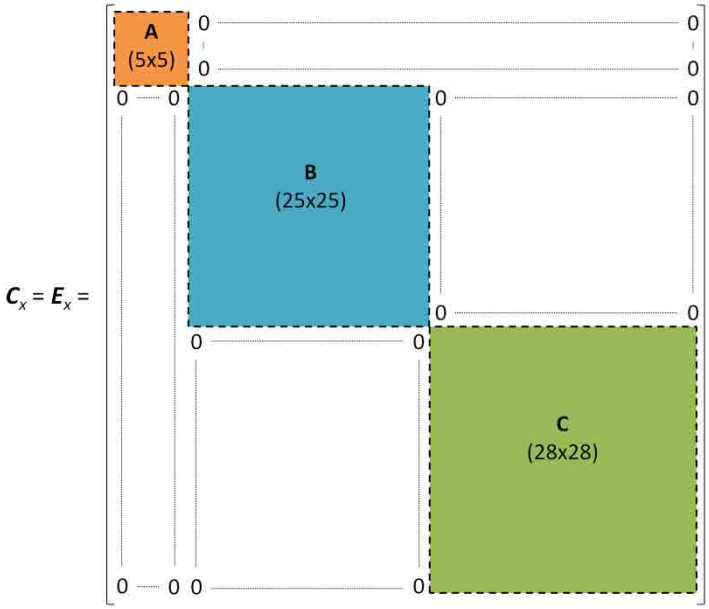

Figure A.22. "Global" Measurements Covariance Matrix. Matrix A (orange) associated with the settlements measurements. Matrix B (blue) associated with the measurements extracted from the sliding micrometer. Matrix C (green) associated with the measurements extracted from the inclinometer.

In the following equations (A1, A2 and A3), the submatrices used to define the "Global" Measurements Covariance Matrix are shown.

$$A = \begin{bmatrix} 1 & 0 & 0 & 0 & 0 \\ 0 & 1 & 0 & 0 & 0 \\ 0 & 0 & 1 & 0 & 0 \\ 0 & 0 & 0 & 1 & 0 \\ 0 & 0 & 0 & 0 & 1 \end{bmatrix} \tag{A.1}$$

$$B = \begin{bmatrix} 1 & 1 & 1 & 1 & 1 & 1 & 1 & 1 & 1 & 1 & 1 & 1 & 1 & 1 & 1 & 1 & 1 & 1 & 1 & 1 & 1 & 1 & 1 & 1 \\ 1 & 2 & 2 & 2 & 2 & 2 & 2 & 2 & 2 & 2 & 2 & 2 & 2 & 2 & 2 & 2 & 2 & 2 & 2 & 2 & 2 & 2 & 2 & 2 \\ 1 & 2 & 3 & 3 & 3 & 3 & 3 & 3 & 3 & 3 & 3 & 3 & 3 & 3 & 3 & 3 & 3 & 3 & 3 & 3 & 3 & 3 & 3 & 3 \\ 1 & 2 & 3 & 4 & 4 & 4 & 4 & 4 & 4 & 4 & 4 & 4 & 4 & 4 & 4 & 4 & 4 & 4 & 4 & 4 & 4 & 4 & 4 & 4 \\ 1 & 2 & 3 & 4 & 5 & 5 & 5 & 5 & 5 & 5 & 5 & 5 & 5 & 5 & 5 & 5 & 5 & 5 & 5 & 5 & 5 & 5 & 5 & 5 \\ 1 & 2 & 3 & 4 & 5 & 6 & 6 & 6 & 6 & 6 & 6 & 6 & 6 & 6 & 6 & 6 & 6 & 6 & 6 & 6 & 6 & 6 & 6 & 6 \\ 1 & 2 & 3 & 4 & 5 & 6 & 7 & 7 & 7 & 7 & 7 & 7 & 7 & 7 & 7 & 7 & 7 & 7 & 7 & 7 & 7 & 7 & 7 & 7 \\ 1 & 2 & 3 & 4 & 5 & 6 & 7 & 8 & 8 & 8 & 8 & 8 & 8 & 8 & 8 & 8 & 8 & 8 & 8 & 8 & 8 & 8 & 8 & 8 \\ 1 & 2 & 3 & 4 & 5 & 6 & 7 & 8 & 9 & 9 & 9 & 9 & 9 & 9 & 9 & 9 & 9 & 9 & 9 & 9 & 9 & 9 & 9 & 9 \\ 1 & 2 & 3 & 4 & 5 & 6 & 7 & 8 & 9 & 10 & 10 & 10 & 10 & 10 & 10 & 10 & 10 & 10 & 10 & 10 & 10 & 10 & 10 & 10 \\ 1 & 2 & 3 & 4 & 5 & 6 & 7 & 8 & 9 & 10 & 11 & 11 & 11 & 11 & 11 & 11 & 11 & 11 & 11 & 11 & 11 & 11 & 11 & 11 \\ 1 & 2 & 3 & 4 & 5 & 6 & 7 & 8 & 9 & 10 & 11 & 12 & 12 & 12 & 12 & 12 & 12 & 12 & 12 & 12 & 12 & 12 & 12 & 12 \\ 1 & 2 & 3 & 4 & 5 & 6 & 7 & 8 & 9 & 10 & 11 & 12 & 13 & 13 & 13 & 13 & 13 & 13 & 13 & 13 & 13 & 13 & 13 & 13 \\ 1 & 2 & 3 & 4 & 5 & 6 & 7 & 8 & 9 & 10 & 11 & 12 & 13 & 14 & 14 & 14 & 14 & 14 & 14 & 14 & 14 & 14 & 14 & 14 \\ 1 & 2 & 3 & 4 & 5 & 6 & 7 & 8 & 9 & 10 & 11 & 12 & 13 & 14 & 15 & 15 & 15 & 15 & 15 & 15 & 15 & 15 & 15 & 15 \\ 1 & 2 & 3 & 4 & 5 & 6 & 7 & 8 & 9 & 10 & 11 & 12 & 13 & 14 & 15 & 16 & 16 & 16 & 16 & 16 & 16 & 16 & 16 & 16 \\ 1 & 2 & 3 & 4 & 5 & 6 & 7 & 8 & 9 & 10 & 11 & 12 & 13 & 14 & 15 & 16 & 17 & 17 & 17 & 17 & 17 & 17 & 17 & 17 \\ 1 & 2 & 3 & 4 & 5 & 6 & 7 & 8 & 9 & 10 & 11 & 12 & 13 & 14 & 15 & 16 & 17 & 18 & 18 & 18 & 18 & 18 & 18 & 18 \\ 1 & 2 & 3 & 4 & 5 & 6 & 7 & 8 & 9 & 10 & 11 & 12 & 13 & 14 & 15 & 16 & 17 & 18 & 19 & 19 & 19 & 19 & 19 & 19 \\ 1 & 2 & 3 & 4 & 5 & 6 & 7 & 8 & 9 & 10 & 11 & 12 & 13 & 14 & 15 & 16 & 17 & 18 & 19 & 20 & 20 & 20 & 20 & 20 \\ 1 & 2 & 3 & 4 & 5 & 6 & 7 & 8 & 9 & 10 & 11 & 12 & 13 & 14 & 15 & 16 & 17 & 18 & 19 & 20 & 21 & 21 & 21 & 21 \\ 1 & 2 & 3 & 4 & 5 & 6 & 7 & 8 & 9 & 10 & 11 & 12 & 13 & 14 & 15 & 16 & 17 & 18 & 19 & 20 & 21 & 22 & 22 & 22 \\ 1 & 2 & 3 & 4 & 5 & 6 & 7 & 8 & 9 & 10 & 11 & 12 & 13 & 14 & 15 & 16 & 17 & 18 & 19 & 20 & 21 & 22 & 23 & 23 \\ 1 & 2 & 3 & 4 & 5 & 6 & 7 & 8 & 9 & 10 & 11 & 12 & 13 & 14 & 15 & 16 & 17 & 18 & 19 & 20 & 21 & 22 & 23 & 24 \\ 1 & 2 & 3 & 4 & 5 & 6 & 7 & 8 & 9 & 10 & 11 & 12 & 13 & 14 & 15 & 16 & 17 & 18 & 19 & 20 & 21 & 22 & 23 & 24 & 25 \end{bmatrix} \tag{A.2}$$

$$C = \begin{bmatrix}
1 & 1 & 1 & 1 & 1 & 1 & 1 & 1 & 1 & 1 & 1 & 1 & 1 & 1 & 1 & 1 & 1 & 1 & 1 & 1 & 1 & 1 & 1 & 1 & 1 & 1 & 1 \\
1 & 3 & 3 & 3 & 3 & 3 & 3 & 3 & 3 & 3 & 3 & 3 & 3 & 3 & 3 & 3 & 3 & 3 & 3 & 3 & 3 & 3 & 3 & 3 & 3 & 3 & 3 \\
1 & 3 & 5 & 5 & 5 & 5 & 5 & 5 & 5 & 5 & 5 & 5 & 5 & 5 & 5 & 5 & 5 & 5 & 5 & 5 & 5 & 5 & 5 & 5 & 5 & 5 & 5 \\
1 & 3 & 5 & 7 & 7 & 7 & 7 & 7 & 7 & 7 & 7 & 7 & 7 & 7 & 7 & 7 & 7 & 7 & 7 & 7 & 7 & 7 & 7 & 7 & 7 & 7 & 7 \\
1 & 3 & 5 & 7 & 9 & 9 & 9 & 9 & 9 & 9 & 9 & 9 & 9 & 9 & 9 & 9 & 9 & 9 & 9 & 9 & 9 & 9 & 9 & 9 & 9 & 9 & 9 \\
1 & 3 & 5 & 7 & 9 & 11 & 11 & 11 & 11 & 11 & 11 & 11 & 11 & 11 & 11 & 11 & 11 & 11 & 11 & 11 & 11 & 11 & 11 & 11 & 11 & 11 & 11 \\
1 & 3 & 5 & 7 & 9 & 11 & 13 & 13 & 13 & 13 & 13 & 13 & 13 & 13 & 13 & 13 & 13 & 13 & 13 & 13 & 13 & 13 & 13 & 13 & 13 & 13 & 13 \\
1 & 3 & 5 & 7 & 9 & 11 & 13 & 15 & 15 & 15 & 15 & 15 & 15 & 15 & 15 & 15 & 15 & 15 & 15 & 15 & 15 & 15 & 15 & 15 & 15 & 15 & 15 \\
1 & 3 & 5 & 7 & 9 & 11 & 13 & 15 & 17 & 17 & 17 & 17 & 17 & 17 & 17 & 17 & 17 & 17 & 17 & 17 & 17 & 17 & 17 & 17 & 17 & 17 & 17 \\
1 & 3 & 5 & 7 & 9 & 11 & 13 & 15 & 17 & 19 & 19 & 19 & 19 & 19 & 19 & 19 & 19 & 19 & 19 & 19 & 19 & 19 & 19 & 19 & 19 & 19 & 19 \\
1 & 3 & 5 & 7 & 9 & 11 & 13 & 15 & 17 & 19 & 21 & 21 & 21 & 21 & 21 & 21 & 21 & 21 & 21 & 21 & 21 & 21 & 21 & 21 & 21 & 21 & 21 \\
1 & 3 & 5 & 7 & 9 & 11 & 13 & 15 & 17 & 19 & 21 & 23 & 23 & 23 & 23 & 23 & 23 & 23 & 23 & 23 & 23 & 23 & 23 & 23 & 23 & 23 & 23 \\
1 & 3 & 5 & 7 & 9 & 11 & 13 & 15 & 17 & 19 & 21 & 23 & 25 & 25 & 25 & 25 & 25 & 25 & 25 & 25 & 25 & 25 & 25 & 25 & 25 & 25 & 25 \\
1 & 3 & 5 & 7 & 9 & 11 & 13 & 15 & 17 & 19 & 21 & 23 & 25 & 27 & 27 & 27 & 27 & 27 & 27 & 27 & 27 & 27 & 27 & 27 & 27 & 27 & 27 \\
1 & 3 & 5 & 7 & 9 & 11 & 13 & 15 & 17 & 19 & 21 & 23 & 25 & 27 & 29 & 29 & 29 & 29 & 29 & 29 & 29 & 29 & 29 & 29 & 29 & 29 & 29 \\
1 & 3 & 5 & 7 & 9 & 11 & 13 & 15 & 17 & 19 & 21 & 23 & 25 & 27 & 29 & 31 & 31 & 31 & 31 & 31 & 31 & 31 & 31 & 31 & 31 & 31 & 31 \\
1 & 3 & 5 & 7 & 9 & 11 & 13 & 15 & 17 & 19 & 21 & 23 & 25 & 27 & 29 & 31 & 33 & 33 & 33 & 33 & 33 & 33 & 33 & 33 & 33 & 33 & 33 \\
1 & 3 & 5 & 7 & 9 & 11 & 13 & 15 & 17 & 19 & 21 & 23 & 25 & 27 & 29 & 31 & 33 & 35 & 35 & 35 & 35 & 35 & 35 & 35 & 35 & 35 & 35 \\
1 & 3 & 5 & 7 & 9 & 11 & 13 & 15 & 17 & 19 & 21 & 23 & 25 & 27 & 29 & 31 & 33 & 35 & 37 & 37 & 37 & 37 & 37 & 37 & 37 & 37 & 37 \\
1 & 3 & 5 & 7 & 9 & 11 & 13 & 15 & 17 & 19 & 21 & 23 & 25 & 27 & 29 & 31 & 33 & 35 & 37 & 39 & 39 & 39 & 39 & 39 & 39 & 39 & 39 \\
1 & 3 & 5 & 7 & 9 & 11 & 13 & 15 & 17 & 19 & 21 & 23 & 25 & 27 & 29 & 31 & 33 & 35 & 37 & 39 & 41 & 41 & 41 & 41 & 41 & 41 & 41 \\
1 & 3 & 5 & 7 & 9 & 11 & 13 & 15 & 17 & 19 & 21 & 23 & 25 & 27 & 29 & 31 & 33 & 35 & 37 & 39 & 41 & 43 & 43 & 43 & 43 & 43 & 43 \\
1 & 3 & 5 & 7 & 9 & 11 & 13 & 15 & 17 & 19 & 21 & 23 & 25 & 27 & 29 & 31 & 33 & 35 & 37 & 39 & 41 & 43 & 45 & 45 & 45 & 45 & 45 \\
1 & 3 & 5 & 7 & 9 & 11 & 13 & 15 & 17 & 19 & 21 & 23 & 25 & 27 & 29 & 31 & 33 & 35 & 37 & 39 & 41 & 43 & 45 & 47 & 47 & 47 & 47 \\
1 & 3 & 5 & 7 & 9 & 11 & 13 & 15 & 17 & 19 & 21 & 23 & 25 & 27 & 29 & 31 & 33 & 35 & 37 & 39 & 41 & 43 & 45 & 47 & 49 & 49 & 49 \\
1 & 3 & 5 & 7 & 9 & 11 & 13 & 15 & 17 & 19 & 21 & 23 & 25 & 27 & 29 & 31 & 33 & 35 & 37 & 39 & 41 & 43 & 45 & 47 & 49 & 51 & 51 \\
1 & 3 & 5 & 7 & 9 & 11 & 13 & 15 & 17 & 19 & 21 & 23 & 25 & 27 & 29 & 31 & 33 & 35 & 37 & 39 & 41 & 43 & 45 & 47 & 49 & 51 & 53 \\
1 & 3 & 5 & 7 & 9 & 11 & 13 & 15 & 17 & 19 & 21 & 23 & 25 & 27 & 29 & 31 & 33 & 35 & 37 & 39 & 41 & 43 & 45 & 47 & 49 & 51 & 55
\end{bmatrix} \quad \text{(A.3)}$$

$C_x^{-1} = E_x^{-1} =$

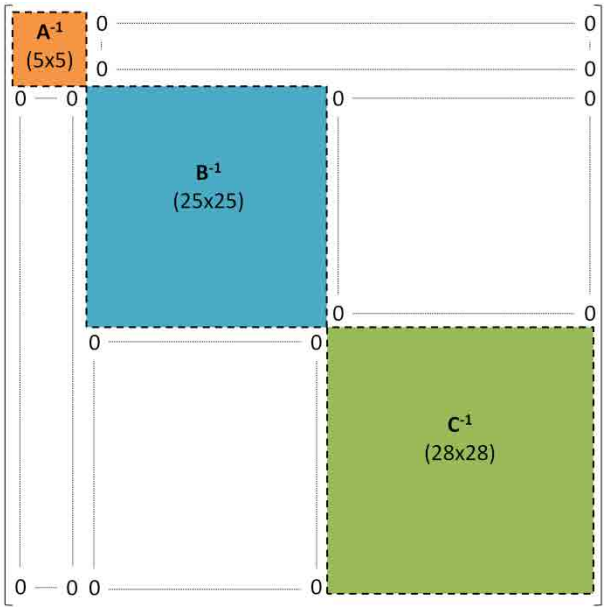

Figure A.23. Invert "Global" Measurements Covariance Matrix. Matrix A^{-1} (orange) associated with the settlements measurements. Matrix B^{-1} (blue) associated with the measurements extracted from the sliding micrometer. Matrix C^{-1} (green) associated with the measurements extracted from the inclinometer.

In the following equations (A4, A5 and A5), the submatrices used to define the Invert "Global" Measurements Covariance Matrix are shown.

$$A^{-1} = \begin{bmatrix} 1 & 0 & 0 & 0 & 0 \\ 0 & 1 & 0 & 0 & 0 \\ 0 & 0 & 1 & 0 & 0 \\ 0 & 0 & 0 & 1 & 0 \\ 0 & 0 & 0 & 0 & 1 \end{bmatrix} \quad \text{(A.4)}$$

$$B^{-1} = \begin{bmatrix}
2 & -1 & 0 & 0 & 0 & 0 & 0 & 0 & 0 & 0 & 0 & 0 & 0 & 0 & 0 & 0 & 0 & 0 & 0 & 0 & 0 & 0 & 0 & 0 \\
-1 & 2 & -1 & 0 & 0 & 0 & 0 & 0 & 0 & 0 & 0 & 0 & 0 & 0 & 0 & 0 & 0 & 0 & 0 & 0 & 0 & 0 & 0 & 0 \\
0 & -1 & 2 & -1 & 0 & 0 & 0 & 0 & 0 & 0 & 0 & 0 & 0 & 0 & 0 & 0 & 0 & 0 & 0 & 0 & 0 & 0 & 0 & 0 \\
0 & 0 & -1 & 2 & -1 & 0 & 0 & 0 & 0 & 0 & 0 & 0 & 0 & 0 & 0 & 0 & 0 & 0 & 0 & 0 & 0 & 0 & 0 & 0 \\
0 & 0 & 0 & -1 & 2 & -1 & 0 & 0 & 0 & 0 & 0 & 0 & 0 & 0 & 0 & 0 & 0 & 0 & 0 & 0 & 0 & 0 & 0 & 0 \\
0 & 0 & 0 & 0 & -1 & 2 & -1 & 0 & 0 & 0 & 0 & 0 & 0 & 0 & 0 & 0 & 0 & 0 & 0 & 0 & 0 & 0 & 0 & 0 \\
0 & 0 & 0 & 0 & 0 & -1 & 2 & -1 & 0 & 0 & 0 & 0 & 0 & 0 & 0 & 0 & 0 & 0 & 0 & 0 & 0 & 0 & 0 & 0 \\
0 & 0 & 0 & 0 & 0 & 0 & -1 & 2 & -1 & 0 & 0 & 0 & 0 & 0 & 0 & 0 & 0 & 0 & 0 & 0 & 0 & 0 & 0 & 0 \\
0 & 0 & 0 & 0 & 0 & 0 & 0 & -1 & 2 & -1 & 0 & 0 & 0 & 0 & 0 & 0 & 0 & 0 & 0 & 0 & 0 & 0 & 0 & 0 \\
0 & 0 & 0 & 0 & 0 & 0 & 0 & 0 & -1 & 2 & -1 & 0 & 0 & 0 & 0 & 0 & 0 & 0 & 0 & 0 & 0 & 0 & 0 & 0 \\
0 & 0 & 0 & 0 & 0 & 0 & 0 & 0 & 0 & -1 & 2 & -1 & 0 & 0 & 0 & 0 & 0 & 0 & 0 & 0 & 0 & 0 & 0 & 0 \\
0 & 0 & 0 & 0 & 0 & 0 & 0 & 0 & 0 & 0 & -1 & 2 & -1 & 0 & 0 & 0 & 0 & 0 & 0 & 0 & 0 & 0 & 0 & 0 \\
0 & 0 & 0 & 0 & 0 & 0 & 0 & 0 & 0 & 0 & 0 & -1 & 2 & -1 & 0 & 0 & 0 & 0 & 0 & 0 & 0 & 0 & 0 & 0 \\
0 & 0 & 0 & 0 & 0 & 0 & 0 & 0 & 0 & 0 & 0 & 0 & -1 & 2 & -1 & 0 & 0 & 0 & 0 & 0 & 0 & 0 & 0 & 0 \\
0 & 0 & 0 & 0 & 0 & 0 & 0 & 0 & 0 & 0 & 0 & 0 & 0 & -1 & 2 & -1 & 0 & 0 & 0 & 0 & 0 & 0 & 0 & 0 \\
0 & 0 & 0 & 0 & 0 & 0 & 0 & 0 & 0 & 0 & 0 & 0 & 0 & 0 & -1 & 2 & -1 & 0 & 0 & 0 & 0 & 0 & 0 & 0 \\
0 & 0 & 0 & 0 & 0 & 0 & 0 & 0 & 0 & 0 & 0 & 0 & 0 & 0 & 0 & -1 & 2 & -1 & 0 & 0 & 0 & 0 & 0 & 0 \\
0 & 0 & 0 & 0 & 0 & 0 & 0 & 0 & 0 & 0 & 0 & 0 & 0 & 0 & 0 & 0 & -1 & 2 & -1 & 0 & 0 & 0 & 0 & 0 \\
0 & 0 & 0 & 0 & 0 & 0 & 0 & 0 & 0 & 0 & 0 & 0 & 0 & 0 & 0 & 0 & 0 & -1 & 2 & -1 & 0 & 0 & 0 & 0 \\
0 & 0 & 0 & 0 & 0 & 0 & 0 & 0 & 0 & 0 & 0 & 0 & 0 & 0 & 0 & 0 & 0 & 0 & -1 & 2 & -1 & 0 & 0 & 0 \\
0 & 0 & 0 & 0 & 0 & 0 & 0 & 0 & 0 & 0 & 0 & 0 & 0 & 0 & 0 & 0 & 0 & 0 & 0 & -1 & 2 & -1 & 0 & 0 \\
0 & 0 & 0 & 0 & 0 & 0 & 0 & 0 & 0 & 0 & 0 & 0 & 0 & 0 & 0 & 0 & 0 & 0 & 0 & 0 & -1 & 2 & -1 & 0 \\
0 & 0 & 0 & 0 & 0 & 0 & 0 & 0 & 0 & 0 & 0 & 0 & 0 & 0 & 0 & 0 & 0 & 0 & 0 & 0 & 0 & -1 & 2 & -1 \\
0 & 0 & 0 & 0 & 0 & 0 & 0 & 0 & 0 & 0 & 0 & 0 & 0 & 0 & 0 & 0 & 0 & 0 & 0 & 0 & 0 & 0 & -1 & 1
\end{bmatrix} \tag{A.5}$$

$$C^{-1} = \begin{bmatrix}
1.5 & -0.5 & 0 & 0 & 0 & 0 & 0 & 0 & 0 & 0 & 0 & 0 & 0 & 0 & 0 & 0 & 0 & 0 & 0 & 0 & 0 & 0 & 0 & 0 & 0 & 0 & 0 & 0 \\
-0.5 & 1 & -0.5 & 0 & 0 & 0 & 0 & 0 & 0 & 0 & 0 & 0 & 0 & 0 & 0 & 0 & 0 & 0 & 0 & 0 & 0 & 0 & 0 & 0 & 0 & 0 & 0 & 0 \\
0 & -0.5 & 1 & -0.5 & 0 & 0 & 0 & 0 & 0 & 0 & 0 & 0 & 0 & 0 & 0 & 0 & 0 & 0 & 0 & 0 & 0 & 0 & 0 & 0 & 0 & 0 & 0 & 0 \\
0 & 0 & -0.5 & 1 & -0.5 & 0 & 0 & 0 & 0 & 0 & 0 & 0 & 0 & 0 & 0 & 0 & 0 & 0 & 0 & 0 & 0 & 0 & 0 & 0 & 0 & 0 & 0 & 0 \\
0 & 0 & 0 & -0.5 & 1 & -0.5 & 0 & 0 & 0 & 0 & 0 & 0 & 0 & 0 & 0 & 0 & 0 & 0 & 0 & 0 & 0 & 0 & 0 & 0 & 0 & 0 & 0 & 0 \\
0 & 0 & 0 & 0 & -0.5 & 1 & -0.5 & 0 & 0 & 0 & 0 & 0 & 0 & 0 & 0 & 0 & 0 & 0 & 0 & 0 & 0 & 0 & 0 & 0 & 0 & 0 & 0 & 0 \\
0 & 0 & 0 & 0 & 0 & -0.5 & 1 & -0.5 & 0 & 0 & 0 & 0 & 0 & 0 & 0 & 0 & 0 & 0 & 0 & 0 & 0 & 0 & 0 & 0 & 0 & 0 & 0 & 0 \\
0 & 0 & 0 & 0 & 0 & 0 & -0.5 & 1 & -0.5 & 0 & 0 & 0 & 0 & 0 & 0 & 0 & 0 & 0 & 0 & 0 & 0 & 0 & 0 & 0 & 0 & 0 & 0 & 0 \\
0 & 0 & 0 & 0 & 0 & 0 & 0 & -0.5 & 1 & -0.5 & 0 & 0 & 0 & 0 & 0 & 0 & 0 & 0 & 0 & 0 & 0 & 0 & 0 & 0 & 0 & 0 & 0 & 0 \\
0 & 0 & 0 & 0 & 0 & 0 & 0 & 0 & -0.5 & 1 & -0.5 & 0 & 0 & 0 & 0 & 0 & 0 & 0 & 0 & 0 & 0 & 0 & 0 & 0 & 0 & 0 & 0 & 0 \\
0 & 0 & 0 & 0 & 0 & 0 & 0 & 0 & 0 & -0.5 & 1 & -0.5 & 0 & 0 & 0 & 0 & 0 & 0 & 0 & 0 & 0 & 0 & 0 & 0 & 0 & 0 & 0 & 0 \\
0 & 0 & 0 & 0 & 0 & 0 & 0 & 0 & 0 & 0 & -0.5 & 1 & -0.5 & 0 & 0 & 0 & 0 & 0 & 0 & 0 & 0 & 0 & 0 & 0 & 0 & 0 & 0 & 0 \\
0 & 0 & 0 & 0 & 0 & 0 & 0 & 0 & 0 & 0 & 0 & -0.5 & 1 & -0.5 & 0 & 0 & 0 & 0 & 0 & 0 & 0 & 0 & 0 & 0 & 0 & 0 & 0 & 0 \\
0 & 0 & 0 & 0 & 0 & 0 & 0 & 0 & 0 & 0 & 0 & 0 & -0.5 & 1 & -0.5 & 0 & 0 & 0 & 0 & 0 & 0 & 0 & 0 & 0 & 0 & 0 & 0 & 0 \\
0 & 0 & 0 & 0 & 0 & 0 & 0 & 0 & 0 & 0 & 0 & 0 & 0 & -0.5 & 1 & -0.5 & 0 & 0 & 0 & 0 & 0 & 0 & 0 & 0 & 0 & 0 & 0 & 0 \\
0 & 0 & 0 & 0 & 0 & 0 & 0 & 0 & 0 & 0 & 0 & 0 & 0 & 0 & -0.5 & 1 & -0.5 & 0 & 0 & 0 & 0 & 0 & 0 & 0 & 0 & 0 & 0 & 0 \\
0 & 0 & 0 & 0 & 0 & 0 & 0 & 0 & 0 & 0 & 0 & 0 & 0 & 0 & 0 & -0.5 & 1 & -0.5 & 0 & 0 & 0 & 0 & 0 & 0 & 0 & 0 & 0 & 0 \\
0 & 0 & 0 & 0 & 0 & 0 & 0 & 0 & 0 & 0 & 0 & 0 & 0 & 0 & 0 & 0 & -0.5 & 1 & -0.5 & 0 & 0 & 0 & 0 & 0 & 0 & 0 & 0 & 0 \\
0 & 0 & 0 & 0 & 0 & 0 & 0 & 0 & 0 & 0 & 0 & 0 & 0 & 0 & 0 & 0 & 0 & -0.5 & 1 & -0.5 & 0 & 0 & 0 & 0 & 0 & 0 & 0 & 0 \\
0 & 0 & 0 & 0 & 0 & 0 & 0 & 0 & 0 & 0 & 0 & 0 & 0 & 0 & 0 & 0 & 0 & 0 & -0.5 & 1 & -0.5 & 0 & 0 & 0 & 0 & 0 & 0 & 0 \\
0 & 0 & 0 & 0 & 0 & 0 & 0 & 0 & 0 & 0 & 0 & 0 & 0 & 0 & 0 & 0 & 0 & 0 & 0 & -0.5 & 1 & -0.5 & 0 & 0 & 0 & 0 & 0 & 0 \\
0 & 0 & 0 & 0 & 0 & 0 & 0 & 0 & 0 & 0 & 0 & 0 & 0 & 0 & 0 & 0 & 0 & 0 & 0 & 0 & -0.5 & 1 & -0.5 & 0 & 0 & 0 & 0 & 0 \\
0 & 0 & 0 & 0 & 0 & 0 & 0 & 0 & 0 & 0 & 0 & 0 & 0 & 0 & 0 & 0 & 0 & 0 & 0 & 0 & 0 & -0.5 & 1 & -0.5 & 0 & 0 & 0 & 0 \\
0 & 0 & 0 & 0 & 0 & 0 & 0 & 0 & 0 & 0 & 0 & 0 & 0 & 0 & 0 & 0 & 0 & 0 & 0 & 0 & 0 & 0 & -0.5 & 1 & -0.5 & 0 & 0 & 0 \\
0 & 0 & 0 & 0 & 0 & 0 & 0 & 0 & 0 & 0 & 0 & 0 & 0 & 0 & 0 & 0 & 0 & 0 & 0 & 0 & 0 & 0 & 0 & -0.5 & 1 & -0.5 & 0 & 0 \\
0 & 0 & 0 & 0 & 0 & 0 & 0 & 0 & 0 & 0 & 0 & 0 & 0 & 0 & 0 & 0 & 0 & 0 & 0 & 0 & 0 & 0 & 0 & 0 & -0.5 & 1 & -0.5 & 0 \\
0 & 0 & 0 & 0 & 0 & 0 & 0 & 0 & 0 & 0 & 0 & 0 & 0 & 0 & 0 & 0 & 0 & 0 & 0 & 0 & 0 & 0 & 0 & 0 & 0 & -0.5 & 1 & -0.5 \\
0 & 0 & 0 & 0 & 0 & 0 & 0 & 0 & 0 & 0 & 0 & 0 & 0 & 0 & 0 & 0 & 0 & 0 & 0 & 0 & 0 & 0 & 0 & 0 & 0 & 0 & -0.5 & 0.5
\end{bmatrix} \quad \text{(A.6)}$$

Additional results of the backanalysis - Using the Instruments Error Structure

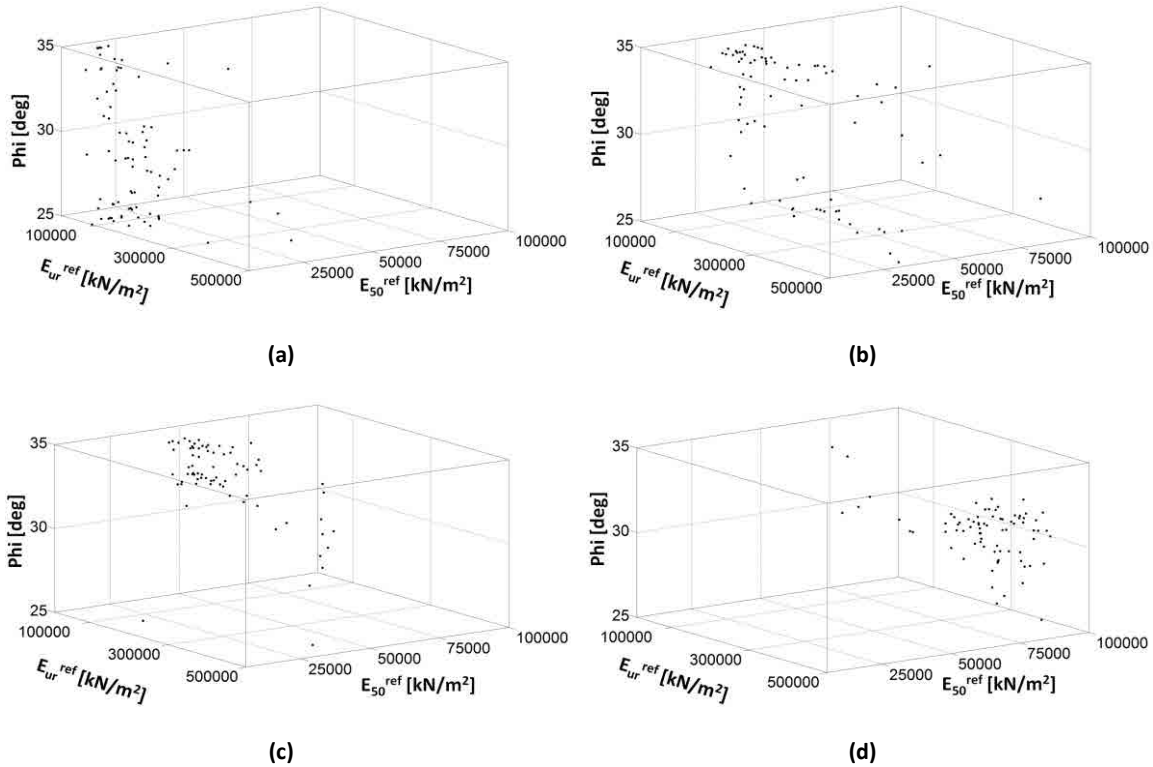

Figure A.24. Final Population after 20 consecutive generations. (a) ΣMStage=0.150. (b) ΣMStage=0.200. (c) ΣMStage=0.225. (d) ΣMStage=0.250. (Using simultaneously both short and long term measurements with the instruments error structure).

ΣMStage	E_{50}^{ref} [kN/m^2]	E_{ur}^{ref} [kN/m^2]	φ [deg]	Error [-]
0.150	13000	47500	35	$5.59 \cdot 10^{-5}$
0.200	25000	95000	35	$5.66 \cdot 10^{-5}$
0.225	36000	142500	35	$5.61 \cdot 10^{-5}$
0.250	52000	180000	35	$5.69 \cdot 10^{-5}$

Table A.1. Best individual for each value of ΣMStage after 20 generations. The error represents the objective function value using simultaneously short and long term measurements with the instruments error structure.

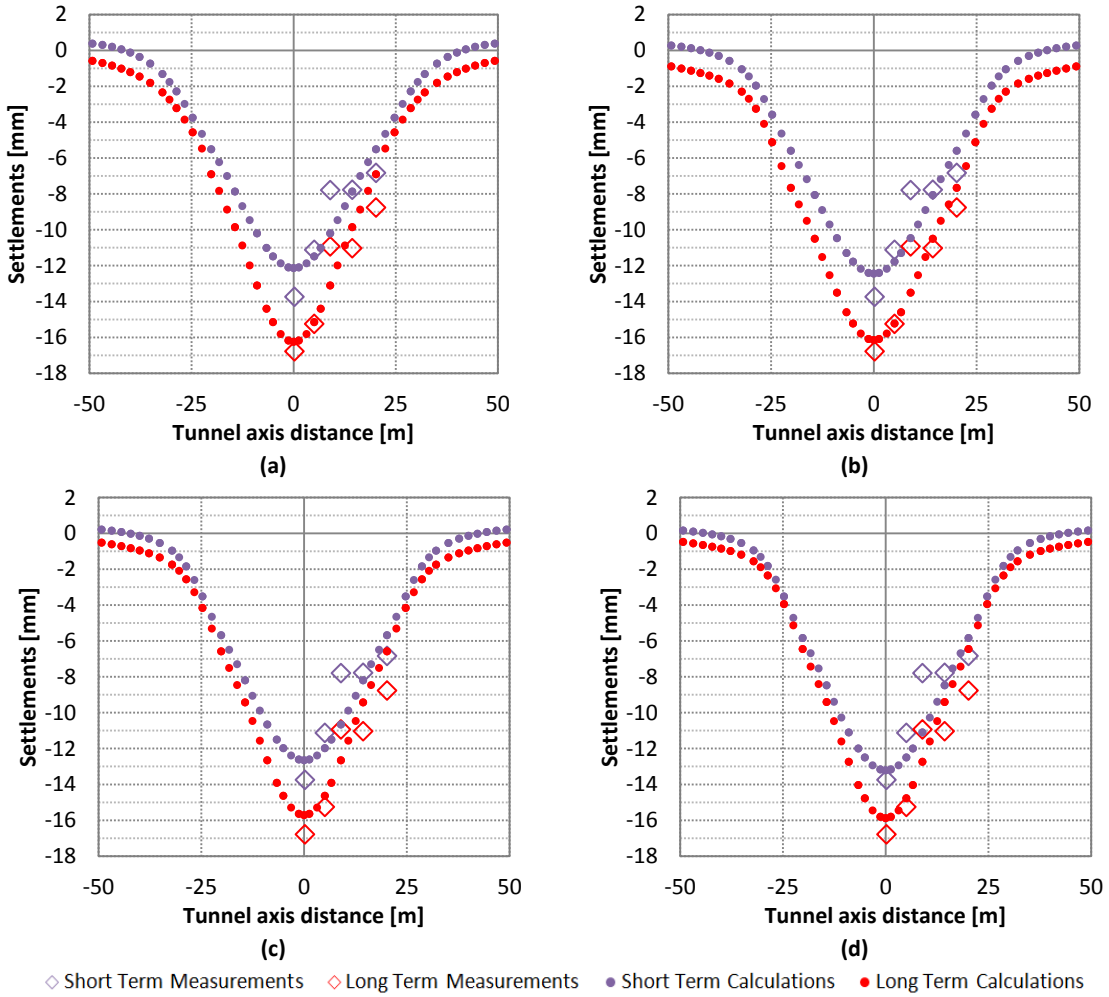

Figure A.25. Comparison between measured and calculated settlements. (a) ΣMStage=0.150. (b) ΣMStage=0.200. (c) ΣMStage=0.225. (d) ΣMStage=0.250. (Using simultaneously short and long term measurements with the instruments error structure)

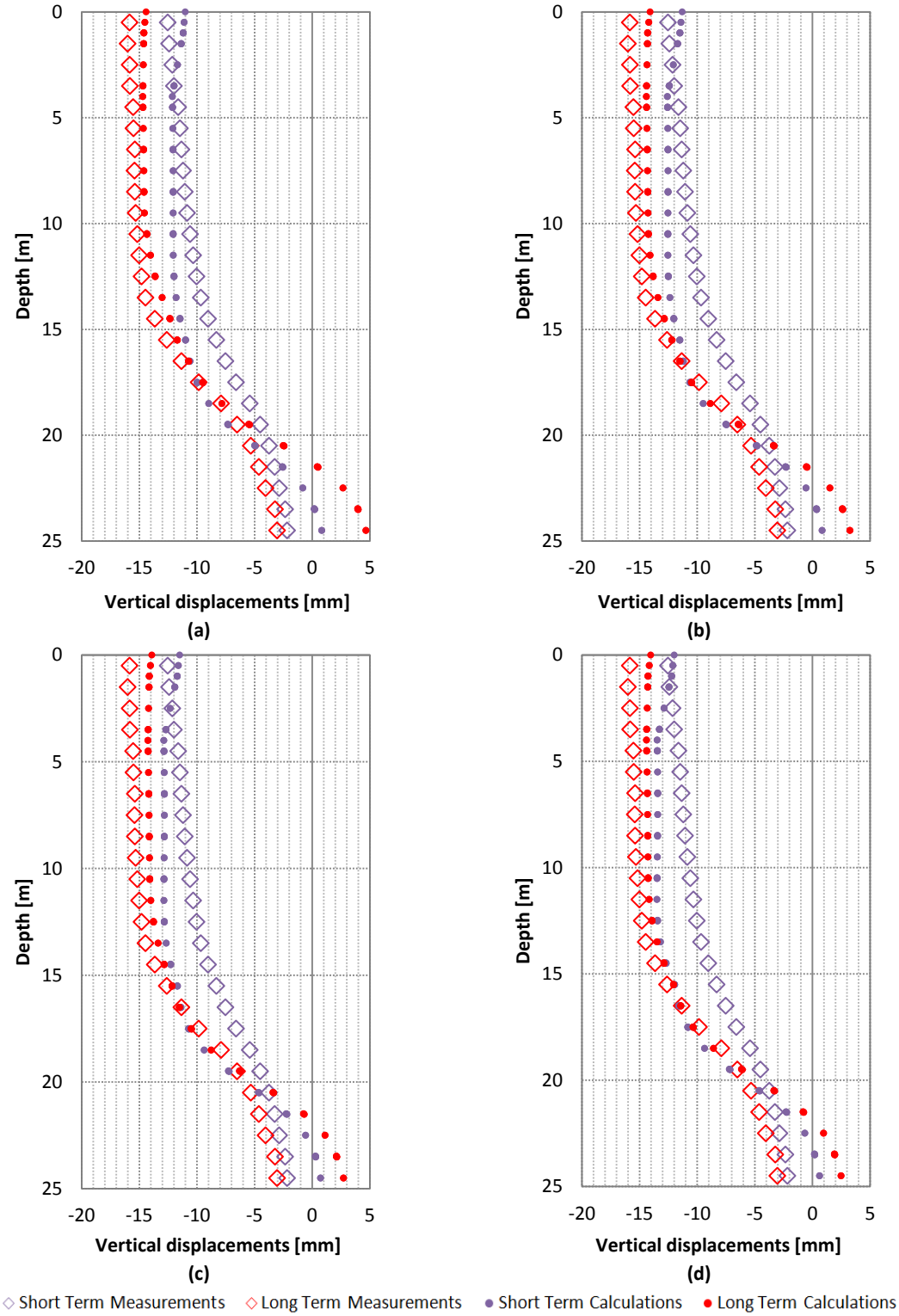

Figure A.26. Comparison between measured and calculated vertical displacements (Sliding Micrometer). (a) ΣMStage=0.150. (b) ΣMStage=0.200. (c) ΣMStage=0.225. (d) ΣMStage=0.250. (Using simultaneously short and long term measurements with the instruments error structure).

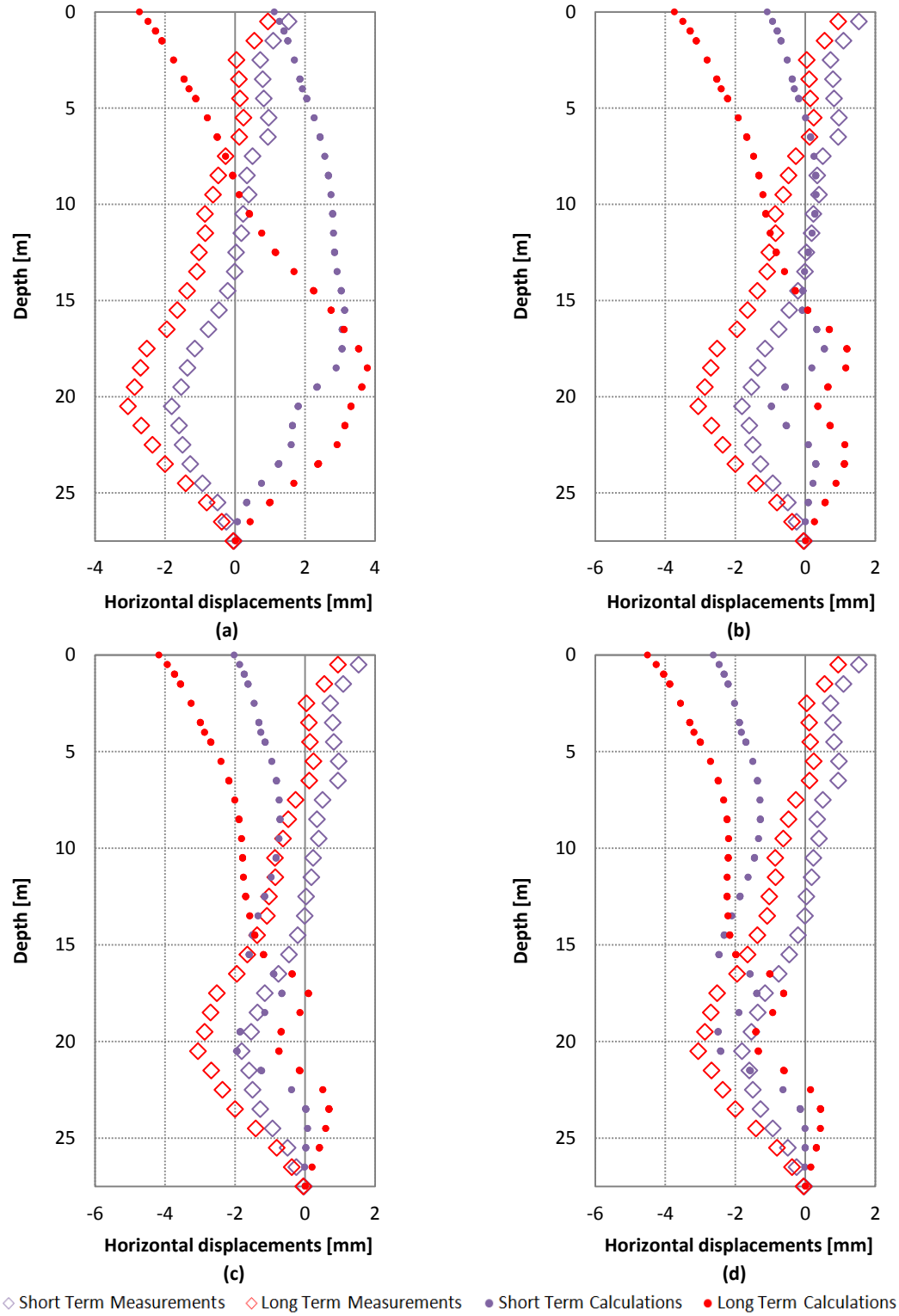

Figure A.27. Comparison between measured and calculated horizontal displacements (Inclinometer). (a) ΣMStage=0.150. (b) ΣMStage=0.200. (c) ΣMStage=0.225. (d) ΣMStage=0.250. (Using simultaneously short and long term measurements with the instruments error structure).